

A ONE-DIMENSIONAL QUANTUM INTERFACE BETWEEN
A FEW ATOMS AND WEAK LIGHT

JEAN-BAPTISTE SYLVAIN BÉGUIN



Ph. D. Thesis

Danish Center for Quantum Optics ([QUANTOP](#))

Niels Bohr Institute ([NBI](#))

Faculty of Science

University of Copenhagen ([UCHP](#)), Denmark

Principal supervisor: Prof. Eugene S. Polzik

Additional supervisors: Assoc. Prof. Jürgen Appel, Assoc. Prof. Jörg H. Müller

This Ph.D. Thesis has been submitted to the Ph.D. School of Science at [UCHP](#).

Ph. D Committee

External experts:

Prof. Vladan Vuletić (MIT-Harvard, Cambridge)

Prof. Leticia Tarruell (ICFO, Barcelona)

Local Head: Prof. Per Hedegård (NBI, Copenhagen)

Submission date: April 16, 2015

Defence date: May 15, 2015

Jean-Baptiste Sylvain Béguin : © 2015

The scientist does not study nature because it is useful; he studies it because he delights in it, and he delights in it because it is beautiful.

— Henri Poincaré

ABSTRACT

Quantum interfaces between light and the collective degrees of freedom of an ensemble of identical atoms have been proposed as a valuable and promising alternative to cavity quantum electrodynamics enhanced interaction with single particles, [Hammerer et al. \(2010\)](#). Many features of the quantum world (e. g. multipartite entanglement, squeezed states), which are central to the future developments of Quantum Information Science and Metrology, can be explored with mesoscopic collective states of atoms.

An efficient quantum interface needs a high optical depth for the atomic ensemble and a measurement sensitivity limited by both the intrinsic quantum noise of light and the quantum projection noise of atoms. This was achieved in the past in a free space optical dipole trap ensemble of $N_{\text{at}} \sim 10^6$ atoms, which triggered the operation of a collective Ramsey atomic clock assisted by entanglement [Appel et al. \(2009b\)](#); [Louchet-Chauvet et al. \(2010\)](#). We have characterized and prepared non-classical collective spin-squeezed states of atoms in this setup, with optical quantum non demolition measurement, [Kiesel et al. \(2012\)](#). We then pursued the goal of generating other non-classical collective states of atoms with non-gaussian statistics, conditioned on discrete heralding optical measurement, [Christensen et al. \(2014\)](#).

In the main part of this thesis, we propose an alternative to free space atomic ensembles to prepare quantum collective states. We build and explore a new interface based on the degrees of freedom between the evanescent fields of an optical nanofiber and fewer atoms $N_{\text{at}} \sim 10^3$. We experimentally show an improvement of more than 2 orders of magnitude in the single-atom coupling strength and we demonstrate a simple method to implement an optical non-destructive measurement of the atomic state populations, which allowed to achieve -14 dB atom number squeezing, in an one-dimensional optical nanofiber lattice trap, [Béguin et al. \(2014\)](#). This shows the ability to explore spin-squeezing and quantum state tomography of non-classical states with negative Wigner functions, using a nanofiber. Finally, we report preliminary observations of collective atomic Bragg scattering in this extreme one-dimensional geometry, in view to realize a switchable atomic mirror, [Chang et al. \(2012\)](#).

RÉSUMÉ

L'intrication et l'interaction collective d'un grand nombre d'atomes identiques avec un champ lumineux cohérent représente une alternative à l'Électrodynamique Quantique en cavité avec des particules uniques, [Hammerer et al. \(2010\)](#). La préparation d'un ensemble d'atomes dans un état de spin collectif, dont les fluctuations quantiques sont comprimées par rapport à celle d'un ensemble non corrélé d'atomes, est un but reconnu et central en métrologie quantique mais aussi pour le traitement de l'information quantique.

La réalisation d'une telle interface quantique collective nécessite une grande section efficace de diffusion entre la lumière et l'ensemble atomique ainsi qu'une précision de mesure limitée en temps réel par le bruit quantique de la lumière et le bruit quantique des atomes. Ce challenge a été réalisé dans des ensembles d'atomes froids, $N_{\text{at}} \sim 10^6$, piégés par les forces optiques de faisceaux laser gaussiens en champ libre. Cela a permis la réalisation d'horloges atomiques de type Ramsey basées sur la manipulation de la cohérence collective de superpositions d'états atomiques, dont la précision dépasse la limite du bruit quantique standard grâce à l'introduction de corrélations non classiques entre les atomes via des mesures optiques non destructives opérées sur l'ensemble des états atomiques [Appel et al. \(2009b\)](#); [Louchet-Chauvet et al. \(2010\)](#). Nous avons préparé et étudié ces états collectifs, [Kiesel et al. \(2012\)](#) et nous avons cherché à réaliser des expériences d'interférométrie quantique entre une onde de spins et un état d'excitation atomique collectif délocalisé, [Christensen et al. \(2014\)](#).

Dans cette thèse, nous proposons une alternative aux ensembles d'atomes préparés en champ libre, basée sur l'interaction entre un plus petit nombre d'atomes, $N_{\text{at}} \sim 10^3$, et les champs évanescents de la lumière se propageant dans une nano-fibre optique. Nous démontrons une amélioration de plus de deux ordres de grandeur dans le couplage entre la lumière et un atome, ainsi qu'une méthode simple pour réaliser la mesure non destructive des états atomiques dont la haute précision permet une réduction d'incertitude de -14 dB sur le nombre d'atomes par rapport à celle sur un nombre aléatoire, piégé dans un réseau optique unidimensionnel, [Béguin et al. \(2014\)](#). Ces résultats montrent la possibilité de réaliser des corrélations quantiques ainsi que la tomographie quantique d'états non classiques présentant une fonction de Wigner négative, en utilisant une nano-fibre optique comme intermédiaire. Enfin, nous reportons des observations préliminaires d'un phénomène de diffusion de la lumière analogue à la diffraction de Bragg dans un ensemble d'atomes piégés autour d'une fibre optique qui permettrait la réalisation d'un miroir atomique pour la lumière, [Chang et al. \(2012\)](#).

RESUMÉ

En kvantemekanisk grænseflade mellem lys og de kollektive frihedsgrader givet ved et ensemble af identiske atomer er blevet foreslået som et lovende alternativ til kavitet-kvante-elektrodynamik som et middel til at øge vekselvirkningen med enkelte atomare partikler [Hammerer et al. \(2010\)](#). Således kan adskillige kvantemekaniske fænomener, f.eks. sammenfiltrering mellem mange partikler og klemte tilstande (eng. henholdsvis entanglement og squeezed states) udforskes ved brug af kollektive tilstande i et mesoskopisk atomart ensemble. Dette er afgørende for den videre udvikling af kvanteinformations videnskab og metrologi.

For at opnå en effektiv kvantemekanisk grænseflade er det nødvendigt både at have en høj optisk dybde af det atomare ensemble samt en målings-sensitivitet der kun er begrænset af kvantestøjen fra henholdsvis lyset (haglstøj) og atomerne (projektionsstøj). Dette er tidligere blevet opnået i et ensemble bestående af $N_{\text{at}} \sim 10^6$ atomer fastholdt i en fritsvævende optisk dipolfælde hvilket gav anledning til udviklingen af et kollektivt Ramsey atomur assisteret af sammenfiltrering mellem atomerne [Appel et al. \(2009b\)](#); [Louchet-Chauvet et al. \(2010\)](#). Vi har karakteriseret og skabt ikke-klassiske kollektive spinklemte atomare tilstande i denne opstilling via optiske kvantebevarende målinger (eng. quantum non-demolition measurements) [Kiesel et al. \(2012\)](#). Efterfølgende forfulgte vi målet om at skabe andre ikke-klassiske kollektive atomare tilstande udvisende ikke-Gaussisk statistik skabt via en varsling fra en diskret optisk måling [Christensen et al. \(2014\)](#).

Størstedelen af denne afhandling består af et forslag til en alternativ opstilling fra hvilken der ligeledes kan skabes kollektive kvantetilstande. Vi har opbygget og udforsket en ny grænseflade baseret påfrihedsgraderne fra et optisk nærfelt (eng. evanescent field) omkring en såkaldt optisk nanofiber og fåatomer $N_{\text{at}} \sim 10^3$. Vi vil her gennemgå en eksperimentel måling der viser en forøgelse af enkelt-atomkoblingsstyrken på mere end to størrelsesordener. Derefter demonstrerer vi en simpel metode hvormed en optisk ikke-destruktiv måling af populationerne af de atomare tilstande kan udføres og fra hvilken en -14 dB reduktion på usikkerheden af antallet af atomer fastholdt i en 1D gitterfælde omkring den optiske nanofiber blev opnået [Béguin et al. \(2014\)](#). Dette viser bl.a. muligheden for, ved hjælp af en nanofiber, at udforske spinklemte tilstande og udføre kvantemekanisk tilstandstomografi af ikke-klassiske tilstande udvisende negative Wigner funktioner. Endelig afrapporterer vi de første observationer af kollektiv Bragg spredning fra atomer siddende in denne ekstreme en-dimensionelle struktur i forsøget på at realisere en atomkontakt - et tnd/sluk atomspejl [Chang et al. \(2012\)](#).

PUBLICATIONS

(Physical Review Letter Editors' choice, highlighted in Physics.)

J.-B. Béguin, E. M. Bookjans, S. L. Christensen, H. L. Sørensen, J. H. Müller, E. S. Polzik, and J. Appel. Generation and detection of a sub-poissonian atom number distribution in a one-dimensional optical lattice. *Phys. Rev. Lett.*, 113:263603, Dec 2014. doi: 10.1103/PhysRevLett.113.263603. URL <http://link.aps.org/doi/10.1103/PhysRevLett.113.263603>

S. L. Christensen, J.-B. Béguin, E. Bookjans, H. L. Sørensen, J. H. Müller, J. Appel, and E. S. Polzik. Quantum interference of a single spin excitation with a macroscopic atomic ensemble. *Phys. Rev. A*, 89:033801, Mar 2014. doi: 10.1103/PhysRevA.89.033801. URL <http://link.aps.org/doi/10.1103/PhysRevA.89.033801>

S. L. Christensen, J.-B. Béguin, H. L. Sørensen, E. Bookjans, D. Oblak, J. H. Müller, J. Appel, and E. S. Polzik. Toward quantum state tomography of a single polariton state of an atomic ensemble. *New Journal of Physics*, 15(1):015002, 2013. URL <http://stacks.iop.org/1367-2630/15/i=1/a=015002>

T. Kiesel, W. Vogel, S. L. Christensen, J.-B. Béguin, J. Appel, and E. S. Polzik. Atomic nonclassicality quasiprobabilities. *Phys. Rev. A*, 86:042108, Oct 2012. doi: 10.1103/PhysRevA.86.042108. URL <http://link.aps.org/doi/10.1103/PhysRevA.86.042108>

ACKNOWLEDGMENTS

I feel privileged to have witnessed the beauty of Quantum Mechanics experimentally under the supervision of Eugene Polzik, who leads the experimental research group in Quantum Optics ([QUANTOP](#)), at the Niels Bohr Institute. I will always remember the first time Eugene showed me the difference between a pure state and a mixed state in a Ramsey clock measurement, after which I started to believe more seriously in Quantum Mechanics. For that, his wisdom, his guidance and the opportunity given to do a Ph.D. thesis in fundamental research among the talented members of the [QUANTOP](#) family, I will always be indebted and grateful to Eugene.

As a result, I am also indebted to the persons who introduced me to the existence of Eugene and [QUANTOP](#). I would like to thank my previous supervisors, Michèle Leduc and Juliette Simonet in Claude Cohen-Tannoudji's group (Laboratoire Kastler-Brossel, Ecole Normale Supérieure, Paris), as well as Chris Westbrook and Denis Boiron in Alain Aspect's group (Laboratoire Charles Fabry, Institut d'Optique, Palaiseau), where I had both my first lab experience and did my Bachelor thesis on the Bose-Einstein condensation of Metastable Helium.

There is no doubt that most of the experimental knowledge and the practical skills that I have acquired are due to Jürgen Appel. I could not have hoped for a better, smarter and enthusiast teacher. I would also like to express my deepest admiration to Jörg Müller and thank him for all the time he invested in sharing his knowledge with me. His talent to reduce a complex problem to simplicity gave a true value to this work.

Now it is time to thank one of the most important person, Stefan Christensen, with whom I shared all the joy and hardship of one the most challenging experiment. Stefan and I started our Ph.D. thesis together on the quantum atomic clock experiment and I will always remember our complementary approach and his hard work. Then, I would like to thank Eva Bookjans who joined me on the nanofiber adventure and contributed significantly to its success. I would like to thank Heidi Sørensen who recently joined on the promising quantum optics experiments based on nanofibers, after mastering its manufacture. She represents my best hopes for the future of our group.

Unfortunately, I do not have enough time to thank individually all the current and past members of [QUANTOP](#) as well as all the people from the Quantum Photonics and Ultracold atom group I had the honour and pleasure to meet and work with and sometimes share a great friendship. Great friends and colleagues are hard to find, difficult to leave and impossible to forget. A special mention is nonetheless de-

served to Emil Zeuthen from the theoretical group, whom I consider as my Danish brother. I thank him for all his support.

To finish I would like to acknowledge Prof. Arno Rauschenbeutel without whom we could not have started the adventure of optical nanofibers, as well as Prof. Mikkel Andersen for enlightening discussions. The experimental projects covered in this Ph.D. work have been financially supported by several funding programs that I would like to acknowledge as well, DARPA, EU (MALICIA, SIQS, QESSENCE), ERC grants and QUANTOP.

CONTENTS

1	GENERAL INTRODUCTION	1
i	COLLECTIVE STATES OF ATOMS AND LIGHT	15
2	CONDITIONAL SQUEEZING OF ATOMS	17
2.1	Motivational idea	18
2.2	Ensemble of atoms	19
2.2.1	Two-level atoms	19
2.2.2	Pseudo spin one-half or two-mode boson	20
2.2.3	Collective coherent spin state	21
2.2.4	Proper complete set of commuting observables	22
2.2.5	Partition projection noise	23
2.2.6	Population difference measurement	24
2.3	Atomic state detection	25
2.3.1	Atomic medium delay and attenuation	25
2.3.2	Atom response principle	26
2.3.3	Characteristic parameters	27
2.3.4	Phase shift measurement advantage	28
2.3.5	Projection noise limited measurement	30
2.4	Conditional spin-squeezing	31
2.4.1	Time continuous measurement	32
2.4.2	Light noise contaminated sample	32
2.4.3	Bayesian estimation	33
2.4.4	Degree of squeezing	34
2.4.5	Degree of shift and future prediction	35
2.4.6	Combined measurements	36
2.4.7	Generic Gaussian Quantum Non Demolition (QND) based squeezing as Kalman filtering	37
2.4.8	Recursive squeezing	38
2.4.9	Classical versus quantum squeezing	39
2.4.10	Spin-squeezing criteria and multipartite correlations	39
3	OPTICAL PHASE DETECTION	
	AT THE QUANTUM NOISE LIMIT	43
3.1	Detection of light	44
3.2	Annihilation operator	44
3.3	Photocurrent	45
3.4	Quantum efficiency	47
3.5	Photocurrent shot noise	49
3.6	Dominant shot noise	49
3.7	Interferometric detection basics	50
3.7.1	Coated beamsplitter	51
3.7.2	Photo-current operators	52
3.7.3	Differential photo-current	52

3.7.4	Balanced homodyne with coherent states	52
3.7.5	Light noise amplification	53
3.7.6	Phase sensitivity	54
3.7.7	Balanced versus unbalanced quantum efficiency	54
3.8	Heterodyning	55
3.9	Single versus double quadrature measurement	56
3.10	Phase estimation via Hilbert transform	57
3.11	Remark on the detected quantum noise	57
3.12	Heterodyne with homodyne sensitivity	58
3.13	single photodetector	60
3.14	Differential homodyne	61
3.15	Remark on optimal loss	61
3.16	Visibility and quantum efficiency	62
3.17	Quantum efficiency in presence of technical noise	62
3.18	Insights into photocurrent measurement	63
3.18.1	Photovoltage versus photocurrent	63
3.18.2	Operation modes	63
3.18.3	Photoconduction and transimpedance stage	64
3.19	Particular limiting noises	65
3.19.1	Background light noise	65
3.19.2	Johnson-Nyquist noise	65
3.19.3	Flicker noise	66
3.20	Summary	66
4	INTERFERENCE BETWEEN AN ATOMIC SPIN WAVE AND A SINGLE POLARITON	67
4.1	Experimental spin-squeezing in a nutshell	68
4.1.1	Atomic levels structure	68
4.1.2	Spatial confinement of the atoms	70
4.1.3	Reservoir of cold atoms	70
4.1.4	Atomic state preparation	71
4.1.5	Collective state preparation	72
4.1.6	Clock state detection with light	72
4.1.7	Dual-color homodyne and \mathcal{J}_z	73
4.1.8	Experimental spin squeezing	75
4.2	W-state preparation and detection	77
5	A NANOFIBER INTERFACE: WHY ?	81
ii	AN INVISIBLE OPEN WAVEGUIDE	85
6	A SUB-WAVELENGTH OPTICAL GUIDE	89
6.1	Maxwell's equations framework	90
6.2	Propagation equation to <i>ansatz</i> solutions	91
6.2.1	Only one cylindrical equation to solve	92
6.2.2	Angular dependence	93
6.2.3	Radial dependence	93
6.2.4	Lossless propagation requirement	94
6.2.5	First general solutions	96

6.3	Continuity and transcendental mode equation	96
6.4	General rotating polarization solutions	97
6.5	General properties	98
6.6	Practical normalization	99
6.7	Hybrid modes propagation and single-mode condition	100
6.7.1	Hybrid mode classes	100
6.7.2	TE and TM modes	101
6.7.3	Cutt-off and mode order	101
7	POLARIZATION AND TOPOLOGY	107
7.1	Rotating polarization	107
7.2	Geometrical phase	108
7.2.1	Longitudinal component	108
7.2.2	Azimuthal harmonics	108
7.3	Quasi-linear polarization	109
8	ABRAHAM-MINKOWSKI ANGULAR MOMENTA	113
8.1	Introduction	113
8.2	Momentum and conservation of energy	113
8.3	Angular momentum density	114
8.3.1	Local definition	114
8.4	Kinetic momentum of the guided modes	115
8.4.1	Free-space linear momentum density	115
8.4.2	Abraham-Minkowski momenta dilemma	116
8.4.3	Cycle-average energy flux	116
8.4.4	Light momentum trajectory	118
8.4.5	Light screw periodicity	119
8.4.6	Modes with quasi-linear polarization	121
8.5	Linear momentum per photon	121
8.5.1	Linear momentum per unit length	121
8.5.2	Photon number per unit length	122
8.5.3	Kinetic momentum per photon	123
8.5.4	Quasi-linear polarized modes	124
8.5.5	Energy transport rate	125
8.6	Angular momentum per photon	126
8.6.1	Total angular momentum per unit length	126
8.6.2	Angular momentum per photon	126
8.7	Decomposition into spin and orbital angular momentum	126
8.7.1	Humblet decomposition	127
8.7.2	Spin per photon	128
8.7.3	Orbital angular momentum	129
8.8	Minkowsky analytical results	129
9	ON THE PHASE VELOCITY	131
9.1	The wave phase	131
9.2	Hybrid phase velocity	131
9.3	Phase and energy helices	133
10	FABRICATION OF A NANOFIBER	135

11 NANOFIBER IRRADIATION IMMUNITY	139
11.1 Femtowatt guided in the fiber	139
11.2 Femtowatt scattering	141
11.2.1 Undesirable effects	142
11.3 Effective scattering cross-section	144
11.3.1 Benefit of light scattering	145
11.4 Fiber taper loss	145
11.5 Summary	146
iii DISCRETE AND CONTINUOUS DETECTION OF ATOMS IN EVANESCENT LIGHT FIELDS	147
12 A NEBULA OF COLD ATOMS ON A ROOM-TEMPERATURE NANOMETRIC WIRE	149
12.1 Vacuum chamber	150
12.2 Optical setup	151
12.3 Magnetic trap considerations	152
12.4 Majorana loss	157
12.5 Basic observations	158
12.5.1 Positioning cold atoms in the vicinity of a nanofiber . . .	159
12.5.2 Reduction of atomic density	159
12.5.3 Qualitative observations on Magneto-Optical Trap (MOT) fluorescence	160
13 DISCRETE SPECTROSCOPY OF A FEW ATOMS	163
13.1 Ultra-violet photodissociation assisted MOT	163
13.2 De-adsorption of atoms induced by weak light	164
13.2.1 Decay of guided mode transmission	164
13.2.2 Photon throughput in presence of Cesium atom vapor . .	165
13.2.3 Recovery of transmission through optical heating	167
13.3 High-sensitive fluorescence spectroscopy	169
13.3.1 Strong evidence for guided spontaneous emitted photons .	169
13.3.2 Estimation of the number of atoms	171
13.3.3 Fluorescence decay	172
13.4 High-sensitive absorption spectroscopy	173
13.4.1 First interaction with guided photons	173
13.4.2 Interleaved measurement of fluorescence and absorption .	173
13.4.3 Absorption spectroscopy	177
13.4.4 MOT coupling lifetime	179
14 SUPERHETERODYNE DETECTION OF ATOMS	181
14.1 Heterodyne detection of absorption	182
14.1.1 Heterodyne lifetime signal	183
14.1.2 Saturation and cooling dynamics	184
14.2 Superheterodyne	186
14.3 Observation of light shifts	191
14.3.1 Blue-detuned light	191
14.3.2 Red-detuned light	193

iv	AN EFFICIENT ATOM-LIGHT CRYSTAL	197
15	DESIGN OF OPTICAL NANOFIBER TRAPS	199
15.1	Diffraction limited optical dipole trap	200
15.2	Roads towards evanescent nanofiber dipole trap	201
15.2.1	Evanescent mirror	202
15.2.2	Along thin wires	202
15.2.3	Hollow core fibers	202
15.3	The simplest nanofiber trap	203
15.4	Dispersive van der Waals interaction	206
15.5	Two-color evanescent dipole trap	207
15.6	Caterpillar trap	212
16	DUAL-HETERODYNE DETECTION OF NANOFIBER TRAPPED ATOMS	215
16.1	Towards trapping atoms	215
16.1.1	Balancing light shifts	216
16.1.2	Unforeseen effect	217
16.1.3	Blue Sisyphus cooling	218
16.2	Running wave trap	220
16.3	Dual-heterodyne detection	220
16.3.1	Detection setup working principles	222
16.3.2	Carrier suppression	225
16.3.3	Dither lock	226
16.4	Optical lattice trap	226
16.4.1	Open transition	230
16.5	Light-atom interface challenges	233
16.5.1	Atomic state population detection	234
16.5.2	Quantum state tomography and spin-squeezing	237
17	NARROW ATOM NUMBER DISTRIBUTIONS IN ONE-DIMENSIONAL LATTICES	241
17.1	Absolute atom number	241
17.1.1	Saturation method	241
17.1.2	Optical pumping transient method	242
17.1.3	Statistical nature of the pumping process	244
17.1.4	Fano factor versus 3-level scheme	246
17.1.5	Nominal number of lattice trapped atoms	246
17.1.6	Dark state pumping kinetics	248
17.1.7	Single-atom optical depth	251
17.2	Measurement strength	254
17.3	Characteristic numbers of scattering events	257
17.4	Low-loss number squeezing	260
17.4.1	Continuous measurement	260
17.4.2	Observation model	262
17.4.3	Atom number squeezing	262
17.4.4	Recursive Bayesian estimation with Markovian loss	264
17.4.5	Variance estimator model	267
17.4.6	Non-linear Riccati model	269

17.4.7 Spin-squeezing outlook	270
17.4.8 Summary	272
18 A ONE-DIMENSIONAL ATOMIC MIRROR	273
18.1 Towards state preparation	273
18.2 Atomic Bragg mirror	275
18.2.1 New setup	275
18.2.2 Bragg reflection condition	276
18.2.3 Reported work	276
18.2.4 The lattice within the lattice	277
18.2.5 Experiments	278
19 CONCLUSION AND OUTLOOK	283
v APPENDIX	285
A ACCOMPANYING MATHEMATICAL DEVELOPMENTS	287
A.1 Wave equations	287
A.2 Relations between cylindrical components	287
A.3 ϕ and r components	288
A.4 Continuity condition derivation	289
A.5 laplace developpment	289
A.6 General solutions for rotating polarization	289
A.7 Normalization constant	290
A.8 Fundamental hydrib mode HE ₁₁ with quasi-linear polarization	291
B ANGULAR MOMENTUM DERIVATIONS	293
B.1 Quasi-linear polarization	294
C OPTICAL LIGHT INDUCED ZEEMAN SHIFTS	297
C.1 Interaction hamiltonian and the symmetry of light	298
C.1.1 Light polarization	298
C.1.2 Atom good quantum number	298
C.2 Scalar, vector and tensor light shifts	299
C.2.1 Effective hamiltonian	299
C.2.2 Atomic polarizability tensor	299
C.2.3 Simplest case: interaction with $F = 1/2$	299
C.2.4 Fictitious magnetic field or spin composition	301
C.2.5 General case $F > 1/2$: tensor shift	301
C.3 State-insensitive optical trap	303
C.3.1 Back-Goudsmit effect	303
C.3.2 Magic and tune-out wavelengths	303
C.3.3 Differential Stark shift	304
C.3.4 Transition shift versus trap loading	306
C.3.5 Magic wavelengths for optical nanofiber traps	308
C.4 A comment on the collisional blockade regime	310
C.4.1 Microscopic trap loading regimes	310
C.4.2 Estimation of the rates	311
D DUAL-HETERODYNE NOTES	315
D.1 Notations	315
D.2 Filtering	316

D.3 Mixing	316
BIBLIOGRAPHY	319

ACRONYMS

NBI	Niels Bohr Institute
QUANTOP	Danish Center for Quantum Optics
UCHP	University of Copenhagen
GHZ	Greenberger-Horne-Zeilinger
EPR	Einstein-Podolsky-Rosen
QIS	Quantum Information Science
QI	Quantum Information
QIP	Quantum Information Processing
QMS	Quantum Metrology and Sensing
QND	Quantum Non Demolition
DQC	Distributed Quantum Computing
EIT	Electromagnetically-Induced Transparency
LIAD	Light-Induced Atom Desorption
MOT	Magneto-Optical Trap
SPOT	Spontaneous-Force Optical Trap
UV	Ultraviolet
CCD	Charge-Coupled Device
SPCM	Single-Photon Counting Module
CW	continuous-wave
ND	neutral density
SSS	spin-squeezed state
EB	Eva Bookjans
AOM	acousto-optic modulator
QED	Quantum Electrodynamics
FORT	Far-off resonant trap
CQED	Cavity Quantum-Electrodynamics

GPS	Global-Positioning System
RMS	root-mean-square
SNR	signal-to-noise ratio
DC	direct current
AC	alternating current
APD	avalanche photodiode
SQL	standard quantum limit
OD	optical depth
CSS	coherent spin state
CW	continuous-wave
MAP	maximum a posteriori
PIN	positive-intrinsic-negative
RF	radio-frequency
NIR	near-infrared
D2	D2
D1	D1
LO	local oscillator
MZ	Mach-Zehnder
ECDL	extended cavity diode laser
BEC	Bose-Einstein condensation
IF	intermediate frequency
BSC	blue Sisyphus cooling
OOE	$1/e$
USB	upper sideband
LSB	lower sideband
EIT	electromagnetically-induced transparency
UHV	ultra-high vacuum
JHM	Jörg Helge Müller
JA	Jürgen Appel
SLC	Stefan Lund Christensen
HLS	Heidi Lund Sørensen

GENERAL INTRODUCTION

As the saying goes, the Stone Age did not end because we ran out of stones. We transitioned to better solutions.

— Steven Chu

The evolution of quantum optics research during the course of the past decades has been spectacular. This has led to increasingly specialized complex experimental and theoretical studies that make it difficult to have a global view of the field. However, this is the mark of a broad and vibrant field of research.

Consequently, I would like to take the opportunity of this thesis introduction to also share some general ideas which may help to identify some of the fundamental challenges that this research field is facing today where the past notions of particles and waves seem to have transitioned to a world of pure physical information.

THESIS INTRODUCTION

Many features of the quantum world – quantum superpositions, multipartite entanglement and squeezed states – are central to the future developments in metrology and quantum information science but also to a better fundamental understanding of the laws of Nature. In quantum optics experiments, an excellent test-bed for exploring these quantum effects, there are as many different implementation schemes and research paths as there are physical systems that exhibit quantum behaviour.

This thesis work particularly focuses on basic interactions between two fundamental quantum systems – a few atoms and weak light. Since the invention of quantum mechanics, the experimental control and manipulation of such simple quantum systems have been long standing and enabling goals, in particular to observe results of thought experiments or perhaps even better to contradict with them. This led both Serge Haroche and David Wineland to be awarded the Nobel Prize in Physics in 2012, who contributed significantly to the study of quantum superpositions and their evolution via light-atom interactions.

In this thesis we explore a compatible alternative to Cavity Quantum-Electrodynamics (CQED) with single particles by exploiting the last

postulate of quantum mechanics, namely the symmetrization postulate which dictates the statistical nature of the quantum state of an ensemble of identical particles, here neutral atoms.

A particular interest and main challenging objective of our experiments is the ability to prepare and observe in real-time quantum superpositions of collective atomic states without destroying them. For this, we will use light as a fundamental tool to manipulate the state of the atoms but also as a soft measurement device to realize quantum non demolition light-atom interactions. In turn, we could use the collective quantum coherence of atoms as a quasi-transparent detector of optical photons. This idea was achieved in the field of [CQED](#) in the group of Serge Haroche on radio-frequency photons trapped between superconducting mirrors using single atom probes. The first non-destructive detection of an optical photon using quantum superpositions of a single atom was achieved only recently, also in [CQED](#) in the group of Gerhard Rempe [Reiserer et al. \(2013\)](#).

All these fundamental challenges among others ask for the realization of an efficient quantum interface between light and atoms. Such an interface demands a high coupling strength while preserving the lifetime of quantum superpositions from loss of coherence or *decoherence*.

This requires a careful and compatible design of the environment for both the atoms and the optical light field. To this end, we will combine the strong confinement and guiding of light with the guiding and trapping of atoms using a sub-wavelength diameter tapered optical fiber – one of the most recent achievement in the field of quantum and atom optics [Vetsch et al. \(2010\)](#); [Goban et al. \(2012\)](#).

This novelty represents a departure from the path originally taken and explored during the first half of this thesis, namely the manipulation of mesoscopic ensembles of cold atoms trapped with light beams propagating in free space. My goal will be to show how we have realized the transition between these two platforms while exploring the benefits of both approaches.

A quantum interface based on an optical nanofiber offers a leap into a one dimensional geometry where mesoscopic ensembles of atoms can be strongly coupled to light on scales thinner than the light wavelength. It represents a promising scalable platform which could be further augmented with the trapping of light, e. g. using fiber Bragg grating cavities or perhaps even better using the atoms themselves as mirrors ([Chang et al. \(2012\)](#)).

As the most recent developments have shown, an optical nanofiber experiment also provides a environment rich in physics, yet to be explored. We believe this fundamentally stems from the full complexity of the dipole electric interaction expressed in three dimensions in this system due to the presence of longitudinal waves of light.

Before I review in detail the contribution and the content of this report, I would like to give a broader and personal perspective on major

challenges of the field in order to share some general motivations. This will help to introduce some definitions and concepts as well as to show the broad interest for exploring light and mesoscopic atomic ensembles interfaces.

This relatively long and detailed thesis report reflects the transition of the experimental research done in the cold atom quantum optics group of [QUANTOP](#), from the very last advanced experiments realized with cold atom ensembles in free space to the construction of a completely new interface that we had to understand and explored step by step. The report is therefore intended to serve as a reference, with a priority on the fundamental, theoretical and experimental challenges I have encountered while being among the main explorers of this very challenging transitional work.

BROAD INTRODUCTION

The quantum computer contradiction ?

In view to implement the idea of the quantum computer, which is among the great excitements behind quantum-enabled technologies, it seems that one is facing a contradiction. One tries to generate more and more important quantum coherence and entanglement while one knows this may lead to a faster and faster loss of coherence and entanglement, as a result of the inexorable leak of information into the environment ([Haroche \(2013\)](#)).

Quantum superpositions (e.g. $|\psi\rangle = |\uparrow\rangle + |\downarrow\rangle$) has been realized on simple quantum systems in the laboratory. Small amounts of multipartite entanglement has even allowed to grow embryos of Schrödinger cats, for instance $|\psi\rangle = |\uparrow\otimes\uparrow\rangle + |\downarrow\otimes\downarrow\rangle$ Bell states or Einstein-Podolsky-Rosen ([EPR](#)) pairs and $|\psi\rangle = |\uparrow\otimes\uparrow\otimes\uparrow\rangle + |\downarrow\otimes\downarrow\otimes\downarrow\rangle$ Greenberger-Horne-Zeilinger ([GHZ](#)) states which are important for quantum teleportation and computing. However, no one has ever seen a macroscopic cat state, that is $|\psi\rangle = |\uparrow\rangle^{\otimes N} + |\downarrow\rangle^{\otimes N}$ for N large. The bigger the cat is, the faster *decoherence* brings it into the classical world (as a mixture) [Zurek \(1991, 2003\)](#). There is however hope in the regime of a mesoscopic number of particles ([Zurek \(2003\)](#)).

Loss of coherence or decoherence can be seen as all phenomena which bring a physical system from the quantum to the classical realm where quantum superpositions (wave-like interference) disappear. Note that the absence of entanglement does not imply classicality ([Ollivier and Zurek \(2001\)](#)). The notion of what is quantum, which lies in the nature of the correlations between physical systems, is still the source of active research (e.g. quantum discord). Intense research is therefore needed and conducted in parallel to preserve a quantum system from the effects of decoherence or even better to correct for it, increasing the developments of quantum information science.

Quantum Information Science (QIS) basically sets what can and cannot be done with Quantum Information (QI), a physical information held in the state of a quantum system.

The meaning of a gain in quantum physics

It may then appear that we, experimentalists, or I should say, observers, have to compete to extract information from a quantum system before the environment, which interacts with the system, takes it away before us. In some sense, this thesis work reflects such attempt to tailor the environment of simple quantum systems by creating an efficient quantum interface between atoms and light.

We will see that the *on-resonant optical depth* has appeared as a figure merit of many realization of interfaces [Hammerer et al. \(2010\)](#). This quantity plays a role analog to the *cooperativity* in cavity Quantum Electrodynamics (QED). However, we should try to keep a broader vision than that given by the characteristics of the achieved interfaces based on the current limits of technology and a benchmark for a quantum interface should be found in a more subtle general interplay between gain and loss of information about a physical system following a particular kind of measurement and what is meant by that. In quantum mechanics, these notions acquire a statistical meaning, e.g. the quantum efficiency of a photo-detector is not a simple gain or scaling factor. In addition, measurement takes a central part as it is a physical process of its own. Measurement precision and estimation through quantum-assisted metrology is bound by the fundamental nature of the state of light and atoms involved in the interaction which is nowadays expressed by the notion of quantum Fisher information and the quantum Cramer-Rao inequality.

A flexibility in measurement bandwidth and the ability to perform real-time observation of quantum fluctuations are also important factors for a quantum interface as we shall see later.

Light and/or atom perspectives

Light and atoms can play asymmetric role in the interface. One may want to learn information from atoms by measuring on light as a meter or by using atoms to measure and probe the state of light. However, during the interaction it is not possible to attribute an independent reality to these two, they are entangled and mutual measurement occurs. In other words, the coupling strength of the interface is a property of the shared or joint system atoms+light. A perspective or unbalanced role may arise when trying to preserve or change the nature of the coherence contained in each systems. We can illustrate this point with the following example. In a number of realizations, one important decoherence mechanism is due to random incoherent scattering between

atoms and light (e. g. spontaneous emission). Although the number of incoherent events or the number of scattered photons is the same as the number of atoms which have scattered a photon, the rate at which one system will decohere depends on the fragility of its coherence, here with respect to one-body loss¹. Losing a part of a composite quantum system may be very detrimental for the encoded multipartite entanglement. The nature of the correlations between its parts, i. e. the nature of the collective state of the system can be robust or not with respect to such partite loss (e. g. GHZ state versus W state). In that respect, a type of superposition states of light, coherent states, also known as “pointer states”, are impervious to entanglement with the environment. They stay coherent states and only suffer relaxation from incoherent scattering into the environment (Haroche and Raimond (2006)). This is a very different behaviour contrary to a superposition of coherent states (see above Schrödinger cat). Although, they are not states of the electromagnetic field with well-defined energy, the above makes them robust atom probes.

Quantum Information Processing

Quantum systems as opposed to classical ones benefit from the essential holism of quantum physics - that the whole can be more than the sum of its parts (partition) - marked by the existence of quantum superposition of states and unfactorisable or nonseparable states of several physical systems. Taking this concept further and concrete, one may want to exploit these quantum features to improve parallel computing and information processing. Digital information is encoded nowadays as separate values of 0 and 1, transcribed for instance in two possible magnetic orientation of a particle. If prepared in a superposition through quantum interference, the correlated degrees of freedom of two such particles could hold the following four values 00, 01, 10, and 11 as a whole. Three particles could hold eight values, four particles sixteen such that N particles could hold 2^N bits of information simultaneously in parallel. Of course, a N -bit classical register could map each of the 2^N combinations but not all of them at once in parallel. This dramatic theoretical exponential scaling of parallel computing power with the number of quantum bits or *qubits* would outperform the amount of data that can be processed by today’s classical computers. This has also the potential of opening new ways of “computing”. Here we also observe that to implement such idea, one will need to manipulate many quantum systems (or a higher Hilbert space per system).

¹ For simplicity we do not comment about dephasing mechanisms here

Quantum algorithms and simulation

The vision of what can be done with quantum computation can be still quite blurry until one recall first that the initial proposal, as suggested by Feynman in a seminal lecture, is to simulate physics with computers.

Nature isn't classical, dammit, and if you want to make a simulation of nature, you'd better make it quantum mechanical, and by golly it's a wonderful problem, because it doesn't look so easy. - Feynman (1981)

Simulating the behaviour of complex physical systems and physical processes seems the first realistic setting for quantum computers. However, Peter Shor and as well Lov Grover at Bell Laboratories made the power of quantum computer clearer through the development of quantum-based algorithms which respectively could factorize large numbers or search entries in database in a time much faster than classical algorithms. Exponential gain in large numbers factorization would for instance render classical cryptographic protocols vulnerable such as RSA (Rivest, Shamir, Adleman). Search engines will also benefit greatly. We highlight here that particles trapped in an optical lattices have proven to be a test-bed of choice for simulating complex physical systems, for instance condensed matter phenomena, disorder or phase transitions linked to the dimensionality of the system.

We would like to also bring a wide perspective of the practical advances of Quantum Information Processing (QIP) in the domain of communication.

Quantum communication, cryptography and teleportation

Demonstrated in the early 1950's by Shannon but first described by Frank Miller (1882), there exists an encryption technique for cryptography with absolute security that is impossible to crack. Well-known as one-time pad systems, the encryption algorithm can be as simple as a xor logic operation between data to be encrypted and a secret key as long as the data. However the key must not be reused to resist cryptanalysis and thus as to be generated with pure randomness. For instance, chaotic sources such as lava lamps or the quantum shot noise of webcams can be used to generate pure random numbers which would make absolute security available to everyone. However, the remaining problem that challenges perfect cryptography is the secure exchange of the key (for symmetric algorithm unlike RSA) between the emitter and the receiver. Geared with the "no-cloning theorem" that forbids the exact copy of an arbitrary quantum state and the uncertainty principle which guarantees that measurements on a quantum system always disturb it, secure key exchange encoded with quantum information is achieved by providing fundamental law of physics to detect any eavesdropping on the quantum communication channel. It is almost impossible to avoid mentioning the initial quantum cryptographic schemes such as BB84 developed by Charles Bennett and Gilles Brassard and

Ekert91 proposed by Arthur Ekert were the information is encoded as qubits of light with different polarization states. The past achievements have revealed entangled states of photons as a prime ingredient for quantum communication. Aside secure cryptographic applications, quantum communication provides a new way of exchanging information with the excellent example of quantum teleportation.

The basics scheme for teleportation involves transporting a qubit Q from one location to another without moving its physical support (e. g. a carrier particle) through the use of a pair of spatially separated entangled states A and B . Following the entanglement of Q with A , B can be transformed into Q after a measurement has been performed on A at the cost of destroying the *original* state Q .

Quantum communication faces the challenge of the distribution of entangled pair of photons over long distance while maintaining entanglement. The realization of quantum repeater devices that can refresh entanglement at regular distance intervals is a potential solution.

All of this could be realized efficiently with a quantum interface between light and atomic ensembles [Hammerer et al. \(2010\)](#). Another field of research would benefit greatly for these developments is metrology.

Quantum Metrology and Sensing (QMS)

Quantum Metrology and Sensing ([QMS](#)) is a very active and fundamental domain of research that nowadays aims at exploiting quantum correlations and entanglement for precision measurement. Quantum metrology enables unprecedented signal-to-noise ratios and resolution of measurements, at sensitivities which would outperform classical systems. Atomic clocks that exploit quantum logic to perform accurate measurement of frequencies can set new time standard used in telecommunication and Global-Positioning System ([GPS](#)) satellite systems for instance. The development of entanglement-enhanced quantum sensors is a well-pursued goal for the measurement of position and displacement (gravitational wave detection), magnetic field sensors (with potential applications for biological analysis). We can also highlight the emergence of optomechanical coupling research for position measurement that triggers the realization of new highly efficient transducers which I have witnessed at [NBI](#) for the last few years.

All the previous discussion may feel a little bit application oriented. On a more fundamental aspect, all the fruits provided by quantum optics experiments followed a century of research aimed at understanding better the nature of light and matter together with its interactions. Taking a deeper step, as mentioned before, any measurement performed on a quantum system disturbed it fundamentally such that the eyes or “sensors” provide us with elements of our own reality which depend on the nature of the detectors we use. If so-called quantum non demolition detectors were easily available, we would have a better understanding

at the elements of the quantum reality to manipulate for instance for QIP and we could prepare and manipulate highly non-classical states.

The choice of a practical candidate

In quantum optics experiments, there are as many different practical candidates as there are physical systems that exhibit quantum behaviour. This, not only in the realm of atomic and nanoscale technologies but also with emergent macroscopic mechanical devices. We can name a few of them: superconducting qubits (based on Josephson-junction), trapped ions, neutral atoms, atom chips, spin qubits in solid state material (quantum dots - artificial atoms, nitrogen vacancy in diamonds, phosphorus atoms in silicon matrix), caged atoms inside fullerene molecules, flying photons, condensed matter entities (Bose-Einstein condensates).

For scalable quantum computing, quantum metrology and all entanglement enabled technologies, two main approaches seem to be pursued. The combination of individual trapped particles or single quantum dots into universal quantum processors. The basic building block of a quantum processor being the quantum logic gate. The second approach, sometimes referred as *top-down*, compared to the previous *bottom-up* one, consists in employing many particle systems to realize special purposes, for instance quantum simulators, quantum register, repeaters and memories. A strong emphasis on so-called Distributed Quantum Computing (DQC) is expressed nowadays which therefore promotes the realization of intermediate platforms to construct networks of small groups of entangled systems. Entangling very large number of qubits is challenging and therefore one might consider combining smaller groups for the initial practical implementations.

It is extremely remarkable that the full quantum control of single quantum systems has been achieved from the standpoint of fundamental science but also for the realization of a single particle logic gate or single particle transistor. However, for the challenges of QIS, which require scalability of such proof-of-principle systems, it seems relevant to envision another road. Qubits are very fragile and preserving the coherence of many single qubits is hard. In order to protect quantum information due to loss of coherence into the environment, Andrew Steane and Peter Shor have developed the first of the quantum-error correction schemes, a currently very active branch of quantum information theory. The idea is simple and consists in spreading the qubit's logical information over many physical quantum systems instead of one. While the Shor code spreads 1 logical qubit over 9 physical qubits, Steane's

provides an equivalent fault-tolerant code with 7 qubits, Laflamme's only 5^2 .

All the above constitutes additional sources of motivation for the development of many-body quantum systems where quantum information would be stored safely over the collective degrees of freedom of the ensemble.

Light and atomic ensembles

Either in the discrete or continuous domain, optical light, with its potential high degrees of freedom³, has proven itself as a robust and reliable support of quantum information. This choice benefits from the great speed of light and therefore high throughput of information. However, exploiting light alone will, at the present state of the art, penalize all the other tasks of QIP which need information storage. A single photon can travel in an optical fiber for about tens of kilometers without being absorbed and breaking the quantum communication link which calls for the realization of quantum repeaters⁴.

A very promising medium to store the information carried by light are atomic ensembles. An ensemble of atoms can interact strongly with light which enables for efficient quantum state transfer between them. A quantum memory for light can be implemented for instance through electromagnetically-induced transparency (EIT). As the main optical properties of atoms are dictated by the valence electrons, alkali atoms offer a prime choice as the simple systems to model and interact with its single valence electron. There are many more merits compared to others systems (e.g. single ions, quantum dots) that we should cover further in this thesis. In addition, many-body ensembles of identical quantum systems render possible the study of collective behaviours, it unravels complex dense matter effects via simulation and it enables the exploitation of coherent enhancements. Various physics phenomena can be explored in different dimensions by a proper arrangement of the atoms in space made through the past groundbreaking development in the manipulation, cooling and control of neutral atoms with light. We note for the moment that neutral atoms offer in general a weaker coupling to light than ions. The latter being in turn more sensitive to environmental field fluctuations. Light, as an electromagnetic wave, interacts with matter through charged particles. Neutral atoms, by definition, have no zero order electrical charge distribution. Thus, light and neutral atom interactions constitute of higher, hence weaker, order effect such as polarization. Contrary to artificially engineered atoms

² According to the quantum Hamming bound, encoding a single logical qubit and providing for arbitrary error correction in a single qubit requires a minimum of 5 physical qubits.

³ For example, orbital angular momentum of light provides higher-dimensional QI encoding.

⁴ Repeater tamper polynomially bit rate degradation.

such as quantum dots, atoms are all identical which makes many-body systems more tractable. Within the diverse quests of quantum information processing, metrology and sensing there is no platform with “winner takes it all” situation. What research tries nowadays is to combined the pros of all past fundamental proof-of-principle achievements into elegant and realistic platforms to keep pushing the boundaries further.

The challenge of detecting light

As detecting light is central to this work and to all the previous tasks, we ought to mention an important point. With all due respect to the field of optics, there are today no detectors that can *detect* light. Contrary to Hertzian waves that can be monitored directly on an antenna, no electronic device has the inertia to follow an optical electromagnetic field. Instead, we only have at our disposal in the laboratories so-called square-law detectors (based on photo-absorption) producing a *response* proportional to an input *photon*⁵ flux. This is a highly destructive measurement process of a fundamental quantum system. Non-linear mixing processes and interferometric measurement such as optical homodyning can bypass the detector bandwidth limitation and allow to record optical phase indirectly, albeit the measured input state of light is still cast into vacuum. The quantum coherence of collective atomic state superpositions may provide a mean and a path for a *transparent* or non-destructive detection of light based on Ramsey spectroscopy of optically-induced Stark shift. Behind this idea also lies the realization of quantum phase gates.

Three enhancement strategies

Most light-matter interactions can be described at first order by the interaction energy between an electrical dipole moment of a charged particle distribution and the electric field of light. Two obvious directions to increase this coupling are to increase the strength of the dipole moment and the strength of the electric field. For atoms, this can imply to consider atomic levels with a large orbital radius such as Rydberg atoms. Or simply to engineer artificial atoms with large oscillator strength such as quantum dots. For light in free space, this can be achieved by a high spatial focusing or tight confinement at the position of the atom. The third general strategy deals with collective enhancement. The interaction can be scaled up or repeated several times as in [CQED](#) where a single photon can propagate and interact many times with a single atom. Instead, before diffraction reduces the effective strength of the electric field of light, light can be made to propagate over many identical dipoles. In the first case, the enhancement of the interaction is

⁵ By a photon, here we mean a light quantum, not a Fock state. [Lamb \(1995\)](#).

given by the cavity finesse. In the second case, the enhancement is given by the number of coherent atoms.

With this introduction to the context, to the challenging goals of the field and to several important aspects of light atomic ensembles interfaces, we are ready to present the structure, the main subjects and experiments realized in this thesis.

THESIS STRUCTURE

My thesis work started initially with the general subject of quantum noise limited measurement in atomic ensembles with continuous variables of light. In essence, the implementation of QND measurement on collective quantum states of atoms which implies the generation of multi-atom entanglement and the creation of so-called collective spin-squeezed states of atoms relevant for Ramsey spectroscopy and magnetometry.

Stefan Lund Christensen (SLC) and I started our theses together on a very advanced setup which were developed during many years by successful previous generations of students. The creation and characterization of spin-squeezed state (SSS) states were already achieved through the operation of a quantum atomic clock beyond the standard atomic projection noise limit, Appel et al. (2009b); Louchet-Chauvet et al. (2010).

The original experimental platform relied on the interaction of light and microwave fields with ensembles of cold Cesium $N_{\text{at}} \sim 10^6$ atoms held in a free space optical dipole trap. While pushing the limit of this proof-of-concept experimental setup which have now been disassembled several months ago, we decided to explore in parallel a novel interface based on an optical nanofiber. This thesis reports will then reflect my parallel efforts in both platforms, starting from a very advanced one, to building a completely new quantum optics setup from zero with the hope to realize an efficient interface between atoms and light.

PART I: After our successful attempts⁶ to reproduce, prepare and improve SSS states, the first experiment oriented itself towards the more challenging task of the creation and characterization of non-gaussian (non-classical) collective state of atoms, which then defined the main line of SLC's thesis. Consequently, I will devote the first part of this thesis to my efforts complementary to Stefan's in the following main subjects:

- Real-time and minimally destructive detection of collective atomic state superpositions at the fundamental quantum light shot noise and atomic projection noise limits. (QND)

⁶ The vacuum setup broke and it took many months for me and Stefan to eliminate classical noise sources and operate measurement at the light shot noise limit.

measurement based on dual-color homodyne detection of atomic phase shifts).

- The preparation and characterization of spin-squeezed states in large ensembles of atoms.
- The hybrid discrete and continuous variable ingredients in the preparation and characterization of the first excited Dicke state.

My goal will be to keep an eye as close as possible to the experiment while trying to provide a simple and accessible theoretical description of the fundamental working principles of collective atomic ensembles which I believe more visual with the help of Bayesian filtering theory.

PART II: In the second part of this thesis, we start exploring a new interface to combine the guiding of light and the trapping of atoms with an optical nanofiber. As I was the first to explore this new system in our group and as there is still a lot to learn from it, I will present an analytical derivation of the light modes and I will try to generalize the theory which should be accessible to the new PhD students. At the end of this part, I will give a brief account on the nanofibers we have manufactured with the help of the group of Prof. Arno Rauschenbeutel.

PART III: In the third part of this thesis, we will sum up briefly many months of construction of a new magneto-optical trap setup for Cold Cesium atoms intended to operate around an optical nanofiber. After a year of development I was joined by Eva Bookjans (EB) who contributed significantly to the construction of the new experimental setup with me. I will present the first successful attempts at interfacing cold atoms with the evanescent field of an optical nanofiber. I will report both discrete (single photon counting) and continuous (heterodyne) measurement performed on a few cold atoms in the magnetic trap.

PART IV: In the last part, we try to realize advanced experiments with atoms trapped in the evanescent field of a nanofiber. We create an optical lattice in the evanescent field of a nanofiber and we develop the first minimally destructive and continuous detection of atomic state in this system, limited by the light shot noise. Together with a robust measurement of the atom number, we realize a significant atom number squeezing and demonstrate an efficient interface between light and nanofiber trapped atoms, in view to implement spin-squeezing and quantum state tomography of non-classical state in this platform. We then communicate on our last exploration, namely, our attempts in the creation of a one-dimensional atomic mirror.

Starting from zero, it was a challenging task to now be able to compete⁷ with the state-of-the-art experiments in the limited PhD time. This report is my attempt to share both the fundamental and technical obstacles in this adventure.

⁷ And the principal ingredient for that, is that we tried to focus on one of the most important element, the detection scheme.

Part I

COLLECTIVE STATES OF ATOMS AND LIGHT

We measure in real time the evolution of collective quantum states of atoms without *destroying* them and with a precision below the standard quantum noise limit.

We present a simple Bayesian approach to the conditional preparation of spin-squeezed states to focus on the physical mechanisms of both optical and atomic homodyne detection in the tomography of non-classical states.

Permutation symmetry of identical particles (atoms and photons) plays a central role.

2

CONDITIONAL SQUEEZING OF ATOMS AN EXPERIMENTAL BAYESIAN APPROACH

*If there would be atoms (...) there would be indistinguishable ones
(...) which is against all the greatest principles of rationality.*

— Leibniz

As long as spontaneous emission remains a single-atom effect, an interface between light and the collective degrees of freedom of an ensemble of identical atoms can provide a powerful and rich in physics alternative to cavity-enhanced interaction with single particles (Hammerer et al. (2010)).

In this composite physical system, the enhancement of electrodynamics interactions has its origin in the *cooperation* (Dicke (1954)) of the many atoms. It stems from the *local indistinguishability*¹ of the identical atoms as the result of the particle exchange symmetry of the interaction performed on the ensemble. This is one of the most mysterious (Feynman (1963)) yet effective prediction from the principles of quantum mechanics when dealing with many identical body systems.

The ability to observe and exploit in real time the evolution of the collective quantum state of the atoms without destroying it, and with a precision measurement only limited by the intrinsic fundamental quantum noise of this system, is one of the most challenging aspect of our and many other experiments.

In this chapter, we introduce with gradual complexity the ideas that have been developed to reach this goal. Over the past years, this challenge has also become a benchmark for the realization of an efficient quantum interface between light and ensembles of atoms. This first chapter is also an opportunity to develop a consistent notation. We present concepts use throughout this thesis work and shared by the two light atomic ensemble interfaces we have studied. In particular, we aim at a simple presentation of the conditional preparation of collective squeezed states achieved experimentally. This is accomplished via

¹ Even in situations where the atoms can be approximately considered independent (e.g. non-overlapping spatial wavefunctions) they can all be coupled to a common-mode interaction thereby loosing their independent reality (w.r.t the nature of such mode, e.g. spatial). One then speaks about the dressed or total collective state of the system.

continuous homodyne measurement of optical light probes interacting homogeneously and dispersively with the atoms for which we propose a description in terms of Bayesian filtering theory at the standard quantum noise limit.

2.1 MOTIVATIONAL IDEA

Suppose we have at our disposal simple quantum systems, e. g. isolated two-level atoms, marked by their ability to exist in a quantum superposition state. In Dirac's formalism we could write the state of an atom $|\psi\rangle$ such that

$$|\psi\rangle = |\varphi_a\rangle + e^{-i\phi} |\varphi_b\rangle, \quad (2.1)$$

where $|\varphi_a\rangle$ and $|\varphi_b\rangle$ are two orthogonal basis states and ϕ an arbitrary quantum phase. It is remarkable that when $|\varphi_a\rangle$ and $|\varphi_b\rangle$ are eigenstates of the atomic system with well-defined energy (also known as stationary states) quantum mechanics tells us that $|\psi\rangle$ is not. Such quantum superposition has to evolve over time. This evolution is encoded in the quantum coherence through the atomic phase $\phi = \Delta E t / \hbar + \phi_0$ where t is the elapsed time, ΔE is the energy difference of the two states $|\varphi_a\rangle$ and $|\varphi_b\rangle$, ϕ_0 the initial prepared phase and \hbar the Planck constant.

The state $|\psi\rangle$ constitutes a fundamental resource to serve as time keeping, i. e. a *quantum clock*. Furthermore, it is clear that any modification of the energy difference ΔE , as from a perturbing interaction energy, will translate into a different rate of phase evolution and will cause the phase of the clock to be ahead or behind the unperturbed isolated atomic phase evolution. This makes the quantum clock a sensor. A sensor that only works during the lifetime of the quantum superposition and whose information retrieval is dictated by the fundamental principles of quantum mechanics.

We note that the strength of the perturbing interaction could be designed such that ϕ get shifted by π creating a transistor (quantum phase gate) between two orthogonal states. Moreover, the measurement of ϕ could be used as a feedback onto the external interaction to lock on universal atomic properties. The application of quantum superpositions to metrology and quantum information are numerous and the previous recall of the principles of Ramsey spectroscopy ([Ramsey \(1990\)](#); [Haroche et al. \(2013\)](#); [Ramsey \(1980\)](#)) do not exhaust all of them.

Neutral atoms have many merits but since they do not have a net electrical charge, their interaction with electromagnetic fields is constituted of higher order moments of the atomic charge distribution. Hence the coupling of a single atom with these fields is in general weak and various strategies need to be devised to build up a significant sensitivity to ϕ , e. g. increase of the field amplitude at the atom position, increase of the atomic moments. Another compatible idea is to use the meso-

scopic enhancement provided by a collection of identically prepared atoms, coherently interacting in a delocalized fashion.

To conclude this section, it is possible to envision very interesting tasks by having many quantum clocks working together. It is possible to synchronize, correlate or entangled them, which allows to improve measurement precision over uncorrelated ensembles of clocks and offers a system ready to realize multiple quantum information processing tasks as presented in the introduction of this thesis. There are as many experimental paths explored as there are systems that exhibit quantum behaviour where the existence of the previous superposition state is central. In our group, we manipulate collective atomic states and I will give in the next section a basic description of such system.

2.2 ENSEMBLE OF ATOMS

For a clear exposition of the physical ideas, I will first give a basic description of our experiments before moving rapidly to its central principles and limitations.

We can prepare ensembles of $N_{\text{at}} \gg 1$ atoms, where initially the atoms are isolated and independent within good approximation. We manipulate and interrogate their internal degrees of freedom by dressing them with electromagnetic fields. The conservation of angular momentum dictates the evolution of the internal atomic states. However, for state preparation and measurement, these fields do not act selectively on each atom. Therefore, identically prepared atoms are *a priori* indistinguishable from each other. As a result, we only probe the collective degrees of freedom of the atomic ensemble, which reflects the underlying permutation symmetry or invariance under particle exchange.

2.2.1 Two-level atoms

We restrict the manipulation of the atomic states to two relatively long-lived states of energy of the atoms and we can prepare any quantum superposition of those states. This constitutes an example of a physical implementation of the quantum bit paradigm. We describe the states by two orthogonal Hilbert vectors $|\uparrow\rangle, |\downarrow\rangle$. In particular, we can prepare an atom in the following symmetric quantum superposition

$$|\rightsquigarrow\rangle = \frac{|\uparrow\rangle + |\downarrow\rangle}{\sqrt{2}}. \quad (2.2)$$

A concrete practical choice of two such states is represented by the so-called clock states of neutral alkali atoms. Specifically, they correspond to the two magnetically insensitive Zeeman sub-levels belonging respectively to the two lowest hyperfine ground states of the atom.

The state (2.2) can be prepared by optical pumping into $|\downarrow\rangle$ followed by a suitable Rabi oscillation duration between the two levels.

2.2.2 Pseudo spin one-half or two-mode boson

Our previous choice of notation for the basis states is motivated by the theoretical equivalent description of a two-level quantum system and a spin one-half particle. The arbitrary Hilbert vectors $|\uparrow\rangle$, $|\downarrow\rangle$ can be formally identified as the only two possible orientations of a fictitious spin one-half projected along an arbitrary given direction². More fundamentally, the state $|\psi\rangle$ of the system can also be described within the density operator formalism. The density operator for the pure state (2.2) is

$$\hat{\rho} = |\psi\rangle\langle\psi| = |\rightsquigarrow\rangle\langle\rightsquigarrow|.$$

Recognizing this operator as a dyad or tensor product Fano (1957), represented in the previous basis as a SU(2) matrix, we can use Schur-Weyl duality to decompose³ ρ into very basic representations of symmetry and antisymmetry under exchange of $|\uparrow\rangle$ and $|\downarrow\rangle$,

$$\rho = \underbrace{\mathbb{1}_2 \frac{\text{Tr}(\rho)}{2} + \begin{pmatrix} \frac{\rho_{\downarrow\downarrow} - \rho_{\uparrow\uparrow}}{2} & \frac{\rho_{\downarrow\uparrow} + \rho_{\uparrow\downarrow}}{2} \\ \frac{\rho_{\downarrow\uparrow} + \rho_{\uparrow\downarrow}}{2} & -\frac{\rho_{\downarrow\downarrow} - \rho_{\uparrow\uparrow}}{2} \end{pmatrix}}_{\text{symmetric}} + \underbrace{\begin{pmatrix} 0 & \frac{\rho_{\downarrow\uparrow} - \rho_{\uparrow\downarrow}}{2} \\ -\frac{\rho_{\downarrow\uparrow} - \rho_{\uparrow\downarrow}}{2} & 0 \end{pmatrix}}_{\text{fully antisymmetric}}. \quad (2.3)$$

These can be easily written in terms of the Pauli matrices $\sigma_x, \sigma_y, \sigma_z$, where z is identified as the arbitrary quantization axis chosen to define $|\uparrow\rangle$ and $|\downarrow\rangle$ earlier. Using the Pauli vector $\vec{\sigma}$ ⁴, one can find a mapping ($\vec{\sigma} \cdot \hat{\mathbf{s}}$) of the density matrix ρ from a vector operator $\hat{\mathbf{s}}$, which shows that the state of the two-level atom is completely described by the components of $\hat{\mathbf{s}}$ defined as,

$$\begin{aligned} \hat{s}_x &= \frac{\hat{\rho}_{\downarrow\uparrow} + \hat{\rho}_{\uparrow\downarrow}}{2} = \frac{1}{2}(|\downarrow\rangle\langle\uparrow| + |\uparrow\rangle\langle\downarrow|), \\ \hat{s}_y &= -i\frac{\rho_{\downarrow\uparrow} - \rho_{\uparrow\downarrow}}{2} = -i\frac{1}{2}(|\downarrow\rangle\langle\uparrow| - |\uparrow\rangle\langle\downarrow|), \\ \hat{s}_z &= \frac{\rho_{\downarrow\downarrow} - \rho_{\uparrow\uparrow}}{2} = \frac{1}{2}(|\downarrow\rangle\langle\downarrow| - |\uparrow\rangle\langle\uparrow|), \\ \text{with } \hat{s}^2 &= \frac{\rho_{\downarrow\downarrow} + \rho_{\uparrow\uparrow}}{2} = \frac{1}{2}(|\downarrow\rangle\langle\downarrow| + |\uparrow\rangle\langle\uparrow|), \quad \rho = \hat{s}^2 \mathbb{1}_2 + \vec{\sigma} \cdot \hat{\mathbf{s}}, \end{aligned}$$

where \hat{s}^2 is the trivial⁵ element of permutation symmetry⁶. It is interesting to examine that the two possible permutation (ladder or jump) operation $\hat{s}^+ = |\downarrow\rangle\langle\uparrow|$ and $\hat{s}^- = |\uparrow\rangle\langle\downarrow|$ do not commute and that a

² Note that a direction is a concept invariant with respect to rotations in \mathbb{R}^3 .

³ $\rho = (\rho - \frac{\text{Tr}(\rho)}{2}\mathbb{1}_2) + \mathbb{1}_2 \frac{\text{Tr}(\rho)}{2}$ where the first traceless matrix can easily be decomposed into a symmetric and antisymmetric matrix by writing the off-diagonal terms as $\rho_{ij} = \frac{\rho_{ij} + \rho_{ji}}{2} + \frac{\rho_{ji} - \rho_{ij}}{2} = \frac{\rho_{ij} + \rho_{ji}}{2} + \frac{\rho_{ij} - \rho_{ji}}{2}$ where $\rho_{ij} = \langle i|\hat{\rho}|j\rangle$

⁴ $\vec{\sigma} = \sigma_x \hat{x} + \sigma_y \hat{y} + \sigma_z \hat{z}$

⁵ the second element being the sign or parity of the permutation, i.e. number of inversions

⁶ And also the Casimir invariant

projective measurement on a basis state is the combination of two successive different permutations⁷ (e.g. $\hat{s}^+ \hat{s}^- = |\downarrow\rangle \langle \downarrow|$), i.e. $[\hat{s}^+, \hat{s}^-] = |\uparrow\rangle \langle \uparrow| - |\downarrow\rangle \langle \downarrow|$. This shows that the three operators are also cyclic permutations of each others⁸ (up to a phase) and invariant⁹ under the action of \hat{s}^2

$$[\hat{s}_i, \hat{s}_j] = i\varepsilon_{i,j,k} \hat{s}_k, \quad (i, j, k) = \{x, y, z\}, \quad (2.4)$$

where $\varepsilon_{i,j,k}$ is the Levi-Civita permutation symbol. From the commutation rules (2.4), one can recognize the Lie algebra representation. In other words, the operators are the infinitesimal generators of rotations. In this two-level space this means that $\hat{\mathbf{s}}$ is formally equivalent to a spin one-half angular momentum. Our selected two atomic states are not necessarily eigenstates of the total atomic angular momentum but their unitary evolution can still be cast into a fictitious spin rotation description to give a visual geometrical representation (Feynman et al. (1957)). We consider the description of $|\uparrow\rangle, |\downarrow\rangle$ as the two eigenstates of a pseudo spin one-half particle projected along a quantization axis z . With regards to the spin-statistic theorem, note that the pseudo spin one-half particles described here are not physical fermions but *two-mode* bosons.

2.2.3 Collective coherent spin state

We can prepare *all the atoms* in the state $|\rightsquigarrow\rangle$. Our measurement method does not act selectively on a particular atom. We act homogeneously on the ensemble in such a way that the interaction is invariant under exchange or permutation of the atoms, initially all independent. The state of the ensemble is described, in good approximation, by the factorizable state

$$|\psi_{\text{css}}\rangle = |\rightsquigarrow\rangle \otimes |\rightsquigarrow\rangle \otimes |\rightsquigarrow\rangle \dots \otimes^{N_{\text{at}}}, \quad (2.5)$$

$$= \bigotimes_{N_{\text{at}}} \left(\frac{|\uparrow\rangle + |\downarrow\rangle}{\sqrt{2}} \right). \quad (2.6)$$

The previous collective state is known as a coherent spin state. A name following a description of the atomic collective state in terms of the pseudo-spin angular momentum or spinor formalism of the single atom, mentioned above (Dicke (1954)). It is indeed customary to introduce the collective spin operators – sum of the pseudo-spin operators of each individual atom,

$$\hat{J}_i = \sum_{k=1}^{N_{\text{at}}} \hat{s}_i^k, \quad \text{where } i = \{x, y, z\}, \quad (2.7)$$

⁷ also known as the Casimir operators

⁸ $(|\downarrow\rangle \langle \downarrow| - |\uparrow\rangle \langle \uparrow|)(|\downarrow\rangle \langle \uparrow| + |\uparrow\rangle \langle \downarrow|) = (|\downarrow\rangle \langle \uparrow| - |\uparrow\rangle \langle \downarrow|)$

⁹ that is commute with

to describe the ensemble. From (2.4), the collective spin operators satisfy the Heisenberg-Robertson uncertainty inequality

$$(\Delta \hat{\mathcal{J}}_x)^2 (\Delta \hat{\mathcal{J}}_y)^2 \geq \frac{1}{4} \left| \langle [\hat{\mathcal{J}}_x, \hat{\mathcal{J}}_y] \rangle \right|^2 = \frac{1}{4} \left| \langle \hat{\mathcal{J}}_z \rangle \right|^2. \quad (2.8)$$

The previous collective state $|\psi_{\text{css}}\rangle$ is known as a minimum uncertainty state in the sense that it saturates the previous inequality. Therefore, any reduction in uncertainty in one component can be achieved with an identical reciprocal increase in another. In the following section, we explain the non-trivial nature of the collective state and operators introduced above.

2.2.4 Proper complete set of commuting observables

Here, we would like to highlight the very important role of atom permutation or exchange symmetry that applies experimentally for homogeneous interrogation of the ensemble. Indeed, the state space spanned by the tensor product of N_{at} pseudo-spin $s = 1/2$ particle or two-mode bosons is tremendous, $(2s + 1)^{N_{\text{at}}} = 2^{N_{\text{at}}}$. A common basis of states employed to describe the atomic collective state, the so-called Dicke states, is the standard coupled spin basis, i.e the angular states $\{|J, M\rangle\}$ of the total spin operators $\{\hat{\mathcal{J}}_z, \hat{\mathcal{J}}^2\}$. In the case where all the atoms are polarized along the same direction as in $|\psi_{\text{css}}\rangle$ along¹⁰ x , the total spin number attained¹¹ is $J = sN_{\text{at}} = N_{\text{at}}/2$. This provides a Dicke state space of $2J + 1 = N_{\text{at}} + 1$ which is very small compare to $2^{N_{\text{at}}}$ for a large number of atoms. These operators (2.7) are not enough to describe completely the atoms, only the ensemble, that is $\{J, M\}$ do not give enough quantum numbers to describe the state of each atoms. Therefore it is important to stress that $|\psi_{\text{css}}\rangle$ is more than the state of the trivial assembly of N_{at} labelled particles. Due to the exchange symmetry of all independent particles

$$\begin{aligned} |\rightsquigarrow\rangle_1 \otimes |\rightsquigarrow\rangle_2 \otimes \cdots \otimes |\rightsquigarrow\rangle_{N_{\text{at}}} &= |\rightsquigarrow\rangle_2 \otimes |\rightsquigarrow\rangle_1 \otimes \cdots \otimes |\rightsquigarrow\rangle_{N_{\text{at}}} \\ &= \underbrace{\quad \quad \quad}_{N_{\text{at}}! \text{ exchanges}} \end{aligned} \quad (2.9)$$

the total quantum state of the ensemble is a general combination of all these (spatially) permuted states. The symmetry group of $N_{\text{at}}!$ permutations or exchange $P_{i,j}$ of an atom i and an atom j commutes¹² with

¹⁰ Readily, the symmetry of $|\rightsquigarrow\rangle$ is such that it is invariant under (is an eigenstate of) \hat{s}_x .

¹¹ Note that the magnitude of the collective spin is $\sqrt{\langle \hat{\mathcal{J}}^2 \rangle} = \sqrt{J(J+1)} \simeq J = N_{\text{at}}/2$ only when $N_{\text{at}} \gg 1$ and should not be confused with the meaning of the total quantum spin number J .

¹² We have shown for instance, in a different kind of permutation symmetry (of the two atomic modes) above that the permutation operators \hat{s}^+ , \hat{s}^- are also the spherical components of the spin operators, in terms of second quantization, also creation and annihilation operators. The symmetric state $|\rightsquigarrow\rangle$ is both an eigenstate of \hat{s}_x and \hat{s}_y .

the above collective spin operators when the collective state is symmetric under spatial particle exchange. One should read $|\psi_{\text{css}}\rangle$ implicitly as a particular symmetric Dicke state $|J = N_{\text{at}}/2, M = 0\rangle$. If we denote as $\{|n\rangle\}$ the basis vectors used to describe the internal atomic states, then according to the symmetrization postulate, the collective state for an ensemble of N_{at} identical bosons (Dalibard and Basdevant (2005))

$$|\psi\rangle = \frac{Q^{-1}}{\sqrt{N_{\text{at}}!}} \sum_P |1 : n_{P(1)}; 2 : n_{P(2)}; N_{\text{at}} : n_{P(N)}\rangle, \quad (2.10)$$

where the sum is carried over all the $N_{\text{at}}!$ particle permutation P . $Q = \sqrt{N_1!N_2!\dots}$ is the constant factor given by the occupation numbers of the different internal states. If all the atoms occupy the internal state $|\rightsquigarrow\rangle$

$$|\psi\rangle = \frac{1}{N_{\text{at}}!} \sum_P |\rightsquigarrow\rangle_1 \otimes |\rightsquigarrow\rangle_2 \otimes \dots \otimes |\rightsquigarrow\rangle_{N_{\text{at}}}, \quad (2.11)$$

and from (2.9)

$$|\psi\rangle = |\rightsquigarrow\rangle^{\otimes N_{\text{at}}} \left(\frac{1}{N_{\text{at}}!} \sum_P 1 \right) \equiv |\psi_{\text{css}}\rangle.$$

From (2.11), the collective state is clearly seen as a constructive interference between all possible (spatial) permutations of the atoms. Such collective superposition is in general sensitive to leak of information that localizes atoms. Conversely, they can be prepared by heralding information, which do not distinguish the atoms and is a common experimental strategy to create higher symmetric Dicke state, e.g. W state for instance Haas et al. (2014); Laurat et al. (2007); Duan et al. (2001).

The robustness of the many-body or collective states with respect to single-body loss depends on the type of delocalized symmetry encoded in the underlying ensemble of atoms. For the coherent superposition state ((2.11)), a loss of an atom is simply equivalent to a loss of only one independent (factorizable) part of the collective state, reducing its size.

In our case and for more general interatomic interference effects (sub/superadiance), permutation symmetry of locally indistinguishable atoms is central (Crubellier et al. (1985)).

2.2.5 Partition projection noise

After the preparation of the collective coherent spin state, we perform a measurement on the ensemble. At some places, I may unfortunately continue to speak in terms of individual atoms in the ensemble although we can only speak objectively about the state of the ensemble, here made of N_{at} atomic independent parts ((2.5)).

We have developed experimental methods based on optical light dispersive interaction with the atoms which allow us to sense the number of atoms populating the states $|\uparrow\rangle$, $|\downarrow\rangle$.

Quantum mechanics forces us to only talk about ensemble average, and the above state of knowledge described earlier has only a statistically meaning. The success probability p to find a given atomic partition in the upper state $|\uparrow\rangle$, after a projective measurement when in the initial state $|\rightsquigarrow\rangle$, is given by the square modulus $|\langle\uparrow|\rightsquigarrow\rangle|^2 = p = 1/2$. This is also the probability to find it in the lower state $|\langle\downarrow|\rightsquigarrow\rangle|^2 = 1/2 = 1 - p$ if we were to measure that one as well. Therefore a measurement of the population of a given state is uncertain and when carried out on an ensemble of such independent partition $|\rightsquigarrow\rangle$, that is $|\psi_{\text{css}}\rangle$, the outcomes will be binomially distributed.

The probability to successfully find N_{\uparrow} atoms in the state $|\uparrow\rangle$ in an ensemble of N_{at} in the collective coherent spin state will be

$$\begin{aligned} p(N_{\uparrow}) &= \frac{N_{\text{at}}!}{N_{\uparrow}!(N_{\text{at}} - N_{\uparrow})!} p^{N_{\uparrow}} (1 - p)^{N_{\text{at}} - N_{\uparrow}}, \\ &= \frac{N_{\text{at}}!}{N_{\uparrow}!(N_{\text{at}} - N_{\uparrow})!} 2^{-N_{\text{at}}}. \end{aligned}$$

The mean and variance of the binomial distribution are given respectively by $N_{\text{at}}p$ and $N_{\text{at}}p(1 - p)$. Hence the expectation value of N_{\uparrow} for the coherent spin state will be $\langle N_{\uparrow} \rangle = N_{\text{at}}/2$ and its variance $(\delta N_{\uparrow})^2 = N_{\text{at}}/4$. This intrinsic statistical uncertainty of the measurement results of N_{\uparrow} is known as projection noise and is fundamentally linked to the nature of the collective state. For large ensembles of atoms, the binomial distribution can be well approximated by a Gaussian or normal distribution (with $p(N_{\uparrow} > N_{\text{at}}) = 0$). The projection noise will then be modelled by a fundamental Gaussian white noise in the experimental measurements.

2.2.6 Population difference measurement

In one experiment, we have been measuring the population difference between the two atomic states. With the previous single state measurement, an unsuccessful measurement outcome cannot be distinguished simultaneously for either $|\rightsquigarrow\rangle$ has collapsed in the complementary state $|\downarrow\rangle$ or the physical particle got lost. The population difference measurement on the ensemble, which can be represented by the operator¹³ as

$$\hat{\mathcal{M}} = \sum_{k=1}^{N_{\text{at}}} (|\downarrow\rangle\langle\downarrow| - |\uparrow\rangle\langle\uparrow|)_k = 2\hat{\mathcal{J}}_z,$$

¹³ The notation $\hat{\mathcal{M}}$ is inspired from the M quantum number of the total spin projection, up to a factor of 2 to remain the population difference.

will be less sensitive to classical fluctuations in the total number of atoms¹⁴. The expectation of the measurement here is $\langle \psi_{\text{css}} | \hat{\mathcal{M}} | \psi_{\text{css}} \rangle = 0$ and its fluctuations will have a variance of $(\langle \psi_{\text{css}} | \hat{\mathcal{M}}^2 | \psi_{\text{css}} \rangle - 0) = N_{\text{at}}$.

2.3 ATOMIC STATE DETECTION

As a concrete implementation of the previous measurements, we experimentally interrogate the population of the two atomic states through optical light probes propagating in the ensemble. When the properties of the probes match the selection rules for a transition from one of the two atomic states $|\downarrow\rangle$ or $|\uparrow\rangle$ to a higher optical excited state of the rich internal energy level structure of the atom we have thus ignored, two well-known phenomena occur on the light probes in the linear interaction regime, namely absorption and dispersion.

The lifetime of the quantum coherence of the atomic state superpositions is ultimately limited by the measurement back-action, often dominated by incoherent spontaneous scattering processes due to probing. We will now go through a basic description of the light-atom interaction with a focus on the detection of the dispersion, or atom induced optical phase shift of light. The dispersion measurement allows to minimize incoherent scattering events without compromising too much the signal-to-noise ratio of the atomic population detection compared to an absorption or fluorescence measurement, while preserving the indistinguishability of the atoms. The signal-to-noise ratio (SNR) of the optical phase shift detection method is limited by the intrinsic quantum noise of the light probes and scales as the square root of spontaneous emission for coherent states of light.

2.3.1 Atomic medium delay and attenuation

Again, for clarity of the concepts and figures of merit we neglect details that add unnecessary complexity. We consider the ensemble of atoms as a dilute homogeneous isotropic medium. We send through the ensemble an optical light probe off-resonant to the adequate above mentioned atomic transition and weaken the light intensity to have a linear response. The general macroscopic response of the ensemble is characterized by a complex index of refraction n , the imaginary part of which is associated with dissipation (absorption). This means for the positive frequency part of the electric field of a transverse plane wave travelling along z with wave-vector $\mathbf{k} = \omega n(\omega) \mathbf{z} / c$ and optical angular frequency ω ,

$$E(z, t)^{(+)} = E_0 e^{-i\omega t} e^{ikz} = E_0 e^{-\frac{\alpha(\omega)}{2} z} e^{-i(\omega t - z/c)} e^{i\varphi(z, \omega)},$$

where $\varphi(z, \omega)$ is the extra phase delay compared to free propagation in vacuum and α the intensity ($\propto |E|^2$) absorption coefficient per unit

¹⁴ $\text{var}(N_{\uparrow} - N_{\downarrow}) = \text{var}(2N_{\uparrow} - N_{\text{at}})$

length. To relate the refractive index to the atomic polarization response, we introduce the isotropic dielectric susceptibility $\chi(\omega)$, which is in general small. Thus we identify

$$\alpha(\omega) = \frac{\omega}{c} \text{Im}(\chi(\omega)) = \frac{2\pi}{\lambda_0} \text{Im}(\chi(\omega)), \quad (2.12)$$

$$\varphi(z, \omega) = \frac{\omega}{2c} z \text{Re}(\chi(\omega)) = \frac{z\pi}{\lambda_0} \text{Re}(\chi(\omega)), \quad (2.13)$$

$$\text{from } n = (1 + \chi)^{1/2} \simeq 1 + \frac{\text{Re}(\chi) + i\text{Im}(\chi)}{2},$$

where c and λ_0 is the speed and light wavelength in vacuum.

We could explain χ in terms of the optical atomic transition properties from a classical Lorentz model of damped harmonic oscillators. In view of further generalization, we adhere to the quantum formalism.

2.3.2 Atom response principle

For instance, the classical or expectation value of each atomic dipole $\hat{\mathbf{p}} = -e\hat{\mathbf{r}}$ under the influence of the electric field is simply given using the density matrix formalism by the trace¹⁵

$$\langle \hat{\mathbf{p}} \rangle = \text{tr}(\boldsymbol{\rho} \mathbf{p}) = \text{tr}(\boldsymbol{\rho} |e\rangle\langle g|) \vec{p} + c.c. = \vec{p} \rho_{ge} + c.c.,$$

where $\boldsymbol{\rho}$ and \mathbf{p} are the matrix representations of the respective operators in the same basis, here the ground and excited state pair ($|g\rangle, |e\rangle$). $\boldsymbol{\rho}$ describes the state of the atom which evolves according Schrödinger's or von Neumann-Liouville's equation as

$$\frac{\partial \boldsymbol{\rho}}{\partial t} = \frac{[\mathbf{H}, \boldsymbol{\rho}]}{i\hbar}, \quad \mathbf{H} = \mathbf{H}_0 - \hat{\mathbf{p}} \cdot (\mathbf{E}^+ + \mathbf{E}^-),$$

$$\mathbf{E}^+ = \vec{\epsilon} E_0 e^{i(kz - \omega t)}, \quad \Omega = \frac{\vec{p} \cdot \mathbf{E}^+}{\hbar}, \quad \vec{p} = \langle e | \hat{\mathbf{p}} | g \rangle.$$

In practice, atoms are never alone, they are dressed by the fluctuating vacuum electromagnetic field. The resulting irreversible evolution of the atom in excited energy levels is taken into account via Fermi golden¹⁶ rule giving the probability to remain at time t in an atomic excited energy level as $1 - \gamma(\omega, p)t$, (here $\dot{\rho}_{ee} = -\gamma\rho_{ee}$).

All the above yields¹⁷ the well-known result (Grynberg et al. (2010))

$$\rho_{eg} = -\Omega \frac{\Delta - i\gamma/2}{\Delta^2 + (\gamma/2)^2 + 2|\Omega|^2},$$

¹⁵ Atoms in a dilute gas possess inversion symmetry. The energy eigenstates of the atom are then either symmetric or antisymmetric, that is $\langle g | \hat{\mathbf{r}} | g \rangle = \langle e | \hat{\mathbf{r}} | e \rangle = \vec{0}$. This also means that an atom in a stable (energy) state has no permanent dipole moment. It needs to be dressed by an external field in order to have a non-zero average moment. And this symmetry can be broken in a solid.

¹⁶ The irreversibility, in contrast to the time-reversal Rabi oscillation phenomenon, arises from the coupling between discrete energy levels to a continuum.

¹⁷ Within the rotating-wave approximation.

where $\Delta = (\omega_{ge} - \omega)$ is the angular frequency detuning between the atomic transition frequency and the light frequency. A volume density of atoms ϱ_{at} will give rise to a macroscopic polarization¹⁸ $\vec{\mathbf{P}} = \varrho_{\text{at}} \langle \hat{\mathbf{p}} \rangle = \epsilon_0 \chi \vec{\mathbf{E}}$, this latter relation holding for a dilute¹⁹ medium.

Projection onto \vec{p} gives $\chi = \varrho_{\text{at}} \rho_{eg} \|\vec{p}\|^2 / (\epsilon_0 \Omega \hbar)$ which from (2.13) leads to

$$\varphi(z, \omega) = \frac{z\pi}{\lambda_0} \text{Re}(\chi(\omega)) = \left(-\frac{z\pi \varrho_{\text{at}}}{\lambda_0 \epsilon_0 \hbar} \right) \|\vec{p}\|^2 \frac{\Delta}{\Delta^2 + (\gamma/2)^2 + 2|\Omega|^2}, \quad (2.14)$$

$$\alpha(\omega) = \frac{2\pi}{\lambda_0} \text{Im}(\chi(\omega)) = \left(\frac{2\pi \varrho_{\text{at}}}{\lambda_0 \epsilon_0 \hbar} \right) \|\vec{p}\|^2 \frac{(\gamma/2)}{\Delta^2 + (\gamma/2)^2 + 2|\Omega|^2}. \quad (2.15)$$

The atomic dipole strength $\|\vec{p}\|^2$ plays a central role. For this basic two-level atom model, γ is fundamentally connected to it via Fermi rule, that is here to the free space density of electromagnetic field modes near λ_0 as

$$\gamma = \frac{8\pi^2}{3\hbar\epsilon_0\lambda_0^3} \|\vec{p}\|^2. \quad (2.16)$$

This allows to rewrite all the above detectable quantities in terms of the experimentally known value of γ .

2.3.3 Characteristic parameters

Most of the figure of merits and physical mechanisms of our light atomic ensemble interface are contained in the previous simple model. Experimentally, we want to obtain the highest atomic signal possible. First of all, we weaken the probe light intensity such that $(|\Omega|^2)$ has a negligible contribution. Otherwise the light intensity would saturate and broaden the atomic response. This fixes the dynamic range of light input intensity for linear atomic response. The saturation intensity being usually defined at the **3 dB** compression point of the atomic response.

Below saturation, we have in this linear regime,

$$\chi(\Delta) \simeq \left(\varrho_{\text{at}} \frac{3\gamma\lambda_0^3}{8\pi^2} \right) \frac{i(\gamma/2) - \Delta}{\Delta^2 + (\gamma/2)^2}, \quad \beta = \left(\frac{\gamma}{2\Delta} \right), \quad (2.17)$$

$$\alpha(\beta) = \alpha_0 \frac{(\gamma/2)^2}{\Delta^2 + (\gamma/2)^2} = \alpha_0 \beta^2 (1 + \beta^2)^{-1}, \quad (2.18)$$

$$\varphi(z, \beta) = -\frac{\alpha_0}{2} z \frac{(\gamma/2)\Delta}{\Delta^2 + (\gamma/2)^2} = -\frac{\alpha_0}{2} z \beta (1 + \beta^2)^{-1}. \quad (2.19)$$

The intensity absorption coefficient per unit length achieves its maximum value $\alpha_0 = 3\varrho_{\text{at}}\lambda_0^2/(2\pi)$ for $\Delta = 0$ where φ vanishes. After

¹⁸ see Maxwell-Gauss relation $\nabla \cdot \mathbf{E} = -\nabla \cdot \mathbf{P} / \epsilon_0$

¹⁹ See the general Clausius-Mossotti relation.

propagation in the atomic sample over a physical linear length l , the intensity of the light probe beam is attenuated by a factor $e^{-\alpha l}$, while its phase has accumulated a delay $\varphi(l) = -\alpha l / (2\beta)$.

The above results provide signals that are sensitive to the population of the atomic ground state by directly measuring the fraction of absorbed probe photons from $N_{\text{ph}}^o / N_{\text{ph}}^i = e^{-\alpha l}$ where N_{ph}^i (resp. N_{ph}^o) is the number of input (resp. output) probe photons or by measuring the number of scattered photons $N_{\text{sc}} = (N_{\text{ph}}^i - N_{\text{ph}}^o)$ and as well as by detecting the imprinted phase shift $\varphi(l)$ independent of the number of probe photons in this linear approximation.

All signal strengths depend on the characteristic quantity of the probing, namely the optical penetration depth of an atomic sample of length l , $d = \alpha l$. Below saturation, the optical depth (OD) is independent of the incident number of photons and only depends on the overlap between the probe beam and the atom spatial distribution.

As long as spontaneous emission is a single-atom effect, the number of scattered photons in the probe volume is the same as the number of atoms which have been scattered. Therefore, in view to preserve quantum superposition of atomic ground states from decoherence induced by these incoherent scattering events, the total average number of scattering events during the interrogation time has to be kept low. Hence the average number of scattering events per atom $n_{\text{sc}} = N_{\text{sc}} / N_{\text{at}} \leq 1$. For atom number measurement and a cyclic atomic transition, this number can be great, limited by plain recoil heating moving the atoms out of the probe beam volume and again ultimately limited by the saturation of the transition. The heating effects due to the optical detection triggered the development of nondestructive techniques (Andrews et al. (1996)) that measure the phase shift imprinted on the forward scattered probe photons rather than measuring absorption or fluorescence (scattered photons). However, the sensitivity or SNR of the underlying interferometric measurement of the phase shift does not necessarily perform better and sometimes worse than that of fluorescence measurement techniques (Lye et al. (2003)). We therefore discuss in the next section within which parameter regime and experimental constraints does the phase shift measurement appear advantageous.

2.3.4 Phase shift measurement advantage

To preserve the symmetry of the collective atomic state under particle exchange, it is important to have no prediction power over the positions of the atoms. To keep the indistinguishability of the atoms, it is important that the light probe interacts homogeneously with the ensemble.

To make all the atoms participate equally²⁰ in the interaction and thereby enhancing their collective effects and minimizing the leak of

²⁰ Maximize the symmetry

local information into the environment, the spatial variation of the number of probe photons can be reduced by detuning the probe light far from the atomic resonance, i. e. by reducing $\beta = \gamma/(2\Delta)$. The fraction of scattered photons becomes in this limit ($d(\beta)$ smaller than 1)

$$\frac{N_{\text{ph}}^i - N_{\text{ph}}^o}{N_{\text{ph}}^i} = 1 - e^{-d(\beta)} \simeq d_0 \beta^2 = d_0 \left(\frac{\gamma}{2\Delta}\right)^2, \quad (\Delta \gg \gamma/2) \quad (2.20)$$

where we have introduced the ensemble on-resonant optical depth $d_0 = \alpha_0 l$. The number of scattered photons will be significant when it is bigger than the intrinsic quantum photon shot noise of the probe light. The above far-off-resonant detuning renders the atomic ensemble transparent during light propagation. It can be made so transparent that it is not possible to distinguish it from the inherent light shot noise, setting at the same time a lower limit in the resolution of atomic state detection based on intensity measurement.

However, while the absorption signal in this limit decays as $1/\Delta^2$, the phase shift decays slower as $1/\Delta$

$$\varphi \simeq -\frac{\alpha_0}{2} l \beta = -\frac{d_0}{4} \frac{\gamma}{\Delta}. \quad (2.21)$$

We will see in the next chapter that our interferometric detection of the optical phase is fundamentally limited by photon shot noise to $\delta\varphi = 1/(2\sqrt{N_{\text{ph}}})$. This gives a fundamental limit to the achievable SNR as²¹

$$\frac{|\varphi|}{\delta\varphi} = d_0 \frac{\gamma}{2\Delta} \sqrt{N_{\text{ph}}} = d_0 \sqrt{\left(\frac{\gamma}{2\Delta}\right)^2 N_{\text{ph}}} = \sqrt{d_0} \sqrt{N_{\text{sc}}}. \quad (2.22)$$

As promised earlier, we show with our simple model that the SNR of atomic energy states detection via measurement of optical phase shift scales fundamentally as the square root of the integrated number of spontaneous emission events (for a coherent state of light). This is valid as long as the on-resonant optical depth remains independent of the number of probe photons (linear regime). Thus the previous result means that if the number of scattering events is constrained, only increasing the on-resonant optical depth helps the measurement precision in the far-off resonant limit.

In addition, since the SNR of the ideal (maximal collection efficiency) record of scattered photons is limited to $\sqrt{N_{\text{ph}}}$ due to intensity shot noise, the dispersive detection becomes advantageous compared to fluorescence detection only for optically thick enough ensembles which satisfy $d_0 \gg \Delta/(\gamma/2)$.

On the other hand $\Delta/(\gamma/2) \gg \sqrt{d_0}$ is required (see (2.20)) for transparency or homogeneous interaction. Therefore, only ODs larger than one are relevant for such experimental schemes.

²¹ Here N_{sc} is given by (2.20) at the same approximation order as φ .

For a given constrained number of scattering events, it is possible to increase the detuning (if other atomic levels are far apart) and reciprocally increasing the number of probe photons without compromising phase detection SNR, as shown by (2.22). This has the merit to offer flexibility in the detection bandwidth by increasing the probe power and reducing the interrogation time in order to overcome uncontrolled dynamics of the atomic signals. However, the probe power is bound to a maximum value for validity of the linear regime or non-saturation of the atomic response.

Note that when the ensemble is not optically thin enough, incoherently scattered photons have a non-negligible probability to be reabsorbed by other surrounding atoms, a phenomenon known as radiation trapping that makes spontaneous emission more detrimental²².

For large resonant ODSs, an experiment based on the measurement of the optical phase is suited for many tasks that require orders of magnitude flexibility in the allowed number of scattering events while providing a light shot noise limited sensitivity over a widely tunable measurement bandwidth.

2.3.5 Projection noise limited measurement

We have seen earlier that if the ensemble of atoms is prepared in the collective coherent spin state, the estimation of the population of one of the atomic ground states, for instance $|\uparrow\rangle$, will contribute to a mean phase shift signal via $\langle N_\uparrow \rangle = N_{\text{at}}/2$. When introducing the effective cross-sectional probe area A , N_{at} corresponds to the number of atoms in the probe volume $V = Al$ as $N_{\text{at}} = \rho_{\text{at}}V$ for our simplified probe mode geometry. The on-resonant optical depth becomes $d_0 = l\alpha_0 = 3N_{\text{at}}\lambda_0^2/(2\pi A) = \sigma_0 N_{\text{at}}/A$, where we have introduced the resonant single-atom absorption cross-section²³ $\sigma_0 = 3\lambda_0^2/(2\pi)$. From (2.21), the expectation value of the phase shift when probing the upper state for an ensemble prepared in the collective state $|\psi_{\text{css}}\rangle$, is then

$$\langle \varphi \rangle = -\frac{\langle d_{0\uparrow} \rangle \gamma}{4 \Delta} = -\frac{\gamma}{4\Delta} \sigma_0 \frac{\langle N_\uparrow \rangle}{A} = -\left(\frac{\gamma}{4\Delta} \frac{\sigma_0}{A} \right) \frac{N_{\text{at}}}{2}. \quad (2.23)$$

The fundamental statistical variance of the measurement due to the projection noise will be

$$(\delta\varphi)_{\text{at}}^2 = \left(\frac{\gamma}{4\Delta} \frac{\sigma_0}{A} \right)^2 (\delta N_\uparrow)^2 = \left(\frac{\gamma}{4\Delta} \frac{\sigma_0}{A} \right)^2 \frac{N_{\text{at}}}{4}.$$

As already mentioned earlier, the total phase shift measurement is fundamentally limited by the intrinsic light shot noise of the probe light, such that the total observed variance will be

$$(\delta\varphi)^2 = (\delta\varphi)_{\text{at}}^2 + (\delta\varphi)_{\text{light}}^2 = \left(\frac{\gamma}{4\Delta} \frac{\sigma_0}{A} \right)^2 \frac{N_{\text{at}}}{4} + \frac{1}{4N_{\text{ph}}}. \quad (2.24)$$

²² Not a single-atom effect anymore

²³ for a closed transition

Clearly, one resolves and at the same time reaches a fundamental atomic projection noise limited precision when $\kappa^2 = (\delta\varphi)_{\text{at}}^2 / (\delta\varphi)_{\text{light}}^2$ becomes larger than one. Here,

$$\kappa^2 = 4 \left(\frac{\gamma}{4\Delta} \frac{\sigma_0}{A} \right)^2 N_{\text{ph}} (\delta N_{\uparrow})^2 = \left(\frac{\gamma}{2\Delta} \frac{\sigma_0}{A} \right)^2 N_{\text{ph}} \frac{N_{\text{at}}}{4}. \quad (2.25)$$

From (2.20), the number of scattered photons

$$N_{\text{sc}} = N_{\text{ph}}^i - N_{\text{ph}}^o = \frac{\sigma_0 \langle N_{\uparrow} \rangle}{A} \left(\frac{\gamma}{2\Delta} \right)^2 N_{\text{ph}}^i,$$

allows to write (2.25)

$$\kappa^2 = \frac{1}{2} d_0 \frac{N_{\text{sc}}}{N_{\text{at}}} = \frac{d_0}{2} n_{\text{sc}} = d_{0\uparrow} n_{\text{sc}}, \quad (2.26)$$

where we have introduced the number of scattered photons per atom n_{sc} and the resonant optical depth of the interacting atomic population $d_{0\uparrow} = \sigma_0 \langle N_{\uparrow} \rangle / A$. For a population difference measurement where the probe photons interact equally with the two ground states $|\uparrow\rangle, |\downarrow\rangle$, one would improve $\kappa^2 = d_0 n_{\text{sc}}$ by a factor of 2. We note that $d_{0\uparrow} = d_0$ if all the N_{at} atoms are prepared in the state $|\uparrow\rangle$. However in this case $\kappa^2 = 0$ as the variance of the collective population measurement $\hat{N}_{\uparrow} = \sum_{k=1}^{N_{\text{at}}} |\uparrow\rangle \langle \uparrow|_k$ as well as $\hat{\mathcal{M}}$ on the collective state $|\uparrow\rangle^{\otimes N_{\text{at}}}$ is 0 (hence $(\delta\varphi)_{\text{at}}^2 = 0$). Conversely, we could interpret κ^2 from the mutual point of view that the atoms are now used as a meter on the coherent state of light. Indeed one can write

$$\kappa^2 = d_0 n_{\text{sc}} = \mathbf{x}_0 \epsilon_{\text{sc}}, \quad \epsilon_{\text{sc}} = \frac{\sigma_0 N_{\text{at}}}{A} \left(\frac{\gamma}{2\Delta} \right)^2, \quad (2.27)$$

where $\mathbf{x}_0 = \sigma N_{\text{ph}} / A$ is a resonant atomic depth and ϵ_{sc} the number of scattered atoms per photon. Here, we have $N_{\text{at}} n_{\text{sc}} = N_{\text{ph}} \epsilon_{\text{sc}}$. Continuing with our simple model, we now show one way to overcome the previous atomic projection noise limit in the estimation of \hat{N}_{\uparrow} or $\hat{\mathcal{M}}$ with QND probing via continuous time measurement of φ (entanglement-assisted metrology).

2.4 CONDITIONAL SPIN-SQUEEZING

The previous model allows to give a simple presentation of the fundamental limit of measurement precision based on coherent states of atoms and coherent states of light. Aside the fact that the predicted limited precision is based on a *prior* knowledge of the state of both the probe light field and of the collective atomic state, it is impractical. This is because quantum mechanics forces us to talk only about ensemble averages which are never fully realized. After three years of insights, I am going to present a visual approach to the conditional reduction of atomic projection noise via optical QND measurement as achieved in Appel et al. (2009b); Schleier-Smith et al. (2010).

2.4.1 *Time continuous measurement*

Experimentally we cannot record data for an infinite amount of time, nor repeat the same experiment infinitely. We have only access to a finite number of realizations from which we estimate all the previous expectation values as well as their uncertainty. In particular the measurement of the phase shift as obtained via homodyne detection, to be presented in details in the next chapter, should be considered as a continuous time record of the atomic population operator outcomes as produced by the instantaneous collective state of the atomic ensemble. In other words, the continuous measurement of the phase will be considered as a process producing a phase variable φ randomly sampled from the initial or prior probability distribution which is dictated by quantum mechanics for the underlying operator $p_i(\hat{\mathcal{M}})$ or $p_i(\hat{\mathcal{N}}_\uparrow)$. Only for a large number of identically prepared coherent spin states $|\psi_{\text{css}}\rangle$ will the distribution $p(\varphi)$ reproduce $p_i(\hat{\mathcal{M}})$.

2.4.2 *Light noise contaminated sample*

For a given experimental realization, we *estimate* the outcome \mathcal{M} of $\hat{\mathcal{M}}$ with the phase data sampled from a detector photocurrent, which is host of the random arrival of probe photons. This random arrival of photons leads to a stochastic fluctuating offset $\delta\varphi(t)$ on the detected phase shift φ . This noisy offset would average to 0 if we could integrate the photocurrent over an infinite time. This corresponds to perform an ideal ensemble average over an infinitely long coherent state of light with constant power. Since this is not realistic, each event of $p(\hat{\mathcal{M}})$ is blurred by a random variable $\delta\varphi(t)$. This calls for quantum filtering theory and Bayesian inference as well presented in [Geremia et al. \(2006\)](#) to optimally extract information from the quantum noise.

By averaging the continuous phase measurement over the interrogation time τ , we can give a “better” estimate of the random outcome of $\hat{\mathcal{M}}$ via the mean of the instantaneous sampled phase values

$$\varphi_s^\tau = \frac{1}{\tau} \int_0^\tau \varphi_s(t) dt = \varphi_{\text{at}}^\tau + \delta\varphi^\tau, \quad (2.28)$$

where $\delta\varphi^\tau$ is a random phase offset drawn from the probability distribution $p(\delta\varphi^\tau)$ of N_{ph} photon arrivals during the time τ . Experimentally this duration can correspond to the time length of a probe square pulse of light sent through the atomic ensemble. For sufficiently large enough N_{ph} value, $p(\delta\varphi^\tau)$ can be considered gaussian or normally distributed by extension of the Poissonian distribution of photons in a coherent state of light.

2.4.3 Bayesian estimation

From our sample mean estimator φ_s^τ we can now infer knowledge about the atomic state by estimating the probability distribution $p(\hat{\mathcal{M}})$ conditioned on the observation φ_s^τ . This allows to test the prior hypothesis or belief about the collective atomic state. According Bayes rule of inference, the probability distribution $p(\mathcal{M}|\varphi_s^\tau)$ of a given outcome \mathcal{M} of the operator $\hat{\mathcal{M}}$ based on the measured sample mean φ_s^τ is

$$p(\mathcal{M}|\varphi_s^\tau) = \frac{p(\varphi_s^\tau|\mathcal{M})p_i(\mathcal{M})}{p(\varphi_s^\tau)}, \quad (2.29)$$

where $p_i(\mathcal{M})$ is the initial prior distribution, $p(\varphi_s^\tau|\mathcal{M})$ the conditional probability to observe the value φ_s^τ from a given outcome \mathcal{M} of the operator $\hat{\mathcal{M}}$ and $p(\varphi_s^\tau)$ the unconditional probability distribution of the measurement φ_s^τ that is

$$p(\varphi_s^\tau) = \int p(\varphi_s^\tau|\mathcal{M})p_i(\mathcal{M}) d\mathcal{M}. \quad (2.30)$$

Clearly, $p(\varphi_s^\tau|\mathcal{M})$ is given by the probability distribution of the noisy phase offset or light shot noise $p(\delta\varphi^\tau)$. As mentioned earlier this can be represented by quantum gaussian white noise

$$p(\delta\varphi^\tau) \sim \mathcal{N}(0, \sigma_l^2) = \frac{1}{\sqrt{2\pi\sigma_l^2}} \exp\left(-\frac{(\delta\varphi^\tau)^2}{2\sigma_l^2}\right), \quad \text{where } \sigma_l^2 = \frac{1}{4\langle N_{\text{ph}} \rangle}$$

with $\langle N_{\text{ph}} \rangle = \Phi\tau$ the number of photons in the time τ for a constant input photon flux Φ . For the moment, we assume that the information about the outcome value \mathcal{M} contained in the time average quantity φ_{at}^τ is faithful²⁴ to the prior probability distribution of $p_i(\mathcal{M})$. Indeed, we neglected for the moment the action of light on the collective atomic state, any measurement back-action, as well as all other perturbation by the environment during the interrogation time τ (limit of small time). In addition, (2.28) implicitly assumes the atomic phase shift and light phase noise smaller than π , i. e. the linearisation of the homodyne signal near the point of highest phase sensitivity²⁵. Because the relevant phase shift signal is independent of the probe photon number within all the above conditions $\varphi_{\text{at}}^\tau = k\mathcal{M}$, $k = -\gamma\sigma_0/(4A\Delta)$ (see (2.23)), it is also independent of the random arrival of photons and of the probe time (as $N_{\text{ph}} = \tau\Phi$). For a sufficiently large number of atoms N_{at} , $p_i(\mathcal{M})$ can also be extended to a normal/gaussian distribution with a variance given by the atomic projection noise $\sigma_{\mathcal{M}}^2 = N_{\text{at}}$ and $\langle \mathcal{M} \rangle = 0$.

$$p_i(\mathcal{M}) \sim \mathcal{N}(\langle \mathcal{M} \rangle, \sigma_{\mathcal{M}}^2) = \frac{1}{\sqrt{2\pi\sigma_{\mathcal{M}}^2}} \exp\left(-\frac{(\mathcal{M} - \langle \mathcal{M} \rangle)^2}{2\sigma_{\mathcal{M}}^2}\right).$$

²⁴ Or at least, that there is a deterministic link between the two, that is fully time correlated to the prior distribution.

²⁵ Otherwise, the observation variable will be a trigonometric function of the atomic variable and non-linear filtering theory should be used

From $p(\varphi_s^\tau|\mathcal{M}) \sim p(\delta\varphi^\tau = \varphi_s^\tau - k\mathcal{M})$, the unconditional measurement distribution $p(\varphi_s^\tau)$ (2.30) is therefore a convolution of two gaussian distributions creating a new gaussian distribution with variance equal to the sum of the variance of $p(\varphi_s^\tau|\mathcal{M})$ and of $p_i(\mathcal{M})$, that is the sum of the phase light noise power and the atomic projection phase noise power. Such is the distribution of the sum of two normally distributed random variables ($\varphi_{\text{at}}^\tau + \delta\varphi^\tau$).

Using the well-known gaussian integrals formula²⁶, we find

$$p(\varphi_s^\tau) = \frac{1}{\sqrt{2\pi(k^2\sigma_{\mathcal{M}}^2 + \sigma_l^2)}} \exp\left(-\frac{(\varphi_s^\tau)^2}{2(k^2\sigma_{\mathcal{M}}^2 + \sigma_l^2)}\right). \quad (2.31)$$

The variance of the estimated distribution $p(\mathcal{M}|\varphi_s^\tau)$ is therefore readily obtained from (2.29) and (2.31)

$$\sigma_{\mathcal{M}|\varphi_s^\tau}^2 = \int (\mathcal{M} - \langle \mathcal{M}(\varphi_s^\tau) \rangle)^2 p(\mathcal{M}|\varphi_s^\tau) d\mathcal{M}, \quad (2.32)$$

or given more directly by writing down the expression ((2.29)) of the newly found probability distribution readily gaussian

$$p(\mathcal{M}|\varphi_s^\tau) = \frac{1}{\sqrt{2\pi}} \sqrt{\frac{k^2\sigma_{\mathcal{M}}^2 + \sigma_l^2}{\sigma_{\mathcal{M}}^2\sigma_l^2}} \exp\left(-\frac{k^2\sigma_{\mathcal{M}}^2 + \sigma_l^2}{2\sigma_{\mathcal{M}}^2\sigma_l^2} (\mathcal{M} - \mathcal{M}_0)^2\right), \quad (2.33)$$

with the following constant being introduced

$$\mathcal{M}_0 = \varphi_s^\tau k \frac{\sigma_{\mathcal{M}}^2}{k^2\sigma_{\mathcal{M}}^2 + \sigma_l^2}. \quad (2.34)$$

We will now discuss the most significant characteristics of this distribution, that is its mean and variance.

2.4.4 Degree of squeezing

Using the above, we arrive at the important result for the variance of the estimated atomic population distribution conditioned on a dispersive light shot noise limited measurement,

$$\sigma_{\mathcal{M}|\varphi_s^\tau}^2 = \frac{\sigma_{\mathcal{M}}^2\sigma_l^2}{\sigma_l^2 + k^2\sigma_{\mathcal{M}}^2} = \sigma_{\mathcal{M}}^2\xi^2, \quad \xi^2 = \frac{\sigma_l^2}{\sigma_l^2 + k^2\sigma_{\mathcal{M}}^2} \quad (2.35)$$

In the previous expression, we deliberately singled out the factor $\xi^2 = \sigma_{\mathcal{M}|\varphi_s^\tau}^2/\sigma_{\mathcal{M}}^2$ in such a way that it quantifies the reduction of uncertainty, the degree of squeezing, which is defined here as the fractional variance of the estimated population measurement with respect to the prior

²⁶ $\int e^{-ax^2-bx} dx = \sqrt{\frac{\pi}{a}} e^{\frac{b^2}{4a}}$ for $(a > 0)$.

variance. Starting with atoms prepared in the collective coherent spin state, we see that the degree of squeezing

$$\xi^2 = \left(1 + \frac{k^2 \sigma_{\mathcal{M}}^2}{\sigma_l^2}\right)^{-1} = \frac{1}{1 + \kappa^2}, \quad (2.36)$$

is given by κ^2 introduced earlier, which is the ratio between the phase noise due to atomic projection noise and the phase noise due to light shot noise. It is clear that if nothing perturbs the collective state, some squeezing is always achieved by continuous measurement.

It is obvious that by averaging over a longer period of time than τ , the phase noise due to the light shot noise will be reduced. If nothing else changes, κ^2 will increase as much and the estimation precision of the population measurement will improve. It is also clear with the previous general Bayesian approach, that the essence of conditional spin-squeezing or the reduction of uncertainty requires the notion of a past/prior knowledge. Without starting in a minimum uncertainty state or coherent spin state (CSS), it is much harder to beat the standard quantum limit (SQL) of measurement precision defined by the fundamental noise level of the collective state CSS.

2.4.5 Degree of shift and future prediction

We note that, besides the previous reduction of the variance compared to the one of the prior distribution $p_i(\mathcal{M})$, the mean value $\langle \mathcal{M} \rangle$ initially zero for a CSS is shifted by an amount \mathcal{M}_0 (see (2.34)). This is remarkable as the mean of a gaussian distribution is also the most probable outcome. This tells that the most likely phase shift to observe in the future conditioned on the above measurement should be $\varphi_0 = k\mathcal{M}_0$. We can write it from (2.34) and (2.36) as

$$\varphi_0 = k\mathcal{M}_0 = \varphi_s^\tau k^2 \frac{\sigma_{\mathcal{M}}^2}{k^2 \sigma_{\mathcal{M}}^2 + \sigma_l^2} = \zeta \varphi_s^\tau, \quad \zeta = \frac{\kappa^2}{1 + \kappa^2}. \quad (2.37)$$

The attentive reader would have noticed that φ_0 does not give directly the observed phase shift of a second successive measurement $\varphi_s^{\tau_2}$ as the recorded data will be obscured by the added uncorrelated light shot noise of the second measurement²⁷ such that the variance of a successive conditioned *phase* measurement is different from $k^2 \sigma_{\mathcal{M}|\varphi_s^\tau}^2$ (see ((2.35))) by

$$\text{var}(\varphi_s^{\tau_2} | \varphi_s^\tau) = \sigma_l^2 + k^2 (\delta \mathcal{M}(\varphi_s^\tau))^2 = \sigma_l^2 + \frac{k^2 \sigma_{\mathcal{M}}^2}{1 + \kappa^2} = \sigma_l^2 (1 + \zeta), \quad (2.38)$$

$$\text{while from (2.35)} \quad \sigma_{\mathcal{M}|\varphi_s^\tau}^2 = (1 - \zeta) \sigma_{\mathcal{M}}^2, \quad \xi^2 = 1 - \zeta. \quad (2.39)$$

²⁷ The light shot noise of the first measurement is already included in the Bayesian update, see for instance in κ^2 .

The previous optimal prediction is sometimes referred to as a maximum a posteriori (MAP) estimation.

2.4.6 Combined measurements

Experimentally, the above means that if we perform a second measurement of the same duration yielding the random variable $\varphi_s^{\tau_2}$, we should²⁸ observe over many experimental realizations (CSS preparations) that the distribution of the latter is correlated to the values of the random variable $\varphi_s^{\tau_1}$ of a first measurement. As derived from (2.37), the observed value of $\varphi_s^{\tau_2}$ will be centered around the conditioned mean $\zeta\varphi_s^{\tau_1}$, when $\varphi_s^{\tau_2}$ was drawn from the same experimental realization as $\varphi_s^{\tau_1}$, meaning that they belong to the same so-called quantum trajectory. The conditional distribution of the second measurement $p(\varphi_s^{\tau_2}|\varphi_s^{\tau_1})$ is therefore also estimated, with the above Bayesian knowledge update, by the probability distribution $p(\varphi_s^{\tau_2} - \zeta\varphi_s^{\tau_1})$. For random variables, it is well-known that for any constant ζ

$$\text{var}(\varphi_s^{\tau_2} - \zeta\varphi_s^{\tau_1}) = \text{var}(\varphi_s^{\tau_2}) + \zeta^2\text{var}(\varphi_s^{\tau_1}) - 2\zeta\text{cov}(\varphi_s^{\tau_2}, \varphi_s^{\tau_1}).$$

As we have shown above that the most probable prediction or best estimate for $\varphi_s^{\tau_2}$ is achieved for $\zeta = \kappa^2(1 + \kappa^2)^{-1}$ (see (2.37)), the derivative of the previous relation with respect to ζ leads optimally to

$$\zeta = \frac{\text{cov}(\varphi_s^{\tau_2}, \varphi_s^{\tau_1})}{\text{var}(\varphi_s^{\tau_1})} = \frac{\kappa^2}{1 + \kappa^2} = 1 - \xi^2. \quad (2.40)$$

Since²⁹ $\text{var}(\varphi_s^{\tau_2} - \zeta\varphi_s^{\tau_1}) = \text{var}(\varphi_s^{\tau_2}|\varphi_s^{\tau_1})$, the combined difference of two successive measurements provides a simple experimental approach that allows to directly visualize the reduction of uncertainty in the estimation of \mathcal{M} . We would like to note that the prior variance should be taken a priori infinite to avoid any bias in the previous estimation process in the absence of concrete information about the initial atomic state. The presentation of the above results was greatly helped by the approximation of all the initial poissonian noise distributions as gaussian distributions, which is valid for sufficiently large numbers. Once this approximation cannot be made anymore, one would have to work with the Poisson and Skellam distributions.

²⁸ if the acquired knowledge or measurement affects the physical reality of the atomic ensemble.

²⁹ we have implicitly selected from all the possible values of the Bayesian estimation based on the first measurement, one value we consider best to estimate the second measurement and which intrinsically here will also minimize on average the spread of the second random variable $\varphi_s^{\tau_2}$ about the conditioned value $\zeta\varphi_s^{\tau_1}$. It is in that sense that the Bayesian estimation overlaps here with a maximum likelihood estimation.

2.4.7 *Generic Gaussian QND based squeezing as Kalman filtering*

Usually it is possible to arrive at all the previous results via a generic QND hamiltonian with input-output relations that uses a more algebraic language approach in an implicit gaussian description of collective atomic and light states observables (see Daniel and Stefan's thesis). In light of the previous Bayesian point of view, this common approach has appeared to me as a Kalman³⁰ filter (Kalman and Bucy (1961)) for which Heisenberg's or Schrödinger's equations give the update rules or evolution of the quantum mechanical statistical state of the system parametrized by the given set of physical observables. Quantum Kalman filtering is one of the simplest³¹ case of recursive Bayesian estimation applied to a quantum trajectory undergoing our time continuous measurement process aimed at gradually *learning* information about the atoms in presence of noise and potential losses. It was adopted for instance for atomic magnetometry in Geremia et al. (2005, 2003). By regarding all the previous measurements of the phase and estimation of the atomic population difference in presence of the stochastic noises (light shot noise and atomic projection) from the point of view of a simple one³² dimensional Kalman filter, it is straightforward to identify the central characteristic of such measurement filter, giving us the optimal Kalman gain for the information about $\hat{\mathcal{M}}$ as

$$\mathcal{K}_g = \frac{\zeta}{k}, \quad \text{with} \quad \xi^2 = (1 - k\mathcal{K}_g). \quad (2.41)$$

This allows us to put into a palpable form what is meant by gain of information and what can later allow to visualize the trade-off between gain and loss of information during such a measurement. We note that the degree of squeezing ξ^2 and the previous gain implicitly depend on the averaging time τ or measurement bandwidth, and should be interpreted in such a way that \mathcal{K}_g is a gain per measurement bandwidth. This should not be forgotten even if in the absence of losses, its role is trivial and because of the stochastic (white) light shot noise, this measurement time bandwidth can be translated at all times into a mean probe photon number for a constant continuous-wave (CW) probe light power. One could extrapolate to the notion of a gain per photon. As a trivial remark, in absence of observation noise (light noise), the Kalman gain of information about the atomic population from the observed phase shift is simply given by the reciprocal phase shift per atom³³ $\mathcal{K}_g = k^{-1}$.

30 random variable in the gaussian description with linear update relations

31 Gaussian distributed random variables and linear update relations.

32 Only one random variable or observable \mathcal{M} is considered here. If we know canonically conjugated observable to \mathcal{M} and their relation, we can increase the dimension of the filter and looked at the *back-action* of the filtering of \mathcal{M} onto these other quantities. Only relevant if we were to also detect them (e. g. anti-squeezing, quantum feedback).

33 or atom per phase shift

2.4.8 *Recursive squeezing*

If the approximation remains valid that any loss or perturbation on the atomic ensemble is negligible, it is possible to keep on squeezing the precision estimation by recursively updating our knowledge based on further measurements. That is repeating the Bayesian update conditioned by new successive measurements, which for simplicity we take of identical duration τ , to have identical phase light shot noise. Because we take the conditional probability distribution of \mathcal{M} based on the previous updates $p(\mathcal{M}|\varphi_s^{\tau_{n-1}} \cdots \varphi_s^{\tau_1})$ as the prior distribution for the n -th measurement update, we have simply from (2.35)

$$\sigma_{\mathcal{M}|\varphi_s^{\tau_n}}^2 = \frac{\sigma_{\mathcal{M}|\varphi_s^{\tau_{n-1}}}^2}{1 + \kappa_{n-1}^2} \quad \text{where } \kappa_{n-1}^2 = k^2 \sigma_{\mathcal{M}|\varphi_s^{\tau_{n-1}}}^2 / \sigma_l^2 \quad (2.42)$$

We find that the general term of the previous recurrence relation is

$$\sigma_{\mathcal{M}|\varphi_s^{\tau_n}}^2 = \left(\frac{1}{\sigma_{\mathcal{M},i}^2} + nc \right)^{-1}. \quad (2.43)$$

where $\sigma_{\mathcal{M},i}^2$ is the variance of the very prior or initial distribution, and where the constant $c = k^2 / \sigma_l^2$ which depends only on the phase shift per atom and on the phase noise due to light shot noise in the measurement time τ . Note that the constant c is independent of the number of atoms and can also be written explicitly here as $c = \left(\frac{\gamma}{2\Delta} \frac{\sigma_0}{A} \right)^2 N_{\text{ph}}$, i. e. as the product of an effective number of photon scattering event per atom during τ and an effective on-resonant optical depth per atom. The result (2.43) means that in the absence of losses and when the measurement is limited only by the quantum light shot noise, the total amount of squeezing after n successive small squeezing steps, is the same as the degree of squeezing achieved by a single measurement with n times less phase noise due to light shot noise, or equivalently n times more photons.

$$\xi_{n\tau}^2 = \frac{1}{1 + n\kappa_{\tau,i}^2}, \quad \text{where } \kappa_{\tau,i}^2 = k^2 \sigma_{\mathcal{M},i}^2 / \sigma_l^2(\tau)$$

If now the state of the ensemble evolves during the time continuous measurement, and if one has a model for that evolution, one needs to update the best estimation for the prior distribution between each step with this extra knowledge. Note that the result (2.43) given by a discrete update is identical to analytically solving (in the limit of short times/few photons) the differential equation $\frac{d}{dn} \sigma_{\mathcal{M}|n}^2 = -c(\sigma_{\mathcal{M}|n}^2)^2$ as done by [Madsen and Mølmer \(2004\)](#). This is the most trivial³⁴ example of a Riccati equation. This is not surprising because the differential equation for the covariance matrix³⁵ in the continuous version of

³⁴ separate the variable to solve it, $d\left(\frac{1}{\sigma_{\mathcal{M}|n}^2}\right) = c dn$ and one has (2.43).

³⁵ Which reduces to the variance here in our one-dimensional presentation

Kalman filtering, known as Kalman-Bucy³⁶ filtering [Bucy \(1970\)](#), is the general matrix Riccati equation, a nonlinear differential equation in the presence of measurement-induced decoherence and noise.

2.4.9 Classical versus quantum squeezing

Apart from the quantum origin of the noises introduced in the previous measurement filtering approach, one might ask where the quantum is. It is in the experimental observation that the achieved degree of squeezing in $(\Delta\hat{M})^2$ or $(\Delta\hat{J}_z)^2$ leads to a conjugated anti-squeezing in the transverse components \hat{J}_x , \hat{J}_y , induced by the minimally destructive interaction with the probe light. The knowledge of the system dissipated through the continuous sampling of \hat{J}_z , affects the quantum state of the ensemble as defined by the Heisenberg principle. In other words, an explicit quantum filtering description would be to recognize that quantum mechanics is a probability theory where the multiple random variables (observables) do not necessarily commute [Bouten et al. \(2007\)](#); [Stockton et al. \(2004\)](#), the Heisenberg principle taken *ab initio* in [Madsen and Mølmer \(2004\)](#); [Colangelo et al. \(2013\)](#).

2.4.10 Spin-squeezing criteria and multipartite correlations

The experimental observation of squeezing suggests the existence of correlation among the initially N_{at} uncorrelated (factorizable) partitions of the initial state³⁷ $|\psi_{\text{css}}\rangle$, that lead to a variation of the collective state partition noise.

Irrespective of the basis or quantization axis \vec{n} , the N_{at} two-level atoms are said to be in a non-separable or entangled state, or the collective atomic state is a many-body entangled state ([Soerensen et al. \(2001\)](#)) when

$$\mathcal{W} = \frac{N_{\text{at}}(\Delta\hat{J}_{n_1})^2}{\langle\hat{J}_{n_2}\rangle^2 + \langle\hat{J}_{n_3}\rangle^2} = \frac{N_{\text{at}}(\Delta\hat{J}_{\parallel})^2}{\langle\hat{J}_{\perp}\rangle^2} < 1. \quad (2.44)$$

Note that this criteria has been derived from the non-separability criterium of the density matrix which does not exhaust all type of non-classical (independent of the measurement basis) correlation ([Zurek \(2003\)](#); [Ollivier and Zurek \(2001\)](#)).

With our choice of quantization axis and when all the atoms are polarized along x , $\langle\hat{J}_y\rangle = 0$, the condition (2.44) reads

³⁶ Here the measurement process is noiseless and the state of the system does not evolve, one only has light observation noise.

³⁷ We remind that the preparation of the coherence spin state or particular symmetric Dicke state, a composite state of N_{at} partition implicitly required particle permutation symmetry of *locally* indistinguishable atoms.

$$(\Delta\hat{\mathcal{J}}_z)^2 < \frac{\langle \hat{\mathcal{J}}_x \rangle^2}{N_{\text{at}}} \quad \text{or} \quad \xi_{\mathcal{W}}^2 \equiv \frac{N_{\text{at}}(\Delta\hat{\mathcal{J}}_z)^2}{\langle \hat{\mathcal{J}}_x \rangle^2} < 1. \quad (2.45)$$

Because for the particular initially prepared coherent spin state $|\psi_{\text{CSS}}\rangle$ we have $\langle \hat{\mathcal{J}}_x \rangle^2 = N_{\text{at}}(\Delta\hat{\mathcal{J}}_z)_i^2$, the degree of squeezing that we have defined from the intuitive notion of the fractional reduction of uncertainty compared to the prior uncertainty,

$$\xi_{\text{ideal}}^2 = \frac{(\Delta\hat{\mathcal{J}}_z(t))^2}{(\Delta\hat{\mathcal{J}}_z(t_0))_i^2} = \frac{\sigma_{\mathcal{M}|\varphi_s}^2}{\sigma_{\mathcal{M}}^2} < 1, \quad (2.46)$$

would constitute an experimental witness of the spin-squeezing criterion \mathcal{W} (Appel et al. (2009b)). This definition of spin-squeezing referred to the prior variance of a CSS, also known as the standard quantum projection noise limit, was introduced by Kitagawa and Ueda (Kitagawa and Ueda (1993)),

$$\xi_{\text{K}}^2 = \frac{(\Delta\mathcal{J}_{\perp})^2}{(\Delta\mathcal{J}_{\perp})_{\text{CSS}}^2}. \quad (2.47)$$

However, in the context of Ramsey spectroscopy or frequency measurement based on the evolution of the quantum coherence ((2.1)), atomic phase or also precession angle of the collective spin, the relevant quantity to estimate precisely is

$$\phi = \tan^{-1} \left(\frac{\langle \mathcal{J}_{\perp} \rangle}{\sqrt{\langle \mathcal{J}^2 \rangle}} \right) \simeq \left(\frac{\langle \mathcal{J}_{\perp} \rangle}{\sqrt{\langle \mathcal{J}^2 \rangle}} \right) \quad (N_{\text{at}} \gg 1). \quad (2.48)$$

Therefore, the improvement of precision compared to the one achieved by an ensemble of uncorrelated atoms or coherent state is quantified by the Kitagawa criteria for ϕ known as Wineland definition for metrologically relevant spin-squeezing (Wineland et al. (1994))

$$\xi_{\mathcal{W}}^2 = \frac{(\Delta\phi)^2}{(\Delta\phi)_{\text{CSS}}^2} = N_{\text{at}} \frac{(\Delta\mathcal{J}_{\perp})^2}{\langle \mathcal{J}^2 \rangle} = \frac{N_{\text{at}}}{2\sqrt{\langle \mathcal{J}^2 \rangle}} \xi_{\text{K}}^2. \quad (2.49)$$

where we have used that $(\Delta\mathcal{J}_{\perp})_{\text{CSS}}^2 = \sqrt{\langle \mathcal{J}^2 \rangle}/2$ (see Heisenberg-Robertson's inequality³⁸ (2.8)) such that $(\Delta\phi)_{\text{CSS}}^2 = (2\sqrt{\langle \mathcal{J}^2 \rangle})^{-1} \simeq 1/N_{\text{at}}$. Because $\sqrt{\langle \mathcal{J}^2 \rangle} < N_{\text{at}}/2$ for any collective state of N_{at} pseudo spin-one half particles different than the coherent spin state, Wineland's squeezing criteria is more demanding, $\xi_{\mathcal{W}}^2 < \xi_{\text{K}}^2$ ($\xi_{\mathcal{W}}^2 = \xi_{\text{K}}^2$ for a CSS). It also corresponds to the many-body entanglement witness reported above (2.45). Consequently, Kitagawa's squeezing is a necessary but insufficient condition for Wineland's squeezing which quantifies the sensitivity to rotation of angular momentum states. This also means that there are

³⁸ Very recently, Lorenzo Maccone found stronger uncertainty relations than Heisenberg-Robertson's uncertainty (Maccone and Pati (2014)).

collective spin states³⁹ with uncertainty reduced compared to a coherent state which are not relevant for Ramsey metrology and which are not multi-atom entangled states.

While it is indeed possible to beat the standard quantum limit achieved by uncorrelated atoms with spin-squeezed states prepared conditionally via QND measurement, there is a fundamental limit to the achievable Wineland squeezing fixed by the Heisenberg principle ($\xi_{\mathcal{W}}^2 > 1/N_{\text{at}}$, Stockton et al. (2003)). The distance to this limit and the achievable degree of squeezing is constrained by a lower bound for the variance of any estimated observable expressed by the Cramér-Rao bound which depends on the quantum Fisher information which is fixed by the nature of the conditional probability distribution of the measurement outcomes of the estimated observable for a particular collective state.

SUMMARY

After starting with the motivational principles of Ramsey spectroscopy, we introduced a standard description of collective ensembles of two-level identical atoms in terms of the pseudo spin-one half formalism. We insisted on the fundamental role of permutation symmetry of N_{at} identical boson particles which constrains the total achievable collective spin to a maximum $J = N_{\text{at}}/2$.

We then presented the collective coherent spin state of N_{at} atoms prepared in a quantum superposition of two long-lived atomic ground states. We distinguished a dispersive and maximally transparent detection method to implement optical QND measurements of the collective populations of these two atomic states with a precision limited by both the intrinsic quantum noise of light and the quantum atomic projection noise.

Such QND measurement allows the continuous and conditional preparation of collective spin-squeezed states which are relevant to entanglement-assisted metrology to improve measurement precision beyond the one achieved by uncorrelated ensembles of atoms. To focus on the physical mechanisms and figures of merits, we presented a simple Bayesian approach to such continuous measurement process without any algebraic Hamiltonian formalism or density matrix stochastic master equation. This was motivated to render accessible and somewhat more visual, the principles of spin squeezing and conditional spin dynamics to the new PhD student arriving on our experiments. The fact that we experimentally only record outcomes ruled by fundamental laws of probability means that our task is often to improve a state of knowledge on a particular physical system conditioned on measurement. Here, we presented the dispersive detection of atomic states with light. In the next chapter, we present how we ultimately measure this light. In the third chapter, we will be ready to only focus on the experimental protocol and results.

³⁹ For instance, a collective mixture.

3

OPTICAL PHASE DETECTION AT THE QUANTUM NOISE LIMIT

Electrons behave (...) in exactly the same way as photons; they are both screwy, but in exactly in the same way.

— Richard P. Feynman

INTRODUCTION

The fundamental ideas exposed in the previous chapter relies on the detection of an atomic signal imprinted on the phase of optical probes. However, as of today, there are no photodetectors available that are fast enough to detect directly the phase of a field oscillating at an optical frequency. In this chapter, we present the experimental methods used to bypass this limitation, which achieve a phase detection sensitivity at the intrinsic quantum noise level of the probes.

Modern quantum optics is born with Roy Glauber's work, through a reinterpretation of the photodetection process [Glauber \(1963a,b\)](#). How we detect light in the laboratory is both central and fundamental. It dictates our point of view on the physical systems we tried to observe first with light. We will first recall some basic notions before we discuss the main and often the only direct physical observable that we record in our experiments, namely a photocurrent.

Consequently, we will describe the main features of different homodyne methods we have implemented experimentally in this thesis in order to estimate the phase of coherent states of light. These methods are non-linear mixing processes which allow to amplify the signal of an input state of light together with its intrinsic noise, well-above the classical technical noise of the detectors. With these methods, one can even resolve single photons per measurement bandwidth. The estimation of optical phase with such interferometric measurements is fundamentally bounded to a so-called [SQL](#) due to the intrinsic quantum noise of the coherent states which do not have a well-defined energy. In connection with the previous chapter, it is important to recall that this limit scales as the square root of spontaneous emission.

3.1 DETECTION OF LIGHT

In our experiments, we use optical light as a meter on atoms. In general, the simplest of our measurement, based on the light-atom interaction, only brings into play the electrical part of the electromagnetic field of light (electrical-dipole hamiltonian). To extract information about the atomic system carried by light, we need to detect at least the electric field of light, which has interacted with the ensemble of atoms. We already encounter then a serious limitation. Contrary to Hertzian waves that can be monitored directly on an antenna, there are today no material detectors available with the inertia to follow a field at an optical frequency.

By default, we only have at our disposal in our experimental setup so-called square-law photodetectors based in general on the absorption¹ of the input light field. To give a concrete example, most of the vital light detectors we have built for this thesis work are based on so-called positive-intrinsic-negative (PIN) junction semiconductor photodiodes.

Measurement is a physical process of its own. It is central in quantum mechanics. The nature of the detectors we use or built dictates the nature of the physical reality we can talk about. So before we give an account of the physical observable we record, we need to recall the important physical meaning of the annihilation operator. As was shown in Glauber (1964), a photodetector is only sensitive to the annihilation operation of the electromagnetic field.

3.2 ANNIHILATION OPERATOR

In classical physics, we often give a complex representation of the electric field. For example, in the simplest case of a single time-harmonic wave $\mathbf{E}(r, t) = 2\mathbf{E}_0(\mathbf{r}) \cos(\omega t - \phi)$, one often retains as a representation $\tilde{\mathbf{E}}(\mathbf{r}, t) = \mathbf{E}_0(\mathbf{r}, \omega, \phi)e^{-i\omega t}$ with $\mathbf{E}(r, t) = \tilde{\mathbf{E}}(\mathbf{r}, t) + c.c$, where c.c denotes the complex conjugate of $\tilde{\mathbf{E}}$. The complex representation is motivated by the great simplification in calculating all the linear equations that the electric field obeys² as long as the superposition principle holds. We observe that classically, it seems *a priori* equivalent to choose either $\tilde{\mathbf{E}}$ or its conjugate $\tilde{\mathbf{E}}^*$ as a complex representation and that in addition, they just appear as mere convenient mathematical tools. In quantum optics, they acquire a different meaning, these are respectively associated to the annihilation and creation operators (here for the simplest single frequency case).

The attentive reader may note that in the above trivial case, $\tilde{\mathbf{E}}$ is also the positive frequency part of the time Fourier decomposition of the

1 This type of detection undergoes a time-reversal symmetric breaking linked to the non conservation of the energy in the light field or irreversible cast of the input state of light into vacuum.

2 For instance, the electromagnetic energy is non-linear in the fields.

electric field. The straightforward generalization of the notion of the complex representation to any (physical) time-varying signal is then taken as the positive frequency part of its Fourier decomposition. This bears the name of the *analytic signal*, α , in classical physics. It leads us to the more general definition of the annihilation operator $\hat{\mathbf{a}}$ as the quantum mechanical reinterpretation of the analytical signal of the electric field or positive frequency part of the field. As is well-known and vital to this thesis, the real and imaginary parts of this complex or non-hermitian quantity, are the quadratures or position and canonical momenta of the light field. We shall see later experimentally how it is further linked to the Hilbert transform of the electric field signal.

The eigenstates of the annihilation operator are the so-called Glauber or coherent states whose eigenvalues are nothing but the classical complex value α , which is the value of the analytic signal of the electric field. These states are the quantum-mechanical reinterpretation of the above classical representation of light, introduced as an electromagnetic field wave. By construction, they are thus known as quasi-classical states. They play an important role as robust³ probes on atoms and provide an adequate description of the light emitted by the laser sources operating above threshold we have built for our experiments. Now that we have recalled the physical meaning of the annihilation operator, we will relate it to the main detection observable in our experiments, the photocurrent. In addition, we will see how the basic photodetection process is fundamentally related to the main concepts of our general experimental work.

3.3 PHOTOCURRENT

Classically one assumes that a photodetector is sensitive to a time-average (due to bandwidth limitation) of the modulus square of the electric field amplitude, i. e. $\propto |\mathbf{E}|^2 \propto \tilde{\mathbf{E}}\tilde{\mathbf{E}}^*$. We have seen previously that the complex electric field $\tilde{\mathbf{E}}$ also denoted positive-frequency part $\tilde{\mathbf{E}}^+$ and its hermitian conjugate (the negative frequency part $\tilde{\mathbf{E}}^-$) are respectively the annihilation and creation operators which in quantum mechanics do not commute⁴. The proper symmetrization of $\tilde{\mathbf{E}}\tilde{\mathbf{E}}^*$ and in the end ordering of this operator was done by Roy Glauber [Glauber \(1964\)](#) through a proper choice of the time arrow dictated by the irreversibility of the light-matter interaction at play in the detector. This is central. In this thesis, you will encounter mainly two categories of light-matter interaction phenomena: irreversible process (e. g. spontaneous emission) and reversible process (e. g. Rabi oscillations). Spontaneous emission exemplifies Fermi's golden rule or Wigner-Weisskopf rule (at

³ Coherent states, also known as “pointer states” are impervious to entanglement with the environment. They stay coherent and only suffer relaxation when coupled to the environment ([Haroche and Raimond \(2006\)](#)).

⁴ This is the direct result of the quantization energy principle.

long time). It is an incoherent irreversible process whereas Rabi oscillations represent a reversible coherent energy exchange⁵. The latter fundamentally appears when the dipole-electric interaction couples isolated discrete atomic energy levels while the former appears when the discrete levels are coupled to a (degenerate) continuum (Grynberg et al. (2010)).

In a general photodiode, discrete electronic energy levels of the semiconductor valence band can be coupled to a continuum of states in the conduction band. The degeneracy of the continuum of excited states weights predominantly the evolution of the light-(electric dipole detector) system in favor⁶ of $-\hat{\mathbf{d}} \cdot \hat{\mathbf{E}}^+$ in front of $-\hat{\mathbf{d}} \cdot \hat{\mathbf{E}}^-$.

A photodetector then only probes mainly the annihilation operator of the input light field, that is $\hat{\mathbf{E}}^+$. While $\hat{\mathbf{E}}^-$ is inexorably lost rapidly into the environment. This decoherence of the negative frequencies into the environment represents a spontaneous breaking of the time-reversal symmetry of the light field evolution⁷, marked by the non-invariance of the light-matter interaction under the exchange of \hat{a} and \hat{a}^\dagger . Whereas in classical physics the negative frequencies of a real-valued signal are superfluous due to the hermitian symmetry of the Fourier transform, they are *complementary* of the positive ones in quantum mechanics due to the non-commutation of the associated operators. As we shall see in a next section, one way to preserve the symmetry in \hat{a} and \hat{a}^\dagger and prevent losing wave (phase) information is the *homodyne* technique. It consists in shifting the origin of frequencies of the light field with respect to the optical frequency associated to the transition energy band gap of the detector. In other words, homodyne is a non-linear mixing process that displaces the energy of vacuum, thereby also amplifying the quantum noise of any coherent state of light.

The evolution of the photodetector state under the presence of the light field leads irreversibility to an excitation in the conduction band and depletion in the valence band. The creation of such electron-hole pair and its routing engineered via p-n regions is not our direct physical signal. What we measure is the electrical current they produce, i.e a count rate of pair production. This rate or photocurrent is given by the probability per unit time to find the detector in an excited state. This is in quantum mechanics given by the modulus square of the transition amplitude of the interaction hamiltonian between the initial and final state. From $-\hat{\mathbf{d}} \cdot \hat{\mathbf{E}}^+$ and our simplified ideal approach, one sees it is proportional to $\langle i | \hat{\mathbf{E}}^- \hat{\mathbf{E}}^+ | i \rangle$ after tracing over all the final states where $|i\rangle$ is the input state of light. The proportionality constant being dependent on the nature of the detector (transition dipole ma-

5 We cannot tell with certainty in which of the two sub systems, light or atom, where the interaction energy, that is the energy of the total system light+atom, is localized.

6 The matrix dipole moment element between the detector ground to the excited state evolves as $e^{i\omega_b t}$ where $\hbar\omega_b$ is the bandgap energy.

7 This is intimately linked to the appearance of light-quanta in quantum optics.

trix element) and geometry⁸. One then recognize the photocurrent as proportional to the ensemble average of the photon number operator⁹ $\hat{n} = \hat{a}^\dagger \hat{a} \propto \hat{\mathbf{E}}^- \hat{\mathbf{E}}^+$. Therefore the photocurrent will exhibit statistics and noise of light-quantum nature in addition to the quantum nature of electricity. In the next section, we present the important meaning of the quantum efficiency of this detection process. It represents one of the major technical limit in the resolution of our measurements.

3.4 QUANTUM EFFICIENCY

We have seen that the photocurrent produced by a photodiode detector represents a sampling of the photon number distribution of the input light state. Detectors are not perfect and in general the mean detected electron count rate is smaller¹⁰ than the mean input photon number due to (assumed) random losses. Let's assume that the input light is a state with well-defined photon number n (a Fock state). For an ideal detector the success probability q to get an electron from one photon is one. Therefore, the conditional probability $P_n(m)$ to obtain m electrons from n photons is also one. In presence of random loss¹¹ $q < 1$. Due to the atomic nature of the electron, its loss has a binary nature. Then, the probability to get 1 electron from 1 photon being q , the conditional probability to get m electrons from n photons $P_n(m)$ is given by the binomial law $P_n(m) = \binom{n}{m} q^m (1-q)^{n-m}$. If now the number of photons is not certain due to the nature of the input light state, for example be it a coherent state, the probability law of the electron events will be the result of a Bernouilli process. Indeed, if $P(n)$ denotes the probability distribution of the photon number of the light state, the probability distribution of the electron number outcomes $P(m)$ is the sum over the photon number of the product of the conditional probability $P_n(m)$ and $P(n)$.

$$P(m) = \sum_n \binom{n}{m} q^m (1-q)^{n-m} P(n). \quad (3.1)$$

Here, $\frac{n!}{m!(n-m)!} = \binom{n}{m}$ is Newton's binomial coefficient. For a coherent state with analytic signal α , the decomposition onto the Fock state basis gives access to the probability of finding the value n for the number of photons

$$P(n) = e^{-|\alpha|^2} \frac{(|\alpha|^2)^n}{n!}. \quad (3.2)$$

⁸ One needs to integrate our ideal point-like atom detector model over the cross-section between the spatial mode of the light field and the detector sensitive area.

⁹ To go from the Dirac bosonic operators to the electric field operators, one only needs in a single-mode description the electric field amplitude of a single photon.

¹⁰ before any possible avalanche amplification stage

¹¹ that we cannot really distinguish from either electron or photon losses.

This is a Poisson distribution with mean value $|\alpha|^2$ such that (3.1) will appear as a convolution between a binomial distribution and a Poisson distribution.

$$\begin{aligned}
P(m) &= \sum_n \binom{n}{m} q^m (1-q)^{n-m} e^{-|\alpha|^2} \frac{(|\alpha|^2)^n}{n!}, \\
&= \frac{q^m e^{-|\alpha|^2}}{m!} \sum_n \frac{1}{(n-m)!} (1-q)^{n-m} (|\alpha|^2)^n, \\
&= q^m e^{-|\alpha|^2} \frac{(|\alpha|^2)^m}{m!} \sum_k \frac{((1-q)|\alpha|^2)^k}{k!}, \quad k = n - m \\
P(m) &= e^{-q|\alpha|^2} \frac{(q|\alpha|^2)^m}{m!}. \tag{3.3}
\end{aligned}$$

Implicitly in the above we have $m \leq n$ ($q \leq 1$). We have just shown that the convolution of the Poisson distribution with mean value $|\alpha|^2$ and the binomial distribution with success q leads to a Poisson distribution for the electron distribution with mean and hence variance both reduced by q compared to the statistics of the input coherent states $P(n)$. This means that one cannot distinguish the output of the previous detector from an ideal one ($q = 1$) with an input coherent state with mean photon number equal to $q|\alpha|^2$. This binomial loss is analog to the effect a beamsplitter produces when mixing the input coherent state with vacuum, with electrical amplitude transmission coefficient \sqrt{q} . $(1 - q)$ percent of the energy is dumped into the (environment) vacuum port. Throughout this thesis, we take q as the definition of the input light state detection quantum efficiency (it is unitless).

It is clear that for a n photon number Fock state, the mean value of the number of produced electrons will be given by the statistical mean of the binomial distribution, nq . But this is also the mean value to be expected for the inefficient detection of a coherent state with mean photon number n . The difference in their nature is to be found in the noise of the photocurrent. The variance of the binomial distribution is $nq(1 - q)$ while for a Poisson distribution the variance is also the mean nq . The electron count rate from a light Fock state is then sub-Poissonian with a Fano factor¹² equal to the quantum inefficiency $(1 - q)$. Even when the photon number is perfectly defined (Fock state, zero variance), the discreteness of the electron gives rise to a photoelectron¹³ shot noise $nq(1 - q)$ on the final photocurrent. Increasing the quantum efficiency thus increases the fidelity of the reconstruction of an input state based on the measurement of its statistical outcomes. We note that the experimental measurement of the quantum efficiency requires in general an external calibration of the power impinging on

¹² ratio of the variance to the poisson variance.

¹³ To clearly claim the origin of the photocurrent noise from the quantum noise of a coherent state of light a sufficiently large q is required.

the detector (unless one has a source of correlated photon pairs, Migdall (2001)).

3.5 PHOTOCURRENT SHOT NOISE

In the previous simple illustration, there is no mention of any detection integration time. Experimentally, we cannot measure for an infinitely long time nor produce infinitely long pulses of light. Therefore $P(m)$ should be considered as a distribution of electrons produced while sampling the input light photon number statistics during a time τ . If Φ denotes a constant input photon flux, n should be replaced in the above by $\Phi\tau$ and the mean of $P(m)$ gives the expectation value of the photocurrent $i = -em/\tau$. The average number of electrons produced per interrogation time or¹⁴ average photocurrent is then equal to $\langle i \rangle = -e \langle m \rangle / \tau = -e/\tau \sum_m mP(m) = -eq|\alpha|^2/\tau$, with $q|\alpha|^2 = \langle n \rangle$ the mean number of *detected* photo-events during the time τ . From,

$$\langle i^2 \rangle = e^2/\tau^2 \sum_m m^2 P(m) = e^2/\tau^2 q|\alpha|^2 (q|\alpha|^2 + 1), \quad (3.4)$$

we deduce that $\sigma_i^2 = \langle i^2 \rangle - \langle i \rangle^2 = e^2/\tau^2 \langle n \rangle = -e/\tau \langle i \rangle$. Introducing the electrical bandwidth of the detector as $B = 1/(2\tau)$, the root-mean-square (RMS) photocurrent noise or shot noise writes as $\Delta i = \sqrt{-2eB \langle i \rangle}$ (see Lye et al. (2003)). We shall discuss this bandwidth later in this thesis.

3.6 DOMINANT SHOT NOISE

If the previous shot noise is the main source of noise on the output photocurrent signal during the interrogation time τ , then we naturally introduce the shot noise limited signal-to-noise ratio of the photocurrent measurement for coherent states of light as

$$\text{SNR} = \left\| \frac{\langle i \rangle}{\Delta i} \right\| = \frac{\sqrt{|\langle i \rangle|}}{\sqrt{2eB}} = \sqrt{\langle n \rangle} = \sqrt{q \langle n_{\text{exp}} \rangle}, \quad (3.5)$$

where $\langle n_{\text{exp}} \rangle$ is the expected average number of photons impinging on the detector during the time τ . For the previous time-resolved detection and a fixed input light power, $\langle n \rangle$ is proportional to the average detection time τ . Therefore, increasing the detection bandwidth decreases the the signal-to-noise ratio. In general, the previous fundamental shot noise limit arising from the quantum nature of light, even for an ideal detection with perfect quantum efficiency $q = 1$, is not directly observable for any detection bandwidth and input light power due to other sources of noise linked to the technical design of the detector contaminating the final readout photocurrent. As we shall see, it is possible

¹⁴ up to the charge of the electron $-e$ where e is the elementary charge.

to bypass these technical limitations using homodyne detection, which allows to resolve in *real-time* (per detection bandwidth) a single photon (if $q = 1$). However, the experimental applicability of such technique or *dynamic range* of the above shot noise limited signal-to-noise will be constrained in bandwidth by this extra sources of electronic noise.

3.7 INTERFEROMETRIC DETECTION BASICS

In this section, we present the concepts behind the detection of the phase shift imprinted by the atoms onto a probe light beam propagating through the atomic sample (see previous chapter).

We have recalled above that for a single radiation mode with optical angular frequency ω , the electric field operator $\hat{\mathbf{E}}^+$ is equivalent to the annihilation operator $\hat{\mathbf{a}}$ for that mode, up to a proper choice of normalization. That is, when the latter creates a *photon*, the electric field operator creates a quantum of electric field amplitude¹⁵ $\varepsilon = \sqrt{\hbar\omega/2\epsilon_0 L^3}$ in such a way that the total energy released in the quantization volume L^3 is $\hbar\omega$. We ignore for the moment the discussion of the polarization and consider that all the fields share the same state of polarization.

We have seen that a standard photodetector is only sensitive to the positive frequency part or analytic signal of the input electric field. Therefore, by reading the photocurrent, it is not possible to access the two quadratures of a probe field *independently* which is necessary to determine the phase of the field. However, the detector state evolves linearly with the input electric field. Thus, as long as the superposition principle holds in the detector, we can obtain a phase sensitive signal by interfering the signal field of interest with a known reference field before the detector. That is, we can replace in the above $\hat{\mathbf{E}}^+ = \hat{\mathbf{E}}_{\text{signal}}^+ + \hat{\mathbf{E}}_{\text{ref}}^+$. The photocurrent will now be given by the expectation value of the operator

$$\hat{\mathbf{E}}^- \hat{\mathbf{E}}^+ = \hat{\mathbf{E}}_{\text{signal}}^- \hat{\mathbf{E}}_{\text{signal}}^+ + \hat{\mathbf{E}}_{\text{ref}}^- \hat{\mathbf{E}}_{\text{ref}}^+ + \hat{\mathbf{E}}_{\text{ref}}^- \hat{\mathbf{E}}_{\text{signal}}^+ + \hat{\mathbf{E}}_{\text{ref}}^+ \hat{\mathbf{E}}_{\text{signal}}^-.$$

The signal is now sensitive to both the positive and negative frequency parts of the signal field. The first two terms are optical rectifications¹⁶. The last two terms represent a non-linear mixing process whereby the signal field is amplified by the reference field.

This is very important as it provides a mean, independent of the nature of the detector, to amplify the quadratures of the signal field but also their quantum fluctuations above the noise sources introduced by the technical detection of the produced photocurrent. It is the key to the detection of single probe photons without photon counting detectors.

¹⁵ This is also the magnitude of the electrical fluctuations of vacuum. Please note that the vacuum electric field noise ϵ depends on the frequency of the mode.

¹⁶ Energy is non-linear in the fields

3.7.1 Coated beamsplitter

Experimentally, the previous interference operation can be realized by overlapping two coherent beams of light into a common spatial mode via a beamsplitter as depicted in figure 3.1.

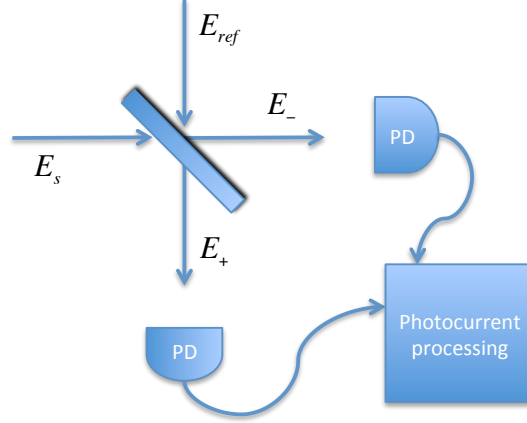


Figure 3.1: Typical coated beamsplitter mixing of the signal field and reference fields. The two output ports are monitored by single photodiode detectors producing the measured photocurrents.

A typical optical beamsplitter is made of a transparent (glass) material with a deposited reflective coating (e. g. fused silica) on one surface whose refractive index is usually lower than that of the glass support. Classical boundary conditions fix that electromagnetic waves experience a phase shift of π upon a reflection from one medium to another with a lower refractive index. The index of air is lower than the coating material giving a π shift whereas there is no shift in reflection from the back side of the splitter after propagation in the glass.

The positive frequency part of the total electric field at the two output ports of the beamsplitter are therefore written as a function of the input fields as

$$\hat{\mathbf{E}}_+^+ = \frac{\hat{\mathbf{E}}_s^+ + \hat{\mathbf{E}}_r^+}{\sqrt{2}}, \quad (3.6)$$

$$\hat{\mathbf{E}}_-^+ = \frac{\hat{\mathbf{E}}_s^+ + e^{-i\pi}\hat{\mathbf{E}}_r^+}{\sqrt{2}}, \quad (3.7)$$

where $\sqrt{2}$ accounts for simplicity for identical power transmission and reflection coefficients of 50%, and $e^{-i\pi}$ the single local dephasing experienced by the field reflected at the interface.

3.7.2 Photo-current operators

The detection of either $\hat{\mathbf{E}}_{\pm}^{\pm}$ will produce the following photo-current operators

$$\hat{I}_{\pm} = \hat{\mathbf{E}}_{\pm}^{-} \hat{\mathbf{E}}_{\pm}^{+} = \frac{1}{2} (\hat{\mathbf{E}}_s^{-} \hat{\mathbf{E}}_s^{+} + \hat{\mathbf{E}}_r^{-} \hat{\mathbf{E}}_r^{+} \pm \hat{\mathbf{E}}_r^{+} \hat{\mathbf{E}}_s^{-} \pm \hat{\mathbf{E}}_r^{-} \hat{\mathbf{E}}_s^{+}), \quad (3.8)$$

$$= \varepsilon^2 \hat{i}_{\pm}, \quad (3.9)$$

$$\hat{i}_{\pm} = \frac{1}{2} (\hat{\mathbf{a}}_s^{\dagger} \hat{\mathbf{a}}_s + \hat{\mathbf{a}}_r^{\dagger} \hat{\mathbf{a}}_r \pm \hat{\mathbf{a}}_r \hat{\mathbf{a}}_s^{\dagger} \pm \hat{\mathbf{a}}_r^{\dagger} \hat{\mathbf{a}}_s), \quad (3.10)$$

where ε is the unit of vacuum noise approximately identical for the relatively small difference in frequencies between the signal and the reference fields we have used. We have introduced the annihilation operators for the reference and signal modes. We note that the two modes are not entangled and the above operators apply onto the tensor product of the two input states before the beamsplitter $\psi = \psi_s \otimes \psi_r$.

3.7.3 Differential photo-current

One might see advantages in measuring the difference between the two previous photocurrents and define a differential photo-current operator \hat{d}_i with

$$\langle \psi | \hat{d}_i | \psi \rangle = \langle \hat{i}_+ - \hat{i}_- \rangle = \langle \hat{\mathbf{a}}_r \hat{\mathbf{a}}_s^{\dagger} + \hat{\mathbf{a}}_r^{\dagger} \hat{\mathbf{a}}_s \rangle = \langle 2\text{Re}(\hat{\mathbf{a}}_r^{\dagger} \hat{\mathbf{a}}_s) \rangle. \quad (3.11)$$

Even though the expectation values of the first two independent terms from (3.9) subtract out, their uncorrelated fluctuations will add in quadrature and still contribute to the total detection noise. The advantage of taking the difference apart from increasing the phase-sensitive signal power is in the suppression of classical intensity fluctuations if both signal and reference mode are derived from the same light source. We shall come back later to the sources of noise on the input light field in addition to the noises linked to the electronic detection as mentioned previously. We imagine here an ideal situation where the only source of noise arises from the quantum nature of light.

3.7.4 Balanced homodyne with coherent states

We consider the signal and reference states as coherent states respectively $|\psi_s(t)\rangle = |\alpha_s(t)\rangle e^{i\varphi_s}$ and $|\psi_r(t)\rangle = |\alpha_r(t)\rangle e^{i\varphi_r}$. Coherent states in our choice of Schrödinger representation evolve simply in time as $\langle \psi_s(t) | \hat{a}_s | \psi_s(t) \rangle = e^{-i\omega_s t} \langle \psi_s(0) | \hat{a}_s | \psi_s(0) \rangle$ in such a way that the expectation value of the differential photocurrent is independent of time following our particular case known as homodyne where $\omega_s = \omega_r$.

$$\langle \psi | \hat{d}_i | \psi \rangle = 2|\alpha_r| |\alpha_s| \cos(\varphi_s - \varphi_r), \quad (3.12)$$

$$= 2|\alpha_r| |\alpha_s| [\cos(\varphi_s) \cos(\varphi_r) - \sin(\varphi_s) \sin(\varphi_r)]. \quad (3.13)$$

The phase of the reference field, φ_r , can be adjusted (mod π) to measure either what will be called the in-phase component of the signal field (for $\varphi_r = 0$) or the one in quadrature (for $\varphi_r = \pi/2$). It is well-known that these are related to the canonical momenta of the field. Indeed, the complex-valued analytic signal can also be written as $\alpha = |\alpha|e^{-i\varphi} = x + ip$. The real (imaginary) part of the analytical signal is known classically as the in-phase (quadrature) component of the field. In quantum optics, this is the expectation value of the real (imaginary) part of the annihilation operator $\sqrt{2}\hat{a} = \hat{X} + i\hat{P}$. The difference in this quick reminder with the canonical momenta being found in the normalization of the field operators, i.e. ε and in the freedom in the electric field amplitude definition. With the previous definition, we can indeed rewrite (3.13) as

$$\langle \psi | \hat{d}_i | \psi \rangle = \langle \hat{i}_+ - \hat{i}_- \rangle = \langle \hat{X}_r \hat{X}_s + \hat{P}_r \hat{P}_s \rangle, \quad (3.14)$$

$$= |\alpha_r| \left(\cos(\varphi_r) \langle \psi_s | \hat{X}_s | \psi_s \rangle + \sin(\varphi_r) \langle \psi_s | \hat{P}_s | \psi_s \rangle \right), \quad (3.15)$$

which recalls the principle of quantum state tomography.

3.7.5 Light noise amplification

Where the quantum description makes a difference is in the fluctuation of the photocurrent. Denoting $\Delta\varphi = \varphi_s - \varphi_r$, it is easy to show that

$$\langle \psi | \hat{d}_i^2 | \psi \rangle = \langle (\hat{i}_+ - \hat{i}_-)^2 \rangle, \quad (3.16)$$

$$= (\hat{\mathbf{a}}_r \hat{\mathbf{a}}_s^\dagger)^2 + (\hat{\mathbf{a}}_r^\dagger \hat{\mathbf{a}}_s)^2 + 2\hat{\mathbf{a}}_r^\dagger \hat{\mathbf{a}}_r \hat{\mathbf{a}}_s^\dagger \hat{\mathbf{a}}_s + \hat{\mathbf{a}}_r^\dagger \hat{\mathbf{a}}_r + \hat{\mathbf{a}}_s^\dagger \hat{\mathbf{a}}_s, \quad (3.17)$$

$$= 4|\alpha_r|^2 |\alpha_s|^2 \left(1 - \sin(\Delta\varphi)^2 \right) + |\alpha_r|^2 + |\alpha_s|^2. \quad (3.18)$$

We then see that if the strength of the reference signal is high enough we can in addition of amplifying the signal in (3.13), also amplify the fluctuations in the signal field quadratures above $|\alpha_s|^2$ and also above the potential technical noise of the detector. We recall that the noise on the photocurrent from coherent states is independent of the relative phase between the signal and the reference, with (3.13), one can find

$$\sigma(\hat{d}_i) = \sqrt{\langle \psi | \hat{d}_i^2 | \psi \rangle - (\langle \psi | \hat{d}_i | \psi \rangle)^2} = \sqrt{|\alpha_s|^2 + |\alpha_r|^2}. \quad (3.19)$$

However the phase sensitivity of the measurement can depend on the phase. The intrinsic quantum mechanical statistical noise (3.19) is only due to the random arrival of photons at the detectors. We recall that $|\alpha_s|^2 = \langle \hat{n}_s \rangle = n_s$ ($|\alpha_r|^2 = \langle \hat{n}_r \rangle = n_r$) is the mean number of photons in the signal (reference).

3.7.6 Phase sensitivity

The measure of the differential photocurrent is said to be phase sensitive when one can resolve a variation in the phase φ_s which is larger than the previous intrinsic noise of the measurement. For a reference phase locked to $\varphi_r = \pi/2$, the mean differential photocurrent will vary to first order by an amount

$$\left| \delta\varphi_s \frac{\partial \langle \psi | \hat{d}_i | \psi \rangle}{\partial \phi_s} \Big|_{\varphi_r = \frac{\pi}{2}} \right| = 2|\alpha_r||\alpha_s| \cos(\varphi_s) \delta\varphi_s, \quad (3.20)$$

upon a variation $\delta\varphi_s$ of the signal phase. This quantity will be significant if it is larger in absolute magnitude than $\sigma(\hat{d}_i)$. We can define a phase sensitivity $\delta\varphi_s$ with respect to the lower bound of the chosen definition of the significance or unit [SNR](#) as

$$\delta\varphi_s = \frac{\sqrt{|\alpha_s|^2 + |\alpha_r|^2}}{2|\alpha_r||\alpha_s| \cos(\varphi_s)} \simeq \frac{\sqrt{|\alpha_s|^2 + |\alpha_r|^2}}{2|\alpha_r||\alpha_s|}, \quad (3.21)$$

where the last equality applies for small phases φ_s , ($\cos(\varphi_s) \sim 1$), which is around the so-called point of highest sensitivity (minimum phase resolution) which happens for φ_s near 0. Otherwise, the phase sensitivity will vary with the phase.

3.7.7 Balanced versus unbalanced quantum efficiency

If the reference field power is much stronger than that of the signal, one can gain a factor of $\sqrt{2}$ in sensitivity compared to the situation where the powers are equal.

For balanced powers $|\alpha_s|^2 = |\alpha_r|^2$, and then from (3.24), one has

$$\delta\varphi_s = \frac{1}{\sqrt{2}|\alpha_s|} = \frac{1}{\sqrt{2}|\alpha_r|} = \frac{1}{\sqrt{2}\langle n_s \rangle}. \quad (3.22)$$

If $|\alpha_r|^2 \gg |\alpha_s|^2$, the noise on the photocurrent signal is dominated by the reference beam fluctuations and therefore the phase sensitivity is limited by the signal fluctuations !

$$\delta\varphi_s = \frac{1}{2|\alpha_s|} = \frac{1}{2\sqrt{\langle n_s \rangle}} \gg \frac{1}{2|\alpha_r|} = \frac{1}{2\sqrt{\langle n_r \rangle}}. \quad (3.23)$$

Apart from the quantum efficiency q , due to the imperfect nature of the detector equivalent to a random loss of signal photons, which will affect the previous sensitivity, any noise free classical gain on the photocurrent will not change this fundamental limit in the [SNR](#).

Experimentally, the power of the reference is never unlimited nor infinite. We could thus rewrite

$$\delta\varphi_s = \frac{\sqrt{|\alpha_s|^2 + |\alpha_r|^2}}{2|\alpha_r||\alpha_s|} = \frac{1}{2\sqrt{q_r} \langle n_s \rangle}, \quad (3.24)$$

and interpret the effect of the finite reference and signal power ratio as an additional detection quantum efficiency q_r , (Appel et al. (2007))

$$q_r = \frac{|\alpha_r|^2}{|\alpha_r|^2 + |\alpha_s|^2} = \left(1 + \frac{|\alpha_s|^2}{|\alpha_r|^2}\right)^{-1}, \quad (3.25)$$

given as the ratio of the intensity noise of the reference beam to the total photocurrent noise, here in absence of extra technical noise only due to the total light intensity impinging on the two photodetectors.

3.8 HETERODYNING

We would like to generalize the previous results to the situation known as heterodyne where the signal and reference fields evolve in time at different frequencies. As we shall see, compared to homodyne, heterodyne has a higher shot noise limited minimum phase resolution. But in many cases during this thesis experimental work, it has appeared very helpful in physical data recording with dominant low frequency technical noise and in the first steps towards the real-time detection of continuous atomic signals.

To avoid rewriting everything, we can simply now consider this difference in frequencies as an extra time-dependent phase. Without loss of generality we now replace $\varphi_s(t) = \varphi_s - \delta\omega t$, where φ_s will always refer to the direct current (DC) phase if not specified.

The differential photocurrent now becomes time-dependent

$$\langle \psi | \hat{d}_i(t) | \psi \rangle = 2|\alpha_r||\alpha_s| \cos(\Delta\varphi - \delta\omega t), \quad (3.26)$$

where we have set $\Delta\varphi = \varphi_s - \varphi_r$. This means now that every half oscillation period $t = \pi/2(\delta\omega)$, the photocurrent measures alternatively the quadratures of the signal, i. e. the quadratures \hat{X} and \hat{P} are sampled independently (for $\varphi_r = 0$) but not *simultaneously*. To extract the phase information, the photocurrent signal is mixed down to baseband, that is, we bring to DC respectively the in-phase and quadrature components by multiplying¹⁷ it electronically respectively with a radio-frequency (RF) wave whose phase can be adjusted to produce either $\cos(\delta\omega t)$ or $\sin(\delta\omega t)$. The components are then averaged (low-pass filtered) over a time $\tau = 2\pi l / \delta\omega$ where l is an integer. For the component in quadrature with the RF phase, we have for instance

$$d_i^{\text{sin}} = \frac{1}{\tau} \int_0^\tau \langle \psi | \hat{d}_i(t) | \psi \rangle \sin(\delta\omega t) dt, \quad (3.27)$$

$$= 2|\alpha_r||\alpha_s| \frac{1}{\tau} \int_0^\tau \cos(\Delta\varphi - \delta\omega t) \sin(\delta\omega t) dt, \quad (3.28)$$

$$= |\alpha_r||\alpha_s| \sin(\Delta\varphi). \quad (3.29)$$

¹⁷ There is no such thing as a multiplier. The electronics frequency mixers we used turn on and off the input signal at a given frequency.

Compared to (3.18) we lose a factor of 2 in signal compared to the homodyne signal. However the noise power also loses a factor of 2 from the previous signal processing such that (3.19) only reduces by $\sqrt{2}$ and therefore one only loses a factor $\sqrt{2}$ in phase-sensitivity compared to (3.24).

$$\delta\varphi_s^{\text{hetero}} = \frac{1}{\sqrt{2q_r \langle n_s \rangle}} = \frac{1}{\sqrt{2q_r \tau \langle \hat{\Phi} \rangle}}, \quad (3.30)$$

where $\langle n_s \rangle$ is the mean number of the signal photons sampled during time τ . Indeed, it is important to identify $|\alpha|^2 = \langle \hat{n} \rangle = \tau \langle \hat{\Phi} \rangle$ where $\hat{\Phi}$ is the photon flux operator. For a fixed input flux or power, we can increase the phase-sensitivity by averaging longer (i. e. more photons).

It is not trivial to estimate the noise power after the classical multiplication by the electronics reference wave at $\sin(\delta\omega t)$. To find the above results we considered that a classical stochastic photocurrent signal is fed to the mixer. This classical photocurrent presents *quantum fluctuations* as the result of the random arrival photons on the photodetector. In this case, the noise is calculated from (3.18) where one should identify $\Delta\varphi \rightsquigarrow \Delta\varphi - \delta\omega t$ to keep the definition $\Delta\varphi = \varphi_s - \varphi_r$. Therefore, the instantaneous noise on the input signal is independent of the phase and random in time. However, upon further mixing at $\delta\omega$ with $\sin(\delta\omega t)$ the instantaneous input noise power becomes time dependent. The only contribution that will remain at DC after time-averaging is the instantaneous noise power component $\sin(\delta\omega t)^2 \delta i^2$ where $\delta i = \sqrt{|\alpha_s|^2 + |\alpha_r|^2}$ is the stochastic light shot noise fluctuations on top of the classical photocurrent which have entered the mixer during the integration time τ such that the time-average or RMS shot noise is $\sqrt{|\alpha_s|^2 + |\alpha_r|^2} / \sqrt{2}$. We will comment on this result in more detail in later sections.

3.9 SINGLE VERSUS DOUBLE QUADRATURE MEASUREMENT

From (3.11), it is clear (if the reference is well-known) that homodyne or heterodyne does not exactly detect a phase but rather the observable $\hat{x} = e^{i\varphi_s} \hat{\mathbf{a}}_s^\dagger + e^{-i\varphi_s} \hat{\mathbf{a}}_s$. Above, we have only commented on single quadrature measurements. In this case, phase information is extracted from the photocurrent, for instance in the balanced homodyne case (3.13) as

$$\varphi_s = \varphi_r + \cos^{-1} \left(\frac{\langle \psi | \hat{d}_i | \psi \rangle}{2|\alpha_r||\alpha_s|} \right). \quad (3.31)$$

This means that the single quadrature measurement requires a *prior* knowledge of both coherent states amplitudes or in classical terms, a calibration of the amplitude of the interference fringe. In addition, the extracted phase φ_s is only defined in a π interval. This contrasts with

an estimation of the phase shift based on *independent* measurements of the two quadratures x and p .

$$\varphi_s = \varphi_r + \tan^{-1} \left(\frac{\langle \psi | \hat{p} | \psi \rangle}{\langle \psi | \hat{x} | \psi \rangle} \right). \quad (3.32)$$

The phase is now well-defined in a 2π interval and there is no explicit need to know the field strengths. However, the drawback is that the independent light shot noise from the independent double quadrature measurement will add in quadrature. In effect, this would mean to acquire twice as many data samples to compensate. For the single quadrature measurement, $\varphi_s - \varphi_r$ is adjusted to the point of maximum phase sensitivity while for the double quadrature measurement, this point needs to be alternatively shifted by $\pi/2$. For heterodyne, this happens *naturally* every half period of the beatnote frequency. This has led us to another strategy we have implemented experimentally at the early stage without enough electronic equipments (see next section).

3.10 PHASE ESTIMATION VIA HILBERT TRANSFORM

In the case of heterodyning, the photocurrent reproduces the narrow-band real quadrature $x(t)$. Clearly, if one could estimate the annihilation operator, i. e. reconstruct the analytic signal $\alpha(t) = x(t) + ip(t)$, then the *instantaneous phase* would be given by the argument of $\alpha(t) = |\alpha|e^{-i\varphi(t)}$ or $i \ln(x(t) + ip(t))$. We can obtain the quadrature $p(t)$ by taking the Hilbert transform of $x(t)$, which is the convolution¹⁸ $p(t) = x(t) \star (1/\pi t)$. $\cos \varphi$ and $\sin \varphi$ are not *independent* here in the sense that they are related by causality¹⁹ and the above Hilbert transform is the mathematical name of the Kramers-Kronig relations²⁰.

3.11 REMARK ON THE DETECTED QUANTUM NOISE

It is possible to find the noise on the differential photocurrent by evaluating

$$\sigma(\hat{d}_i) = \sqrt{\langle \psi | \hat{d}_i^2 | \psi \rangle - (\langle \psi | \hat{d}_i | \psi \rangle)^2} = \sqrt{|\alpha_s|^2 + |\alpha_r|^2}, \quad (3.33)$$

where $\hat{d}_i = \hat{i}_+ - \hat{i}_-$ is the differential photocurrent operator. Even though (3.33) would give the right answer for the homodyne case and for the instantaneous noise of heterodyne, it might be misleading to use such an operator to predict the noise after the entire detection chain. It can lead to physical aberration if the photocurrent is further up or down frequency mixed. This is because we actually do not measure

18 In frequency domain, it is equivalent to a $-\pi/2$ phase shift of the positive frequencies and a $\pi/2$ of the negatives ones. This leads to destructive interference of the negative frequencies when added onto the original signal x .

19 In quantum mechanics, measuring x before p is different than the reversed order.

20 that the imaginary part is the Hilbert transform of the real part.

$\hat{i}_+ - \hat{i}_-$. Rather, the expectation value of the latter contributes to the probability per unit time of creating a photo-electron.

Each detector produces a *classical* photocurrent corresponding to a time continuous sampling of the expectation value of the operator \hat{i}_\pm . The term $(\pm \hat{\mathbf{a}}_r \hat{\mathbf{a}}_s^\dagger \pm \hat{\mathbf{a}}_r^\dagger \hat{\mathbf{a}}_s)/2$ has a well-defined expectation value for coherent states whereas $(\hat{\mathbf{a}}_s^\dagger \hat{\mathbf{a}}_s + \hat{\mathbf{a}}_r^\dagger \hat{\mathbf{a}}_r)/2$ does not. The latter has intrinsic ensemble average quantum fluctuations that lead to a stochastic noise added on top of the former *classical* well-defined signal, due to the random arrival of photons on the detectors. This only source of quantum noise on the photocurrent is independent for each detector in such a way that they will add in quadrature if one measures a differential photocurrent. While on average, the differences of these optical rectification terms cancel out. We could then write the differential photocurrent signal as $s(t) = i(t) + \delta i(t)$ where $i(t)$ is the time evolution of the well-defined expectation value $\langle \psi | \hat{d}_i(t) | \psi \rangle$ and $\delta i(t)$ is a random offset increment from the statistical ensemble average uncertainty of $\hat{\mathbf{a}}_s^\dagger \hat{\mathbf{a}}_s + \hat{\mathbf{a}}_r^\dagger \hat{\mathbf{a}}_r$. As in Brownian motion, $\delta i(t)$ is not differentiable at time t and should be understood as a value sampled from the distribution of the photon arrival times here for coherent states of light.

Therefore, it is clear that upon mixing the output noisy photocurrent difference with $\sin(\delta\omega t)$, the added random fluctuations will also be multiplied. After a time-average multiple of the mixing period, these do not contribute to the mean value of the signal. However, the noise power of the photocurrent, independent of the phase sensitive part $i(t)$ of the signal, will be reduced by half after the time average

$$\int_0^\tau \sin(\delta\omega t)^2 \delta i^2 dt / \tau = \delta i^2 / 2.$$

The above remark is important as it allows us to simply use the classical representation to describe the signal as long as the quantum aspect, here in the existence of a fundamental light shot noise from coherent states, is taken into account in the final SNR.

3.12 HETERODYNE WITH HOMODYNE SENSITIVITY

We would like to anticipate on the ideas we have implemented for the second of our main investigated thesis project. We have noticed that the previous penalty of $\sqrt{2}$ in phase sensitivity of single heterodyne compared to homodyne can be overcome for the same total light power in the signal. Consider that the signal is now made of the superposition of two coherent fields with opposite phase φ_s and separated in frequencies by $2\delta\omega$. In addition, the fields have equal strength and their frequencies are symmetric compared to that of the reference field. We have $\hat{\mathbf{E}}_s^+ = \hat{\mathbf{E}}_{s_+}^+ + \hat{\mathbf{E}}_{s_-}^+$ and $|\psi_s\rangle = |\psi_{s_+}\rangle \otimes |\psi_{s_-}\rangle$. Their explicit representation is $|\psi_{s_\pm}(t)\rangle = e^{-i\omega_\pm t} |\alpha_{s_\pm} e^{\pm i\varphi_s}\rangle$ where $|\alpha_{s_+}| = |\alpha_{s_-}|$ and $\omega_\pm = \omega_r \pm \delta\omega$, ω_r being the optical frequency of the reference field.

Starting from (3.13) which involves the sum of $\hat{a}_r^\dagger \hat{a}_s$ and its hermitian conjugate operator (twice the classical real part).

$$\begin{aligned} \langle \psi | \hat{d}_i | \psi \rangle &= \langle \psi | \hat{a}_r^\dagger \hat{a}_s + \text{h.c.} | \psi \rangle \\ &= 2|\alpha_{s_+}| |\alpha_r| [\cos(\delta\omega t - (\varphi_r + \varphi_s)) + \cos(\delta\omega t - (\varphi_s - \varphi_r))]. \end{aligned} \quad (3.34)$$

From the previous result, it seems that upon the previous demodulation and averaging procedure, we might obtain twice the information about φ_s as with the earlier single heterodyne. Actually not twice but $\sqrt{2}$, as we will now see when comparing the methods for identical invested light power. Both methods require to lock the phase of the reference φ_r and the previous observation can be read directly from (3.34) if we measure $\Delta\varphi = \varphi_s$ i.e. $\varphi_r = 0$. This would give for the quadrature component

$$d_i^{\text{sin}} = \frac{1}{\tau} \int_0^\tau \langle \psi | \hat{d}_i(t) | \psi \rangle \sin(\delta\omega t) dt, \quad (3.35)$$

$$= 2|\alpha_r| |\alpha_{s_\pm}| \sin(\varphi_s). \quad (3.36)$$

Because our two sub-signals have equal strength and each carries half of the total power of the total single signal in the single heterodyne method, we identify $|\alpha_s| = \sqrt{2}|\alpha_{s_\pm}|$ for comparison. In addition their respective light noise contributions are uncorrelated (product states). To deduce the phase sensitivity it is easier to see first that in the limit of a stronger reference beam power, only the shot noise of the reference contributes to the noise power which is averaged as before and then reduced by a factor of 2 due to the demodulation. Therefore, (3.23) gives here

$$\delta\varphi_s = \frac{1}{2\sqrt{2}|\alpha_{s_\pm}|} = \frac{1}{2|\alpha_s|} = \frac{1}{2\sqrt{\langle n_s \rangle}}, \quad (3.37)$$

where we have used the previous identification showing that the symmetrical dual heterodyne method yields the same phase sensitivity as homodyne if the powers in the total signal field are identical. The general expression for the phase sensitivity is readily obtained by using again a quantum efficiency

$$q_r' = \frac{b|\alpha_r|^2}{|\alpha_r|^2 + |\alpha_{s_+}|^2 + |\alpha_{s_-}|^2}, \quad (3.38)$$

where the factor of $b = 2$ is due to the reduction in the noise powers from the averaged demodulation and can be considered as an extra detection inefficiency. It is a matter of choice to keep the earlier definition of q_r and consider the demodulation efficiency $b = 2$ such that

$$\delta\varphi_s = \frac{1}{2\sqrt{bq_r}|\alpha_{s_\pm}|} = \frac{1}{\sqrt{2bq_r}|\alpha_s|} = \frac{1}{\sqrt{2bq_r} \langle n_s \rangle}, \quad (3.39)$$

as $|\alpha_s| = \sqrt{2}|\alpha_{s_\pm}|$, where $q_r = q_r'/b$. Therefore, as long as the noises of the two signals add in quadrature and the signal measures *twice* the

phase compared to single heterodyne we recover the 3 dB penalty in signal power to noise power. Indeed, for a strong reference power $q_r \sim 1$, we find the same result as (3.23). All the previous results are based on (3.34), it is therefore important to mention that to arrive at the latter, we have assumed that the optical rectification terms $\hat{\mathbf{a}}_s^\dagger \hat{\mathbf{a}}_s + \hat{\mathbf{a}}_r^\dagger \hat{\mathbf{a}}_r$ in (3.9) have been filtered out by the detection chain. Whereas for homodyne both terms are DC components, for the dual-heterodyne procedure, the term associated to the signal $\hat{\mathbf{a}}_s^\dagger \hat{\mathbf{a}}_s$ will give rise to a frequency component at $2\delta\omega$ due to interference between the sub-signals. This needs to be filtered out. We will present in more detailed this dual-heterodyne technique later in the thesis at the heart of the nanofiber experiment which is really not suited to detect classical phase dispersion but really suited to measure anomalous dispersion.

3.13 SINGLE PHOTODETECTOR

If only one photodetector is available in the laboratory, then one only measure either the outcomes of \hat{i}_+ or \hat{i}_- . In this situation, the terms responsible for the quantum fluctuations are on average not subtracted out and clearly expose themselves as a non-zero noisy offset. Assuming this offset is subtracted for homodyne measurement via calibration, we can show that the phase sensitivity, for a general beamsplitter with $R : T$ intensity reflection and transmission coefficients, is obtained from²¹

$$\langle \psi | \hat{i}_\pm | \psi \rangle = R|\alpha_s|^2 + (1-R)|\alpha_r|^2 \pm 2\sqrt{R(1-R)} \cos(\phi_s - \phi_r).$$

If we assume that the light power of the reference at the detector is infinitely strong compared to the signal power at the detector, $R|\alpha_s|^2 \ll (1-R)|\alpha_r|^2$

$$\delta\varphi = \frac{1}{2\sqrt{R}|\alpha_s|} = \frac{1}{2\sqrt{R}n_s}, \quad (3.40)$$

or in terms of the mean fraction of signal photons lost, Tn_s , $T = 1 - R$,

$$\delta\varphi = \frac{1}{2\sqrt{(1-T)n_s}}. \quad (3.41)$$

If the signal shot noise is not negligible compared to the reference shot noise (finite reference power) we will write as earlier

$$\delta\varphi = \frac{1}{2\sqrt{q_r(1-T)n_s}}, \quad (3.42)$$

$$\text{where } q_r = \left(1 + \frac{1-T}{T} \frac{|\alpha_s|^2}{|\alpha_r|^2} \right)^{-1}. \quad (3.43)$$

In the case of single heterodyne, the mean DC offset can be high-pass filtered and as before we loose a factor $\sqrt{2}$ in phase sensitivity from the effective bandwidth of the mixing signal process.

²¹ we have assumed that the coating and anti-reflection coating coefficients are identical.

3.14 DIFFERENTIAL HOMODYNE

From the previous relations, it is straightforward to find the result for the general unbalanced ($R \neq T$) differential homodyne measurement with two photodetectors monitoring the two outputs ports ($\langle \psi | \hat{i}_+ | \psi \rangle - \langle \psi | \hat{i}_- | \psi \rangle$). We find, as long as the energy is conserved by the linear optics beamsplitter ($R + T = 1$),

$$\delta\varphi = \frac{1}{2\sqrt{q_r n_s}}, \quad (3.44)$$

$$\text{where } q_r = f(R) \left(1 + \frac{|\alpha_s|^2}{|\alpha_r|^2}\right)^{-1} \quad \text{and } f(R) = 4(1-R)R. \quad (3.45)$$

The most efficient detection that yields the minimum phase resolution is found at the maximum of $f(R)$. Readily, the balanced mode ($R = T = 1/2$) is the optimal one. This is because, even though the shot noises from both detectors add in quadrature and are independent of R and T from the conservation of energy, the phase sensitive signal depends on the amplitude of the fields, proportional to the square roots of the reflection and transmission coefficients.

3.15 REMARK ON OPTIMAL LOSS

A few insights can be gained by considering that a too familiar technical limitation is not a fundamental one. It is obvious that with a single detector and an infinite resource of reference field power, the minimum phase resolution limited by the signal photons is achieved for the minimum fraction of signal photon loss R . However, if the ratio $x = |\alpha_r|^2/|\alpha_s|^2$ is finite before mixing on a beamsplitter, a realistic situation, what is the optimal value for R ? In the differential measurement, which conserves the total energy found before the beamsplitter, the optimal value of R is found independent of x . For a single port measurement, we find instead that there exists an optimal beamsplitter reflection coefficient given by

$$R = \frac{1}{\sqrt{x} + 1} \quad \text{with } x \geq 0. \quad (3.46)$$

Here x is always positive and R is the intensity reflection coefficient of the reference beam always positive and smaller than 1. We assume that the technical noise of the detectors is not a fundamental limit and we have neglected it so far. The obvious question will be to compare the optimal phase resolution in this situation with the differential balanced homodyne case. The quantum efficiency of two-port homodyne is optimal for $R = 1/2$ and is $q_r^{\text{bh}} = x/(x+1)$. The optimal quantum efficiency for single port homodyne and optimal $R(x)$ is given by

$$q_r = \frac{x}{(\sqrt{x} + 1)^2}, \quad (3.47)$$

which saturates to 1 for large x . Thus, we have

$$\frac{q_r^{\text{bh}}}{q_r} = 1 + \frac{2\sqrt{x}}{1+x}. \quad (3.48)$$

Already at $x \sim 10^3$, the quantum efficiency a 50 : 50 differential balanced homodyne measurement would provide is only 5% times greater than the quantum efficiency a single port homodyne measurement with a 95 : 5 beamsplitter (5% of signal power loss) would achieve. This observation explains why we decided to build a simple and robust single photodiode detector in the nanofiber experiment to save time for all the other important things to be built as well.

3.16 VISIBILITY AND QUANTUM EFFICIENCY

Another important imperfection that can be cast into an additional detection quantum inefficiency is the quality of the mode overlap (e. g. polarization mismatch, spatial mode overlap, beam size and divergence etc) between the probe (signal) field and the optical local oscillator, called up until now reference field.

This quality is experimentally estimated by measuring the interference fringe visibility \mathcal{V} given by the beatnote intensity contrast (see for instance [Oblak et al. \(2005\)](#)). An imperfect visibility ($\mathcal{V} \ll 1$) is equivalent to an attenuation of the probe field strength (and of the beatnote) by \mathcal{V} . Therefore, it is also equivalent to a loss of probe photons of $(1 - \mathcal{V}^2)$. Or as before, it is equivalent to the effect of a beamsplitter with intensity transmission coefficient $V = \mathcal{V}^2$ where V is the quantum efficiency associated to the imperfect visibility \mathcal{V} .

$$\mathcal{V} = \frac{I_{\max} - I_{\min}}{I_{\max} + I_{\min} - 2f} = \frac{\langle \psi | \hat{d}_i(t) | \psi \rangle_{\Delta\varphi=\pi} - \langle \psi | \hat{d}_i(t) | \psi \rangle_{\Delta\varphi=0}}{\langle \psi | \hat{d}_i(t) | \psi \rangle_{\Delta\varphi=\pi} + \langle \psi | \hat{d}_i(t) | \psi \rangle_{\Delta\varphi=0}} \quad (3.49)$$

$$\mathcal{V} = \frac{2\sqrt{I_r I_s}}{I_r + I_s} \quad (3.50)$$

where f is a possible electronic detection measurement offset. Because the quantum efficiency scales quadratically with the visibility it should be made as close as possible to unity.

3.17 QUANTUM EFFICIENCY IN PRESENCE OF TECHNICAL NOISE

In a realistic technical implementation, extra classical noise pollutes the photocurrent signal. We denote by χ the electronic technical noise power and we assume it is independent of the input light. Therefore, it simply adds in quadrature to the photon shot noise power and its

effect can be accounted for a modification of the detection quantum efficiency. Here for balanced homodyne,

$$q_r = \left(1 + \frac{|\alpha_s|^2 + \chi(\tau)}{|\alpha_r|^2}\right)^{-1}. \quad (3.51)$$

In the next section we shall discuss the main dominant sources of noise contributing to $\chi(\tau)$. To stay in the right units, $\chi(\tau)$ should be interpreted in (3.51) as a photon shot noise equivalent electronic noise. Readily, we explicitly showed that such noise power can have an arbitrary (not necessarily stochastic) frequency spectrum, where as before τ is the measurement averaging time. $\chi(\tau)$ is the average technical noise power during time τ . The overall detection quantum efficiency in presence of technical noise now becomes measurement time dependent. This is extremely important because it means that a perfect characterization or state reconstruction fidelity of an input light field is constrained to a usually narrow detection band where light shot noise dominates classical technical noise.

I do not have enough time to go through all the technical details of the design of all the light shot noise limited photodetectors we have built for the experiments. I will at least finish this chapter by saving what I believe to be the most important working ideas and ingredients.

3.18 INSIGHTS INTO PHOTOCURRENT MEASUREMENT

3.18.1 Photovoltage versus photocurrent

In general, when one uses electrical sensors as measurement devices in the laboratory, one often has to make a choice between measuring either a voltage or an electrical current. The winner method is often the one which has the best combination of a wide linearity in response with respect to the input signal (large linear dynamic range), a quick time response and a low-level of measurement induced noise. One has to make this choice for light sensing.

3.18.2 Operation modes

The photocurrent produced from the semi-conductor junction of a photodiode needs to be measured. With a zero external bias voltage, the photodiode operates in the so-called photovoltaic mode where the produced photo-electron current cannot flow out of the semi-conductor and therefore accumulates at its electrodes (after being diffused by the n-p doped regions) while effectively charging it and building a voltage across. The already accumulated charges shield the new coming ones (capacitance effect). The sensitivity of the diode depends on the voltage across its junction and therefore this can build a nonlinear response

with respect to the incident light energy. Such a detection mode can be interesting to integrate very weak input light power (solar cells). However, in order to measure such voltage signal one needs to connect the diode electrodes to a voltmeter or oscilloscope with a high input impedance. Otherwise current will be drawn from the charged diode junction which would lower the signal voltage. Even though this is achievable²², a photodiode has a small but non-negligible junction capacitance which in series to such high impedance measurement point will make the light measurement sensitivity very slow.

3.18.3 Photoconduction and transimpedance stage

For these reasons, we almost always operate our light detection in the photoconductive mode where instead we detect a signal current by applying a constant external reversed bias voltage to the photodiode. This provides energy for the photo-electrons to flow out of the diode by lowering their potential barrier. This also helps to prevent recombination of electron-hole pairs effectively reducing²³ the capacitance of the junction and therefore increasing speed. The applied voltage has the drawback to ease the apparition of a leakage *dark current* from charge carriers thermally excited in the conduction band. The dark current²⁴ is in general not significant for photodiodes as their junction has a relatively high shunt resistance (for a $\sim 10\text{ V}$ bias voltage). While for photon counting based on avalanche photodiode (APD), the dark current is relatively high due to the much higher required bias voltage. Clearly, this limitation or temperature dependent dark current, is more serious when the detector bandgap is designed for the energy of infrared light. Cooling an APD is therefore a common strategy albeit increasing the complexity of a setup.

A typical PIN photodiode detector therefore can be viewed as a relatively simple and compact low-level electrical current source. To measure such a current, it is possible to measure a voltage drop across a resistance in series. Increasing the resistance will increase the voltage or signal gain and as we will mention in the next section it will also reduce an intrinsic added thermal noise present in Ohmic circuits known as Johnson-Nyquist noise. However, increasing this load resistance will also increase the time response and reduce the detection bandwidth of the electronic circuit.

Complementary to the voltage measurement where a high impedance is required to avoid drawing current and affecting the voltage across the diode, here measuring the photocurrent via a voltage drop without disturbing the voltage across the diode (i. e. keeping the bias voltage constant) calls also for an intermediate transimpedance buffer stage. The

²² using a voltage buffer or differential operational amplifier.

²³ increase the depletion width

²⁴ In the ideal photovoltaic mode, there is no dark current.

latter gives an output voltage signal proportional to the photocurrent while keeping the bandwidth of the detection circuit independent of any output load thanks to a fast feedback loop to the bias voltage. The voltage noise of the transimpedance amplifier always adds up on the measurement and usually is the limiting source of noise, in particular at high frequency where the Johnson noise decreases.

3.19 PARTICULAR LIMITING NOISES

The addition of noises, which are independent of the light power, and therefore add in quadrature on the final photocurrent, is not necessarily a sign of a poor detection design. We can name a few of them.

3.19.1 Background light noise

An obvious source of noises is the detection of an unwanted light flux (often spectrally broad but also scattered laser light²⁵) impinging the detector. This also leads to a background shot noise if the background photons arrive randomly. We have seen earlier $\sigma_{\text{sn}} = \sqrt{-2eB \langle i \rangle} = \sqrt{2e^2 B q \Phi_{\text{exp}}}$ where the expected input photon flux is $\Phi_{\text{exp}} = \tau \langle n_{\text{exp}} \rangle$. This flux can be augmented by a background photon flux Φ_b efficiently detected within the optical bandwidth in such a way that the total shot noise becomes $\sigma_{\text{sn}} = \sqrt{2e^2 B q (\Phi_{\text{exp}} + \Phi_b)}$.

3.19.2 Johnson-Nyquist noise

The raw photocurrent produced by light is generally weak. To detect it, we need to transport it into an electronic circuit. The final signal we process in our experiments is generally a voltage signal to be acquired by an (often digital) oscilloscope. This voltage is often obtained by a transimpedance amplification stage of the photocurrent. An electronic circuit operating at a non-zero temperature is prone to the thermal agitation of electrons in the Ohmic elements of the circuit (such as the feedback resistance of the amplifier or the load resistance of the detector). This fluctuation is identified as a black-body radiation thermal equilibrium which due to the finite temporal response of any realistic electrical system (electrical bandwidth B) leads to the well-known Nyquist relation of the RMS thermal noise or voltage²⁶ variance $\sigma_v^2 = 4k_B T R B$ across a ohmic resistor R and T the temperature. This average kinetic energy of the conduction electrons due to thermal equilibrium gives rise to a electric current noise or Johnson-Nyquist noise $\sigma_{\text{jn}} = \sqrt{4k_B T B / R}$. The thermal noise can also load a capacitance such that the RMS voltage across the capacitor reads $\sqrt{k_b T / C}$ where C is

²⁵ detrimental or highly noticeable during photon counting and requires good shielding.

²⁶ we recall that a voltage is an energy per unit charge.

the capacitance. It appears as a filtering of the previous current noise by a low-pass filter bandwidth $B = 1/(4RC)$.

3.19.3 *Flicker noise*

While the previous noise dominates at high frequencies, another source of noise dominates at low frequency, $\sigma_f \sim \sqrt{1/f^x}$ (where x is a real number close to 1.0) known as flicker noise. The sources of this noise are very diverse (e.g. surface charges). In phase-sensitive (homodyne) detection, this noise can be bypassed by chopping the incident input light in case the information encoded on light is contained near zero frequencies. This strategy has been implemented in the atomic clock setup.

3.20 SUMMARY

In this chapter, we have presented in a simple form the essential ideas that we have applied and developed experimentally, with the help of Jürgen Appel (JA) in the two light-atom interface experiments, in order to be able to detect in real time (continuously) the optical phase of light probes with a precision only limited by the intrinsic noise of the probe, ideally independently of the technical classical noise in the detection process. The most important quantity is the overall detection quantum efficiency and we identified the main sources of imperfections which reduce it.

This chapter is intended to be a reference for the merits of the different measurement schemes we have implemented, balanced/unbalanced single/dual port homodyne/heterodyne/dual-heterodyne and it fulfills a lack. Understanding the light detection process is one of the most important enabling step in the realization of advanced experiments in quantum optics, here in particular to implement optical QND measurement of atomic states. As a result, the first two chapters contain most of the challenging principles that we need and will use to understand the measurement reported in the next chapter and in the remainder of this report.

We recommend to read the very recent work published in [Locke and Fertig \(2013\)](#) where the suppression of the heterodyne precision penalty has also been observed in parallel to our experimental work.

4

INTERFERENCE BETWEEN AN ATOMIC SPIN WAVE AND A SINGLE POLARITON

We can easily forgive a child who is afraid of the dark; the real tragedy of life is when men are afraid of the light.

— Plato

INTRODUCTION

The two previous chapters contain enough material to understand the experiments we are going to describe in this chapter. We will start by giving an overview of the experimental setup that realizes a quantum interface between free space optical light modes and the collective degrees of freedom of mesoscopic ($N_{\text{at}} \sim 10^6$) ensembles of cold Cesium atoms. We shall highlight the challenging parts in both atomic state preparation and non-destructive light measurement at the shot noise limit. We will present the experimental achievement of spin squeezing in this system in conditions suited to implement a quantum atomic clock. Then, we will show the steps that have been required to generate higher symmetric Dicke states at the frontier between continuous and discrete variables measurements. The objective is to insist on the experimental aspect and keep our comments as descriptive as possible.

Fundamentally, we would like to extend heterodyne interferometry with light modes to collective atomic modes. The interference between a reference atomic local oscillator (mesoscopic collective two-mode atomic coherent state or simply spin wave) and any *mode-matched* collective internal atomic state (if possible highly quantum, i. e. a collective Fock state or simply a polariton) to be characterized is realized with a 50 : 50 internal atomic state beamsplitter (played by a $\pi/2$ Rabi pulse). The SNR of this atomic state tomography is analogously limited by the intrinsic noise of the signal atomic state and the atomic detection quantum efficiency. The challenge is therefore both in the preparation of non-classical atomic states (high purity) and in their faithful (high fidelity) characterization limited by the latter quantum efficiency which is function of atomic mode losses, atomic mode-matching visibility and importantly the ratio of atomic local oscillator noise to total atomic state detection noise and finally how large the size of this atomic local oscillator can be before its intrinsic noise becomes dominated by

classical atomic state noise. We note the further exciting prospect of squeezing the collective local oscillator (LO) atomic coherent states conditioned on QND light measurement to beat the underlying SQL.

4.1 EXPERIMENTAL SPIN-SQUEEZING IN A NUTSHELL

Because during the second part of my thesis work a completely new experimental setup for cold atoms was built I should go into more practical details about the manipulation and trapping of atoms later and I will try to keep a minimal technical approach here to focus on the fundamental measurements.

4.1.1 Atomic levels structure

As mentioned in the first chapter, a practical choice of two long-lived atomic states is given by the so-called clock states of neutral Cesium atoms. Specifically, they correspond to the two magnetically insensitive Zeeman sub-levels belonging respectively to the two lowest hyperfine ground states of the atom. They can be identified in figure 4.1 which offers a zoom into the hyperfine structure of the ground and first excited states of the Cesium atom.

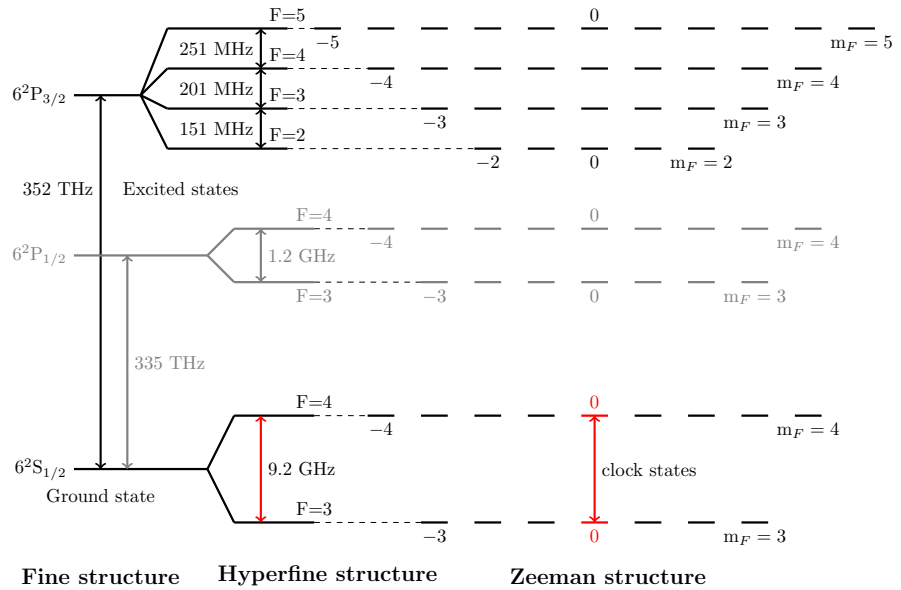


Figure 4.1: Representation of the hyperfine and Zeeman atomic states of the first fine structure doublet of neutral Cesium atoms.

We briefly recall the physical origin of these two states and introduce a few notations.

Cesium atoms possess an unpaired single valence electron. Relativistic effects and interaction of the electronic spin ($S = 1/2$) with its orbital angular momentum (L) give rise to the fine structure of the

atomic energy levels shown on the left of the figure which is particularly strong for Cesium. The ground state configuration of the atom is $6^2S_{1/2}$ for which the electronic orbital momentum is nul ($\mathbf{L} = 0$, S orbital) and therefore the total electronic angular momentum $\mathbf{J} = \mathbf{L} + \mathbf{S}$ is only due to the single valence electron spin such that $\mathbf{J} = 1/2$. The first excited state of the electron into the P orbital ($L = 1$) gives rise to the fine structure splitting doublet $\mathbf{J} = \{1/2, 3/2\}$, shown by the terms $6^2P_{1/2}, 6^2P_{3/2}$ on the drawing.

These two excited levels can be coupled to the ground state via permitted¹ electric dipole transitions and they form respectively the (doublet) D1 (895 nm or 335 THz) and D2 (852 nm or 352 THz) lines.

The nucleus of Cesium has a ground state spin $\mathbf{I} = 7/2$. The interaction between the nuclear spin and the total electronic angular momentum gives rise to an additional energy splitting, the hyperfine structure shown in the middle of figure 4.1. The total angular momentum of the atom (electronic + nuclear) $\mathbf{F} = \mathbf{I} + \mathbf{J}$ implies the existence of a hyperfine doublet $\mathbf{F} = 3, 4$ for the ground state corresponding to the two stationary opposite orientations of the electron spin with respect to the nuclear spin. The frequency difference between these two states is *exactly*² 9.192 631 770 GHz. The hyperfine structure of the excited state of the D2 (D2) line is made of four levels $\mathbf{F} = 2, 3, 4, 5$ the frequency extend of which is about two orders of magnitude smaller than the ground state hyperfine splitting contrary to the arbitrary scale of the drawing.

Because of the magnetic moment induced by the angular momentum, the energy of an atom depends on the orientation of its angular momentum in space when immersed in a magnetic field (e. g. Earth magnetic field). This gives rises to the additional energy splitting structure or Zeeman magnetic levels shown in the right of figure 4.1 for the only $2\mathbf{F} + 1$ stable azimuthal orientations of the atomic magnetic moment³ allowed by quantum mechanics with respect to the external magnetic field direction.

To anticipate the following sections, we recall that the selection rules for electric dipole transitions between two Zeeman hyperfine levels $|F, m_F\rangle \leftrightarrow |F', m_{F'}\rangle$ are is $\Delta F = F - F' = 0, \pm 1$ and $\Delta m_F = m_F - m_{F'} = 0, \pm 1$ with the exception that when $F = F'$, the transition from a Zeeman level $m_F = 0$ to $m'_{F'} = 0$ is forbidden. The D2 line exhibits then two forbidden electric dipole transition in the optical

¹ As long as the atom possesses inversion symmetry, its stable energy states are either symmetric or anti-symmetric under inversion of the atomic charge distribution. This means that the atoms have no (permanent) electrical dipole moment in a given (stationary) energy state.

² The unit of time (s) and hence frequency is defined upon it until another standard replaces it.

³ Which orientation that minimizes the energy of the atom (parallel or anti-parallel to the magnetic field) is given by the sign of the Landé factors, negative for $F = 2$ and $F = 3$ (except for the D2 excited state where it vanishes). All the others are positive.

domain $|F = 4, m_F = 0\rangle \leftrightarrow |F' = 4, m_{F'} = 0\rangle$ and $|F = 3, m_F = 0\rangle \leftrightarrow |F' = 3, m_{F'} = 0\rangle$ that may be useful for dark optical pumping. Note that electric dipole transitions within the same electronic orbital are forbidden (due to inversion symmetry) but magnetic dipole transitions are allowed. In particular, the clock states can be manipulated with a magnetic field oscillating in the microwave domain.

4.1.2 *Spatial confinement of the atoms*

To manipulate the internal and collective states of atoms one needs to be able to observe and interrogate all the atoms together homogeneously in a sufficient time with a sufficient interaction strength. To this end, atoms are held in a tightly confined volume in space by a cylindrically symmetric trap potential. This trap is a standard far off-resonant (1064 nm) light force gradient arising from a gaussian laser beam mode spatially focused down to waists of about 50 μm and a nominal power of about 5 W. The trap light wavelength is designed to attract ground state Cesium atoms at the intensity maxima of the light field, that is, at the beam focus. Note that this simple trap is atomic state sensitive. That is, we only trap atoms that spend predominantly their time in the ground state $6^2\text{S}_{1/2}$. The applied light force will be approximatively considered conservative on the atom observation time scales.

4.1.3 *Reservoir of cold atoms*

Because such optical dipole trap is relatively shallow (maximum AC Stark shift of a few MHz), the atoms need to be pre-cooled in order to be confined in the field of view of the gaussian trap beam. The atomic trap is realized inside a low vacuum chamber with all optical beams entering from outside via a near-infrared (NIR) coated rectangular glass cell connected to the chamber. A three-dimensional MOT designed for the D2 line of Cesium is built around the cell. It allows to cool Cesium atoms directly from a background vapor of Cesium atoms released in the vacuum chamber via dispensers. To compare to slowing and cooling of thermal atomic beams, loading from a background pressure has the disadvantage to reduce the mean free time of atoms between collisions. Yet, the background pressure is optimized for a high repetition rate of experimental realizations that require the creation of a new MOT and loading of the optical trap (about a second). The lifetime of the now cold atoms once transferred in the above optical dipole trap will be limited by collisions with the room-temperature background atoms to several milliseconds.

4.1.4 Atomic state preparation

After loading into the dipole trap, an external DC magnetic field oriented along the gravity axis is applied onto the atoms (about 1.5 G). The trapped atoms are initially populating randomly the Zeeman levels of the hyperfine ground states, that is, the angular momenta of the atoms in the ensemble point in the allowed random directions about the external magnetic field. With dark state optical pumping one can prepare a pure ensemble of atoms which all populate one and the same clock state. We denote by π for parallel, when the linear polarization of an external electric or magnetic field is parallel to the quantization axis or external bias magnetic field direction. We denote by σ (for senkrecht, German word for perpendicular) when the polarization is perpendicular to the quantization magnetic field direction. By σ^+ (σ^-) when it is in addition right-hand (left-hand) circular polarized along the magnetic field direction.

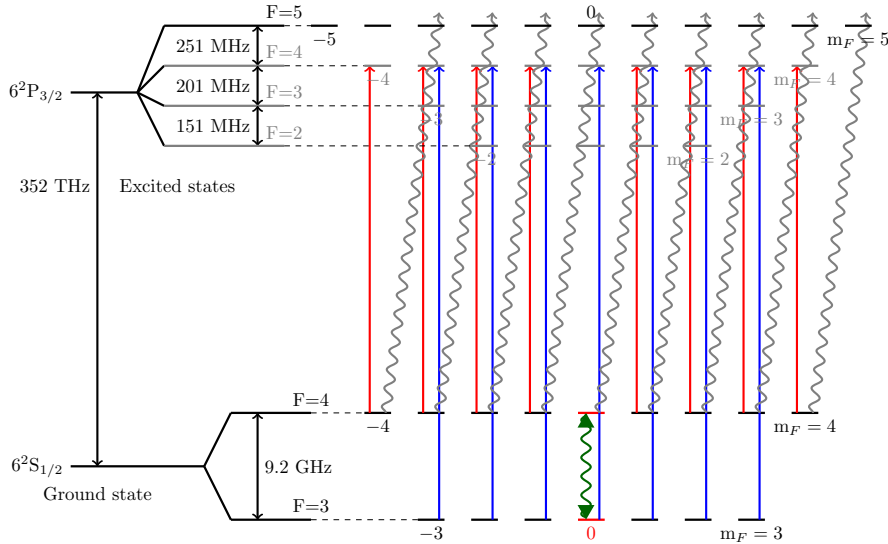


Figure 4.2: Optical dark state preparation and purification. (red) pumping light; (blue) repumping light; (grey) heating light; (green) pumping microwave.

The preparation of a pure ensemble of atoms populating the same Zeeman level is performed in four steps. We illustrate the different required light pulses in figure 4.2. From now on, we use the simplified notation $|F = X, m_F = Y\rangle = |X, Y\rangle$, a single number will always refer to the total angular momentum value F and primed quantities to the excited manifold of the D2 line. First, two quasi-resonant optical fields with π polarization address simultaneously the atoms on $|3\rangle \rightarrow |4'\rangle$ (repumping light, blue color) and on $|4\rangle \rightarrow |4'\rangle$ (pumping light, red color). The repumping light brings all the lowest energy atoms into the hyperfine manifold $|4\rangle$ and also counteracts the allowed decays into $|3\rangle$ of atoms excited into $|4'\rangle$ by the pumping light. Excited atoms can de-

cay by emitting photons with π , σ^+ or σ^- polarizations. As a result, the ensemble starts to build a macroscopic fraction of atomic population in the clock dark state $|4, 0\rangle$ which cannot be excited by the π -polarized pumping light to $|4', 0'\rangle$ (forbidden dipole electric transition). The atoms brought into $|4, 0\rangle$ after a few optical pumping-decay cycles remain in this state.

The second step consists in turning the pumping light off and shortly after, the repumping light as well exactly in that order. Next, with the help of a quasi-resonant microwave magnetic field with π polarization (dark green arrow), the atoms are pumped (saved) into the lowest clock state $|3, 0\rangle$. Finally the atoms not successfully transferred remaining in any Zeeman level of the $|4\rangle$ manifold are heated away from the trap using⁴ blue detuned σ^+ polarized light on the $|4\rangle$ to $|5'\rangle$ transition (gray snaky arrows). With this sequence, one can prepare pure ensemble of atoms in the same state while losing only about 20 – 30% of the atoms.

4.1.5 *Collective state preparation*

The collective coherent spin state is prepared with a $\pi/2$ Rabi resonant microwave pulse between the two clock states. The wavelength of such microwave frequency is on the centimeter scale. That is, the ensemble of atoms is homogeneously and coherently irradiated. In addition, the power of the microwave magnetic field falls into the Watt regime (for kHz Rabi frequency), where the classical (coherent) wave approximation is very good.

4.1.6 *Clock state detection with light*

The spatial distribution of cold atoms in the focus of the dipole trap forms an elongated cigar (prolate) shape. Optical light probes are sent to and propagate through the atomic ensemble along the longitudinal axis of the atomic trap. The probes are also gaussian beams focused at the atom position. The perturbation induced by the atoms in the optical probes is detected via homodyne interferometry, a technique introduced in the previous chapter. More precisely, the heart of the experiment setup is a Mach-Zehnder (MZ) interferometer one arm of which is aligned along the atomic trap axis as shown in the simplified sketch 4.4.

Two off-resonant optical light probes with identical π polarization addressing the D2 line of the Cesium atoms are sent into the same spatial mode and port of the interferometer. The frequency difference between them being on the order of the hyperfine splitting of the ground state. As shown in figure 4.3, the orange (resp. purple) probe frequency is chosen such that the light field will experience a phase shift if there is

⁴ Experimentally, we use one of the MOT beam propagating along the bias magnetic field.

atomic energy populating the ground state $|4\rangle$ (resp. $|3\rangle$). The probe detunings are large enough to apply the homogeneous (transparent ensemble, atoms interacting equally) condition mentioned in the first chapter.

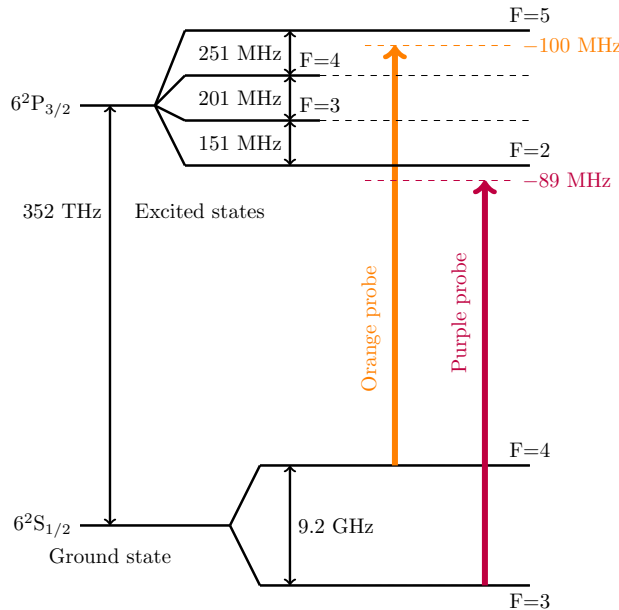


Figure 4.3: Optical probe frequencies.

In addition, for identical probe intensities, the detunings with respect to the hyperfine levels of the atomic optical excited state have been chosen such that the AC stark shifts induced by the two light probes on the two atomic ground states are identical in magnitude but opposite in sign while the two light probes experience phase shifts of both identical sign and magnitude for an atom in any of the two states. These magic frequencies allow to cancel the differential AC stark shift or shift in transition frequency of the ground states. This concern is relevant for ultraprecise atomic clock based on the measurement of the hyperfine transition frequency but also to preserve the collective state coherence from dephasing effects due to inhomogeneous AC stark shifts from the spatial distribution⁵ of the atoms in the trap with respect to the spatial variation of the probe intensity.

4.1.7 Dual-color homodyne and \mathcal{J}_z

In this section, we give more details about the homodyne detection of the two color probes and how one can measure the population difference between the two clock states. We give a simple and light view of the principle of the experimental setup in figure 4.4.

The (optical) length difference of the MZ interferometer between the probe path going through the atomic ensemble trap and the reference

⁵ In addition, the conservatively trapped atoms are moving (quite harmonically) in the gaussian dipole trap

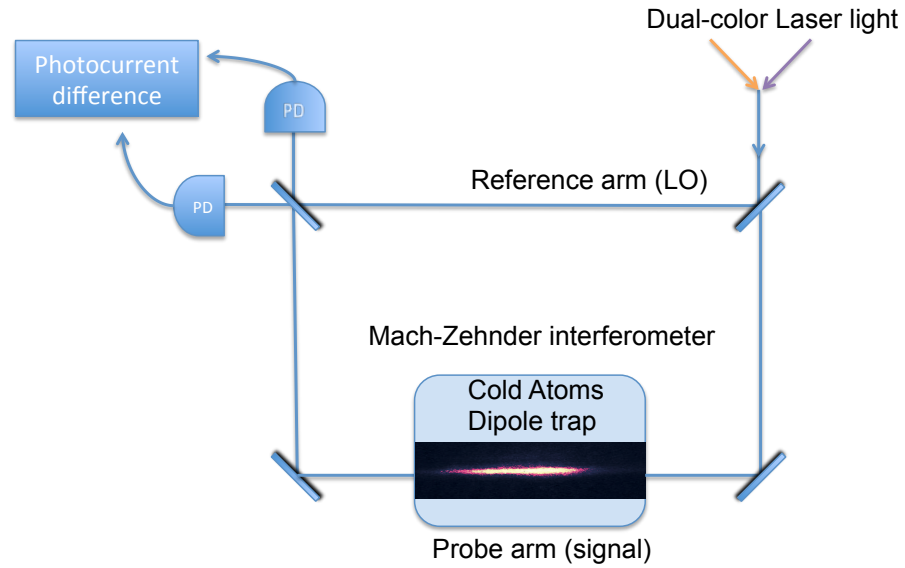


Figure 4.4: Simplified principle of the atomic state population measurement.

(LO) arm path is different from zero. In other words, the interferometer is not operated at the so-called white light position, for which the accumulated phase difference between the LO arm and the probe arm at the interferometer output is independent of the absolute frequency of the propagating optical field. This is convenient to suppress the effect of laser frequency noise⁶ on the detected interference fringe. Here however, the path length difference was chosen such that the accumulated phase difference for the orange probe is out of phase or 180 degrees shifted compared to that of the purple probe, which differ in absolute frequency by about 9 GHz. There is an infinite integer multiple choice for the MZ interferometer path difference to obtain such a condition and the one that yields the lowest length difference is chosen to remain as little insensitive as possible to previously mentioned frequency noise. The phase of a given probe is extracted from differential homodyning (presented in the previous chapter) which allows to subtract out relatively slow classical intensity noise. In addition, the photodetectors are not fast enough (maximum 100 MHz bandwidth) to be sensitive to a beatnote between the two probe colors. Therefore, one should regard the final detected photocurrent for simultaneous probing with the two colors as produced from the superposition of two independent fringe intensities.

As the interference fringes of the two color probes are out-of-phase, the recorded fringe sum photocurrent is only sensitive to the differential phase between the probes. As the two color probes share a common spatial mode, any classical noise (acoustic, thermal) that induces fluc-

⁶ Also, there is no such thing as a monochromatic laser source and any finite frequency width may lead to significant detected phase noise if the interferometer length difference is relatively large.

tuations in the optical path lengths will subtract out when the fringe amplitudes of the two colors are equal. A piezo mounted on one of the [MZ](#) interferometer mirror is used to stabilize the path length difference at the exact non-white light position by adjusting a piezo offset voltage, using the fringe signal from an extra independent laser probe. In addition, the interferometer path length is lock at the zero crossing of the fringe amplitude such that the differential phase between the two colors is measured at the point of maximum phase sensitivity. This technical detection scheme implements in effect a measurement proportional (for small differential phase shifts near the zero crossing) to \mathcal{J}_z or to the population difference between the two clock states as the two probes experience atomic phase shift imprints of equal sign due to the previous choice of detunings to the excited atomic energy levels. When the atoms are in the equal quantum superposition of the two clock states (2.2), the mean detected differential phase is zero, and the detected photocurrent is maximally sensitivity to differential phase variation arising for instance from the quantum fluctuations of the collective atomic state. The rejection of classical fluctuations is good enough such that the [MZ](#) setup operates at light shot noise limited phase sensitivity in adequate measurement time scales (see previous chapter).

4.1.8 *Experimental spin squeezing*

We report in figure 4.5, a typical record of the raw differential photodetection signal after the atoms were prepared in the collective coherent spin states. The atoms are interrogated with $10\ \mu\text{s}$ pulses⁷ generated using acousto-optic modulator ([AOM](#))s. The first 20 pulses, corresponds to the simultaneous interaction with both probes while the last two give access to the phase shifts experienced by the individual colors.

After such measurement sequence, the atoms are pumped to one of the clock states to estimate the number of atoms. Then the atoms are re-prepared in the coherent collective spin state and the same interrogation sequence is repeated providing measurements with different total atom number decaying over the course of the experiment.

As in (2.28), the integration of a pulse signal gives access to a mean integrated phase value. However, a calibration of the fringe amplitudes for given probe powers is required to convert the measured displaced voltage into a phase (as in (3.31)). In figure 4.5, the spikes correspond to the real time observation of phase noise due to probe photon shot noise which is also contaminated by the atomic projection noise. In absence of atoms, the shot-to-shot fluctuations of this value reproduce the probability distribution of N_{ph} mean photon arrivals during the pulse

⁷ Aside simplifying the analysis of the effect of a given number of invested probe photons, such periodic interrogation allows to encode or carry the relevant atomic phase information at a frequency higher than slow classical frequency noise, in particular the [DC](#) electronic noise of the photodetectors.

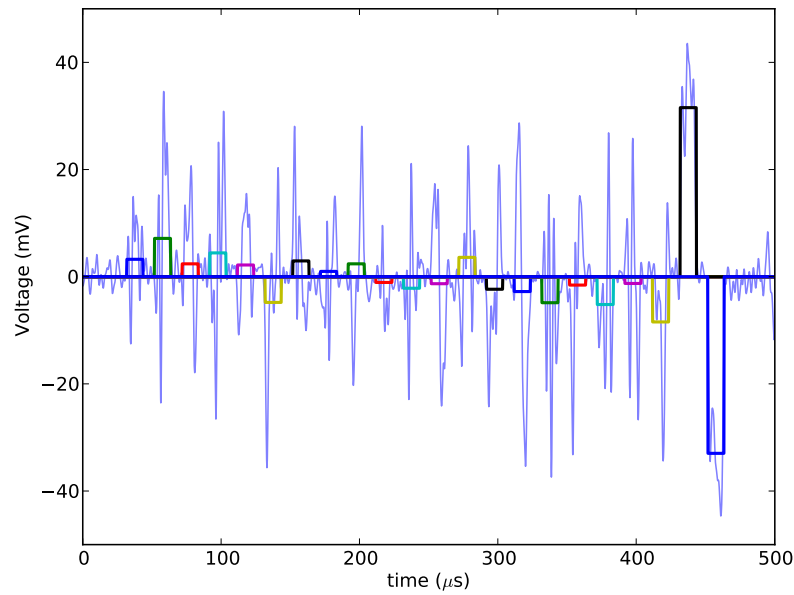


Figure 4.5: Raw homodyne photocurrent voltage while probing a coherent spin state of atomic populations. (see main text)

duration τ for coherent states if the detected phase noise is dominated by light shot noise. As long as the measured phases from the different pulses remain independent (random noise), the scaling of the reciprocal phase noise power (reciprocal phase variance) should increase linearly with the number of integrated pulses or the number of probe photons (see previous chapter) until (relatively low frequency) classical correlations (covariance) between the pulses (e.g. drift of differential phase baseline of the MZ interferometer, laser noise) affect such scaling and become the dominant source of phase noise in a given integration time.

In figure 4.5, I explicit show with the coloured pulses, the mean signal value extracted from an integration time window around the probe pulses. By repeating this kind of measurement many times with atoms initially prepared in a coherent spin state, one will obtain a statistical distribution of such pulse heights which should reproduce the expected statistical outcomes for the collective atomic state. The number of photons in a given pulse may be so small that the statistical variance of the associated phase will be dominated by the light shot noise which would prevent the observation of the phase noise due to atomic noise. However, because the photon shot noise from the different pulses is uncorrelated (or as long as it is) we can reduce the light shot noise contribution by combining successives together in order to resolve better the atomic noise. Unfortunately I do not have time to go through the technical details and the data analysis of this experiment. This has also been done several times in the litterature [Appel et al. \(2009b\)](#);

Louchet-Chauvet et al. (2010). I just wanted to give a simple companion to the group litterature and showing how a *'real* signal looks like.

In presence of atoms prepared in the CSS, the analysis of the detected phase noise should reveal the random atomic projection noise (see (2.24)). In addition, the noise power should scale linearly with the size or number of atoms in the prepared collective coherent state. Here, such number of atoms is estimated indirectly as well by a detected phase shift. One way to estimate the absolute number of atoms is to know the proportionality constant (phase shift per atom) denoted k in the first chapter. While the mean detected atomic phase shifts are proportional to k , the phase noise power (variance) due to projection noise is proportional k^2 and both scale linearly with the number of atoms N_{at} . Therefore the extracted slope of the linear scaling of the phase noise power with the mean phase shift for different atom numbers give access to k .

The demonstration of spin squeezing requires a calibration of the decoherence induced by the invested probe photons. This is done by measuring the Ramsey fringe constrast of the coherent spin-state with and without interacting probe photons.

My first contribution to this experiment, aside from making it operational again with SLC, has been to track and improve on the classical noise sources affecting the phase shift measurement. A bit after, I showed that we could actually observe squeezing without the need to subtract the classical drift of the interferometer between successive collective state preparation. Indeed, in the past group litterature, the squeezing was observed on the so-called two-point variance measurement. We then started to investigation more optimal ways to reject classical noise by combining pulses with different weights and this ultimately led me to adhere to the more general Bayesian filtering approach.

In collaboration with theoretical research on non-classical criteria, we published our experimental results on the preparation of spin-squeezed states in Kiesel et al. (2012). After that, I focused with JA our investigations of the atomic projection noise in presence of a relatively high external magnetic field 20 G, which will make the clock states sensitive to magnetic field fluctuations and will contaminate the observed atomic noise. We observed that we could still resolve the quantum noise of the atoms and decided to explore experimentally the proposal of SLC for the creation of more exotic quantum states in an atomic ensemble. I will finish this chapter by giving a few more details on this last project.

4.2 W-STATE PREPARATION AND DETECTION

Due to the time constrain in writing this thesis as well as the many experiments explored in this work, I will only give the essential ideas as well as my basics point of view on the attempts I tried with SLC

which could be summed up as the preparation and characterisation of a non-classical state stored in a quantum memory based on mesoscopic ensembles of atoms. It represents a hybrid approach where the non-classical state is prepared via discrete events and the characterization of the state is performed using continuous variable measurement.

Our initial ambition was to prepare the first excited symmetric Dicke state, a non-classical state with a negative Wigner function or non-Gaussian marginal probability distribution. The proposal was published in [Christensen et al. \(2013\)](#) and our experimental efforts lead to the results published in [Christensen et al. \(2014\)](#).

The general idea is the following. With optical pumping and state purification steps, we can prepare a pure ensemble where all the atoms are populating initially the upper ground state clock level

$$|\psi\rangle = |\uparrow\rangle \otimes |\uparrow\rangle \otimes |\uparrow\rangle \cdots \otimes^{N_{\text{at}}} \equiv |0\rangle. \quad (4.1)$$

In other words, all the atoms are pseudo-spin polarized along the axis z . We now send an excitation beam propagating through the atomic ensemble. This excitation light addresses the ground state $|\uparrow\rangle$ to a higher optical excited state of the atom, allowing for the possibility of light scattering on the atomic ensemble. However, the excitation light pulse is weak and sufficiently detuned such that it interacts homogeneously with all the atoms. In an ideal scheme, an atom which would be excited can only decay back to the lower ground state $|\downarrow\rangle$, while emitting a scattered photon (in our case anti-Stock photon).

By detecting such a photon in the light field scattered by the ensemble of atoms in the forward propagation direction of the excitation pulse (which has a different frequency than the anti-Stock photon), the measurement heralds the preparation of a delocalized collective excitation

$$|\psi\rangle = \frac{1}{\sqrt{N_{\text{at}}}} \sum_{l=1}^{N_{\text{at}}} |\uparrow\rangle \otimes |\downarrow\rangle_l \otimes |\uparrow\rangle \otimes |\uparrow\rangle \otimes \cdots \otimes |\uparrow\rangle_{N_{\text{at}}} \equiv |W\rangle. \quad (4.2)$$

This state is the generalization of the so-called W state. It can be interpreted as the delocalized interference of a single polariton $|\downarrow\rangle$ and a coherent spin wave with all the remaining atoms in $|\uparrow\rangle$. We can rotate this picture as follows. In order to characterize this state and to measure its marginal statistics via the experimental atomic population difference probing method, we apply homogeneously on the ensemble, a $\pi/2$ microwave Rabi pulse to drive coherently the atomic states ($|\uparrow\rangle \rightarrow |\rightsquigarrow\rangle$, $|\downarrow\rangle \rightarrow |\leftarrow\rangle$) which transforms the W state into

$$|W'\rangle = \frac{1}{\sqrt{N_{\text{at}}}} \sum_{l=1}^{N_{\text{at}}} |\rightsquigarrow\rangle \otimes |\leftarrow\rangle_l \otimes |\rightsquigarrow\rangle \otimes |\rightsquigarrow\rangle \otimes \cdots \otimes |\rightsquigarrow\rangle_{N_{\text{at}}}. \quad (4.3)$$

In absence of the delocalized spin flip or excitation, the collective atomic state after this Rabi pulse would be instead the unperturbed coherent spin state,

$$|\psi_{\text{css}}\rangle = |\rightsquigarrow\rangle \otimes |\rightsquigarrow\rangle \otimes |\rightsquigarrow\rangle \dots \otimes^{N_{\text{at}}}.$$

However, our experimental measurement proposal with a free space dipole trap ensemble of atoms together with the complexity of the atomic level structure is such we cannot prepare with 100% certainty the state W conditioned on the detection of the scattered single photon following that the latter photon has a finite probability to arise from other origins (described in details in the supplementary material of [Christensen et al. \(2014\)](#)). This non-determinism in the state preparation implies that the prepared and interrogated state is a general mixture of the two pure states $|\psi_{\text{css}}\rangle$ and $|W'\rangle$, best described by the density matrix formalism as

$$\hat{\rho} = (1 - p) |\psi_{\text{css}}\rangle + p |W'\rangle, \quad (4.4)$$

where p is the purity or the conditional probability to prepare the W state. In the reported experiments, we had $p = 38\%$, limited mainly by the (technical) quality of the rejection of the writing or excitation light.

Finally, the second important quantity to mention is the atomic state detection quantum efficiency q , analog to the quantum detection efficiency for optical state measurement presented in the previous chapter. $|0\rangle$ or $|\psi_{\text{css}}\rangle$ in the measurement basis, plays the role of a vacuum state for the underlying single excitation state. Our ability to perform the ideal characterization of (4.4) or indirectly $|W'\rangle$ through a calibration of the reference state $|\psi_{\text{css}}\rangle$ is limited by state-independent technical and fundamental noise of the light measurement (see κ^2 in the first chapter), and other imperfections analog to loss of detection signal and imperfect visibility of the atomic state similar to optical homodyne interferometry. In the reported experiments we had $q = 27\%$. This imperfect detection efficiency contributes to a final effective purity

$$p_{\text{eff}} = pq \simeq 10\%. \quad (4.5)$$

As a result, there is no hope to claim non-classicality by reconstructing a negative Wigner function here (this demands $p > 0.5$). However, we observed a significant increase in the atomic spin projection noise of the heralded state compared to a coherent spin state. Our hopes for improvement both in state purity and overall atomic state detection quantum efficiency lies in the new one-dimensional light-atom interface I started to build from zero and whose first exploration will be the subject of the remaining parts of this thesis report.

5

A NANOFIBER INTERFACE: WHY ?

Hobson's choice, the choice of taking what is offered or nothing at all.

— Named after Thomas Hobson (1544-1631), of Cambridge, England, who rented horses and gave his customer only one choice, that of the horse nearest the stable door.

The choice to build a new interface from zero to exploit light-atom interactions based on an optical nanofiber is an important departure, not arbitrary, and it may be the first question a new student may want to ask when joining our group in the future. However, it may also be the most difficult question as there is no single exhaustive answer to why we decided to go for this system. And the reader will find in all the remaining chapters of this thesis a broad list of new features brought by this system. Perhaps, the value of an experimental hypothesis or explored path is best judged by the experimental results that I will present in the next parts. However, in view of the transition from the old setup to this new interface we have developed, it is important to highlight how a nanofiber could help in the realization of many tasks for QIS and metrology but also in simple terms for fundamental research in the field of light-atom interactions.

They can be different levels of understanding and perspectives. Here is my personal and non-exhaustive opinion to serve as a smooth transition to the next part of this thesis. The choice of a nanofiber is clearly not a Hobson's choice.

Although it is true that the nanofiber project represents historically for us a technical improvement to achieve better some of the fundamental ideas developed in the past setup, it cannot be reduced only to a technical device or aspect. It provides a new system rich in physics. It is a new environment for light and neutral atoms. It exhibits new symmetries and degree of freedoms for light and the manipulation of atoms. The use of an optical nanofiber is first intimately connected to the reasons why we use light and neutral atoms.

Contrary to ions, neutral atoms, by definition, do not possess a net electric charge. This means that light which is an electromagnetic field, does not interact with neutral atoms at first sight. The reader may then ask why not using ions instead. As mentioned in the introduction of this thesis, there is no "the winner takes it all" situation. Ions will

be for instance sensitive to environment stray fields and will also exhibit different collective behaviours and spatial densities due to obvious electrical inter-particle interactions (e.g. ion crystals), which may also turned out to be useful.

A general light-atom interaction will thus find its source in higher symmetries of the atomic charge distribution, e.g. electric dipole moment, leading to relatively weaker¹ coupling. Already there at the first next order, atoms do not even possess a permanent dipole moment. This is due to the fundamental reflection symmetry of the atomic charge distribution that ensures the stability of the atoms. The light-atom interaction will therefore be limited by the characteristics of the transient or induced dipole of the atom.

As a result and as is well-known, a whole range of linear quantum optics experiments based on light-matter interaction is described, at first order, by a basic electric-dipole interaction

$$V = -\mathbf{d} \cdot \mathbf{E}, \quad (5.1)$$

from which one can extract the two obvious roads for improving a light-atom interface such as ours. To increase the interaction, one will try to find material system with a high electric polarizability to increase the dipole moment \mathbf{d} (e.g. quantum dot, Rydberg atoms). The obvious second road consists in increasing the strength of the electric field of light \mathbf{E} at the position of the dipole. Or equivalently, to increase the effective electric field of a single photon at the atom position. An additional path to improve the overall interaction is a multi-pass or collective approach. Light is swift and do not interact long with the dipole before it continues its path at the speed of light. CQED as is well-known, is exactly based on the idea to trap light or to allow multi-pass interaction every cavity round trip with the dipole. The alternative approach of collective ensembles is to use many identical dipoles on the single pass trajectory of light. Of course, the last two ideas can be combined together.

Our choice of light-atom interface finds a trade-off among all these basic ideas. In particular, for the first proof-of-concepts of interfaces based on atomic ensembles, the setup was based on the state-of-the-art techniques to manipulate and trap atoms with light in free space. To increase the strength of the electric field of light at the position of the atoms, (5.1), one would focus light on the ensemble of atoms. In view of the best enhancement of the interaction and effective total optical depth, which depends on the overlap of the light beam and the spatial distribution of the atoms, it is important that, as many and as strongly, atomic dipoles couple to the light beam. Although it would be possible to prepare ensembles of atoms as elongated as possible along the beam path direction, the diffraction phenomenon constrains the

¹ Compared to the electromagnetic forces exerted by the nucleus on the electrons for instance.

length of the homogeneous field of view of the light beams over the atomic ensemble (Rayleigh range) and the peak intensity of the light beam (which depends on the beam waist). In free space, diffraction imposes a trade-off between the highest field strength achievable by focusing and the spatial extend of the high field region. And we have not mentioned yet the technical task of achieving a good collection efficiency of the light once transmitted through the ensemble. For optically dense ensembles of atoms, the geometry of the atomic ensemble can lead to new limiting or helping effects, such as lensing effect that would affect the light scattered by the atoms (e. g. diverging forward scattered light).

Building a new interface between light and atoms based on a nanofiber will help to improve on many of such aspects. As we will see, the field of light carried by the fundamental mode of the nanofiber, which we will design to interact with Cesium atoms, is a type of Bessel field. This means that it does not diffract over the propagation length. The field strength therefore remains homogeneous along the propagation direction. This, while at the same time, confining light on transverse dimensions which are smaller than the light wavelength itself. At already a few picowatt light power, the evanescent field intensity reaches the regime of non-linear response of optical atomic transitions. Systematic effects in dense ensembles mentioned above, for example radiation trapping whereby a photon spontaneously scattered by one atom would scatter neighboring ones before leaving the ensemble, would be reduced by the extreme 1D geometry of the nanofiber interface. In view of metrologic applications, such dimension would be interesting for instance to measure gradients of electric and magnetic fields using the atoms as sensors. But there is more to gain than from the geometry of this new platform.

Until now I only put a stress on the strengths of both electric field and atomic dipole while an important aspect of the light-atom interaction lies fundamentally in the orientation of the electric field vector and the dipole vector. In free space, the polarization of light is constrained to live in a plane orthogonal to the light propagation direction. In a nanofiber medium, light is not simply a transverse electromagnetic field anymore. In particular, in the fundamental mode, we will see that it is a hybrid combination of transverse and longitudinal waves. In addition, these waves oscillate in quadrature. This gives to the total polarization of the field a richer three-dimensional complexity. For example, it is possible to change the dominant polarization at the atoms position, π or σ , without changing the propagation direction of light and without changing the quantization axis for the atoms. This has also important consequences for the directionality of the dipole emission pattern of the atoms with respect to the propagation direction of light. The probability of forward (resp. backward) light scattering into a given nanofiber guided mode can be enhanced and made Zeeman state dependent². All

² Photon path could be entangled with particular internal atomic states.

these new opportunities come with the existence of orbital momentum of light carried by nanofiber modes which gives a new twist to light-atomic ensembles for the rapidly-evolving field of quantum information with orbital angular momentum states of light.

Obviously, the inherent compatible and existing fiber technology for this platform, together with its scalability potential, adds to the previous and already long list of exciting perspectives. It is time to discover this new interface in the next parts of this thesis.

To finish, I would just like to emphasize that our attempts at an interface between light and atoms based on a nanofiber was primarily designed in view of the coherent manipulation of long-lived atomic states, here the hyperfine ground states of Cesium.

Part II

AN INVISIBLE OPEN WAVEGUIDE

INTRODUCTION

Wings are a constraint that makes it possible to fly.

— Robert Bringham

In addition to the results reported in the first part, this thesis work represents the first investigations into the realization of an efficient interface between cold atoms and light based on an optical nanofiber, in our group. Therefore, I will save in this part some important personal theoretical efforts in view to understand and to describe the most important properties of light waves propagating into such system. You will find some answers I would have enjoyed to find at the beginning of this thesis. In particular, that the equations I was trying to solve and understand were already found a while ago by Charles Kao (Physics Nobel Prize 2009). However, the field has not ceased to grow over the past three years through a better understanding of the full complexity and symmetry of light guided in an optical nanofiber. Especially through the efforts of Fam Le Kien with whom I shared a few correspondence.

In contrast to sound waves, electromagnetic waves are usually given as a good physical example of transverse waves in the most familiar situation where they *freely* propagate in space. A list of such familiar properties tend to vanish when light propagates in a nanofiber. However the new unfamiliar properties offer a system richer in physics yet to be explored; non-diffracting, inhomogeneous and longitudinal waves which carry orbital momentum. Many non-trivial yet fundamental questions can be raised in this system. What is the *spin* of a photon in a medium of refractive index n ?

The manipulation of both internal and external degrees of freedom of atoms with light is dictated by the principles of linear and angular momenta conservation. It might then appear fundamental to find these in such a system which distinguishes the role of the canonical and kinetic momenta of light, [Barnett and Loudon \(2010\)](#).

In 2009, Charles Kuen Kao was awarded the Nobel Prize in Physics for groundbreaking achievements concerning the transmission of light in fibers for optical communication.

If you really look at it, I was trying to sell a dream ... There was very little I could put in concrete to tell these people it was really real.
– C. K. Kao

The revolution in communication based on the transmission of optical energy through optical fibers, has had a formidable impact on research and societies. Aside from the lightning growth of fiber networks all around the world, sending optical light through pure glass wires is also very elegant and glass is both abundant and fully recyclable.

In a seminal paper of 1966, co-written with George Hockham (Kao and Hockham (1966)), clad glass fibers are proposed as a transmission medium for optical communication. Such fiber waveguides consist of a glass core surrounded by a glass cladding of lower refractive index. Glass fibers have definitely proved to be a medium of choice for optical light communication and manipulation, thanks to sufficiently³ low propagation losses. However, one limitation of this medium in the quest to transmit optical signals over longer and longer distances would be the co-existence of many signal modes⁴ which would propagate at different velocities. This will be the source of signal distortions. Therefore, one also meet a great interest in so-called single-mode fibers which are available today, unfortunately at the cost of a generally weak guidance.⁵ However, one will discover that the apparent impossibility of a single-mode operation together with a strong guidance and strong confinement of light is not a fundamental limitation.

We would like to quote a remark from Kao's original article:

At the visible wavelengths, the operation of a dielectric waveguide with free space as its outer medium is difficult. The physical size, which is now in the submicron range, becomes a serious snag [...] The radius for low-loss operation is considerably less than the wavelength [...] This will cause the waveguide to be invisible.

Delightfully, it happens nowadays that the order of magnitude of the silica glass wire diameters achievable are below the wavelength of optical light waves Tong et al. (2003). A dream that would have been even much harder to sell for Charles Kao in 1966. Kao's "serious snag" is part of our thesis project. Not only does the waveguide becomes invisible, the light guided by the fiber can now be accessed from the outside. It can therefore be interfaced with other systems such as atoms. This is remarkable in a view of scalability and insertion of quantum interfaces into the already existing optical fiber network all over the world.

In the first chapters, we will derive, solve and put our focus on the fundamental equations for the propagation of electromagnetic waves in a optical nanofiber. In other words, we will study Charles Kao's transcendental equation without approximation. These solutions are important for light-atom interactions, for the design of atom traps based on the optical dipole force and also for a better understanding of the nature of light in this system. In the remaining chapters, I will briefly recall how we manufactured optical nanofibers with the help of the group of Pr. Arno Rauschenbeutel, located⁶ at the University of Mainz. Then, I will give some preliminary observations on light propagating in a nanofiber prepared in a ultra-high vacuum (UHV) chamber.

3 A few decibel per kilometer.

4 this term will make itself clearer and more precise in the next chapter.

5 bending radii that guided light can negotiate before radiating out of the waveguide.

6 Now, in Vienna.

6

THINER THAN LIGHT A SUB-WAVELENGTH OPTICAL GUIDE

Ideas do not always come in a flash but by diligent trial-and-error experiments that take time and thought.

— Charles Kao

INTRODUCTION

We will start the study of the nanofiber light-atom interface by first presenting a description of the light propagation in a fiber medium with dimensions smaller than the light wavelength, using the classical electromagnetic wave theory. We tried to reduce the complexity of the problem to a simple and accessible step-by-step derivation. The results presented here in details, although sometimes technical, are not only important in view of the manipulation of atoms with light using an optical nanofiber but also in view of understanding the richer properties of light expressed in this particular medium.

It is remarkable that in such a situation, where the wavelength of light becomes bigger than the transverse size of a fiber, light can still be guided. The most important properties are certainly that this light propagation is theoretically lossless, and that the light is strongly guided and accompanied with a non-diffracting and confined evanescent field outside the fiber. This guided evanescent field is an appealing phenomenon in view to strongly couple light with a surrounding medium (e.g atoms) which may possess subwavelength scattering cross-sections.¹ The framework of electromagnetic wave propagation is very general. It renders the description of this phenomenon feasible and interesting despite the simplicity of the model of reality we devise in the next section. Besides, these solutions are also required in view to quantize the fields, for whom would like to study nanofiber quantum electrodynamics (e. g. Purcell enhancement).

The common single-mode fibers one buys everyday from the industry are weakly-guiding fibers. The single-mode operation is achieved through the design of fibers with small core-cladding refractive index difference (N.A \sim 0.15). As a result, one usually approximates

¹ overcoming diffraction limitation when manipulating light waves in free space

Maxwell's equations to the previous domain of validity which renders the solutions of the fiber eigenvalue problem more tractable. Here, we show how to solve the problem exactly with no such approximation and we will therefore not use the industry standard vocabulary (e.g. LP modes).

6.1 MAXWELL'S EQUATIONS FRAMEWORK

We consider the description of a standard passive optical fiber as an open waveguide made of a cylindrically symmetric step-index medium with inner core radius a . n_1 will always refer to the refractive index of the core and n_2 will be the refractive index of the cladding. In order to extrapolate this simple model to our nanofibers, it is important to mention that an air-cladd optical nanofiber will be obtained by creating a tapered section in a standard fiber through combined heating, pulling and stretching of the fiber media. The transition from the standard fiber to the nanosection is assumed adiabatic and the values of the refractive indexes in this section should be adapted. For instance, n_2 will now refer to the refractive index of vacuum in the nanofibers section as the small core medium of the initial standard fiber merged with its initial cladding medium into a single core medium leaving the role of cladding to the surrounding fiber environment.

$$\text{step index } n(r) = \begin{cases} n_1 & \text{if } r < a, \\ n_2 & \text{if } r > a. \end{cases} \quad \text{with } n_1 > n_2.$$

In order to find how light fields distribute in and around such heterogeneous dielectric subwavelength structure, we will study the solutions of the propagation wave equations, starting from Maxwell's macroscopic relations for the case of *linear, isotropic and transparent non-magnetic dielectric* media².

Macroscopic Maxwell's equations:

$$\nabla \cdot \mathbf{D} = 0 \quad \text{with} \quad \mathbf{D} = \epsilon_0 \mathbf{E} + \mathbf{P}, \quad (6.1)$$

$$\nabla \times \mathbf{E} = -\mu_0 \frac{\partial \mathbf{H}}{\partial t}, \quad (6.2)$$

$$\nabla \cdot \mathbf{H} = 0 \quad \text{with} \quad \mathbf{H} = \frac{\mathbf{B}}{\mu_0}, \quad (6.3)$$

$$\nabla \times \mathbf{H} = \frac{\partial \mathbf{D}}{\partial t}. \quad (6.4)$$

For simplicity but also generalization to various optical light frequencies spectrum, we will only consider monochromatic (angular frequency ω) and harmonic solutions for the fields.

² Bold letters denote vector quantities

From the above assumed properties of the medium, we would then have as one constitutive relation, the linear polarization response

$$\mathbf{P}(t, \mathbf{r}) = \epsilon_0 \chi(\omega, r) \mathbf{E}(t, \mathbf{r}).$$

We have introduced $\chi(\omega, r)$, here the direct Fourier transform of the linear response of the medium, also known as the first order dielectric susceptibility. Just because we only consider here first order responses does not imply that a silica glass nanowire would not be a good candidate for non-linear optics. Abundance, low cost of silica glass and ready fiber communication technology attract non-linear optics research with electrically(thermally)-poled silica optical fibers. Although silica glass has no second-order nonlinearity (glass is centrosymmetric), second-harmonic generation (SHG) in silica optical fibers was observed (Österberg and Margulis (1986)).

6.2 PROPAGATION EQUATION TO *ansatz* SOLUTIONS

We can rewrite Maxwell's equations in terms of the electric and magnetic fields \mathbf{E} and \mathbf{H} . Following the electric induction in the medium, we indeed have

$$\mathbf{D}(t, \mathbf{r}) = \epsilon_0(1 + \chi(\omega, r)) \mathbf{E}(t, \mathbf{r}) = \epsilon(r) \mathbf{E}(t, \mathbf{r}), \quad (6.5)$$

where $\epsilon(r)$ is the dielectric permittivity of the medium, $\epsilon_r = \epsilon(r)/\epsilon_0 = (1 + \chi)$ the relative permittivity, $n(r) = \sqrt{1 + \chi} = \sqrt{\epsilon_r}$ the refractive index of the medium ($\epsilon(r) = n^2 \epsilon_0$). Thereafter, one would obtain the following general wave equations (see A.1):

Wave equation for \mathbf{E}

$$\Delta \mathbf{E} - \mu_0 \epsilon \frac{\partial^2 \mathbf{E}}{\partial t^2} = -\nabla \left[\frac{\mathbf{E} \cdot \nabla(\epsilon)}{\epsilon} \right]. \quad (6.6)$$

Wave equation for \mathbf{H}

$$\Delta \mathbf{H} - \mu_0 \epsilon \frac{\partial^2 \mathbf{H}}{\partial t^2} = \nabla \epsilon \times \mathbf{E}. \quad (6.7)$$

Since $\epsilon(r)$ is constant when $r \neq a$, one can solve the homogeneous version of our wave equations (6.6) and (6.7) in the core and the cladding independently. Finally, one would merge the solutions using the continuity conditions for the fields at $r = a$.

From the circular symmetry around the fiber axis and invariance of all refractive indices along this axis, a cylindrical coordinate system (r, ϕ, z) with the z axis parallel to the fiber axis suggests itself to describe the fields. As we are interested at the very least in propagation of light inside the fiber, we are inclined to investigate solutions that propagate

in the z -direction, that we will characterize by the propagation constant β . The coupling requirement of any input wave-front into the fiber physically fixes constraints on β and will thus play a central role in our description.

To sum up our previous discussion, we will start with solving the wave equations for the following *ansatz* forms³:

$$\mathbf{E}(r, \phi, z, t) = \text{Re}\{\mathcal{E}(r, \phi) \exp [i(\omega t - \beta z)]\}, \quad (6.8)$$

$$\mathbf{H}(r, \phi, z, t) = \text{Re}\{\mathcal{H}(r, \phi) \exp [i(\omega t - \beta z)]\}, \quad (6.9)$$

where we have introduced complex amplitudes to make use of the numerous linear relations.

ANSATZ

As quoted by Feynman in Lectures on Physics, the best way to solve an equation is to already know the solution. But more pragmatically, the state of the electromagnetic fields can be decomposed completely over a given vectorial basis, for instance the three-dimensional plane waves. The choice of the basis being guided for simplicity by the symmetry of the problem. The translational invariance along the fiber axis leads to the separation of the problem into longitudinal and transverse components. β represents the longitudinal component of the gradient of the phase wave-front, i.e the longitudinal wave-vector component.

It should be noted that the previous choice of Ansatz solutions implies a spontaneous breaking of the time-reversal symmetry. Solutions that propagate forward, increasing z , for increasing time t , are singled out. Causality requirements are also implicitly contained in the susceptibility χ .

6.2.1 Only one cylindrical equation to solve

An helpful property arises from the separation of one coordinate (here z) in the field expressions. In Appendix A.2, we have arranged 's equations by pairs such that one can clearly express the components \mathcal{E}_r , \mathcal{H}_r , \mathcal{E}_ϕ and \mathcal{H}_ϕ only in terms of \mathcal{E}_z and \mathcal{H}_z . Therefore we only need to solve the wave equations for \mathcal{E}_z and \mathcal{H}_z (which are both identical). Besides, the z -component of the Laplacian operator is much simpler. Hence (6.6) and (6.7) become for $r \neq a$:

$$\left[\frac{\partial^2}{\partial r^2} + \frac{1}{r} \frac{\partial}{\partial r} + \frac{1}{r^2} \frac{\partial^2}{\partial \phi^2} + (k^2 - \beta^2) \right] \begin{Bmatrix} \mathcal{E}_z(r, \phi) \\ \mathcal{H}_z(r, \phi) \end{Bmatrix} = 0, \quad (6.10)$$

where $k = \omega n/c$, c being the speed of light in free space. This equation can be further separated in ϕ and r such that $\mathcal{E}_z(r, \phi) = R(r)\Phi(\phi)$. Denoting the separation constant

³ Calligraphic letters will refer to complex field quantity.

$$l^2 = -\frac{1}{\Phi} \frac{\partial^2 \Phi}{\partial \phi^2},$$

we now see that the radial part is a solution of a differential Bessel equation of order l , up to a change of variable $\rho^2 = r^2(k^2 - \beta^2)$:

$$\left[r^2 \frac{\partial^2}{\partial r^2} + r \frac{\partial}{\partial r} + r^2(k^2 - \beta^2) - l^2 \right] R(r) = 0, \quad (6.11)$$

$$\left[\rho^2 \frac{\partial^2}{\partial \rho^2} + \rho \frac{\partial}{\partial \rho} + \rho^2 - l^2 \right] R(\rho) = 0. \quad (6.12)$$

The last equation being rewritten in the more suggestive form of a Bessel equation.

6.2.2 Angular dependence

The solution to the angular dependence equation given previously by the separation constant l is trivial. In general, the angular dependence Φ of the field will then be a linear superposition of $\{\exp[+il\phi], \exp[-il\phi]\}$. Here, we would like to introduce already the notation \mathcal{E}_z^\pm to distinguish between both terms, that refers to $e^{\pm il\phi}$ in the angular dependence of the field solution. In addition, we acknowledge that the constant l must be an integer. Indeed, $\Phi(\phi)$ must be single-valued, which here translates into 2π -periodicity $\Phi(\phi + 2\pi) = \Phi(\phi)$.

6.2.3 Radial dependence

As any second order equation, (6.11) admits two linearly independent solutions. However, we also need to distinguish between the sign of $(k^2 - \beta^2)$:

$k^2 > \beta^2$: The analytical solutions of (6.11) are known as the Bessel function J_l of the first kind of order l and Neumann function Y_l of order l (known as the Bessel function of the second kind).

$k^2 < \beta^2$: (6.11) becomes what is known as the modified Bessel equation,

$$\left[r^2 \frac{\partial^2}{\partial r^2} + r \frac{\partial}{\partial r} - \left(r^2(\beta^2 - k^2) + l^2 \right) \right] R(r) = 0, \quad (6.13)$$

whose solutions are analogous Bessel functions (also known as the modified Bessel functions) of the first and second kind, I_l and K_l respectively.

We then get the following general⁴ solutions for the radial part, depending on the previous value of β , where h and q are real constant:

$$R_1(r) = aJ_l(hr) + bY_l(hr) \quad \text{with} \quad h^2 = k^2 - \beta^2, \quad (6.14)$$

$$R_2(r) = cI_l(qr) + dK_l(qr) \quad \text{with} \quad q^2 = \beta^2 - k^2. \quad (6.15)$$

One can also reformulate these solutions in terms of another basis set, namely the two linearly independent Hankel functions. Hankel functions are to the Bessel functions (cylindrical harmonics) what $e^{\pm i\theta}$ are to the trigonometric functions (the circular harmonics, i.e sine and cosine). We prefer to work with non-complex constants. Inasmuch as the previous expressions are about to be greatly simplify in the next section.

6.2.4 Lossless propagation requirement

Now, we are going to add physical appreciations for the nature of light propagation in the fiber which will constrain β . We require radially confined light in the core with only evanescent field in the cladding for lossless mode propagation in the whole fiber.

As mentioned before, the wave-vector in the core and the cladding is naturally decomposed into a longitudinal component and a transversal component with respect to the fiber axis. A wave-vector can be complex and propagation is identify with its real part while the imaginary part represents attenuation of the fields. No propagation occurs if all wave-vectors are pure imaginary. If all wave-vectors are real, light will be instead freely radiating without confinement. The moduli of the radial and longitudinal components satisfy $k^2 = k_{\perp}^2 + \beta^2$ where $k = 2\pi n/\lambda$.

For lossless propagation along the fiber axis, β is real. The sign of $k^2 - \beta^2$ basically tells us whether the fields are now radially radiating or decaying. The value of k depends on the local refractive index. If we want to guide and confine light along the fiber axis, we cannot allow for radiation outside, that is in the assumed infinitely thick surrounding cladding. k_{\perp} will thus have to be purely imaginary in the cladding. To work with real constant, we will set $k_{\perp} = -iq$.

Mathematically, while the normal Bessel functions oscillate, the modified ones exponentially vanish or explode (figure 6.1). Therefore, to satisfy the guiding requirement we demand $R(r)$ to be of the kind of (6.14) in the core and of the kind (6.15) outside. In addition, the fields must be finite at the center of the fiber $r = 0$ and they should vanish in the limit $r \rightarrow \infty$. To that end, one would have to set the constants $b = 0$ and $c = 0$ since Y_l diverges towards 0 and I_l diverges for $r \rightarrow \infty$. We are then left with two functions, J_l in the core which has a finite value at $r = 0$ and K_l for the cladding field which vanishes at $r \rightarrow \infty$.

The previous conditions translate for β as follows : In the core ($r < a$), $k^2 = k_0^2 n_1^2$ and we thus require $k^2 > \beta^2$. Outside ($r > a$), $k^2 = k_0^2 n_2^2$

⁴ We will focus on a particular order l of Bessel functions.

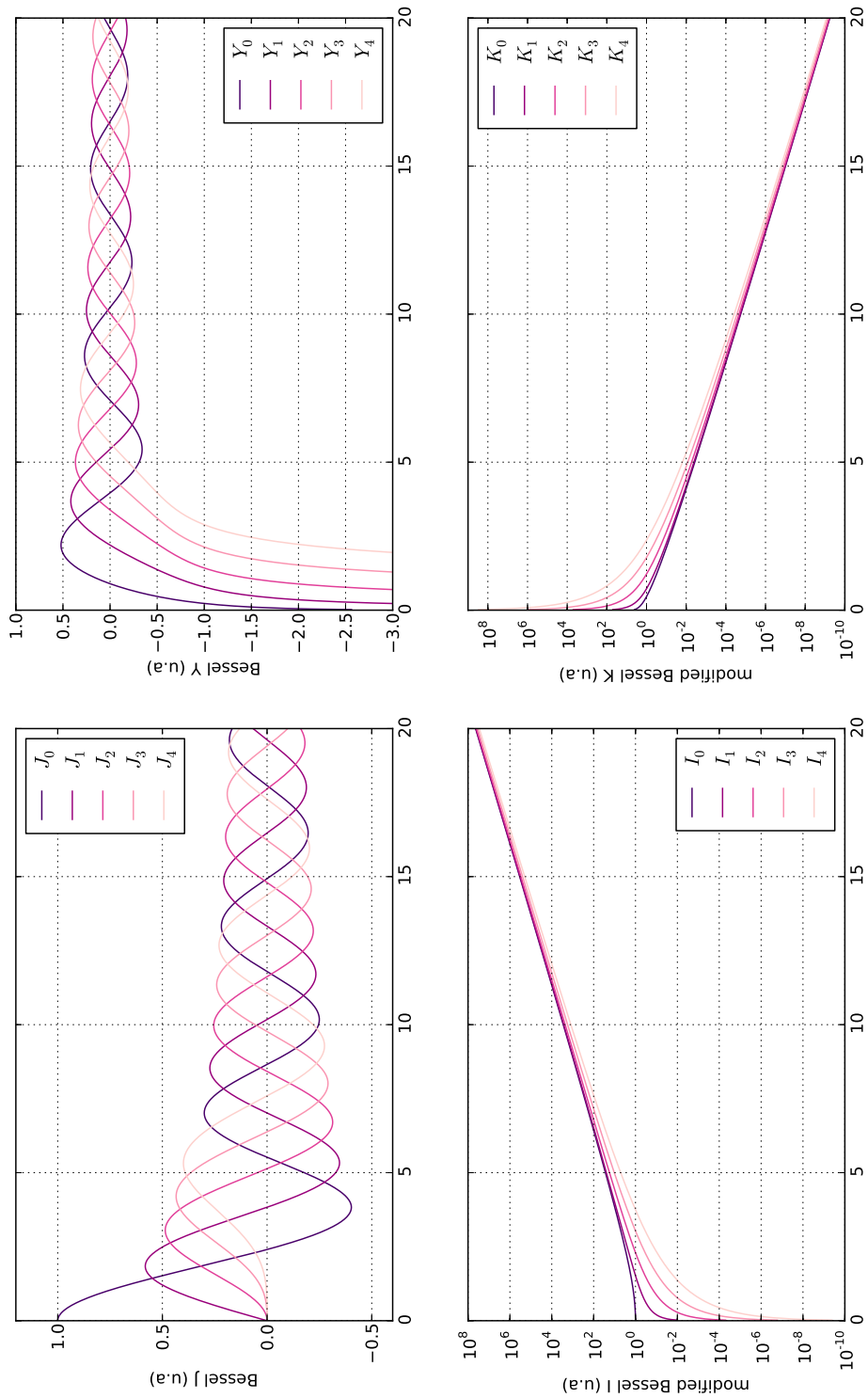


Figure 6.1: Behaviour of Bessel and modified Bessel functions.

and we require instead $\beta^2 > k^2$. Finally one has to satisfy the important condition

$$k_0^2 n_2^2 \leq \beta^2 \leq k_0^2 n_1^2 \quad \text{with} \quad k_0^2 = \frac{\omega^2}{c^2}. \quad (6.16)$$

6.2.5 First general solutions

It follows the general form of the field components \mathcal{E}_z and \mathcal{H}_z . As mentioned above (6.10), we can deduced all remaining field components with the knowledge of \mathcal{E}_z and \mathcal{H}_z alone. All the expressions are given in Appendix A.3.

In the core, $r < a$,

$$\mathcal{E}_z^\pm(r, \phi) = \mathcal{A} J_l(hr) \exp[\pm il\phi] \quad (6.17)$$

$$\mathcal{H}_z^\pm(r, \phi) = \mathcal{B} J_l(hr) \exp[\pm il\phi] \quad (6.18)$$

$$h = \sqrt{k_0^2 n_1^2 - \beta^2} \quad (6.19)$$

Outside, $r > a$,

$$\mathcal{E}_z^\pm(r, \phi) = \mathcal{C} K_l(qr) \exp[\pm il\phi] \quad (6.20)$$

$$\mathcal{H}_z^\pm(r, \phi) = \mathcal{D} K_l(qr) \exp[\pm il\phi] \quad (6.21)$$

$$q = \sqrt{\beta^2 - k_0^2 n_2^2} \quad (6.22)$$

where \mathcal{A} , \mathcal{B} , \mathcal{C} , \mathcal{D} are normalization factors to be related by continuity conditions for the fields at $r = a$. They will be finally expressed in terms of the total light field power. However, before we proceed, we are going to show that these boundary conditions put even more constraints on the propagation constant β and we will observe how only particular values for β are singled out from the continuous range obtained at (6.16). This will lead to the definition of the modes that will propagate through the thin part of the fiber. From these results, we will then see how to achieve single-mode propagation for instance.

6.3 CONTINUITY AND TRANSCENDENTAL MODE EQUATION

The continuity conditions for the fields at $r = a$ demand that all component parallel to the core-cladding interface, E_z , E_ϕ , H_z and H_ϕ should be preserved (A.4). This means four different conditions and we have

four factors \mathcal{A} , \mathcal{B} , \mathcal{C} and \mathcal{D} to find. We can thus solve the following linear algebraic system:

$$\begin{aligned}
 \mathcal{A}J_l(ha) - \mathcal{C}K_l(qa) &= 0 & (E_z) \\
 \mathcal{B}J_l(ha) - \mathcal{D}K_l(qa) &= 0 & (H_z) \\
 \mathcal{A} \left[\pm \frac{l\beta J_l(ha)}{h^2 a} \right] + \mathcal{B} \left[i \frac{\omega\mu_0}{h} J'_l(ha) \right] + \mathcal{C} \left[\pm l\beta \frac{K_l(qa)}{q^2 a} \right] + \mathcal{D} \left[\frac{i\omega\mu_0}{q} K'_l(qa) \right] &= 0 & (E_\phi) \\
 \mathcal{A} \left[-\frac{i\omega\epsilon_1}{h} J'_l(ha) \right] + \mathcal{B} \left[\pm l\beta \frac{J_l(ha)}{h^2 a} \right] + \mathcal{C} \left[\frac{-i\omega\epsilon_2}{q} K'_l(qa) \right] + \mathcal{D} \left[\pm l\beta \frac{K_l(qa)}{q^2 a} \right] &= 0 & (H_\phi)
 \end{aligned}$$

with $J'_l(hr) = \frac{dJ_l(hr)}{d(hr)}$ and $K'_l(qr) = \frac{dK_l(qr)}{d(qr)}$

We will get a non-trivial solution, that is non-zero fields, whenever the determinant of the previous system is zero. Its Laplace's development (A.5) can be ultimately factorised such

$$\begin{aligned}
 (l\beta)^2 \left\{ \left(\frac{1}{qa} \right)^2 + \left(\frac{1}{ha} \right)^2 \right\}^2 &= \frac{\omega^2}{c^2} \left(\frac{J'_l(ha)}{haJ_l(ha)} + \frac{K'_l(qa)}{qaK_l(qa)} \right) \\
 &\times \left(n_1^2 \frac{J'_l(ha)}{haJ_l(ha)} + n_2^2 \frac{K'_l(qa)}{qaK_l(qa)} \right).
 \end{aligned} \tag{6.23}$$

For a given angular frequency ω , as h and q depend solely on β , there will be a solution for propagation of the fields only if β is solution of the previous transcendental equation (6.24). As long as these solutions are within the range 6.16, we will call the corresponding allowed electromagnetic field solutions the modes that can propagate losslessly through the fiber or simply, guided modes. Each mode will be identified by a given pair of indices (l, m) , where l is the considered order of the Bessel functions and m denotes an ordinal intersection number starting from 1, associated with the particular value β for that mode when graphically solving (6.24). This will be precised in section 6.7.

6.4 GENERAL ROTATING POLARIZATION SOLUTIONS

Directly from the previous linear system 6.3,

$$\frac{\mathcal{A}}{\mathcal{C}} = \frac{\mathcal{B}}{\mathcal{D}} = \frac{K_l(qa)}{J_l(ha)} \quad \text{and} \quad \frac{\mathcal{D}}{\mathcal{C}} = \frac{\pm i l \beta}{\omega\mu_0} \left[\frac{1}{h^2 a^2} + \frac{1}{q^2 a^2} \right] \left(\frac{J'_l(ha)}{haJ_l(ha)} + \frac{K'_l(qa)}{qaK_l(qa)} \right)^{-1} \tag{6.24}$$

are sufficient relations to express all fields in terms of only one constant, say \mathcal{C} . This arbitrary constant will be further set upon the total input power of light 6.6 to normalize the field expressions conveniently. We report here their general expressions as they constitute the backbone of this chapter. Where β , as well as h , q and thus the fields are given for a particular mode (l, m) , see A.6 for more details.

In the core section ($r < a$):

$$\begin{aligned}
\mathcal{E}_z^\pm(r, \phi) &= \mathcal{C} J_l(hr) \frac{K_l(qa)}{J_l(ha)} \exp[\pm il\phi] \\
\mathcal{E}_r^\pm(r, \phi) &= \mathcal{C} \frac{K_l(qa)}{J_l(ha)} \frac{i\beta}{2h} [J_{l+1}(hr)(1+ls) - J_{l-1}(hr)(1-ls)] \exp[\pm il\phi] \\
\mathcal{E}_\phi^\pm(r, \phi) &= \pm \mathcal{C} \frac{K_l(qa)}{J_l(ha)} \frac{\beta}{2h} [J_{l+1}(hr)(1+ls) + J_{l-1}(hr)(1-ls)] \exp[\pm il\phi] \\
\mathcal{H}_z^\pm(r, \phi) &= \pm s \frac{i\beta}{\omega\mu_0} \mathcal{C} \frac{K_l(qa)}{J_l(ha)} J_l(hr) \exp[\pm il\phi] \\
\mathcal{H}_r^\pm(r, \phi) &= \pm \mathcal{C} \frac{K_l(qa)}{J_l(ha)} x \left[J_{l-1}(hr) \left(ls - \frac{\omega^2 \epsilon_1 \mu_0}{\beta^2} \right) - J_{l+1}(hr) \left(ls + \frac{\omega^2 \epsilon_1 \mu_0}{\beta^2} \right) \right] \exp[\pm il\phi] \\
\mathcal{H}_\phi^\pm(r, \phi) &= \mathcal{C} \frac{K_l(qa)}{J_l(ha)} ix \left[J_{l+1}(hr) \left(\frac{\omega^2 \epsilon_1 \mu_0}{\beta^2} + ls \right) + J_{l-1}(hr) \left(ls - \frac{\omega^2 \epsilon_1 \mu_0}{\beta^2} \right) \right] \exp[\pm il\phi]
\end{aligned}$$

In the cladding section ($r > a$):

$$\begin{aligned}
\mathcal{E}_z^\pm(r, \phi) &= \mathcal{C} K_l(qr) \exp[\pm il\phi] \\
\mathcal{E}_r^\pm(r, \phi) &= -\mathcal{C} \frac{i\beta}{2q} [K_{l+1}(qr)(1+ls) + K_{l-1}(qr)(1-ls)] \exp[\pm il\phi] \\
\mathcal{E}_\phi^\pm(r, \phi) &= \pm \mathcal{C} \frac{\beta}{2q} [K_{l-1}(qr)(1-ls) - K_{l+1}(qr)(1+ls)] \exp[\pm il\phi] \\
\mathcal{H}_z^\pm(r, \phi) &= \pm s \frac{i\beta}{\omega\mu_0} \mathcal{C} K_l(qr) \exp[\pm il\phi] \\
\mathcal{H}_r^\pm(r, \phi) &= \pm \mathcal{C} y \left[K_{l+1}(qr) \left(ls + \frac{\omega^2 \epsilon_2 \mu_0}{\beta^2} \right) + K_{l-1}(qr) \left(ls - \frac{\omega^2 \epsilon_2 \mu_0}{\beta^2} \right) \right] \exp[\pm il\phi] \\
\mathcal{H}_\phi^\pm(r, \phi) &= -\mathcal{C} iy \left[K_{l+1}(qr) \left(\frac{\omega^2 \epsilon_2 \mu_0}{\beta^2} + ls \right) + K_{l-1}(qr) \left(\frac{\omega^2 \epsilon_2 \mu_0}{\beta^2} - ls \right) \right] \exp[\pm il\phi] \\
\text{with } s &= \left[\frac{1}{h^2 a^2} + \frac{1}{q^2 a^2} \right] \left(\frac{J'_l(ha)}{ha J_l(ha)} + \frac{K'_l(qa)}{qa K_l(qa)} \right)^{-1} \\
h &= \sqrt{k_0^2 n_1^2 - \beta^2}, \quad x = \frac{\beta^2}{2h\omega\mu_0} \\
q &= \sqrt{\beta^2 - k_0^2 n_2^2}, \quad y = \frac{\beta^2}{2q\omega\mu_0}
\end{aligned}$$

We would like now to give a few immediate remarks about the previous wave field solutions.

6.5 GENERAL PROPERTIES

First, the amplitudes of the field components are described by Bessel functions. This leads to the particularly interesting behaviour of Bessel

waves. They do not spread radially while propagating along the fiber axis (along z). This means that they do not diffract and spread out as they propagate as compare to Hermite or Laguerre-gaussian laser modes for instance. This property makes these nanofiber field solutions extremely interesting for light beams where tight focus and collimation are very important e.g optical tweezers, strong single atom light interactions. Nowadays, Bessel beams can be procuded for instance via axicons⁵.

We can also note that the fields are in general (for any order l) not transverse. Indeed, the components of the fields along the propagation direction (here z) do not vanish. We shall encounter the consequences of these properties latter.

Outside the core, the field amplitudes are in good approximation exponentially decaying with the decay constant $\Lambda = 1/q$. On the other hand, $k_0^2 n_2^2 \leq \beta^2$. Therefore, one limit of guidance happens when q vanishes, that is when the mode extension outside the core of the fiber is largest, here infinitely wide. Light is indeed not confined anymore. We can give an estimate of the order of magnitude of the light evanescence length from 6.16 $\Rightarrow 0 \leq q^2 \leq k_0^2 (n_1^2 - n_2^2)$. Setting $n_2 = 1$ and $n_1 \sim 1.5$ for silica glass, Λ is about a few hundred nanometers for infrared light ($1\mu\text{m}$). We shall study more precisely the mode evanescence in later chapters.

An immediate consequence of the ratio \mathcal{D}/\mathcal{C} in (6.24) being \pm pure imaginary is that \mathcal{E}_r^\pm and \mathcal{E}_ϕ^\pm are $\pm\frac{\pi}{2}$ phase-shifted. This means that $\{\mathcal{E}_r^+, \mathcal{E}_\phi^+\}$ will represent a real transverse field to the fiber axis \mathbf{E}_\perp with clockwise rotating polarization, and $\{\mathcal{E}_r^-, \mathcal{E}_\phi^-\}$ with counter-clockwise rotating polarization. We prefer to speak in terms of *rotating* polarization since \mathcal{E}_z^\pm and \mathcal{H}_z^\pm are in general non-zero. As a result, one can only hope to obtain a *quasi*-linear transverse polarization from an equal superposition of the $+$ and $-$ solutions. The polarization gradients of the guided modes shall be studied as well in later chapters. Another consequence of the angular dependance of the optical phase $\Phi^\pm = \omega t - \beta z \pm l\phi$ is that the wavefront of these solutions is not planar. It is rather *helical*. We shall study this property in close relation to the fact that a guided mode can carry orbital angular momentum.

6.6 PRACTICAL NORMALIZATION

We now express and relate the normalization constant \mathcal{C} in terms of the light power we send through the fiber along its axis. This relates directly to the physical quantity we can effectively measure. The total

⁵ A special lens with a conical surface.

light power will be given by the average value, over one optical period $2\pi/\omega$, of the transverse flux of the Poynting vector :

$$\begin{aligned}\mathcal{P}^{in} &= \int_0^{2\pi} \int_0^a \langle S_z^{in} \rangle_{\frac{2\pi}{\omega}} r d\phi dr, \\ \mathcal{P}^{out} &= \int_0^{2\pi} \int_a^\infty \langle S_z^{out} \rangle_{\frac{2\pi}{\omega}} r d\phi dr,\end{aligned}$$

$$\text{with } S_z = [\mathbf{E} \times \mathbf{H}]_z,$$

which, following the definition of our complex⁶ fields (6.8) and accounting for the cycle-average, gives

$$\langle S_z \rangle_{\frac{2\pi}{\omega}} = \frac{1}{2} [\mathcal{E} \times \mathcal{H}^*]_z.$$

We find, for both \pm rotating polarizations,

$$\mathcal{C} = \sqrt{\frac{4\omega\mu_0\mathcal{P}^{tot}}{\pi a^2\beta}} \left(\left(\frac{K_l(qa)}{J_l(ha)} \right)^2 \mathcal{T}_l^{in} + \mathcal{T}_l^{out} \right)^{-\frac{1}{2}} \text{ with } \mathcal{P}^{tot} = \mathcal{P}^{in} + \mathcal{P}^{out}. \quad (6.25)$$

All new terms introduced can be found in Appendix A.7 together with the detailed derivation of (6.25).

6.7 HYBRID MODES PROPAGATION AND SINGLE-MODE CONDITION

We now focus the discussion on the modes that can propagate in the nanofiber and study the characteristic equation (6.24). In order to contemplate the emergence of new modes while sweeping the wavelength of input light we need a good representation for this transcendental equation. Of course, one could be simply satisfied by numerically solving (6.24) for given interesting parameters. As mentioned above, the normal Bessel functions are oscillating functions while the modified Bessel functions have exponential behaviours. In order to graphically appreciate contributions, from both kind of Bessel functions independently, which are currently entangled in (6.24), for any variation of λ , one needs to isolate $\frac{J'_l(ha)}{haJ_l(ha)}$ terms from $\frac{K'_l(qa)}{qaK_l(qa)}$ terms. This become more evident and was brought to mind when considering the case where $l = 0$. Therefore, as (6.24) is quadratic in $\frac{K'_l(qa)}{qaK_l(qa)}$ and $\frac{J'_l(ha)}{haJ_l(ha)}$, one can achieved this separation by solving for one or the other, the former second order equation.

6.7.1 Hybrid mode classes

Solving for the J' 's gives:

$$\Delta = \left(\frac{K'_l(qa)}{qaK_l(qa)} \right)^2 \left[(n_1^2 + n_2^2)^2 - 4n_1^2 n_2^2 \right] + 4n_1^2 \left(l \frac{\beta}{k_0} \right)^2 \left\{ \left(\frac{1}{qa} \right)^2 + \left(\frac{1}{ha} \right)^2 \right\}^2 \geq 0$$

⁶ \mathcal{H}^* denotes the complex conjugate of \mathcal{H} .

$$(6.26)$$

where Δ , the discriminant of the second order polynomial equation, is positive⁷.

The roots follow :

$$\begin{aligned} \frac{J'_l(ha)}{haJ_l(ha)} &= - \left(\frac{K'_l(qa)}{qaK_l(qa)} \right) \left(\frac{n_1^2 + n_2^2}{2n_1^2} \right) \\ &\pm \sqrt{\left(\frac{n_1^2 - n_2^2}{2n_1^2} \right)^2 \left[\left(\frac{K'_l(qa)}{qaK_l(qa)} \right)^2 + \left(\frac{2l\beta k_0 n_1}{h^2 q^2 a^2} \right)^2 \right]}. \end{aligned} \quad (6.27)$$

An immediat result which stems from our transition to a first order transcendental equation is that we have shuffled the forest of modes in two classes following the \pm sign. By directly plugging these solutions into (6.24) one can see an associated property to each class. For the class + we have $\mathcal{E}_z > \mathcal{H}_z$, for the class - we have $\mathcal{H}_z > \mathcal{E}_z$. Hence the notation for these so-called hybrid modes Snitzer (1961), EH_{lm} and HE_{lm} .

6.7.2 TE and TM modes

A special case arises when $l = 0$. Because $\left(\frac{K'_l(qa)}{qaK_l(qa)} \right)$ is negative, the previous two possible roots reduce to

$$\text{class (+)} \quad \frac{J'_l(ha)}{haJ_l(ha)} = - \frac{K'_l(qa)}{qaK_l(qa)}, \quad \text{class (-)} \quad \frac{J'_l(ha)}{haJ_l(ha)} = - \frac{n_2^2}{n_1^2} \left(\frac{K'_l(qa)}{qaK_l(qa)} \right). \quad (6.28)$$

Class (+) respectively (Class (-)) solutions corresponds to vanishing constants \mathcal{A} and \mathcal{C} respectively (\mathcal{B} and \mathcal{D}), that is $\mathcal{E}_z = 0$ respectively ($\mathcal{H}_z = 0$), see (6.24). For all HE_{0m} modes, the component \mathcal{H}_z then vanishes and we will label these *transverse magnetic* modes, TM_m . Respectively, for all EH_{0m} , the component \mathcal{E}_z vanishes and we label these *transverse electric* modes, TE_m . Using geometrical optics, one can quickly picture the distinction between transverse and these hybrid modes with longitudinal components. The light ray either goes straight through our rigid fiber model or propagates from reflections onto the walls.

6.7.3 Cutt-off and mode order

In this section, we will understand visually how the fiber modes are identified and how they arise for different optical input light wavelength. We have graphically represented (top figure 6.2) the left- and right-hand

⁷ indeed, $(n_1^2 + n_2^2)^2 - 4n_1^2 n_2^2 = (n_1^2 - n_2^2)^2 \geq 0$

LABEL	MODES	DESCRIPTION
TE	Transverse Electric	No electric field in the propagation direction
TM	Transverse Magnetic	No magnetic field in the propagation direction
TEM	Transverse ElectroMagnetic	No electric and magnetic fields in the propagation direction
HE, EH	Hybrid modes	Non-zero electric and magnetic fields in the propagation direction

Table 6.1: Mode terminology

sides of the two kind of first order transcendental equations (6.28) as functions of ha to see relative changes between both sides for different values of the wavelength λ . This becomes more apparent by recalling the following important fixed relation that always holds here

$$h^2 + q^2 = \left[\frac{2\pi}{\lambda} \right]^2 (n_1^2 - n_2^2). \quad (6.29)$$

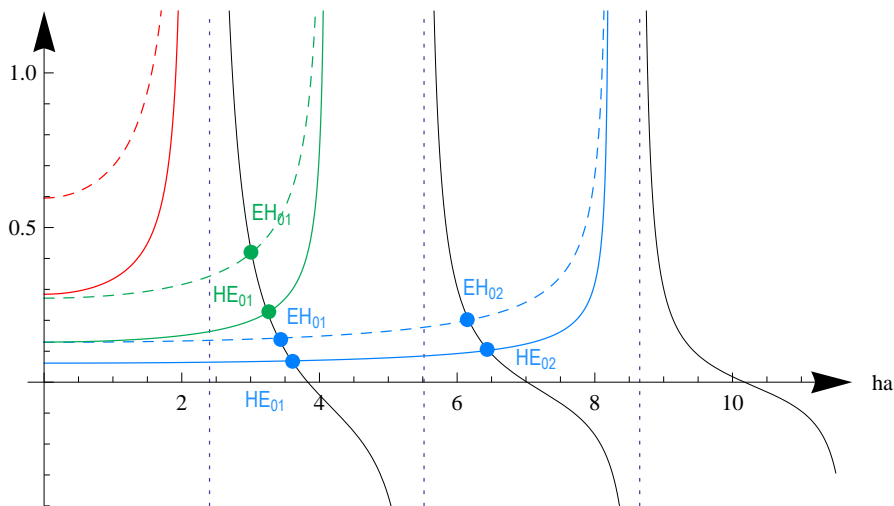
For a given wavelength, the number of possible modes depends on how many times the right-hand side of (6.28) intersects the left-hand side before it diverges. For a given order l , we identify each intersection point with the ordinal number m starting with 1. We know that $\frac{1}{qa} \frac{K'_l(qa)}{K_l(qa)}$ diverges whenever $qa = 0$, that is, as follows from equation (6.29), when

$$ha = \frac{2\pi a}{\lambda} \sqrt{n_1^2 - n_2^2} \equiv V_{cut}. \quad (6.30)$$

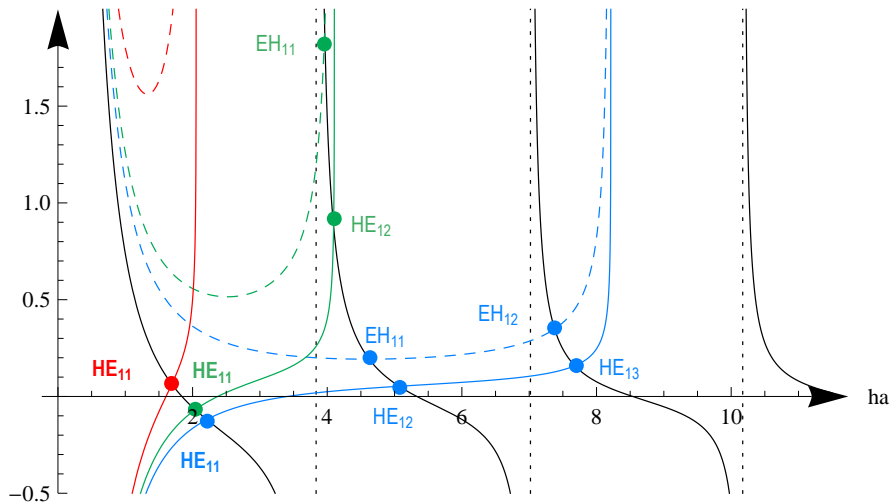
This characteristic constant of the problem acts as a cut-off parameter for the number of sustained modes of a given wavelength.

NUMERICAL APERTURE The parameter V_{cut} is the wave analogue of the geometrical numerical aperture. The numerical aperture being the sine of the critical angle for total internal reflection. $NA = \sin \theta_c = \sqrt{n_1^2 - n_2^2}/n_0$, where n_0 is the refractive index of the medium into which the fiber is immersed.

The cut-off parameter can be easily understood as follows. The core of the fiber, in order to guide and confine light waves acts as a transverse ring resonator or a circular cavity for that part of the light field which propagates radially. Hence the appearance of a discrete number of modes that matches constructive interference conditions for the radial field. However, there is a primordial *sine qua non* condition to be satisfied to guide light along the fiber axis. Light has to fall back at



(a) First modes with $l = 0$



(b) First modes with $l = 1$

Figure 6.2: (black) left side of transcendental equation, else right side (dashed lines for EH modes, solid lines for HE modes) {red 800 nm, green 400 nm, blue 200 nm}, $a = 200$ nm, $n_1 = 1.4469$, $n_2 = 1$ (a) . (b) case $l = 1$.

the core-cladding interface. Indeed, h is the radial component of the light wave-vector, that can be written $h = k_0 \sin \theta$ with ($\beta = k_0 \cos \theta$, $k_0 = 2\pi/\lambda$) when measuring the angle θ from the fiber axis. As well known from Snell's law, total internal reflection only happens if θ is smaller than the critical angle satisfying $\sin \theta_c = \sqrt{n_1^2 - n_2^2}$. Only when $\sin \theta$, that is h/k_0 , is smaller than V_{cut}/a light is reflected. For higher values, as shown by the divergence of all the coloured traces in figure 6.2, the fiber will not confine light along z . This should be retained as the

first meaning of the cut-off parameter. When the previous condition is met, due to the wave nature of the light, the reflected Bessel waves will interfere destructively in general except for the discrete values of ha or equivalent, discrete values of β .

From top figure 6.2 (see red curve), one can then state for instance that the fiber will not allow any $l = 0$ modes to propagate if the cut-off parameter is smaller than the first vertical asymptote of (6.28)'s left side. The positions of all these vertical asymptotes are given by the zeros of the Bessel function $J_l(ha)$ according to (6.28)'s left side. The first zero of $J_0(x)$ (a well-known value) is reached when $x = x_0 \approx 2.405$.

Following bottom figure 6.2, one can choose the wavelength of light for a given fiber such that $\frac{2\pi a}{\lambda} \sqrt{n_1^2 - n_2^2} < 2.405$ which allows the existence of only one mode, the mode HE_{11} . In fact, this mode will always exist. It is the so-called fundamental mode of the optical nanofiber. As near cut-off as it might be, also synonym of weak-guidance, there will always be an intersection on our previous graph that translates the existence of the fundamental mode.

To finish we give a visualization of the tranverse field intensity distribution for the first height fiber hybrid modes based on our derivations in figure 6.3.

SUMMARY

In this chapter, I have presented in a simple way how to solve the guided modes which are allowed to propagate in an optical nanofiber. This work represents my very first efforts in our nanofiber projects, which have then allowed to deduce and model all the important characteristics for light-atom interactions in the evanescent fields of a nanofiber.

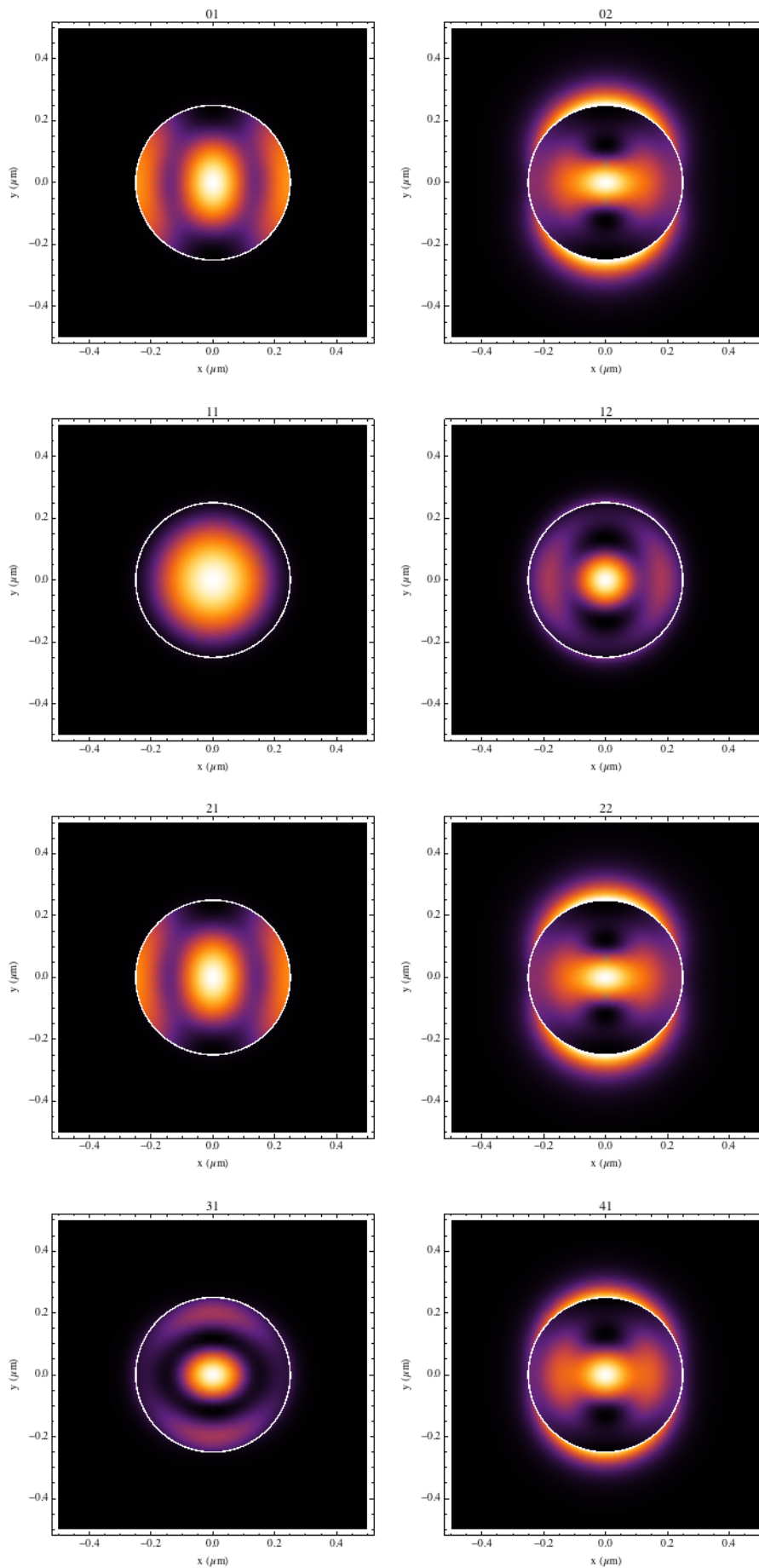


Figure 6.3: Mode map: Transverse field intensity distribution for the first height nanofiber modes with rotating polarization.

POLARIZATION AND TOPOLOGY

*Point set topology is a disease
from which the human race will soon recover.*

— Henri Poincaré

7.1 ROTATING POLARIZATION

We first start by plotting the transverse electric vector field for the general solutions found in the previous chapter, at different propagation time instants.

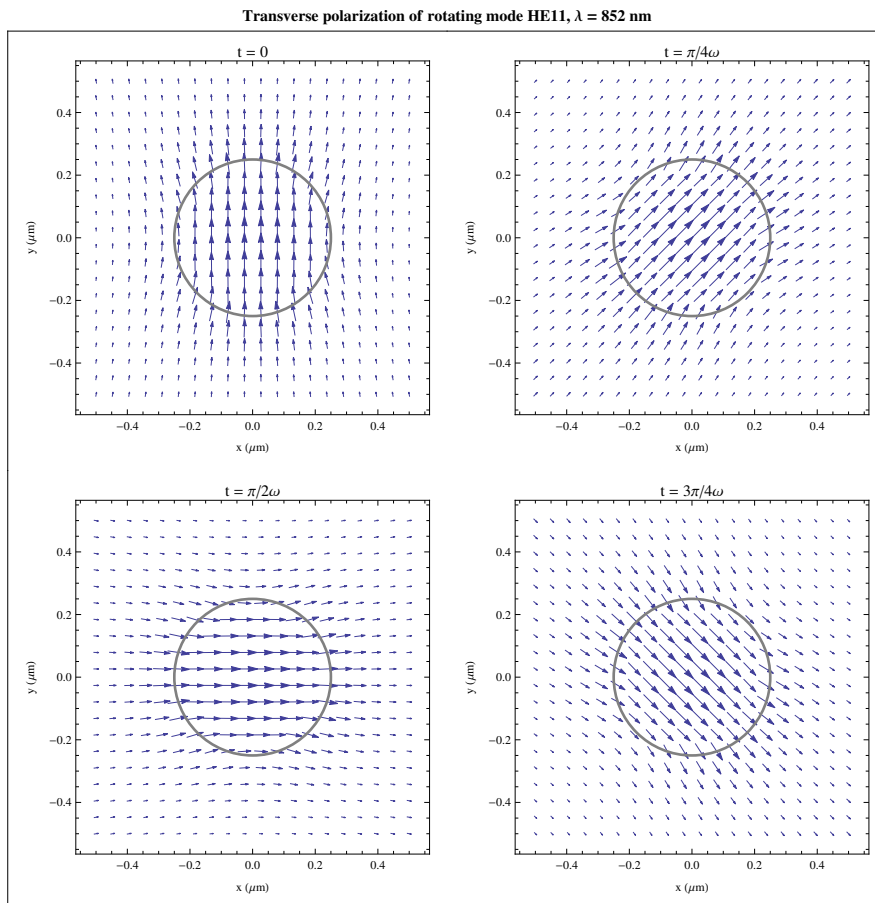


Figure 7.1: Transverse polarization field of the fundamental mode solution.

Visually (figure 7.1), these solutions correspond to a global rotation of the transverse orientation of the electric field, the solutions denoted (+) corresponding to clockwise polarization rotation, and (-) to counter-clockwise rotation.

7.2 GEOMETRICAL PHASE

A quick look at the cylindrical components of the electric field solution reveals the geometrical nature of the phase. As noted before, the phase of the field components depends on the cylindrical angle ϕ .

$$\begin{aligned}\mathcal{E}_z^\pm(r, \phi) &= \mathcal{C}K_l(qr) \exp[\pm il\phi] \\ \mathcal{E}_r^\pm(r, \phi) &= -\mathcal{C}\frac{i\beta}{2q} [K_{l+1}(qr)(1+ls) + K_{l-1}(qr)(1-ls)] \exp[\pm il\phi] \\ \mathcal{E}_\phi^\pm(r, \phi) &= \pm\mathcal{C}\frac{\beta}{2q} [K_{l-1}(qr)(1-ls) - K_{l+1}(qr)(1+ls)] \exp[\pm il\phi]\end{aligned}$$

This means that in general, the hybrid guided modes of the nanofiber are characterized by a helical wavefront shape.

Cophasal or constant optical phase points describe an helix. Helical modes are remarkable from the presence of a topological phase singularity at the beam axis (here the fiber axis). This constitutes the feature of vortices, therefore a helical mode is an optical vortex. We shall see later that a pure helical mode with phase $l\phi$ corresponds to a light field carrying orbital momentum equal to $l\hbar$.

7.2.1 Longitudinal component

Readily, the longitudinal component $\mathcal{E}_z^\pm(r, \phi)$ exhibits a pure helical phase. In figure 7.2, we plot the spatial distribution of this component for the fundamental mode. Clearly, one observes the topological singularity and the discontinuity about the fiber axis.

7.2.2 Azimuthal harmonics

However, the phase evolution of the transverse components $\mathcal{E}_r^\pm(r, \phi)$ and $\mathcal{E}_\phi^\pm(r, \phi)$, is different from the longitudinal one. Indeed, the cylindrical basis is a local basis. Therefore, the transverse polarization of the field, given by the azimuthal invariant transverse field amplitude components, \mathcal{E}_r and \mathcal{E}_ϕ given above will actually depend harmonically on ϕ . This transformation from the cylindrical basis to a fixed cartesian one is nothing but a rotation around the fiber axis, that is adding or annihilating a unit of orbital angular momentum.

$$\mathbf{e}_r = \mathbf{e}_x \cos \phi + \mathbf{e}_y \sin \phi = \left(e^{i\phi} \mathbf{e}_{-1} - e^{-i\phi} \mathbf{e}_1 \right) / \sqrt{2} \quad (7.1)$$

$$\mathbf{e}_\phi = -\mathbf{e}_x \sin \phi + \mathbf{e}_y \cos \phi = i \left(e^{i\phi} \mathbf{e}_{-1} + e^{-i\phi} \mathbf{e}_1 \right) / \sqrt{2} \quad (7.2)$$

The best basis to discuss angular momentum properties is the spherical or irreducible tensor basis.

$$\mathbf{e}_{-1} = \frac{\mathbf{e}_x - i\mathbf{e}_y}{\sqrt{2}}, \quad \mathbf{e}_0 = \mathbf{e}_z, \quad \mathbf{e}_1 = -\frac{\mathbf{e}_x + i\mathbf{e}_y}{\sqrt{2}}. \quad (7.3)$$

Readily, the transverse field polarization will then contain a superposition of azimuthal harmonics, a superposition of helical modes with $(l \pm 1)\phi$. For the fundamental mode HE_{11} with $l = 1$, the transverse field will be a superposition of an azimuthally invariant mode (with $l = 0$) and an helical mode with $l = 2$. The rotation of the polarization is independent of these properties. It comes from the relative constant dephasing of $\pm\pi/2$ between the two transverse components.

7.3 QUASI-LINEAR POLARIZATION

From a balanced superposition of direct and counter-clockwise rotating polarization modes, we can obtain modes with constant field direction. The field oscillates along this direction and cancel out every half-period.

The cylindrical components of two orthogonal quasi-linear polarized fields are given by

$$\mathcal{E}_{i\uparrow}(r, \phi) = \frac{\mathcal{E}_i^+(r, \phi) + \mathcal{E}_i^-(r, \phi)}{\sqrt{2}}, \quad i = \{r, \phi, z\} \quad (7.4)$$

$$\mathcal{E}_{i\rightarrow}(r, \phi) = \frac{\mathcal{E}_i^+(r, \phi) - \mathcal{E}_i^-(r, \phi)}{\sqrt{2}}, \quad i = \{r, \phi, z\} \quad (7.5)$$

To finish this short chapter, I would like to show one of the main novelty of nanofiber light modes. They are a superposition of longitudinal and transverse waves. As a result, even if the field as quasi-linear transverse polarization, its longitudinal polarization field is not necessarily linear. In figure 7.5, we show the longitudinal (YZ) plane polarization field for light propagating along the fiber axis (Z) with transverse linear polarization along X . In the plane (YZ) the polarization of the light field clearly rotates and is therefore highly elliptical.

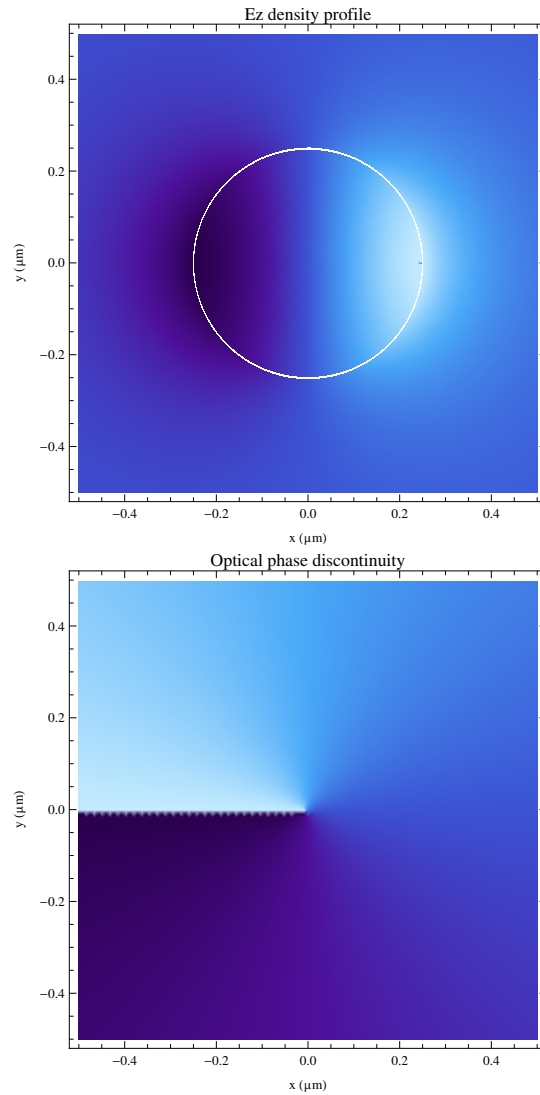


Figure 7.2: (top) Intensity distribution of the longitudinal field component. The field has a zero at $(0,0)$. (bottom) Transverse phase distribution, discontinuity $\phi = \pi$. The longitudinal wave for the fundamental mode with transverse rotating polarization is a pure helical mode, it has a vortex-like geometrical phase.

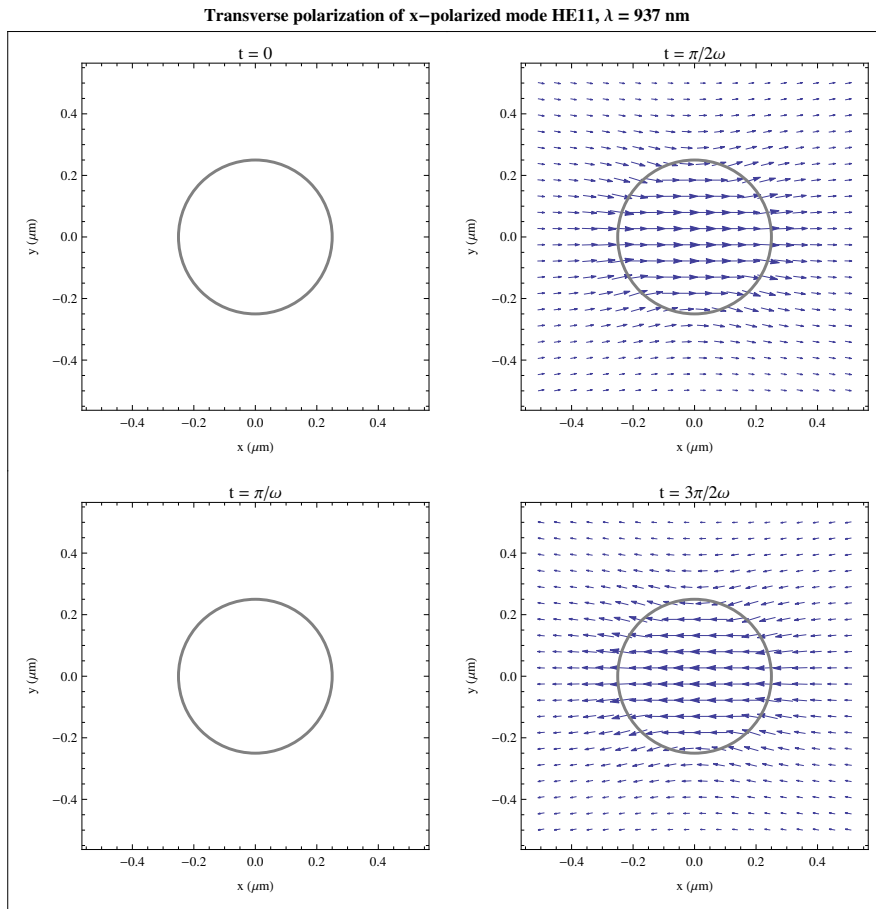


Figure 7.3: Transverse polarization field of the fundamental mode from a balanced superposition of clockwise and counter-clockwise rotating fields.

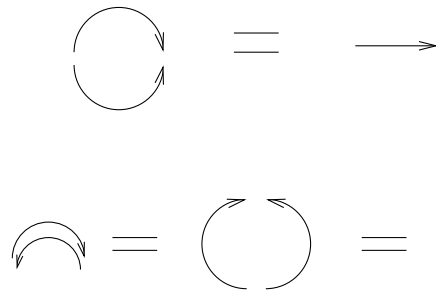


Figure 7.4: Graphical translation of the previous relations

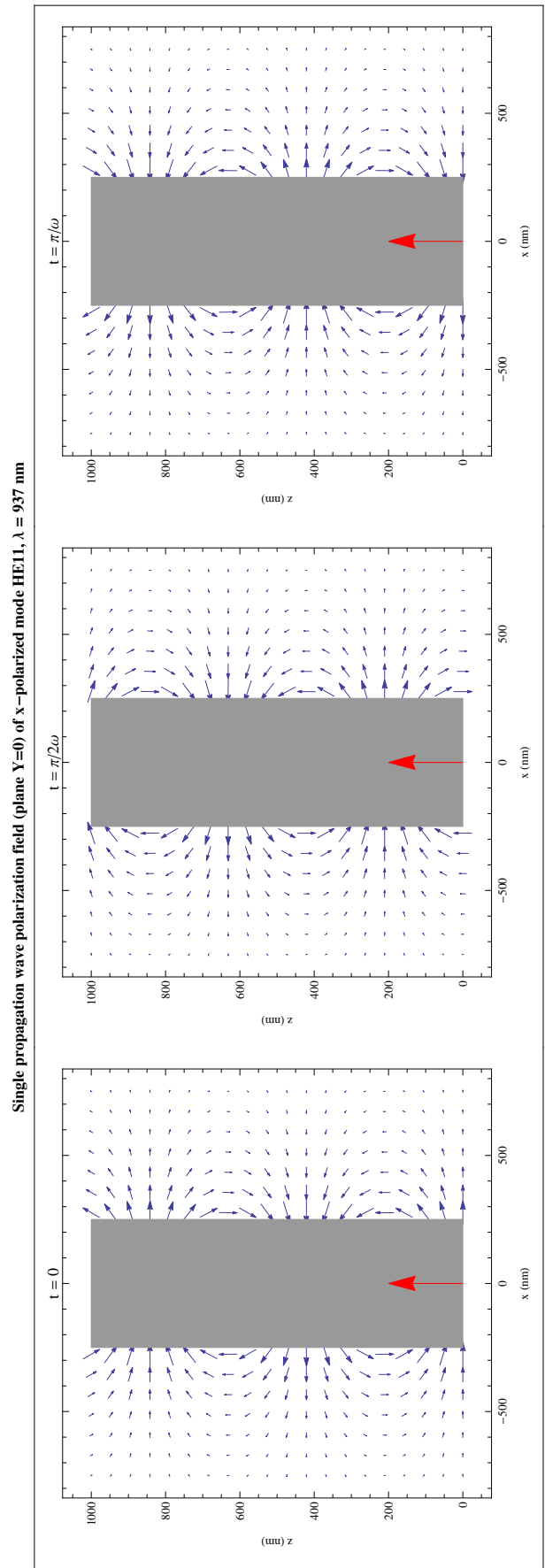


Figure 7.5: YZ longitudinal polarization field of the fundamental mode for a transverse linearly X polarized field.

8

ABRAHAM-MINKOWSKI ANGULAR MOMENTA

A very small cause which escapes our notice determines a considerable effect that we cannot fail to see, and then we say that the effect is due to chance.

— Henri Poincaré.

8.1 INTRODUCTION

The main objective of this chapter is to study the mechanical properties of the nanofiber light fields. For instance, one will see that photons from the hybrid guided light modes propagating in and around an optical nanofiber carry orbital angular momentum in addition to its standard spin angular momentum components. Photons with no well defined spin will challenge, for instance, the pure optical pumping of single atomic Zeeman levels. The evanescent field of the fundamental mode of the nanofiber that we used to trap, manipulate and probe the atoms carries orbital momentum and its three-dimensional polarization field can lead to non-trivial light shifts on the atomic states. In addition, the optical pumping of orbital angular momentum can cause atoms to experience torques and azimuthal shift such as rotational Doppler and recoil shifts. We will find the trajectory of the energy flow and show that in its fundamental mode, the nanofiber interface behaves as a light screw.

This chapter follows the pioneer work of Le Kien and also the recent progress on the fundamental dilemma between the Abraham and Minkowski momenta of light. We generalize the theory of [Kien et al. \(2006\)](#) and provide detailed analytical results for any mode order¹.

8.2 MOMENTUM AND CONSERVATION OF ENERGY

Light has mechanical properties. This is a well-known experimental fact. However, it is interesting to trace it back as a requirement from the energy conservation principle and the theory of relativity. One can also argue that energy and momentum are components of the same

¹ We have not found any references to compare with, except for the fundamental mode.

four-vector. Indeed, it is *classically* clear that electromagnetic energy can not be conserved globally. The energy that would disappear at a given point A in space would have to reappear somewhere else at another distant point B, simultaneously, to conserve the total energy in the universe. The concept of simultaneity being relative, the energy conservation principle would not be satisfied for all observers.

Electromagnetic energy has to be conserved locally. In absence of matter, this writes

$$\frac{\partial u}{\partial t} + \nabla \cdot \mathbf{S} = 0 \quad (8.1)$$

where u is the energy density and \mathbf{S} the energy flux. In words, the electromagnetic energy that disappears in the infinitely small volume dV , has to flow through the boundaries of dV . It was Poynting (1884) who gave the expression widely accepted² for the flux of electromagnetic energy \mathbf{S} in vacuum.

To this quantity of energy that is flowing in free space, one can associate, directly from the result of Einstein, the linear momentum $\mathbf{p} = \mathbf{S}/c$. Because this momentum is transported at the constant speed of light c , the density of linear momentum in vacuum will be

$$\mathbf{g}(\mathbf{r}, t) = \frac{\mathbf{S}(\mathbf{r}, t)}{c^2}. \quad (8.2)$$

8.3 ANGULAR MOMENTUM DENSITY

In the previous section, we have mentioned how the local conservation of electromagnetic energy suggests the existence of the linear momentum of light. Light possesses another degree of freedom, linked to rotational motion, well-known as angular momentum. It is as well a fundamental mechanical characteristic of light.

8.3.1 Local definition

From the knowledge of the local linear momentum density of light at a certain point \mathbf{r} in space, we deduce the local angular momentum density at \mathbf{r} . Readily,

$$\mathbf{j}(\mathbf{r}, t) = \mathbf{r} \times \mathbf{g}(\mathbf{r}, t). \quad (8.3)$$

The first main step in order to study \mathbf{j} , is then to determine the value of linear momentum carried by the guided modes inside and outside the nanofiber.

All the final analytical results of this chapter are based on the expressions of the general solutions for the guided modes with rotating

² There are indeed other valid expressions for energy density and flux

polarization we have found earlier, see Appendix A.6. There, we considered modes propagating towards the positive direction of the nanofiber axis (\mathbf{z}). For an observer looking down the negative direction of the fiber axis, the transverse field components with phase term $+l\phi$ represent clockwise rotation, $-l\phi$ counterclockwise rotation. Indeed, with a proper choice of phase (time) origin, the cylindrical angle of constant phases is,

$$\pm l\phi(t) = \beta z \mp \omega t.$$

For the sake of generality, we take all cases into account, as well as quasi-linear polarized fields.

8.4 KINETIC MOMENTUM OF THE GUIDED MODES

It is well-known that a photon carries a free-space kinetic or linear momentum $\mathbf{p} = \hbar\mathbf{k}$, where here the wave-vector of light \mathbf{k} as magnitude ω/c . ω being the angular frequency of the light mode and c the speed of light in free-space.

However, in a medium of refractive index n , where \mathbf{k} gets multiplied by $n(\omega)$, one may think that the linear momentum of a photon within the medium is

$$\mathbf{p} = \hbar\mathbf{k}n. \tag{8.4}$$

This is not correct.

CANONICAL MOMENTUM Even though the latter expression is the momentum that an atom would absorb if placed in the same medium. The reason being that atoms, in a medium, absorb the canonical momentum of light, [Barnett and Loudon \(2010\)](#); [Barnett \(2010\)](#). It is the canonical momentum which is the generator of translations of the light fields in quantum mechanics.

Instead, the kinetic momentum of a photon in the medium is

$$\mathbf{p} = \frac{\hbar\mathbf{k}}{n}. \tag{8.5}$$

8.4.1 Free-space linear momentum density

Adding the electromagnetic power loss into motion of charged particles to the right-hand side of (8.1), Poynting showed that the electromagnetic energy flux is given by the cross-product of the electric and magnetic fields. As referred to in the introduction, one can find without ambiguity the linear momentum density in vacuum,

$$\mathbf{g}_{\text{Abra}} = \frac{\mathbf{E} \times \mathbf{H}}{c^2}. \tag{8.6}$$

8.4.2 *Abraham-Minkowski momenta dilemma*

In media, we have indeed the choice between either \mathbf{E} and \mathbf{D} , or \mathbf{H} and \mathbf{B} . The displacement field and the induction fields give rise to another possible expression for a density of field momentum due to Minkowski

$$\mathbf{g}_{\text{Mink}} = \mathbf{D} \times \mathbf{B}. \quad (8.7)$$

The expression (8.6) given in vacuum is also valid in a refractive medium (Abraham). It took a century to solve the dilemma of choice between these two previous expressions until 2010 [ref barnett]. Indeed, both theoretical examples and experimental tests confirmed the validity of both momenta. We now know that the Minkowski momentum represents the canonical momentum of the fields. This momentum is relevant in diffraction experiments and light-atom interaction.

This choice dilemma exists therefore also for the angular momentum (8.3) of any light field in a medium. We will provide results for both cases even though we will focus on the true kinetic quantities using Abraham expression.

8.4.3 *Cycle-average energy flux*

From the definition of the complex field amplitudes we chose (6.8), the cycle-average Poynting vector can be written as follows, if the harmonic optical frequency components at 2ω are neglected,

$$\langle \mathbf{S} \rangle = \langle [\mathbf{E} \times \mathbf{H}] \rangle_{\frac{2\pi}{\omega}} = \frac{1}{2} \text{Re} [\mathcal{E} \times \mathcal{H}^*]. \quad (8.8)$$

NO RADIAL FLOW A quick inspection at the coefficients A.6 shows that $\mathcal{E}_\phi^\pm \mathcal{H}_z^{\pm*} - \mathcal{E}_z^\pm \mathcal{H}_\phi^{\pm*}$ is pur imaginary, both inside and outside the nanofiber. Therefore we conclude that there is no mean radial flow of energy, $\langle \mathbf{S}_r \rangle = 0$. This important property also holds for an equal superposition of clockwise and counter-clockwise rotating polarizations. As expected from the definition of guided modes, we see here that the energy is indeed confined along the longitudinal fiber axis (\mathbf{z}).

CIRCULATION Here one might observe the consequence of the existence of longitudinal components of the fields. The azimuthal component of the cycle-average Poynting vector is different from zero (and only depends on r). The electromagnetic energy of the guided modes circulates around the nanofiber axis. This is very important as it will give

birth to angular momentum in a direction parallel to the fiber axis. We found,

$$\begin{aligned} \langle \mathbf{S}_\phi^\pm \rangle &= \frac{1}{2} \text{Re} [\mathcal{E}_z^\pm \mathcal{H}_r^{\pm*} - \mathcal{E}_r^\pm \mathcal{H}_z^{\pm*}] \\ \langle \mathbf{S}_\phi^\pm \rangle_{\text{in}} &= \mp \mathcal{N}^2 \frac{\hbar}{\omega \mu_0} \frac{s}{s_1} \xi J_l(hr) \left[J_{l+1}(hr)(2ls_1 + 1 + l^2 s s_1) - J_{l-1}(hr)(2ls_1 - 1 - l^2 s s_1) \right] \\ \langle \mathbf{S}_\phi^\pm \rangle_{\text{out}} &= \pm \mathcal{N}^2 \frac{q}{\omega \mu_0} \frac{s}{s_2} K_l(qr) \left[K_{l+1}(qr)(2ls_2 + 1 + l^2 s s_2) + K_{l-1}(qr)(2ls_2 - 1 - l^2 s s_2) \right] \\ \text{where } \xi &= \left(\frac{q}{\hbar} \frac{K_l(qa)}{J_l(ha)} \right)^2, \quad \mathcal{N} = \mathcal{C} \frac{\beta}{2q}, \quad s_i = \frac{\beta^2}{k^2 n_i^2} s \quad (i = 1, 2). \end{aligned}$$

The last two constants were introduced to compare our results with [ref lekien].

$\langle \mathbf{S}_\phi \rangle$ is however null for quasi-linear polarized modes which still possess longitudinal components.

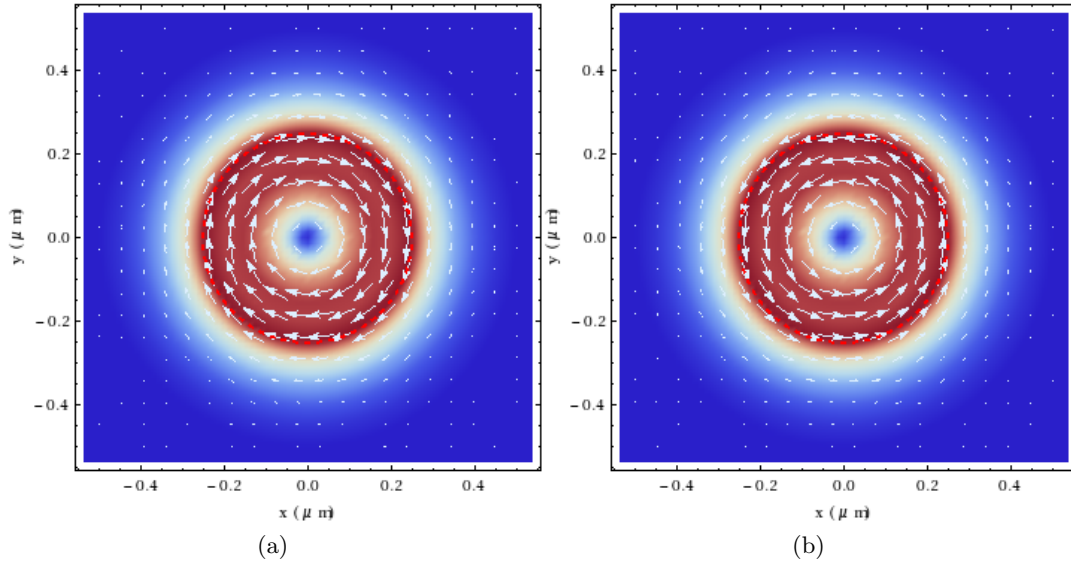


Figure 8.1: Transverse Poynting vector field density of the fundamental HE_{11} mode. (a) for (+) solutions, clockwise rotating polarization (b) for (-) solutions, counter-clockwise rotating polarization.

LONGITUDINAL FLOW We already found the longitudinal component of the cycle-average energy flux in the previous chapter in order to normalize the field expressions to the total transverse input power in the fiber. Here we rewrite it and try to keep the symmetry in the expressions. One can notice in the constants, as above, a normalized

wavelength (s/s_i) and an effective impedance (transverse for (h, q) and longitudinal for β).

$$\begin{aligned} \langle \mathbf{S}_z^\pm \rangle &= \frac{1}{2} \operatorname{Re} \left[\mathcal{E}_r^\pm \mathcal{H}_\phi^{\pm*} - \mathcal{E}_\phi^\pm \mathcal{H}_r^{\pm*} \right] \\ \langle \mathbf{S}_z^\pm \rangle_{\text{in}} &= \mathcal{N}^2 \frac{\beta}{\omega \mu_0 s_1} \xi \left[J_{l+1}^2(hr)(1+ls)(1+ls_1) + J_{l-1}^2(hr)(1-ls)(1-ls_1) \right] \\ \langle \mathbf{S}_z^\pm \rangle_{\text{out}} &= \mathcal{N}^2 \frac{\beta}{\omega \mu_0 s_2} \left[K_{l+1}^2(qr)(1+ls)(1+ls_2) + K_{l-1}^2(qr)(1-ls)(1-ls_2) \right] \end{aligned}$$

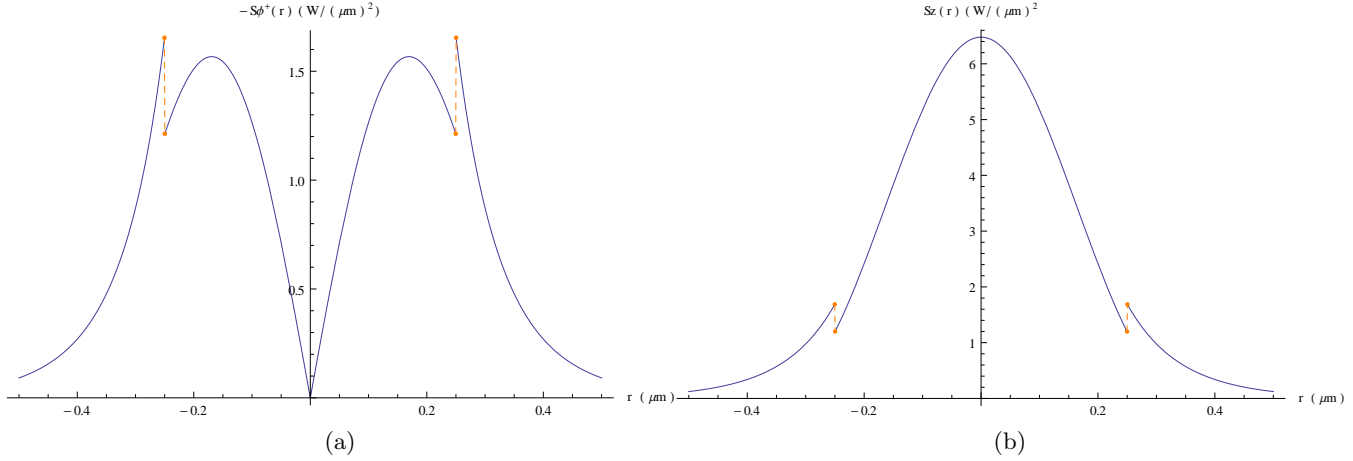


Figure 8.2: Magnitude of energy flow components as a function of the distance to the fiber axis for the fundamental HE_{11} mode with rotating polarization. (a) Transverse energy flow (b) Longitudinal energy flow.

We have now reached our first goal. Indeed, from equations (8.2) and (8.6), we obtain the cycle-average kinetic momentum density of the guided modes. Before we proceed further, it is interesting to study the trajectory of the linear momentum.

8.4.4 Light momentum trajectory

At a fixed distance away from the fiber axis, the cylindrical components of $\langle \mathbf{S} \rangle$ are constant. They do not depend on z nor do they on the angle ϕ . However, the cylindrical basis is a local basis. Therefore the direction of $\langle \mathbf{S} \rangle$ will vary along the fiber axis. From the constant azimuthal circulation and axial translation of the Poynting vector (having no radial flow), its trajectory will then describe a spiral. This is how the light energy is kept guided and confined all along the nanotapered section. See figure 8.3.

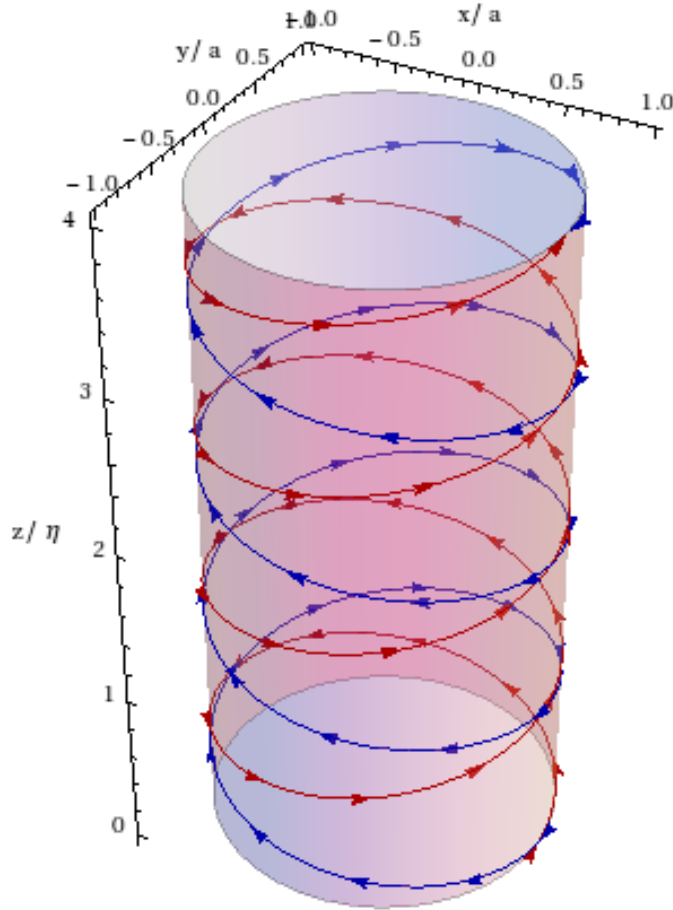


Figure 8.3: Classical trajectory of a photon particle at the nanofiber surface, blue (+) mode, red (-) mode.

8.4.5 Light screw periodicity

An important feature of the linear momentum trajectory is its longitudinal periodicity. Besides, it clearly depends on the spiral radius. In order to obtain an analytical expression for the spatial period, we seek for a 2π increase in the rotation angle $\alpha(z)$ of the spiral, during propagation.

The transverse arc length increase, during an infinitesimal path step, is directly linked to the increase in the rotation angle by $r d\alpha$. It is coupled to an infinitesimal increase dz along the fiber axis. One can see that the previous arc length is given by $dz|S_\phi|/S_z$. Thus, we have

$$\frac{d\alpha}{dz} = \frac{1}{r} \frac{|S_\phi|}{S_z}.$$

As commented above, the components of $\langle \mathbf{S} \rangle$ do not depend on z . A direct integration gives,

$$\alpha(z) = \frac{z}{r} \frac{|S_\phi|}{S_z} + \alpha_0$$

where α_0 is an arbitrary starting angle constant. From $\alpha(z + \eta) - \alpha(z) = 2\pi$, the wanted spatial period is found to be

$$\eta = 2\pi(rS_z)/|S_\phi|. \quad (8.9)$$

LIGHT SPIRAL MECHANICAL ADVANTAGE The previous parameter would be interesting in a view of designing a light screw for example. Indeed, the mechanical advantage of this screw would clearly depend on η , which characterizes the increase in linear motion during one revolution. An optimal screw will then be found by maximizing the period η while the light intensity transported in the evanescent leads is sufficient.

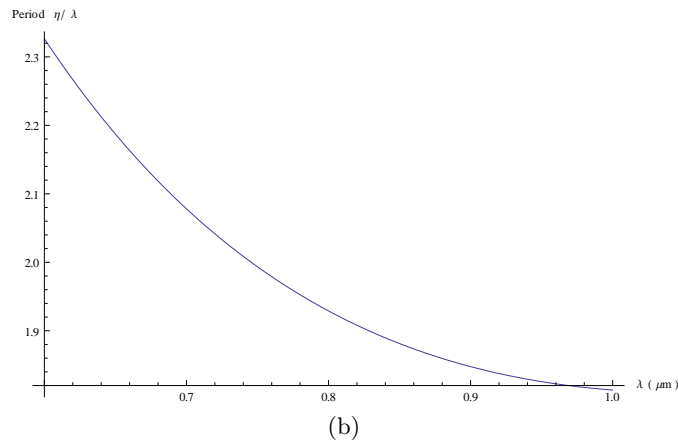
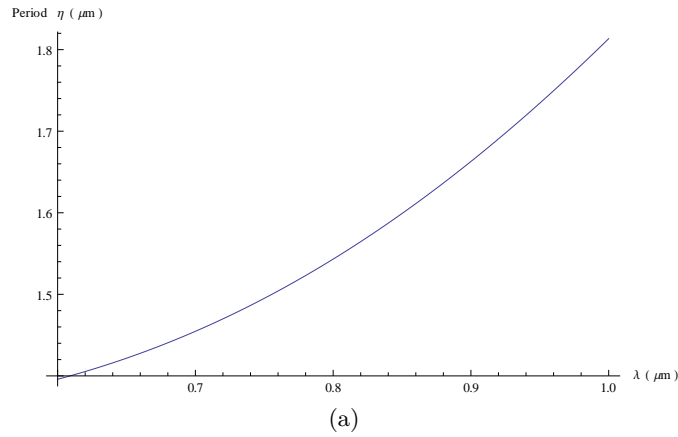


Figure 8.4: (a) Light screw period versus light wavelength (b) Ratio of light screw period to the light wavelength.

It would be very interesting to investigate how the spiral depends on the light wavelength, on the fiber radius and the refractive index

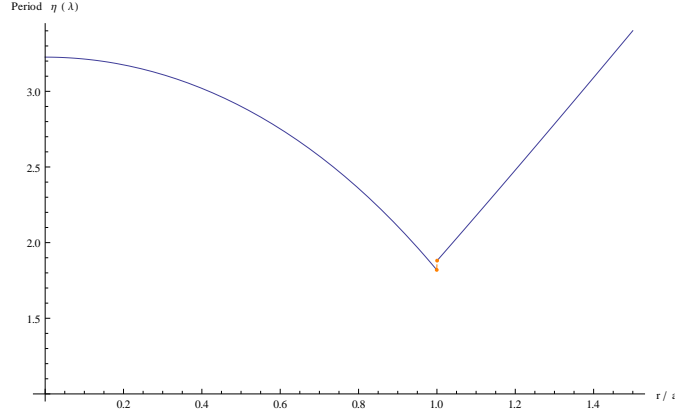


Figure 8.5: Light screw period as a function of the distance to the fiber axis.

difference in order to optimize the previous spatial period in the design of optical light screw.

8.4.6 Modes with quasi-linear polarization

We report our analytical results for modes with equal superposition of (+) and (-) rotating polarization, that is quasi-linearly polarized modes. Clearly, the azimuthal symmetry of the longitudinal energy flow is now broken. Only the longitudinal component remains. Light energy does not circulate anymore around the fiber axis.

$$\begin{aligned}
 \langle \mathbf{S}_z^p \rangle_{\text{out}} &= \left[K_{l+1}^2(qr)(1+ls)(1+ls_2) + K_{l-1}^2(qr)(1-ls)(1-ls_2) \right] \times \mathcal{N}^2 \frac{\beta}{\omega\mu_0} \frac{s}{s_2} \\
 &\quad - 2(l^2 s s_2 - 1) \cos(2l\phi + 2\alpha) K_{l+1}(qr) K_{l-1}(qr) \times \mathcal{N}^2 \frac{\beta}{\omega\mu_0} \frac{s}{s_2} \\
 \langle \mathbf{S}_z^p \rangle_{\text{in}} &= \left[J_{l+1}^2(hr)(1+ls)(1+ls_1) + J_{l-1}^2(hr)(1-ls)(1-ls_1) \right] \times \xi \mathcal{N}^2 \frac{\beta}{\omega\mu_0} \frac{s}{s_1} \\
 &\quad + 2(l^2 s s_1 - 1) \cos(2l\phi + 2\alpha) J_{l+1}(hr) J_{l-1}(hr) \times \xi \mathcal{N}^2 \frac{\beta}{\omega\mu_0} \frac{s}{s_1}
 \end{aligned}$$

8.5 LINEAR MOMENTUM PER PHOTON

In this section, we want to evaluate the final average linear momentum distributed per photon in the guided modes and compare it to $\hbar k$. To this end, we will normalize the linear momentum to unit propagation length, which has to be finite and then to the number of photons per unit length.

8.5.1 Linear momentum per unit length

The linear momentum per unit length \mathbf{G} is given by integration of the linear momentum density over the infinite transverse plane to the fiber

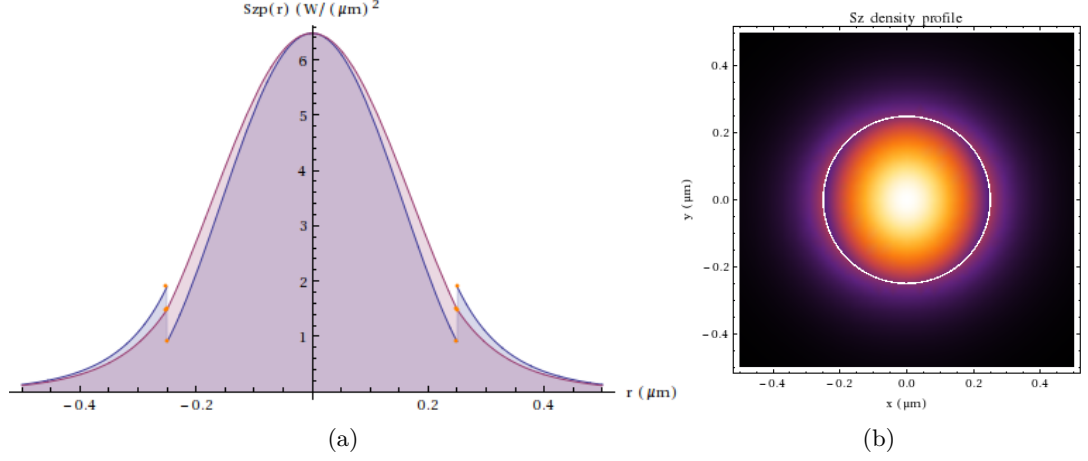


Figure 8.6: Example of the transverse intensity distribution of the longitudinal Poynting vector component S_z for the quasi-linearly polarized fundamental mode (a) Radial intensity profile along the azimuthal direction $\phi = 0, \phi/2$ (b) Transverse density. We observe a broken symmetry $\phi = 0, \phi/2$.

axis. Because of the azimuthal invariance of $\langle \mathbf{S}_\phi \rangle$, only the longitudinal component of the average Poynting vector will contribute to the vector \mathbf{G} .

$$\mathbf{G} = \mathbf{z} \int_0^{2\pi} d\phi \int_0^\infty \frac{\langle \mathbf{S}_z \rangle}{c^2} r dr \quad (8.10)$$

$$\begin{aligned} \mathbf{G}_z &= \pi a^2 \mathcal{N}^2 \frac{\beta \epsilon_0}{\omega} \frac{s}{s_1} \xi \left[(1 + ls)(1 + ls_1) \mathcal{L}_{l+1}^J(a) + (1 - ls)(1 - ls_1) \mathcal{L}_{l-1}^J(a) \right] \\ &+ \pi a^2 \mathcal{N}^2 \frac{\beta \epsilon_0}{\omega} \frac{s}{s_2} \left[(1 + ls)(1 + ls_2) \mathcal{L}_{l+1}^K(a) + (1 - ls)(1 - ls_2) \mathcal{L}_{l-1}^K(a) \right], \end{aligned}$$

with for compactness (Lommel integrations)

$$\begin{aligned} \mathcal{L}_l^J(r) &= \left[J_l^2(hr) - J_{l-1}(hr) J_{l+1}(hr) \right] \\ \mathcal{L}_l^K(r) &= \left[K_{l-1}(qr) K_{l+1}(qr) - K_l^2(qr) \right]. \end{aligned}$$

8.5.2 Photon number per unit length

The electromagnetic energy density is given by :

$$u = \frac{1}{2} (\mathbf{D} \cdot \mathbf{E} + \mathbf{B} \cdot \mathbf{H}) \quad \text{or} \quad \langle u \rangle_{2\pi/\omega} = \frac{1}{4} \left(\epsilon_0 n^2 |\mathcal{E}|^2 + \mu_0 |\mathcal{H}|^2 \right) \quad (8.11)$$

with our definition of the complex amplitudes. It is then remarkable that the cycle-average electromagnetic energy per unit length is simply given by the electric field,

$$U = \frac{\epsilon_0}{2} \int_0^{2\pi} d\phi \int_0^\infty n(r)^2 |\mathcal{E}|^2 r dr. \quad (8.12)$$

Indeed, according an important theorem, the reciprocity theorem, that applies to guided modes, one can show that the total magnetic energy per unit length equates the total electric energy per unit length. We have verified analytically the validity of this result for all mode order. The difficulty being that the magnetic energy contribution inside (outside) the fiber is different from the electric energy inside (outside). Only the totals are equal. Equation (8.12) turns out to be a consequence of the fundamental eigenvalue relation 6.3.

$$\begin{aligned} U_{in} &= \mathcal{N}^2 \pi a^2 \epsilon_0 n_1^2 \xi \left[\mathcal{L}_{l+1}^J(a)(1+ls)^2 + \mathcal{L}_{l-1}^J(a)(1-ls)^2 + 2 \frac{h^2}{\beta^2} \mathcal{L}_l^J(a) \right] \\ U_{out} &= \mathcal{N}^2 \pi a^2 \epsilon_0 n_2^2 \left[\mathcal{L}_{l+1}^K(a)(1+ls)^2 + \mathcal{L}_{l-1}^K(a)(1-ls)^2 + 2 \frac{q^2}{\beta^2} \mathcal{L}_l^K(a) \right] \end{aligned}$$

For the fundamental mode with $l = 1$, we report the analytical expression in Appendix B. The number of photons per unit length in a given rotating polarization mode $\pm l$ reads

$$n_\gamma = \frac{U_{in} + U_{out}}{\hbar \omega}. \quad (8.13)$$

8.5.3 Kinetic momentum per photon

We finally obtain the average linear momentum per photon in the considered modes,

$$\mathbf{p}_\mathbf{a} = \mathbf{z} \frac{\mathbf{G}_z}{n_\gamma}. \quad (8.14)$$

HOMOGENEOUS LIMIT For the sake of curiosity, let us consider from our model the singular case of an homogeneous medium. We take the limiting case where no polarization gradient subsists between the core and the cladding, that is, $n_1 = n_2 = n$. The latter condition implies both $\beta = k_0 n$ (for example see (6.16)) and $h^2 = -q^2$. The fields components also greatly simplifies following $s = 0$. Because the eigenvalue relation vanishes to $\frac{J'_l(ha)}{haJ_l(ha)} = -\frac{K'_l(qa)}{qaK_l(qa)}$, one can show that $\xi \mathcal{L}_l^J(a) \rightarrow \mathcal{L}_l^K(a)$ that gives

$$\begin{aligned} \mathbf{G}_z &\rightarrow \pi a^2 \mathcal{N}^2 \frac{\epsilon_0 k_0^2 n^2}{\omega \beta} \left[\xi \left(\mathcal{L}_{l+1}^J(a) + \mathcal{L}_{l-1}^J(a) \right) + \mathcal{L}_{l-1}^K(a) + \mathcal{L}_{l+1}^K(a) \right] \\ n_\gamma &\rightarrow \frac{\pi a^2 \mathcal{N}^2 \epsilon_0 n^2}{\hbar \omega} \left[\xi \left(\mathcal{L}_{l+1}^J(a) + \mathcal{L}_{l-1}^J(a) \right) + \mathcal{L}_{l-1}^K(a) + \mathcal{L}_{l+1}^K(a) \right] \end{aligned} \quad (8.15)$$

A lot of terms cancel out and the linear momentum per photon reduces to the well-known and expected result given in the introduction for

the Abraham momentum (8.5) in a linear isotropic and homogeneous dielectric medium of refractive index n .

$$\mathbf{p}_n = \frac{\hbar k_0^2}{\beta} \mathbf{z} = \frac{\hbar k_0}{n} \mathbf{z}.$$

This is indeed the value one would expect for a plane wave travelling in the fiber axis direction \mathbf{z} , for which $\mathbf{g}_{\text{Abra}} = \mathbf{z} \cdot (n\epsilon_0|\mathbf{E}|^2/c)$ and a uniform density of photons that amounts to $\epsilon_0 n^2 |\mathbf{E}|^2 / (\hbar\omega)$. One could have also predicted this result if one recognized that the hitherto simplified eigenvalue relation describes transverse electromagnetic modes (TEM, i.e both TM and TE at the same time, because the two classes will be degenerated in this case.

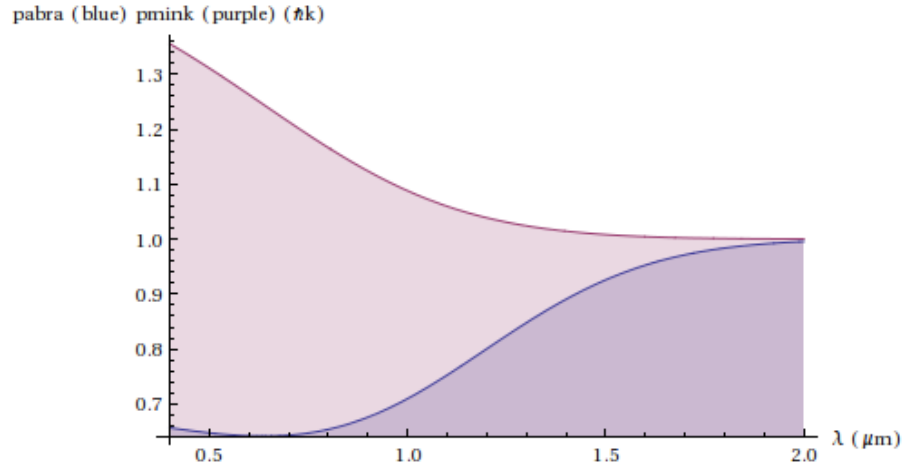


Figure 8.7: Average Abraham (blue) and Minkowsky (pink) momenta per photon in the fundamental mode as a function of the wavelength.

8.5.4 Quasi-linear polarized modes

The azimuthal symmetry is broken for quasi-linear polarized modes. For instance, the electric field intensity appearing in (8.12) depends now on the azimuthal angle ϕ . The corresponding expressions for $|\mathcal{E}|^2$ are reported in Appendix B. However, one can show that the energy per unit length vehicled by a normalized equal superposition of the clockwise and counter-clockwise modes, remains unchanged. Therefore, the results given above for U_{in} and U_{out} , in case of any rotating mode, are also valid for a quasi-linear polarized mode.

This observation also applies to the longitudinal component of the cycle-average Poynting vector given before 8.4.6, for which the azimuthal harmonic component will average out after transversal integration (8.10). Thus, the linear momentum per unit length transported by the quasi-linear polarized modes \mathbf{G}_z is also identical to the expression found earlier for the rotating modes.

8.5.5 Energy transport rate

In this chapter, we have obtained an analytical expression for both the energy density per unit length U and the transversal energy flow $c^2\mathbf{G}$. Clearly, the ratio of the latter to the former has the dimension of a velocity. It represents indeed, the rate at which the energy carried in a hybrid mode propagates in the longitudinal direction (parallel to the fiber axis). From (8.12) and (8.10) one can write

$$\begin{aligned}
 A &= n_1^2 \xi \left[(1+ls)(1+ls_1)\mathcal{L}_{l+1}^J(a) + (1-ls)(1-ls_1)\mathcal{L}_{l-1}^J(a) \right] \\
 B &= n_2^2 \left[(1+ls)(1+ls_2)\mathcal{L}_{l+1}^K(a) + (1-ls)(1-ls_2)\mathcal{L}_{l-1}^K(a) \right] \\
 C &= n_1^2 \xi \left[\mathcal{L}_{l+1}^J(a)(1+ls)^2 + \mathcal{L}_{l-1}^J(a)(1-ls)^2 + 2\frac{h^2}{\beta^2}\mathcal{L}_l^J(a) \right] \\
 D &= n_2^2 \left[\mathcal{L}_{l+1}^K(a)(1+ls)^2 + \mathcal{L}_{l-1}^K(a)(1-ls)^2 + 2\frac{q^2}{\beta^2}\mathcal{L}_l^K(a) \right],
 \end{aligned}$$

$$\frac{c^2\mathbf{G}_z}{U} = \frac{\omega}{\beta} \left(\frac{A+B}{C+D} \right), \quad (8.16)$$

where the fraction in parenthesis is a dimensionless quantity. In the short chapter [ref], we have shown that the magnitude of the phase velocity in the direction of the fiber axis is $v_{\text{ph}} = \omega/\beta$. Therefore, in the very special case of no modal dispersion, that is for the limiting case of an isotropic homogeneous medium without dispersion where $n_1^2 = n_2^2$, the group velocity will be identical to the phase velocity and the energy transport rate is then given by v_{ph} . In free space, it is well-known that the electromagnetic energy density and power are related via the speed of light c as such $P = cu$.

We found very interesting that even when one neglects the dispersion of the core and cladding media of the nanofiber, i.e $dn_1/d\omega = dn_2/d\omega = 0$, the energy transport rate is not given by the longitudinal phase velocity, but rather still by the longitudinal group velocity $d\omega/d\beta = 1/\beta(\omega)'$. This is due to the refractive index step. In the end, one obtains an other way of getting an analytical expression for the group velocity. In order to show that

$$\mathbf{v}_{\text{gr}} \cdot \mathbf{z} = \frac{1}{\beta'} = \frac{c^2\mathbf{G}_z}{U} = \frac{\omega}{\beta} \left(\frac{A+B}{C+D} \right) \quad (8.17)$$

we compared (8.16) to a differentiation of the fundamental transcendental eigenvalue equation of the fiber. We have treated the analysis for the transverse modes in Appendix B.

8.6 ANGULAR MOMENTUM PER PHOTON

From the required previous steps, we now want to find the angular momentum per photon for any mode order. Following the definition (8.3) and the Poynting vector expression 8.4.3, the cycle-average local Abraham angular momentum density is³

$$\mathbf{j}(\mathbf{r}) = r\mathbf{r} \times [\langle \mathbf{S}_z \rangle \mathbf{z} + \langle \mathbf{S}_\phi \rangle \Phi] = r \langle \mathbf{S}_\phi \rangle \mathbf{z} - r \langle \mathbf{S}_z \rangle \Phi. \quad (8.18)$$

8.6.1 Total angular momentum per unit length

Again, the last term in (8.18) will not contribute to the total angular momentum per unit length, such that the latter only depends on $\langle \mathbf{S}_\phi \rangle$. Its only non-zero component is therefore along \mathbf{z} .

$$\mathbf{J}^\pm = \frac{\mathbf{z}}{c^2} \int_0^{2\pi} \int_0^\infty r \langle \mathbf{S}_\phi^\pm \rangle r \, d\phi \, dr. \quad (8.19)$$

To avoid reporting heavy formulas, the way we found to integrate the latter can be found in Appendix B and we obtained the following results

$$\begin{aligned} \mathbf{J}_{\text{in}}^\pm &= \mp \mathcal{N}^2 2\pi a^2 \frac{\epsilon_0}{\omega} \frac{s}{s_1} \xi l \left[J_l^2(ha)(1 + l^2 s s_1) - J_{l-1}(ha)J_{l+1}(ha)(2s_1 + 1 + l^2 s s_1) \right] \\ \mathbf{J}_{\text{out}}^\pm &= \pm \mathcal{N}^2 2\pi a^2 \frac{\epsilon_0}{\omega} \frac{s}{s_2} l \left[K_{l-1}(qa)K_{l+1}(qa)(2s_2 + 1 + l^2 s s_2) - K_l^2(qa)(1 + l^2 s s_2) \right]. \end{aligned}$$

Readily, only modes with $l > 0$ possess axial angular momentum.

8.6.2 Angular momentum per photon

As for the kinetic momentum per photon, we normalize the angular momentum per unit length to the number of photons per unit length and obtain the average angular momentum carried per photon⁴ travelling along the fiber axis,

$$\mathbf{j}_\gamma^\pm = \frac{\mathbf{J}_{\text{in}}^\pm + \mathbf{J}_{\text{out}}^\pm}{n_\gamma}. \quad (8.20)$$

From our previous study of the energy flow circulation, we have observed that the angular momentum per photon is null for quasi-linear polarized modes.

8.7 DECOMPOSITION INTO SPIN AND ORBITAL ANGULAR MOMENTUM

We have seen previously that once the linear momentum density of the fields is known, the total local angular momentum follows naturally.

³ $(\mathbf{r}, \Phi, \mathbf{z})$ are the cylindrical basis unit vectors.

⁴ in this chapter photon means a quantum of light energy.

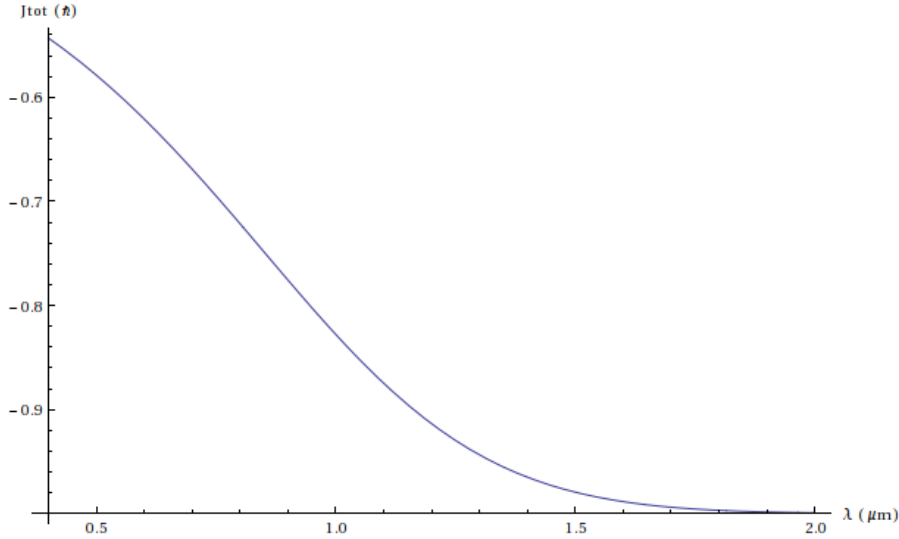


Figure 8.8: Total angular momentum as a function of the wavelength λ . i. e. the projection on the fiber axis is negative for (+) clockwise rotating polarization.

However, this total momentum can result from two different contributions as far as we know. Early quantum mechanics experimental facts taught us indeed that light can carry an intrinsic angular momentum, commonly referred to as spin. Keeping in mind that our treatment of the electromagnetic field description is classical, we will try to decompose \mathbf{j}_γ^\pm in spin and orbital angular momentum contributions.

8.7.1 Humblet decomposition

Following [ref lekien], we safely start with the Abraham definition,

$$\mathbf{J}^\pm = \mathbf{J}_{\text{spin}}^\pm + \mathbf{J}_{\text{orb}}^\pm = \epsilon_0 \iint \mathbf{r} \times (\mathbf{E}^\pm \times \mathbf{B}^\pm) r \, dr \, d\phi \quad (8.21)$$

and then introduce the potential vector \mathbf{A} from the familiar result that for a charge free electromagnetic field in the Coulomb gauge ($\nabla \cdot \mathbf{A} = 0$) follows $\mathbf{E} = -\frac{\partial \mathbf{A}}{\partial t}$ and $\mathbf{B} = \nabla \times \mathbf{A}$. Replacing the new expression for the magnetic induction field \mathbf{B} , one can show that (8.21) becomes three terms, that we will call Humblet's decomposition [ref]. This decomposition is unfortunately not unique because all the terms are not gauge invariant. However, one of the terms can be associated to the spin contribution. This term is

$$\mathbf{J}_{\text{spin}}^\pm = \epsilon_0 \iint (\mathbf{E}^\pm \times \mathbf{A}^\pm) r \, dr \, d\phi. \quad (8.22)$$

The quantity involved under the integration sign clearly does not depend explicitly on the position \mathbf{r} in space where the angular momentum is computed (see (8.3), (8.21)). It is intrinsic. Moreover, one can observe that this spin is different from zero if $\frac{\partial \mathbf{A}}{\partial t}$ and \mathbf{A} are not proportional.

A fact that occurs when the direction of the field changes, here, rotates, over time.

Clearly, the appearance of the potential vector, unlike \mathbf{E} , makes the previous spin definition not unique, not gauge invariant. One can be very disappointed and unsatisfied by this fact until one realizes that the spin of a photon is not a physical observable.

Indeed, the claim is that only observable physical quantity matters and it has appeared to experience that it is not possible to measure the spin of a photon while the latter propagates in a direction orthogonal to the photodetector. The observable, that is the only measurable physical quantity here is the helicity, which corresponds to projections of the spin along directions parallel to the photon propagation direction.

INVISIBLE GAUGE ? Interestingly, one can show [James H. Crichton] that the gauge freedom introduced by the potential vector in (8.22) will give rise to an extra spin density term in a direction orthogonal to the propagation direction of the photon, which is not measurable. For a brightful example, one can consider a transverse electromagnetic field where the classical photon particule trajectories point in the same direction (i.e a plane wave). The nabla operator ∇ can be replaced by $i\mathbf{k}$ in that case and one can then show that adding an arbitrary gradient gauge field to \mathbf{A} adds a term orthogonal to \mathbf{k} in the spin density.

8.7.2 Spin per photon

Going back to our definition of the complex amplitudes, together with the definition of the potential vector given the previous paragraph, we have

$$\mathbf{A} = \frac{\mathcal{A}e^{i(\omega t - \beta z)} + \mathcal{A}^*e^{-i(\omega t - \beta z)}}{2}$$

with $\mathcal{A} = i\frac{\mathcal{E}}{\omega}$ from $\mathbf{E} = -\frac{\partial\mathbf{A}}{\partial t}$.

Taking the cycle-average of (8.22), then rewrites

$$\langle \mathbf{J}_{\text{spin}}^{\pm} \rangle = i\frac{\epsilon_0}{2\omega} \iint (\mathcal{E}^{\pm*} \times \mathcal{E}^{\pm}) r dr d\phi = -\frac{\epsilon_0}{\omega} \mathbf{z} \iint \text{Im}(\mathcal{E}_r^{\pm*} \mathcal{E}_{\phi}^{\pm}) r dr d\phi.$$

The last result showing that the only non-zero component of the spin per unit length is along \mathbf{z} can be found in Appendix B. It relies on the elimination of the radial part from the field expressions and the azimuthal part vanishes from their azimuthal invariance.

$$(\mathcal{E}_r^* \mathcal{E}_{\phi})_{\text{in}}^{\pm} = \pm i \mathcal{N}^2 \xi \left[J_{l-1}^2(qr)(1-ls)^2 - J_{l+1}^2(qr)(1+ls)^2 \right] \quad (8.23)$$

$$(\mathcal{E}_r^* \mathcal{E}_{\phi})_{\text{out}}^{\pm} = \pm i \mathcal{N}^2 \left[K_{l-1}^2(qr)(1-ls)^2 - K_{l+1}^2(qr)(1+ls)^2 \right] \quad (8.24)$$

They are pure imaginary and bring the important result

$$\begin{aligned}\langle \mathbf{J}_{\text{spin}}^{\pm} \rangle_{\text{in}} &= \pm \frac{\epsilon_0}{\omega} \pi a^2 \mathcal{N}^2 \xi \left[(1 + ls)^2 \mathcal{L}_{l+1}^J(a) - (1 - ls)^2 \mathcal{L}_{l-1}^J(a) \right] \\ \langle \mathbf{J}_{\text{spin}}^{\pm} \rangle_{\text{out}} &= \pm \frac{\epsilon_0}{\omega} \pi a^2 \mathcal{N}^2 \left[(1 + ls)^2 \mathcal{L}_{l+1}^K(a) - (1 - ls)^2 \mathcal{L}_{l-1}^K(a) \right].\end{aligned}$$

Normalizing the result to the density of photon per unit length (see (8.13) finally yields the average spin per photon,

$$\mathbf{j}_{\gamma, \text{spin}}^{\pm} = \frac{\langle \mathbf{J}_{\text{spin}}^{\pm} \rangle_{\text{in}} + \langle \mathbf{J}_{\text{spin}}^{\pm} \rangle_{\text{out}}}{n_{\gamma}}. \quad (8.25)$$

8.7.3 Orbital angular momentum

The orbital angular momentum contribution can be deduced by subtracting the total angular momentum from the previous spin contribution.

$$\langle \mathbf{J}_{\text{orb}}^{\pm} \rangle = \langle \mathbf{J}^{\pm} \rangle - \langle \mathbf{J}_{\text{spin}}^{\pm} \rangle. \quad (8.26)$$

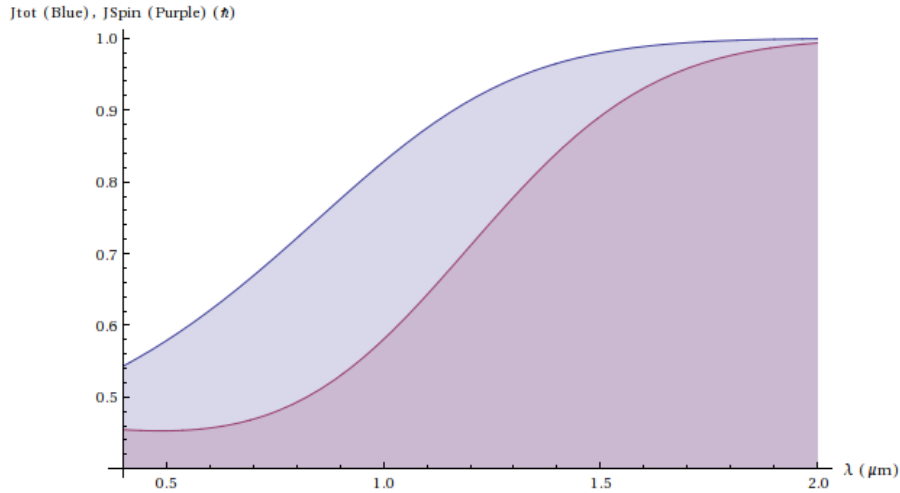


Figure 8.9: (Pink) Total angular momentum. (Blue) Spin angular momentum. The difference gives the contribution of orbital momentum (blue area).

8.8 MINKOWSKY ANALYTICAL RESULTS

Within the framework of our model, it is clear that we have from the definitions (8.6) and (8.7) that

$$\mathbf{g}_{\text{Mink}} = n(r)^2 \cdot \mathbf{g}_{\text{Abra}}. \quad (8.27)$$

Hence, to get the analytical results for the Minkowski formulation one should just multiply the expressions obtained for the Abraham formulation inside the nanofiber by n_1^2 and by n_2^2 respectively outside.

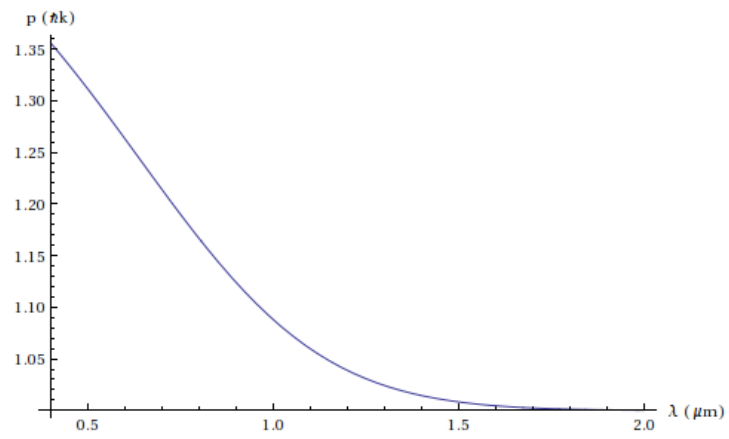


Figure 8.10: Minkowski momentum per photon as a function of the wavelength, for the fundamental of the nanofiber.

 ON THE PHASE VELOCITY

Sometimes, you have to go through a phase whether you like it or not.

— Tina Weymouth

In this very short chapter, we would like to share a short observation about the consequence of the helicity of the hybrid modes on the phase velocity. We will show that the general phase velocity of any mode depends on its polarization state and can differ from the familiar result ω/k for transverse waves.

9.1 THE WAVE PHASE

Another look at the phase dependence of the general hybrid modes ref[appendix]

$$\Xi = \omega t - \beta z \pm l\phi = \omega t - \xi(\mathbf{r}), \quad (9.1)$$

where ϕ is here a cylindrical angle, clearly reveals that the surfaces of constant phase, or cophasal surfaces, are not planar but helical. By taking a time snapshot of the phase wave, the phase points readily define a helix with rotation angle

$$\phi(z) = \frac{2\pi}{\zeta} z - \phi_0 \quad (9.2)$$

where ζ is the spatial period of the helix, $\zeta = (2\pi l)/\beta$ and ϕ_0 is an arbitrary time origin angle. Before drawing any further comments about the wave-front, we would like to introduce the phase velocity.

9.2 HYBRID PHASE VELOCITY

The rate in time of the phase of a certain frequency component of a wave propagating in space, is well understood and known as the phase velocity. Although the phase velocity does not behave as a vector, its reciprocal, the phase slowness does. The phase velocity is usually given as a scalar accounting for the speed of the wavefront in the direction of the gradient of the phase.

Indeed, at an infinitesimally close time $t + dt$, the phase value $\Xi(\mathbf{r}, t)$ will be found at $\mathbf{r} + d\mathbf{r}$, if

$$\omega(t + dt) - (\xi + d\xi) = \omega t - \xi \quad \rightarrow \quad \omega dt = d\xi = \nabla\xi \cdot d\mathbf{r}.$$

In more words, the spatial displacement $d\mathbf{r}$ from \mathbf{r} of the phase during the time dt along a arbitrary direction defined by a unit vector \mathbf{u} , $d\mathbf{r} = dr\mathbf{u}$, is obtained from

$$\omega dt = (\nabla\xi \cdot \mathbf{u}) dr \quad \rightarrow \quad \frac{dr}{dt} = \frac{\omega}{\nabla\xi \cdot \mathbf{u}}. \quad (9.3)$$

The rate dr/dt represents the speed at which the wave-front propagates in the direction \mathbf{u} . As the phase increases in the direction of the gradient, $\mathbf{u} = \nabla\xi / \|\nabla\xi\|$, one naturally defines the phase velocity as

$$v_{\text{ph}} = \frac{\omega}{\|\nabla\xi\|} = \frac{\omega}{\|\mathbf{k}\|} \quad (9.4)$$

where we have introduced the wave-vector \mathbf{k} as being by definition the gradient of the phase delay $\xi(\mathbf{r})$ to the origin of time (9.1). Its direction indicates locally the wavefront propagation direction. In general, \mathbf{k} and the Poynting vector \mathbf{S} are not collinear vectors. That is to say that the propagation direction of the wavefront does not necessarily correspond to the direction of the energy flow transported by the wave.

With the cylindrical gradient given by

$$\nabla\xi = \frac{\partial\xi}{\partial r}\mathbf{r} + \frac{1}{r}\frac{\partial\xi}{\partial\phi}\mathbf{\Phi} + \frac{\partial\xi}{\partial z}\mathbf{z},$$

the wave-vector of the general hybrid modes with rotating polarization becomes

$$\mathbf{k} = \beta\mathbf{z} \mp \frac{l}{r}\mathbf{\Phi}. \quad (9.5)$$

Therefore, it is only for the transverse electric and transverse magnetic modes TE, TH ($l = 0$) plus all modes with quasi-linear polarization that $\mathbf{k} = \beta\mathbf{z}$ and that the propagation constant β represents the angular wavenumber. For modes with rotating polarization, this is no longer the case. For the former, the phase velocity $v_{\text{ph}} = \omega/\beta$ and for the latter

$$v_{\text{ph}} = \frac{\omega}{\sqrt{\beta^2 + (l/r)^2}}. \quad (9.6)$$

However, the *longitudinal* phase speed (ω/β , for $\mathbf{u} = \mathbf{z}$) is readily kept unchanged.

9.3 PHASE AND ENERGY HELICES

One could have carefully noticed after introducing the wave-vector \mathbf{k} that the spatial period of the phase helix (see above (9.2)) ζ can be rewritten as

$$\zeta = 2\pi(r|k_\phi|)/k_z, \quad (9.7)$$

that we wish to compare with the period η of the energy flow helix found in ref[chapter]

$$\eta = 2\pi(rS_z)/|S_\phi|. \quad (9.8)$$

The apparent role inversion of the azimuthal and longitudinal components of the wave-vector in (9.7) compare to (9.8) arises from the fact that \mathbf{k} is locally normal to the phase helix whereas the Poynting vector describes tangentially the energy helix. Indeed, for the vector $\mathbf{T} = q(\beta r\Phi + l\mathbf{z})$ orthogonal to \mathbf{k} , q being a arbitrary real number, we have $\zeta = 2\pi(rT_z)/|T_\phi|$.

We have already seen how η depends on the distance to the fiber axis in the previous chapter. Because on the other hand here ζ is however constant, it gives a visual way of showing that in general, the propagation direction of the energy in a hybrid mode of a nanofiber is different from the wave-vector, i.e the propagation direction of the wavefront. This is to be expected for an inhomogeneous wave, i. e. when the co-phasal surfaces are not co-amplitude surfaces. Here, the co-amplitude surfaces depend both on the cylindrical angle ϕ and on the radial coordinate r , unlike Ξ .

10

FABRICATION OF A NANOFIBER

In this very brief chapter, we just save some accounts about the fabrication of the nanofiber we have used.



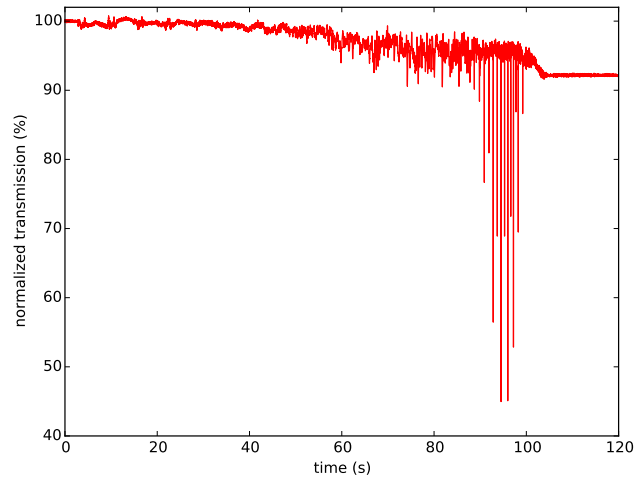
Figure 10.1: Success in making a 500 nm tapered-diameter fiber glued on a U -shaped glass holder. From left to right, Daniel Reitz, Jelmer Renema, Rudolph Mitsch, Jürgen Appel, and myself behind the camera capturing this great event.

The nanofibers for this second thesis work were built at the end of July, 2010 during my master thesis. The nanofibers were made at the University of Mainz (South Germany) in the group of Pr. Arno Rauschenbeutel where myself, Jelmer Renema¹, Jürgen Appel learned how to make (and break) nanofiber tapers with the generous help of Rudolph Mitsch and Daniel Reitz (see figure 10.1). Several fibers were produced and brought back to Copenhagen. However, we have used one and the same nanofiber for all the experiments. The nanotapers were built out of passive fibers ($6/125\text{ }\mu\text{m}$ core/cladding diameters), nLight Liekki™(exact part number P07-050C-01-1A5B).

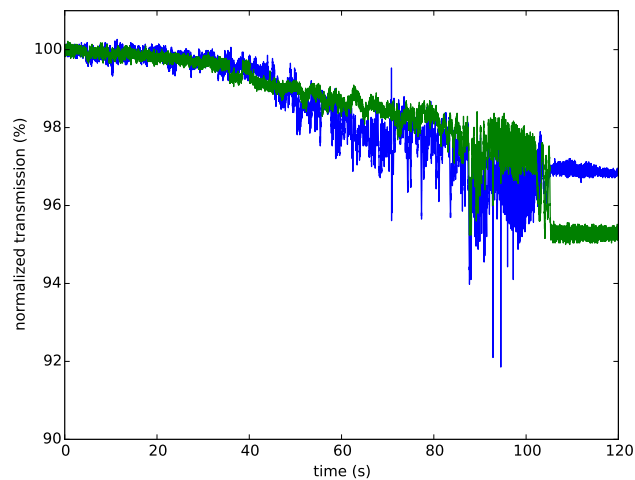
In figure 10.2 we report the measurement of the transmission of 852 nm laser light propagating in the fibers during the pulling process which last for about 105 seconds. The transmission is normalized to the

¹ A former PhD student at [QUANTOP](#) who staid only a few months with us

initial transmission of the unprocessed fiber. The transmission of the used nanofiber is about 92% while it is a bit higher for the spare fibers (which were not transported next in a low vacuum tube to Copenhagen). The choice of this fiber was motivated by the fact that we managed to put two such nanofibers glued in parallel on the holder, however one of them did not survive when we arrive at [NBI](#).



(a) Used nanofiber



(b) Spare nanofibers

Figure 10.2: Output power of 852 nm laser light transmitted through the fiber during the pulling process. The transmission is normalized to the transmission for the initially unpulled fiber. (a) The transmission is about 92% and corresponds to the fiber (used in this thesis). (b) are the records for the two spare fibers we also created. (200 Hz data point sampling rate)

The fabrication process consists in heating a section of a conventional single-mode fiber while pulling it in a such way to produce a desired

target shape. Here, starting from the diameter of the standard fiber, there is a linear ramp in which the fiber is tapered down from $125\ \mu\text{m}$ (in diameter) to almost $10\ \mu\text{m}$. From these $10\ \mu\text{m}$ one has some kind of continuous and adiabatic decrease of the fiber diameter down to $500\ \text{nm}$. From here on, the diameter stays at $500\ \text{nm}$ over the $5\ \text{mm}$ long fiber waist and then increases in the same way as it decreased in the first part (symmetric taper). This whole tapering happens over $\sim 35\ \text{mm}$.

NANOFIBER IRRADIATION IMMUNITY

A very small cause which escapes our notice determines a considerable effect that we cannot fail to see, and then we say that the effect is due to chance.

— Henri Poincaré.

INTRODUCTION

The collection and channelling of optical photons from external light sources was observed at the tapered section of the fiber. This short chapter offers evidences for impurities at the fiber surface from which both experimental limitations and experimental resources are drawn. Static light scattering induced by such impurities can introduce unwanted light intensity landscapes modulation and polarization gradients which are detrimental for optical traps and coherent probing in the vicinity of the fiber surface. However, such scattering effects can in turn be exploited to infer characteristics about the light propagating in the fiber at the tapered section which allows to control for instance the polarization state of the evanescent light propagating in the fiber as we will see in the third part of this thesis.

Although this is a very basic yet first observation, it also demonstrates the strong irradiation immunity of the nanofiber waist. A key ingredient that enables to resolve for instance a few atoms in the evanescent field of the fiber.

11.1 FEMTOWATT GUIDED IN THE FIBER

I just report the first minute measurement performed once a Single-Photon Counting Module (SPCM) detector was carefully aligned with one of the two output modes of the fiber. The fiber was already integrated in a setup ready to trap cold atoms in a MOT around the tapered section of the fiber that I will present in a different chapter. Before to perform any experiments with atoms I had a few simple questions in mind; Can one see guided photons collected at the nano-tapered section of the fiber from light beams crossing over it, for instance the MOT beams ? How big is the signal ? And would that be a limitation for

instance for fluorescence spectroscopy of atoms actively pumped in the MOT ?

Counting photons here is limited to a background photon count rate due to surrounding light sources. This rate was reduced by shielding the apparatus from the laboratory light pollution to about 2 kHz (raw electric events). It is as broadband as the light quantum efficiency spectrum of the detector (visible light domain). When the detector sensitive area is physically blocked the count¹ rate goes down to below 0.3 kHz. We will refer to such a device quality dependent rate as the dark count rate of the detector. The background signal was low enough that we were able to observe with significance (signal-to-noise ratios ranging from 6 to 16) -120 dBm of light power incoming from the fiber. Please note that the other end of the fiber was not blocked (no mirror etc).

The first photons we clearly detected originated from the MOT beams crossing over the fiber at the taper location. The design of the MOT trap has been reported in the next part. Three orthogonal pairs of collimated laser light beams intersect at the nanofiber. Each beam contains two different light sources for cooling and repumping sharing the same spatial mode. Blocking and unblocking physically either of the two lights yield the following mean detected count rates: (cooler) 30.34 kHz \pm 0.17 kHz (repumper) 10.62 kHz \pm 0.06 kHz. The average total cooler (resp. repumper) light power was 2.40 (resp. 1.15) \times 6 mW.

An estimate P for the detected light power transmitted through the fiber can be given from the raw count rates with the knowledge of the energy E_λ of a photon with wavelength $\lambda = 852\text{nm}$ (cooler and repumper light wavelengths), the corresponding detector quantum efficiency $\eta_{\text{SPCM}}(\lambda) = 0.45$ and accounting for 3% loss through propagation across the optical elements from the fiber output to the detector semi-conductor chip.

$$\text{SPCM count rate} \times \frac{E_\lambda}{\eta_{\text{SPCM}}(\lambda)(1 - \text{loss})} = P \quad (11.1)$$

The light power associated to the number of detected cooler photons in the fiber mode is $P_{\text{cooler}} = 15.2 \text{ fW}$. It must be mentioned that the detector monitored only one output of the fiber and there was no intentional back reflection of light at the second output. The fraction of cooler light, as well as repumper light, collected at the taper of the fiber yet detectable is then very weak. It is 12 orders of magnitude smaller than the total light power committed to create the magneto-optical trap ($\sim 20 \text{ mW}$). This constitutes a very high rejection of external irradiation on the waist of the nanofiber, although the MOT beams are relatively large compare to the nanofiber geometry.

The collected power from the repumper is lower than the cooler, $P_{\text{repumper}} = 4.65 \text{ fW}$ but the ratio $P_{\text{cooler}}/P_{\text{repumper}}$ is somewhat larger

¹ Building the counting and failsafe electronics for the SPCM was among the first circuits I worked on for the nanofiber experiment

than the ratio of the above respective estimated total input powers. This could indicate a difference in the effective scattering cross-sections for these two light sources but their frequencies only differ by about 10 GHz. It is more probable to be the result of a systematic error in the measurement of the input powers that might be due to different polarization inputs into the MOT couplers.

11.2 FEMTOWATT SCATTERING

A simple hypothesis to understand the observation of guided photons from the MOT beams would be to consider that the fraction of light from the MOT beams that collides with the glass fiber surface gets coupled into it and propagates further to the detector. For the sake of simplicity, let me neglect any diffraction effect and even overestimate cross-section geometries. For instance, consider a virtual rectangular bounding box around the cylindrical taper of the fiber. The MOT beams are collimated gaussian beams. The order of magnitude of their waist is a centimeter. Over such a length, that is taken as the length of the bounding box, an overestimated mean value of 10 μm for the fiber taper diameter can be retained as the height of the box. The observed ratio of 10^{12} between the total MOT light power and the guided power is clearly incompatible with the ratio of a MOT beam waist to the transverse size of the fiber that can reach at most 10^4 when considering extremes. For instance, a 1 cm beam waist and a fiber diameter of 500 nm. Moreover, the real taper has a diameter of 500 nm over a distance of 5 mm and then 10 μm over 1.7 cm on each side before growing up to 125 μm . So this too simple beam crossing hypothesis cannot explained by far the detected count rates.

In the optical domain, silica glass has a refractive index bigger than $\sqrt{2}$. This means that the optical numerical aperture of an air-cladd silica glass fiber is always bigger than 1. The numerical aperture is the sine of the critical input light ray angle measured from the fiber axis above which light rays cannot be guided by the fiber, through total internal reflection. Therefore, even light rays (very well collimated beams) with grazing incidence can couple and be guided into an air-cladd silica glass fiber from its ends. This translates into: even light with grazing incidence cannot couple and then be guided into an air-cladd silica glass fiber from its surface (the two diopter normals being at right-angle). As long as geometrical optics is valid, i. e. as long as one can assume that the well collimated MOT beams are not diffracted at the fiber, coupling of light into the fundamental single mode of the fiber is expected to be strongly suppressed.

A contrario, if the above hypothesis were valid, one would have found an easy way to estimate the diameter of the taper section of the fiber by detecting guided light from an external beam.

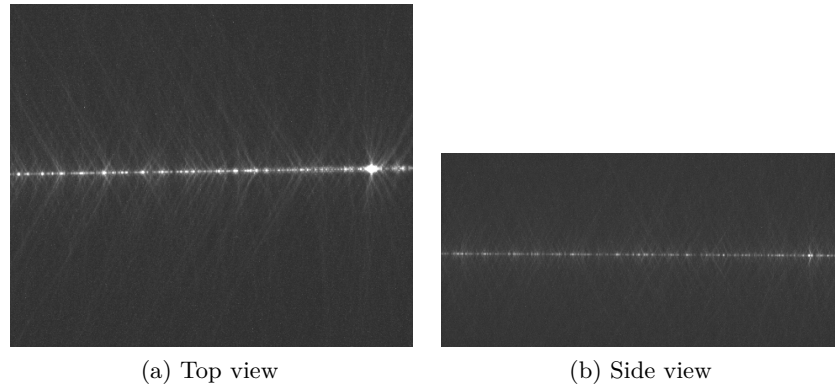


Figure 11.1: CCD images of the 5 mm nanofiber section when 852 nm probe light is guided in the fiber.

The weak detected power from the MOT lights arised therefore most probably from leaking photons or impurities at the fiber surface acting as scattering centers. It has not been attempted to distinguish between the two hypotheses for this particular experiment where the two phenomena are likely to be realized at once. Yet, polarization measurements performed on the output guided light could reveal a signature for Rayleigh scattering. Indeed, light scattering by particles smaller than the wavelength of light exhibits a dipole radiation emission pattern. Due to the strong suppression of emission along the direction of the dipole moment, such scattering will be sensitive to the input polarization. ?? and ?? evidence inhomogeneous scattering of light propagating in the tapered section of the fiber. Here, light is scattered outside the fiber. One should note that the wavelength used on figure ?, $\lambda = 633$ nm, is near the fundamental mode cut-off of the nanofiber. This implies a relatively large evanescent decay length for the fraction of light travelling outside the fiber as well as a bigger overlap with surface impurities. Even if one can have the feeling that this chapter is not that important, one should remember that defect, impurities and scattering centers prevent the realization of many proposals that requires nano and photonic structures combined with optical trap for cold atoms.

11.2.1 *Undesirable effects*

The consequences of the latter observation should be considered a little bit more quantitatively. Indeed, conversely scattering centers that enable surrounding light to channel into the guided mode may in turn scatter photons off a probe beam propagating in the fiber at the tapered section. More, in the situation where light is send through the fiber to create a static evanescent optical light dipole trap potential for neutral atoms, a non-negligible scattering rate will superimpose a spatial modulation of light intensity as well as the introduction of polarization gradients. These effects are expected to be mainly static as

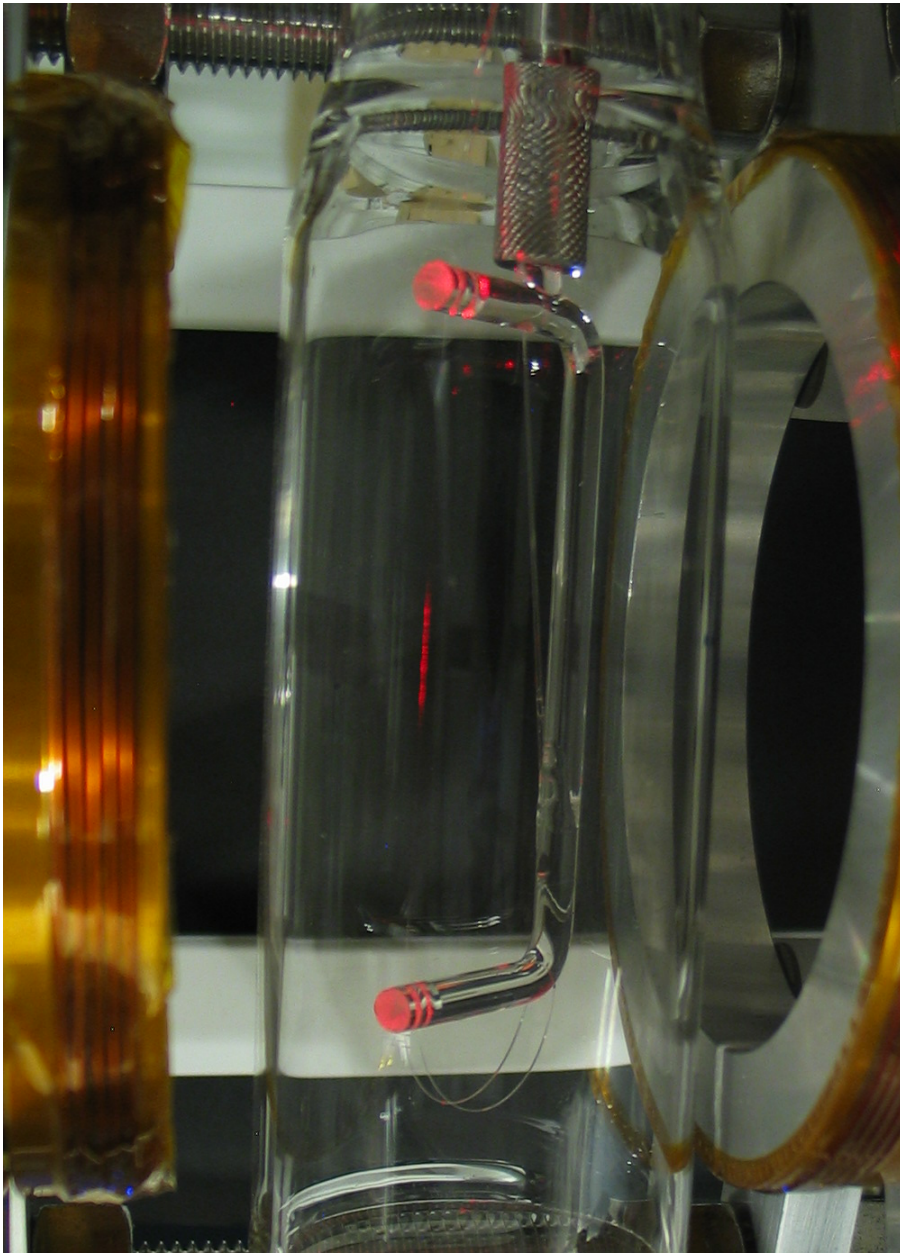


Figure 11.2: A photograph of the nanofiber inside the vacuum chamber. He-Ne laser light sent in the fiber, reveals through scattering, the position of the 35 mm long tapered section.

long as the fiber does not expand or contract thermally nor vibrate. Besides, I have observed that when sending cooler or repumper lights through the fiber, I can perturb a cloud of atoms in a magneto-optical trap via scattering off the fiber even when the center of mass of the cloud is several millimeters away from the fiber surface. Finally, it can be mentioned that the observed leak light will pollute measurements aimed at collecting the fluorescence from surrounding cold atoms.

11.3 EFFECTIVE SCATTERING CROSS-SECTION

An effective scattering cross-section σ_{eff} can be introduced to quantify the probability that a photon from the MOT light beams will couple into the forwarded nanofiber guided mode. We only want to give orders of magnitude.

$$P_{\text{guided}} = \sigma_{\text{eff}} I_{\text{MOT}} \quad (11.2)$$

Counter-propagating MOT beams do not interfere as they have opposite circular polarization. However, their overlap will lead to polarization gradients. MOT beams propagating in the same direction in the same plane will interfere. All interference and diffraction effect are neglected and the measurement is not polarization sensitive.

Furthermore, because of the size of the MOT beam waist compare to the fiber waist and the fact that the beam wave-vectors add up to 0 at the crossing (center of the MOT), the scattered photons are assumed to originate from a wide distribution of spatial directions. The intensity of a MOT beam at the intersection with the fiber is approximated to the peak intensity of a gaussian beam equal to $P/\pi w_0$ with waist w_0 and power P :

$$\sigma_{\text{eff}} = \frac{\pi w_0}{6 \times P_{\text{beam}}} P_{\text{guided}}. \quad (11.3)$$

For cooler light only, $\sigma_{\text{eff}} = 3.3 \cdot 10^{-2} \mu\text{m}^2$ or $\sigma_{\text{eff}} = 1.4 \cdot 10^{-2} \lambda_{\text{D2}}^2$ for a centimeter large waist. By way of comparison, the effective cross-section is 5 orders of magnitude bigger than the disc area of a Cesium atom, 22 \AA^2 (radius 266 pm). However, it is about five time smaller than the on-resonance light scattering cross-section of the D2 line transition of Cesium ($\sigma = 1.4 \cdot 10^{-13} \text{ m}^2$).

Lets consider the hypothesis that photons guided and propagating in the taper section will scatter into MOT beam directions and all other radiation modes with the previous effective cross-section. An estimate for the fraction of light lost through impurities scattering after propagating a length w_0 along the taper, will be given by the ratio of σ_{eff} to πb^2 where b is a worse-case average fiber radius of $1 \mu\text{m}$ over the length w_0 . This would lead to 1% loss. This number is compared to a measure of the taper transmission in 11.4, independently of the fiber input coupling efficiency. For the same mean radius b , one can infer an impurity surface coverage on the order of 1 ppm ($\sim \sigma_{\text{eff}}/bw_0$).

11.3.1 *Benefit of light scattering*

Sometimes, what appears to be a major source of limitation for a particular experiment can be turned into a powerful resource for another experiment. An experimental technique has been implemented to measure and engineer the polarization state of light at the taper section of the fiber. It is based on the principle of Rayleigh scattering mentioned above. The measurements are depicted in details in chapter REF. Without the presence of impurities scattering light, such information would be otherwise difficult to access. The quality of the polarization at the taper is crucial for a non-exhaustive list of experimental abilities: light induced trap geometries, pure optical pumping of targeted atomic population (addressing single zeeman level) or Faraday rotation experiments.

11.4 FIBER TAPER LOSS

The effective propagation loss through the taper of the fiber was evaluated using the cut-back technique. For a fixed light input mode-matching into the fiber mode, the transmitted light power was compared from two measurements. The light power emerging at the output of the fiber was measured. Then the fiber was shortened by cutting it off at its input end, before the taper. Finally, the power emerging at the new output of the fiber was measured. The former power found 8% lower than the latter. This represents a significant attenuation of about 1 dB. The expected attenuation for 852 nm light and a passive silica glass fiber is about $5 \cdot 10^{-3}$ dB after a propagation length of one meter. The splicing² losses that might have been introduced to preserve the length of the fiber are trusted to be as well negligible (~ 0.02 dB, BBT FiberopticTM). Therefore the cut-back method can attribute 92% transmission to the tapered part of the fiber, when located in ultra-high vacuum chamber. This number can be compared to the performances achieved by Arno Rauschenbeutel's group where our fiber was manufactured: 97% (REF PRL 104 2010). In Sague thesis, spectroscopy of cold atoms were achieved with an identically profiled optical tapered fiber with 93% transmission. These losses are most likely attributed to the adiabatic conversion between the weakly guided mode LP01 of the untapered fiber to the strong hybrid fundamental mode HE11 of the nanosection and vice-versa. This is shown by monitoring the transmission of the fiber during the pulling process to create the taper (REF). The contribution to the 8% due to impurities scattering photons off the light field evanescent out of the tapered section was overestimated small ($\sim 1\%$). It is negligible compare to the adiabatic conversion loss.

² For the cut-back technique, about a meter of the same kind of fiber was spliced at one end of the existing fiber. This part was cut half for the mentioned measurement. The loose half was spliced back at the other end of the initial fiber.

11.5 SUMMARY

- A. A number of about 20 photons in 1 ms from the MOT light channeled into the fiber tapered section was observed. It represents tens of femtowatt light power.
- B. The hypothesis of simple scattering from the MOT light beams intersecting with the tapered section was refuted. Otherwise, it would be possible to infer the diameter of the taper section.
- C. These photons are most probably either leaking and/or channel into the guided mode with the help of impurities at the fiber surface acting as scattering centers as evidenced by imaging the fiber.
- D. An estimate for the impurity surface coverage was given ~ 1 ppm. The effects of scattering onto guided probe light and future evanescent dipole trap lights were mentioned and expected to be small. Further, there are expected to be negligible compare to light scattering occurring at the adiabatic transition parts of the fiber. This highlight the important quality of the nanofiber waist: strong immunity to external irradiation. A key ingredient to resolve a few MOT atoms.
- E. Measurement of the taper transmission loss via the cut-back technique was explained and reported. It is at least 10 times bigger than the impurity scattering rate.

Part III

DISCRETE AND CONTINUOUS DETECTION OF ATOMS IN EVANESCENT LIGHT FIELDS

We build a completely new three-dimensional magneto-optical trap setup for cold Cesium atoms, which is compatible with the operation of an optical nanofiber.

We demonstrate the realization of an interface between a very small number of cold atoms ($N_{\text{at}} \sim 10$) and the fundamental guided mode of an optical nanofiber. We realize both fluorescence and absorption spectroscopy of the atoms with weak light field, which we detect with single photon counting techniques. Then, we construct a shot noise limited heterodyne measurement setup and we realize the first continuous detection of atoms in a nanofiber evanescent field.

Then, we build a *radio* or superheterodyne detection scheme to record simultaneously both the continuous absorption and dispersion of atoms. Finally, we observe inhomogeneous light shifts induced by far-detuned guided light.

12

A NEBULA OF COLD ATOMS ON A ROOM-TEMPERATURE NANOMETRIC WIRE

A bit of mould is a pleiad of flowers; a nebula¹ is an ant-hill of stars.

— Victor Hugo

INTRODUCTION

In this chapter, we will present the experimental realization of a three-dimensional magneto-optical trap for cold Cesium atoms, which is compatible with the existence of a room-temperature optical nanofiber located about the center of the trap, see figure 12.1.

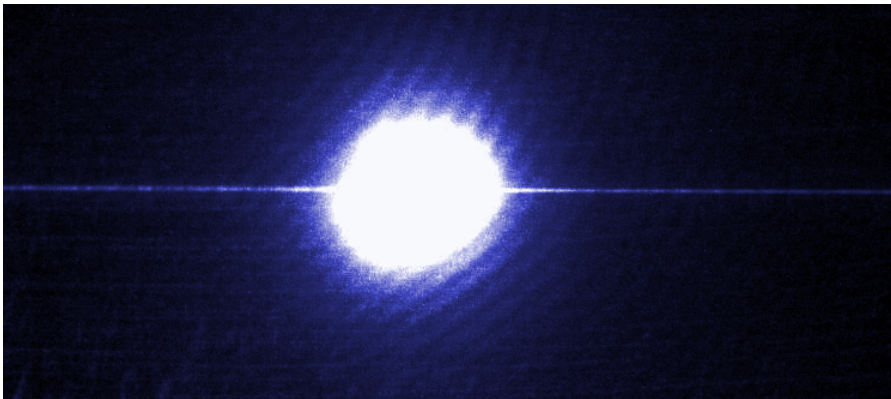


Figure 12.1: Nebula of Cold Cesium atoms in equilibrium around a 500 nm diameter thin fiber.

This constitutes the first enabling step in order to create an interface between cold atoms and the evanescent field guided by an optical nanofiber. It is as well the required resource and the setup to have, in view to load and confine cold neutral atoms into the shallow but conservative evanescent field traps. Although the operation of a MOT has become the workhorse of many quantum optics experiments based on cold neutral atoms, it took many months of my PhD time to build a completely new setup, starting from the vacuum chamber choice, as-

¹ Nebula is the Latin word for cloud, a term introduced by the astronomer William Herschel who also discovered infra-red light. This term seems to be then appropriate to describe the Cesium cloud emitting in the infrared.

sembling and preparation till the construction of all the adequate laser sources and all the electronics to control it as well as the magnetic field sources. Unfortunately, I do not have time to write about these steps in details² and I will only present the necessary schematics together with images of the setup, while writing down some important principles that I would like to remember and also transmit to the next generation of students who would work on the setup. Then, I will start giving the first few basic observations on the effect of the nanofiber onto atoms which were successfully cooled and trap in this new MOT setup.

12.1 VACUUM CHAMBER

Along the lines of the vacuum tubes I built to transport the manufactured nanofibers from Mainz to Copenhagen, we³ tried to build a vacuum chamber as simple as possible, with a small volume (wine bottle volume) and an easy optical beam access to create a MOT from outside the chamber (see figure 12.2). If I would have to redo the chamber today, I would probably go for a rectangular glass cell instead of the cylindrical one we had available at the time and also rethink the design of the nanofiber holder because of its relatively long moment arm which favors acoustic vibrations of the nanofiber.



(a) Cylindrical glass cell

(b) Chamber ready to bake out

Figure 12.2: Photographs during the construction of the vacuum chamber to host the nanofiber. The glass cell and the electrical feedthrough connections to the Cesium dispensers are clearly visible. In addition, one can see on the right, a part of the attached ion pump reservoir and finally a valve.

To release on-demand an ultrapure vapor of Cesium atoms in the chamber, we used common dispensers from the company SAES (see figure 12.3). I would also like to show a photograph of the flange, which

² It has been documented internally as best as possible.

³ Me and Jelmer Renema, a former PhD student who participated for the first few months on the project.

supports the nanofiber holder (figure 12.3 (b)) to be inserted straight from the right flange of figure 12.2 (a) to the center of the glass cell.

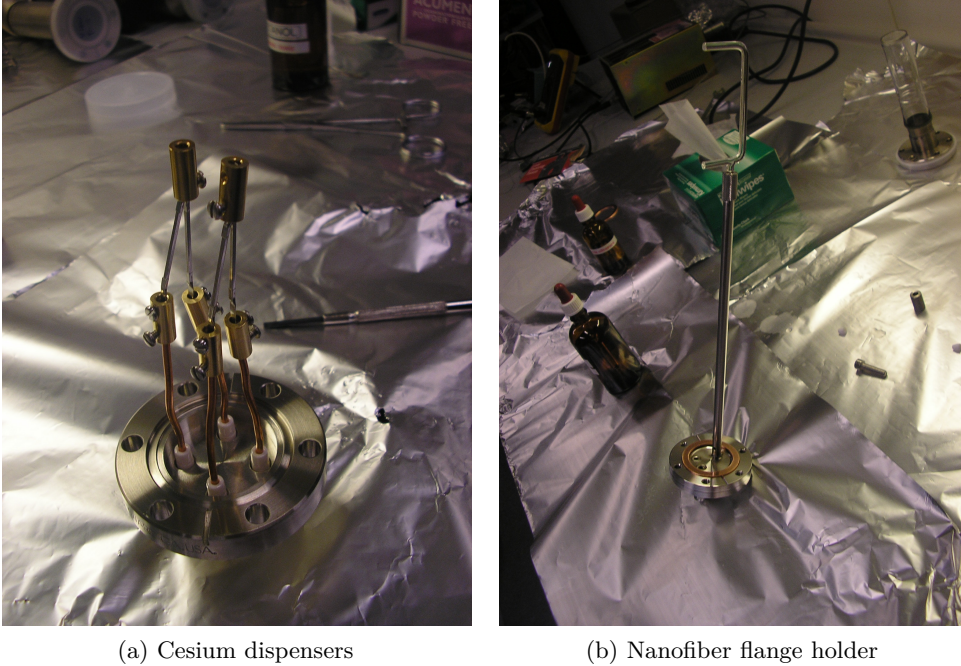


Figure 12.3: (a) Photograph showing two pairs of Cesium dispensers mounted with electrical connections through a flange. (Each pair has two Cesium dispensers (grey metallic bars) connected in series.). In (b) One can see the steel rod that will support the nanofiber.

12.2 OPTICAL SETUP

Two extended cavity diode laser (ECDL) light sources using 150 mW and 852 nm laser diodes were built for the realization of the MOT lights. One is dedicated to laser cooling on the cycling transition of the D2 line of Cesium $|4\rangle \rightarrow |5'\rangle$, the so-called cooler. The other one, the so-called repumper, is used to repump the atoms populating the ground state $|3\rangle$ into the ground state $|4\rangle$ via the $|3\rangle \rightarrow |4'\rangle$ transition. Although radiative decay from $|5'\rangle$ to $|3\rangle$ is not allowed at first order, atoms can be depumped from $|4\rangle$ to $|3\rangle$ via spin exchange collisions, which would stop the cooling mechanism. The repumper laser frequency was stabilized, using a magnetically shielded room-temperature glass cell containing a saturated vapor of Cesium atoms, via the technique of Doppler-free saturation polarization spectroscopy (Wieman and Hänsch (1976)). While we accumulated experience with standard saturation absorption spectroscopy, the polarization one proved to be more robust and stable. In addition, it was easy and relatively quick to set up as it does not require frequency modulation of the laser light. The laser was locked on one significant Doppler-free cross-over resonance, the frequency corresponding

to a transition from $|3\rangle$ to the middle of $|2'\rangle$ and $|3'\rangle$. The repumper frequency is then adjusted and brought closed to $|4'\rangle$ using the first diffraction order of a double-pass AOM (shift of about $+2\times 125$ MHz). The cooler laser frequency is stabilized against the repumper with a versatile and inexpensive phase-locked loop method (Appel et al. (2009a)). In short, the relative frequency of the cooler compared to the one of the repumper is measured by recording the interference beatnote of these two light sources, on a fast photodiode. The frequency of the cooler is meant to address the cycling $|4\rangle \rightarrow |5'\rangle$ transition. The cooler light used for the MOT is derived in addition from an extra +1 diffraction order of a single-pass AOM centered at 80 MHz, to allow fast switching times of the cooler light.

We invested in a fiber splitter array that takes two input⁴ fibers and produce 6 relatively well power balanced fiber outputs to create three pairs of counter-propagating MOT beams. The cooler and repumper lights are sent independently into these two separate input fibers and are then mixed⁵ together into the output fibers, which are all polarization maintaining. We built simple output fiber coupler tubes containing first a polarization beam splitter cube⁶, a quarter waveplate and then a magnifying lens to create centimeter wide and collimated beams with the appropriate circular polarization. With this solution, the setup readily gained in compactness compared to other free-space MOT designs.

Now that we have presented two of the three ingredients required to create a MOT (i. e. Cesium atoms, laser lights), we give some comments about the magnetic trapping part.

12.3 MAGNETIC TRAP CONSIDERATIONS

The magneto-optical trap combines laser Doppler cooling and magnetic trapping. Although there is no general theory for it in 3D (William D. Phillips, Les Houches 1964) its experimental working principle is well-known and I will not explain⁷ it here. I will just insist on practical details I would like to save for the future and give selected references.

Whereas cooling increases the density in velocity space, trapping increases the density in position space. The restoring force here is pro-

⁴ There are actually two extra inputs but which only connect to four of the outputs. They could be used to add easily other light frequencies such as depump light for instance.

⁵ Very useful for instance to check for any AOM leakage frequency order using a fast fiber coupled detector.

⁶ reflected port of the cube goes into a small diode detector to measure each beam power

⁷ Moreover, the common description uses only a basic approach with ground $J = 0$ to excited $J = 1$ atomic levels. This is a very particular case of a level structure which hides the possibility of stimulated emission between orthogonal polarization modes of light and other subtle effects that might appear in the presence of both polarization gradients and degenerate atomic levels.

duced by modifying the radiative light force through the Zeeman effect by application of an inhomogenous magnetic field ($\mathbf{B} = bz\mathbf{z}$). The MOT makes then use of both linear and angular momenta transfert and circumvent the optical Earnshaw theorem⁸.

The magnetic field gradient produced along all the three dimensions is generated from a pair of anti-helmoltz coil that creates a quadrupolar magnetic field distribution.

The group of William Phillips reported, together with Harold Metcalf, Migdall et al. (1985), the first magnetically trap gas of neutral atoms in such a quadrupole trap configuration. Therefore, it may be relevant (to someone building a new one) to read Bergeman et al. (1987) for the analytical results of the different magnetostatic configurations explored such as the quadrupole trap, the baseball trap (also coined “yin-yang” trap) or the Ioffe trap. One finds that the exact expression of the magnetic field from a circular current loop I with radius R located at the distance d from the origin (along the cylindrical basis axis z sharing the loop axis) can be written in terms of the complete elliptic integral of the first kind K of the second kind E , (in SI units)

$$\begin{aligned}
 B_z &= \frac{\mu_0 I}{2\pi} \frac{1}{\sqrt{(R+\rho)^2 + (z-d)^2}} \\
 &\times \left(K(k^2) + \frac{R^2 - \rho^2 - (z-d)^2}{(R-\rho)^2 + (z-d)^2} E(k^2) \right), \quad (12.1) \\
 B_\rho &= \frac{\mu_0 I}{2\pi\rho} \frac{z-d}{\sqrt{(R+\rho)^2 + (z-d)^2}} \\
 &\times \left(-K(k^2) + \frac{R^2 + \rho^2 - (z-d)^2}{(R-\rho)^2 + (z-d)^2} E(k^2) \right), \\
 B_\phi &= 0, \\
 \text{with } k^2 &= \frac{4R\rho}{(R+\rho)^2 + (z-d)^2}.
 \end{aligned}$$

The quadrupole magnetic field is produced from a pair of coils with opposite currents (anti-Helmholtz). The total field near the origin ($z = 0, \rho = 0$) expands to third order as

$$B_z = 3\mu_0 I \frac{dR^2}{(d^2 + R^2)^{5/2}} z + \mu_0 I \frac{15 R^2 (4d^2 - 3R^2)}{24 (d^2 + R^2)^{9/2}} (4z^3 - 6\rho^2 z) + \dots \quad (12.2)$$

$$B_\rho = -\frac{3}{2}\mu_0 I \frac{dR^2}{(d^2 + R^2)^{5/2}} \rho + \mu_0 I \frac{15 R^2 (4d^2 - 3R^2)}{16 (d^2 + R^2)^{9/2}} (\rho^3 - 4\rho z^2) + \dots \quad (12.3)$$

⁸ The first experimental demonstration of the magneto-optical trap is reported in Raab et al. (1987). The principle of Doppler cooling for neutral atom was presented by Hänsch and Schawlow (1975) in a quite short article (and the same year by David Wineland and Hans Dehmelt for trapped ions). And then in a Cesium vapor cell Monroe et al. (1990)

The axial and radial gradients differ by a factor of 2. Whereas the third order vanishes for $R = d\sqrt{4/3}$, the gradient is maximized for $R = 2d$,

$$\frac{\partial B_z}{\partial z} = 2 \frac{\partial B_\rho}{\partial \rho} = \mu_0 I \frac{48}{25\sqrt{5}R^2}. \quad (12.4)$$

As in the original article, the gradient is actually estimated from the first order⁹ term in the general situation

$$B_z = 3\mu_0 I \frac{dR^2}{(d^2 + R^2)^{5/2}} z, \quad (12.5)$$

$$B_\rho = -\frac{3}{2}\mu_0 I \frac{dR^2}{(d^2 + R^2)^{5/2}} \rho. \quad (12.6)$$

This is a very standard configuration that was also used in the old experiment. However, with the benefit of hindsight gained after the construction and from the axial geometry of the nanofiber, I would really like to consider the idea to create an elongated¹⁰ MOT along the fiber axis direction by changing the aspect ratio of the magnetic field gradients (i. e. imposing a two-dimensional quadrupole field) in order to obtain a higher optical depth from MOT atoms flying in the nanofiber evanescent field and to increase the effective loading length in view of nanofiber evanescent field traps.

In addition to the magnetic trap coils, three pairs of Helmholtz coils were built to compensate for the local Earth magnetic field, by superimposing a static offset field. For the Helmholtz configuration, coils that may be used as well to produce quantization bias fields to split atomic Zeeman levels, the axis curvature is an important parameter

$$B_z = \mu_0 I \frac{R^2}{(d^2 + R^2)^{3/2}} z + \mu_0 I \frac{3R^2(4d^2 - R^2)}{2(d^2 + R^2)^{7/2}} (z^2 - \rho^2/2) + \dots \quad (12.7)$$

$$B_\rho = -\mu_0 I \frac{3R^2(4d^2 - R^2)}{2(d^2 + R^2)^{7/2}} (\rho z) + \dots \quad (12.8)$$

(valid up to fourth order, there are no third orders). For $2d = R$, the second orders cancel

$$B_z = \mu_0 I \frac{8}{5\sqrt{5}R} + \dots \quad (12.9)$$

$$B_\rho = 0 + \dots \quad (12.10)$$

All the above results considered a theoretical single spire coil. For MOT coils and the Earth field nulling ones, we do not need to consider the thickness of the wires for the field calculation, from their relatively

⁹ The polynomial expansion is given up to order 9 in the above cited article.

¹⁰ while this might decrease the radius of the so-called circle of death for Majorana losses, I observed that blue-detuned MOT light propagating in the nanofiber could play the role of a plug (personal dreams of Bose-Einstein condensation around a fiber).

large distance to the center of the trap. This means that for N spire coils with I_0 as the single coil current, just replace $I = NI_0$ in the previous results. The series expansions deduce rapidly from the power series expression of the elliptic integrals.

For a nominal coil current of 5.5 A, 40 spires and a minimum coil radius of 4 cm, the expected optimal longitudinal gradient (12.4) is about 0.15 T/m or 15 G/cm. It is possible to already give an estimation of the expected size of the MOT clouds knowing the previous magnetic gradient, according to an estimation based on the equipartition theorem (Cohen-Tannoudji and Guéry-Odelin (2011), page 343). The RMS size of the MOT is expected to be a few tens of micrometers, which really underestimates the observed size of the achieved clouds. This is because for sufficiently large atom number, the MOT becomes a gas rich in physics with atom-atom interactions limited for instance by radiation trapping¹¹.

An important parameter to consider when building a coil is the electrical power dissipated and whether one needs to implement a cooling mechanism. The power dissipated by the coil would be $P = RI_0^2$ where the resistance of the coil R can be evaluated from the resistivity of copper in our case, $\rho \sim 1.7 \times 10^{-2} \Omega \text{ m}$ (value at room temperature), and the approximated length $l \simeq 2\pi Nr_m$ where r_m is the mean radius of the coil, $R = \rho l / A$. I used copper wires from the company R/S components¹³ with 1.25 mm thickness (1.3 measured). Each MOT coil has 41 windings. For a given magnetic field gradient, the current I_0 varies inversely proportional to N , however the mean resistance of the coil R is proportional to N/A in such a way that P is inversely proportional to NA the entire coil section. In designing a coil one would try to reduce therefore the effective coil cross section and not necessarily the number of spires.

$$P = \frac{2\pi r_m \rho I_0^2}{NA}.$$

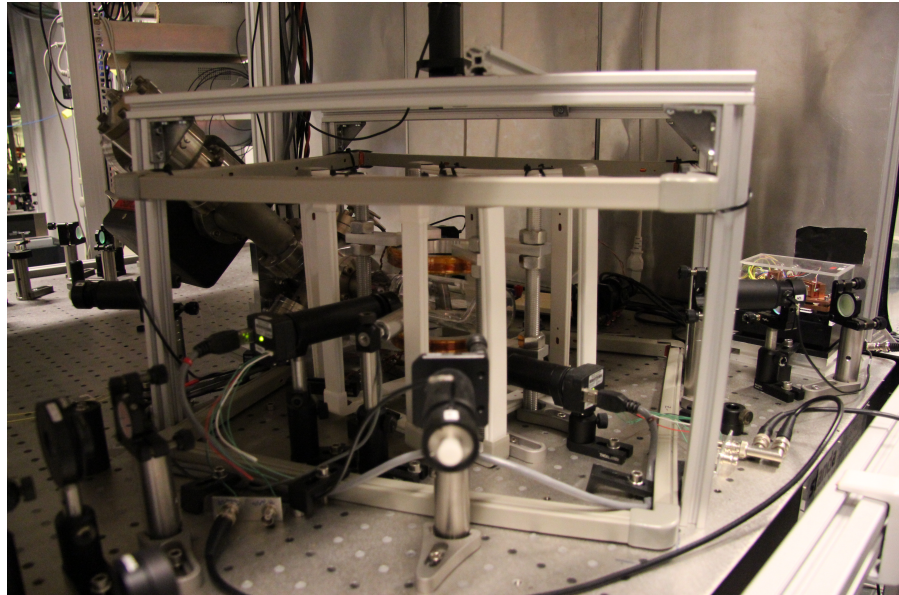
Unlike, the resistance R , the resistivity ρ of a material is an intrinsic property. Copper wires of any shape and length have about the same resistivity.

$$\rho = \frac{RA}{l}$$

where A is the wire cross-section and l its length.

¹¹ The emission and reabsorption of photons between atoms in the MOT is analog to a repulsive Coulombian force that limits the volume of a MOT. This happens when the MOT becomes optically dense. Light-assisted collision also starts to play a bigger role.

¹³ Each MOT coil has 41 windings. Heating test: The current is set to 5 A. The corresponding voltage for the first coil is after 2 hours 1.19 V. Putting the other one in serie leads to voltage 2.39 V which means the coils have roughly the same resistance. $R = 240 \text{ m}\Omega$.

(a) Close-up at the MOT coils (wrapped with heat resistance tape¹²)

(b) Wide view of the compact MOT setup

Figure 12.4: Photographs of the constructed MOT setup. The grey and white plastic frames enclose the three pairs of compensation coils.

When the mean radius of a coil r_m is large compared to the mean thickness of the wire layer $2a$, the inductance of a coil is [Ramo et al. \(1994\)](#)

$$L \simeq N^2 r_m \mu_0 \left(\ln \left(\frac{8r_m}{a} \right) - 2 \right).$$

The previous estimation supposes that the surrounding environment of the coils have a permeability μ close to μ_0 (vacuum) that should not affect the inductance. Moreover, it is important to keep rings away or open them otherwise their finite resistance will cause eddy currents that can sustain magnetic fields for relatively long times after the coils are switched. We note that the stability of the magnetic field here is much less critical than for Bose-Einstein condensation (BEC) experiments or experiments based on Feshbach resonances for instance. Thermal expansion of the coil might lead to fluctuations of a few mG that might be critical otherwise. A measure of the capacitance of the coil, that depends on the geometry of the wires and their arrangement or more directly measuring the resonance frequency of the coil might be appropriate if one needs to consider RF effects.

12.4 MAJORANA LOSS

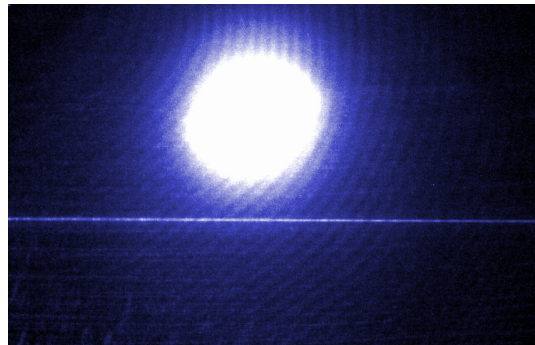
By adjusting the (restoring force) gradient of the B field one can control the size or density of the atomic cloud. One has to keep in mind that a magnetic trap works on weak field seeker atomic state (extreme Zeeman levels) and that magnetic traps are prone to Majorana losses. Indeed, atoms moving near the center of the trap can experience rapid (non-adiabatic) variations of the magnetic field. In particular, the B field direction is reversed across the center of the trap. If this change happens on a timescale shorter than the Larmor frequency $\omega_L \sim \mu_B B / \hbar$, atoms can remain polarized into a non-trapping Zeeman state and be expelled. Superimposing a static magnetic field just displaces the zero of the quadrupole field and is then not enough to prevent such non-adiabatic spin flip when an atom passes the center. Atoms which do not possess a trajectory in the trap with a sufficiently high orbital momentum and which approach the center of the trap below the radius of the so-called “circle of death” will be lost.

This effect is relevant for tight confinement and the pursue of high density to reach Bose-Einstein condensation for example. In view to load microscopic optical dipole traps created in the evanescent field of an optical nanofiber, one might wonder whether one should spatially overlap the center of the MOT with the taper of the fiber where the local density of MOT atoms might be affected by this so-called magnetic “hole”. In that respect, I would like to report a qualitative observation of a clear increase in the fluorescence light emitted by a cloud of magneto-optically trapped atoms centered on the nanofiber while milliwatt blue-detuned light (over a range of many linewidths) to the cooling transition $|4\rangle \rightarrow |5'\rangle$ is guided in the nanofiber. This indicates that we might have observed an analog of the blue-detuned optical plug effect, one of the ingredient that suppresses the Majorana “hole” as reported for the first Bose-Einstein condensation of sodium Davis et al. (1995). A nanofiber at the center of a MOT guiding in its evanescent field blue-detuned

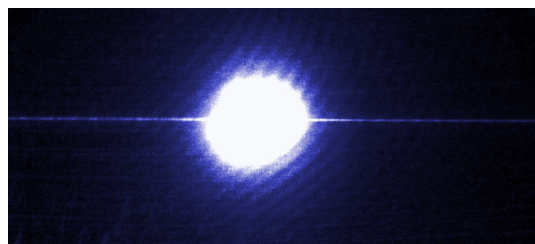
light of mW power would produce a similar repulse barrier force as the focused gaussian beam used by the group of Pr W. Ketterle. This may allow for high magnetic confinement around a nanofiber and might help to reach BEC around a nanofiber. In absence of blue-detuned light (repulse barrier), the room-temperature nanofiber and cold atoms collisions are inelastic (a momentum of 300 K is given to the atoms which are then ejected). When the repulsive barrier is on, the collisions are instead elastic and the particle loss rate is lower than without the barrier.

12.5 BASIC OBSERVATIONS

We now report more basic experimental observations during the very first attempts at interfacing cold atoms with a nanofiber once a CCD based imaging of the fluorescence emitted by the MOT was set up. We aligned a pair of digital cameras to image the light emitted at the nanotaper from orthogonal directions (one looking from the side of the fiber propagation axis, and the other one from below). The camera model is Point Grey Firefly FFMV-03M2M (Firewire, IEEE 1394). Each camera images the fiber with the help of a $f = 50$ mm lens.



(a) MOT above nanofiber



(b) MOT on nanofiber

Figure 12.5: CCD photographs of the fluorescence (fake color) of a MOT of Cesium atoms on and sideways to the nanofiber. The aspect ratio is 1:1 and the horizontal dimension corresponds to about 2 mm.

12.5.1 *Positioning cold atoms in the vicinity of a nanofiber*

The first step in engineering interactions between atoms and the nanofiber was to bring cold atoms in the evanescent mode volume. This was accomplished by modifying the surrounding magnetic field in all directions of space via the three orthogonal pairs of Helmholtz coils. These coils were primarily designed to cancel the Earth magnetic field by superimposing a static offset magnetic field at the location of the atoms. It has the effective property of moving the center of the quadrupole magnetic field¹⁴ that creates the trapping potential seen by the cold atoms. A magneto-optical trap is a spontaneous-light force trap. Thus the trapped atom will keep on emitting photons, here in a 4π solid angle. The size and the shape of the cloud can be imaged by detecting the spontaneous fluorescence with CCD cameras sensitive to near-infrared photons. A remarkable change in fluorescence is observed when overlapping the center of the atomic cloud onto the nanofiber waist (see figure 12.5).

12.5.2 *Reduction of atomic density*

Figures 12.6 and 12.7 evidence a quantitative reduction as large as 70% in the collected fluorescence when the cloud is brought onto the fiber waist. This effect is symmetric with respect to the fiber axis, i.e. the fluorescence will grow again when the cloud is moved further below the fiber. This eliminates possible systematic effects due to misalignment between the laser beams and the quadrupole magnetic field center. The observed reduction in fluorescence seems to happen in all directions although we have only imaged the MOT from two angles. The shutter speed of the camera was adjusted such that the maximum count per pixel was lower than half the saturation value of a given pixel. The calibration of the CCD pixel counts in terms of the detected input photon flux is not needed for the relative comparison of the cloud fluorescence.

The background light scattered by the nanofiber and other impurities at the surface of the chamber glass cell is quite static and it can be well subtracted out. The spontaneous emission is proportional to the number of atoms in the trap. This fluorescence is assumed to be also proportional to the atomic cloud density if the cloud is still relatively dilute. Therefore, this observation would witness an important decrease in the effective atomic density which directly affects the number of atoms in the evanescent probe volume of the fiber. It turned out that this shrink in the fluorescence was observed as well in [Nayak et al. \(2007\)](#). A compatible decrease of 2/3 in the atomic density was reported.

¹⁴ The center of the quadrupole field can be identified by looking at oscillations in the MOT position when turning on and off the quadrupole field for instance.

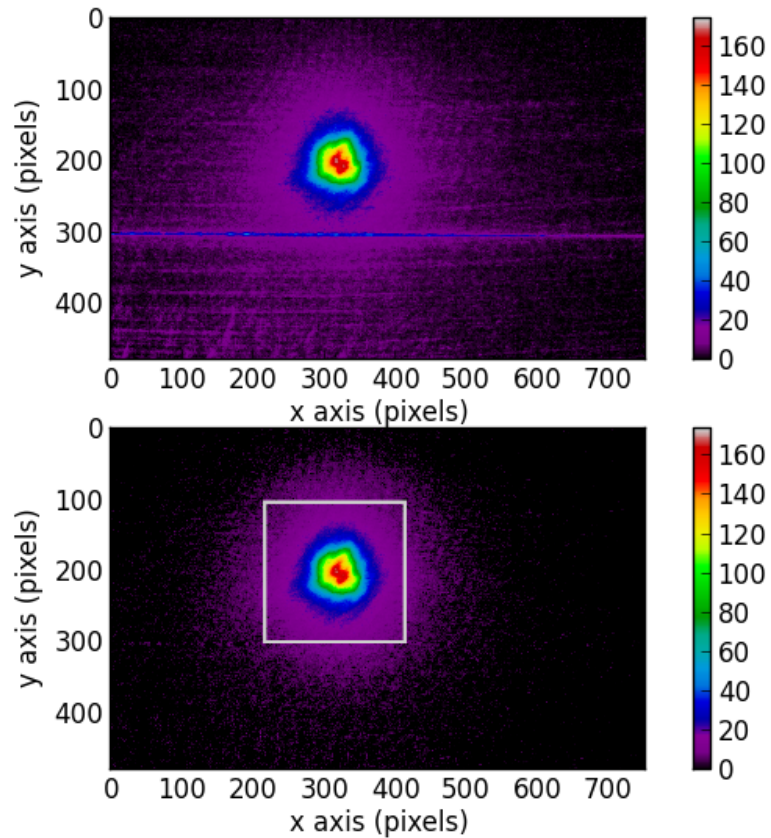


Figure 12.6: Fluorescence imaging (pixel counts) of a cloud of cold Cesium atoms positioned above the nanotaper of the fiber. The y axis corresponds to the gravity axis. (bottom) Background subtracted counts.

A different equilibrium between higher atom loss in the vicinity of the fiber surface and the loading rate of cold atoms in the trap volume may be inferred. One can bear in mind that the fiber is a relatively hot object compare to MOT atoms (Doppler cooling temperature $\sim 125 \mu\text{K}$). The fiber is indeed at room temperature, it behaves like a hot needle, whose thermal conductivity ($\sim 1 \text{ W m}^{-1} \text{ s}^{-1}$) is weak compared to metals. This makes it challenging if one would like to cool the fiber rapidly.

12.5.3 Qualitative observations on MOT fluorescence

It is somewhat interesting to observe that the previous decrease of fluorescence when the MOT is brought on the fiber can be recovered when MOT light is sent through the fiber. However, not only locally in the evanescent field of the fiber. The fluorescence revives in the entire field of view of the cameras wherever one positions the MOT.

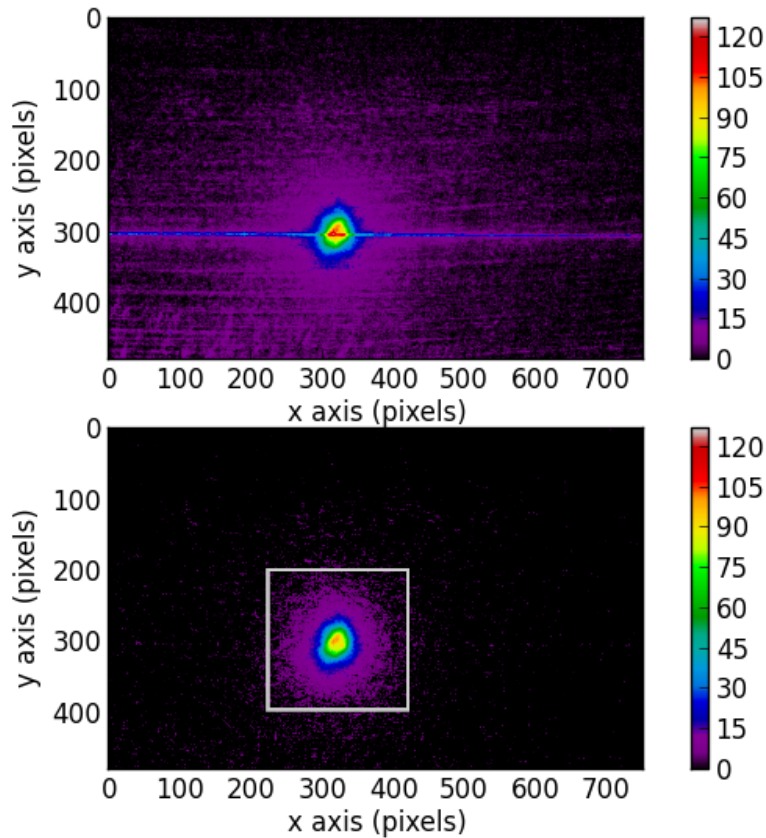


Figure 12.7: Fluorescence imaging (pixel counts) of a cloud of cold Cesium atoms positioned on the nanotaper of the fiber. The y axis corresponds to the gravity axis. (bottom) Background subtracted counts.

MOT cooling and repumping light propagating in the fiber affects the fluorescence. This is not surprising. However, the fluorescence is only noticeably recovered when the frequency of the cooling light is blue-detuned compared to the $|4\rangle \rightarrow |5'\rangle$ D2 transition, and as far as 1 GHz (larger detunings in that order of magnitude has not been attempted). The fluorescence is not recovered when light is red detuned by more than 2 linewidths from resonance. However, the fluorescence is not affected by light which is very far detuned to the Cesium D2 line, propagating in the fiber evanescent field. No effects were noticed with 780 nm and 1064 nm for instance, for light powers up to several milliwatts.

In addition, in the presence of 852 nm guided light, we observed a net mechanical displacement of the atom cloud for narrow continua of frequencies centered on resonance with the expected atomic hyperfine transition frequencies of Cesium. The cloud of atoms is pushed in a direction mainly parallel to the fiber axis. This is probably due to the

radiation pressure unbalancing induced by the extra light propagating in the fiber. Moreover, the displacement of the cloud is in the same direction as the fiber light propagation direction, evidencing static momentum conservation. This simple effect could be interesting in view to drag cold atoms, on very short time scales, onto longer spatial distances along the fiber than the cloud diameter. To finish with these basic observations, which were huge steps for me at the earliest stage of the construction of the experiment, especially countless hours in the hope to observe any starting signal of interaction between light propagating the fiber with surrounding atoms, I would like to mention that the observed variations in the fluorescence of a MOT due to resonant light propagating in the nanofiber offered me a cheap and visual¹⁵ way to perform hyperfine spectroscopy of the atomic levels and more importantly it will give to someone a fine tuning knob of the equilibrium number of atoms in the magnetic trap.

SUMMARY

In this short chapter, we reported the successful construction and demonstration of a three-dimensional magneto-optical trap for Cesium atoms operated in the presence of a room-temperature nanofiber. We observed that the equilibrium atomic density or number of trapped atoms in the MOT is readily affected by this intruder. However, we discovered that the atom loss mechanism introduced by the presence of the nanofiber can be tampered by sending near resonant blue-detuned light in the nanofiber. This may rise some interesting questions as whether it is possible to cool this nano fiber object using surrounding cold atoms.

¹⁵ I also observed some interesting spatial pattern in the fluorescence of the atom cloud when varying the polarization of the light guided in the nanofiber. Perhaps, it could be used to map the polarization field of the light scattered by a nanofiber.

13

DISCRETE SPECTROSCOPY OF A FEW ATOMS

Cesium melts in the sun of California.

— Eugene Simon Polzik

In this chapter, we experimentally demonstrate, by counting single photons, the observation of both external channeling and scattering of weak light guided in the fundamental mode of a nanofiber by the action of a few number of cold atoms in the vicinity of the fiber tapered section surface. These results represent the first interfacing and coupling of cold atoms with the nanofiber. This achievement was made possible through the discovery and removal of adsorbed atomic layers, which are coating the fiber glass surface.

13.1 ULTRA-VIOLET PHOTODISSOCIATION ASSISTED MOT

Driven by curiosity, we¹ explored the effects light from a Ultraviolet (UV)-laser (~ 405 nm) pen could potentially have on a cloud of atoms trap in the MOT sitting on the nanofiber. We shone this well-collimated light through the glass cell of the vacuum chamber in random directions. Unexpectedly, we observed a rapid increase in the global fluorescence emitted by the atomic cloud. We would like to relate this observation to a phenomenon discovered by accident by Gozzini et al. (1993) in a cell containing a Sodium vapor. This effect is known as Light-Induced Atom Desorption (LIAD). It can be summarized as follows; light is shone on the inner wall of the cell containing an atomic vapor; alkali-atom coatings are desorbed from the wall; the density of the background atomic vapor in the cell increases. This leads to an increased loading rate of atoms in the MOT and to a new equilibrium with the atom loss rate. A higher number of atoms are trapped thereby augmenting² the stationary fluorescence emission.

We set up a proper UV-light source, so as to take advantage of LIAD to save the lifetime of the Cesium getters. A single packaged diode (TO3A-H390-180 Roithner lasertechnik) was mounted near the glass

¹ Me and EB

² I would like to mention failed attempts to observe any effect on room-temperature Cesium microcells of a neighboring experimental research setup (Eugene Polzik's teleportation experiment) where the cells are coated with paraffin.

cell. The diode outputs light in the range 382 nm - 390 nm. We ran it at a current of 140 mA such that we do not need to cool it. We clearly saw the same effect. The use of this new source of light allows one to run a MOT experiment without the use of getters for several days until the walls of the chamber are *cleaned*.

13.2 DE-ADSORPTION OF ATOMS INDUCED BY WEAK LIGHT

In this section, we report on a more subtle effect concerned with most likely Cesium atoms sticking on the surface of the optical nanofiber located in the chamber.

13.2.1 *Decay of guided mode transmission*

The first attempts at a nanofiber-based light-atom ensemble interface were focused on the detection of the emission of light as well as the absorption of light from cold atoms in a MOT, through interaction with the evanescent guided mode of the nanofiber at the tapered section. Enough confidence about the position of the atomic cloud on the fiber was provided with imaging from two CCD cameras. However, no precise measurement of the quality of the overlap was known as well as whether atoms could reach close enough to the fiber surface. The first signal observed from Cesium atoms flying by the fiber surface was a channeling of spontaneously emitted photons by excited MOT atoms into the fiber and guided in its fundamental mode towards a SPCM. This initial detected photon rate was only four times as big compared to leakage photons coming from all the laser light beams forming the trap. This weak atomic signal was not enough to claim any coupling in the evanescent volume as these photons could have been emitted anywhere in the atom cloud, indirectly scattered or channeled at the adiabatic taper transitions of the fiber.

With optimism, it was hoped that conversely, photons from resonant probe light sent into the fiber guided mode would be absorbed by those *same* average flying atoms located in the evanescent probe field. Starting from an absorption detection signal one could then seek to improve it with optimizing the position of the MOT controlled by external bias magnetic fields or adjust the atomic cloud density and other parameters we can control. However a lot of peculiar and erratic effects were experienced until we could observe evidences for cold atom absorption. Those effects cannot be neglected in general for photon-counting based spectroscopy with atoms around a nanofiber. Yet, they opened the road towards the first successful interaction between guided mode photons and cold Cesium atoms as shown in the next sections.

13.2.2 Photon throughput in presence of Cesium atom vapor

In figure 13.1, we report transmission data for weak (pW) probe light sent through the fiber, while a magneto-optically trapped ensemble of cold atoms evolves around the tapered section.

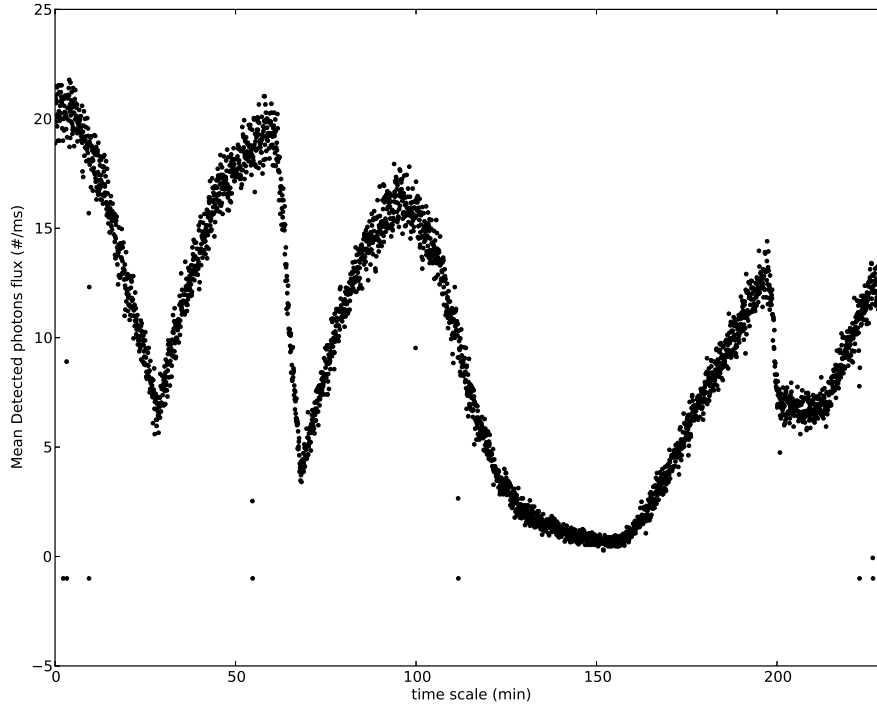


Figure 13.1: Evolution of the transmission of weak probe light propagating in the nanofiber guided mode over the course of 4 hours. The few outliers with negative count values correspond to saturation events of the single-photon counting detector.

Each point in the figure represents an average over 32 photon counting gated time bins, each of 1 ms duration, separated by a 10 ms time interval. The MOT preparation and loading time was set to 2 s, after which these 32 measurements, corresponding to gate pulses controlling the SPCM, were acquired. From the knowledge of the absolute input probe power of 20 μW , the fiber coupling efficiency of 55% together with the calibration of neutral density filters used to avoid saturation of the detector as well as preventing the expected saturation of the resonant Cesium transition (in the high intensity area of the evanescent field), the quantum efficiency of the SPCM for 852 nm and optical path losses, one expects a detected CW photon flux of about $\Phi = 22 \text{ kHz}$.

Many observations are contained in figure 13.1 that compiles four hours of data acquisition. First of all, one clearly notice a strong decrease and increase in photon transmission, over the course of the ac-

quisition with a typical time scale of several minutes. As reported in figure 13.2, these events are fully correlated to the activation and deactivation of the Cesium dispensers employed to populate the vacuum chamber with a sufficient background atomic vapor pressure to prepare millimeter size MOT clouds. One can note that as the detected light intensity decreases the fluctuation on the photon number signal decreases as expected from the photon shot noise of coherent states of light. We clearly observe that more than 90% of the probe photons can be lost and scattered off the detection mode.

Different dynamical behaviours in the transmission can be noticed such as the plato at $t \sim 200$ min when the previously mentioned ultraviolet light source was turn on and irradiates the vacuum chamber. Many times we would conclude that the use of the UV-light source led to a faster increase of the background Cesium vapor pressure in the glass cell and maintained it quite constant. For every two points in the graph of figure 13.2, that is every MOT reloading phase, the magnetic field gradient, vital for the creation an atomic cloud on the fiber is turn on and off. We clearly see no difference or dependence on the observed probe absorption. What can be the cause of more than 90% drop in transmission of weak probe light if not atoms from the trap ?

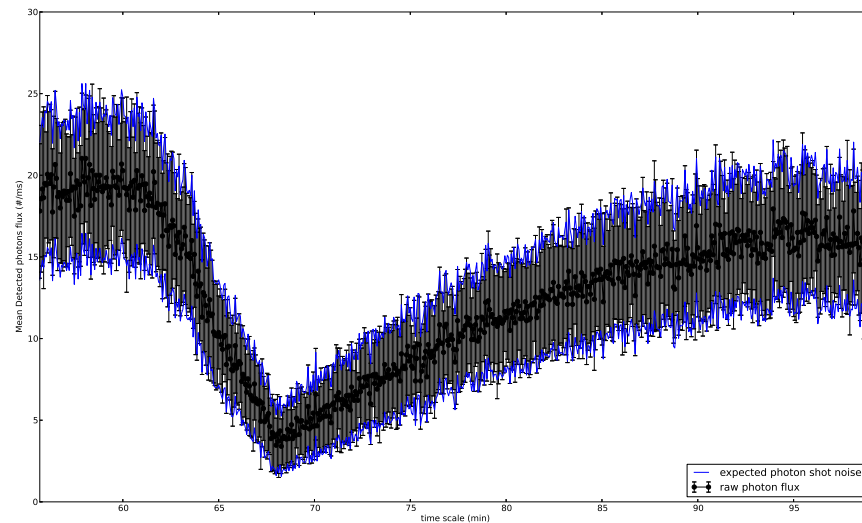


Figure 13.2: Decrease in the photon number transmitted through the guided mode of the nanofiber. Each black error bar represents the standard deviation of the 32 raw photon counts used to compute the mean. The blue traces correspond to the expected photon shot noise for coherent states of light.

Our main relevant observations are listed as follows. The absorption of the probe photons clearly depends on:

- Cesium dispenser electric current intensity

- Duration of the active time of the dispensers
- Ultra-violet irradiation of the chamber

Whereas it is:

- Insensitive to the magnetic field gradient vital to create a **MOT**
- Insensitive to the probe light frequency over a ~ 1 GHz interval centered around the $|4\rangle \leftrightarrow |5'\rangle$ Cesium optical transition
- Independent of the position of the **MOT** cloud, when displaced by twice its millimeter diameter away from the nanofiber, in all direction.
- Not due to an over-exposure of the **SPCM** detector by having **CW** probing.
- Not due to a systematic drifts in the nanofiber input light coupling efficiency.
- Not due to polarization rotation due to heating of the fiber, the measurement being insensitive to the probe light polarization.
- Insensitive to optical repumping light on the $|3\rangle \leftrightarrow |4'\rangle$ Cesium transition.

Therefore, it was more likely that the observations betrayed the formation and deposition of layers of Cesium compound on the surface of the nanofiber. Acting as broadband scattering centers, they absorb or redistribute photons from the guided mode into free space radiation modes. The formation of this layer as well as its time scale, would be favorized by a higher and higher Cesium vapor background pressure in the experimental chamber. In general, typical time scales for the evolution of the background pressure fall in the several minutes domain. Hopefully, the recovery of the transmission can be achieved and controlled quite easily as we have found. Without caring for this effect, experiments based on collecting the fluorescence or absorption of a probe within a **MOT** will give rise to lower signal-to-noise ratios, depending indirectly on the background atomic pressure (related to the size of the atomic cloud one wants to achieve).

13.2.3 *Recovery of transmission through optical heating*

To make a long series of attempts short, the transmission was seen to recover when checking the nanofiber input coupling efficiency at higher probe power (a few μW) by removing neutral density (**ND**) filters. The recovery of the transmission is possible by sending quite different laser light wavelength in the fiber mode (tested with 780, 852 or **1060 nm**). Whereas the removal process could be a consequence a thermo-optical

effect discovered during early tests of the nanofiber (nanofiber length expansion and contraction induced by light pulses), we privileged heating rather than a direct mechanical action due to light to explain it.

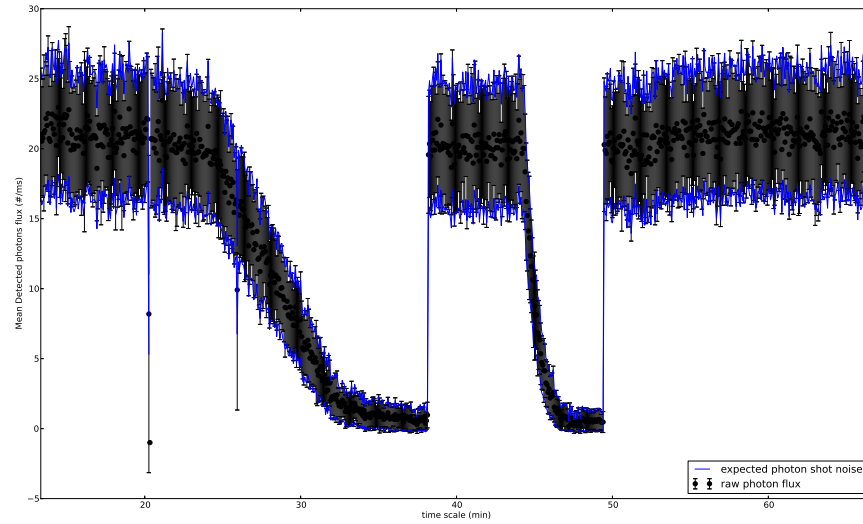


Figure 13.3: Decay of probe transmission, 20 minutes after the Cesium dispensers are turned on. Then the mechanical shutter of a $60\ \mu\text{W}$ $1060\ \text{nm}$ light beam coupled to the nanofiber mode is open between the SPCM counting measurements. 10 minutes later, the shutter is left closed.

Even though the light power sent involved is quite weak, the light intensity grows inversely as the square of the probe beam area. The intensity at the tapered section of the nanofiber whose radius equal $250\ \text{nm}$ can produce enough heating of the silica glass in such a way that it leads to a longitudinal fiber expansion of up to several hundred micrometers.

We then added in the setup an additional beam to send in the fiber to clean the nano-taper surface with evanescent light before performing photon counting measurement. Even if the cleaning light power is relatively weak, it would totally blind the SPCM detector and without descent filtering it cannot be done in parallel even if the wavelength used is far apart from the probe wavelength. At the beginning, an AOM was set to turn on and off on short time scales ($< 1\ \mu\text{s}$) this so-called cleaning-heating light pulse between the 32 time bin measurement done with the photon detector. However, a measured rejection of 10^7 was not even enough to prevent saturation of the SPCM from AOM diffraction order leakage light. A mechanical shutter was built instead, based on a 5200 rpm laptop hard drive to physically chop the cleaning beam. This beam was activated only once a time before the 32 photon counting measurements due to the low mechanical speed but was sufficient to avoid any noticeable decrease of the probe transmission. Figure 13.3

clearly shows how effective is this cleaning pulse but also how fast the transmission decays back in its absence. The decay time depends on the background pressure, here needed to create a normal MOT cloud size (~ 1 millimeter diameter). Figure 13.4 exhibits the cleaning effect with 852 nm light by chopping manually the beam but also reveals complete absorption of any probe photon that would propagate in the fiber over a very long experimental time if no cleaning was performed.

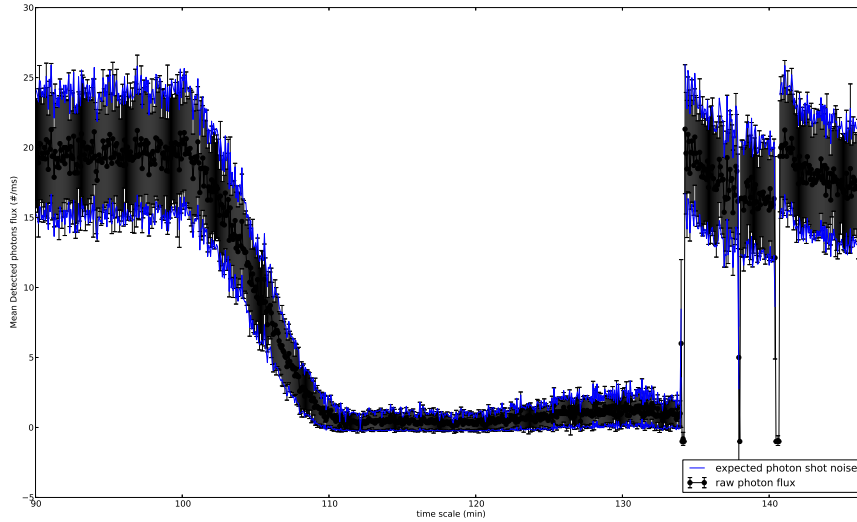


Figure 13.4: Cleaning with probe light

13.3 HIGH-SENSITIVE FLUORESCENCE SPECTROSCOPY

13.3.1 *Strong evidence for guided spontaneous emitted photons*

It has been experimentally shown in the previous section that in conditions required to create a common size MOT atomic cloud, the background atom pressure in the vacuum chamber is sufficient to spawn the formation of an atomic layer on the nanofiber section that dramatically affects the transmission of probe photons guided by the nanofiber. The coupling of photons emitted by excited cold Cesium atoms into the nanofiber mode when in the vicinity of the fiber surface is therefore also strongly perturbed and can be suppressed by such coating. In figure 13.5, we report a successful observation of such spontaneously emitted photons with a high signal-to-noise ratio by implementing the above cleaning procedure with 60 μ W of 1060 nm fiber coupled light pulses between the photon counting time bins. We show a careful hunting and dissection of all the possible photon sources that are detected by the SPCM, which contribute to a common random photon noise background. A logarithm scale helps to present these contributions as in fig-

ure 13.6. Deprived independently from two of the three vital ingredients to realized a magneto-optical trap of cold atoms (the third one being atoms), the different experimental runs indicate that the observed high fluorescence signal arises from MOT trapped atoms and apparently not observable for atoms in an optical molasse (see cycle number around 200). Contrary to the absorption effect reported in the previous section, this fluorescence signal depends strongly on the frequency of the trap lasers (about two atomic linewidths).

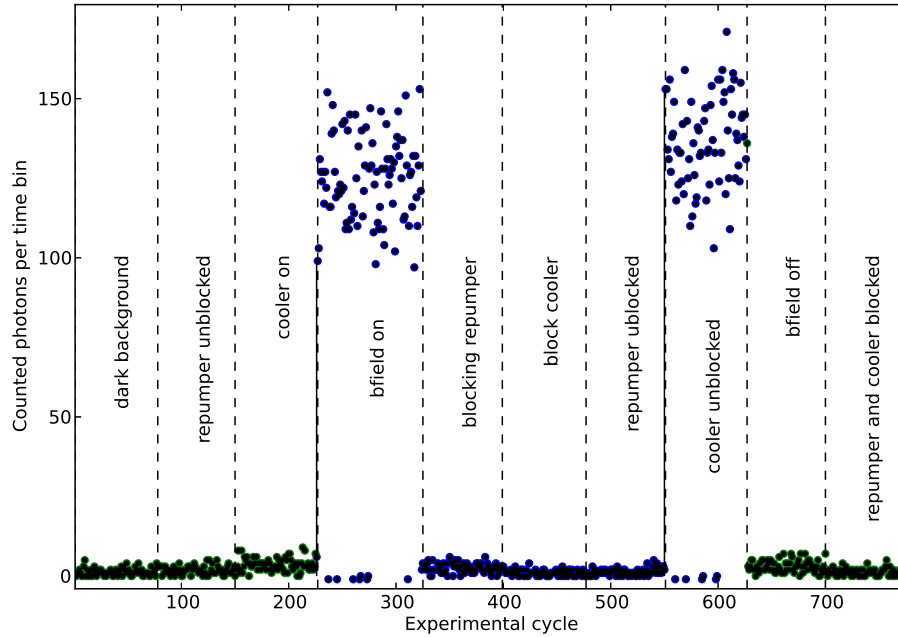


Figure 13.5: Experimental evidences of the detection of guided photons spontaneously emitted from cold Cesium atoms in a magneto-optical-trap surrounding a nanofiber. The achieved fluorescence signal is more than 100 times the background counts of photon leakage into the fiber mode.

We note that photon statistics could be studied if the detected photons could be time stamped - could one observe photon bunching in the emission of the few atoms responsible for the signal in figure 13.5? (within the time of flight in the evanescent mode volume). Interestingly, the noise on the shot-to-shot fluorescence counts is larger than a poissonian photon shot noise, as can be seen clearly on figure 13.5. More so if we stress again that each plotted data point is a mean number of 32 photon counting time bins. This can be attributed to fluctuation in the number of atoms leaving and entering the evanescent mode volume from one MOT loading to the next. On the assumption of both random entrance and exit of atoms, one would expect the noise to scale as the square root of the mean number of atoms in the evanescent mode. We

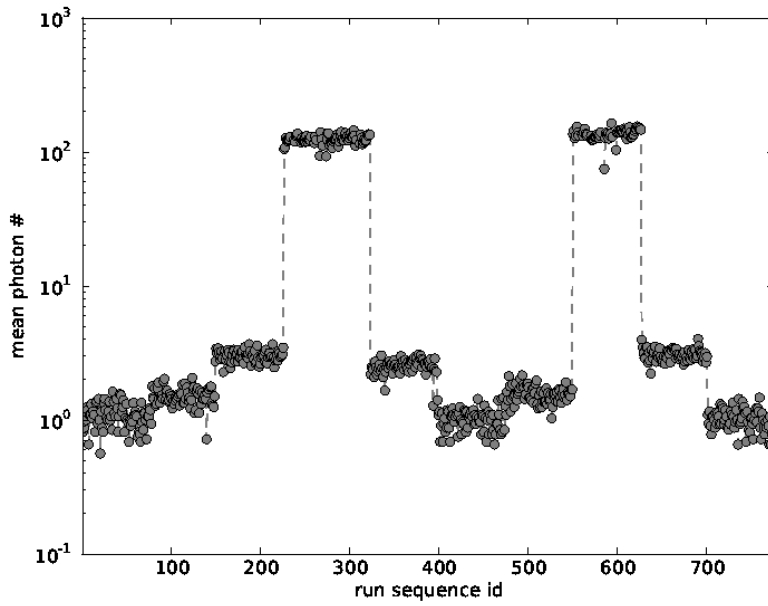


Figure 13.6: Logarithm scale of the data presented in 13.5.

try to estimate the number of atoms responsible for the fluorescence signal in the next section.

Our fluorescence measurements open the road for studying dynamics of the fluorescence for various trap parameters. It could for instance be used in a time-of-flight experiment to measure atomic cloud temperatures and to detect an atom clouds falling due to gravity on the nanofiber.

13.3.2 Estimation of the number of atoms

In this section, we follow and invert the estimation of the detected fluorescence photon count f_c as done in [Nayak et al. \(2007\)](#) $f_c = N_{\text{at}} R \beta T \eta$, in order to infer the effective atom number N_{at} responsible for the detected fluorescence.

The fluorescence photon count is mainly proportional to the number of Cesium atoms in the effective evanescent probe volume and proportional to the atomic scattering rate R . However, without precise knowledge of the spatial distribution of these atoms in the vicinity of the fiber surface, one can only give effective parameters. The transient interaction time between these atoms and the evanescent field of the guided light mode is expected longer than the optical spontaneous emission lifetime of the [D2](#) line.

The atomic scattering rate R depends on the total [MOT](#) laser intensity, the [MOT](#) beam detunings and the saturation intensity of the

emitting atomic transition. The SPCM detector is quite broadband and its quantum efficiency around 852 nm is about $\eta = 0.45$.

The fraction of fluorescence collected in the nanofiber mode depends on the coupling efficiency of the spontaneously emitted photons to the guided mode $\beta \simeq 6\%$, which depends on the atom distance to the fiber surface, was computed in Le Kien et al. (2005a). T represents the transmission on the photon path from the nanofiber to the detector.

As it turns out that our experimental conditions are very similar to that of Nayak et al. (2007), we use directly the same value for the atomic scattering rate and the QED enhancement factor of spontaneous emission. We estimate an effective atom number $N_{\text{at}} \simeq 9$ using $f_c = 75 \text{ kHz}^3$, $T = 0.97 \times 0.046$ due to optical loss and a protection neutral density filter in front the detector, and $R = 6.8 \text{ MHz}$.

From the previous deduced value of an average of 9 atoms, one could expect that the signal explores deviation of 30% around its mean value for a Poissonian distribution of atoms entering and leaving the evanescent volume. This would be in reasonable agreement with the fluctuations observed in figure 13.5. Finally, the estimation of the number of atoms allows to give an estimate of the resonant optical depth per atom d/N_{at} to $\sim 10\%$ as the probe transmission measurement estimates d a little higher than 1 for the same experimental conditions.

13.3.3 Fluorescence decay

We ask experimentally what happens now if the cleaning procedure is turned off for experimental conditions associated to the previous fluorescence records. Figure 13.7 reports the evolution of the number of spontaneously emitted photons detected over time when the 1060 nm cleaning light is physically blocked.

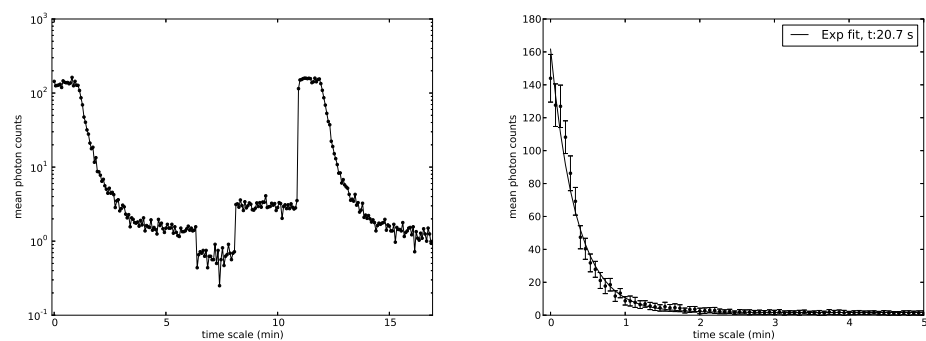


Figure 13.7: Decay dynamics of the fluorescence

The formation of atomic layers deposited on the fiber leads to an exponential decay of the fluorescence signal. This could either be the

³ In figure 13.5, the time bin duration was 2 ms

consequence of an increase in the mean radial distance for flying MOT atoms to approach the fiber surface, the evanescent field coupling decaying rather exponentially or this atomic crust would absorb or scatter the fluorescence photons preferentially into free space radiation modes. I remarked that the decay time of the fluorescence was somewhat different from the decay time of the transmission of fiber guided probe light. However, they always seemed to stay in a constant ratio, the fluorescence decreasing about twice as fast as the transmission.

13.4 HIGH-SENSITIVE ABSORPTION SPECTROSCOPY

Having reported high fluorescence signals from external photons, emitted by cold atoms present most likely in the vicinity of the fiber surface, and channeled into the fiber guided mode, we now report high absorption signals of weak light sent into the fiber by cold atoms present in the evanescent field at the tapered section.

13.4.1 *First interaction with guided photons*

An important experimental step towards the manipulation of atoms with light guided in the nanofiber is to observe atoms interacting with such light. Here we perform transmission measurement and reports clear absorption signals from resonant probing on the $|4\rangle \rightarrow |5'\rangle$ transition of cold Cesium atoms evolving in a MOT speared by a nanofiber. We have been able to observe up to 70% absorption from one millimeter diameter atom clouds.

The detection is similar to that of the fluorescence measurement. We report in figure 13.8 the average value of identical 32 photon counting time bins as before (with cleaning pulses etc). The green points corresponds to experimental runs in the absence of the quadrupole magnetic field required to trap atoms, while the blue points when the latter was present and a MOT was loaded for about 2s. Points in red indicates saturation events of the detector during any of the 32 time bins while the points in magenta spot records with bunching (at least two consecutive) of 0 photons detected. Clearly, the mean detected photons from the guided mode of the fiber drops from its reference value (green) when a MOT is created on the fiber (blue). In addition, the figure witnesses that at the beginning of the sequence, we alternatively switched the quadrupole magnetic field every experimental realization. Then it shows different phases where the magnetic field was left on for a while then turned off for a while and also when we blocked the probe light.

13.4.2 *Interleaved measurement of fluorescence and absorption*

Now being able to detect both fluorescence and absorption of photons by atoms, we had many experimental questions, for instance: Is the

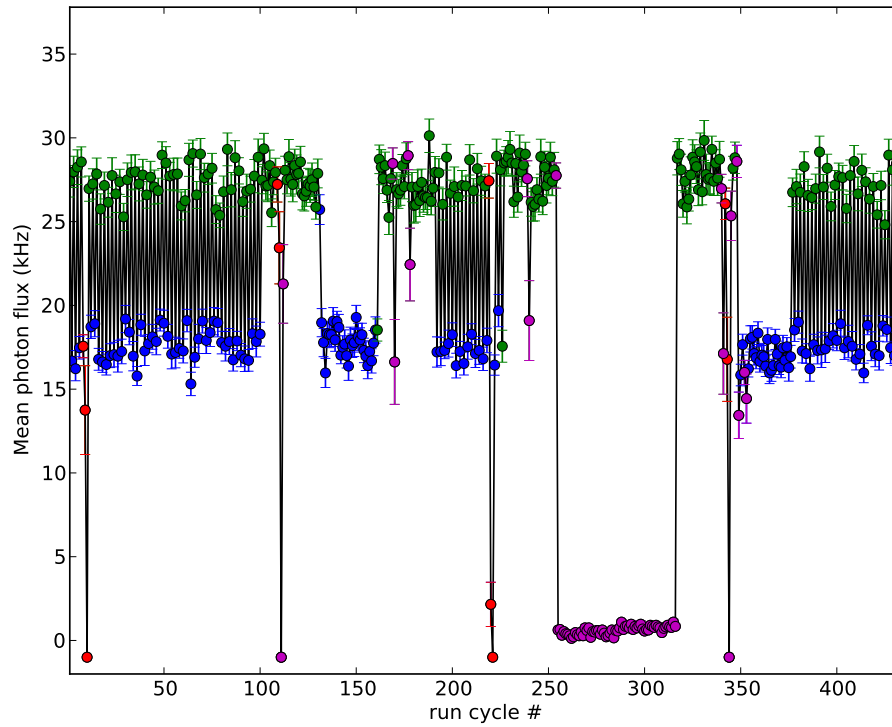


Figure 13.8: Consistent observation of guided probe light absorption in presence of cold Cesium atoms trapped in a MOT overlapping with the nanofiber. (See main text for legend)

absorption signal maximized when the fluorescence signal is maximized? We were also curious to compare in general the dynamics of the fluorescence as compare to probe light transmitted by the nanofiber.

This quite sideways experimental details led us in fact to obtain the biggest signals from MOT atoms. In this short section I would like to report the implementation of interleaved fluorescence and absorption measurement on quite short time scales. It also evidences a somewhat good duty cycle for applications of MOT atoms interfaced to a nanofiber. The sequence is as follows.

It was not possible to perform both fluorescence⁴ and absorption spectroscopy from the common fiber observation mode with the broadband and incoherent detection of photons with the SPCM. Therefore the idea consists in alternating probe light pulse sent through the fiber and the cooling light of the MOT. The trap is loaded with atoms and stays in equilibrium for 2 s (we could have reduced this value) while an open shutter let the cleaning light beam going through the nanofiber. Then, the latter shutter is closed and blocks the cleaning beam. Then the cooler light of the MOT is gated off for 1 ms while simultaneously

⁴ which requires cooler light that would saturate the absorption.

probe light, controlled with an AOM, is allowed to propagate in the fiber for the same gate duration to perform absorption spectroscopy. For the next 10 ms, cooling is re-activated and cold atoms are recaptured into the trap. For the next 1 ms, the cooler is kept on while the probe is off, allowing to observe atom fluorescence without probe photons in the fiber mode. This alternated cooling-probing process is repeated 16 times until all the 32 registers of the SPCM counting electronics are filled. Indeed, the photon detector is gated on and counts photons during the 1 ms time bins. We note that our measurement demonstrated a duty cycle of 10 ms for operations on MOT atoms to perform on demand fluorescence or absorption spectroscopy.

Each point in figures 13.9 and 13.10 is an average over 16 counting photon bins following the previous sequence.

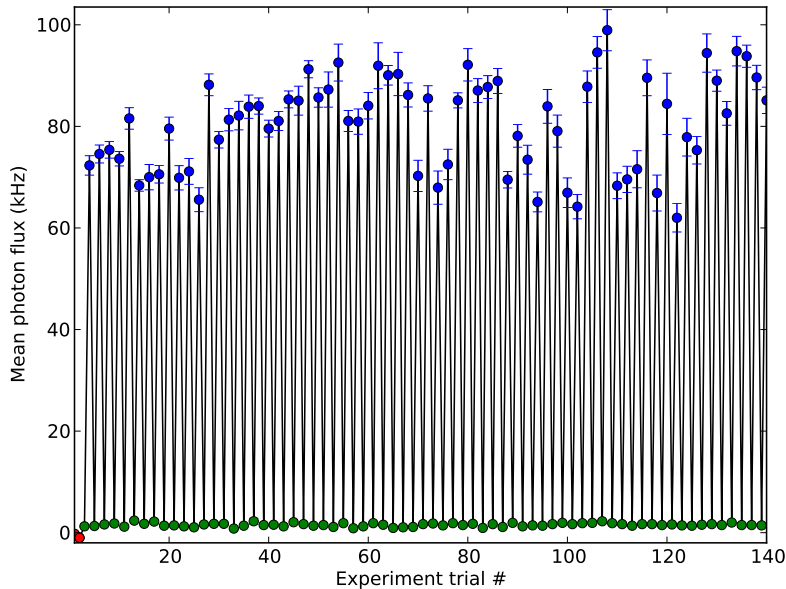


Figure 13.9: Interleaved fluorescence and absorption detection. Here only the average over the photon counting bins corresponding to fluorescence detection is shown. The probe is resonant with the $|4\rangle \rightarrow |5'\rangle$ transition. (Red) Saturation event of the SPCM (Blue) Magnetic trap ON (Green) Magnetic trap OFF.

These figures report the raw detected photon flux. A rapid estimates of the collected fluorescence emission rate into the fiber can be obtained by multiplying the raw fluxes by a factor 50.

$$F = \frac{D}{qn(1-l)} \simeq 50 \cdot D$$

where,

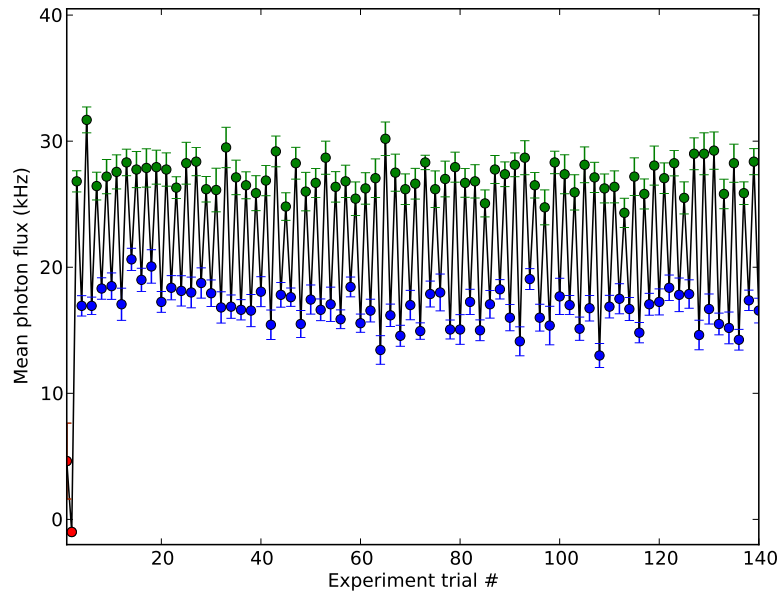


Figure 13.10: Interleaved fluorescence and absorption detection. Here only the average over the photon counting bins corresponding to absorption detection is shown. The probe is resonant with the F4F5 transition. (Red) Saturation event of the SPCM (Blue) Magnetic trap ON (Green) Magnetic trap OFF.

$$\begin{aligned}
 q &= 0.45 && \text{quantum efficiency of SPCM at } 852 \text{ nm}, \\
 D &&& \text{raw detected photon flux,} \\
 n &= 4.6\% && \text{neutral density filter in front of detector,} \\
 l &= 3\% && \text{optical path loss to detector .}
 \end{aligned}$$

Readily on figure 13.9, no photons in the fiber mode are detected in absence of magnetic field. We note that in the detection time window, the mean number of dark counts is less than 1. In contrast, a clear photon flux is detected when MOT atoms evolve in the vicinity of the nanofiber. In figure 13.10, contrary to figure 13.9, a high photon flux is detected in absence of a magnetic trap. Indeed, here probe photons are sent into the fiber mode for absorption spectroscopy. In presence of atoms in the trap, the signal reduces due to probe photon absorption or scattering.

To end this section, we present the latest absorption measurement we have performed with single photons once we optimized all trap parameters using the previous techniques in figure 13.11. In particular here, the magnetic field gradient was increased (5.5 A current) as well as the overall position of the MOT cloud on the nanofiber. The observed signals are very sensitive to the latter.

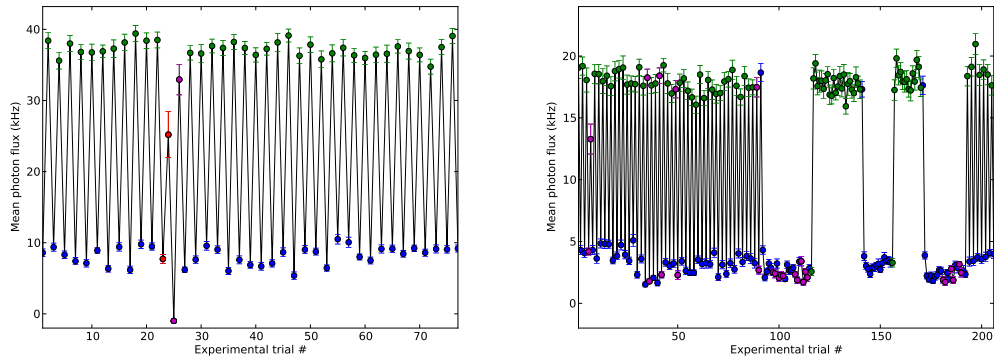


Figure 13.11: Optical depth greater than 1.5 is observed from MOT atoms via absorption measurement. The probe is resonant with the $|4\rangle \rightarrow |5'\rangle$ transition. (Red) Saturation event of the SPCM (Blue) Magnetic trap ON (Green) Magnetic trap OFF. (Purple) “Suspicious” counts (more than 2 consecutives 0 photons).

The absorption is clear and strong. Readily, a transmission smaller than 25% is observed corresponding to an effective resonant optical depth of 1.5.

13.4.3 Absorption spectroscopy

By developing further the experimental control which were nearly un-existent, I was able to modify the frequency of the probe laser every MOT loading realization and therefore I could start investigating the resonant property of the interacting atoms. As can be seen in figure 13.12 from the discontinuous steps in absorption, the optical frequency of the probe is was detuned by random steps around the $|4\rangle \rightarrow |5'\rangle$ transition. This ensures experimental consistency, reproducibility and remove potential biases when measuring the lineshape of the interacting atomic transition.

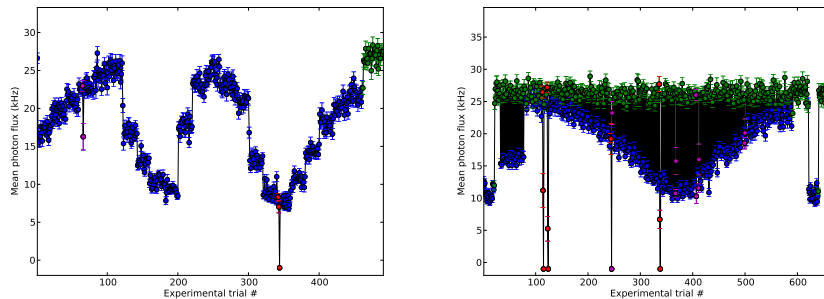


Figure 13.12: Raw absorption spectroscopy around the expected $|4\rangle \rightarrow |5'\rangle$ transition: discontinuous and continuous frequency sweeps of the guided probe light.

From this data, we can reconstruct the probe transmission versus probe detuning with respect to the expected resonant transition frequency. The result is shown in figure 13.13.

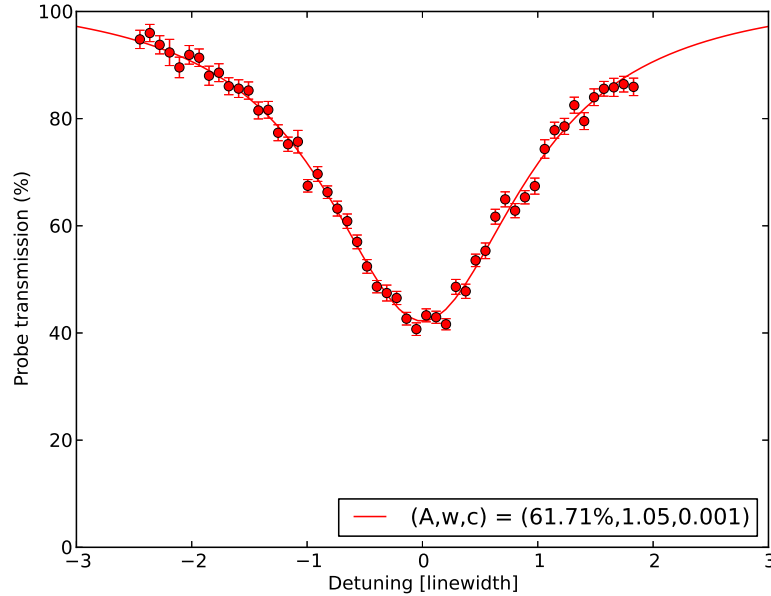


Figure 13.13: Transmission/absorption spectroscopy of the cyclic $|4\rangle \rightarrow |5'\rangle$ Cesium transition, at the photon shot noise limit. $\Gamma \simeq 1.05\Gamma_0$.

The transmission T is linked to the total atomic optical depth d as $d(\Delta) = -\ln T(\Delta)$, where Δ is the probe detuning. A Lorentzian model for the optical depth fits very well to the data and reveals that the observed atomic resonance as a linewidth almost identical to the expected value for Cesium and that the position or resonance frequency shows no shift compared to the expected Cesium frequency. The resonant optical depth here is $d \simeq 1$.

By pushing the limit of the probe laser lock, we can scan the excited state of the atoms over more than 500 MHz and one will observe, as reported in figure 13.14, different and similar narrow resonances positioned quasi exactly at the expected resonance frequency of the different excited hyperfine states of Cesium. The absolute value of the resonant optical depth depends on the effective number of atoms in the evanescent probe field, which depends on the surrounding atomic cloud density. However, the relative strength of the resonant optical depths depends on the relative absorption strength of these atomic hyperfine transitions. The extracted values of d from the resonant transmissions show a very good agreement with the strengths given in Steck (2010).

We therefore experimentally justify the choice of the probing transition $|4\rangle \rightarrow |5'\rangle$ to obtain the highest response and interaction with this relatively small effective number of atoms $N_{\text{at}} \sim 10$ in the evanescent field.

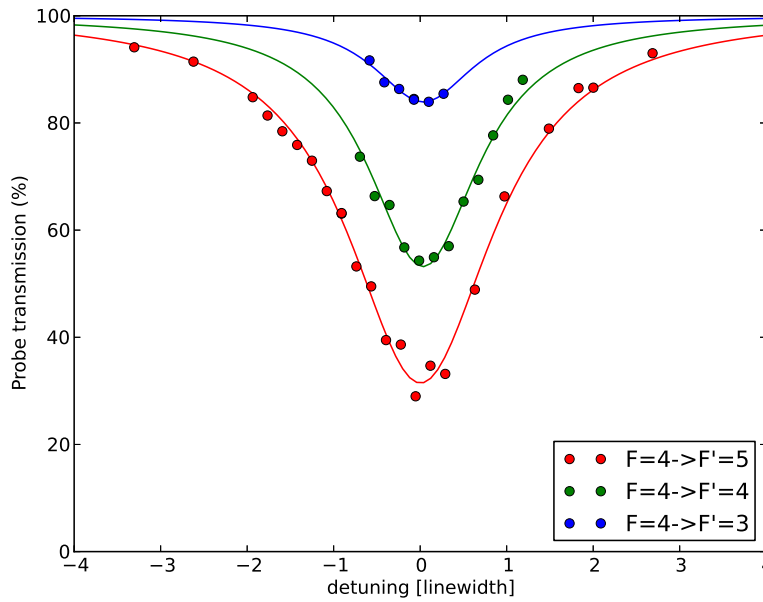


Figure 13.14: Spectroscopy of the observed and allowed hyperfine excited state transitions from the ground state $|4\rangle$.

13.4.4 *MOT* coupling lifetime

Using the photon counting technique and the initial experimental basic and somewhat slow control, I tried to measure precisely the lifetime of the atomic signal in the evanescent field.

For measurement that involves quite short time scale, it is relevant to now look into the different photon time bins instead of averaging them as before.

In figure 13.15, I report the lifetime of the resonant absorption signal when the cooling *MOT* light is suddenly switched off. The repumping light is still active to counteract any depumping that could be caused by the probe light. In the shown data, the content of the 32 *SPCM* registers are displayed. Each corresponds to an acquisition time of 500 μs , each bin being separated by a 1 *ms* interval. The absorption is seen to decay exponentially with time constant of about 4 *ms*. One can note that for this measurement with cold *MOT* atoms, the signal transmission starts at about 1/8 of its maximum value in absence of atoms. This corresponds to a resonant optical depth close to 2, which is remarkable for the small resident number of atoms present on average in the evanescent field.

The signal lifetime also tells us that cold atoms flying around the nanofiber, after stopping *MOT* magnetic confinement and laser cooling, may still give a significant residual background signal on this time scale. This would be important in view of probing atoms which would be trapped in optical dipole force built in the evanescent field of the

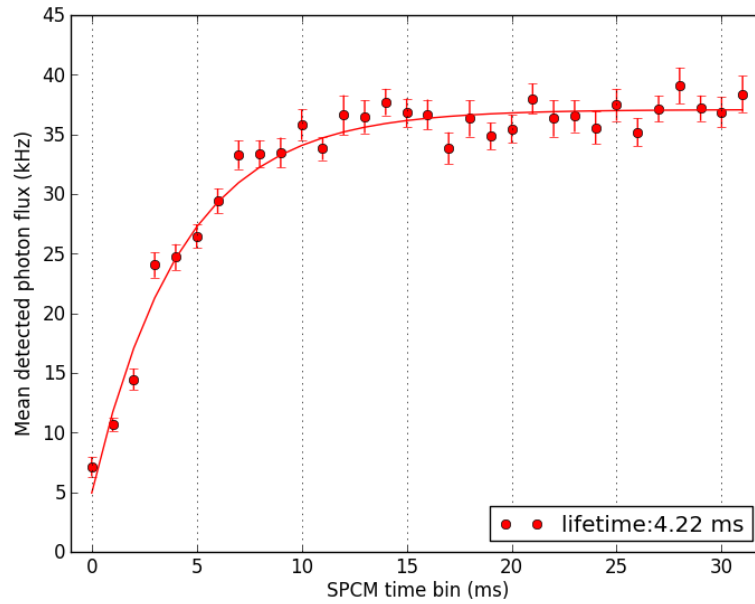


Figure 13.15: Evolution of the number of fiber guided and resonant probe photons, as a function of time, when the quadrupole magnetic field and laser cooling of the MOT has stopped.

nanofiber that requires to be loaded from a MOT around the fiber. One way to remove this background signal, corresponding to the expansion and fall of the cold atom MOT reservoir, when probing on the $|4\rangle \rightarrow |5'\rangle$ transition, would be to implement a phase of optical depumping of these atoms into a dark state. Or simply, to probe the atoms after a sufficiently long trap storage time if the trap lifetime is sufficient.

SUMMARY

In this chapter, we have presented the first observations and experiments performed on cold atoms, which demonstrate significant interaction with the evanescent and guided light mode of an optical nanofiber. We have detected a few cold atoms by counting a few photons emitted by these atoms in the fiber mode but also we have observed the reciprocal absorption of guided probe photons.

We were then able to perform fluorescence and absorption spectroscopy by counting photons guided in the nanofiber with significant signal-to-noise ratios which are limited by photon shot noise. We have observed resonant optical depth as large as $d \simeq 2$, which is remarkable for the small nanofiber geometry. The result indicates that the order of magnitude of the single-atom optical depth is about 10%. All the presented achievements were made possible by understanding the formation of atomic layers, which can coat the fiber surface and prevent or bias the observation of cold atoms.

SUPERHETERODYNE DETECTION OF ATOMS

Anyone who has had actual contact with the making of the inventions that built the radio art knows that these inventions have been the product of experiment and work based on physical reasoning, rather than on the mathematicians' calculations and formulae. Precisely the opposite impression is obtained from many of our present day text books and publications.

— Edwin Armstrong

INTRODUCTION

In this chapter, we make a leap from discrete variables to continuous variables by demonstrating the first experimental steps in the real-time and continuous detection of atoms in the evanescent field of an optical nanofiber. First, I will present some preliminary observations using the heterodyne technique introduced in chapter 2. In particular, we will see the real-time detection and narrow-band absorption of weak (~ 100 pW) fiber guided probe light by MOT atoms.

Second, following the experimental principles of Edwin Armstrong developed during the war to detect weak high frequency radio waves, I will present a superheterodyne measurement which allows to detect a phase shift induced by atoms. This technique was implemented only during the early stage of the construction of the experiment because of the limitations from many missing elements. The coherent signal from atoms can be brought to an acoustic frequency, this may allow one to *hear* cold atoms in real time. Using the superheterodyne technique, we were then able to measure simultaneously both the absorption and the dispersion from atoms while changing the probe light frequency across the atomic resonance. As we will report in the last part of this thesis, this allowed us to obtain a clear view of the effects of evanescent dipole light force on MOT atoms in order to capture them in the evanescent field.

In view of collective measurement and realization of QND interaction based on the detection of atomic states via phase shift imprints (see first chapter), we need a coherent detection of the probe light field propagating in the fiber. Once we finished to build an adequate low-

noise photodetector, we initially tried to implement first the heterodyne technique to detect coherently quasi-resonant atomic absorption from MOT atoms (figure 14.1).

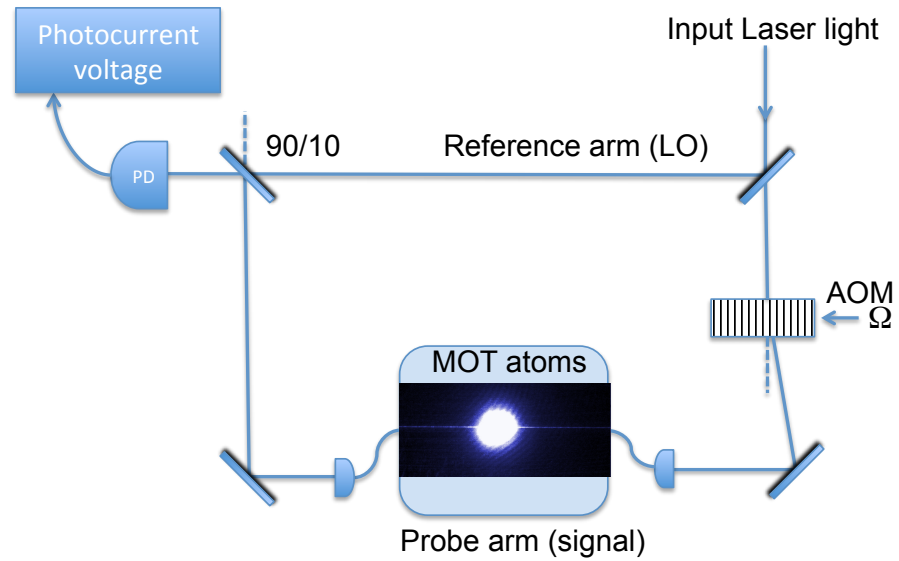


Figure 14.1: Simplified experimental principle of the single-port heterodyne detection of cold atoms in the evanescent field of a nanofiber. The interference between the probe field and the optical local oscillator reference oscillates at the RF (angular) frequency $\Omega = 2\pi \times 62.5 \text{ MHz}$.

Unfortunately, even using very weak (non-saturating) probe powers ($\sim 1 \text{ pW}$), we failed to observe any consistent signals due to all the subtle effects conspiring reported in the previous chapter.

Although we then succeeded to observe a few percent absorption after implementing the cleaning method it appeared very difficult to optimize and improve the heterodyne signal (see figure 14.2). It happened that the amount of fluorescence photons emitted by these atoms into the nanofiber mode was the most effective and sensitive signal to look at in order to optimize delicately many of the parameters affecting the average overlap between the MOT cloud and the fiber in the vicinity of the taper surface.

14.1 HETERODYNE DETECTION OF ABSORPTION

Once a significant absorption of guided probe light was observed with single photon counting (see previous chapter) it was clear that one should be able to observe such atomic signal using heterodyne detection for the same probe parameters (power and frequency detuning), unless an extremely poor overall detection quantum efficiency.

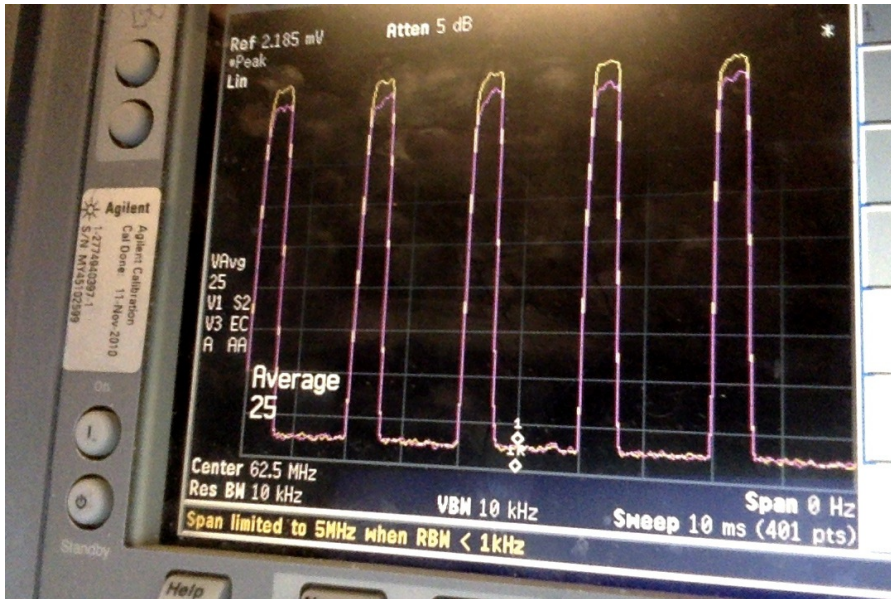


Figure 14.2: Indication of guided probe absorption. August 2013, 28th. (yellow) MOT gradient coils OFF (pink) ON. $\sim 6\%$ absorption. Pulsed probing (cooler off when probe on).

14.1.1.1 *Heterodyne lifetime signal*

To continue along the lines of the last reported data in the previous chapter, we report in figure 14.3 a similar measurement of the lifetime of the atomic absorption (probe transmission) signal which is demonstrated using continuous heterodyne detection.

The traces shown were recorded with a spectrum analyser in zero-span mode measuring the RMS alternating current (AC) coupled voltage of the output of our homemade single PIN photodiode detector in a 10 kHz narrow bandwidth centered around 62.5 MHz. Indeed, the optical local oscillator had a frequency lower than that of the probe light by 62.5 MHz for this heterodyne technique, the absolute frequency of the probe was adjusted near the expected $|4\rangle \rightarrow |5'\rangle$ transition frequency, while maximizing the observed absorption. Please note that the signal is directly proportional to the beatnote between the LO and the probe, that is, proportional to the electric field amplitude of the probe. The lowest trace represents the detected signal when the probe is (blocked) in the vacuum state, that is, the sum of LO shot noise and electronic noise. The highest trace is the signal in absence of MOT atoms showing the signal level for a DC probe light power of ~ 100 pW at the position of the atoms. When a MOT is prepared, the cooling light is switched off while the spectrum analyser is triggered simultaneously and records such 10 ms long traces. Each shown trace is an average over 10 consecutive acquired traces corresponding to re-preparation of a millimeter size atom cloud for about 2 s. Note that this data represent a real-time detection of atomic signal and our choice to show overages over 10 traces

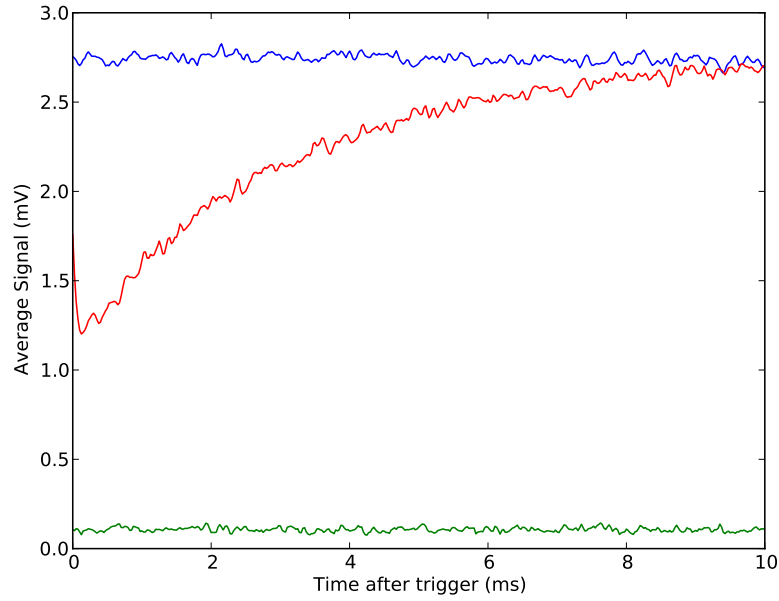


Figure 14.3: Continuous evolution of the narrow band (10 kHz) RMS heterodyne beatnote amplitude, proportional to the electric field amplitude of the fiber guided probe in presence of MOT atoms in the nanofiber evanescent field. At the initial trigger time, the MOT cooling light is turned off, the repumping light is kept active. (Probe frequency blue-detuned +62.5 MHz compared to optical LO, absolute PLL LO frequency 896×9.744 MHz). Each trace is an average over 10 (traces) experimental realizations. Probe power at the atoms ~ 100 pW, LO power at detector ~ 550 μ W. (top blue) Signal with MOT quadrupole magnetic field off (no cold atoms) (bottom green) Vacuum probe signal (probe blocked i. e. electronic noise + optical LO shotnoise). 1060 nm (~ 60 μ W) cleaning pulse 10 ms before measurement.

is just for clarity of the presentation to reduce the light shot noise. See figure 14.5 for a single-shot measurement limited by the light noise.

14.1.2 Saturation and cooling dynamics

In this short section, we save a few evidence, using the heterodyne signal, of the saturation and lower absorption of the guided probe when the MOT is in a stationary regime, that is, when laser cooling is active on the atomic cycling transition $|4\rangle \rightarrow |5\rangle$, which is being used to probe the atoms. For the previous and current reported data, the repumper light was always active during the continuous measurement.

As shown in figure 14.4, the longer the cooler is kept off, the longer it takes to recover an identical absorption level compared to the initial one. In the subfigure 14.4(d), we show a noteworthy duty cycle for constant high absorption in a view of experiments and applications based on

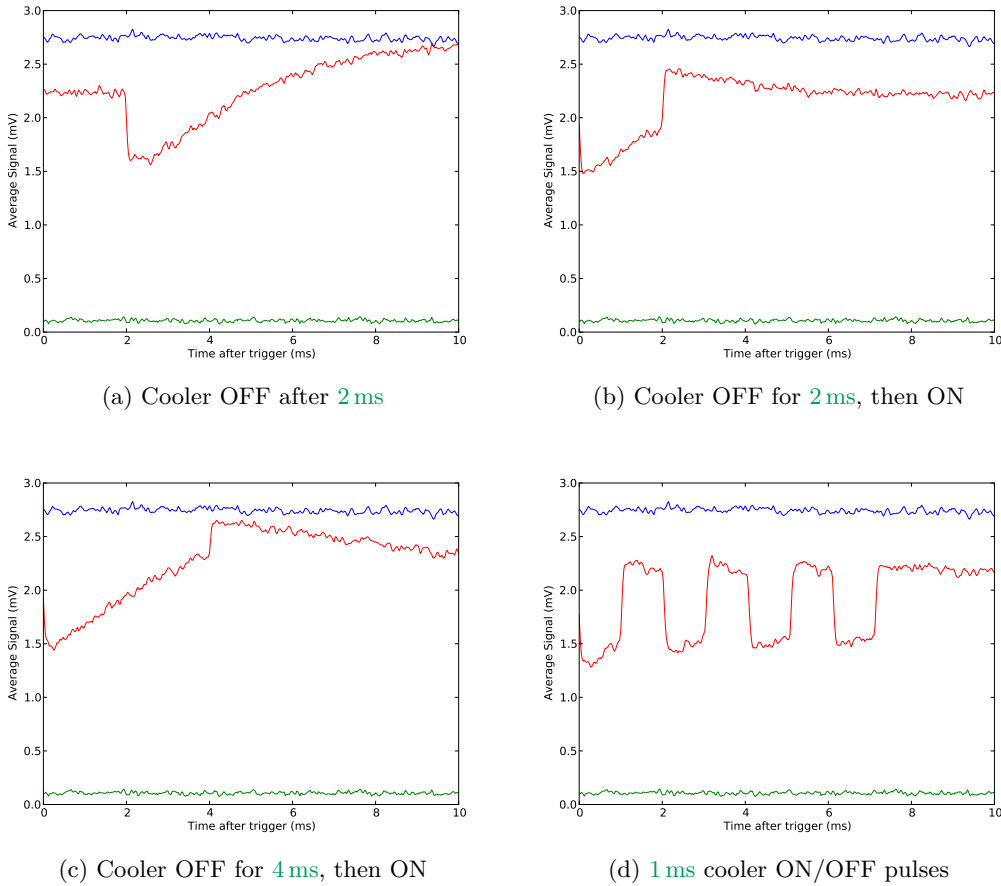


Figure 14.4: Continuous heterodyne detection of MOT atoms in the nanofiber evanescent field. Same experimental conditions as in figure 14.3.

MOT atoms. I would like to mention the qualitative observation that, when sweeping the probe frequency across the atomic resonance while the saturating cooling light was simultaneously exciting the atoms, I noted some weak discontinuities in the absorption of the probe that may indicate the possible observation of Mollow resonances but I have not had the time to redo this measurement. Indeed, as soon as absorption was detected coherently, the next experimental challenge to achieve was to be able to detect a phase shift imprint on the probe induced by the atoms. This required a fast detection method adapted to very weak probe light, if possible simple and rapid to implement, and as little sensitive to classical phase noise (I did not have any hardware built yet to stabilize and lock the interferometer arms showing in figure 14.1.). Before I present the first experimental successful measurement, I will briefly introduce in the next section the experimental setup and the technique used to reach this goal with nearly few experimental control at the early stage of the experiment.

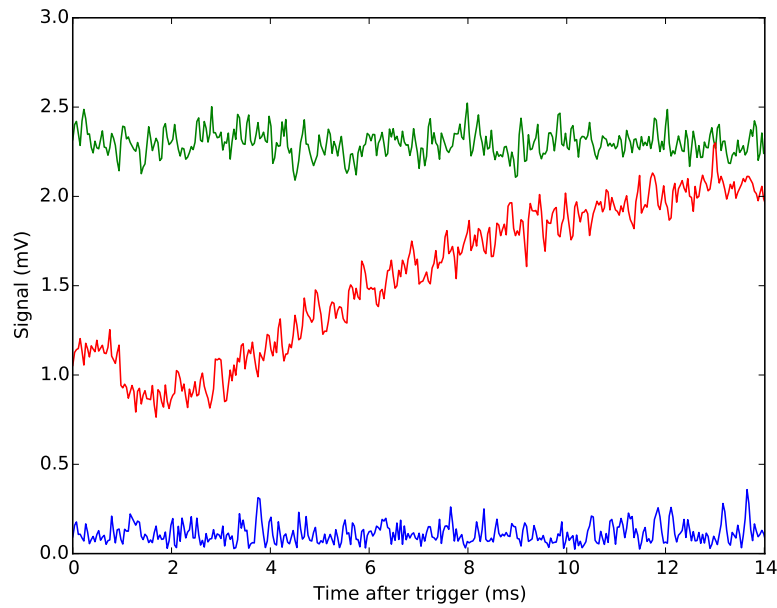


Figure 14.5: Single-shot continuous transmission of the probe light field in a **10 kHz** bandwidth. The cooler is turned off after $t = 1$ ms.

14.2 SUPERHETERODYNE

In this section, I will try to explain in simple terms how one can detect with little experimental equipment an atomic phase imprint from **MOT** atoms onto a weak probe light field propagating in the nanofiber.

The raw output voltage of the photodetector carrying the beat note¹ between the probe field and the optical **LO** at **62.5 MHz** is band-pass filtered by combining a low-pass filter (DC - **60 MHz**) and a high-pass² filter (**27.5 - 800 MHz**). Then it is electronically amplified before it is mixed³ down with a **RF LO** to an intermediate frequency (**IF**). With the **RF LO** frequency of **62.4 MHz**, the detected signal is carried at an ultra-acoustic frequency⁴ of **100 kHz**. In this frequency domain, the electronics is relatively simpler to build compared to the **RF** domain. It felt easier to build a narrow low-pass filter window⁵ (**1 MHz**) on the **IF** frequency than a narrow bandpass around **62.5 MHz**. This idea, known as superheterodyne, was inspired by Edwin Armstrong who developed

1 oscillation of the optical intensity arising from the superposition of light with different optical frequencies

2 Low-pass: Mini-circuits SLP-70+, High-pass: Mini-circuits SHP-25+

3 Or frequency multiplied. However, there is no such thing as a frequency multiplier. Physically, it is a diode ring mixer. The input signal is switched on and off with the **RF LO** frequency.

4 the heterodyne signal at $62.4 + 62.5$ **MHz** will be strongly filtered.

5 In order to be able to observe enough signal in real-time compared to the broadband detection noise, for instance, when using an oscilloscope which had **100 MHz** bandwidth.

this technique during the first world war in a view to detect weak high frequency enemy radio waves, by mixing down the detected frequency spectrum to intermediate frequencies where amplifiers (rectifiers etc) were available. In addition, the reason I chose to mixed down to 100 kHz instead of baseband (DC, 0 Hz) is directly linked to the goal of detecting an atomic phase shift and that I did not have built yet a system to stabilize the interferometer path length⁶ or the relative phase between the probe field and the optical LO.

In addition, I did not have yet a 90° phase shifter and another RF mixer working around 62.5 MHz. Therefore, I could not record *independently* signals sensitive to each quadrature of the probe field. With a non-zero mix down frequency, I would get them periodically (every mix down oscillation period) and faifully if this frequency is high enough compared to classical acoustic frequencies in the interferometer but also to the dynamics of the expected atomic phase shift.

I will now explain how to extract information about the phase of the probe light field. The ultra-acoustic signal $x(t)$ is recorded with a digital oscilloscope. Therefore, it is important to mention that the RF local oscillator signal generated for frequency mixing, the RF wave generated to supply the AOM (62.5 MHz) creating the probe light (+1 AOM diffraction order) frequency shifted compared to the optical LO and also the base time axis of the recording oscilloscope device are derived from a common time reference. By taking the Hilbert transform of the recorded signal $\mathcal{H}(x(t)) = p(t)$, one can reconstruct the (annihilation) analytic signal (see chapter 2) $a = x + ip$ which gives access to both the *instantaneous* amplitude ($|x|^2 + |p|^2$) and phase ($i \ln a$ or $\tan^{-1} p/x$). However to obtain the DC phase, one mixes down the analytic signal to DC. Before adding more details to the data post-processing, I will now present the measurement sequence.

Because we have observed previously absorption of the probe light by MOT atoms and more strikingly as a clear step in transmission when the cooler light was turned off (no saturation of the probing transition), we were hoping to observe a step in the phase for the same atomic event. This follows the well-known ideas behind the Kramers-Kronig's relations (dispersion from absorption) linked to causality, which are also connected by the Hilbert transform. The experimental sequence is as follows. A MOT is loaded on the nanofiber for 2 s, at the end of which a cleaning light pulse of 1060 nm is sent in the fiber to avoid accumulation of Cesium layers on the fiber surface between experimental realizations. The CW probe light propagating in the nanofiber is quasi-resonant with the atomic transition $|4\rangle \rightarrow |5\rangle$ and has a power of about 100 pW. The optical heterodyne signal mixed down into the superheterodyne signal oscillating at 100 kHz is then recorded for 5 ms on the oscilloscope after

⁶ which would make a noisy and randomly unstable homodyne detection sensitivity. Note also that it was my first personal attempts at doing heterodyne at a few hundred pW probe power as well

a trigger event at $t = 0$ ms. During the first 2 ms, one has a normal MOT situation where both the cooler and repumper light is ON. For the next 1 ms, where we put all our attention, both the cooler and repumper are turned OFF (the repumper is turned off 100 μ s after the cooler to ensure a maximum number of atoms pumped on the probing transition). The repumper is kept OFF for the rest of the sequence. In the need of a rapid reference measurement with no atoms, the cooler is turned ON for 1 ms, from $t = 3$ ms to $t = 4$ ms and then OFF for the rest of the sequence. We record 200 different experimental realizations (MOT loading) and we report on figure 14.6 the average instantaneous amplitude and phase. Note that because the initial phase delay of the superheterodyne signal compared to the trigger instant of the oscilloscope varies from one record to the next, we do a manual “dual-trigger” on the data by phase shifting each record signal to have them in phase at $t = 0$ ms before averaging over all traces. Our goal is to observe a step in the phase.

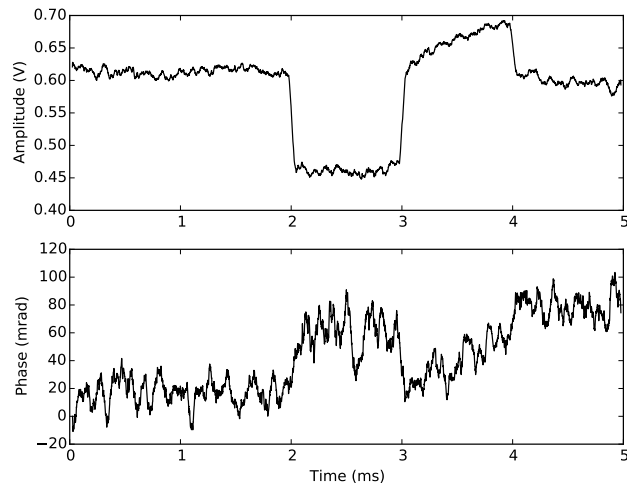


Figure 14.6: Amplitude and DC phase extracted from the Hilbert transform of the superheterodyne beatnote.

In addition, we have performed a running average of 50 μ s on the data points. In figure 14.6, we clearly observe a step in the transmitted probe field amplitude but also in the phase after $t = 2$ ms when the MOT lights are suppressed. This very first observed step in phase is not significant compared to the noise but this is remarkable in view of our main objective. In addition, I should recall that for this measurement the probe light was quasi-resonant with the atomic transition for which little atomic dispersion is expected (see chapter 1). To quantify the observations, one would like to have a reference measurement with no atomic signal in a time closeby to avoid phase drift due to classical noise. When I first saw that turning the cooler light ON during the interval $t = 3$ ms to 4 ms would reduce completely the absorption, I

first believed that the measurement interval 4 ms to 5 ms with all light off except the probing one, would be a good measurement interval for a reference signal for no atomic signal. Curiously, one obtains nearly the same signal levels as compared to the initial MOT phase situation. It appeared to me that the main reason for that observation would be the ineffective pumping of the atoms into the probe dark state $F' = 3$. Therefore I added yet another laser source to the experiment whose frequency was quasi-resonant to the $|4\rangle \rightarrow |4'\rangle$ transition, which would provide optical depumping. This light was sent into the same spatial mode as the MOT beams. Now, with both cooler and optical depumping light active during step (3), we obtain a reference signal with no atoms and the signal reported in figure 14.7.

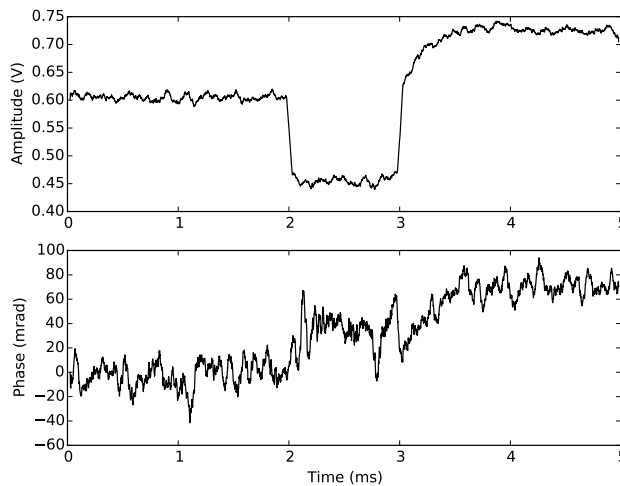


Figure 14.7: amplitude and phase step

We repeated this measurement idea for various probe frequency detunings across the $|4\rangle \rightarrow |5'\rangle$ transition and we obtained the various following curves.

By compiling all the information gained into a common graph as a function of the probe detuning with respect to the probing cyclic transition, one can obtain a combined dispersion and detected atomic absorption (see figure 14.9). Note that the data reported in this new figure were taken on a different day and for a different MOT density, from the traces acquired in 14.8. Here, we show the last data taken with optimization of all experimental parameters.

Each point is an average over 200 realizations. We directly plot the measured optical depth (the error bar are smaller than the point in the figure). From 14.8, one can extract the relative change in transmission due to atoms between $t = 2$ ms to 3 ms compared to the assumed reference full transmission of the probe $t = 4$ ms to 5 ms (we average the raw data over 600 μ s at the center of these intervals). The optical depth is deduced as before from the opposite natural logarithm of the

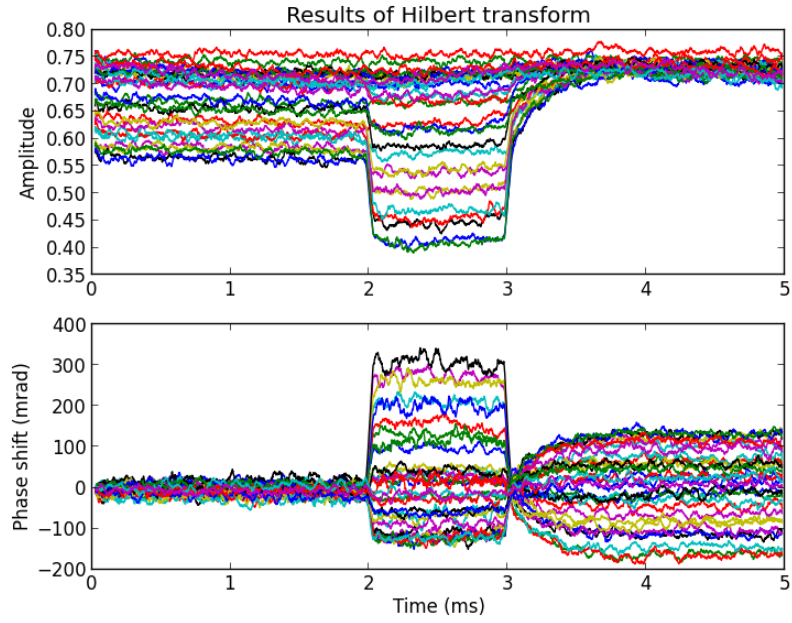


Figure 14.8: Results of Hilbert transforms for various probe detunings.

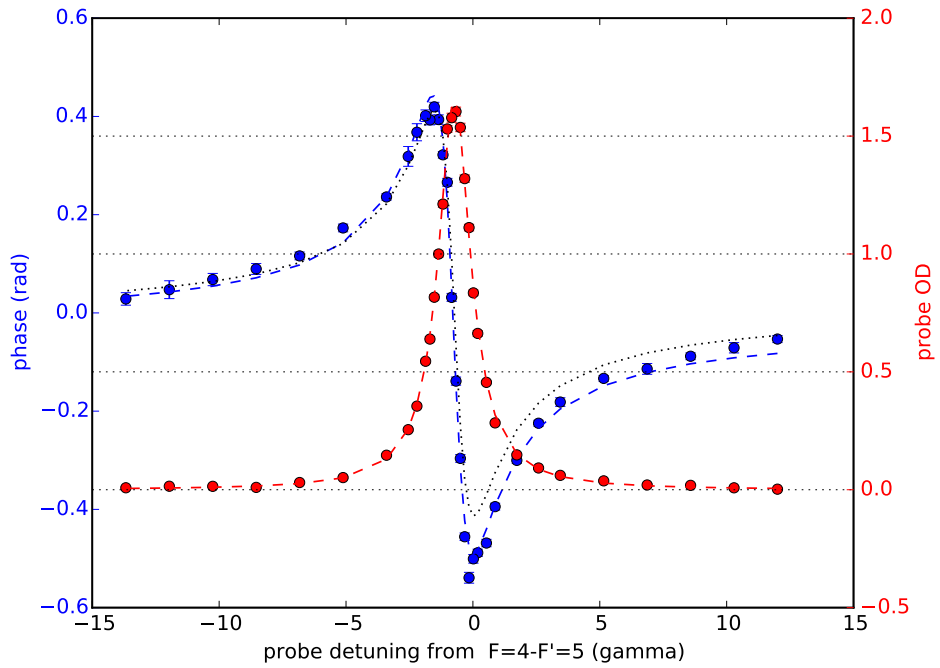


Figure 14.9: Simultaneous measurement of atomic absorption and dispersion using the superheterodyne and Hilbert transform method.)

probe transmission⁷, $d = -\ln T$. We fit independently, the phase dis-

⁷ The amplitude of the detected beatnote signal is proportional to the electric field strength of the probe, such that one should not forget to square it to deduce transmission of probe intensity

persion and optical depth to the expected model for a non-saturated two-level atom (see first chapter, (2.17)). The black dotted fit is the expected phase shift from the Lorentzian optical depth ($\varphi = -d(\Delta)\Delta/\gamma$, see (2.17) with $d = \alpha l$). Both measured phase shift and attenuation indicates a red shift of the atomic transition of about 0.73γ where $\gamma = 5.234 \text{ MHz}$ is the expected linewidth of the transition. Note that the frequency axis given in the figure is expected from the experimental calibration of the probe frequency (polarization spectroscopy+PLL lock+AOM shift) and may be prone to systematic error (as experienced in Dawkins et al. (2011)) although we are quite confident about it. The quadrupole magnetic field was ON during the measurement and atoms in a MOT are mainly in weak field seeking state (lowest Zeeman levels $m_f = -4$) this could indicate such Zeeman red shift. On the other hand, the probe power at the atoms for the measurement was about 30 pW . The line presents as well broadening (about $\delta\nu = 1.6\gamma$). In addition, we note a slight asymmetry of the phase shift value (offset of about -25 mrad). We remind that this simple two-level model ignores the presence of the hyperfine structure of the excited states of the atoms, which might be responsible for this small deviation. The optical depth and phase shifts which are observed are quite remarkable as they originate from a few MOT atoms flying in the evanescent field of the nanofiber.

14.3 OBSERVATION OF LIGHT SHIFTS

I would like now to anticipate the results of the next chapters concerned with trapping of atoms using optical dipole forces in the evanescent field of the nanofiber. This is because I believe that the superheterodyne detection method, even imperfect, played a big initial role in the future success of the nanofiber experiment. It allowed to apprehend visually what happens to the detected atomic signals for instance when one send in the nanofiber significant far blue or red detuned light power.

14.3.1 *Blue-detuned light*

Let me start with the simplest case. It is expected that when ground state Cesium atoms are illuminated by a spatial inhomogeneous light field, that is far blue detuned compared to the D2 (here 780 nm), they would experience predominantly an optical dipole force, which would attract the atoms (the atomic dipoles) towards the intensity minima of the light field. Because the evanescent field carried by the fundamental mode of the nanofiber is quasi exponentially decaying a way from the fiber surface, one expect that the application of blue-detuned field will repell atoms away from the fiber surface. One would then expect a higher mean distance of approach of atoms in equilibrium with the new repelling force and the confining MOT light forces. As a result, because the strength of the electric field of the guided probe light also

carried by the fundamental mode decreases as well away from the fiber surface, one would expect a decrease of the observed optical depths when increasing the power of the blue-detuned light field. In addition, the typical effective mode cross section of the fundamental mode is relatively so small ($\sim 1 \mu\text{m}^2$) that for a few milliwatt of power, one would expect to observe already a few megahertz light shift of the atomic transition.

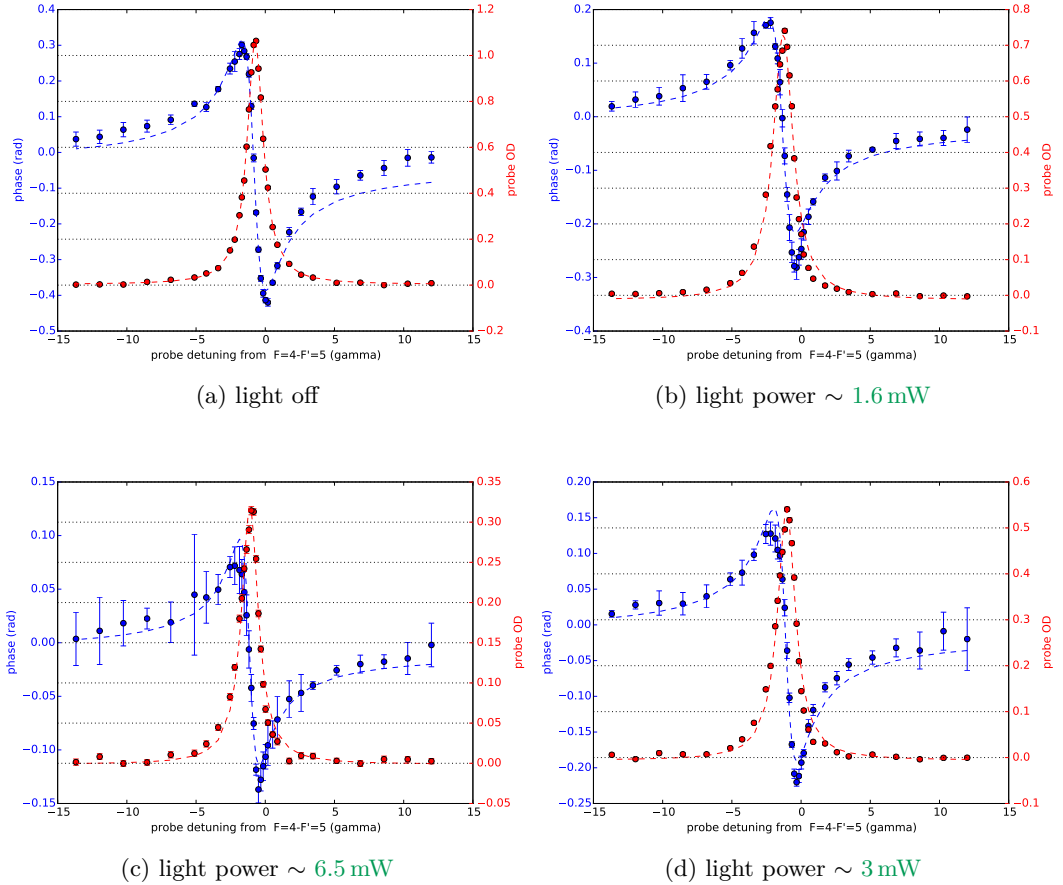


Figure 14.10: Continuous heterodyne detection of MOT atoms in the nanofiber evanescent field in presence of 780 nm evanescent light.

We report in figure 14.10 a few selected measurement where we approximately doubled the 780 nm light power. Compared to the typical values obtained from the observed atomic response in absence of such a light, we do not observe any extra broadening of line which is still always on average about 1.5γ . Secondly, we do not see clear frequency shift of the atomic resonance as the light power is increased. However, we observe a clear variation of the maximum detected optical depth.

We report in figure 14.11 a more quantitative display of the various values for all the different light powers we have tried. The maximum or resonant optical depth measured is seen to decay quasi exponentially as the light power is increased with a $1/e$ decay constant of 5.2 mW. Note

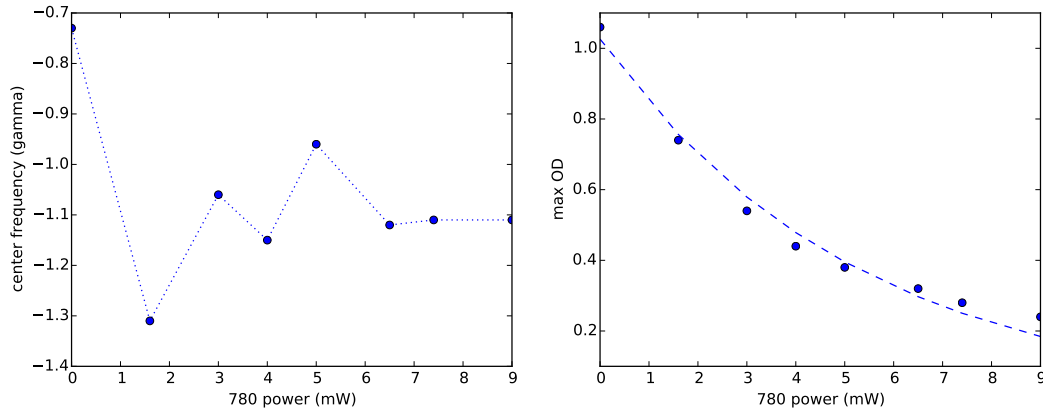


Figure 14.11: Effects of far blue-detuned light on the observed resonant optical depth and resonance frequency.

that if one knows by how much the mean distance between the atoms and the fiber surface is changed as a function of the light power, one could map the evanescent field profile of the probe light. Interestingly, the position of the resonant atomic frequency, with respect to the expected position, seems to oscillate until it reaches a stationary value at high power. Note also that there is at least a clear jump in the atomic resonant frequency from no light to a few milliwatt. In addition, the observed atomic light shift is red, which is expected for blue-detuned light (on a two-level atom). The atomic transition frequency is reduced compared to the expected frequency of the transition $|4\rangle \rightarrow |5'\rangle$ from 3 to 2 MHz. We could explain that the observed light shift does not increase with the light power because it depends primarily on the light intensity at the atom position, which here depends on the mean position of the atoms with respect to the fiber surface. As the light power increases, the mean distance of approach to the fiber surface increases as the atoms are more and more shielded from the fiber surface by this static elastic barrier. Because the light field decreases away from the fiber surface, this tampers the linear increase of the light shift with light power. In the next subsection, we report observation with far red-detuned light.

14.3.2 Red-detuned light

In this section, we report similar measurement as before but using far red-detuned light instead. We have built an ECDL laser operating at 1057 nm. In contrast with the above expectation for blue-detuned light, we expect very simply that the atoms will now be attracted towards the fiber surface. The atoms approaching closer to the fiber surface will couple stronger and stronger with the evanescent probe light field. This should increase the resonant optical depth with increased light powers.

As reported in figure 14.12 and clearly shown as well in figure 14.13 (a) this is not what is observed. The maximum optical depth actually

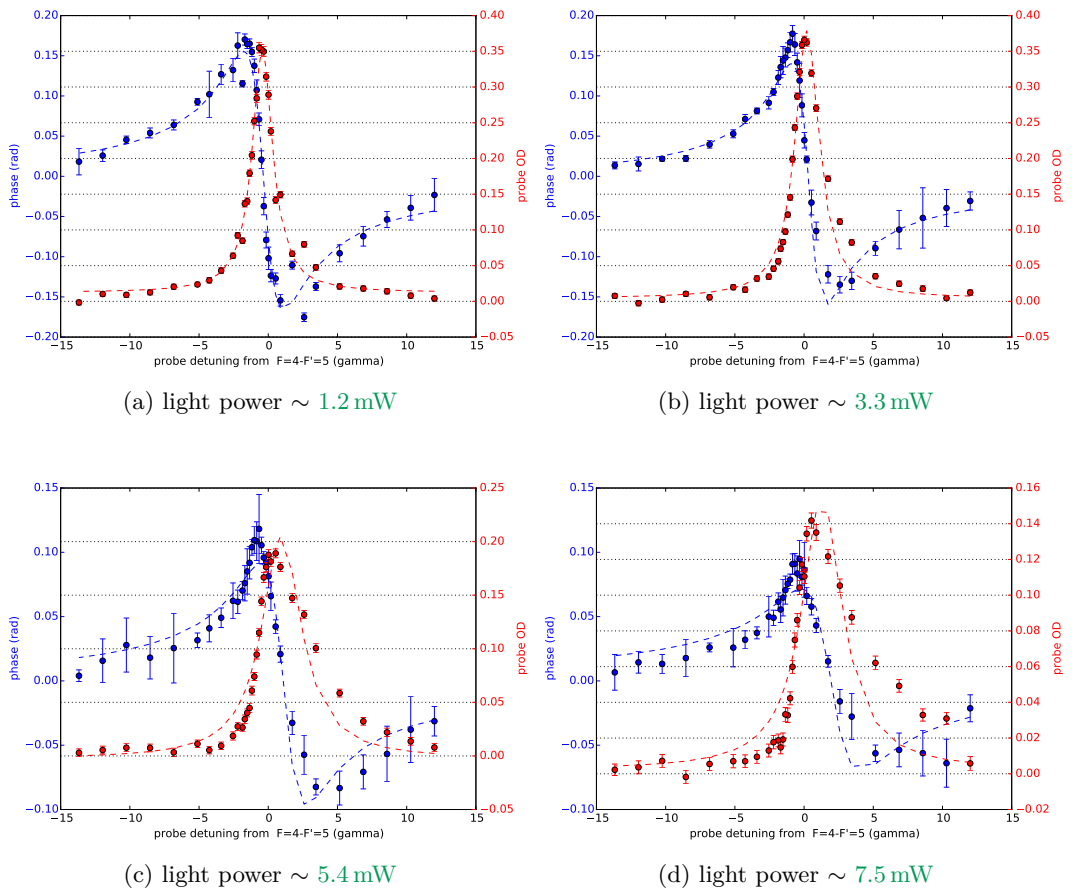


Figure 14.12: Continuous heterodyne detection of MOT atoms in the nanofiber evanescent field in presence of 1057 nm evanescent light.

decreases with increased light power. The most remarkable feature of the atomic response compared to the previous observations with blue-detuned light is the presence of a clear broadening of the atomic signal. In addition, this broadening, which grows as the light power gets increased, is interestingly asymmetric. Because of such a broadening, it becomes difficult to estimate properly an atomic resonance frequency. However, it is seen and perhaps better in figure 14.13 (a), that the atomic response is now (blue) shifted towards higher transitions frequency as expected from red-detuned light. In addition, also in contrast with the results for blue-detuned light, the frequency shift is seen to increase steadily and linearly from its starting value with no light, (see figure 14.13 (b)). We only reported values for the lowest powers where the center frequency is extracted from the Lorentzian fit which are in reasonable correspondence with the data.

The reduced maximum optical depth could be explained by considering that the atoms are now accelerated towards the fiber surface by the attractive red-detuned field. They will crash on the surface or may scatter away. Consequently, the mean time spent by MOT atoms en-

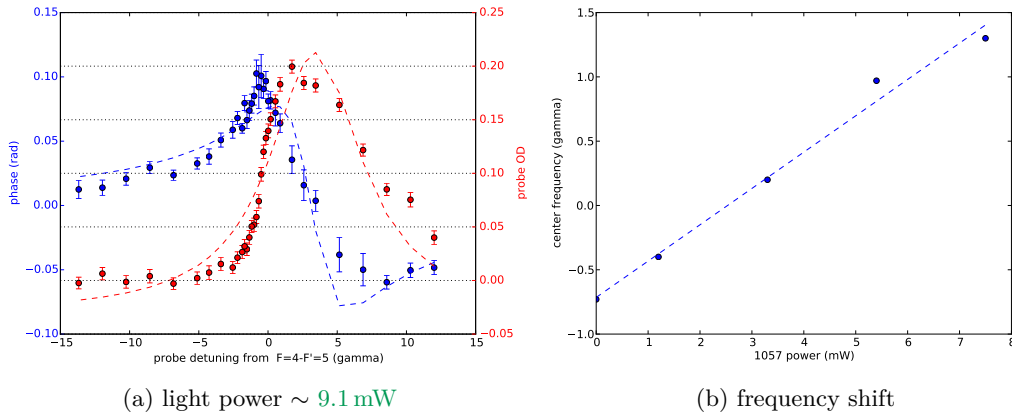


Figure 14.13: (a) effects of blue detuned light on resonant OD and resonant frequency (b) effects of red detuned light on resonant frequency

tering the evanescent field of the nanofiber is smaller resulting in an average lower atom density in the evanescent field. The broadening of the signal could be explained by a signal arising from different atoms present in the evanescent field of the probe but which are located on average at different positions in the red-detuned evanescent field, thereby experiencing different light shift. Note that the red-detuned light field penetrates deeper outside the nanofiber more than twice as much as the blue-detuned one (see next chapter).

Based on all these observations, the next natural experimental question was to observe whether for instance the reduction in resonant optical depth caused by the repulsive blue-detuned light could be compensated by simultaneously imposing a red-detuned light field. And also whether the strong broadening would still be present. These results were among the first obtained in order to trap atoms using a two-color evanescent field around a nanofiber. We will present subsequent steps after a more theoretical chapter about such nanofiber traps.

SUMMARY

In this chapter, we have made the first successful transition from discrete to continuous variable detection of atomic signal. We started by performing absorption spectroscopy from the variation of the beat note intensity of the probe field with a reference local oscillator using a simple single-port heterodyne measurement scheme. The results provided a new point of view on the atoms and confirmed the observations realized with photon counting in the previous chapter. Then, we presented an experimental method, called superheterodyning, which we have developed to detect the phase shift imprinted on the probe light field by the atoms, without any lock and classical phase stabilization of the probe and reference arm path length difference. Moreover, the continu-

ous measurement of the phase shift was extracted from only ~ 100 pW probe field power. With this great initial tool, which allows to visualize simultaneously atomic dispersion and absorption, we could observe directly the effects of both far blue and red detuned light propagating in the evanescent field of the nanofiber. One can clearly observe light shifts and broadening, which are not necessarily trivial. However, the qualitative results are fantastic as they show the possibility of non-dissipative guided light interactions with atoms in the evanescent field and the perspective of confining these atoms in the evanescent probe field for long interrogation times.

Part IV

AN EFFICIENT ATOM-LIGHT CRYSTAL

We create two one-dimensional optical lattices for Cesium atoms in the evanescent field of an optical nanofiber.

We develop a minimally destructive probing method which allows to measure continuously the atomic state population at the light shot noise limit. With Bayesian filtering we demonstrate up to -14dB atom number squeezing.

Finally, we explore the novel perspective of a creating an atomic mirror in this system.

15

DESIGN OF OPTICAL NANOFIBER TRAPS

As the saying goes, the Stone Age did not end because we ran out of stones. We transitioned to better solutions.

— Steven Chu

INTRODUCTION

In this chapter, we prepare the description of the experiments based on atoms optically trapped around a nanofiber, reported in this last part of the thesis. We will go through some essential principles of optical dipole traps based on evanescent fields of light and we will highlight the merits of nanofibers to create them.

A magneto-optical trap also called in the past a spontaneous optical force trap, is a non-conservative trap. During their lifetime in the trap, atoms undergo successively incoherent light scattering events, which among other constrains is detrimental for the type of quantum state engineering and study of coherent interactions with cold atoms in our scope. Rather, a MOT constitutes a precious reservoir of cold atoms needed to load conservative traps that are a few millikelvin shallow for neutral alkali atoms.

Neutral atoms require to be polarized in a so-called weak-field-seeker state to be captured in a quadrupole magnetic trap. Such states with non-zero magnetic moment are also by definition sensitive to external magnetic field fluctuations. In that respect, optical dipole traps based on induced electric dipole interaction with far-detuned light are more versatile as the above restriction is absent. Moreover, one can control the dependence of the trap depth on the internal atomic states. However, as mentioned elsewhere in this thesis, one must look at the flipside of the coin for high resolution spectroscopy since trapping mechanisms that rely on the internal electric charge distribution of the neutral atom, will perturb by definition the internal atomic energy levels, limiting the measurement accuracy of atomic frequencies (e. g. in atomic clocks).

Note that the induced nature of the dipole force is the only way to create a conservative trap for atoms with light as neutral atoms do not have a permanent dipole moment that would otherwise violate the

reflection symmetries (Cohen-Tannoudji and Dupont-Roc (1972)) of the fundamental interactions at the root of the stability of atoms.

15.1 DIFFRACTION LIMITED OPTICAL DIPOLE TRAP

In the disordered atomic ensembles based experiments operated during the first part of this thesis we have optically trapped cold Cesium atoms using the simplest optical dipole trap that has many advantages.

Proposed theoretically on two-level neutral atoms in three dimensions by Ashkin (1978), the first demonstration of optically trapped atoms was reported in Chu et al. (1986). As mentioned before, neutral atoms does not have permanent dipole moment, however one can be induced optically by the time-dependent electric field of light. The electrically induced dipole moment $d = \alpha(\omega)E$ (linear response) is characterised by the dynamic atomic polarizability $\alpha(\omega)$, with ω the optical field frequency. The interaction of the induced dipole moment back onto the electric field of the light provides a conservative force in presence of gradients of the electric field (in addition to the dissipative radiation pressure force contribution linked instead to the gradient of the phase of the field.)

The potential energy of the atom is $U = -\alpha(\omega)E^2/2$ that leads to the force $F = -\nabla U = \alpha(\omega)\nabla(E^2)/2$. α^1 is positive for an atom in its ground state and would be attracted toward the highest electric field region. The dipole potential can be described in terms of the optical Stark shift of the atomic energy levels, that lowers the ground state energy by U and increases the excited state by the same quantity. This picture relies on an atom dressed by the field, a process that is linked to the coherent redistribution of photons with different momenta through stimulated emission. An atom which spends most its time in the ground state could be confined by the gradient of an optical field. The simplest case that was also design in our experiment is a focused Gaussian beam whose frequency is far-detuned from the atomic transition to reduce the incoherent scattering due to the radiation pressure force component (critical in particular in the axial direction).

The spatial distribution of the intensity of such beam writes

$$I(r, z) = I_0 \left(\frac{w_0}{w(z)} \right)^2 \exp \left(\frac{-2r^2}{w(z)^2} \right),$$

$$\text{with } I_0 = \frac{E_0}{2\eta}, \quad w(z) = w_0 \sqrt{1 + \left(\frac{z}{z_0} \right)^2}.$$

η is the vacuum impedance, w the beam waist of the Gaussian beam and $z_0 = \pi w_0^2/\lambda$ the depth of the focus or Rayleigh range.

In the past experiment, a 5 W laser Gaussian beam with a wavelength $\lambda = 1064 \text{ nm}$ was focused down to a waist of about 50 μm . The

¹ Here we consider the real part of the polarizability

coolest atoms, that is, with the lowest kinetic energy will experience an harmonic potential near the focus of the laser beam.

$$U(r, z) \simeq U_0 \left(-1 + \frac{2r^2}{w_0^2} + \frac{z^2}{z_0^2} \right) = -U_0 + \frac{1}{2}m\omega_r^2 r^2 + \frac{1}{2}m\omega_z^2 z^2. \quad (15.1)$$

Since in general $w_0 \gg \lambda$, this kind of trap is very anisotropic $\omega_z \gg \omega_r$. We note that the trap frequencies depend on the electric field amplitude $E_0 = E(r=0, z=0)$ in contrast to the harmonic frequency of a mass-spring independent of the gravity field. The confinement can be made deeper and tighter by respectively increasing the peak light intensity and decreasing the beam waist w_0 for the radial confinement or the focal depth z_0 for the axial confinement. As can be seen clearly from the divergence angle of the beam $\tan \theta = w(z)/z \sim \lambda/\pi w_0$, the smaller the confinement volume, the higher the diffraction of the beam. When the angle θ is non-negligible the paraxial approximation for the validity of the above Gaussian beam expression starts to fail.

It is possible to design a trap based on a electromagnetic mode different than the previous TEM_{00} that does not diffract, that is whose radial intensity profile is independent of the propagation ordinate z on the optical axis. Bessel beams do not diffract but are more difficult to produce in free space. Gaussian dipole traps allow to achieve sufficiently deep and localized optical potential down to several optical wavelengths which allows relatively high atomic densities. The lifetime of the atoms in the trap is limited by (in absence of the background gas collisions) the random fluctuation of the light forces that boil the atoms out of the trap.

In general, a realistic atom possesses many ground state levels. If all are displaced by the same amount via optical Stark shift, a situation that occurs for far enough detuned light, then the general trap properties are quite simplified and independent of the light polarization.

The potential energy of the dipole force can write for a two-level atom [Ashkin \(1978\)](#); [Renn et al. \(1995\)](#)

$$U = \hbar \frac{\omega_L - \omega_0}{2} \ln \left(1 + \frac{\Omega^2/2}{(\omega_L - \omega_0)^2 + \Gamma^2/4} \right) \sim \hbar \frac{\Omega^2}{4(\omega_L - \omega_0)},$$

where the last relation is valid for large detuning $|\Delta = \omega_L - \omega_0|$ compared both to the Rabi frequency $\Omega = dE/\hbar$ and the linewidth of the transition Γ . The rate of spontaneous emission or scattering rate $\gamma = \Gamma\Omega^2/4(\omega_L - \omega_0)^2$ satisfies in this limit $\gamma = \Gamma/U/(\hbar\Delta)$ that is $\gamma \ll U/\hbar$ (see [Grimm et al. \(2000\)](#)).

This scattering rate is responsible for heating of the atoms in the trap through the transfert of random momentum recoil energy.

15.2 ROADS TOWARDS EVANESCENT NANOFIBER DIPOLE TRAP

It seems that the experimental road towards using today the evanescent optical field of a sub-micrometer diameter dielectric glass fiber, to trap

and guide atoms through the dipole force, has emerged at the crossing of several past investigations of which we would like to mention a few examples.

15.2.1 *Evanescent mirror*

When light impinges at the interface between two media of different refractive indices at an angle satisfying the total internal reflection condition, no light propagates in the medium with the lowest refractive index. However an evanescent field penetrates it that decays exponentially on the order of the light wavelength. By using blue detuned light, one can then create a repulsive potential barrier on a glass surface that will elastically reflect cold atoms falling onto it. The idea of such evanescent electromagnetic mirror for neutral atoms was proposed by [Cook and Hill \(1982\)](#). Based on this principle, a so-called gravitational cavity can be created with a concave glass surface for this first mirror and the gravity potential acting as the second mirror. This was demonstrated in the group of Claude Cohen-Tannoudji ([Aminoff et al. \(1993\)](#)) and in other groups using prisms.

15.2.2 *Along thin wires*

Magnetic traps for neutral particles (e.g. neutrons, neutral atoms) which possess a magnetic moment were extensively investigated. In particular, contrary to the mechanism underlying the magneto-optical trap where atoms are attracted towards a minimum of a magnetic field, high-field-seeking state magnetic trapping was pursued and the simplest proposal turned out to be the interaction with the magnetic field produced by a thin current-carrying wire, [Blümel and Dietrich \(1991\)](#) (neutrons) [Vestergaard Hau et al. \(1995\)](#) (neutral atoms). This was successfully demonstrated by [Schmiedmayer \(1995\)](#) trapping and guiding Sodium atoms over a distance of one meter along a $150\ \mu\text{m}$ diameter current-carrying tungsten wire. The magnetic field from the wire only provides an attractive force for the atomic magnetic moment that would lead the particle to crash on the wire. A potential minimum for the atom is provided by considering the centrifugal repulsive barrier that arises from the orbital motion of the particle around the wire.

15.2.3 *Hollow core fibers*

During the same period, on the other hand, optical traps for neutral atoms were developed in conjunction with analogous glass wires or optical fibers in attempts to combine trapping and guiding of atoms with the guiding of light. In particular the transmission and manipulation of an atomic flow through an hollow-core cylindrical optical waveguide using the optical dipole force from the core evanescent guided mode was

suggested in [Ol'Shanii et al. \(1993\)](#). This was successfully demonstrated by guiding Rubidium atoms through a red-detuned evanescent optical field inside a fiber hollow core with a $40\ \mu\text{m}$ diameter [Renn et al. \(1995\)](#). The channeling of atoms inside such fibers was then optimized using instead blue-detuned light and smaller hollow core diameters down to $2\ \mu\text{m}$ ([Ito et al. \(1996\)](#)).

15.3 THE SIMPLEST NANOFIBER TRAP

As soon as it became technologically possible to fabricate sub-wavelength diameter optical fibers [Tong et al. \(2003\)](#), the first proposal that consists in trapping and guiding atoms, instead, outside the core of the fiber, was published. This idea consists in attracting atoms towards the fiber surface using far red-detuned evanescent optical light while balancing the attraction with the repulsive centrifugal force from the orbital motion of atoms as in Jörg Schmiedmayer experiment for instance ([Schmiedmayer \(1995\)](#)). The evanescent light is produced by the fundamental mode of the fiber with transverse rotating polarization which does not break the circular symmetry. In the first proposal [Balykin et al. \(2004\)](#), the modes taken for the discussion are weakly guided modes which is questionable as the authors pointed themselves out. We would to give our remarks on it here.

The existence of a stable trap from the balancing of the centrifugal force is possible if the fiber evanescent field does not diverge faster than the centrifugal barrier, that is faster than $1/r^2$. We found in earlier chapters that the transverse electric field distribution for any fiber mode order (with rotating transverse polarization) outside the core writes

$$|\mathcal{E}|^2 = 2\mathcal{N}^2 \left[K_{l+1}^2(qr)(1+ls)^2 + K_{l-1}^2(qr)(1-ls)^2 + 2\frac{q^2}{\beta^2} K_l^2(qr) \right].$$

The (quantum) centrifugal potential energy for the orbital motion of the cold atoms in a fiber transverse plane is given by

$$C = \frac{\hbar^2}{2M} \frac{m^2 - 1/4}{r^2}.$$

Please note that when the orbital quantum number m is null $L_z = m\hbar$, z being the fiber axis, the centrifugal potential energy is attractive. To grasp this very counterintuitive term that I should highlight that appears in two dimensions, a very interesting study is presented in [Cirone et al. \(2001\)](#) about this so-called quantum anticentrifugal force.

For the fundamental mode HE_{11} with azimuthal number $l = 1$, the effective far-detuned potential can be read,

$$W/E_{\text{rec}} = -\chi \left[K_2^2(qr)(1+s)^2 + K_0^2(qr)(1-s)^2 + 2\frac{q^2}{\beta^2} K_1^2(qr) \right] + \frac{m^2 - 1/4}{k^2 r^2},$$

$$\text{with } \chi = -\frac{\hbar}{E_{\text{rec}}} \frac{\Omega_s^2/\Delta}{\left[K_2^2(qa)(1+s)^2 + K_0^2(qa)(1-s)^2 + 2\frac{q^2}{\beta^2} K_1^2(qa) \right]}$$

where Ω_s is the Rabi frequency at the fiber surface, $E_{\text{rec}} = k^2 \hbar^2 / 2M$ is the single photon recoil energy and χ the coupling constant with the atom following the spirit of [Balykin et al. \(2004\)](#). Clearly the existence of local extrema for the potential is given by the nulling of its first derivative leading to the following equation

$$y(x) = 2q^2 \frac{m^2 - 1/4}{k^2 \chi}, \quad (15.2)$$

with

$$\frac{y(x)}{x^3} = K_2(x) [K_3(x) + K_1(x)] (1+s)^2 + 2K_0(x)K_1(x)(1-s)^2 + 2\frac{q^2}{\beta^2} K_1(x) [K_2(x) + K_0(x)].$$

Contrary to the case of evanescent fields from weakly guided modes, the previous expression is more complex and we will simply try to answer whether a stable trap exists for a fiber radius $a = 0.25 \mu\text{m}$ and a few wavelengths. We have plotted on figure [15.1](#), the function y for the different parameters. The condition for the existence of an extremum of potential energy W is clearly that the right-hand side of [\(15.2\)](#) is smaller than the maximum value of y . This seems to be satisfied for all given wavelengths. However, when there is one solution, the extremum is a maximum. For instance, only for the long wavelength such as $\lambda = 2 \times 780 \mu\text{m}$ one can foreseen a local minimum². Instead of going into a complex analysis let just ask whether it is realistic to form a stable trap for cold atoms. One would like to bring the atoms close enough to the fiber surface such that one can interact strongly with adequate probe light such as 852 nm for Cesium atoms. A good estimate for the fiber surface distance is our fiber radius $a = 250 \text{ nm}$. The orbital quantum number we want to trap can be estimated for a realistic millikelvin cold atom from a [MOT](#) reservoir. If we take this temperature for the rms transverse velocity component, that is $v = \sqrt{k_B T / 2M}$, but $v = L_z / Mr \simeq \hbar m / 2Ma$ ($r = 2a$ being the distance to the fiber axis). For $T = 1 \text{ mK}$, we find $m \sim 185$. The centrifugal potential energy would then be about 5.2 MHz at $r = 2a$.

² one should look at the sign of the second derivative

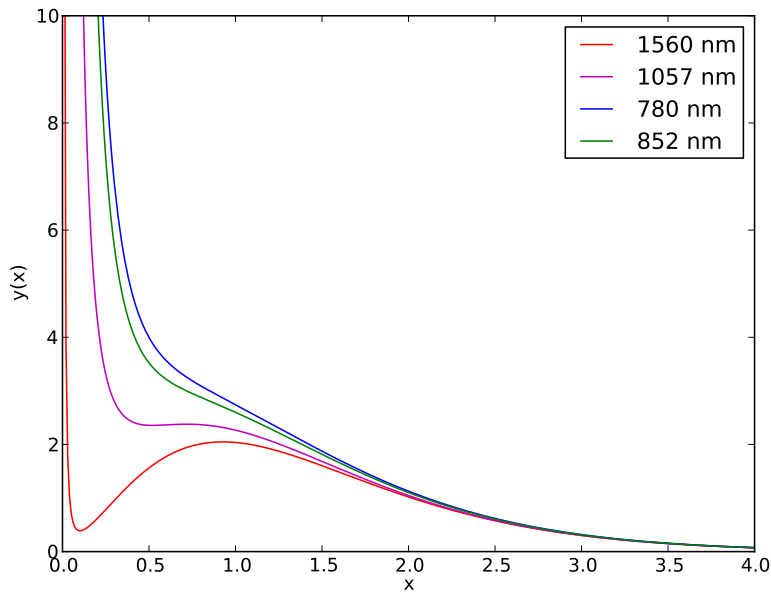


Figure 15.1: Function y

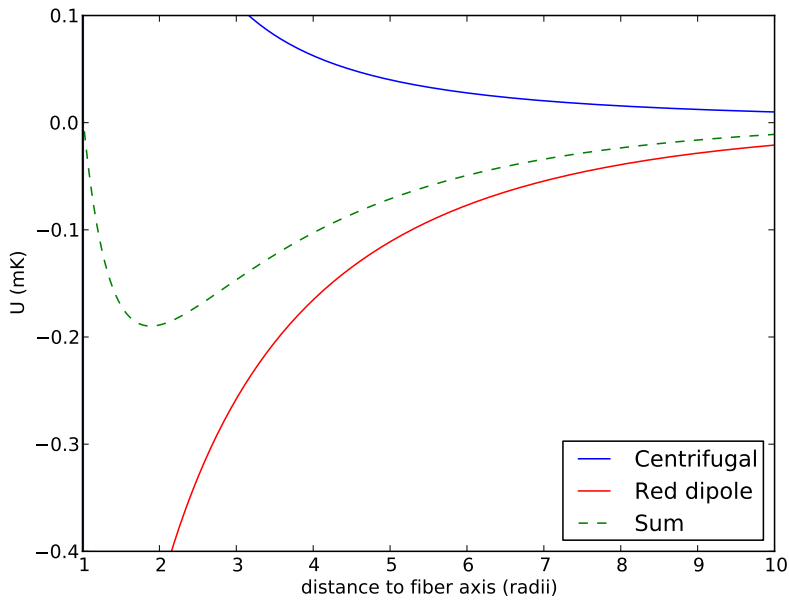


Figure 15.2: Centrifugal force based trap, $m = 185$ power 19 mW , $\lambda = 1560 \text{ nm}$

We find that trapping cold atoms close the surface of an optical nanofiber with radius $a = 250 \text{ nm}$ with the above wavelengths, might be possible near the telecom wavelengths, based solely on red-detuned dipole force in the fundamental mode with rotating polarization balanced by the centrifugal force. However, for all the near-infrared wave-

lengths this seems less realistic and differs somewhat from the results of [Balykin et al. \(2004\)](#) that we explain graphically in figure 15.3. In this first proposal, the weakly guided mode expressions were used, that leads to $y(x) = x^3 K_0(x) K_1(x) \equiv \text{ref}(x)$. The LP mode $K_0^2(x)$ diverges slower than the exact solution for the fundamental mode HE_{11} compared to the centrifugal barrier in $1/r^2$.

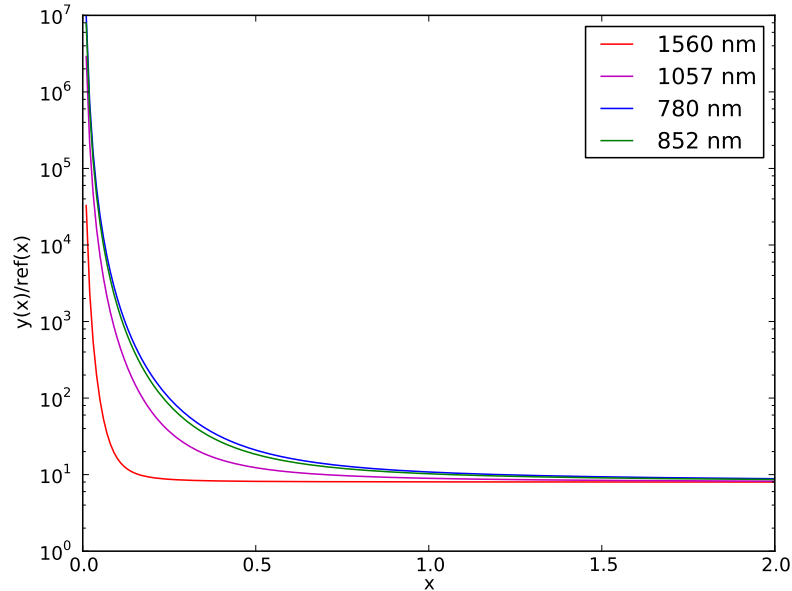


Figure 15.3: ratio y/ref

Instead one needs to investigate repulsive barriers other than the centrifugal one, that would diverge as fast as the single red-detuned evanescent field. A first simple answer would then be naturally to superimpose a blue-detuned evanescent field of the same mode. We note that when the optical potential minimum get closer and closer to the fiber surface, a dielectric object, one must consider its influence via van der Waals and Casimir-Polder types of interaction.

15.4 DISPERSIVE VAN DER WAALS INTERACTION

A fluctuating dipole would induce a dispersive (in contrast to inductive for a permanent dipole) van der Waals interaction with the nanofiber medium. One can understand simply this force as the result of the electric field produced by the fluctuating dipole that is reflected by the fiber surface back to the dipole location with certain Fresnel coefficients. This potential energy correction for trapping atoms, is up to the current knowledge of the author often referred to the formula reported in [Le Kien et al. \(2004\)](#). However, most the time, the planar van der Waals approximation is used in the literature even though we have

an exact analytical expression for it. This is questionable in as much as V/V_{planar} already differs by a factor of 2 a few hundred nanometers from the fiber surfaces.

This exact expression for the van der Waals interaction originates from the group of Jacques Robert in France³. The formula we report here is a special case of a more general result for an infinite metallic nanowire which involves non-local responses of the material. But for a dielectric, using the quasi-static approximation to solve Maxwell's equation to find the reflection coefficients appropriate to the cylindrical geometry is just an analytical puzzle. There will not be any plasmonic resonances and the formula can be deduced for any degree of multipolar expansion of the source potential [Boustimi et al. \(2002\)](#) and [Boustimi et al. \(2003\)](#). Within the isotropic dipole approximation and SI units (Boustimi results are in CGS from $\text{div } \Phi = -4\pi\delta\rho$),

$$V = \frac{\hbar}{\pi^2} \frac{1}{4\pi\epsilon_0} \sum_{n=-\infty}^{+\infty} \int_0^\infty dk \left[k^2 K_n'^2(kr) + \left(\frac{n^2}{r^2} + k^2\right) K_n^2(kr) \right] \int_0^\infty d\xi \alpha(i\xi) G_n(k, a, i\xi), \quad (15.3)$$

with

$$G_n(k, a, \omega) = \Delta_n(k, a, \omega) \frac{I_n'(ka)}{K_n'(ka)},$$

$$\Delta_n(k, a, \omega) = \Delta_n^{loc} = \frac{[\epsilon(\omega) - 1] I_n(ka) K_n'(ka)}{I_n(ka) K_n'(ka) - \epsilon(\omega) I_n'(ka) K_n(ka)},$$

where care should be taken to distinguish the derivatives of the modified Bessel functions, a being the radius of the fiber, r the radial distance of the dipole to the fibre axis, k a dummy math variable, α the frequency-dependent atomic polarizability and ϵ the dynamical permittivity of the dielectric (silica) (i.e $\epsilon = n^2$).

The planar approximation expression is given by [McLachlan \(1964\)](#),

$$V = -\frac{C_3}{(r-a)^3}, \quad (15.4)$$

$$C_3 = \frac{\hbar}{4\pi} \frac{1}{4\pi\epsilon_0} \int_0^\infty d\xi \alpha(i\xi) \frac{\epsilon(i\xi) - \epsilon_0}{\epsilon(i\xi) + \epsilon_0},$$

where the constant C_3 , depends on the atomic polarizability α .

15.5 TWO-COLOR EVANESCENT DIPOLE TRAP

The first proposal of an atom trap using a two-color evanescent light field around a nanofiber was published in [Le Kien et al. \(2004\)](#). However, the idea to use a two-color far off resonant dipole force with evanescent fields to create a potential for neutral atoms was proposed by [Ovchinnikov et al. \(1991\)](#) as a new kind of gradient light force trap in contrast to strongly focused Gaussian beams in free space.

³ The author master's thesis co-director.

Aside from the well-known possibility to use evanescent fields to trap atoms through far-off-resonant dipole force near a surface, it is primordial to understand the advantages of optical nanofibers through the main characteristics of the atom traps : the trap depth, the trap limited coherence time and the heating trap lifetime.

As mentioned before [Cook and Hill \(1982\)](#) suggested to reflect slow atoms by a non-uniform evanescent light field penetrating outside a dielectric surface through total internal reflection. Yet, they discussed only the case of a blue-detuned light field but introduced the concept of gravitational cavities which all led latter to the idea of atomic cavity with light-induced mirrors [Balykin and Letokhov \(1989\)](#). The first experimental realization of an atomic mirror using blue-detuned evanescent field to reflect a thermal atomic beam was reported in [Balykin et al. \(1987\)](#). Soon, it was realized naturally that the reflection of atoms could be made atomic-state selective as the detuning between the light field depends on the atomic state and its sign can revert, that is, the evanescent field can attract the atoms towards the dielectric surface if red-detuned which leads to atomic diffuse reflection instead of specular reflection as in the case of blue-detuning. This was demonstrated in [Balykin et al. \(1988\)](#) by selectively reflecting the two hyperfine ground states ($3S_{1/2}$, $F=2$ and $F=1$) of thermal sodium beams. This development triggered the idea to combine two evanescent fields with different atomic detunings to create an atomic trap [Ovchinnikov et al. \(1991\)](#).

The main idea here is to produce a short-range repulsive force and a long-range attractive force, similar to the repulsive and attractive forces acting between two atoms in a molecule.

— Yuri B. Ovchinnikov

(Balykin et al., 1988) (also give expression for dipole force with log, well.. (Cook and Hill, 1982) also does)

The russian group has been very prolific in the pioneer development of the manipulation of atom with light. The previous proposal yet suggested in conjunction with the use of prisms highlight the characteristic of such trap which helps to bring atoms very close to a dielectric surface in a tiny trap volume ($V \sim 10^{-10} \text{ cm}^3$) with trap lifetime bigger than a second. Tiny trap volumes⁴ help to reach the Lamb-Dicke regime necessary for resolved sideband cooling for instance. Instead of using the evanescent modes of a flat planar dielectric surface, the group of Jeff Kimble suggested to build a two-color evanescent light dipole trap for neutral atoms based on a pair of whispering gallery modes breathing at the surface of quartz microspheres [Mabuchi and Kimble \(1994\)](#). Atoms can then be confined in stable orbits in such toroidal potential and strongly coupled to the microsphere modes.

[Barnett et al. \(2000\)](#) proposed to trap atoms above a rectangular optical waveguide ($0.8 \mu\text{m} \times 0.2 \mu\text{m}$) which provides a trap depth of

⁴ which increase the trap vibrational energy spacing compared to a single photon recoil energy.

200 μK for Cesium atoms based on two evanescent fields with different polarizations in the single fundamental mode of the waveguide. Atoms could then be trapped in a non-diffracting linear channel or pipeline at a distance of $\lambda/2$ above the dielectric slab surface.

We note that in this proposal the important trap properties are studied and the trap light induced optical Stark shift on the Zeeman magnetic sublevels or fictitious magnetic field is presented.

From all this study of history we learn a vital parameter to consider when designing a two-color evanescent field.

Barnett's elegant proposal as a free-standing optical waveguide is demonstrated not suited for integrated optical waveguide or photonic circuit. The reason, yet simple, is extremely important in view of the advantage of nanofibers. [Burke et al. \(2002\)](#) theoretically investigated the design of neutral atom nanotraps with photonic circuit. One learns that Barnett's two-color design is sensitive to scattered light from any defect of the waveguide structure. Indeed, the net trapping potential formed by the two color evanescent fields is small while the absolute force each individual field produces is great from their great light power. The trap is the result of a very delicate balance and any perturbations of these large powers will result in a great effect on the trap. A single-color trap would be of great advantage in that respect such as the dark-spot blue-detuned trap implemented in hollow core fibers for instance.

All this development leads us to identify a figure of merit for two-color evanescent traps, the normalized decay length difference Λ , and qualitative behaviours with the following simple treatment. Lets consider that the evanescent mode function can be well estimated by an exponential, as is the case for the planar prism in [Ovchinnikov et al. \(1991\)](#). The one dimensional net trapping potential from the superposition of a blue-detuned light field and a red-detuned one, with respective decay lengths b and r writes

$$U(x) = Be^{-x/b} - Re^{-x/r},$$

where B (resp. R) is proportional to the square of the electric field intensity of the blue-detuned (resp. red-detuned) field at the dielectric surface. One easily finds that the single extremum of the total potential is given by

$$x_m = -\ln\left(\frac{bR}{rB}\right) \frac{br}{r-b} = -\ln\left(\frac{bR}{rB}\right) \frac{r}{\Lambda},$$

where $\Lambda = (r-b)/b$ is the normalized difference decay length.

A minimum trap potential outside the dielectric exists for $r > b$ (as is the case for the nanofiber fundamental mode where higher wavelength penetrates deeper in the cladding) provided that the light intensity of the blue field at the surface is higher than that of the red, $B > R$. For a fixed optimization of both field intensities, the trap minimum approaches the waveguide surface the higher Λ is. After some math-

emational gymnastics, one can show that in addition the depth of the trap

$$U(x_m) = -Be^{-x_m/b}\Lambda = -\Lambda B \left(\frac{b}{r}\xi\right)^{r/(b\Lambda)},$$

scales linearly with Λ for small values, where $\xi = R/B$ is the ratio of the field intensities at the waveguide surface. By increasing Λ , the potential gets deeper which also means that one can reduce the total light power (red+blue) invested. This in turn will increase the trap coherence time by reducing the scattering rate (for fixed atomic detunings). It will also make the trap depth more robust with respect to power fluctuations in each color. Therefore, the strategy in designing a two-color trap would be to get the highest possible Λ within the atomic line and dielectric geometry constrains.

... see goodness factor in (Barnett et al., 2000)

This is where one of the advantage of thin optical fiber comes greatly at the foreground compared to other systems. The decay length constant of the evanescent guided modes of a nanofiber can be characterized as shown in previous chapters by the reciprocal of the transverse radial wave-vector component $q = k_0\sqrt{\beta(\lambda)^2/k_0^2 - n_2^2}$ with $k_0 = 2\pi/\lambda$. When the diameter of the core is small enough, $1/q$ becomes a rapidly varying function of the light wavelength such that Λ augments within the range of the wavelengths that are allowed below the cut-off of the fundamental mode. We have for instance: $\Lambda_{blue} = 1/q = 0.20 \mu\text{m}$ for $\lambda = 780 \text{ nm}$ and $\Lambda_{red} = 0.44 \mu\text{m}$ for $\lambda = 1057 \text{ nm}$ for a nanofiber radius of 250 nm ($n_1 = 1.452$, $n_2 = 1$). This gives for the normalized decay length $\Lambda = 1.2$ to be compared for instance with $\Lambda = 0.47$ for the design of a one-dimensional trap above a rectangular dielectric waveguide Barnett et al. (2000). The previous values were given assuming a circularly symmetry mode of the nanofiber (with rotating polarization) whereas Barnett's was already optimized by considering two orthogonal polarizations in the single fundamental mode which differs in decay length (TM modes being closer to cut-off than TE modes). Clearly, due to the strong refractive index step at the fiber nanotapered, transverse linearly polarized mode breaks the symmetry which leads to a great anisotropy of the transverse intensity profile. See for instance figure 15.4.

One can then feel already that for a given total two-color light power and fixed trap wavelengths, the best strategy is to use two orthogonally *quasi*-linearly polarized mode in the fundamental mode to obtain the biggest relative difference in decay lengths, that is the biggest Λ . As seen above, a stable trap will happen along a direction where $\Lambda_{red} > \Lambda_{blue}$ as long as the intensity of the blue field at the fiber surface is the highest.

Based on the previous discussion it seems natural that further improvement of nanofiber traps will be found in the increase of Λ through the use of higher guided mode orders. In fact, by superimposing higher modes with different polarizations one could then create a deep and

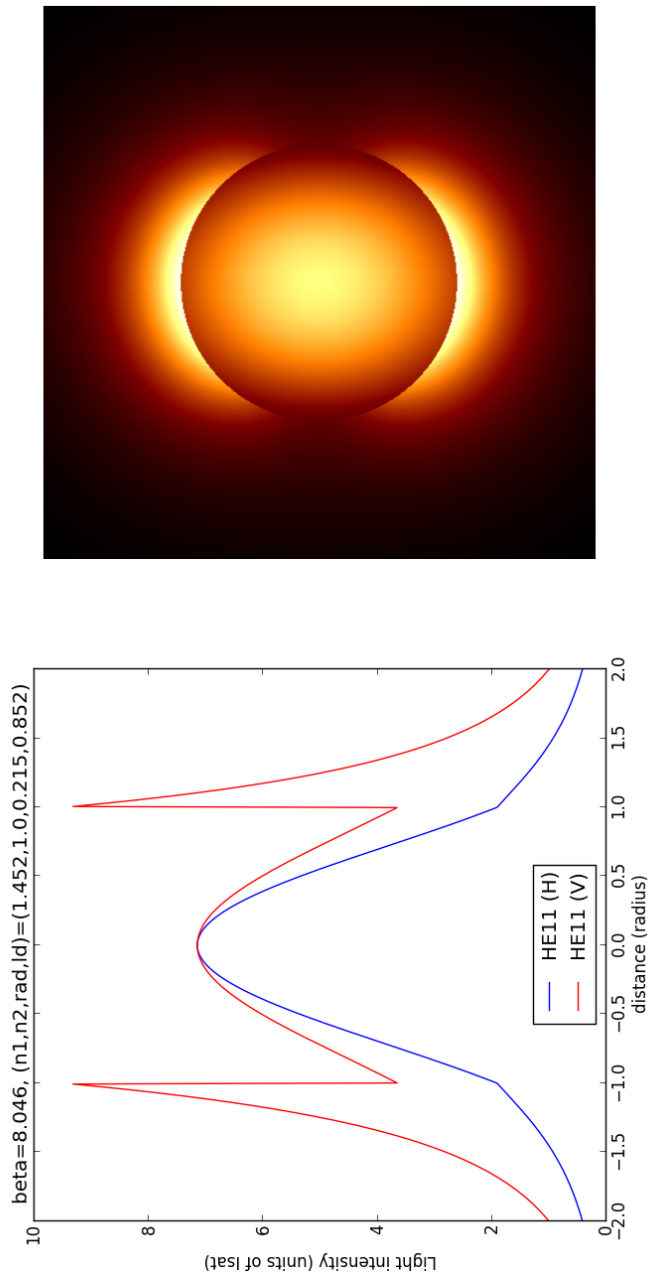


Figure 15.4: Transverse intensity profile of the fundamental mode with transverse quasi-linear polarization for $\lambda = 852 \text{ nm}$.

more robust single color blue-detuned trap, [Sagué et al. \(2008\)](#), in the spirit as the hollow core fiber traps for instance.

I will now briefly describe the two trap configurations we have implemented experimentally.

15.6 CATERPILLAR TRAP

The first two-color evanescent trap we have implemented consists in two running wave and co-propagating beams with orthogonal transverse linear polarization. From the above discussion and the quite elliptical spatial distribution of the intensity (see 15.4), the trap minima will form two lines diametrically opposed, all along and above the fiber surface. However, I will not reproduce here the theoretical model for that case as this one as a serious limitation. If you remember, we saw in chapter 7, that a transverse quasi-linearly polarized mode has a significant ellipticity in the longitudinal plane containing the fiber axis and the transverse polarization. As a result here for orthogonal transverse trap light polarizations, atoms will experience unwanted vectorial Stark shifts.

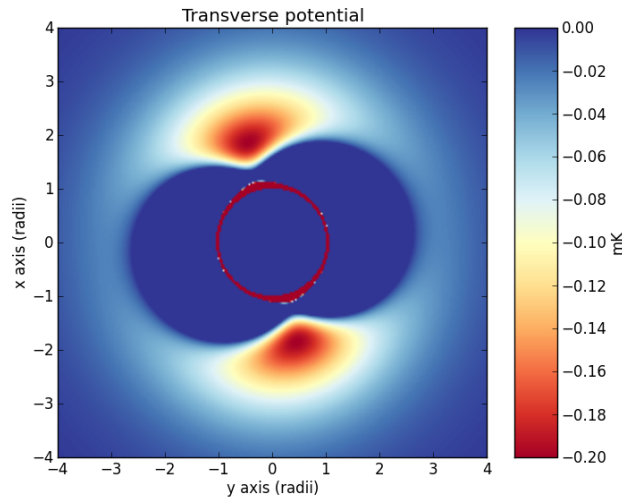


Figure 15.5: 20 degrees imperfection in the polarization orientation of the blue trap light with respect to the orientation of the red trap. Same parameters as in figure 15.6.

Instead, we have implemented a slightly different trap configuration where now the red-detuned color is made to propagate in both fiber directions in a such way that it forms a standing wave. In addition, the fact that the longitudinal wave components are in quadrature to the transverse wave components means that whenever the transverse counterpropagating waves interfere constructively, the longitudinal ones interfere destructively. In other words, at the anti-nodes of the standing wave, there is no longitudinal field and hence elliptical polarization.

The details of the trap configuration is shown in figure 15.6, where we have used our daily experimental trap power parameters. In short,

the trap forms two one-dimensional arrays of trapping minima, that is, two linear optical lattices.

The control of the polarization of the light field at the nanotaper is therefore important to create such traps. For instance, we show in figure 15.5 how the transverse potential is affected if the polarization of the blue trap is tilted by 20 degrees. In addition, this will affect the longitudinal ellipticity of the polarization at the trap minima.

It might appear challenging to control the polarization as the nanotaper was shaped in a nonpolarization maintaining fiber. There is a need to know and control the polarization of at least three different wavelengths, two for the trap (780 nm, 1057 nm) and at least one for probing on the D2 line of Cesium at 852 nm. This is primordial. Unfortunately, I do not have time to go into these details if I want to focus on the most important experimental results for this report. Our measurement and polarization control protocol is similar to Vetsch et al. (2012). In addition, I will still attempt to save a personal review of more advanced issues concerned with optical light shifts, magic wavelengths and the expected collisional blockage loading regime for these microscopic nanofiber traps in Appendix C.

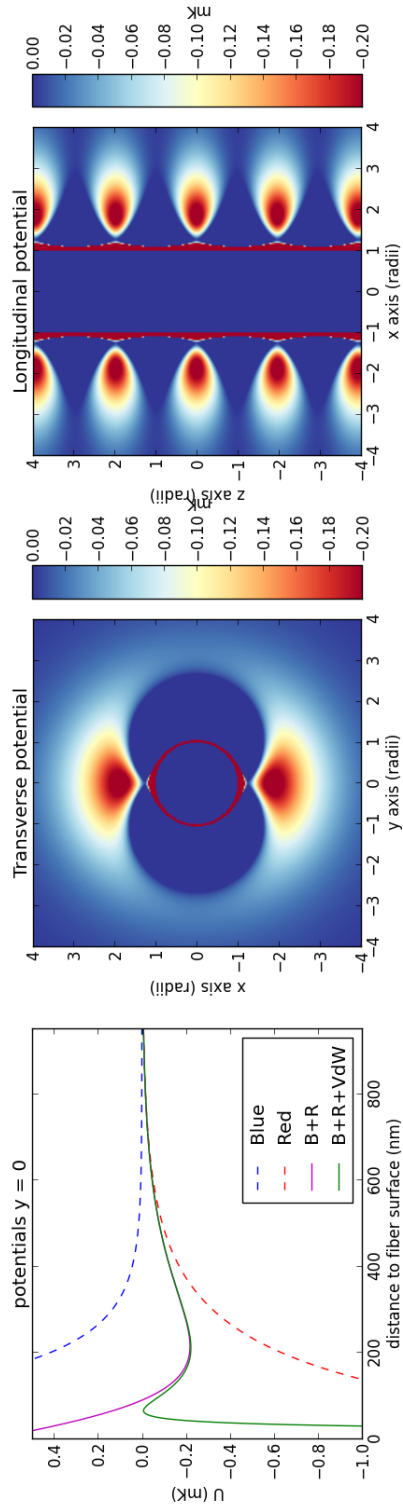


Figure 15.6: Calculated optical potential for Cesium atoms with a single running wave blue-detuned $\lambda_{\text{blue}} = 780 \text{ nm}$ light field with transverse linear x polarization, orthogonal to a red-detuned $\lambda_{\text{red}} = 1057 \text{ nm}$ standing wave light field with transverse linear y polarization. The nanofiber radius is $a = 250 \text{ nm}$ and the total trap powers are $P_{\text{red}} = 2 \times 1.1 \text{ mW}$, $P_{\text{blue}} = 12 \text{ mW}$.

16

DUAL-HETERODYNE DETECTION OF NANOFIBER TRAPPED ATOMS

*It is through science that we prove, but through intuition
that we discover.*

— Henri Poincaré

INTRODUCTION

In this chapter, we present experimental results on cold atoms successfully trapped in the evanescent field of a nanofiber. The key ingredient in this achievement was the implementation of the blue Sisyphus cooling (BSC) or gray molasses technique.

After some initial observations on atoms trapped in a running wave trap configuration, we load cold atoms in an optical lattice created in the evanescent field. More precisely, we create two one-dimensional optical lattices within the fundamental mode of the fiber. Finally, we introduce a new and somewhat natural progression of the detection method compared to earlier chapters. We report the first real-time detection of atoms in a nanofiber trap with a precision measurement limited by the intrinsic quantum noise of the probe light.

Then, we extract experimental information that will be relevant in view of atom number measurement, quantum state tomography and spin-squeezing.

16.1 TOWARDS TRAPPING ATOMS

Our first attempts at trapping atoms in the evanescent field of the nanofiber were focused on using one the simplest trapping configuration, a single running wave red-detuned light field (1057 nm) with transverse quasi-linear polarization together with a single running wave blue-detuned light field (780 nm) with orthogonal transverse quasi-linear polarization.

16.1.1 *Balancing light shifts*

With the experimental observation of the effects of such fields on MOT atoms as reported in chapter 14 with the help of the superheterodyne experimental technique, the strategy towards confining atoms near the fiber surface using these dipole forces was first to observe whether the reduction in optical depth and broadening effect due to the red-detuned field alone (attractive force) for instance could be compensated by an appropriate amount of power of blue-detuned light (repulsive force). The next step would be to increase the delay between the atomic signal measurement and the switching of the MOT forces to see whether cold atoms remain in the evanescent field without MOT confinement.

As shown in figure 16.1, the first step was indeed possible and this seemed a promising starting point to trap atoms.

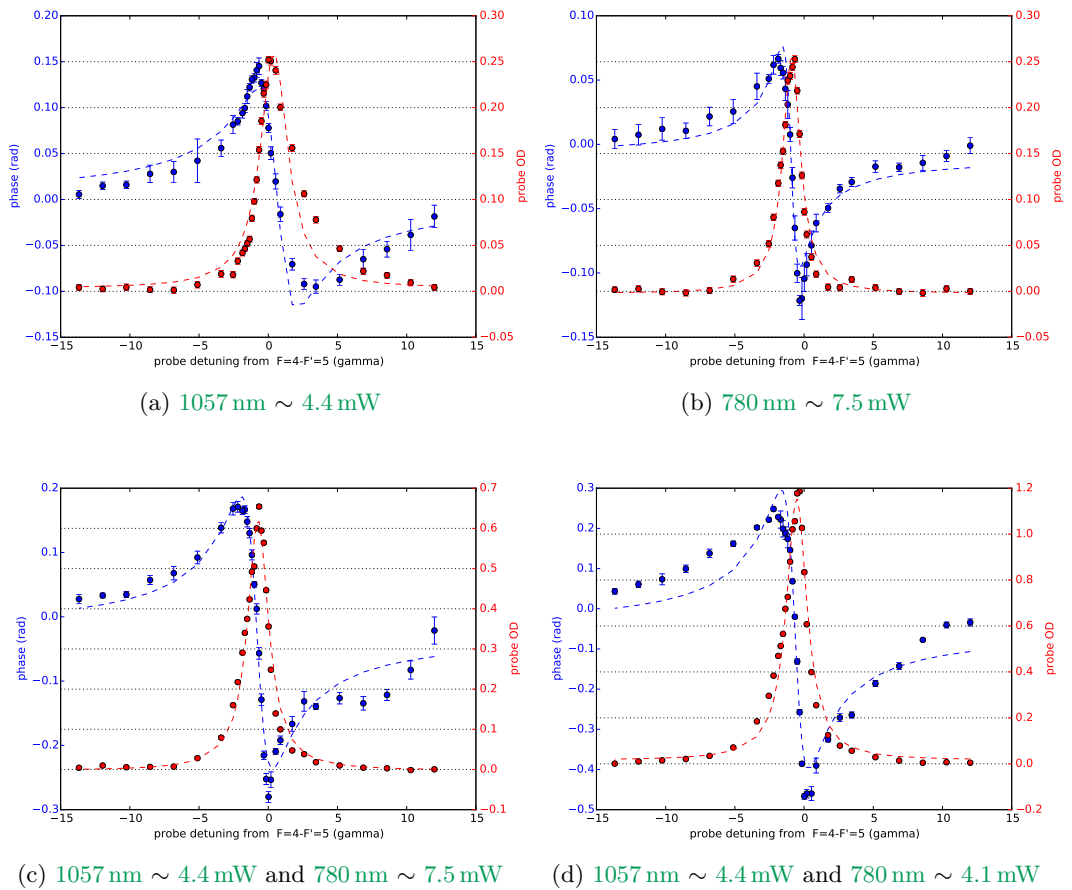


Figure 16.1: Recovery of optical depth and reduction of broadening through balancing of attractive and repulsive light shifts.

However, I started to notice little dimples in the blue side of the phase dispersion signal as in figure 16.1 (c). We discuss this in the next section.

16.1.2 *Unforeseen effect*

A finer scan of the atomic response with shorter probe frequency steps in the blue side of the atomic resonance revealed a somewhat peculiar dispersive step. This is shown in figure 16.2. Note that I would not have been curious to zoom in that frequency region with the knowledge of an atomic transmission signal alone where there was no noticeable effect.

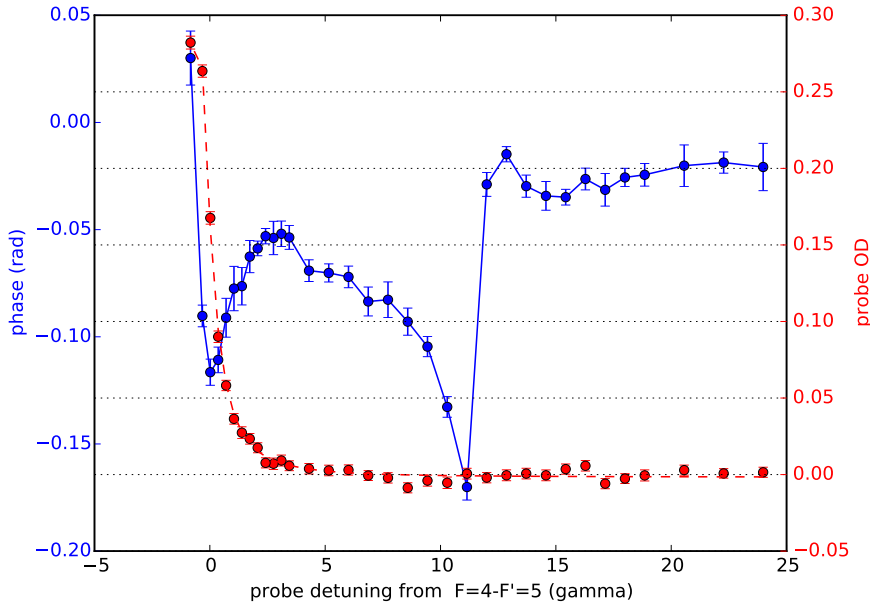


Figure 16.2: Atomic dispersion without absorption ? 1057 nm \sim 4.0 mW and 780 nm \sim 8.2 mW, MOT off measurement delay 4 ms

This relatively sharp feature in the atomic dispersion happens at the interesting blue detuning of $\simeq 12\gamma$ which is equivalent to the frequency shift of 62.5 MHz between the probe field frequency (+1 AOM diffraction order) sent into the nanofiber and the optical local oscillator used for the heterodyne detection. By using the -1 AOM diffraction order to probe the atoms, the atomic feature is now observed on the red side of the atomic resonance at a detuning of about $\simeq -12\gamma$ from the atomic resonance. After a thorough investigation of the probe light spectrum and any AOM leakages that I shall touch upon later, the origin of the observed effect was to be found elsewhere. This led me to find one of the most cumbersome paradoxical yet limiting effect not written in textbooks. Basically, enough photons from the optical LO impinging on the photodiode of the detector used for heterodyne detection can be scattered back into the probe mode and back into the nanofiber mode at the atoms location. Even by tilting the photodiode, adding optical isolators on the probe path and using the high quality optical elements is not necessarily enough. The idea of the optical LO is to be sufficiently strong to amplify the very weak probe field. Optical LO powers are in

general in the order of a milliwatt. Cesium atoms are already saturated by a few picowatt near the fiber surface which requires a lot of efforts to have a high rejection ratio of backscattered light into the probe mode. Of course, the probability to absorb such photons decreases as the detuning square $1/\Delta^2$. Only when the LO photons approaches the atomic resonance as in figure 16.2, the upshifted probe interrogating the atoms at $\Delta \simeq +12\gamma$ experiences atoms perturbed by the now resonant LO photons (red-shifted to the probe by exactly 12γ). This effect may actually be interesting to exploit as the field probe experiences a controllable and significant dispersion (delay) without being absorbed. Using a SPCM to measure the amount of LO photons scattered back into the nanofiber mode, we managed to reduce it to an average photon flux of 10 kHz for about 700 μW of optical LO power at the heterodyne photodetector.

Although we found in figure 16.1 settings for which a good (high optical depth, little broadening) atomic signal seems to be recovered for a given trap power balancing, the observed resonant optical depth as a function of the time delay between the measurement and the end of the MOT phase decreases as rapidly as the MOT expansion signal observed until now. This suggested that atoms are probably too hot compared to the prepared trap depths. We could not simply increase as much as one wants this trap depth by increasing the trap light powers. We indeed mentioned elsewhere in this thesis the observation of the thermal expansion of the nanofiber and a beginning of non-linear behaviour at about a total power of 15 mW above which we believed the fiber would break. This always forced us to be very careful and an extra heterodyne interferometric detection of the fiber length was designed in addition using the red trap light which would turn all the lasers off in case the nanofiber length will reach a limit of a few hundreds of micrometer.

Based on the hypothesis that the atoms were too hot and that the operation of a MOT is not necessarily compatible with the simultaneous presence of microscopic dipole traps, we modified the MOT setup and built extra control to implement BSC.

16.1.3 Blue Sisyphus cooling

Having done my Bachelor thesis with Denis Boiron and Chris Westbrook (Alain Aspect's Helium BEC group in Paris), I was familiar with the idea of blue Sisyphus cooling also known as gray molasses, Boiron et al. (1996, 1998), which allows to reduce the kinetic energy of atoms below the Doppler temperature. BSC is a phenomenon rich in physics that I will not cover but only state what we did experimentally. The initial standard bright MOT setup was adjusted to basically invert the role of the cooler and the repumper laser. For a duration of 20 ms, we create a linear ramp that reduces the frequency of the cooler light by about 62 MHz, red-detuning it away from $|4\rangle \rightarrow |5'\rangle$, and now blue-detuned

to $|4\rangle \rightarrow |4'\rangle$. The frequency of the repumper is also ramped down by about 12 linewidths in 15 ms, starting at the same time as the previous ramp, while its power is also linearly attenuated to zero, contrary to the cooler. The gradient magnetic field is also ramped down to zero during the repumper transient. Note that during this operation, the two-color evanescent dipole trap light is on and their powers adjusted as above. BSC results in sub-Doppler cooled atoms which have been transferred to a dark state for the cooler, namely the hyperfine ground state $|F' = 3\rangle$. At the end of the sub-Doppler cooling technique, any remaining MOT light is turned off and we let the atoms evolving in the dark. After some waiting time, weak quasi-resonant probe light is sent through the nanofiber to perform the continuous heterodyne detection of probe absorption while the repumper light is turned on to observe any potential dark state atoms present in the evanescent field. We report in figure 16.3 the first data acquired.

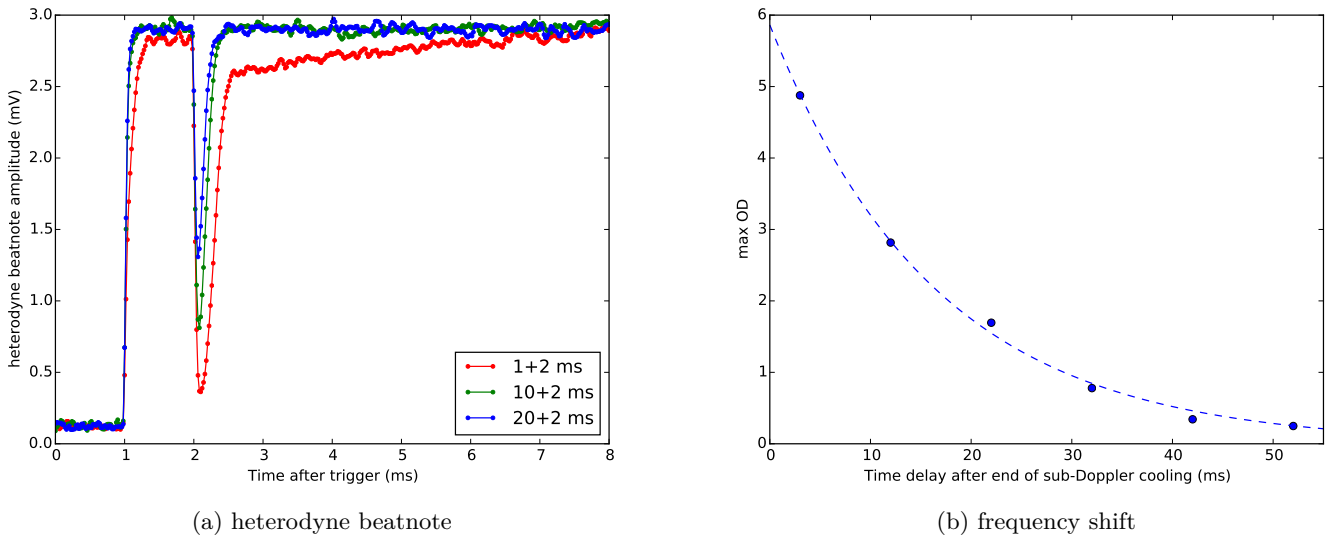


Figure 16.3: (a) Continuous heterodyne beatnote (10 kHz bandwidth). The elapsed time between the end of the sub-Doppler cooling where all MOT light and magnetic gradients are off and $t = 0$ ms is indicated in the legend, after $t = 1$ ms the probe is turned on, after $t = 2$ ms repumping light is turned on (b) decay of the quasi-resonant optical depth versus repumping waiting time. 1057 nm ~ 4.0 mW and 780 nm ~ 8.0 mW.

The first observation of nearly 5 times higher optical depths than observed without the sub-Doppler cooling together with a 1/e (OOE) decay time of about 16.5 ms (figure 16.3 (b)) gives strong support in favor of the success of the transfert of cold Cesium atoms in the evanescent dipole trap. We measured with the superheterodyne technique the absorption and dispersion curves across 80 linewidths that I will not report to lighten this section. However, the position of the atomic res-

onance is observed slightly blue-shifted compared to the resonance in absence of sub-Doppler cooling by ~ 2 MHz (or ~ 100 μ K). As shown in figure 16.3 (a), the probe (field) transmission is seen with two different dynamics when probing the atoms shortly after the end of the sub-Doppler. One observes a slower decaying tail but also an attenuation of the probe transient when turning the probe AOM on at $t = 1$ ms where the trapped atoms have not been repumped into the probe transition ($t = 2$ ms repumper on). We attribute this signal to residual atoms from the initial MOT reservoir which have not been transferred into the dipole trap. It takes a few milliseconds for the residual MOT cloud background to expand and fall due to gravity. The relatively short lifetime of the absorption dip indicates a relatively strong effect (heating) of the probing light (here ~ 30 pW) on the atoms. This is why I would like to highlight that this first data acquired do not represent an optimum configuration of all trap parameters. We will see later in this chapter how much this signal, constituting a good starting point, has been improved.

16.2 RUNNING WAVE TRAP

We explored many parameters (e. g. influence of probe polarization etc) to improve the optical depth and to have an experimental understanding on the sensitive ones. Here I would like to report the maximum optical depth observed for 51 different trap power configurations, (see figure 16.4). For each couple of powers, we had to sweep the probe frequency across the atomic resonance in order to extract the resonant optical depth.

Based on all the previous achievement, we did not spend more time on this running wave trap configuration and directly set the next goal of trapping atoms in an optical lattice around the nanofiber for the appeal of trapping single atom per site in the collisional blockade regime and also in view to reject fictitious magnetic field induced by the red-detuned trap at the position of the atoms. Before I present our results in such system, I am going first to describe the method we have developed to detect in real time the atomic state populations in a minimally-destructive and homogeneous way (see chapter 1) in order to implement optical QND measurement in the future.

16.3 DUAL-HETERODYNE DETECTION

The detection method we are about to present was designed with having in mind the most stringent level of measurement precision, namely collective spin squeezing prepared by QND probing with light (see first chapter). Because this requires sufficiently high resonant optical depth while at the same time both the homogeneous interaction of the probe light with all the atoms and a low scattering probability per atom,

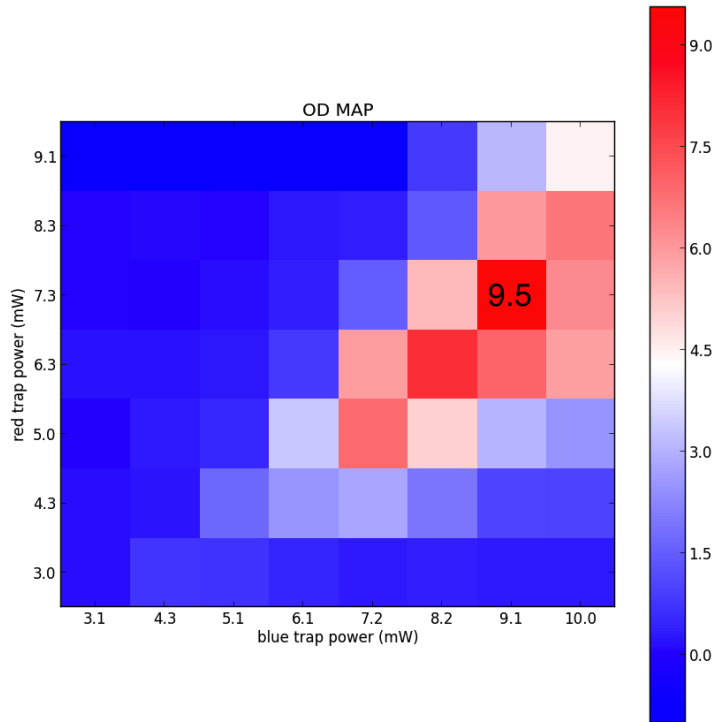


Figure 16.4: Evolution of the resonant optical depth as a function of the trap power configuration.

one needs an appropriate probe detuning for the dispersive detection of the atomic state. Actually, in the limit of large detuning Δ where the dispersive signal falls off as $1/\Delta^2$, the detuning is constrained with the probe power for a fixed scattering rate per atom. A constant integrated spontaneous emission keeps the SNR of the atomic state phase detection constant (see chapter 1). The relative freedom in detuning should be kept in mind even though the method I will present was designed with a fix detuning for simplicity of implementation.

Historically, this fix detuning was chosen as $\Delta = 67.5 \text{ MHz}$. However, because the RF signals were generated from a waveform with a DDS dividing a reference signal at 500 MHz , we decided to use $\Delta = 62.5 \text{ MHz}$ to avoid phase jitter on the signal as the frequency are in a integer ratio.

Because the atomic dispersion response for a two-level atom is antisymmetric (anomalous dispersion) across the resonance, two probes of light detuned symmetrically about the atomic resonance will experience atomic phase shifts of opposite signs. A measurement which would be sensitive to the phase difference $\Delta\phi$ between the two probes, would yield twice the atomic phase shift signal while at the same time sub-

tracting out any common-mode classical phase noise that both probes would experience propagating along the probe path (in the same spatial mode). The last point is very important as the probe path is host of many sources of noise (mainly acoustic, nanofiber vibrating). In order to observe the quantum projection noise of collective atomic states around the nanofiber in a non-destructive fashion, we need to be able to perform dispersive measurement in real-time at the light shot noise limit. We therefore need to suppress as much as possible classical noise within a desired measurement bandwidth. We have implemented a detection scheme which realizes a differential measurement of the phases of two probes based on the heterodyne technique. Let me highlight already that however the detected differential phase is $\delta\varphi = \Delta\phi/2$ such that one will not measure twice the atomic phase shift with this technique. However, as shown in chapter 2, the detection method removes the usual 3 dB penalty in SNR power of heterodyne compared to homodyne. That is the SQL of the method is identical to homodyne with a single probe with at the same time cancelling common-mode classical noise. In addition, the choice of the detuning to render the atomic ensemble transparent also took into account the possible perturbation induced by the presence of the neighboring other excited hyperfine levels of Cesium. As it is relatively far detuned enough to the other hyperfines lines, a nearly symmetric placement of the red and blue detuned probes (with equal intensities) across the atomic resonance will cancel the differential AC stark shift induced by the probes on the ground state, removing another source of measurement back-action.

In the following we give more details on how the technique works and show a simplified drawing of the experimental detection setup in figure 16.5.

16.3.1 *Detection setup working principles*

Starting from a laser light beam source with a frequency tuned to the resonance of the atomic transition $|4\rangle \rightarrow |5'\rangle$, two light beams are splitted off. One of them will be used as the optical local oscillator while the other one first propagate through an AOM to create two light probe beams from the +1 and -1 diffraction orders. By analogy with carrier-supressed frequency modulation, we will name the + diffraction order the upper sideband (USB) and the - diffraction order the lower sideband (LSB). The AOM diffraction operates in the non-linear Raman-Nath regime, for which the diffraction efficiency is low ($\sim 10\%$). With a zero input beam incidence angle, we create two symmetrically deviated beams about the zero-order diffraction beam. The three spatially separated output beams, are collimated and made parallel with a lens such that the separation distance between the sideband beams matches the one of a calcite beam combiner.

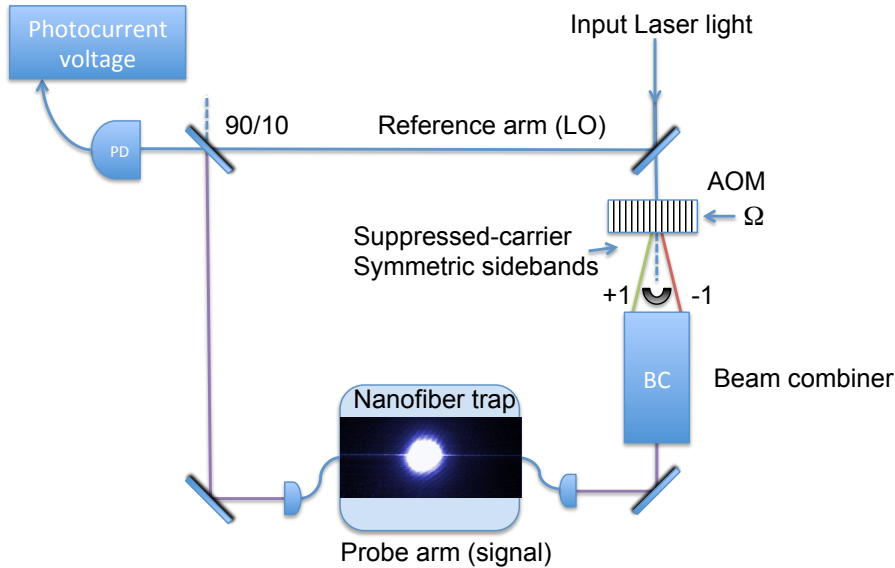


Figure 16.5: Simplified probing scheme based on two **LO** symmetric probe light fields recombined into a common spatial mode and common polarization.

Indeed, we use a birefringent beam combiner to create a beam containing both **USB** and **LSB** but free from zero-order light. This probe beam is spatially filtered by propagating in a fiber and then sent into the nanofiber.

The **AOM** is driven by an **RF** wave at a frequency $f = 62.5 \text{ MHz}$ ($\Omega = 2\pi f$) in such a way that the sidebands are symmetrically red and blue detuned¹ to the frequency of the optical local oscillator by $\pm\Omega$.

The optical path length difference between the probe path and of the reference path of the optical **LO** was made as close as possible to zero to operate the interferometer at the white light position (over several gigahertz).

Besides the symmetric placement of the probes about the atomic resonance, they are also symmetrically placed around the heterodyne local oscillator. This confers the homodyne sensitivity (first chapter) but also helps to understand simply the rejection of classical phase noise. Indeed, the interference between the probe beam containing the two optical angular frequencies $\omega_{\pm} = \omega_{\text{LO}} \pm \Omega$ with the optical **LO** (ω_{LO}) will give rise to a total beatnote signal oscillating at Ω given by the contributing sum of two independent beatnote of each sideband frequency with the optical **LO**. Of course, the light field will also contain optical beatnote frequencies around $2\omega_{\text{LO}}$ which are too fast for the detector. However, the interference between the two sidebands at 2Ω , independent of the optical **LO** will be detected. This signal will be relatively weak and most importantly it is not enhanced (amplified) by the optical **LO** (and we will filter it out). Similar to the superhetero-

¹ we defined the detunings in term of the angular frequencies.

dyne detection presented in previous chapters, the photocurrent signal is multiplied electronically by an RF local oscillator which is in phase with the driving field of the AOM producing the probe sidebands. Using an I-Q demodulator, we actually extract both in-phase and quadrature components of the signal with respect to the RF phase which can be adjusted.

We show in appendix D that after the required filtering of the unwanted frequency components at DC and at 2Ω , the in-phase and quadrature component (with respect to the RF LO phase) of the beat-note signal carried at Ω are proportional to following expressions.

In-phase component:

$$\begin{aligned}\mathcal{S}(t)^{in} &\propto \mathcal{E}_{LO} \{ \mathcal{E}_1 \cos(\Phi_{LO} - \Phi_1) + \mathcal{E}_2 \cos(\Phi_2 - \Phi_{LO}) \} \\ \mathcal{S}(t)^{in} &\propto \mathcal{E}_{LO} \{ \bar{\mathcal{E}} \cos(\Phi_{\text{ref}}) \cos(\Delta\bar{\Phi}) + \Delta\bar{\mathcal{E}} \sin(\Phi_{\text{ref}}) \sin(\Delta\bar{\Phi}) \}\end{aligned}\quad (16.1)$$

Quadrature component:

$$\begin{aligned}\mathcal{S}(t)^q &\propto \mathcal{E}_{LO} \{ \mathcal{E}_1 \sin(\Phi_{LO} - \Phi_1) + \mathcal{E}_2 \sin(\Phi_2 - \Phi_{LO}) \} \\ \mathcal{S}(t)^q &\propto \mathcal{E}_{LO} \{ \bar{\mathcal{E}} \cos(\Phi_{\text{ref}}) \sin(\Delta\bar{\Phi}) - \Delta\bar{\mathcal{E}} \sin(\Phi_{\text{ref}}) \cos(\Delta\bar{\Phi}) \}\end{aligned}\quad (16.2)$$

Where we have introduced the electric field amplitude of the sidebands $\mathcal{E}_{1,2}$ and their DC phase $\Phi_{1,2}$.

$$\begin{aligned}\bar{\Phi} &= \frac{\Phi_1 + \Phi_2}{2}, \quad \Delta\bar{\Phi} = \frac{\Phi_2 - \Phi_1}{2}, \\ \bar{\mathcal{E}} &= \frac{\mathcal{E}_1 + \mathcal{E}_2}{2}, \quad \Delta\bar{\mathcal{E}} = \frac{\mathcal{E}_2 - \mathcal{E}_1}{2}, \\ \Phi_{\text{ref}} &= \Phi_{LO} - \bar{\Phi}.\end{aligned}$$

When the intensities of the sidebands are balanced (equal) the previous expressions shows that a classical phase fluctuation is transformed into amplitude modulation (modulation which is in phase for both detected quadratures). A simple description of the signal will be the following. When the probe optical path length changes, the interference fringe pattern of one sideband with the LO moves left while the fringe pattern of the interference of the other sideband moves right by the same amount. As the total signal is the sum of this independent fringes, a change of optical path length translates into a change of total fringe amplitude. This also means a change in slope or sensitivity for differential phase measurement.

Indeed, because of common-mode phase noise rejection $\rightarrow \Delta\bar{\Phi} = \Delta\bar{\Phi}_{\text{atomic}}$. However, $\bar{\Phi} = \Phi_{\text{physical length}} + \bar{\Phi}_{\text{atomic}}$ where $\Phi_{\text{physical length}}$ is the probe path phase delay in absence of atoms. When the sidebands are symmetric around the atomic resonance and if the atomic dispersion profile is odd to a good approximation, we should nearly have $\bar{\Phi}_{\text{atomic}} \sim 0$ in a such way that

$$\Phi_{\text{ref}} \cong \Phi_{LO} - \Phi_{\text{physical length}}.$$

To have the best sensitivity over the atomic phase shifts we want to extract the term proportional to $\sin(\Delta\Phi)$. As we want the same coupling with the atoms for the two sidebands, we need $\Delta\mathcal{E} \sim 0$. Thus, measuring $\mathcal{S}(t)^q$ when $\Phi_{ref} = 0 [2\pi]$ would be adequate.

In simple terms, the technique is bad for measuring classical phase shift but good for anomalous dispersion.

16.3.2 Carrier suppression

To look at the frequency spectrum contained in the probe fiber sent to the nanofiber, we beat the guided light with an external laser reference (here the cooler). We show the beatnote spectrum in figure 16.6 recorded with a spectrum analyzer. We have modified the frequency axis to refer it to the external reference laser frequency (cooler) involved in the beatnote.

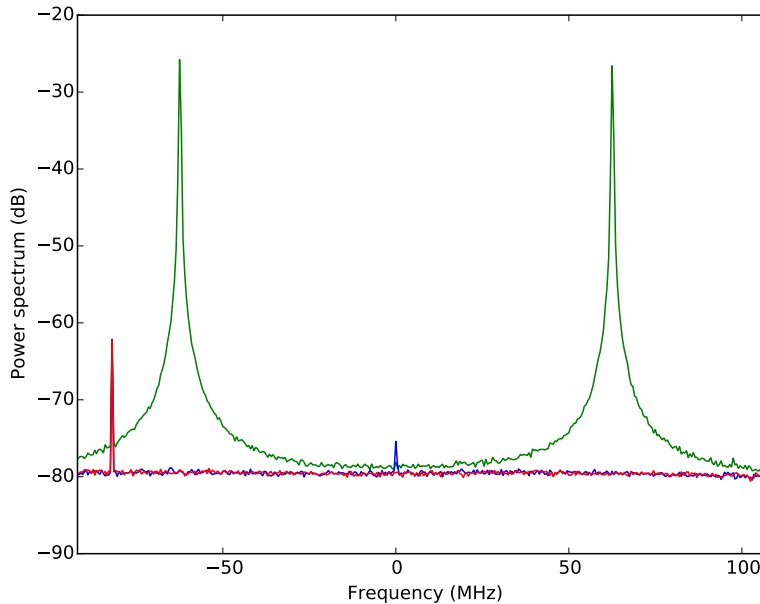


Figure 16.6: Frequency content of the total probe light field sent to the nanofiber trapped atoms. Resolution bandwidth 10 kHz (RMS). The origin here corresponds to the frequency of the external reference laser frequency involved in the interference. (See main text for legend)

When the probe light is blocked, the red trace gives a calibration or reference for the spectral content of the cooler. It reveals the presence of an 80 MHz sideband (red peak on the left) due to the way we sampled this light source from an AOM and this is not relevant here. When the probe light is unblocked but the probe AOM creating the sidebands is off (blue trace) we observe zero-order leakage. When the AOM is activated (green trace) we clearly observe the two symmetric

sidebands and we conclude that the carrier leakage is more than 50 dB less than the sideband power. In addition, part of this leakage light is converted in sideband energy when the AOM is activated. Therefore, any carrier photon are strongly suppressed. Although a single resonant leakage photon has $(1 + 4\Delta^2/\Gamma^2) \simeq 577$ more chance to scatter an atom than a sideband photon, there will be less than 10^{-5} carrier photons compared to sideband photons. Therefore the sideband photons will be the dominant source of scattering and heating effects in a given continuous measurement time. Here, I wanted to build the quickest and simplest (prototype) setup, which implies that the optical LO frequency is resonant to the atomic transition. However, it is possible to use two different AOMs to bypass this design.

16.3.3 Dither lock

As mentioned above, classical phase noise drift between the probe path and the reference LO path is converted into amplitude modulation of the differential phase measurement. This means that classical phase drift is equivalent to a change in sensitivity of the measured phase shift. To counteract this, I built a simple servo loop (dither lock) with the help of JA a to feedback the phase of the LO with a piezo mirror to always maximize the absolute value of S_{in} . Trust me, it hurts me not to be able to take more time in this important details, they are just too many of them in this single PhD time.

16.4 OPTICAL LATTICE TRAP

As mentioned earlier, as soon as the sub-Doppler cooling method worked and we managed to confine atoms near the fiber surface with the help of basic dipole trap forces, we tried to realize an optical lattice trap by using instead two counterpropagating red-detuned light field. By that time we gained more knowledge about the system and improved many noise sources. In the next chapter, we shall summarize all these points and gives a more quantitative analysis of the system when presenting the results connected to Béguin et al. (2014). Here I would like to present more naturally how all our ideas came about. Let me start by illustrating concretely the idea of the dual-heterodyne method by first showing the atomic response from atoms trapped in two one-dimensional optical lattices around the nanofiber. Using the superheterodyne technique and probing the atoms with only one of the two sidebands give the data shown in figure 16.7.

Each curve compiles only 10 averages. Aside from fitting very well to the two-level atom model, the recorded data reveal clearly the sign inversion of the dispersion for the two sidebands. With respect to the LO reference phase, for a given atomic detuning, the phase of one sideband is retarded while the other is advanced.

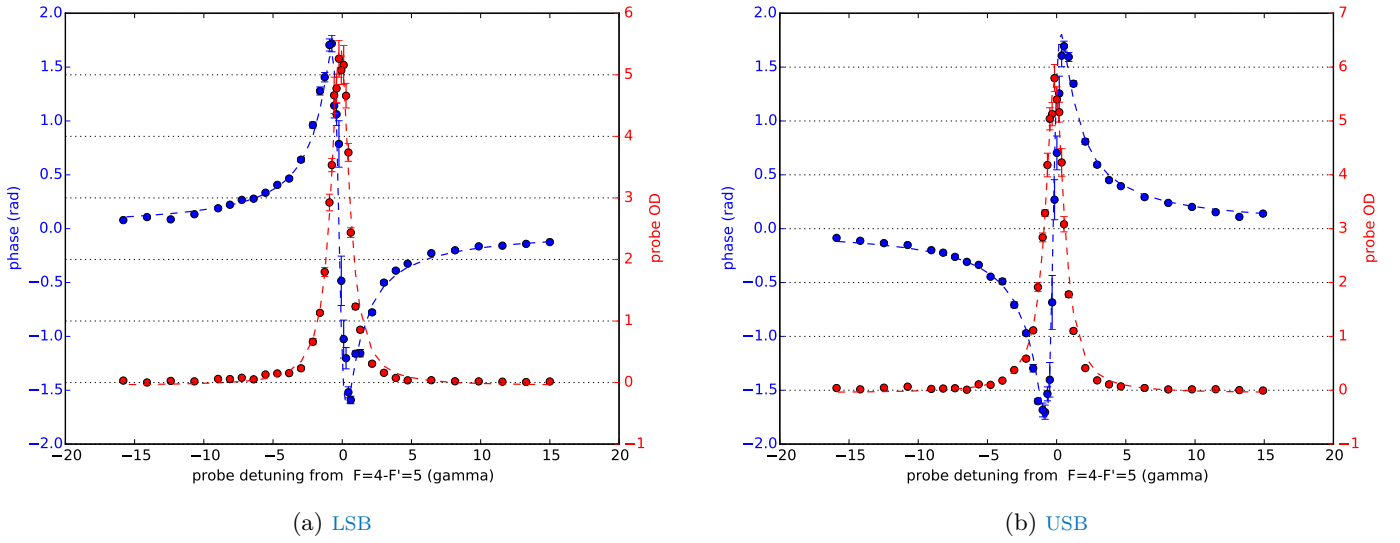


Figure 16.7: Atomic dispersion and absorption from lattice trapped atoms, detected with superheterodyning (a) Using the single LSB (b) Using the single USB. Each point is a 10 trap loading realizations average.

Now, It would like to show what happens when you send both sidebands together. After balancing the sidebands, activating the interferometer dither lock and adjusting the phase of the RF LO such that the demodulated quadrature component is zero in absence of atoms, we observed the first raw signals reported in figure 16.8. The step in the quadrature signal is equivalent to about 150 mrad close to what is seen in figure 16.7 for a single sideband.

I would like now to show some initial albeit imperfect data which demonstrates our first attempts at the real-time detection of atomic phase shift. In figure 16.9, we report the detected atomic phase shift taken 4 ms after the end of the trap loading. We show the measurement for 5 different total probe powers. Figure 16.9 (a) shows real-time or single shot measurement where a post-processing running average of 20 μ s was performed for clarity of the data. This time is also short compared to the observed quasi-exponential dynamics of the atomic signal. The continuous phase is extracted from $\tan^{-1} \mathcal{S}(t)^{in} / \mathcal{S}(t)^q$.

One first clearly notices that the noise on the recorded signals depends on the probe power. Using the first 2 ms signal without pumped atoms, we extract the Allan deviation shown in figure 16.9 (d). Briefly, from a single trace, we average the first data point over a time $\tau \leq 1$ ms giving us a mean phase φ_1 . We do the same on the successive data points giving us a mean phase φ_2 and then compute the difference $\varphi_1 - \varphi_2$. We then calculate the standard deviation of the difference over many traces. For uncorrelated photon shot noise limited phase measurement during τ , this Allan deviation should scale as the $\sqrt{\tau}$.

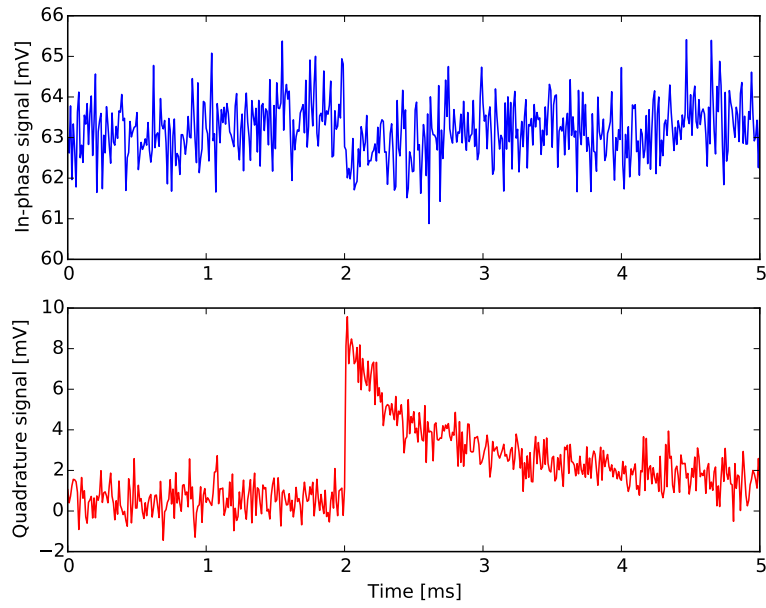


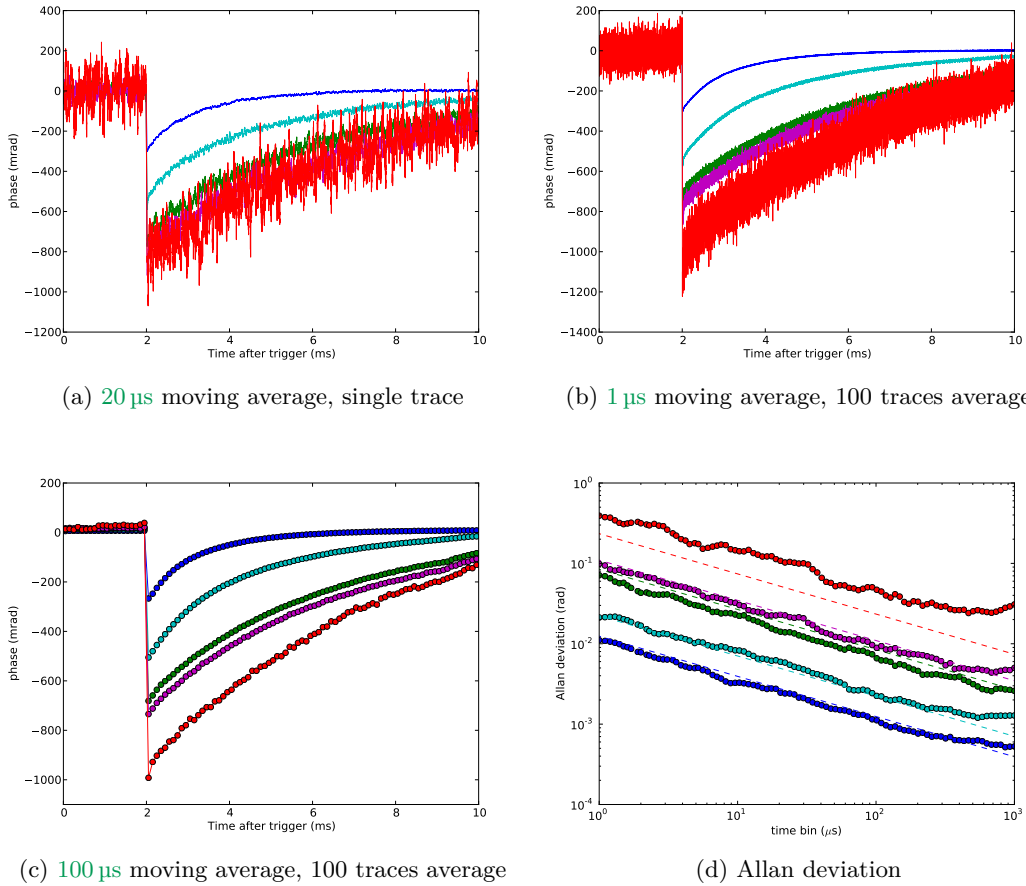
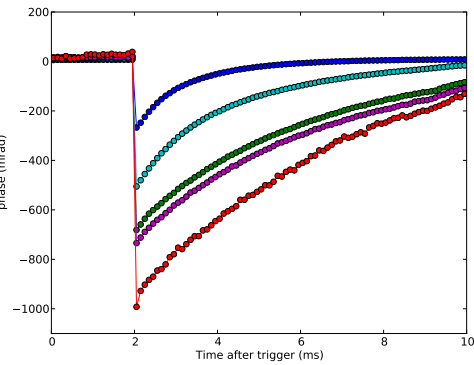
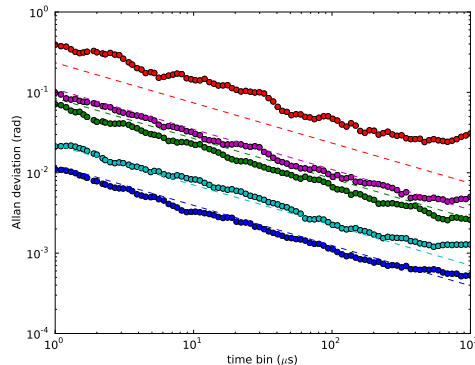
Figure 16.8: Raw demodulated quadratures, $\mathcal{S}(t)^{in}$ and $\mathcal{S}(t)^q$ (average over 100 traces). At $t = 2$ ms, the lattice trapped atoms are pumped into the probing transition.

In most cases, the detected phase noise scales as expected from the standard quantum noise limit due to the photon shot noise of coherent state. The dashed curves are not fits but the expected phase noise levels taking into account all the quantum inefficiencies for the presented measurement.

The phase noise starts to reveal a limit and a different scaling once the phase noise due to light shot noise become smaller than the sources of classical noise. In particular, we always observed a limit once the time scale or measurement averaging time was comparable to the dominant nanofiber vibration frequency of 280 Hz. The discrepancy between the expected phase noise from the expected probe power for the lowest power is caused by systematic errors in the creation of the very weak powers using stacks of ND filters which tend to affect the coupling efficiency of the probe beam into the nanofiber.

This systematic error is not a limitation for the future measurement and the probe powers to be used will be higher.

The maximum observed phase shifts are quite remarkable for one who observed the same order of magnitude with $N_{at} \simeq 10^6$ in the first setup with a free space dipole trap ensemble. Curiously, one may notice that the maximum observed phase shift depends on the choice of probe power in figure 16.9. This feature would indicate a saturation of the atomic transition for instance. However, the probe powers used were far below the expected saturation ~ 100 nW (see next chapter). Here, the probe sidebands are detuned from the resonance by 12γ and the

(a) 20 μs moving average, single trace(b) 1 μs moving average, 100 traces average(c) 100 μs moving average, 100 traces average

(d) Allan deviation

Figure 16.9: Continuous dual-heterodyne measurement of the atomic phase shift on the $|4\rangle \rightarrow |5'\rangle$ transition, for various probe powers. The atoms are initially in the dark state $|3\rangle$ and are CW repumped onto $|4\rangle$ at $t = 2$ ms. (red) 10 pW, (purple) 47 pW, (green) 78 pW, (cyan) 1.1 nW, (blue) 3.6 nW.

explanation for the observed effect is to be found in the simple preliminary design of the interferometer lock. The dither lock, which was implemented to stabilize the optical path length difference between the probe and the optical LO, used the probing beam itself. It required the probe light to be active all the time in the nanofiber and in particular during the sub-Doppler cooling transfert of cold atoms into the lattice trap. This readily affects the number of atoms which can be loaded in the trap. By adding the option to freeze the slow servo loop of the stabilization feedback, we could then turn the probe off during the trap loading phase which only last 20 ms, but also we could stop the lock while measuring on the atoms. In figure 16.10 and as well the following figures, we show phase shift measurement where this experimental issue was fixed. One observes quasi identical maximum phase shift from a few picowatt to a few nanowatt total probe power. Any slight differ-

ence most likely arises from drift of the total number of atoms loaded into the trap over the course of the many experiment realizations.

Contrary to 16.9 (a), which shows remarkable single-shot measurement, 16.9 (b) shows an important aspect which is the reproducibility of the experiments. It compiles 100 different lattice trap loading with the same trap light parameters. The main experimental variable which would affect significantly the accuracy of the measurement or drift of the observed phase shift is the change in the number of atoms caused by a variation of the MOT reservoir density.

So far, the measurement we have presented (fig 16.9 but also 16.10 (a)) were concerned with the continuous probing of the $|4\rangle \rightarrow |5'\rangle$ transition while repumping light is turned on. In figure 16.10 (b) we report measurement where only a pulse of repumping light was shone on the atoms at $t = 2\text{ ms}$ for a duration of $500\text{ }\mu\text{s}$. During this time, the probe light was also turned off. The data shown are only an average over 2 trap loadings and post-processed with a running average of $100\text{ }\mu\text{s}$ (or 10 kHz measurement bandwidth). Clearly, compared to the result in figure 16.10 (a), the atomic signal is now lost faster. This is particularly evident for the highest probe powers. It indicates that the dynamics of the atomic signal in absence of repumping light is dominated by probe induced optical pumping and heating for the relatively high powers. However, for the very weak powers, the decay is quite similar to the one with repumping light which would evidence in contrast that the dynamics of the atomic signal is not limited by those probe induced effects.

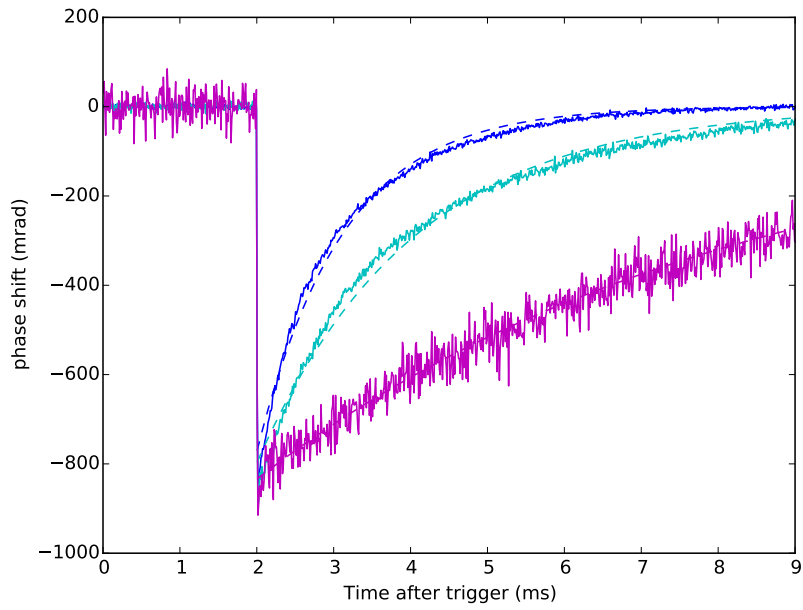
We will continue to discuss these important observations in more details in connection with the data reported in the next section.

16.4.1 *Open transition*

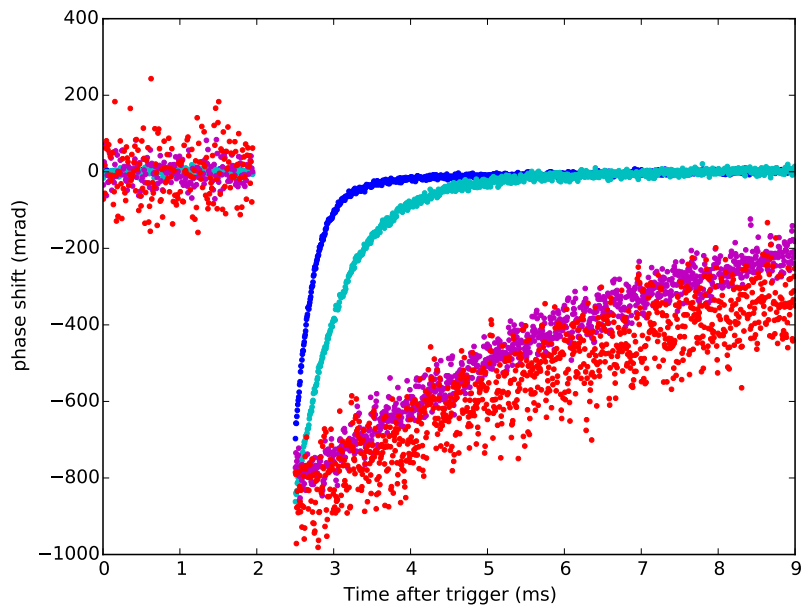
By changing the absolute frequency of the probe laser source, which is identical to the optical LO frequency, it is possible to perform the differential phase detection of the atomic ground state population $|4\rangle$ by probing around another excited hyperfine level. Here, we report such measurement for the $|4\rangle \rightarrow |4'\rangle$ transition (figure 16.11). The phase shift imprinted on the probe depends on the oscillator strength of the atomic transition. The cycling transition $|4\rangle \rightarrow |5'\rangle$ possesses the strongest of the D2 line. One may then obtain weaker atomic responses for another choice but also open more loss channels of atomic signal due to permitted optical pumping channels.

The transition $|3\rangle \leftrightarrow |4'\rangle$ is indeed allowed (dipole electric) and atoms initially in $|4\rangle$ which absorbed probe photons and are then excited to $|4'\rangle$, can decay back into $|4\rangle$ or $|3\rangle$.

In figure 16.11 we have reported three different configurations of repumping light while probing the atoms continuously with the dual heterodyne technique. At $t = 2\text{ ms}$, which corresponds to 4 ms after the



(a) CW repumping



(b) No CW repumping

Figure 16.10: Continuous dual-heterodyne measurement of the atomic phase shift on the $|4\rangle \rightarrow |5'\rangle$ transition with (a) and without (b) CW repumping, for various probe powers. ($100\ \mu\text{s}$ moving average on a single trace). (red) $10\ \text{pW}$, (purple) $47\ \text{pW}$, (cyan) $1.1\ \text{nW}$, (blue) $3.6\ \text{nW}$.

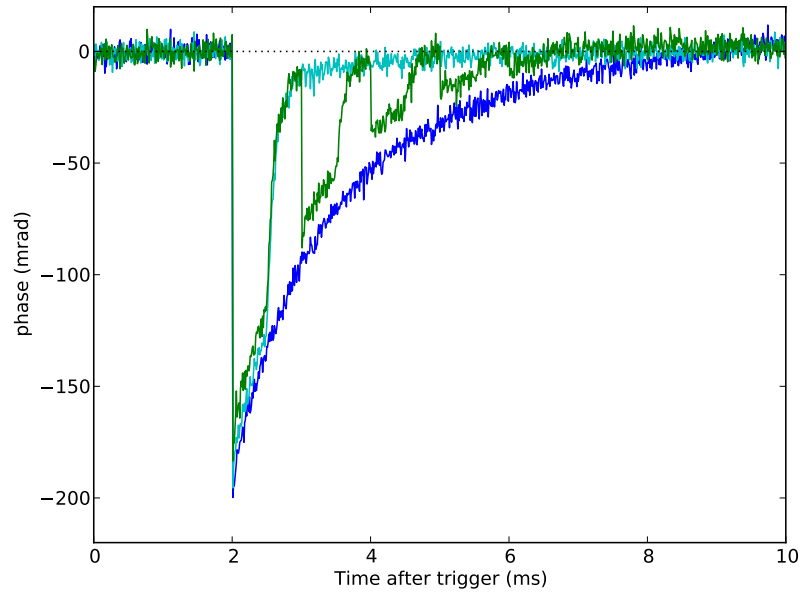


Figure 16.11: Dual-heterodyne probing on the $|4\rangle \rightarrow |4'\rangle$ transition for different repumping light configuration on the $|3\rangle \rightarrow |4'\rangle$ transition. (dark blue) CW repumping, (green) pulsed repumping, (cyan) single pulse of repumping light. (Average over 100 traces and $1\ \mu\text{s}$ running average). Probe power $2.8\ \text{nW}$

end of the sub-Doppler cooling trap transfert, the repumper was either turned on continuously (blue curve), turned on only for a pulse duration of $500\ \mu\text{s}$ (cyan curve) or pulsed with a repetition period of $1\ \text{ms}$ (green curve). The measurement were taken in that order such that the small reduction in maximum observed phase shift is due to reduction in the size of the MOT reservoir over time. This data shows that the dynamics of the atomic signal for the used total probe power here $2.8\ \text{nW}$ (detuning 12γ) is dominated by hyperfine pumping induced by probing. This depumping can be counteracted by continuous repumping or by restoring the dark state atoms at a later time which have not been lost from the evanescent field dipole trap.

Similar to the data presented above, we report on figure 16.12 and figure 16.13 the continuous probing on the open transition $|4\rangle \rightarrow |4'\rangle$ for continuous and single pulse repumping for the same various probe powers. The data were taken under the same condition as figures 16.9 and 16.10. The measurements confirm indeed the reduction of the maximum phase shift but also reveal an even faster loss of atomic signal. In figure 16.13, one can notice that, for the highest probe powers, the atomic signal quickly decays but then only slowly it reaches the initial phase shift level before optical repumping. We attribute this weak signal to an effect caused by residual atoms from the initial MOT reservoir around the nanofiber.

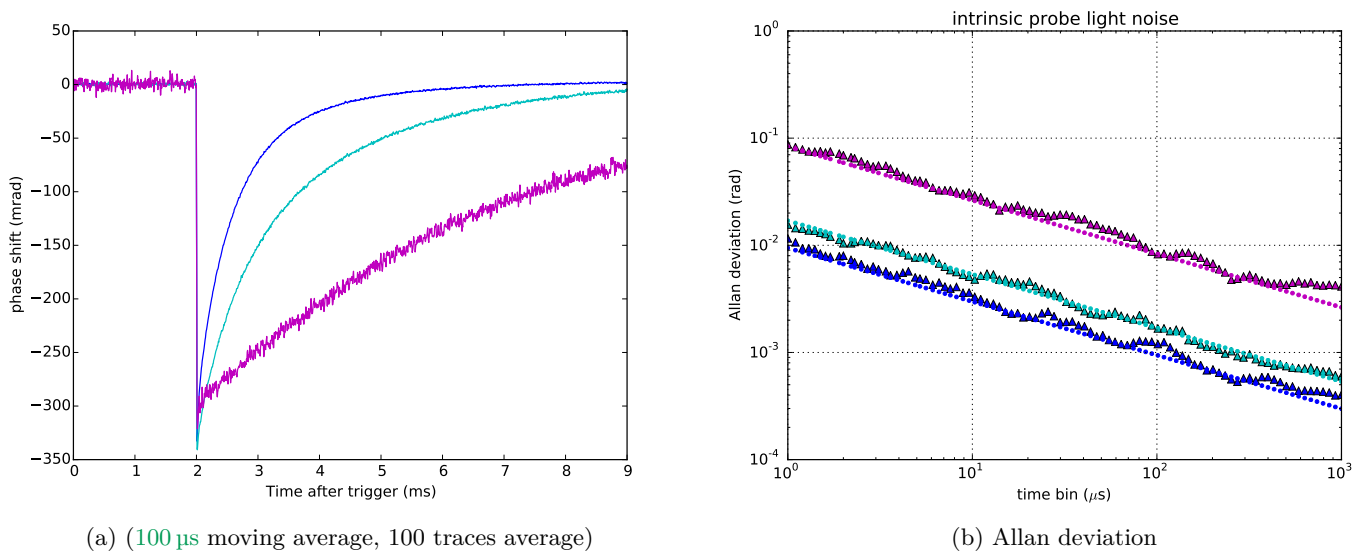


Figure 16.12: Continuous dual-heterodyne measurement of the atomic phase shift on the $|4\rangle \rightarrow |4'\rangle$ transition, for various probe powers. The atoms are initially in the dark state $|3\rangle$ and are CW repumped onto $|4\rangle$ at $t = 2$ ms. (purple) 47 pW, (cyan) 1.1 nW, (blue) 3.6 nW.

After all these observations, that we wanted to keep as qualitative as possible, we comment in the next section how they are important for many tasks to be realized with light-atom interfaces.

16.5 LIGHT-ATOM INTERFACE CHALLENGES

Atoms strongly coupled to the guided mode of an optical nanofiber are a very promising platform for many quantum optics experiments. And over the past three years, new and more interesting studies have been reported. However, no detection method was reported which would allow to observe the evolution of the atomic state in real-time. The other important point is that the measurement can be performed down to the fundamental intrinsic quantum noise limit of the probe light. On the one hand one, this one of the greatest benefit of the homodyne technique which allow to amplify even the probe vacuum state above the detector technical noise. On the other hand, this is due to the rejection of classical noise.

In order to improve the precision measurement of the underlying interferometric detection of the probe beyond the SQL, one may use non-classical state of light with lower intrinsic noise such as squeezed state of light. However, the phase noise will now depend on the phase. Indeed, one quadrature of the probe field will be squeezed but the other one will be anti-squeezed. In addition such non-classical states are in general very fragile with respect to energy loss and tend to decohere

rapidly into the environment. All of this is in contrast with coherent states which are robust probes. Coherent states stay coherent and only suffer from relaxation when coupled to the environment.

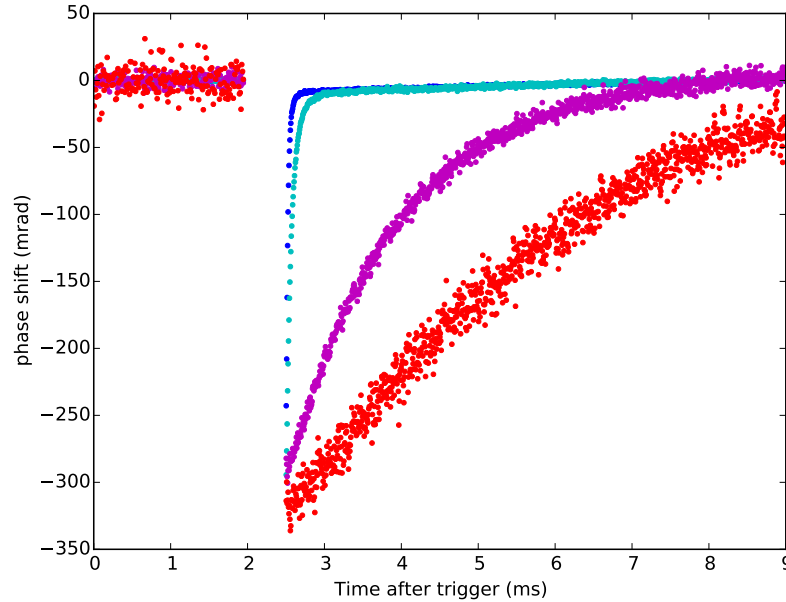


Figure 16.13: Continuous dual-heterodyne measurement of the atomic phase shift on the $|4\rangle \rightarrow |4'\rangle$ transition without CW repumping, for various probe powers. (10 μ s moving average, 100 traces average). (red) 10 pW, (purple) 47 pW, (cyan) 1.1 nW, (blue) 3.6 nW.

It is important to highlight that experimentally, a shot-noise limited measurement precision is bound to a lower limit (for the phase detection) given by residual classical noise. This classical noise is in general independent of the number of probe photons. Of course, it is always possible to reduce enough the number of probe photons to always make phase noise due to light shot noise dominate over the classical noise.

Although the observed phase shifts are quite high what is most important for many experimental challenges is often the signal-to-noise ratio per measurement bandwidth. At the light of the previously reported phase shift measurement, we would like to discuss in connection with [Béguin et al. \(2014\)](#), three main characteristic challenging levels in atomic state detection with light, namely atom number measurement, quantum state tomography of non-classical states and finally spin squeezing.

16.5.1 Atomic state population detection

If ones' goal is to detect simply the highest atomic signal or the number of atoms in the lattice trap in real-time, one can pump all the atoms into the ground state $|4\rangle$ and one can use the dual-color probing scheme

on the strongest transition $|4\rangle \rightarrow |5'\rangle$ to detect a phase shift. The latter being proportional to the atomic state population, a knowledge or calibration of the conversion factor (phase per atom) would give access to the number of atoms. We ignore classical phase noise for the moment and consider that the measurement is always light shot noise limited. Then the uncertainty on the number of atoms is ultimately limited by the light shot noise. For a given probe power, and if the atomic signal remains constant, one can keep on improving the measurement SNR by averaging the atomic signal over longer times which is equivalent to increasing the number of invested probe photons. However, the atomic signal only lives for a finite duration experimentally.

First of all, independently of any measurement process, the atomic signal is prone to loss of atoms which have a limited lifetime in the trap. This is in general mainly caused by collisions with the background atom gas in the chamber as well as heating from the only approximately conservative trap light forces. These effects can be considered in good approximation as random loss processes and characterized by a OOE lifetime τ_{bg} . Therefore, this means that there exists already a minimum probe power to achieve a given SNR. Indeed, the loss of SNR due to loss of atomic signal over time, independently of the number of probe photons, can be overcome by probing with higher power P and averaging the atomic signal over a duration short compared to the characteristic lifetime of the signal. While the mean signal would decrease exponentially with averaging time, the phase noise due to light shot noise would decrease as $1/\sqrt{Pt}$. The other way, using lower powers and longer averaging time, will eventually lead² to a poorer SNR. τ_{bg} represents therefore a minimum atomic measurement bandwidth limited by the temperature and the quality of the confinement of the atoms.

On the other side, one will encounter a maximum bound to the probe power, namely, the saturation power of the atomic transition for which the atomic response ceases to be independent of the probe power and suffers a reduction and broadening for example. Obviously, one should not ignore technical limitations and the photodetector should provide a light shotnoise limited photocurrent with linearity in response over the wide range of probe powers.

The dynamics of the atomic signal within this probe power range is even richer as we have ignored so far the dissipation which always come along with the dispersive interaction between the atoms and the probing light. Although the probe sidebands are far detuned from the addressed atomic transition, there is still a finite probability that the atoms will absorb probe photons. The polarizability of the atom depends on the atomic state and the excitation of the atoms will lead to a different phase shift. We will ignore this effect as the radiative

² there is a difference between an atomic signal decreasing exponentially with time or with a number of probe photons.

lifetime of the excited states is relatively short and we consider that far from the saturation power, the fraction of excited atoms is small. Atoms which are excited to $|5'\rangle$ can only decay back to first order to the ground $|4\rangle$ and therefore we do not lose atomic signal on average (closed transition). However, if an atom would be excited to $|4'\rangle$, it has the possibility to relax into a dark state for the probe and this will lead to a decrease of the atomic signal. The **LSB** which is blue detuned to the $|4'\rangle$ level can pump atoms into the hyperfine ground state $|3\rangle$. By using continuous repumping light one can counteract this internal state loss channel. However this may participate in probe-induced heating of atoms. Indeed, every time an atom absorbs incoherently a probe or repump photon, the atom experiences a recoil momentum. This increases its kinetic energy on average and eventually give it enough energy to escape the evanescent dipole trap, leading to a loss of atomic signal³.

The last two probe-induced mechanisms lead to an optical pumping rate and a heating rate which are expected to grow linearly with the input probe photon flux below saturation. For sufficiently high probe powers, it is possible therefore to overcome the dynamics of the atomic signal due to background collisions for instance. In this limit, where the rates are proportional the probe photon flux, the average **SNR** becomes characterized by the number of scattering events which happened during the averaging time.

The phase shift measurement we have reported above shows that our detection method is widely tunable in bandwidth. In addition, from the various probe powers, one can outrun the decoherence and loss not induced by the measurement itself already with probe powers that are still hundred times below the atomic saturation power. In this situation, the strength of the measurement will be given by the number of probe photons. The measured signal lifetime τ_{meas} for interrogation performed on the $|4\rangle \rightarrow |5'\rangle$ transition with continuous repumping will only be affected by probe heating and atomic decay in the dark (without probe) such that

$$\frac{1}{\tau_{\text{meas}}} = \frac{1}{\tau_{\text{heat}}(P)} + \frac{1}{\tau_{\text{bg}}} \quad (16.3)$$

where the heating rate $1/\tau_{\text{heat}}$ is expected proportional to the input probe photon flux. Clearly, in the limit of small probe powers (τ_{heat} large) the time constant $\tau_{\text{meas}} \simeq \tau_{\text{bg}}$ extracted from the small probe power data in figure 16.10 or in figure 16.9 would give access to the lifetime of the atoms in the trap. This should be independent of the probe transition (here either $|4\rangle \rightarrow |5'\rangle$ or $|4\rangle \rightarrow |4'\rangle$). Another way to measure this lifetime that will be free from residual probe induced effects, will be to record the maximum observed phase shift as a function of the time delay between the end of the sub-Doppler cooling transfer

³ In addition, our two-color evanescent trap is state-sensitive. It is designed to trap atoms that spend predominantly their time in the ground state.

of the atoms in the trap and the beginning of the phase shift measurement. We found $\tau_{\text{bg}} = 6.8 \text{ ms}$ for the data presented so far. It is also possible to measure the decay of the total resonant optical depth d_0 as a function of time in the trap via an absorption measurement. However, it becomes difficult to distinguish between nearly zero transmissions for large optical depths.

After a careful study of the trap light laser sources, we reduced significantly⁴ the intensity noise on the trap light which allowed to increase the lifetime $\tau_{\text{bg}} \simeq 20 \text{ ms}$ comparable to the values of $\sim 12 \text{ ms}$ reported respectively in Goban et al. (2012) without extra pulsed polarization gradient cooling in the trap.

For relative high probe powers such that $\tau_{\text{heat}}^{-1}(P) \gg \tau_{\text{bg}}^{-1}$, one can extract $\tau_{\text{meas}} \simeq \tau_{\text{heat}}(P)$. However, in absence of repumping light, the atomic signal suffers from an extra loss rate and we have

$$\frac{1}{\tau_{\text{meas}}} = \frac{1}{\tau_{\text{hf}}(P)} + \frac{1}{\tau_{\text{heat}}(P)} + \frac{1}{\tau_{\text{bg}}} \quad (16.4)$$

where the rate of hyperfine pumping in the dark state $|3\rangle$, $1/\tau_{\text{hf}}$, is also expected to grow linearly below saturation with the input probe photon flux. This rate could be then measured step by step for probe powers that outrun the decay in the dark, and performed with and without repumping light as we have reported earlier, i. e. $\tau_{\text{hf}} = (\tau_{\text{meas}}^{-1} - \tau_{\text{heat}}^{-1})^{-1}$. In the next section, we explain why these parameters among others are important to evaluate in view of important tasks for quantum information processing and quantum-assisted metrology with light atomic ensemble interfaces.

16.5.2 Quantum state tomography and spin-squeezing

We have seen in the first chapter of this thesis that for one of the most stringent tasks, namely collective spin-squeezing, not only do we want to detect an atomic state signal with a high SNR in real-time, we also need to be able to resolve as well the intrinsic atomic noise on the detect signal. In the situation where the atoms would be prepared in a collective coherent spin state, we need to be able to resolve the phase noise due to atomic projection noise imprinted on the probe light, above the phase noise due to light shot noise. This is more demanding but any significant finite κ^2 would allow to prepare the collective atomic state in a squeezed state. However, the last but not least challenging requirement is that the measurement should preserve the quantum state of the atoms while achieving the real-time projection noise precision measurement. The absorption of a probe photon will destroy the quantum superposition of the two ground states of an atom in the CSS. Therefore, the average number of scattering events per atom during the measurement has to be smaller than 1.

⁴ As quiet as a DC source of light over 20 MHz, which actually allows one to observe nanofiber torsion mode frequencies in the shot noise of the trap light.

However, for state tomography, which is essential to characterize the preparation of a target state, the measurement can be destructive and hence less stringent than spin squeezing. The idea there would be to measure the components (populations) of a given quantum atomic state onto a complete set of basis atomic states, for instance using the two clock states. However, for the best reconstruction fidelity, the populations of the basis states should not be mixed. Here, this means that when measuring the population in $|4\rangle$ via $|4\rangle \rightarrow |5'\rangle$, one should not repump population in the other basis state $|3\rangle$ into $|4\rangle$ which would bias the tomography. Therefore, probe-induced hyperfine pumping will be the limiting measurement back-action mechanism for tomography (when the heating rate is much slower than hyperfine pump rate).

In addition, for the characterization of non-classical states, for which a well-known and clear indicator of quantum interference is the reconstruction of a negative Wigner quasi-probability distribution, a minimum degree of squeezing of -3 dB is required. In the language of this thesis, we mean $\kappa^2 \geq 1$ or also that less than half of the total detected quantum noise should be due to light shot noise. And we have not mentioned the often imperfect purity of the prepared state to observe negativities such that realistically, higher degrees of squeezing will help.

In [Béguin et al. \(2014\)](#), we have shown through the experimental demonstration of -14 dB number squeezing, that all three challenging levels could be accomplished. In particular, we predicted through a pessimistic model that -8 dB would be available for quantum state tomography and we extrapolated that our probing method should allow for the preparation of less than -4 dB squeezed collective spin states. Of course, the last two points need to be realized experimentally and they have not been done so far in this new nanofiber system.

For a given optical depth per atom, the best achievable spin squeezing can be inferred from the number of atoms and the probe-induced scattering rate per atom. The latter cannot be extracted directly from τ_{meas} and the knowledge of both τ_{heat} and τ_{bg} for probing on the $|4\rangle \rightarrow |5'\rangle$ transition as atoms relaxing back to $|4\rangle$ after being scattered will not lead to a decay of the detected atomic signal. Of course, a proper measurement of the decoherence induced by probing will be a measure of the reduction of the Ramsey fringe contrast once quantum state preparation will be available. An estimation of the scattering rate leading to decoherence can however be inferred from measurement performed on the $|4\rangle \rightarrow |4'\rangle$ for which there is a fixed decay branching ratio from the excited state to either $|4\rangle$ or $|3\rangle$ and then extrapolating to the scattering rate when probing on $|4\rangle \rightarrow |5'\rangle$ from the knowledge of the relative line strengths.

Actually, this step gave us the idea to implement a robust and fast measurement method to count the number of atoms in the lattice trap. This allowed then to estimate the average single-atom coupling strength in our light-atom interface. A calibration of the average detected phase

per atom combined with both the real-time resolution and minimally destructive dispersive detection of the atoms allowed to prepare very narrow atom number distribution in the trap. We presents these experimental results in the next chapter.

SUMMARY

In this experimental and qualitative chapter, we wanted to show the steps we took in the development of a simple and working detection technique of atomic state populations. We also started by creating an optical lattice around a nanofiber, which was loaded via [BSC](#). This was an important experimental step. Then, we have reported the first real time measurements of atomic phase shifts ever observed in a nanofiber experiment. In addition, we managed to perform this dispersive continuous measurement at the light shot noise limit, with flexibility in measurement bandwidth. Then, we have shown the different dynamics of the atomic state population signal in presence of heating, optical pumping and background collisions.

NARROW ATOM NUMBER DISTRIBUTIONS IN ONE-DIMENSIONAL LATTICES

*It is far better to foresee even without certainty
than not to foresee at all.*

— Henri Poincaré

INTRODUCTION

In this chapter, we demonstrate the generation and detection of sub-Poissonian atom number distributions in optical lattices created in the evanescent field of an optical nanofiber. First, we use the versatile heterodyne detection to measure the absolute number of atoms in the nanofiber trap by recording optical pumping transients. Then, we use a calibrated minimally destructive dispersive detection of the atoms to prepare very narrow atom number distributions, which are estimated using the principles of continuous Bayesian filtering theory presented in the first chapter of this thesis.

The minimally destructive preparation of very narrow atom number distributions and the knowledge of its statistics in real time is a valuable asset for strongly correlated systems ([Eckert et al. \(2008\)](#)) and many advanced multi-atom experiments.

17.1 ABSOLUTE ATOM NUMBER

We could not resolve spatially (optically) the atoms in their single lattice site around the nanofiber using fluorescence imaging for instance. Instead, we interrogate the entire ensemble of atoms with light propagating in the fiber and we estimate the absolute number of atoms by measuring the field transmitted by the atoms.

17.1.1 *Saturation method*

In [Vetsch et al. \(2010\)](#), [Goban et al. \(2012\)](#) and in most recent experiments concerned with an [EIT](#) based memory using a nanofiber, the absolute number of atoms is estimated from a measurement of the total power absorbed by the ensemble of atoms. There, one exploits the

non-linear response of the atoms obtained by driving an atomic dipole transition ($|4\rangle \rightarrow |5'\rangle$) in the regime of probe light intensity saturation. The idea is that on resonance, a fully saturated Cesium atom radiates a nominal power on the cycling transition $|4\rangle \rightarrow |5'\rangle$ of

$$p = \frac{E_0}{2\tau_{\text{rad}}} \simeq 3.8 \text{ pW}.$$

Here, $E_0 = \hbar\omega_0 \simeq 0.233 \text{ aJ}$ is the energy of the 852 nm emitted photons and $\tau_{\text{rad}} = 1/(2\pi \cdot 5.234 \text{ MHz}) \simeq 30.4 \text{ ns}$ is the radiative lifetime ($1/2\tau_{\text{rad}}$ saturated decay rate) of the excited state $|5'\rangle$. Below saturation, the average power scattered by an atom is proportional to the input probe photon flux.

By monitoring the total absorbed probe power after propagation through the ensemble of atoms, as a function of the input probe power, one should observe two regimes. The absorbed power will first grow linearly with the input probe power until it progressively saturates when the fraction of atoms which are saturated by the input probe power becomes significant. Dividing the total absorbed power, corresponding to all the atoms being saturated, by p , will give an estimate of the total number of atoms. Although we can and did implement this method, we developed an alternative and robust technique based on optical pumping transients, which allows to estimate much faster the number of atoms with a good resolution and accuracy.

17.1.2 *Optical pumping transient method*

The atom number is determined here from optical pumping or dark state population trapping. At first sight, the simple idea behind this method is to measure the number of probe photons required to pump the trapped atoms in a dark state or to bleach the ensemble of atoms. The technique was brought to our knowledge by Jörg Helge Müller (JHM), based on the idea of the photon counting technique reported in Pino et al. (2011) for the detection of Bragg excitations.

We probe the atoms with a single sideband, which is resonant to the $|4\rangle \rightarrow |4'\rangle$ transition. The atoms, which have been excited to any Zeeman levels of the state $|4'\rangle$, can¹ decay back into either one of the two ground state manifolds, $|3\rangle$ or $|4\rangle$ (see figure 17.1). The lowest hyperfine ground state $|3\rangle$ of this three-level or Λ -type level system is relatively far detuned $\sim 9 \text{ GHz}$ from the probe frequency in such a way that we can neglect the interaction with the probe light on the allowed $|3\rangle \rightarrow |4'\rangle$ transition.

As a result, the atoms which relaxed into the dark state $|3\rangle$ will not interact any further with the probe light and hence will stop absorbing

¹ Note that the possible atomic population trapping into the forbidden transition $|4, 0\rangle \leftrightarrow |4', 0\rangle$ (for π linear polarization) can be avoided by a suited magnetic field orientation.

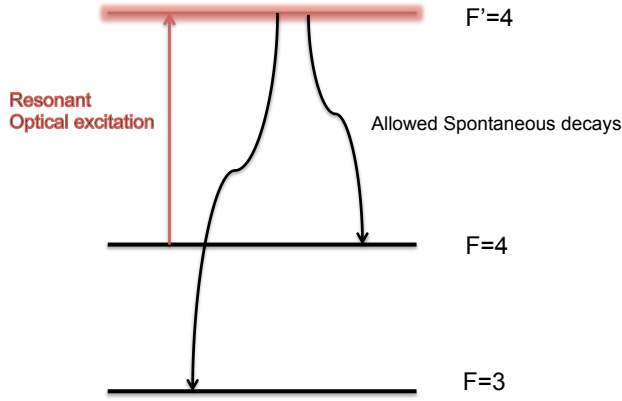


Figure 17.1: Three-level atomic scheme with resonant probing for atom number measurement based on dark state pumping.

probe photons. Starting initially with all the atoms in the state $|4\rangle$, the resonant weak probe light, which would be first completely absorbed and scattered by the optically dense ensemble of atoms, will have its transmission increasing again over time as the atomic population in $|4\rangle$ decreases due to optical pumping, until the full transmission of the probe light is recovered.

This method can be modelled quite simply below optical saturation of the atomic transition. According to Lambert-Beer's law, the output probe photon flux $\Phi_{\text{out}}(t)$ is given by the optical penetration depth of the atomic ensemble $d(t)$ as a function of the input probe photon flux $\Phi_{\text{in}}(t)$,

$$\Phi_{\text{out}}(t) = \Phi_{\text{in}}(t) \exp(-d(t)). \quad (17.1)$$

All the atoms are assumed to populate initially the state $|4\rangle$ and we introduce the optical depth per atom α_{at} such that

$$d(t) = N_{\text{at}}(t)\alpha_{\text{at}}. \quad (17.2)$$

The single-atom coupling strength α_{at} depends on the oscillator strength of the interacting atomic transition, here the $|4\rangle \rightarrow |4'\rangle$ transition. We assumed that α_{at} is independent of time and identical for each atom. $\alpha_{\text{at}} = \sigma/A_{\text{eff}}$ depends on the overlap between the effective atomic cross-section σ and the effective mode area A_{eff} of the evanescent probe field at the position of the atoms. In order to estimate the number of atoms in the trap from the number of missing probe photons, we need to know the average number of photon scattering events k required to transfert an atom from $|4\rangle$ to the dark state $|3\rangle$.

The evolution of the number of atoms N_{at} in the ground state $|4\rangle$ would then be given by the differential equation

$$\frac{dN_{\text{at}}}{dt} = -\frac{1}{k} (\Phi_{\text{in}}(t) - \Phi_{\text{out}}(t)). \quad (17.3)$$

The quantity we measure experimentally is the transmission of the probe field deduced from the acquisition of the two quadratures $x^2 + p^2$ of the probe field via heterodyne detection. By combining all the previous relations, we find for the evolution of the optical depth

$$\frac{dd(t)}{dt} = -\frac{\alpha_{\text{at}}}{k} (\Phi_{\text{in}}(t) - \Phi_{\text{out}}(t)) = -\frac{\alpha_{\text{at}}}{k} \Phi_{\text{in}}(t) [1 - \exp(-d(t))]. \quad (17.4)$$

Using a constant input probe power or photon flux Φ_{in} , the solution of (17.4) is

$$d(t) = \ln [1 + (\exp(d(t=0)) - 1) \exp(-\alpha_{\text{at}} \Phi_{\text{in}} t / k)], \quad (17.5)$$

which models the experimentally measured transmission $T(t)$ as

$$T(t) = \frac{\Phi_{\text{out}}(t)}{\Phi_{\text{in}}(t)} = \exp(-d(t))$$

$$T(N_{\text{at}}, \alpha_{\text{at}}, t) = \frac{1}{1 + [\exp(\alpha_{\text{at}} N_{\text{at}}) - 1] \exp(-\alpha_{\text{at}} \Phi_{\text{in}} t / k)}. \quad (17.6)$$

The merit of this method is that it allows not only to estimate the number of atoms with good accuracy and speed in a single optical pumping transient record but also it allows to independently estimate the optical depth per atom which enters as an additional free parameter. Before I show some experimental results, I would like to give remarks on the statistical nature of the optical pumping process and also how to find the value of k which is required in (17.6).

17.1.3 Statistical nature of the pumping process

First of all, the average number of photon scattering events k , required to transfer an atom from $|4\rangle$ to the dark state $|3\rangle$, is evaluated using the knowledge of the partial decay rates of the excited state $|4'\rangle$ into the two possible ground states $|3\rangle$ and $|4\rangle$. These partial rates are respectively $5/12\Gamma$ and $7/12\Gamma$, where the branching ratio $7/5$ is independent of the Zeeman levels. To find these values we did the following.

In the Cesium data reference [Steck \(2010\)](#), only the hyperfine line strengths from ground to excited states are tabulated in Table 8, based on the equation (41). What we want are the strengths from excited to ground states. By inverting the role of the ground and excited state in equation (41) of [Steck \(2010\)](#) together with the invariance of 6-J Wigner coefficients from column permutation and invariance of the dipole matrix element, we have

$$\tilde{S}_{F',F} = S_{F,F'} \frac{(2F+1)(2J'+1)}{(2F'+1)(2J+1)}.$$

² Γ is the decay rate equal to $2\pi \cdot 5.234 \text{ MHz}$ for the D2 line of Cesium

From $S_{4,4'} = 7/24$ we find $\tilde{s}_{4',4} = 2 \times 7/24 = 7/12$. From $S_{3,4'} = 15/56$ we find $\tilde{s}_{4',3} = 5/12$.

In order to find k , we consider first $P(n)$, the survival probability distribution of an atom in $|4\rangle$ after n scattering events. Obviously, after $n = 0$ scattering event, the survival probability is $P(0) = 1$. We denote $q = P(1) = 7/12$ the probability to spontaneously decay back into the original state after one scattering event ($n = 1$). $1 - q = p = 5/12$ will be the probability to decay back into the dark state $|3\rangle$. It is easy to find that the survival probability after n events is given by $P(n) = q^n$.

Therefore, the success probability that it takes n successive trial scattering events to pump an atom into the dark state $|3\rangle$ is given by³

$$\chi(n) = pP(n-1), \quad (n \geq 1). \quad (17.7)$$

It is more than instructive to recognize that χ is the geometric distribution law⁴ with parameter $p = 1 - q$. Its mean and variance are well-known and given respectively by $p/(1 - q)^2$ and q/p^2 .

χ is normalized here following that $(1 - q) = p$. Indeed,

$$\sum_{n=1}^{+\infty} \chi(n) = p \sum_{m=0}^{+\infty} P(m) = p \lim_{n \rightarrow +\infty} \frac{1 - q^{n+1}}{1 - q} = \frac{p}{1 - q} = 1.$$

The expectation value for the number of scattering events to pump the atom, which gives the value of k , is indeed

$$k = \langle n \rangle = \frac{\sum_{n=1}^{+\infty} n\chi(n)}{\sum_{n=1}^{+\infty} \chi(n)} = (1 - q) \sum_{n=1}^{+\infty} nP(n-1), \quad (17.8)$$

$$= (1 - q) \frac{\partial}{\partial q} \sum_{n=1}^{+\infty} q^n = (1 - q) \frac{\partial}{\partial q} \lim_{n \rightarrow +\infty} \left(\frac{1 - q^{n+1}}{1 - q} - 1 \right), \quad (17.9)$$

$$k = \frac{1}{1 - q} = 2.4. \quad (17.10)$$

Using twice the derivative trick, one will find for the variance of the pumping process

$$\text{var}(n) = \langle n^2 \rangle - \langle n \rangle^2 = \frac{q}{(1 - q)^2} = \frac{q}{p^2} \simeq 3.36.$$

The variance is larger than the mean. Therefore, the statistical pumping process is super-Poissonian. Looking at these statistical moments leads one to find an interesting result. The Fano factor \mathcal{F} ,

$$\mathcal{F} = \frac{\text{var}(n)}{\langle n \rangle} = \frac{q}{1 - q} = \frac{q}{p} = \frac{7}{5} = 1.4, \quad (17.11)$$

³ $(n - 1)$ failed previous attempts followed by the finally expected success

⁴ which is the discrete model of a radioactive decay or death, $P(n) = q^n = e^{n \ln(q)} \simeq e^{-pn}$ but only when $\ln(q) = \ln(1 - p) \sim -p$ for $p \ll 1$.

which we use to qualify the statistical nature of the process, i. e. whether the process is sub-Poissonian $\mathcal{F} < 1$, Poissonian $\mathcal{F} = 1$ or super-Poissonian $\mathcal{F} > 1$, is given by the branching ratio of the transitions. Here for the used atomic levels, the optical pumping process is expected super-Poissonian.

17.1.4 Fano factor versus 3-level scheme

With the benefit of such statistical hindsight, it is interesting to note that the transitions $|4\rangle \rightarrow |4'\rangle$ and $|3\rangle \rightarrow |4'\rangle$ have about the same strengths ($7/24$ and $15/56$). This means that if one would have used instead the swapped Λ -level system with initially all the atoms in $|3\rangle$ and the dark state $|4\rangle$, the optical depth per atom α_{at} would have been similar but the branching ratio would have been inverted in such a way that the process would become sub-Poissonian, $\mathcal{F} = 5/7 = 0.71$, for a quasi-identical optical thick ensemble.

The small \mathcal{F} and the small q is, k becomes close to 1 and therefore the optical pumping transient is faster. It takes less photons to bleach the ensemble of atoms and therefore less photon shot noise. Of course, the probability of a scattering event at a given time t is also conditioned by the probability distribution of probe photon arrivals at t . For coherent states of light, the number of photons in a fixed time window follows the Poisson distribution. The distribution of the population of pumped atoms at t will be contaminated by input photon shot noise. However, a more deterministic pumping process (smaller \mathcal{F}) would help to reduce the statistical error in repeated optical transient measurement.

In that respect, for the future, I would like to draw the attention on the D1 (D1) line of Cesium which seems even more promising. Interestingly, the partial decay rates are swapped compared to the D2 line, $\tilde{s}_{4',4}(D1) = \tilde{s}_{4',3}(D2)$ and $\tilde{s}_{4',3}(D1) = \tilde{s}_{4',4}(D2)$ such that the previous inversion of the branching ratio happens naturally on the D1 line without inverting the role of the ground states, i. e. keeping all atoms initially in $|4\rangle$ and pumping into the dark state $|3\rangle$. In addition, the strength of the interacting transition $|4\rangle \rightarrow |4'\rangle$ and hence the effective single-atom coupling α_{at} , would be stronger on the D1 line, here for Cesium by a factor $10/7$. Actually, this observation seems to be valid for all alkali atoms⁵. Note that Rubidium 87 seems to achieve a perfect symmetric scenario (and hence on both D1 and D2 line) with a unit Fano factor or branching ratio, using the two ground states $|1\rangle$ and $|2\rangle$ and the hyperfine excited state $|2'\rangle$.

17.1.5 Nominal number of lattice trapped atoms

We report in figure 17.2 atom number measurement data when probing the atoms with a continuous 852 nm input light power of 5.0 pW

⁵ I only checked for Cesium 137 and Rubidium 85.

resonant to the $|4\rangle \rightarrow |4'\rangle$ transition. The data reported is an average over 178 consecutive lattice trap loading realizations. It is important to mention that this pumping measurement is performed with a trap storage time of 10 ms after the end of the sub-Doppler cooling transfer to avoid reliably residual effects due to background cold atoms from the initial MOT reservoir flying in the probe evanescent field. The measurement of the probe transmission is performed at the light shot noise limit by recording in real time the evolution of the probe field quadratures using heterodyne detection.

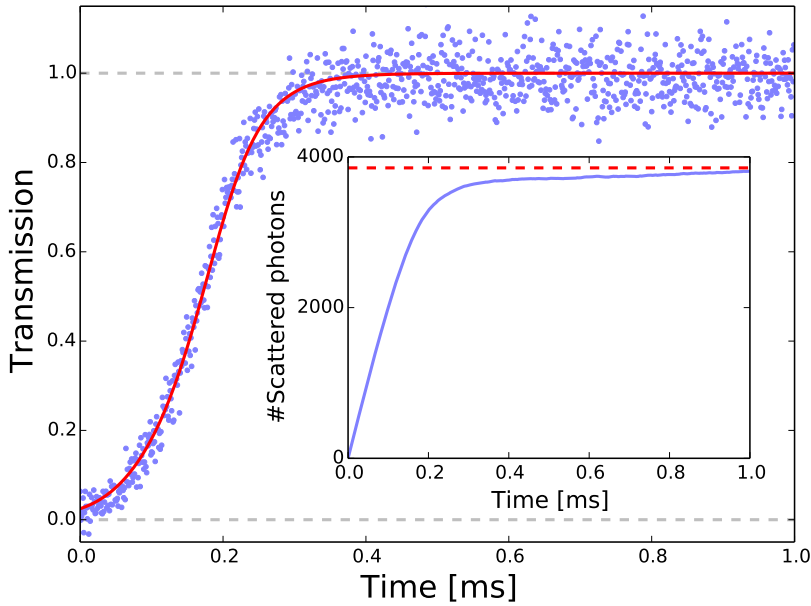


Figure 17.2: Atom number measurement based on optical pumping transients. The inset shows the cumulative integration of the number of missing scattered photons. Dividing the asymptotic value by k is equivalent to extracting $N_{\text{at}} = 1606$ from the transmission curve fit.

For the presented data, we report a mean⁶ number of trapped atoms,

$$N_{\text{at}} = 1606 \pm 4^{\text{stat}} \pm 161^{\text{sys}}, \quad (17.12)$$

where the statistical error on the mean number of atoms is given for an average over 178 transients. The systematic error accounts for the propagation of calibration uncertainty of the overall quantum detection efficiency of probe photons using the heterodyne technique. This uncertainty which amounts⁷ to 10% experimental confidence, dominates all

⁶ Mean over individual transient fits

⁷ A fractional uncertainty of 10% in the inferred number of scattered photons from the detected number of photons with a finite quantum detection efficiency (and losses) q_e , leads to same fractional uncertainty in the number of atoms, i. e. $N_{\text{at}} = N_{\text{ph}}/k$ and $q_e N_{\text{ph}} = N_{\text{ph,detect}}$.

other possible sources of systematic effects which may bias the estimation of the number of atoms. It is important to stress that this systematic calibration source of error does not vary between atom number measurement realizations and it is left to the care of the experimentalist in the preparation of the setup.

It is important to mention that because the method requires the knowledge of k , any modification of the partial decay rates of the atoms from a modification of the electromagnetic vacuum near the surface of the dielectric nanofiber medium should be considered. However, this kind of Purcell enhancement is expected smaller than a percent at the position of the atoms. In addition, the branching ratio would not be affected at first order.

The optical pumping technique in itself is robust against effects which have limited in the past the accurate determination of the number of atoms such as laser detuning, polarization, population redistribution among Zeeman sub-levels and inhomogeneous broadening of the probe transition by trap light (see for instance [Chen et al. \(2001\)](#)). The number of spontaneous emission cycles needed to bleach the ensemble of atoms and used to estimate the atom number, is independent of such effects which may however affect the atomic cross-section or single-atom coupling.

We have seen that the optical pumping transient method gives access independently to the single-atom coupling α_{at} . We discuss this point in the next section.

17.1.6 *Dark state pumping kinetics*

Inspired by memories of acid-base titration and pH measurement in chemistry, it is interesting to look at the information contained in the *equivalent* time or inflection point

$$t_{\text{eq}} = k \frac{\ln [\exp(\alpha_{\text{at}} N_{\text{at}}) - 1]}{\alpha_{\text{at}} \Phi_{\text{in}}}, \quad (17.13)$$

for which the probe transmission $T = 0.5$ (see (17.6)) and where the first derivative of T achieves its maximum. Reading this time directly gives access to the initial atom number for sufficiently optically thick initial ensemble,

$$t_{\text{eq}} \simeq \frac{N_{\text{at}} k}{\Phi_{\text{in}}}, \quad \exp(d(t=0)) \gg 1 \quad (17.14)$$

which happens when the average number of probe photons which have entered the ensemble, $t_{\text{eq}} \Phi_{\text{in}} / k$, is sufficient to bleach the initial number of atoms N_{at} . Note that (17.14) is independent of the single light-atom coupling α_{at} .

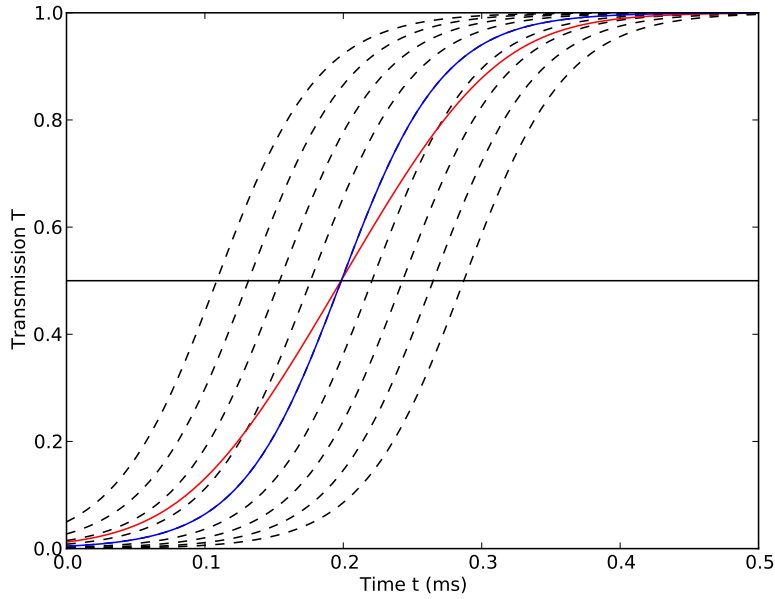


Figure 17.3: (Black dashed lines) Simulated transmission for a fixed single-atom coupling $\alpha_{\text{at}} = 0.3\%$ and various atom number $N_{\text{at}} = (1000, 1200, 1400, 1600, 1800, 2000, 2200, 2400, 2600)$. (Red solid line) average over the various transmissions, (blue solid line) transmission from average atom number $\langle N_{\text{at}} \rangle = 1800$.

In contrast, the information contained in the slope of T at t_{eq} , which is also the maximum speed of the transmission transient,

$$\left. \frac{\partial T}{\partial t} \right|_{t=t_{\text{eq}}} = \frac{\alpha_{\text{at}} \Phi_{\text{in}}}{4k}, \quad (17.15)$$

is independent of the number of atoms and is directly proportional to the per-atom optical depth α_{at} .

From these two results, one will be able to understand simply the effects of averaging over several optical pumping transients which may be prone to fluctuations in N_{at} or α_{at} from one lattice trap loading to the next. Another way than (17.14) to see that the atom number measurement method is robust against variations in the single light-atom coupling for initially thick ensembles is to consider that N_{at} is obtained simply⁸ from the asymptotic value of the cumulative number of *expected* yet missing probe photons, given by subtracting the area or integrated transmission transient from the rectangular area obtained in absence of atoms (see inset of figure 17.2).

We sum up all our observations in the following figures. In figure 17.3, we simulate the effect of large variation in the number of atoms for fix single-atom coupling in shot-to-shot transient transmission. In figure 17.4, we show the opposite case, fluctuations in coupling constant for

⁸ dividing by k the missing probe photons

constant atom number. One sees that for the best estimation of α_{at} or reduction of random photon shot noise by using averaging over many transients, one should not simply fit to the average transient response but extract an average single-atom coupling constant from individual fit values.

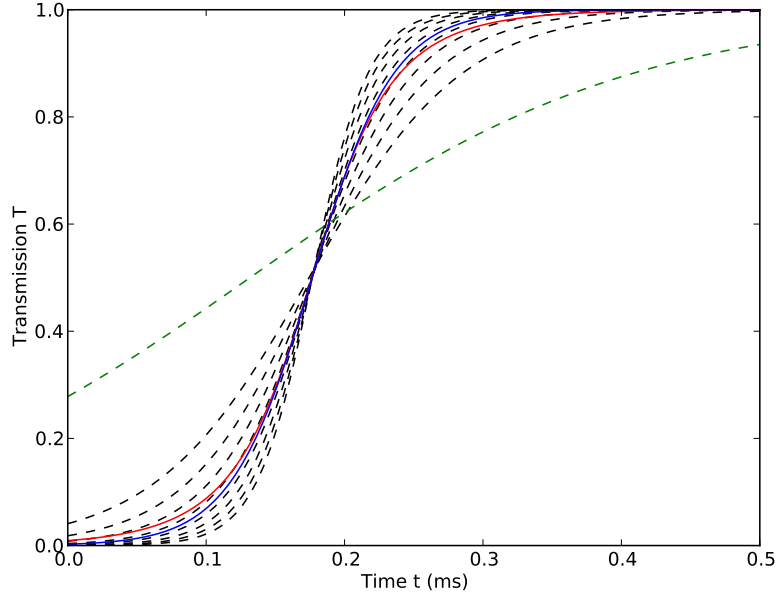


Figure 17.4: (Black dashed lines) Simulated transmission for a fixed atom number $N_{\text{at}} = 1600$ and fluctuating single-atom coupling $\alpha_{\text{at}} = (0.2, 0.25, 0.3, 0.35, 0.4, 0.45, 0.5, 0.55)\%$. (Red solid line) average over the various transmissions, (blue solid line) transmission from average single-atom coupling $\alpha_{\text{at}} = 0.375\%$. (Green dashed line) $\alpha_{\text{at}} = 0.08\%$ the initial ensemble is not optically thick ($d \sim 1.3$).

For the data associated to (17.12) reported in figure 17.2, we found

$$\langle \alpha_{\text{at}} \rangle = 0.32\%, \quad (17.16)$$

which corresponds to the per-atom optical depth while probing on the $|4\rangle \rightarrow |4'\rangle$ transition where we expected atoms to be isotropically distributed in the Zeeman sub-levels. The linear polarization of the probe was aligned parallel to the polarization of the red trap.

It is possible to extrapolate the expected optical depth for probing isotropically the atoms on the $|4\rangle \rightarrow |5'\rangle$ transition from the knowledge of the different coupling strengths between the different Zeeman levels. One will find an average relative coupling strength of ~ 2.095 which should scale up $\langle \alpha_{\text{at}} \rangle$ on the cycling transition, taking into account the forbidden transition $|4, 0\rangle \rightarrow |4', 0\rangle$. This value is compatible with the ratio of the line strengths $[(11/18)/(7/24)]$ reported in Table 8 of Steck (2010). In addition, the most favorable interaction strength would be gained in interrogating the atoms using the closed transition $|4, 4\rangle \rightarrow$

$|5', 5\rangle$ with σ^+ polarized light. From Clebsch-Gordan coefficients, one expects to gain another factor of ~ 2.46 . Therefore, one would estimate from (17.16) a per-atom optical depth $\langle\alpha_{\text{at}}\rangle = 1.65\%$ on this strong closed $|4, 4\rangle \rightarrow |5', 5\rangle$ transition.

17.1.7 *Single-atom optical depth*

Although it is possible to make extrapolations, it is better to measure more directly the single-atom optical depth. The atom number measurement cannot be applied to extract directly the maximum or resonant single-atom coupling on the cyclic $|4\rangle \rightarrow |5'\rangle$ transition. However, with the knowledge of the total number of atoms combined with a resonant transmission measurement while probing the transition $|4\rangle \rightarrow |5'\rangle$, which gives access to the total resonant optical depth of the ensemble d_0 , one can estimate $\alpha_0 = d_0/N_{\text{at}}$ for that transition. This has been the method applied in other nanofiber experiments (combined with the saturation method to estimate N_{at}).

The results presented in the previous sections were acquired at the earliest stages of the experimental progress of the setup. In particular, the OOE trap storage time was somewhat on the lower side, $\tau \sim 6.8$ ms, due to excess intensity noise on the homebuilt laser sources to produce the trap lights. After improving on this, the storage time extended up to 20 ms. In figure 17.5, we report examples of transmission measurement of the total resonant optical depth for various trap storage times. More precisely, we record directly on a spectrum analyser the heterodyne beatnote amplitude (in a narrow bandwidth 10 kHz) between an optical LO and the probe light transmitted through the nanofiber, as seen in the previous chapter. Therefore, the amplitude of the signal here is proportional to electric field amplitude or to the square root of the probe intensity transmission.

Remarkably, one can observe that the ensemble of trapped atoms in the nanofiber evanescent field is so optically thick that almost no probe light is seen transmitted through the nanofiber mode for a few milliseconds until continuous scattering of probe photons heats the atoms away from the nanofiber trap. It is then clear that for optically thick ensembles, it is difficult to distinguish or measure precisely optical depths as this requires to be able to distinguish tiny fraction of transmitted light. For instance, for $d_0 = 5, 10, 11$ the transmission would already be as small as $T = \exp(-d_0) \simeq 6.7 \times 10^{-2}, 4.5 \times 10^{-5}, 1.6 \times 10^{-5}$. This makes it difficult in as much as in order to avoid power broadening and saturation of the atomic transition which would affect the detected optical depth, it is primordial to keep the input probe power low, therefore increasing the relative fraction of intensity light shot noise⁹ if the measurement is not limited already by technical detection noise. The first

⁹ which is already a few percent in a bandwidth limited by the atomic heating loss rate for probe picowatt power

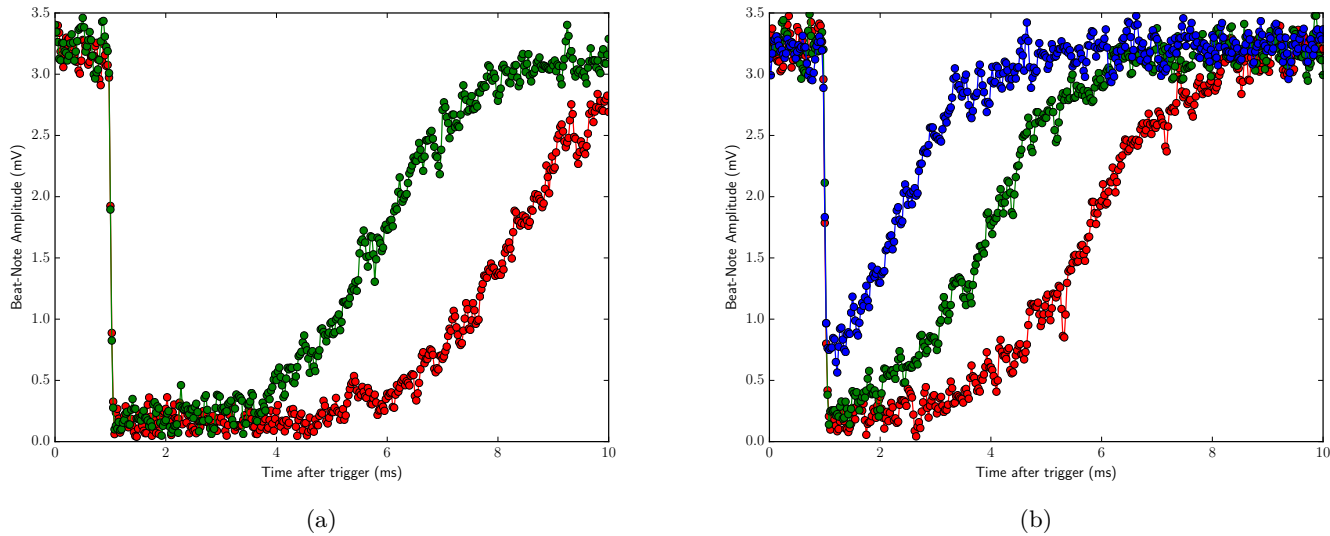


Figure 17.5: Narrow band (10 kHz) continuous heterodyne beatnote showing the transmission of the probe electric field after propagation through the nanofiber trapped atoms. At $t = 1$ ms the atoms are repumped continuously onto the probe transition. The optical depth is so large that the probe light is completely absorbed over several milliseconds until atoms are lost due to heating. The various curves correspond to different accumulated storage times τ before the measurement trigger at $t = 0$ (a) (red) $\tau = 20$ ms, (green) $\tau = 25$ ms. (b) (red) $\tau = 40$ ms, (green) $\tau = 50$ ms, (blue) $\tau = 60$ ms.

obvious strategy to improve the precision would be to average over many measurements and to trap fewer¹⁰ atoms such that d_0 is not too large and one could infer an effective resonant single-atom optical depth. Another strategy that has been done is to measure the optical depth as a function of the probe detuning (see figure 17.6) which is expected to be Lorentzian. However, as such, the maximum of a Lorentzian or resonant optical depth is strictly linked to its width and the resonant optical depth cannot be distinguished from potential broadening¹¹ of the atomic transition.

Instead, we decided to follow another approach allowed by the dispersive detection of atoms. From (2.19), which is a consequence of

¹⁰ without changing the conditions of trap loading, i. e. collisional blockade regime

¹¹ For a Lorentz fit, the maximum is not a free parameter compared to the line width. Even in absence of broadening, it implies an a priori knowledge of the linewidth Γ which is actually linked to the atomic transition cross-section.

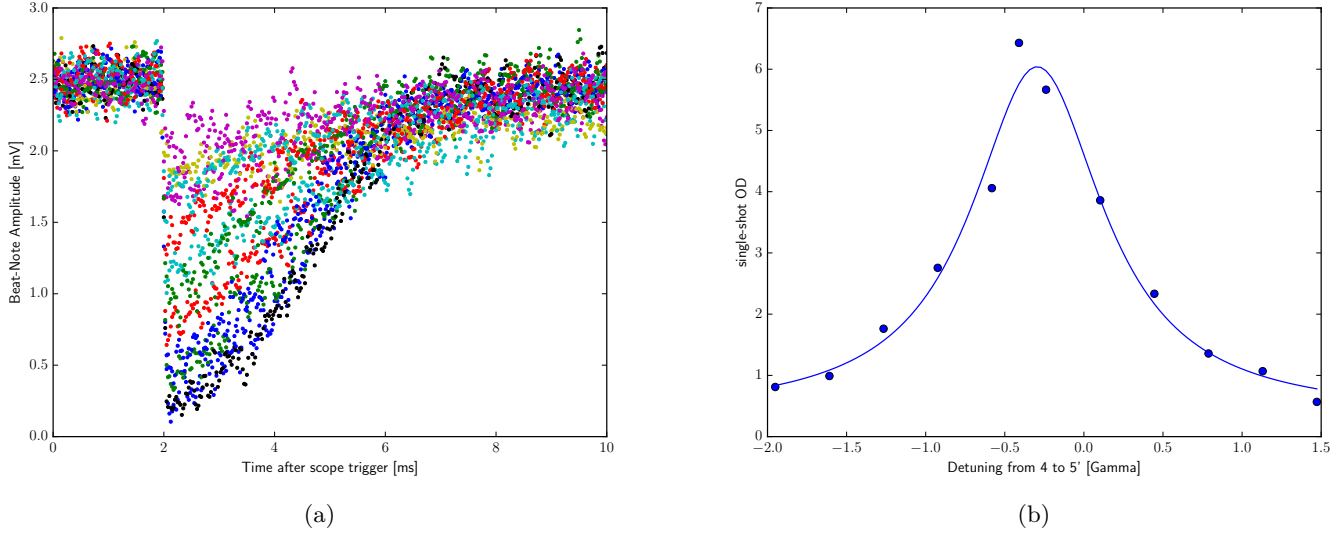


Figure 17.6: Optical depth measurement as a function of the probe detuning to the cyclic transition. The measurement is performed after a storage time of **20 ms** with fewer atoms than in figure 17.5 to distinguish the variations in probe transmission. (b) Lorentzian fit to the extracted optical depth agrees well with the data and give a linewidth almost identical (1.01Γ) to the expected atomic transition width.

Kramers-Kronig's relations, there is a fundamental link between the observed accumulated phase shift and the resonant optical depth d_0 as

$$\varphi(d_0, \beta) = -\frac{d_0}{2} \frac{(\gamma/2)\Delta}{\Delta^2 + (\gamma/2)^2} = -\frac{d_0}{2} \beta (1 + \beta^2)^{-1}, \quad (17.17)$$

$$\varphi(d_0, \beta) \simeq -\frac{d_0}{2} \beta = -\frac{d_0}{2} \frac{\gamma}{2\Delta} \quad \text{or} \quad d_0 \simeq -\varphi(\Delta) \frac{4\Delta}{\gamma} \quad (\Delta \gg \gamma/2). \quad (17.18)$$

Therefore, a direct measurement of the imprinted phase shift, which can be performed at the shot noise limit with a good **SNR**, combined with the robust measurement of the number of atoms for the same experimental conditions, would give a reliable estimation of the effective resonant single-atom optical depth $\alpha_0 = d_0/N_{\text{at}}$.

For the relatively far-detuned dual-heterodyne measurement of the total accumulated phase shift $\varphi(\Delta)$, we have $\Delta/(\gamma/2) \simeq 24$ or $\beta \simeq 1/24$ such that $(1 + \beta^2)^{-1} \simeq 1$ and (17.18) is an excellent approximation¹² in such way that $\alpha_0 \simeq |\varphi(\Delta)|4\Delta/(\gamma N_{\text{at}})$. To remove conservatively any doubt about the origin¹³ of the atomic signals, we perform both an atom number measurement and a phase shift measurement after a trap

¹² which would be limited by the applicability of the 2-level atom approximation, i. e. correction effects due to the presence of other hyperfine levels

¹³ as mentioned before, after a storage time of **1 ms** a residual signal from background cold atoms in the evanescent field, falling due to gravity and free flying after the

storage time of $t = 40$ ms. For a millimeter size MOT overlapping the nanofiber, we measured an average number of atoms $N_{\text{at}} = 4.2 \times 10^2 \pm 42^{\text{sys}}$ and observed an average accumulated maximum phase shift of $\varphi = -0.085$ rad giving an estimation of $\alpha_0 = 9.8 \times 10^{-3}$ or $\alpha_0 = 2.4\%$ on the closed transition.

The expected effective single-atom optical depth is given by the ratio of the atomic cross-section σ to the effective probe mode area A_{eff} which depends on the position of the atoms. At the expected nominal trap minimum position $r_{\text{min}} = 200$ nm for the used trap powers, the effective probe mode area¹⁴ $A_{\text{eff}}(r_{\text{min}}, \phi = 0)$ for 852 nm is $\sim 2.6 \mu\text{m}^2$, where $\phi = 0$ means that the transverse quasi-linear polarization of the probe field is aligned with the standing wave red trap field transverse polarization. This area is to be compared to the expected resonant isotropic atomic cross-section (π polarization) for the $|4\rangle \rightarrow |5\rangle$ transition $\sigma = 0.14 \mu\text{m}^2$ (Steck (2010)) or if extrapolated to the closed transition to $\sigma = 0.35 \mu\text{m}^2$ for (σ^+ polarization). I would like to save also that $A_{\text{eff}}(r_{\text{min}}, \phi = \pi/2)$ is $\sim 7.4 \mu\text{m}^2$ if the probe polarization is aligned along the blue trap (see figure 17.7).

Although the observed effective single-atom optical depth is lower than the expected value which assumes perfect trap and probe polarizations as well as ground state-cold atoms at the exact trap minima, $\alpha_0 = 2.4\%$ versus $\alpha_{\text{th}} = 13\%$, it still represents an improvement of more than 2 orders of magnitude compared to the signal from a single atom obtained in the free space optical dipole trap experiment (Appel et al. (2009b)) presented in the first part of this thesis. With this great improvement, we can already draw some important conclusions about the ability of our light shot noise limited phase detection scheme to resolve in real time any intrinsic atomic noise on the signal.

17.2 MEASUREMENT STRENGTH

Before we go on more advanced results, it is important to recap, from the knowledge of the single-atom optical depth, several important characteristics of our dispersive interface between nanofiber trapped atoms and light.

We have seen in earlier chapters that the SQL of the dual-heterodyne technique imposes a minimum shot noise limited phase resolution given by

$$\delta\varphi = \frac{1}{2\sqrt{qN_{\text{ph}}}}. \quad (17.19)$$

MOT is turned off, can contribute to a few percent on the signal. However, after 10 ms this is completely negligible and we never noticed residual signals.

¹⁴ $A_{\text{eff}} = P_{\text{total}}/I(r, \phi)$

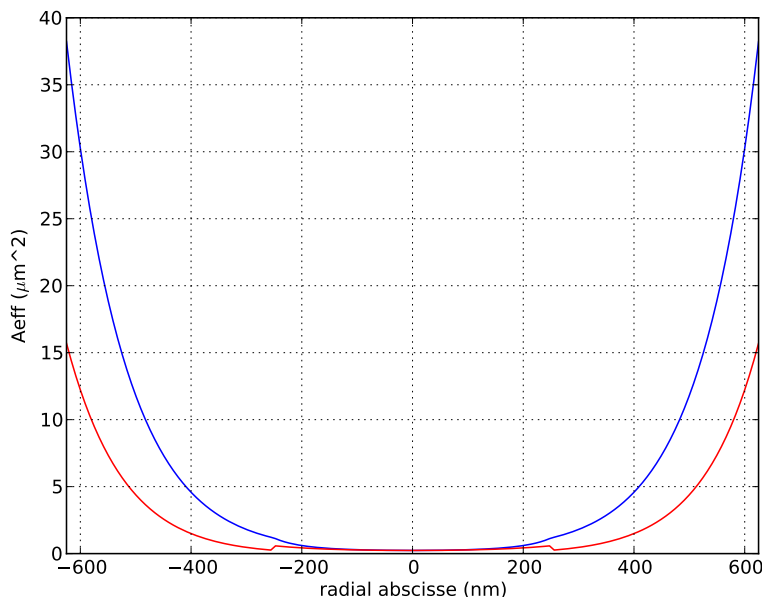


Figure 17.7: Theoretical effective mode area A_{eff} for the nanofiber fundamental mode with transverse quasi-linear polarization, as a function of the radial distance to the fiber axis. (Red) Along the polarization direction. (Blue) Orthogonal to the transverse polarization.

When N_{ph} is the number of photons at the position of the atoms, the nominal value for the overall quantum efficiency of our experimental setup is given by

$$q = \epsilon(1 - l)\eta\mathcal{V} \simeq 0.4, \quad (17.20)$$

where $\epsilon = 0.89$ is the finite quantum efficiency of the photodetector, $l = 0.3$ is the transmission loss¹⁵ along the probe light propagation from the atom positions to the detector, η is the ratio¹⁶ of optical LO photon shot noise to total detection noise (electronic plus LO shotnoise) and \mathcal{V} is the quantum efficiency associated to the mode matching between the probe field and the optical LO, i.e. $\mathcal{V} = V^2$ where $V = 0.9$ is the interference fringe visibility.

Now, from the knowledge of the single-atom optical depth α_{at} or more precisely from the above calibration of the measured phase shift per atom $\varphi_1 = 0.204 \text{ mrad}$, one will see that it only takes $N_{\text{ph}} = (2\sqrt{q}N_{\text{at}}\varphi_1)^{-2} \sim 4$ photons to detect in a single-shot, routinely trapped ensembles of $N_{\text{at}} = 2000$. This happens more precisely when the SNR ratio of accumulated phase shift signal $\varphi_{\text{at}} = N_{\text{at}}\varphi_1$ to shot noise limited detection noise $\delta\varphi$ becomes greater than 1,

$$\text{SNR} = \frac{\varphi_{\text{at}}}{\delta\varphi} = \frac{N_{\text{at}}\varphi_1}{\delta\varphi} = \left(2\sqrt{qN_{\text{ph}}}\right) N_{\text{at}}\varphi_1. \quad (17.21)$$

¹⁵ limited by the insertion loss of an optical isolator

¹⁶ which depends on the power of the optical LO

Assuming artificially that the total accumulated phase shift signal φ_{at} does not depend on the number of probe photons, it would take $N_{\text{ph}} = (2\sqrt{q}\varphi_1)^{-2} \simeq 1.5 \times 10^7$ to reach a single-atom resolution.

Of course, as we have seen in the previous chapter, the atomic signal is not immortal and its lifetime is first naturally limited by the trap storage time τ_{bg} , which combines the effects of trap light heating and background gas collisions. This makes the atomic signal-to-noise ratio explicitly dependent on time. Therefore, the best signal-to-noise ratio depends on the measurement bandwidth or on the averaging time of the signal. However, when we are fundamentally measuring at the photon shot noise limit, the noise only depends on the mean number of invested probe photons during the averaging time τ with $N_{\text{ph}} = \tau\Phi_{\text{in}}$ where Φ_{in} is the input probe photon flux. Therefore, without compromising the fundamental signal-to-noise, one can outrun the dynamics of atom loss due to the finite trap lifetime τ_{bg} by reducing the measurement time τ below τ_{bg} by increasing the input photon flux or probe power. We have seen in the previous chapter that this is indeed possible for probe powers which are still far for the regime of saturation and non-linear atomic response. With the measured value of the resonant optical depth per atom α_0 , one can calculate the expected saturation power at the probe sideband detuning for unpolarized atoms on the cycling transition as

$$P_{\text{sat}}(\Delta) = \frac{\Gamma}{2} \frac{(1 + 4(\Delta/\Gamma)^2)}{\alpha_0} \hbar\omega_0 \simeq 224 \text{ nW}, \quad (17.22)$$

following that

$$\begin{aligned} I_{\text{sat}}(\Delta) &= \frac{\hbar\omega_0}{\sigma(\Delta)} \frac{\Gamma}{2}, \\ \sigma(\Delta) &= \frac{\sigma_0}{(1 + 4(\Delta/\Gamma)^2)}, \\ \alpha &= \frac{\sigma}{A_{\text{eff}}} \quad \text{and} \quad A_{\text{eff}} = \frac{P}{I}, \end{aligned} \quad (17.23)$$

as long as $\Gamma = \tau_{\text{rad}}^{-1} = 2\pi \cdot 5.23 \text{ MHz}$ is not modified by Purcell effects. If the optical depth per atom would be as expected for atoms positioned exactly 200 nm away from the fiber surface, one would have $P_{\text{sat}}(\Delta) \simeq 40 \text{ nW}$. (See above the difference in measured and expected α). In any case, this gives several orders of magnitude in the allowed probe powers to outrun the background collision loss without reaching saturation of the atomic transition.

In this regime, the dynamics of the atomic signal becomes now only limited by probe photon induced effects. Therefore, the best measurement signal-to-noise becomes a trade-off between the gain of atomic information learned by probe photons and achieved through reduction of measurement stochastic shot noise, via averaging for instance, combined with the measurement back-action which reduces the atomic signal during the measurement time. For atomic population measurement, the limiting back-action mechanism is loss of atoms from heating induced

by the random scattering of probe photons. Here, optical pumping is not a fundamental limitation and the loss of atomic signal due to probe induced dark state pumping can be prevented by a suited repumping light source. Nevertheless, both limiting effects are characterized by a loss rate which, below saturation of the atoms, is expected proportional to the input photon flux. As a result, the strength of the measurement is completely¹⁷ characterized by the average number of probe photon scattering events per atom and therefore it does not depend explicitly on time in this regime. Consequently, we developed in the next section all these ideas with a consistent notation and simple formalism only based on numbers of scattering events.

17.3 CHARACTERISTIC NUMBERS OF SCATTERING EVENTS

In the first chapter of this thesis (2.20), we saw that in the far-detuned limit ($\Delta \gg \gamma/2$), which is a good approximation for the dual-heterodyne dispersive measurement, the stationary number of probe photons scattered into free space by an ensemble of 2-level atoms is given by

$$\begin{aligned} N_{\text{sc}} &= N_{\text{ph}}^{\text{in}} - N_{\text{ph}}^{\text{out}} = (1 - e^{-d(\beta)})N_{\text{ph}}^{\text{in}}, \\ &\simeq d_0\beta^2 N_{\text{ph}}^{\text{in}} = d_0 \left(\frac{\gamma}{2\Delta}\right)^2 N_{\text{ph}}^{\text{in}}. \end{aligned}$$

Remembering that $d_0 = \alpha_0 N_{\text{at}}$, we introduce the average number of scattering events per atom n_{sc} as

$$n_{\text{sc}} = \frac{N_{\text{sc}}}{N_{\text{at}}} = \alpha_0 \left(\frac{\gamma}{2\Delta}\right)^2 N_{\text{ph}}^{\text{in}}. \quad (17.24)$$

For a given measurement with constant input photon flux Φ_{in} , the observation of the exponential decay or loss of the mean atomic phase shift signal (or mean atom number) with the characteristic OOE time constant τ_{loss} allows to introduce the equivalent average number of scattering events n_{loss} after which an atom would be lost as

$$n_{\text{loss}} = \alpha_0 \left(\frac{\gamma}{2\Delta}\right)^2 \tau_{\text{loss}} \Phi_{\text{in}}. \quad (17.25)$$

To all the various time constants linked to the various loss mechanisms presented in the previous chapter, one can then associate a corresponding critical number of scattering events in a such way that the general average number of scattering events to loose an atom from the ground state $|4\rangle$ in absence of repumping, reads

$$n_{\text{loss}} = \left(\frac{1}{n_{\text{bg}}} + \frac{1}{n_{\text{heat}}} + \frac{1}{n_{\text{hf}}} \right)^{-1}, \quad (17.26)$$

following the same relation between the decay rates. As mentioned earlier, τ_{bg} is independent of the probe light and therefore n_{bg} is directly

¹⁷ in the far-detuned or homogeneous probing limit

proportional to the input photon flux. Thus, the hierarchy between the different numbers depend on the choice of probe powers. In the remaining, we will assume that the probe power was chosen high enough such that $n_{\text{bg}} \gg \max(n_{\text{heat}}, n_{\text{hf}})$.

In contrast, the heating decay rate $1/\tau_{\text{loss}} = 1/\tau_{\text{heat}}$ is expected to be proportional to the input photon flux Φ_{in} below saturation of the atomic transition. As a result (see (17.25)), the average number of scattering events to heat an atom away from the trap is independent of the input probe power. It is a constant characteristic of the external degrees of freedom of the atom in the nanofiber trap. For the nanofiber lattice trap experiments presented in this thesis, the nominal depth at the trap minimum is about $200 \mu\text{K}$ which is equivalent to $\sim 10^3 E_{\text{recoil}}$ where $E_{\text{recoil}} = 198 \text{ nK}$ is the recoil energy of a Cesium atom for momentum exchange on the D2 line. As the average increase in kinetic energy of an atom per spontaneous scattering cycle is $2E_{\text{recoil}}$ (see Wolf et al. (2000), recoil heating is a two-photon process), we expect $n_{\text{heat}} \simeq 500$. For the data presented in the last chapter and acquired before improving on the intensity noise of the trap light, we had the puzzling observation that n_{heat} was varying with the probe power P , $n_{\text{heat}} \simeq 380$ for $P = 3.6 \text{ nW}$, while $n_{\text{heat}} \simeq 190$ for $P = 1.1 \text{ nW}$ and $n_{\text{heat}} \simeq 56$ only for $P = 0.15 \text{ nW}$. This would indicate that the heating rate grows slower than linear with the probe power (see (17.25)). After we improved on the trap light sources, a study conducted by Freja Thilde Pedersen, clearly concluded that the observed heating rate was now proportional to the input probe power for the tested powers ranging from few picowatts to few nanowatts. Unfortunately, we did not have enough time to perform a calibration of the single-atom optical depth associated to these measurements. A measured value significantly lower than $n_{\text{heat}} = 500$ could indicate that the temperature of the atoms loaded in the nanofiber lattice trap is relatively high compared to the expected trap depth.

Similarly, the rate of hyperfine pumping of atomic population into the dark state $|3\rangle$, which is rendered possible by the finite detunings of the probe sidebands to the excited state $|4'\rangle$, is expected proportional to the input photon flux. Hence n_{hf} is also a constant. It can be calculated from the knowledge of the relative strength of the $|4\rangle \rightarrow |4'\rangle$ transition compared to the $|4\rangle \rightarrow |5'\rangle$ transition, the partial decay rate from $|4'\rangle$ to the ground state $|3\rangle$ and finally with the different sideband detunings with respect to the $|4\rangle \rightarrow |4'\rangle$ transition. More precisely, as the probe sidebands are symmetrically detuned with respect to the excited state $|5'\rangle$, the average number of scattering events per atom n_{hf} (referred to the $|4\rangle \rightarrow |5'\rangle$ transition) required to pump an atom into the ground

state $|3\rangle$ will be given by the harmonic mean of the relative scattering event of each probe sideband alone. We have¹⁸

$$n_{\text{hf}} = 2rk \left(\frac{1 + 4(\Delta/\Gamma)^2}{1 + 4(\Delta_l/\Gamma)^2} + \frac{1 + 4(\Delta/\Gamma)^2}{1 + 4(\Delta_u/\Gamma)^2} \right)^{-1}, \quad (17.27)$$

$$\simeq 67$$

where $r = 2.1$ for isotropically distributed atoms and π -polarized light probing, $k = 2.4$ as found earlier, and Δ is the identical sidebands detuning with respect to $|4\rangle \rightarrow |5'\rangle$ while Δ_l (resp. Δ_u) is the detuning of the lower (resp. upper) sideband to the $|4\rangle \rightarrow |4'\rangle$ transition. Probing with the lower (resp. upper) sideband alone would give $n_{\text{hf}} \simeq 45$ (resp. $n_{\text{hf}} \simeq 124$). The experimental observed values deduced from τ_{hf} and α_0 (see (17.25)) is in good agreement with the theory $n_{\text{hf}} = 67$.

The relation (17.21) is equivalent to the expression (2.22) we already derived in the first chapter, except that we are now taking into account the quantum efficiency of the photodetection. It is nothing but the consequence of the Kramers-Kronig's relations between absorption and dispersion written in the far-detuned limit. Combining them at the single-atom level, i. e. using ((2.20) and (2.21)) or equivalently ((17.18) and (17.24)), gives probably one of the most important relation

$$\varphi_1^2 = \frac{\alpha_0}{4} \frac{n_{\text{sc}}}{N_{\text{ph}}}, \quad (17.28)$$

which leads to

$$\text{SNR} = \frac{\varphi_{\text{at}}}{\delta\varphi} = N_{\text{at}} \sqrt{q\alpha_0 n_{\text{sc}}}. \quad (17.29)$$

As the mean atomic state population follows the back-action of the scattering events as

$$N_{\text{at}}(t) = N_{\text{at}}^i \exp(-t/\tau_{\text{loss}}),$$

$$N_{\text{at}}(n_{\text{sc}}) = N_{\text{at}}^i \exp(-n_{\text{sc}}/n_{\text{loss}}),$$

where N_{at}^i is the initial mean number of atoms, we can predict a simple effective evolution as

$$\text{SNR} = N_{\text{at}}^i e^{-\frac{n_{\text{sc}}}{n_{\text{loss}}}} \sqrt{q\alpha_0 n_{\text{sc}}} \quad (17.30)$$

which is maximum for $n_{\text{sc}} = n_{\text{loss}}/2$.

It is interesting to translate the meaning of the previous ratio of mean atomic signal to light shot noise as the ability to resolve any other intrinsic fluctuation in the signal which are not due to the light shot noise. Indeed, for a given significant SNR, one is able to resolve relative fluctuation of $1/\text{SNR}$, here ((17.30)) in the number of atoms

¹⁸ $n_{45}^{-1} = (2 * 0.5)\alpha_{45}(\Gamma/2\Delta)^2$, $n_{44l}^{-1} = \alpha_{44}(\Gamma/2\Delta_l)^2$, $n_{44u}^{-1} = \alpha_{44}(\Gamma/2\Delta_u)^2$, $\alpha_{45}/\alpha_{44} = r$, $n_{\text{hf}} = k[(0.5n_{44u}/n_{45} + 0.5n_{44l}/n_{45})^{-1}]$

populating a given ground state. In the limit of low loss (high n_{loss}), we have

$$\frac{N_{\text{at}}}{\text{SNR}} = \frac{1}{\sqrt{q\alpha_0 n_{\text{sc}}}} \left(1 + \frac{n_{\text{sc}}}{n_{\text{loss}}} \right), \quad (17.31)$$

which shows the characteristic competition between in the one hand, the increase in resolution thanks to the decrease in phase light shotnoise with increasing n_{sc} and on the other hand, the decrease in resolution as intrinsic fluctuations in the number of atoms cannot be distinguished better than the random variation in the atom number caused by the random scattering losses induced by the measurement.

We already encounter these ideas when dealing with the conditional reduction of noise in the preparation of collective spin-squeezed state of atoms via QND measurement. We also presented this principle from the point of view of the continuous Bayesian filtering theory. In the next section, we apply these ideas and we develop a strategy for the real-time detection and preparation of very narrow (close to Fock state) atom number distributions.

17.4 LOW-LOSS NUMBER SQUEEZING

In contrast to the previous presentation of characteristic parameters of the light-atom interface, we will now use the language of Bayesian probability as introduced in the first chapter of this thesis. This allows us to describe more precisely what is meant by the state of knowledge about a given physical quantity inferred by experimental measurement.

17.4.1 *Continuous measurement*

Consider the following concrete experimental measurement which can be generalized to many other experimental situations. First, we trap atoms in the nanofiber lattice trap which are initially populating the lowest internal ground state $|3\rangle$. After a storage time of $t = 10$ ms, we prepare all the atoms into the ground state $|4\rangle$ using a suited repumping light on the $|3\rangle \rightarrow |4'\rangle$ transition. The repumping remains active for the rest of the experiment such that the only loss mechanisms would be heating and background gas collisions. Simultaneously, we continuously interrogate dispersively the atomic population of the ground state $|4\rangle$ using the two probe sidebands heterodyne technique which address the strong atomic transition $|4\rangle \rightarrow |5'\rangle$. We report such real-time or single shot dispersive observation of the atoms in figure 17.8.

Associated to this measurement, all the various important parameters are provided. The total probe power at the atoms is $P = 154$ pW. A calibration of the overall detection quantum efficiency gives $q = 0.4$ which is consistent with an Allan deviation measurement calibration

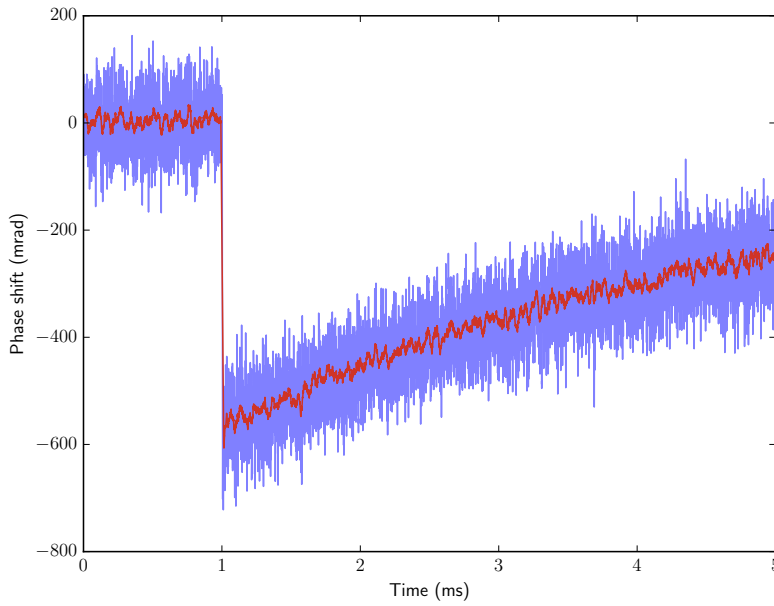


Figure 17.8: (Purple) Real-time detected atomic phase shift at the light shot noise limit. (Red) Same raw data processed with a running average of $20\ \mu\text{s}$. The measurement is performed after a storage time of $10\ \text{ms}$, the total probe sideband power at the atom position is $154\ \text{pW}$. At $t = 1\ \text{ms}$, the atoms are continuously repumped into $|4\rangle$.

showing in addition that the real-time or single-shot measurement is light shot noise limited for an averaging time longer than a millisecond. For the same experimental preparation of the setup and initial conditions, a calibration of the phase shift per atom is achieved through an atom number measurement combined with a dispersive measurement (dual-sideband technique) after a storage time of $t = 40\ \text{ms}$, for which the calibration is free of any potential biasing from residual cold atoms flying from the initial MOT reservoir. This gives $\varphi_1 = 0.204\ \text{mrad}$.

We now ask the challenging question - how much can we infer about the atom number distribution in the lattice trap via the calibrated dispersive measurement performed at the intrinsic stochastic quantum light noise limit in presence of random atom loss? In short, how much information can we extract about the atom number observable from the continuous measurement with light. In particular, we would like to track in real time the evolution of the atom number, which is driven by both reaction and dissipation induced by the interaction with light, in a such a way that we could estimate what is the atom number with high precision after a given measurement time t .

To this goal, remember the ideas introduced in the first chapter about the continuous Bayesian filtering theory.

17.4.2 Observation model

We consider the regime of a short averaging time τ during which the atom number loss is negligible and the average number of probe photons is high enough such that the measurement noise, or the stochastic poissonian light shot noise for a probe in a coherent state, is well described by Gaussian white noise. This means that our observation model of the atom number is achieved through the average of the instantaneous sampled phase values $\varphi_s(t)$

$$\varphi_s^\tau = \frac{1}{\tau} \int_0^\tau \varphi_s(t) dt = \varphi_{\text{at}}^\tau + \delta\varphi^\tau, \quad (17.32)$$

together with the prior calibration of the phase shift per atom φ_1 . The average atomic contribution to the measured signal given by

$$\varphi_{\text{at}}^\tau = \varphi_1 N_{\text{at}}^\tau,$$

is to be understood as an a priori random short-time average variable drawn from the initially unknown probability distribution $p(N_{\text{at}}^\tau)$ to have a mean atom number N_{at}^τ . This short-time average atom number $N_{\text{at}}^\tau(t)$ constitutes our quasi-continuous estimator of the number of atoms which is closest to the real value of $N_{\text{at}}(t)$ when $\tau \rightarrow 0$ or when τ is sufficiently small compared to the characteristic evolution time of the number of atoms. Here, the probe power was chosen such that the [OOE](#) lifetime of the mean number of atoms is limited by the probe induced heating rate which outruns the loss rate due to background gas collisions. This time (~ 4 ms, [fig 17.8](#)) is long enough for a fine data acquisition of the signal dynamics. Therefore, a good quasi-continuous atom number estimator is obtained here by taking $\tau = 5$ μs .

In the observation model (17.32), $\delta\varphi^\tau$ corresponds to an observation noise. As in the first part of this thesis, $\delta\varphi^\tau$ is to be understood as a random phase offset drawn from the probability distribution $p(\delta\varphi^\tau)$ of qN_{ph} detected photon arrivals during the time τ which is responsible for the homodyne phase noise due to photon shot noise. The average number of photons during τ is $N_{\text{ph}} = 3.3 \times 10^3 \gg 1$, hence the following Gaussian white noise approximation

$$p(\delta\varphi^\tau) \sim \mathcal{N}(0, \sigma_\tau^2) = \frac{1}{\sqrt{2\pi\sigma_\tau^2}} \exp\left(-\frac{(\delta\varphi^\tau)^2}{2\sigma_\tau^2}\right), \quad (17.33)$$

$$\text{with } \sigma_\tau^2 = \frac{1}{4q \langle N_{\text{ph}} \rangle_\tau}.$$

17.4.3 Atom number squeezing

Based on the principle of Bayesian inference presented earlier, we can give an estimate of the probability distribution of the atom number conditioned on the dispersive measurement φ_s^τ as

$$p(N_{\text{at}}^\tau | \varphi_s^\tau) = \frac{p(\varphi_s^\tau | N_{\text{at}}^\tau) p_i(N_{\text{at}}^\tau)}{p(\varphi_s^\tau)}, \quad (17.34)$$

where $p_i(N_{\text{at}}^\tau)$ is the initial or prior atom number distribution, $p(\varphi_s^\tau | N_{\text{at}}^\tau)$ is the conditional probability to observe the value φ_s^τ from a given atom number N_{at}^τ and $p(\varphi_s^\tau)$ is the unconditional probability for finding the measurement outcome φ_s^τ . It is given by

$$p(\varphi_s^\tau) = \int p(\varphi_s^\tau | N_{\text{at}}^\tau) p_i(N_{\text{at}}^\tau) dN_{\text{at}}^\tau. \quad (17.35)$$

$p(\varphi_s^\tau | N_{\text{at}}^\tau)$ is readily given by the atom number observation model (17.32) in such a way that the probability to measure φ_s^τ conditioned on having a given value of N_{at}^τ is given by the probability distribution of the light shot noise $\delta\varphi^\tau$ (17.33),

$$p(\varphi_s^\tau | N_{\text{at}}^\tau) \sim p(\delta\varphi^\tau = \varphi_s^\tau - \varphi_1 N_{\text{at}}^\tau) = \frac{1}{\sqrt{2\pi\sigma_\tau^2}} \exp\left(-\frac{(\varphi_s^\tau - \varphi_1 N_{\text{at}}^\tau)^2}{2\sigma_\tau^2}\right). \quad (17.36)$$

Therefore, if we would know the prior distribution $p_i(N_{\text{at}}^\tau)$, which implicitly means some degree of state preparation knowledge, we would be able to tell $p(N_{\text{at}}^\tau | \varphi_s^\tau)$. The uncertainty in the initial number of atoms could be understood as a very large prior variance $(\Delta N_{\text{at}}^i)^2$. We could also say that there is a certain likelihood that the number of atoms trapped in the optical lattice is clamped between a minimum and a maximum filling number, which we can describe as uniform probability distribution. In absence of more knowledge, we have to gradually learn more information by repeated measurement. And one of the strong point of the Bayesian method is that any prior knowledge hypothesis can be rapidly confirmed or rejected from measurement inference.

We saw in the first part of this thesis the two effects of such continuous light shot noise limited measurement on the prior distribution when dealing with collective atomic states. Namely, the measurement would induce both a change in the mean atom number, hence refining the most probable atom number value, and a reduced variance, improving the precision on such value. A model for the evolution of the variance of the atom number estimator after a finite measurement of duration τ , based on the results of (2.35), would write here as

$$(\Delta N_{\text{at}})^2 = \left(\frac{1}{(\Delta N_{\text{at}}^i)^2} + c \right)^{-1}, \quad (17.37)$$

$$\text{where } c = \frac{\varphi_1^2}{\sigma_\tau^2} = q\alpha_0 n_{\text{sc}}. \quad (17.38)$$

Here n_{sc} is the mean number of photon scattering events per atom during the finite measurement integration time τ . In absence of informative

prior $((\Delta N_{\text{at}}^i)^2 \rightarrow \infty)$, one has $\Delta N_{\text{at}} = \sigma_\tau / \varphi_1 \equiv \Delta N_{\text{at}}^{\text{light}}$ which trivially means that the uncertainty in the atom number is the one which cannot be distinguished from the uncertainty in the phase noise due to light shot noise. However, please note that ΔN_{at} does not depend on the number of atoms as expected from a dispersive measurement. In the general case, one can observe that (17.37) reads as half of the harmonic mean of $(\Delta N_{\text{at}}^i)^2$ and $(\Delta N_{\text{at}}^{\text{light}})^2$.

Now comes the difficult part. By applying a recursive Bayesian estimation from a repeated number of l successive measurement steps or identical time bins τ as above, we could keep on improving the precision on the atom number. We would have as shown in the first chapter ((2.43)), the same result as (17.37) where instead n_{sc} is the mean number of photon scattering events per atom during the total integration time $l\tau$. However, the atom number estimation is not only subject to observation light noise but also to a fundamental so-called process noise which we cannot observe directly and constitutes the measurement back-action. We present the recursive strategy in presence of such loss in the next section.

17.4.4 Recursive Bayesian estimation with Markovian loss

The previous Bayesian inference results are based on the assumption that the atom number does not evolve during the observation time which is not realistic in presence of significant loss. In presence of random or non-deterministic loss, the evolution of the atom number also becomes non-deterministic. A Bayesian inference step therefore becomes additionally probabilistic and conditioned on a given realized measurement trajectory of the detected phases.

We consider the evolution of the atom number between the measurement steps as a (memoryless) Markov process. This means that the probability to lose an atom during a measurement step is fixed and independent of the measurement step. From the observation of the exponential decay of the mean phase shift or atom number signal, we know that it takes on average $n_{\text{loss}} \simeq n_{\text{heat}} = 56$ photon scattering events to loose an atom. To fix ideas, during the time step $\tau = 5 \mu\text{s}$ for which $N_{\text{ph}} = 3.3 \times 10^3$, the average number of scattering events per atom is $n_{\text{sc}\tau} \simeq 0.057$ (see (17.24)) such that $\eta = n_{\text{sc}\tau} / n_{\text{heat}} \ll 1$. A loss of an atom is a discrete event which will be described by the Bernoulli distribution with loss success η . Assuming uncorrelated single particle loss, the probability to have N_l atoms in the trap in the l -th measurement step given that the atom number was N_{l-1} in the previous step would be given by the binomial distribution:

$$p(N_l | N_{l-1}) = \binom{N_{l-1}}{N_l} (1 - \eta)^{N_l} \eta^{N_{l-1} - N_l}, \quad (17.39)$$

so that on average the atom number evolves as

$$\langle N_l \rangle = N_0 e^{-l\eta} = N_0 e^{-\frac{t}{\tau}\eta}. \quad (17.40)$$

The light shot noise is also stochastic and not correlated between the different measurement steps. Under the Markov assumption the probability distribution for the atom number state simply writes

$$p(N_l | N_1, \dots, N_{l-1}) = p(N_l | N_{l-1}), \quad (17.41)$$

and since the phase measurement outcome φ_l only depends on the current atom number state

$$p(\varphi_l | N_1, \dots, N_l) = p(\varphi_l | N_l). \quad (17.42)$$

Therefore, the probability distribution for the atom number after the measurement step l conditioned on all the previous phase measurement steps up to l included is

$$p(N_l | \varphi_1, \dots, \varphi_l) = \frac{p(\varphi_l | N_l) p(N_l | \varphi_1, \dots, \varphi_{l-1})}{\mathcal{Z}}, \quad (17.43)$$

where $p(N_l | \varphi_1, \dots, \varphi_{l-1})$ is the prior probability distribution of having N_l atoms, which was inferred from all previous measurements and atom evolution, and \mathcal{Z} is the unconditional probability to measure φ_l ,

$$\mathcal{Z} = \sum_{N_l=0}^{\infty} p(\varphi_l | N_l) p(N_l | \varphi_1, \dots, \varphi_{l-1}).$$

After a measurement or update step $l-1$ (17.43), a new prior or best estimation distribution for the atom number N_l is made based on the freshly inferred estimation $p(N_{l-1} | \varphi_1, \dots, \varphi_{l-1})$ and on the transition or evolution probability $p(N_l | N_{l-1})$ in a such way that

$$p(N_l | \varphi_1, \dots, \varphi_{l-1}) = \sum_{N_{l-1}=0}^{\infty} p(N_l | N_{l-1}) p(N_{l-1} | \varphi_1, \dots, \varphi_{l-1}), \quad (17.44)$$

which takes into account the stochastic trajectory of the atom number.

Starting with an initial uniform probability distribution for the atom number $p(N_0)$ ($N_0 < 4400$) we apply this recursive Bayesian estimation to a real-time or single-shot measurement of the calibrated atom number phase shift measurement. We report the results in figure 17.9.

We introduce again the Fano factor F which quantifies the reduction in the atom number fluctuations as compared to a Poisson distribution as $F = (\Delta N_{\text{at}})^2 / \langle N_{\text{at}} \rangle$. A unity Fano factor may be considered as reaching the SQL if we were dealing with quantum atomic projection noise. Here, a value of F below unity corresponds to atom number squeezing. The Fano factor of the atom number estimator as a function

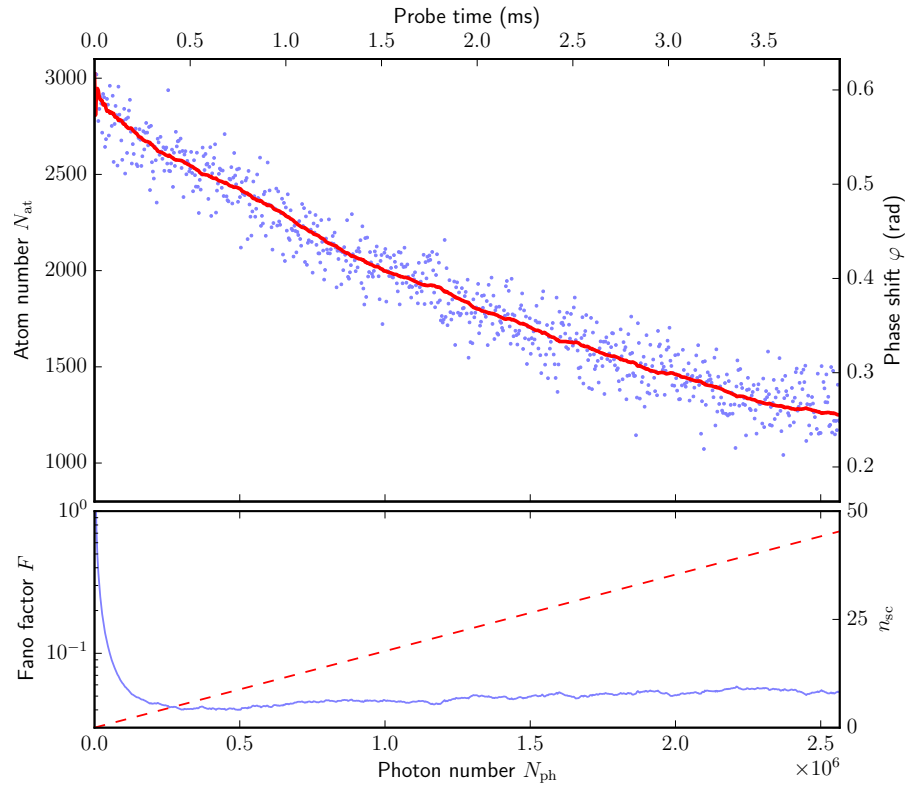


Figure 17.9: (Top panel) Quasi-continuous Bayesian estimation of the atom number based on the single-shot dispersive measurement shown in figure 17.8. The blue points represent data samples averaged over $\tau = 5 \mu\text{s}$. The red curve is the evolution of the mean atom number estimator. (Lower panel) Logarithm scale of the Fano factor as a function of time or equivalently as the number of invested probe photons.

of time or equivalently as a function of the number of probe photons reveals a minimum of

$$F_{\text{min}} = -14 \text{ dB}, \quad (17.45)$$

from the knowledge acquired by 5×10^5 probe photons. This is remarkable inasmuch as this high precision is achieved for a loss of only 14% of the initial atoms. As shown in the reported figure, the Fano factor converges rapidly to its minimum value and only slowly increases over time as the number of lost atoms or average number of scattering events n_{sc} increases.

However, there is a clear distinction to make between the accuracy with which a given number of atoms can be prepared in the trap according to plan and the precision with which the achieved number of trapped atoms is known.

Here, the data reported in figure 17.9 demonstrates that we can prepare ensembles with arbitrary atom numbers between 1000 – 2500 with Fano factors well below -10 dB . To fix some ideas, this means that one can resolve $\sqrt{F} \langle N_{\text{at}} \rangle \sim \pm 8$ atoms in a ensemble containing a mean

number of atoms $N_{\text{at}} = 1000$ (or about ± 10 atoms in an ensemble of $N_{\text{at}} = 2500$ at the minimum Fano factor). In figure 17.10, we show that such preparation is well reproducible using 200 experimental realizations.

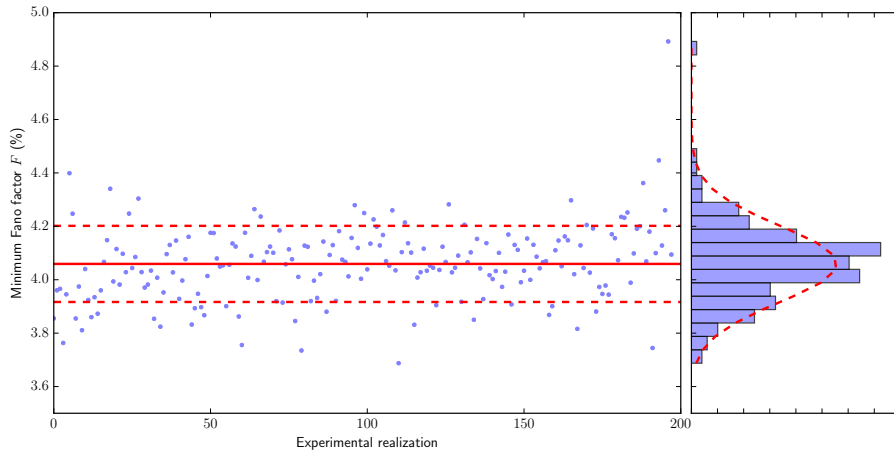


Figure 17.10: (Left) Accuracy of the minimum Fano factor achieved for 200 single-shot measurements. (Right) Histogram

Note that the data analysis based on the recursive Bayesian estimation was done numerically and it would be very instructive to have an analytical model to understand the behaviour of the variance of the atom number estimator. We address this point in the next section. Also note that the method could be ran backward to infer precisely the initial number of atoms instead of the *present* one.

17.4.5 Variance estimator model

We will use first a simplified model for the variance of the estimator $(\Delta N_{\text{at}})^2$ based on the model used for the impressive atom number estimation resolution achieved in Zhang et al. (2012). From this work, one has

$$(\Delta N_{\text{at}})^2 = \frac{c_1}{\tau} + c_2\tau, \quad (17.46)$$

where c_1 and c_2 are constant. In the previously mentioned article, (17.46) was applied to model the atom number fluctuations from a measure of the two-point or Allan atom number variance as a function of the averaging time τ . This model was also used for a similar impressive atom number counting in a different system, Hume et al. (2013).

The first term in (17.46) is analog to (17.37) in absence of prior variance. It is identical to the contribution of light shot noise $(\Delta N_{\text{at}}^{\text{light}})^2$ (i. e. $c_1^{-1} \equiv q\alpha_0\dot{n}_{\text{sc}}$). The second term models the added partition noise due to the random loss of atoms. For our experiments, we consider this as the Poissonian atom loss due to probe light scattering into free space.

In terms of the integrated number of scattering events during a single averaging measurement duration τ , the model (17.46) will write

$$(\Delta N_{\text{at}})^2 = \left(\frac{1}{(\Delta N_{\text{at}}^i)^2} + q\alpha_0 n_{\text{sc}} \right)^{-1} + N_{\text{at}} \frac{n_{\text{sc}}}{n_{\text{loss}}}. \quad (17.47)$$

where we incorporated any prior knowledge variance. The first term corresponds to a gain of knowledge¹⁹ while the second corresponds to a loss of information or increase in entropy due to random loss of atom into the environment. From the appropriate derivative of (17.47), one readily finds the optimal number of scattering events n_{sc} for the minimum variance and minimum Fano factor as

$$n_{\text{sc}} = \left(\frac{n_{\text{loss}}}{N_{\text{at}} q \alpha_0} \right)^{1/2}, \quad (17.48)$$

in a such way that

$$(\Delta N_{\text{at}})_{\text{min}}^2 = \left(\frac{4N_{\text{at}}}{n_{\text{loss}} q \alpha_0} \right)^{1/2}, \quad (17.49)$$

$$F_{\text{min}} = \left(\frac{4}{N_{\text{at}} n_{\text{loss}} q \alpha_0} \right)^{1/2}. \quad (17.50)$$

For atom number state preparation, where $n_{\text{loss}} = n_{\text{heat}}$ this model predicts, for the measured $n_{\text{heat}} = 56$, a metrologically relevant²⁰ Fano factor of $F = -10.7 \text{ dB}$ for an ensemble of $N_{\text{at}} = 2500$ remaining atoms and optimal $n_{\text{sc}} = 2.4$. It is first interesting to mention that although this simple model is a bit pessimistic compared to (17.45), it will nonetheless predict an impressive precision for quantum state tomography. This is because although quantum state tomography is more stringent and do not allow repumping light, our probing method is minimally destructive enough to acquire a lot of knowledge for such a low average number of scattering events per atom $n_{\text{loss}} = n_{\text{heat}} = 56$ which turns out to be comparable to the average number of scattering events to depump an atom from $|4\rangle$ to the ground state $|3\rangle$, $n_{\text{hf}} = 67$. For quantum state tomography, we would have in absence of repumping light, which cannot be used to avoid mixing of basis state populations²¹,

$$n_{\text{loss}} = \left(n_{\text{heat}}^{-1} + n_{\text{hf}}^{-1} \right)^{-1}. \quad (17.51)$$

Here $n_{\text{loss}} \simeq 31$ which gives a prediction of $F = -8 \text{ dB}$ where we considered that $N_{\text{at}} = 1250$, i. e. performing a tomographic characterization of a collective hyperfine coherence where half of the atoms populate the interrogated basis state. This should be compared with $F = -3 \text{ dB}$

¹⁹ It is interesting to remark that in absence of prior knowledge or variance which in some sense bias the estimation, the estimation of the atom number is bound to a minimum $(\Delta N_{\text{at}})^2 \geq (q\alpha_0 n_{\text{sc}})^{-1}$ from which one can read the Fisher information of the conditional probability distribution for N_{at} according to the Cramér-Rao bound.

²⁰ The Fano factor is calculated with respect to the current remaining number of atoms.

²¹ when preparing collective spin state based on such two hyperfine ground states

required to observe negative Wigner function in the characterization of non-classical states. Note that the optimal $n_{sc} = 2.5$ is quasi-identical to the one for atom number measurement.

Although the model (17.47) is of great help and describe the behaviour of the atom number fluctuations in the different limiting regimes of negligible and high atom loss, we have to keep in mind that it constitutes a great simplification of the recursive Bayesian estimation, namely a single averaging step.

If all the non-deterministic processes could be described as Gaussian, we could propagate simply all the results of function convolutions in the recursive estimation and have an analytical and deterministic equation of evolution for the variance of the estimated parameter. In other words, the quasi-continuous Bayesian description would become the Kalman-Bucy description. Such is actually the essence of the Gaussian description formalism of continuous variables in quantum mechanics.

Based on the fundamental role of the Riccati equation in quantum mechanics (Schuch (2014)) in the evolution of the width of a wave-packet and some hindsight given in the first chapter of this thesis, I would like to propose a refine prediction for the evolution of the variance in the next section.

17.4.6 Non-linear Riccati model

We noted in the first chapter of this thesis that in absence of loss, the evolution of the variance $(\Delta N_{at})^2 \equiv v(t)$ is solution of the simple Riccati equation

$$\frac{dv}{dt} = -cv^2. \quad (17.52)$$

In presence of an additional rate of increase r of the variance due to the random loss of atoms, we would like to solve instead

$$\frac{dv}{dt} = -cv^2 + r(t), \quad (17.53)$$

where the rate is expected to vary in time, here exponentially as does the mean number of lost atoms $N_{at}^i (1 - \exp(-t/\tau_{loss}))$. (17.53) would become a non-trivial non-linear differential equation. However, lets consider the lowest order of complexity where the rate r can be assumed constant. We assume that the recursive Bayesian estimation is performed over a duration for which the loss of atoms is small. This is actually the observed experimental situation. Then one can solve exactly the equation. Before I give the solution found with the help of JHM, let me first mention the two important characteristic values of this non-linear equation, namely the prior variance or initial condition v_0 and the asymptotic or stationary variance v_∞ readily given by zeroing the derivative in (17.53)

$$v_\infty = \sqrt{\frac{r}{c}}. \quad (17.54)$$

There are two different solutions which depend on whether the prior variance is larger or smaller than the asymptotic variance, which does not depend on the prior variance. When $v_0 > v_\infty$, the asymptotic variance also becomes the minimum variance that can be reached. The solution writes

$$v(t) = v_\infty \frac{1 + \frac{v_0 - v_\infty}{v_0 + v_\infty} \exp(-2\sqrt{crt})}{1 - \frac{v_0 - v_\infty}{v_0 + v_\infty} \exp(-2\sqrt{crt})}, \quad (17.55)$$

which is equivalent to a time shifted hyperbolic cotangent

$$v(t) = v_\infty \coth(\sqrt{crt} + t_0), \quad (17.56)$$

$$t_0 = \frac{1}{2} \ln \left(\frac{v_0 - v_\infty}{v_0 + v_\infty} \right) = \frac{1}{2} \ln \left(\frac{1 - v_\infty/v_0}{1 + v_\infty/v_0} \right). \quad (17.57)$$

In the case where the prior variance is larger than the stationary variance or if one starts with no prior knowledge ($v_0 \rightarrow +\infty$), $t_0 \rightarrow 0$ in such a way that the evolution of the atom number variance is simply

$$v(t) \simeq v_\infty \coth(\sqrt{crt}). \quad (17.58)$$

For the case $v_0 < v_\infty$ (initial squeezing), the hyperbolic cotangent is to be replaced by the hyperbolic tangent.

Here, $c = c_1^{-1} = q\alpha_0\dot{n}_{sc}$ and $r = c_2 = N_{at}\dot{n}_{sc}/n_{loss}$ and we have

$$(\Delta N_{at})_{\min}^2 = v_\infty = \sqrt{\frac{N_{at}}{n_{loss}q\alpha_0}}. \quad (17.59)$$

Interestingly, this result is twice smaller than (17.50) and therefore will correct for the apparent pessimistic discrepancy of about 3 dB in the first simple variance estimation model. Instead of predicting $F = -10.7$ dB, we predict that the Bayesian estimation of the minimally destructive probing measurement should reach close to $F = -13.7$ dB when the loss are small which is in very good agreement with the observed value of $F = -14$ dB. Hence, the expected precision for tomography would improve even further.

When the approximation of a constant rate loss r is not valid anymore, for instance in the case that t becomes comparable to τ_{loss} , we can physically expect the solution to follow locally the behaviour of (17.57) towards a continuously renewed asymptotic value v_∞ .

17.4.7 Spin-squeezing outlook

The previously reported precision is a promising perspective for continuous measurement induced collective spin squeezing. However, this is one of the most challenging tasks as the allowed measurement strength or number of scattering events per atom has to be weak. The number of allowed spontaneous emission events need to be below unity $n_{sqz} = n_{sc} \leq 1$ as any spontaneous scattering event will project or

make the state of an atom collapse. One can draw two immediate consequences. As the measurement strength is weak, the role of the prior state knowledge (prior variance) becomes significant (see (17.47)). However, at the same time, the contribution of the loss of atoms becomes negligible $n_{\text{sc}} \ll n_{\text{loss}}$ (second term in (17.47)). The dominant measurement back-action mechanism, which outruns the other effects, and needs to be addressed for quantum collective states, becomes the reduction of Ramsey contrast following the scattering induced decoherence of atomic (hyperfine) state superpositions. This effect needs to be taken into account for a metrologically relevant degree of squeezing.

To estimate the achievable degree of spin-squeezing, we consider the scenario of an initially prepared ensemble of N_{at} 2-level atoms in the equatorial plane of the collective Bloch sphere or coherent collective (spin) superposition of the two hyperfine ground states as in the first part of this thesis. We applied the weak dispersive measurement to the ground state $|4\rangle$ where therefore only half of the atomic population resides. As a result, the prior variance of the coherent spin state is $(\Delta N_{\text{at}})^2 = N_{\text{at}}/4$ and the average number of scattering events per atom is halved as half of the sample population in $|3\rangle$ is far-detuned and do not interact with the probe light. After the interaction, the incoherent photon scattering implies a reduction of the transverse²² collective spin component, which here is identical to the size of the collective spin such that we have $\langle \mathbf{J} \rangle \rightarrow \exp(-n_{\text{sc}}/2) \langle \mathbf{J} \rangle$ (see Saffman et al. (2009)). Putting all this together (with (2.44)) gives the metrologically relevant (Wineland) degree of squeezing

$$\xi \equiv \frac{1}{(e^{-n_{\text{sc}}/2})^2} \frac{(\Delta N_{\text{at}})^2}{N_{\text{at}}/4} = \frac{1}{1 + q\alpha_0 N_{\text{at}} n_{\text{sc}}/4} e^{n_{\text{sc}}}, \quad (17.60)$$

$$= \frac{1}{1 + qd_0 n_{\text{sc}}/4} e^{n_{\text{sc}}}, \quad (17.61)$$

where d_0 is the ensemble resonant optical depth. The optimum degree of squeezing is achieved for

$$n_{\text{sc}} = 1 - \frac{4}{qd_0}, \quad (17.62)$$

$$\text{with } \xi_{\text{min}} = \frac{4}{qd_0} \exp\left(1 - \frac{4}{qd_0}\right) = (1 - n_{\text{sc}}) \exp(n_{\text{sc}}). \quad (17.63)$$

Any meaningful and useful squeezing is achieved for $n_{\text{sc}} > 0$ or when the effective optical depth $qd_0 > 4$. We see that in the limit of high optical depths (for a descent detection efficiency q), the degree of squeezing scales as $\sim 1/d_0$. From (17.63), the degree of squeezing is readily optimized for $n_{\text{sc}} = 1$, corresponding to a reduction of Ramsey fringe contrast of $\exp(-n_{\text{sc}}/2) = 61\%$. For ensembles of $N_{\text{at}} = 2500$ pseudo-spin particles and probing on the closed transition $|4, 4\rangle \rightarrow |5, 5\rangle$, which

²² compared to the quantization axis

would be relevant for instance for quantum-assisted magnetometry using the hyperfine coherence from $|4, 4\rangle$ to $|3, 3\rangle$, one can expect up to -4.2 dB metrologically relevant squeezing.

17.4.8 *Summary*

In this chapter, we started by presenting a novel and simple, fast and robust absolute atom number measurement method based on recording optical pumping transients with heterodyne detection. With the knowledge of the calibrated phase shift per atom, we have applied our dual-heterodyne dispersive method proposal to the non-destructive real-time and light shot limited detection of atomic population state. The proposed method reveals impressive resolution for very low average number of scattering events per atom $n_{sc} < 3$. As a result, the fundamentally limited measurement precision left for more stringent tasks such as quantum state tomography and spin-squeezing, in ensemble of atoms interfaced to our nanofiber, will be still significant and demonstrate the future possibility of the generation of collective atomic entanglement using the principles of optical QND measurement.

In this interface, we have gained more than 2 orders of magnitude in the coupling of a single-atom compared to past experiments with ensembles in free space dipole traps.

18

A ONE-DIMENSIONAL ATOMIC MIRROR

The scientist is not a person who gives the right answers, he is one who asks the right questions.

— Claude Lévi-Strauss

This chapter contains results which have not been published yet and deals with progress in the exploration of coherent and collective effects in a nanofiber interface.

An essential step missing towards the realization of tomography of non-classical states as well as spin-squeezing, following the successful demonstration of a real-time high-resolution and minimally destructive probing for QND measurement, is the coherent manipulation and preparation of quantum atomic states (e. g. Ramsey interrogation). We will briefly sum up the experimental work achieved in this direction before we rapidly move on a different project in progress. Namely, the realization of a one-dimensional atomic Bragg mirror in the evanescent field of an optical nanofiber.

18.1 TOWARDS STATE PREPARATION

In a few lines, which sum up a few months, we have accomplished a few experimental progress towards quantum state engineering, which we focus on the manipulation of the coherence between the two hyperfine ground states of Cesium. We have interfaced to the nanofiber setup, a microwave source (free space antenna) with a power of about 10 W, identical to the one used in the old experiment. In the past, we could drive, with a similar source, Rabi frequencies up to 50 kHz. This relatively low frequency for such high driving field power is due to the nature of the ground state hyperfine transition which is electrically forbidden (first order) and therefore is driven through the interaction between the magnetic moment of the atom and the magnetic field of the microwave radiation. This expected Rabi frequency would be suited for our goals if the coherence time of the levels would be long enough compared to the Rabi period of 20 μs , which was already close to 100 μs for the free space dipole trap atomic ensemble. A pessimistic intuition for the expected coherence time in the nanofiber interface arose from the existence of fictitious magnetic fields due to the non-trivial polar-

ization field of the nanofiber trap light. As we have seen earlier in this thesis, Zeeman atomic levels can be mixed or coupled when the atoms are dressed by a light field with a significant ellipticity. This would lead for instance to a loss of coherence between the initially prepared Zeeman clock states. This led us to develop in parallel another technique to drive Rabi oscillations faster, optically, namely via a two photon transition or Raman stimulated transition. The time invested in assembling the Raman setup will also open the possibility for the study of Raman sideband cooling. We have not had the time yet to make this important quantum state preparation step as we encountered another important one that I will present in the next section. However, let me just report in figure 18.1 an important achievement showing the successful observation of microwave photon interaction with Cesium atoms trapped in a lattice around an optical nanofiber.

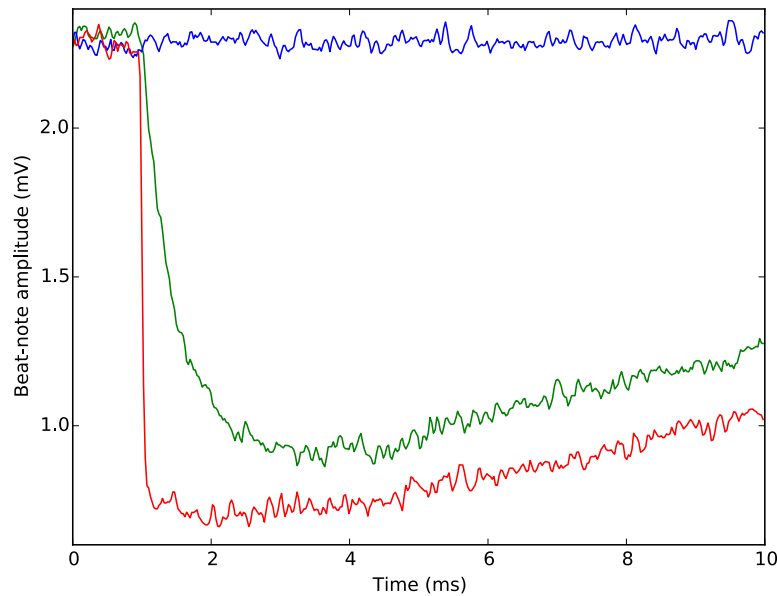


Figure 18.1: Continuous heterodyne detection of the transmitted probe field resonant to $|4\rangle \rightarrow |5\rangle$. The atoms are initially in the dark state $|4\rangle$. (blue trace) field transmission in absence of atoms (no quadrupole MOT field), (red trace) At $t = 1$ ms CW optical repumping on $|3\rangle \rightarrow |4\rangle$, (green trace) repumping with an external microwave sweep. (see main text)

The data reveal a microwave pumping transient following a 10 ms long linear sweep of the external microwave field frequency irradiating the atoms (2 MHz around the resonant transition frequency of ~ 9.1926 GHz). In short, this figure shows the first atomic detection of microwave radiation by nanofiber trapped atoms in our group. Atoms are initially trapped in the lowest ground state $|3\rangle$. We continuously perform heterodyne detection of resonant probe light on the $|4\rangle \rightarrow |5\rangle$

transition. Instead of being pumped into the ground state $|4\rangle$ via external repumping light on the $|4\rangle \rightarrow |4'\rangle$, as we have done several times in the past, here the atoms are driven into the upper hyperfine state by the continuous external microwave field interaction which led to the observation of the resonant absorption of probe photons. To observe continuously (in real-time) Rabi oscillations, the atomic state population needs to be detected non-destructively. And promising steps have been done through the observation of the same microwave interaction but as a transient in the phase shift of the dispersively detection hyperfine state using the dual-sideband probing technique. I believe that this important experimental objective will be achieved soon in the future, once we will finish the characterization of Landau-Zener sweeps.

18.2 ATOMIC BRAGG MIRROR

In parallel to the previous developments, we invested time at the end of this thesis, to rebuilt completely the detection setup. It took more than four months of intense work to get the setup operational again with the trapping of atoms in optical lattices and their non-destructive detection.

18.2.1 *New setup*

This decision was first triggered by the lack of independent polarization degrees of freedom for all the different light sources, which are combined and propagate into the same nanofiber mode, but also in order to improve the overall detection quantum efficiency. Although the latter $q \simeq 0.4$ is descend, we can improve it by transforming our prototype detection setup. In particular, we built new shot noise limited photodetectors peaked around the 62.5 MHz heterodyne frequency. Contrary to the single photodiode prototype detector used so far, these new detectors are differential detectors based on two photodiodes. This will allow to perform balanced heterodyning without wasting 90% of the optical LO power and 10% of the probe signal, resulting in higher quantum efficiency from the higher ratio of LO shotnoise to electronic noise and lower probe photon loss.

Not only did we rebuild and optimize the detection system, we built two of them arranged symmetrically about the nanofiber in such a way that we can perform the dual-sideband QND measurement independently and simultaneously from both propagation fiber ports. This also means that while probing the atoms along a given propagation direction and measuring the properties of the forward scattered probe field in transmission, we can at the same time monitor the light field in reflection which may be scattered back by the atoms into the fiber guided mode.

We started to investigate the back-reflection properties of the probe light interacting with atoms trapped in the nanofiber lattice, which is a spatially periodic atomic structure, well known to allow for collective or interference effects such as Bragg diffraction or scattering analog to crystal diffraction.

18.2.2 *Bragg reflection condition*

For the one-dimensional fiber mode geometry, constructive interferences between all the light fields scattered by the periodically trapped Cesium atoms may indeed be possible in back-reflection or in other words in a direction corresponding to a deviation angle of the incident light by π , if the well-known Bragg condition is met,

$$2d \sin(\theta) = n\lambda, \quad (18.1)$$

$$d = \frac{\lambda}{2}n. \quad (18.2)$$

where θ is half the deviation angle (so here $\sin(\theta) = 1$), d is the atomic spacing or lattice period, λ the light wavelength and n the diffraction order (natural number). Note that the intensity of the back-reflected light depends on the atomic scattering cross section.

From (18.2), we see that the Bragg condition in reflection is fulfilled if the atomic spacing is a multiple integer of $\lambda/2$. Unfortunately, this condition is not satisfied for a probe wavelength resonant to the Cesium D2 line scattering cross section ($\lambda_p = 852 \text{ nm}$) as it is incommensurate with the nanofiber optical lattice trap sites period, built from the far red-detuned ($\lambda_r = 1057 \text{ nm}$) standing wave, i. e. $d = \lambda_r/2$. Actually, these values are the wavelengths in vacuum and the longitudinal wavelength ($2\pi/\beta$) of the guided fundamental mode is lower due to the effective waveguide refractive index (e. g. $\lambda_p = 852 \text{ nm} \rightarrow 745 \text{ nm}$).

Consequently, collective back-scattering would be largely suppressed in our interface and any observed back-scattering would be similar to the one expected from a disordered medium. Before we show the technique we have implemented experimentally to bypass the above limitation and observe Bragg reflection, I would like to mention the only (to my knowledge) two recent articles reporting observations and properties of light reflected off a nanofiber lattice trap.

18.2.3 *Reported work*

First, in Goban et al. (2012), reflected light from the disordered situation (incommensurate lattice trap period and probe wavelength) is reported by counting photons, i. e. detecting reflected photons. No absolute reflection coefficient is given. The study was focused on the reflection spectrum, more precisely the frequency dependence of the reflected light. It reveals a resonant Lorentzian spectrum with a min-

imum linewidth given by the natural transition linewidth of Cesium which however presents broadening proportional to the lattice disorder or entropy defined as $S = \ln \binom{N_{\text{at}}}{n_{\text{site}}}$, where $\binom{N_{\text{at}}}{n_{\text{site}}}$ is the binomial coefficient with n_{site} the number of lattice sites.

In [Reitz et al. \(2014\)](#), the entire article is dedicated to the back-scattering properties, also for the disordered situation and measurement performed via photon counting. It reports absolute values of the light power reflected by the atoms which presents a saturation behaviour with the input power. From the article data, one finds that the typical reflected DC equivalent light power (inferred from the number of photons in the 200 ns measurement time bin) is about 10 pW for an ensemble of $N_{\text{at}} = 500$ atoms. This power is reflected from a typical resonant and saturating input light power of 10–20 nW representing saturated reflection coefficients ranging from 1×10^{-4} to 1×10^{-3} . In addition, the reflected light is seen scattered into different polarization modes than the incident light polarization.

18.2.4 *The lattice within the lattice*

With the help of Prof. Anders Sørensen and Ivan Iakoupov from the theoretical quantum optics group, working in close collaboration with our experiments, we have found a way to bypass the natural mismatch between the lattice periodicity and the wavelength resonant to the Cesium atomic scattering cross section. This would allow to observe for the first time in this system collective back-scattering and allow to realize an atomic mirror from a few trapped atoms with total reflection coefficients on the order of 50%. The theoretical study is based on the transfert matrix formalism [Deutsch et al. \(1995\)](#). In that respect it would be possible to realize the interesting hybrid idea ([Chang et al. \(2012\)](#)) of reaching the regime of cavity QED with atomic ensembles using the atoms themselves as the mirrors.

To fulfill the Bragg condition for a wavelength resonant to the strong D2 atomic transition, our approach consists in pumping periodically and spatially the internal atomic states with the help of a pumping standing wave field. One should now view the nanofiber optical lattice dipole trap as a mere tool to hold the atoms in place and consider to imprint the *correct* pattern of periodic atomic cross sections for light diffraction, by manipulating the internal states of the atoms.

Initially prepared in the lowest hyperfine ground state $|3\rangle$, atoms which will seat at the anti-nodes of the optical pumping standing wave field, which is resonant to the $|3\rangle \rightarrow |4\rangle$ transition, will be pumped into the ground state $|4\rangle$, while the atoms seating at the nodes will remain in their initial dark state $|3\rangle$ for the probe light resonant to the $|4\rangle \rightarrow |5'\rangle$ that we hope to be Bragg reflected. As we exploit hyperfine pumping, the optical period of the imprinted pattern is nearly half ($\lambda/2$) of the incident probe wavelength. I personally expect this idea to work even

better for Rubidium atoms and alkali atoms with a lower ground state hyperfine splitting. Indeed, although the frequency difference between the pump and the probe is only about ~ 9.2 GHz for Cesium that corresponds to a difference of only 22 pm in wavelengths to satisfy the Bragg condition, the accumulated phase delay and therefore phase mismatch will reach close to 0.6 mrad for after a nominal maximum 5 mm nanofiber propagation length.

Nonetheless, this research project is appealing as the created atomic mirror, which can be used to reflected single photon backward in a fiber with a high probability from a few atoms, is switchable and is created on-demand by optical pumping. Note that one can choose between making a bright or dark pattern lattice. Above we presented the bright lattice case but one could start initially with the atoms in $|4\rangle$ and depump into $|3\rangle$ using the $|4\rangle \rightarrow |4'\rangle$ transition. This would have the other great advantage of improving the phase matching following that the frequency difference between the pump and the probe would now fall into a few hundred of megahertz. Such mirror is expected to have a very narrow bandwidth, limited by the incident resonant light spectrum and not the atomic transition linewidth as in the case of disordered ensembles. In addition, the state-selective nature of the cold atom mirror makes it appealing to be controlled by small external field perturbations. Last but not least, it may be possible, via optical pumping into particular Zeeman levels, to make the collective reflection strongly polarization dependent. It seems therefore that there will be a lot of interesting things to explore for the next generation of PhD students¹. In the next section, I will describe a few experimental measurement and data acquired showing progress in this direction.

18.2.5 Experiments

From the current light sources constrains of our experimental setup, I initially offered to implement with EB the idea of the bright lattice to start this adventure and to learn as much as possible. Heidi Lund Sørensen (HLS) has now joined us on this adventure and will be the principal PhD student on the experiment.

As a novelty compared to the litterature, I propose to use our versatile heterodyne detection chain to monitor any back-reflected light from the nanofiber. This means that we are looking at a field of light which is potentially reflected and will most importantly interfere with an optical local oscillator. This has several advantages including that we do not need to filter the photons coming from all the relatively intense trap light propagating in the nanofiber, using for instance high quality

¹ If you read this, I sometimes asked myself whether the coupling efficiency into a fiber could be greatly improved via Bragg scattering. In particular, it would be interesting to see if one could couple light into the nanofiber mode from outside, at the taper position, exploiting the Bragg condition at a different angle after preparation of an atomic mirror.

volume Bragg gratings as in other experiments. Certainly the most important point is that the detection will allow to monitor continuously over time the evolution of the light field reflected by the atoms.

In figure 18.2, I report the first demonstration of continuous and coherent detection of light reflected by a periodically pumped ensemble of atoms (bright configuration).

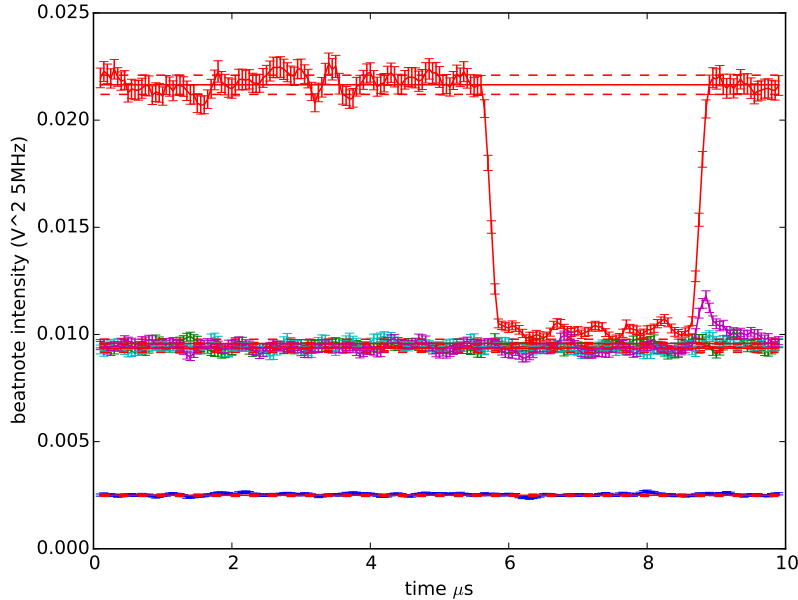


Figure 18.2: Continuous narrow-band detection of reflected light from ordered nanofiber trapped atoms. (See main text for the legend).

The experimental protocol is as follows. First we trap Cesium atoms in the nanofiber lattice trap and wait for a storage time of $t = 10 \text{ ms}$ to remove any potential bias from residual flying MOT atoms. The atoms are initially in the lowest hyperfine state $|3\rangle$ and we send a single sideband resonant to the $|4\rangle \rightarrow |5'\rangle$ to probe the atoms, which then initially do not interact with the ensemble. We record, for $10 \text{ }\mu\text{s}$, the raw photocurrent heterodyne beatnote at 62.5 MHz and extract the reflected detected field intensity in a narrow resolution bandwidth (5 MHz) to have similar conditions as the photon counting experiments that reported consistent reflected photon signals only for the first 200 ns (Reitz et al. (2014)). The lowest constant signal in figure 18.2 is the total electronic noise of the detection chain. The green level near 0.010 V^2 corresponds to optical LO shot noise plus electronic noise. In other words it is the reference level corresponding to detection of a vacuum reflected input field. The significant red signal corresponds to a calibration measurement at a relatively high input probe power (several hundred of nanowatt), which reveals the existence of a finite amount of classical light which is always reflected by all the optical elements on the probe path, the dominant ones being the nanofiber input and out-

put couplers. As clearly seen, the input probe is turned off rapidly at $t = 5.5 \mu\text{s}$ with an AOM to create a time window at the center of which we will prepare the atomic ensemble in the bright Bragg lattice with a 500 ns standing wave repumping pulse. The cyan signal which cannot be distinguished from the vacuum signal level corresponds to the same calibration classical back-reflection when the input probe power is now adjusted to 10 nW . Delightfully, repeating the previous cyan measurement in presence of nanofiber trapped atoms with the periodic optical pumping scheme reveals the apparition of a reflected pulse of light (purple curve) as soon as the probe light field is sent towards the atoms when its AOM is turned back on. This is really the first signal observed and I need to highlight that the measurement is quite challenging. The detected pulse contains less than half a photon measured with heterodyning and all the shown data corresponds to an average over 500 hundred experimental realizations to resolve clearly this very weak signal. While for this first data the absolute reflection coefficient is on the order of 1×10^{-4} we are nowadays approaching the few percent level by a better understanding of the quality of the standing wave repump parameters and the fact that the theory was originally calculated for single input probe photons. Here our first attempts were motivated to observe first what has been reported before and the probe power used there were meant to saturate disordered atomic ensembles.

We can repeat the experiment by blocking only one of the beams forming the optical repumping standing wave, creating a disordered ensemble of atoms, and we will fail to the reflected peak. This peak is sensitive to various parameters and in particular to the input probe frequency with respect to the $|4\rangle \rightarrow |5'\rangle$ transition. By adjusting the starting origin of the data acquisition we can look at later times which reveal the existence of a flat tail following the peak as seen in figure 18.3.

This tail is also present when blocking one of the standing wave repumping beams, which gives indication that this might represent a signal from disordered atoms. The Bragg diffraction condition is perfectly realized if atoms are not moving, which is not realistic in the nanofiber trap (expected trap oscillation frequencies from 0.1 to 1 MHz). And we can understand that the perfect phase matching for Bragg diffraction will be rapidly smeared out by many effects. Because of the relatively long lifetime of the trail signal, one can average or decrease the heterodyne detection bandwidth to improve the signal in contrast to the short lifetime of the coherent pulse.

To finish this chapter, I would like to mention the observation of revivals or oscillations in the reflected light field as in figure 18.4 after an attempt to improve the contrast of the repumping standing wave. We need to understand better all the characteristics of this new system and we are currently exploring the creation of the dark atomic Bragg

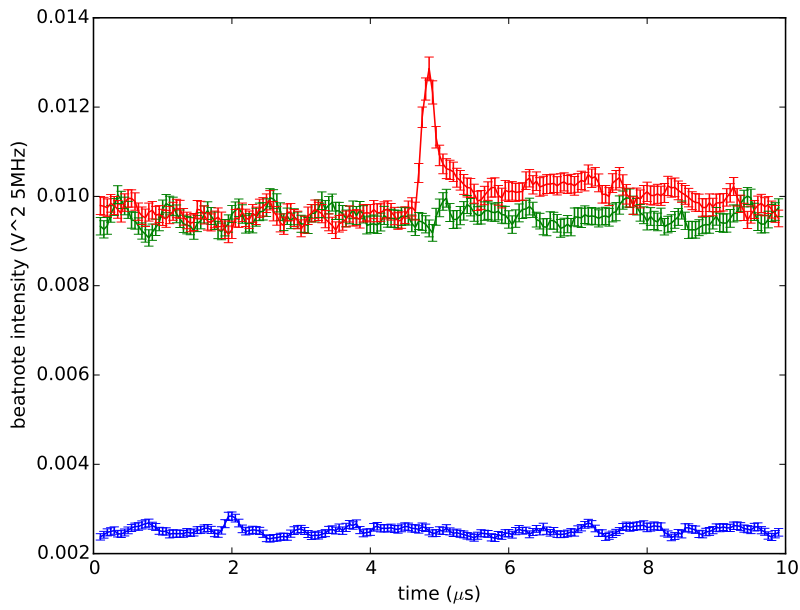


Figure 18.3: Longer acquisition of the reflection signal showing a double structure, a peak and trailing tail. (Blue) electronic noise, (Green) vacuum signal, (Red) Reflected light from ordered atoms

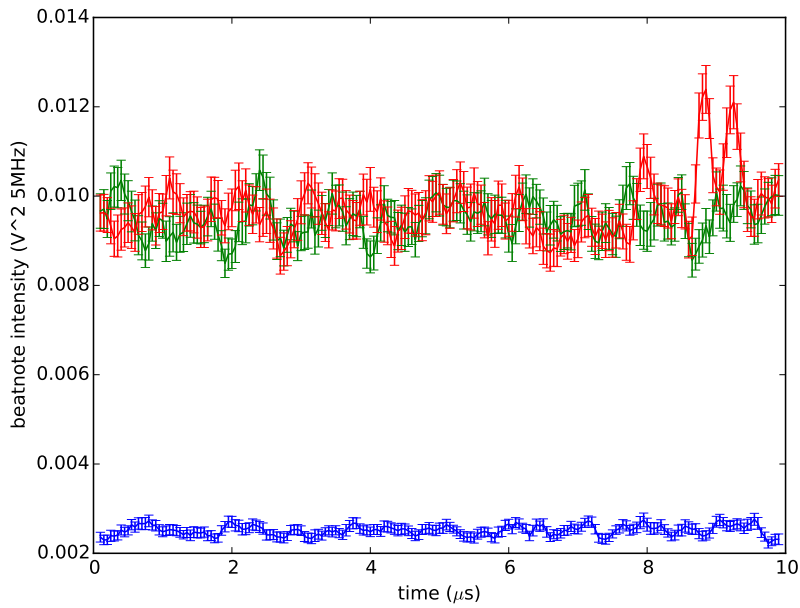


Figure 18.4: Observation of oscillations in the reflected light field. (Blue) electronic noise, (Green) vacuum signal, (Red) Reflected light from ordered atoms

lattice scheme and the effects of external bias fields and input probe polarization on the reflected signals.

SUMMARY

In this chapter, we started by reporting some progress towards the coherent preparation of quantum superposition of atomic states in nanofiber trapped atoms. Then, we presented the possible realization of collective Bragg scattering in reflection from nanofiber trapped atoms with a simple idea based on periodically pumped atomic states. Finally, we reported some preliminary exciting experimental results showing the observation of reflected light fields from ordered atoms, which are detected continuously with the heterodyne technique.

CONCLUSION AND OUTLOOK

We have finally reached the conclusion of this thesis report. In the first part, I tried to present in a simple form the experimental work and ideas conducted with [SLC](#) on the manipulation and preparation of non-classical collective states of atoms in free space optical dipole trap ensembles of cold Cesium atoms. With complementary experimental efforts, we succeeded in the preparation and characterization of collective spin-squeezed states of atoms, which were demonstrated highly non-classical albeit Gaussian states, in [Kiesel et al. \(2012\)](#). We then pursued the experimental goal of creating the first excited Dicke state or the creation of a single delocalized atomic spin excitation in the ensemble, heralded by a forward scattered photon. We next tried to characterize this state via atomic state interferometry and continuous measurement of atomic state populations. We observed a significant macroscopic increase in the quantum noise of the heralded state as compared to a coherent spin state [Christensen et al. \(2014\)](#).

Although I spent two intense years working on these projects, I had the parallel challenging proposal of building a completely new experimental quantum optics setup for cold Cesium atoms in view to create a new interface based on an optical nanofiber. As a result of the limited time constraint of a PhD, I tried to focus my efforts on the development of a simple and versatile detection scheme for the various tasks of light atomic ensemble interfaces. It was a challenge to explore both theoretically and experimentally this new experiment and I ought to save the important enabling steps to the future generation of students who will work on the setup. This explains why this report is detailed on the nanofiber interface exploration.

We successfully demonstrated an interface between light and atoms trapped in an optical lattice in the evanescent field of a nanofiber [Béguin et al. \(2014\)](#). We realized the first non-destructive real-time and light shot noise limited detection of atomic state population around the fiber.

The future seems then well defined. We will next try to prepare non-classical collective states of atoms around an optical nanofiber. We will also continue to explore the realization of an atomic Bragg mirror. To give a few ideas of improvement in this interface, I can mention the prospect of nanofibers with fiber Bragg gratings (cavity) to enhance the

interaction. On the atomic side, one can also imagine to manipulate and couple Rydberg atoms to a nanofiber. Due to their high orbital radius ($\sim 100 \text{ nm}$) one has to take care of the effects of the fiber surface or align the electronic orbital plane parallel to the fiber surface.

I would like to finish by showing a rapid theoretical calculation I did at the very first order, of the effect of bending our optical nanofiber, on the transverse intensity profile of the evanescent fundamental mode with linear polarization, see figure 19.1. Would it be possible to create a nanofiber loop or create a ring-cavity-like resonator where atoms are trapped all around its circumference ? According to figure 19.1, the local transverse evanescent field is not seen affected by a loop radius as small as $50 \mu\text{m}$. However, the mode starts to *whisper* towards the outer loop diameter or outer right edge side on the figures for $5 \mu\text{m}$.

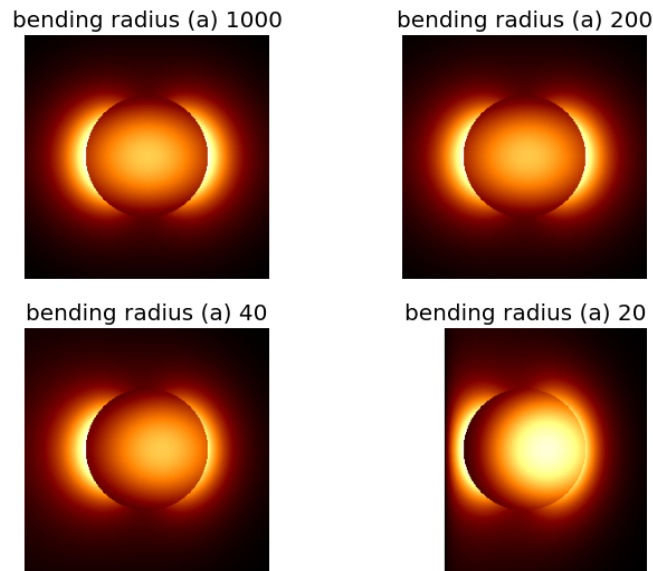


Figure 19.1: Transverse intensity profile of the nanofiber fundamental mode with quasi-linear transverse polarization (horizontal in this figure) and $\lambda = 1057 \text{ nm}$. The bending curvature radii are given in units of the nanofiber radius $a = 250 \text{ nm}$.

Part V

APPENDIX

A

ACCOMPANYING MATHEMATICAL DEVELOPMENTS

A.1 WAVE EQUATIONS

- Wave equation for \mathbf{E} : Taking the curl of (6.2), inserting (6.4) and using a useful vectorial relation leads to

$$\nabla \times (\nabla \times \mathbf{E}) = -\mu_0 \frac{\partial(\nabla \times \mathbf{H})}{\partial t} = -\mu_0 \epsilon \frac{\partial^2 \mathbf{E}}{\partial t^2} = \nabla(\nabla \cdot \mathbf{E}) - \Delta \mathbf{E}$$

Plus (6.1), $\nabla \cdot [\epsilon(r)\mathbf{E}] = \mathbf{E} \cdot \nabla \epsilon(r) + \epsilon(r)\nabla \cdot \mathbf{E} = 0$ that gives $\nabla \cdot \mathbf{E} = -[\mathbf{E} \cdot \nabla(\epsilon)] / \epsilon$

$$\Delta \mathbf{E} - \mu_0 \epsilon \frac{\partial^2 \mathbf{E}}{\partial t^2} = -\nabla \left[\frac{\mathbf{E} \cdot \nabla(\epsilon)}{\epsilon} \right] \quad (\text{A.1})$$

- Wave equation for \mathbf{H} :

$$\Delta \mathbf{H} - \mu_0 \epsilon \frac{\partial^2 \mathbf{H}}{\partial t^2} = \nabla \epsilon \times \mathbf{E} \quad (\text{A.2})$$

A.2 RELATIONS BETWEEN CYLINDRICAL COMPONENTS

We can explicit the relations between all the components of the fields with the help of the following operators in cylindrical coordinates :

$$\begin{aligned} \nabla \cdot \mathbf{A} &= \frac{1}{r} \frac{\partial}{\partial r} [rA_r] + \frac{1}{r} \frac{\partial A_\phi}{\partial \phi} + \frac{\partial A_z}{\partial z} \\ \nabla \times \mathbf{A} &= \left[\frac{1}{r} \frac{\partial A_z}{\partial \phi} - \frac{\partial A_\phi}{\partial z} \right] \mathbf{u}_r + \left[\frac{\partial A_r}{\partial z} - \frac{\partial A_z}{\partial r} \right] \mathbf{u}_\phi + \frac{1}{r} \left[\frac{\partial}{\partial r} (rA_\phi) - \frac{\partial A_r}{\partial \phi} \right] \mathbf{u}_z \end{aligned}$$

$$\nabla \times \mathcal{E}]_r = \frac{1}{r} \frac{\partial \mathcal{E}_z}{\partial \phi} + i\beta \mathcal{E}_\phi = -i\omega \mu_0 \mathcal{H}_r$$

$$\nabla \times \mathcal{H}]_\phi = -i\beta \mathcal{H}_r - \frac{\partial \mathcal{H}_z}{\partial r} = i\omega \epsilon \mathcal{E}_\phi$$

$$\begin{aligned}\frac{1}{r} \frac{\partial \mathcal{E}_z}{\partial \phi} - \frac{\omega \mu_0}{\beta} \frac{\partial \mathcal{H}_z}{\partial r} &= i \frac{h^2}{\beta} \mathcal{E}_\phi \\ \mathcal{H}_r &= i \frac{1}{\beta} \frac{\partial \mathcal{H}_z}{\partial r} - \frac{\omega}{\beta} \epsilon \mathcal{E}_\phi\end{aligned}$$

$$\begin{aligned}\nabla \times \mathcal{E}]_\phi &= -i\beta \mathcal{E}_r - \frac{\partial \mathcal{E}_z}{\partial r} = -i\omega \mu_0 \mathcal{H}_\phi \\ \nabla \times \mathcal{H}]_r &= \frac{1}{r} \frac{\partial \mathcal{H}_z}{\partial \phi} + i\beta \mathcal{H}_\phi = i\omega \epsilon \mathcal{E}_r\end{aligned}$$

$$\begin{aligned}\frac{\beta}{h} \left\{ \pm m \frac{\mathcal{B} J_m(hr)}{hr} - i \frac{\omega \epsilon_1}{\beta} \mathcal{A} \frac{\partial J_m(hr)}{\partial(hr)} \right\} &= \mathcal{H}_\phi \\ \frac{1}{r} \frac{\partial \mathcal{H}_z}{\partial \phi} + \frac{k_0^2 n_1^2}{\beta \omega \mu_0} \frac{\partial \mathcal{E}_z}{\partial r} &= i \frac{h^2}{\beta} \mathcal{H}_\phi \\ \frac{\omega \mu_0}{\beta} \frac{1}{hr} \frac{\partial \mathcal{H}_z}{\partial \phi} + \frac{\partial \mathcal{E}_z}{\partial(hr)} &= i \frac{h}{\beta} \mathcal{E}_r\end{aligned}$$

$$\begin{aligned}\nabla \times \mathcal{E}]_z &= \frac{1}{r} \left[\frac{\partial}{\partial r} (r \mathcal{E}_\phi) - \frac{\partial \mathcal{E}_r}{\partial \phi} \right] = -i\omega \mu_0 \mathcal{H}_z \\ \nabla \times \mathcal{H}]_z &= \frac{1}{r} \left[\frac{\partial}{\partial r} (r \mathcal{H}_\phi) - \frac{\partial \mathcal{H}_r}{\partial \phi} \right] = i\omega \epsilon \mathcal{E}_z\end{aligned}$$

A.3 ϕ AND r COMPONENTS

$$\begin{aligned}\mathcal{E}_\phi^\pm(r < a, \phi) &= \frac{\beta}{h} \left\{ i\mathcal{B} \frac{\partial J_l(hr)}{\partial(hr)} \frac{\omega \mu_0}{\beta} \pm l\mathcal{A} \frac{J_l(hr)}{hr} \right\} \exp[\pm il\phi] \\ \mathcal{E}_\phi^\pm(r > a, \phi) &= -\frac{\beta}{q} \left\{ i\mathcal{D} \frac{\partial K_l(qr)}{\partial(qr)} \frac{\omega \mu_0}{\beta} \pm l\mathcal{C} \frac{K_l(qr)}{qr} \right\} \exp[\pm il\phi] \\ \mathcal{E}_r^\pm(r < a, \phi) &= -\frac{\beta}{h} \left\{ i\mathcal{A} \frac{\partial J_l(hr)}{\partial(hr)} - (\pm l) \frac{\omega \mu_0}{\beta} \mathcal{B} \frac{J_l(hr)}{hr} \right\} \exp[\pm il\phi] \\ \mathcal{E}_r^\pm(r > a, \phi) &= \frac{\beta}{q} \left\{ i\mathcal{C} \frac{\partial K_l(qr)}{\partial(qr)} - (\pm l) \frac{\omega \mu_0}{\beta} \mathcal{D} \frac{K_l(qr)}{qr} \right\} \exp[\pm il\phi] \\ \mathcal{H}_r^\pm(r < a, \phi) &= -\frac{\beta}{h} \left\{ (\pm l) \frac{\omega \epsilon_1}{\beta} \mathcal{A} \frac{J_l(hr)}{hr} + i\mathcal{B} \frac{\partial J_l(hr)}{\partial(hr)} \right\} \exp[\pm il\phi] \\ \mathcal{H}_r^\pm(r > a, \phi) &= \frac{\beta}{q} \left\{ (\pm l) \frac{\omega \epsilon_2}{\beta} \mathcal{C} \frac{K_l(qr)}{qr} + i\mathcal{D} \frac{\partial K_l(qr)}{\partial(qr)} \right\} \exp[\pm il\phi] \\ \mathcal{H}_\phi^\pm(r < a, \phi) &= \frac{\beta}{h} \left\{ (\pm l) \mathcal{B} \frac{J_l(hr)}{hr} - i \frac{\omega \epsilon_1}{\beta} \mathcal{A} \frac{\partial J_l(hr)}{\partial(hr)} \right\} \exp[\pm il\phi] \\ \mathcal{H}_\phi^\pm(r > a, \phi) &= -\frac{\beta}{q} \left\{ (\pm l) \mathcal{D} \frac{K_l(qr)}{qr} - i \frac{\omega \epsilon_2}{\beta} \mathcal{C} \frac{\partial K_l(qr)}{\partial(qr)} \right\} \exp[\pm il\phi]\end{aligned}$$

A.4 CONTINUITY CONDITION DERIVATION

A.5 LAPLACE DEVELOPPMENT

$$(l\beta)^2 \left\{ \frac{1}{q^4 a^2} + \frac{1}{a^2 q^2 h^2} + \frac{1}{h^2 a} \left(\frac{1}{q^2 a} + \frac{1}{h^2 a} \right) \right\} - \frac{J'_l K'_l \omega^2 \mu_0}{JK} \frac{1}{hq} (\epsilon_1 + \epsilon_2) - \omega^2 \mu_0 \left(\epsilon_1 \left(\frac{J'_l}{Jh} \right)^2 + \epsilon_2 \left(\frac{K'_l}{Kq} \right)^2 \right) = 0$$

A.6 GENERAL SOLUTIONS FOR ROTATING POLARIZATION

Inside :

$$\begin{aligned} \mathcal{E}_z^\pm(r, \phi) &= \mathcal{C} J_l(hr) \frac{K_l(qa)}{J_l(ha)} \exp[\pm il\phi] \\ \mathcal{E}_r^\pm(r, \phi) &= \mathcal{C} \frac{K_l(qa)}{J_l(ha)} \frac{i\beta}{2h} [J_{l+1}(hr)(1+ls) - J_{l-1}(hr)(1-ls)] \exp[\pm il\phi] \\ \mathcal{E}_\phi^\pm(r, \phi) &= \pm \mathcal{C} \frac{K_l(qa)}{J_l(ha)} \frac{\beta}{2h} [J_{l+1}(hr)(1+ls) + J_{l-1}(hr)(1-ls)] \exp[\pm il\phi] \\ \mathcal{H}_z^\pm(r, \phi) &= \pm s \frac{i\beta}{\omega\mu_0} \mathcal{C} \frac{K_l(qa)}{J_l(ha)} J_l(hr) \exp[\pm il\phi] \\ \mathcal{H}_r^\pm(r, \phi) &= \pm \mathcal{C} \frac{K_l(qa)}{J_l(ha)} \frac{\beta^2}{2h\omega\mu_0} \left[J_{l-1}(hr) \left(ls - \frac{\omega^2 \epsilon_1 \mu_0}{\beta^2} \right) - J_{l+1}(hr) \left(ls + \frac{\omega^2 \epsilon_1 \mu_0}{\beta^2} \right) \right] \exp[\pm il\phi] \\ &= \pm \mathcal{C} \frac{K_l(qa)}{J_l(ha)} \frac{\beta^2}{2h\omega\mu_0} \left[J_{l-1}(hr)(ls-1) - J_{l+1}(hr)(ls+1) - 2l \frac{h^2}{\beta^2} \frac{J_l(hr)}{hr} \right] \exp[\pm il\phi] \\ \mathcal{H}_\phi^\pm(r, \phi) &= \mathcal{C} \frac{K_l(qa)}{J_l(ha)} \frac{i\beta^2}{2h\omega\mu_0} \left[J_{l+1}(hr) \left(\frac{\omega^2 \epsilon_1 \mu_0}{\beta^2} + ls \right) + J_{l-1}(hr) \left(ls - \frac{\omega^2 \epsilon_1 \mu_0}{\beta^2} \right) \right] \exp[\pm il\phi] \end{aligned}$$

Outside :

$$\begin{aligned}
\mathcal{E}_z^\pm(r, \phi) &= \mathcal{C}K_l(qr) \exp[\pm il\phi] \\
\mathcal{E}_r^\pm(r, \phi) &= -\mathcal{C}\frac{i\beta}{2q} [K_{l+1}(qr)(1+ls) + K_{l-1}(qr)(1-ls)] \exp[\pm il\phi] \\
\mathcal{E}_\phi^\pm(r, \phi) &= \pm\mathcal{C}\frac{\beta}{2q} [K_{l-1}(qr)(1-ls) - K_{l+1}(qr)(1+ls)] \exp[\pm il\phi] \\
\mathcal{H}_z^\pm(r, \phi) &= \pm s \frac{i\beta}{\omega\mu_0} \mathcal{C}K_l(qr) \exp[\pm il\phi] \\
\mathcal{H}_r^\pm(r, \phi) &= \pm\mathcal{C}\frac{\beta^2}{2q\omega\mu_0} \left[K_{l+1}(qr)(ls + \frac{\omega^2\epsilon_2\mu_0}{\beta^2}) + K_{l-1}(qr)(ls - \frac{\omega^2\epsilon_2\mu_0}{\beta^2}) \right] \exp[\pm il\phi] \\
\mathcal{H}_\phi^\pm(r, \phi) &= -\mathcal{C}\frac{i\beta^2}{2q\omega\mu_0} \left[K_{l+1}(qr)(\frac{\omega^2\epsilon_2\mu_0}{\beta^2} + ls) + K_{l-1}(qr)(\frac{\omega^2\epsilon_2\mu_0}{\beta^2} - ls) \right] \exp[\pm il\phi] \\
\text{with } s &= \left[\frac{1}{h^2a^2} + \frac{1}{q^2a^2} \right] \left(\frac{J_l^*(ha)}{haJ_l(ha)} + \frac{K_l^*(qa)}{qaK_l(qa)} \right)^{-1} \\
&\text{using} \\
K_l^*(qr) &= -\frac{1}{2} [K_{l+1}(qr) + K_{l-1}(qr)] \\
K_{l+1}(qr) &= \frac{2l}{qr} K_l(qr) + K_{l-1}(qr) \\
J_l^*(hr) &= -\frac{1}{2} [J_{l+1}(hr) - J_{l-1}(hr)] \\
J_{l+1}(hr) &= \frac{2l}{hr} J_l(hr) - J_{l-1}(hr)
\end{aligned}$$

A.7 NORMALIZATION CONSTANT

For both $^1 \pm$ rotating polarizations,

$$\begin{aligned}
\langle S_z^{in} \rangle_{\frac{2\pi}{\omega}} &= \left(\mathcal{C} \frac{K_l(qa)}{J_l(ha)} \right)^2 \frac{\beta^3}{4h^2\omega\mu_0} \times \\
&\left\{ J_{l+1}^2(hr)(1+ls) \left[\frac{h^2}{\beta^2} + 1 + ls \right] + J_{l-1}^2(hr)(1-ls) \left[1 - ls + \frac{h^2}{\beta^2} \right] \right\} \\
\langle S_z^{out} \rangle_{\frac{2\pi}{\omega}} &= \mathcal{C}^2 \frac{\beta^3}{4q^2\omega\mu_0} \times \\
&\left\{ K_{l+1}^2(qr)(1+ls) \left[1 + ls - \frac{q^2}{\beta^2} \right] + K_{l-1}^2(qr)(1-ls) \left[1 - ls - \frac{q^2}{\beta^2} \right] \right\}
\end{aligned}$$

and from Lommel's integrals

$$\int_0^r J_l^2(hr) r \, dr = \frac{r^2}{2} [J_l^2(hr) - J_{l-1}(hr)J_{l+1}(hr)]$$

¹ Using $\omega^2\epsilon_1\mu_0/\beta^2 = h^2/\beta^2 + 1$ and $\omega^2\epsilon_2\mu_0/\beta^2 = 1 - q^2/\beta^2$

$$\begin{aligned}
\mathcal{P}^{in} + \mathcal{P}^{out} &= \mathcal{C}^2 \frac{\beta \pi a^2}{4\omega \mu_0} \left(\left(\frac{K_l(qa)}{J_l(ha)} \right)^2 \mathcal{T}_l^{in} + \mathcal{T}_l^{out} \right) \\
\mathcal{T}_l^{in} &= (1+ls) \left(1 + \frac{\beta^2}{h^2} (1+ls) \right) \left[J_{l+1}^2(ha) - J_l(ha) J_{l+2}(ha) \right] \\
&+ (1-ls) \left(1 + \frac{\beta^2}{h^2} (1-ls) \right) \left[J_{l-1}^2(ha) + J_l^2(ha) - \frac{2(l-1)}{ha} J_l(ha) J_{l-1}(ha) \right] \\
\mathcal{T}_l^{out} &= (1+ls) \left(1 - \frac{\beta^2}{q^2} (1+ls) \right) \left[K_{l+1}^2(qa) - K_l(qa) K_{l+2}(qa) \right] \\
&+ (1-ls) \left(1 - \frac{\beta^2}{q^2} (1-ls) \right) \left[K_{l-1}^2(qa) - K_l^2(qa) + \frac{2(l-1)}{qa} K_l(qa) K_{l-1}(qa) \right]
\end{aligned}$$

Finally

$$\mathcal{C} = \sqrt{\frac{4\omega \mu_0 \mathcal{P}^{tot}}{\pi a^2 \beta}} \left(\left(\frac{K_l(qa)}{J_l(ha)} \right)^2 \mathcal{T}_l^{in} + \mathcal{T}_l^{out} \right)^{-\frac{1}{2}} \text{ with } \mathcal{P}^{tot} = \mathcal{P}^{in} + \mathcal{P}^{out}. \quad (\text{A.3})$$

A.8 FUNDAMENTAL HYDRIB MODE HE₁₁ WITH QUASI-LINEAR POLARIZATION

Inside the core:

$$\begin{aligned}
\mathcal{E}_x(r, \phi) &= \mathcal{C} \frac{i\beta}{h\sqrt{2}} \frac{K_1(qa)}{J_1(ha)} \left[J_2(hr)(1+s) \cos(2\phi - \phi_0) - J_0(hr)(1-s) \cos(\phi_0) \right] \\
\mathcal{E}_y(r, \phi) &= \mathcal{C} \frac{i\beta}{h\sqrt{2}} \frac{K_1(qa)}{J_1(ha)} \left[J_2(hr)(1+s) \sin(2\phi - \phi_0) - J_0(hr)(1-s) \sin(\phi_0) \right] \\
\mathcal{E}_z(r, \phi) &= \sqrt{2}\mathcal{C} J_1(hr) \frac{K_1(qa)}{J_1(ha)} \cos(\phi - \phi_0)
\end{aligned}$$

Outside² :

$$\begin{aligned}
\mathcal{E}_x(r, \phi) &= -\mathcal{C} \frac{i\beta}{q\sqrt{2}} \left[K_2(qr)(1+s) \cos(2\phi - \phi_0) + K_0(qr)(1-s) \cos(\phi_0) \right] \\
\mathcal{E}_y(r, \phi) &= -\mathcal{C} \frac{i\beta}{q\sqrt{2}} \left[K_2(qr)(1+s) \sin(2\phi - \phi_0) + K_0(qr)(1-s) \sin(\phi_0) \right] \\
\mathcal{E}_z(r, \phi) &= \sqrt{2}\mathcal{C} K_1(qr) \cos(\phi - \phi_0)
\end{aligned}$$

² One can notice that \mathcal{E}_z is $\pi/2$ dephased from the transverse components $\{\mathcal{E}_x, \mathcal{E}_y\}$ then also leading to rotating polarization while observing light from a plan parallel to the fiber axis.

B

ANGULAR MOMENTUM DERIVATIONS

(since $J_{-1} = -J_1$ and $K_{-1} = K_1$)

$$\begin{aligned}
 U_{in} &= \mathcal{N}^2 \pi a^2 \epsilon_0 n_1^2 \xi \left[\left(J_2^2(ha) - J_1(ha)J_3(ha) \right) (1+s)^2 + \left(J_0^2(ha) + J_1^2(ha) \right) (1-s)^2 \right. \\
 &\quad \left. + 2 \frac{h^2}{\beta^2} \left(J_1^2(ha) - J_0(ha)J_2(ha) \right) \right] \\
 U_{out} &= \mathcal{N}^2 \pi a^2 \epsilon_0 n_2^2 \left[\left(K_1(qa)K_3(qa) - K_2^2(qa) \right) (1+s)^2 + \left(K_1^2(qa) - K_0^2(qa) \right) (1-s)^2 \right. \\
 &\quad \left. + 2 \frac{q^2}{\beta^2} \left(K_0(qa)K_2(qa) - K_1^2(qa) \right) \right]
 \end{aligned}$$

We first find the need to rewrite $\langle \mathbf{S}_\phi^\pm \rangle$,

$$\begin{aligned}
 \langle \mathbf{S}_\phi^\pm \rangle_{in} &= \mp \mathcal{N}^2 \frac{h}{\omega \mu_0} \frac{s}{s_1} \xi J_l(hr) \left[J_{l+1}(hr)(2ls_1 + 1 + l^2 s s_1) - J_{l-1}(hr)(2ls_1 - 1 - l^2 s s_1) \right] \\
 \langle \mathbf{S}_\phi^\pm \rangle_{in} &= \mp \mathcal{N}^2 \frac{h}{\omega \mu_0} \frac{s}{s_1} \xi J_l(hr) \left[2ls_1(J_{l+1}(hr) - J_{l-1}(hr)) + (1 + l^2 s s_1)(J_{l+1}(hr) + J_{l-1}(hr)) \right] \\
 \langle \mathbf{S}_\phi^\pm \rangle_{in} &= \mp \mathcal{N}^2 \frac{h}{\omega \mu_0} \frac{s}{s_1} \xi J_l(hr) \left[2ls_1(-2J'_l(hr)) + (1 + l^2 s s_1) \left(\frac{2l}{hr} J_l(hr) \right) \right] \\
 \langle \mathbf{S}_\phi^\pm \rangle_{in} &= \mp \mathcal{N}^2 \frac{h}{\omega \mu_0} \frac{s}{s_1} \xi \left[-2ls_1 \frac{dJ_l^2(hr)}{d(hr)} + (1 + l^2 s s_1) \left(\frac{2l}{hr} J_l^2(hr) \right) \right]
 \end{aligned}$$

$$\begin{aligned}
 \int_0^r r^2 \langle \mathbf{S}_\phi^\pm \rangle_{in} dr &= \mp \mathcal{N}^2 \frac{h}{\omega \mu_0} \frac{s}{s_1} \xi (-2ls_1 A + (1 + l^2 s s_1) B) \\
 A &= \int_0^r r^2 \frac{dJ_l^2(hr)}{d(hr)} dr = \int_0^{x/h} x^2 \frac{J^2(x)'}{h^3} dx = \frac{1}{h^3} \left\{ [x^2 J^2(x)]_0^{x/h} - 2 \int_0^{x/h} x J^2(x) dx \right\}
 \end{aligned}$$

The last term is a Lommel integration as well as B ,

$$\begin{aligned}
 A &= \frac{1}{h} \left\{ r^2 J_l^2(hr) - r^2 J_l^2(hr) + r^2 J_{l-1}(hr)J_{l+1}(hr) \right\} = \frac{r^2}{h} J_{l-1}(hr)J_{l+1}(hr) \\
 B &= \int_0^r r \frac{2l}{h} J_l^2(hr) dr = \frac{l}{h} r^2 \left[J_l^2(hr) - J_{l-1}(hr)J_{l+1}(hr) \right]
 \end{aligned}$$

Rotating modes

Inside the fiber

$$|\mathcal{E}|^2 = 2\mathcal{N}^2\xi \left[J_{l+1}^2(hr)(1+ls)^2 + J_{l-1}^2(hr)(1-ls)^2 + 2\frac{h^2}{\beta^2}J_l^2(hr) \right] \quad (\text{B.1})$$

Outside

$$|\mathcal{E}|^2 = 2\mathcal{N}^2 \left[K_{l+1}^2(qr)(1+ls)^2 + K_{l-1}^2(qr)(1-ls)^2 + 2\frac{q^2}{\beta^2}K_l^2(qr) \right] \quad (\text{B.2})$$

B.1 QUASI-LINEAR POLARIZATION

$$\begin{aligned} \mathbf{E}p &= \frac{\mathbf{E}^+ + \mathbf{E}^-}{\sqrt{2}} = \text{Re} \left[e^{i(\omega t - \beta z)} \frac{\mathcal{E}^+ + \mathcal{E}^-}{\sqrt{2}} \right] = \text{Re} \left[\mathcal{E}p \cdot e^{i(\omega t - \beta z)} \right] \\ \mathcal{E}p &= \frac{\mathcal{E}^+ + \mathcal{E}^-}{\sqrt{2}} \end{aligned}$$

Inside

$$\begin{aligned} \mathcal{E}p_z(r, \phi) &= \sqrt{2}C \frac{K_l(qa)}{J_l(ha)} J_l(hr) \cos(l\phi) \\ \mathcal{E}p_r(r, \phi) &= C \frac{K_l(qa)}{J_l(ha)} \frac{i\beta}{\sqrt{2}h} [J_{l+1}(hr)(1+ls) - J_{l-1}(hr)(1-ls)] \cos(l\phi) \\ \mathcal{E}p_\phi(r, \phi) &= C \frac{K_l(qa)}{J_l(ha)} \frac{i\beta}{\sqrt{2}h} [J_{l+1}(hr)(1+ls) + J_{l-1}(hr)(1-ls)] \sin(l\phi) \\ \mathcal{H}p_z(r, \phi) &= -\sqrt{2}C \frac{K_l(qa)}{J_l(ha)} \frac{sl\beta}{\omega\mu_0} J_l(hr) \sin(l\phi) \\ \mathcal{H}p_r(r, \phi) &= C \frac{K_l(qa)}{J_l(ha)} \frac{i\beta^2}{\sqrt{2}h\omega\mu_0} \times \\ &\quad \left[J_{l-1}(hr) \left(ls - \frac{\omega^2\epsilon_1\mu_0}{\beta^2} \right) - J_{l+1}(hr) \left(ls + \frac{\omega^2\epsilon_1\mu_0}{\beta^2} \right) \right] \sin(l\phi) \\ \mathcal{H}p_\phi(r, \phi) &= C \frac{K_l(qa)}{J_l(ha)} \frac{i\beta^2}{\sqrt{2}h\omega\mu_0} \times \\ &\quad \left[J_{l+1}(hr) \left(\frac{\omega^2\epsilon_1\mu_0}{\beta^2} + ls \right) + J_{l-1}(hr) \left(ls - \frac{\omega^2\epsilon_1\mu_0}{\beta^2} \right) \right] \cos(l\phi) \end{aligned}$$

Outside

$$\begin{aligned}
 \mathcal{E}p_z(r, \phi) &= \sqrt{2}C K_l(qr) \cos(l\phi) \\
 \mathcal{E}p_r(r, \phi) &= -i \frac{C\beta}{\sqrt{2}q} \cos(l\phi) [K_{l+1}(qr)(1+ls) + K_{l-1}(qr)(1-ls)] \\
 \mathcal{E}p_\phi(r, \phi) &= -i \frac{C\beta}{\sqrt{2}q} \sin(l\phi) [K_{l+1}(qr)(1+ls) - K_{l-1}(qr)(1-ls)] \\
 \mathcal{H}p_r &= i \frac{C\beta^2}{\sqrt{2}q\omega\mu_0} \sin(l\phi) \left[K_{l+1}(qr) \left(ls + \frac{\omega^2 \epsilon_2 \mu_0}{\beta^2} \right) + K_{l-1}(qr) \left(ls - \frac{\omega^2 \epsilon_2 \mu_0}{\beta^2} \right) \right] \\
 \mathcal{H}p_\phi &= -i \frac{C\beta^2}{\sqrt{2}q\omega\mu_0} \cos(l\phi) \left[K_{l+1}(qr) \left(ls + \frac{\omega^2 \epsilon_2 \mu_0}{\beta^2} \right) - K_{l-1}(qr) \left(ls - \frac{\omega^2 \epsilon_2 \mu_0}{\beta^2} \right) \right] \\
 \mathcal{H}p_z &= -\frac{sl\beta}{\omega\mu_0} C K_l(qr) \sqrt{2} \sin(l\phi)
 \end{aligned}$$

To vary arbitrarily the direction of the quasi-transverse polarization direction, one can introduce for convenience an arbitrary dephasing constant term between the left and right rotating parts of the field. Let it be 2α , such that the cartesian components of the fields become, after contravariant rotation,

$$\begin{pmatrix} \mathcal{E}_x \\ \mathcal{E}_y \\ \mathcal{E}_z \end{pmatrix} = \begin{pmatrix} \cos \phi & -\sin \phi & 0 \\ \sin \phi & \cos \phi & 0 \\ 0 & 0 & 1 \end{pmatrix} \begin{pmatrix} \mathcal{E}_r \\ \mathcal{E}_\phi \\ \mathcal{E}_z \end{pmatrix}$$

Inside,

$$\begin{aligned}
 \mathcal{E}p_x(r, \phi, \alpha) &= C \frac{K_l(qa)}{J_l(ha)} \frac{i\beta}{\sqrt{2}h} [J_{l+1}(hr)(1+ls) \cos(\phi(l+1) + \alpha) - J_{l-1}(hr)(1-ls) \cos(\phi(l-1) + \alpha)] \\
 \mathcal{E}p_y(r, \phi, \alpha) &= C \frac{K_l(qa)}{J_l(ha)} \frac{i\beta}{\sqrt{2}h} [J_{l+1}(hr)(1+ls) \sin(\phi(l+1) + \alpha) + J_{l-1}(hr)(1-ls) \sin(\phi(l-1) + \alpha)] \\
 \mathcal{E}p_z(r, \phi, \alpha) &= \sqrt{2}C \frac{K_l(qa)}{J_l(ha)} J_l(hr) \cos(l\phi + \alpha)
 \end{aligned}$$

Outside,

$$\begin{aligned}
 \mathcal{E}p_x(r, \phi, \alpha) &= -i \frac{C\beta}{\sqrt{2}q} [K_{l+1}(qr)(1+ls) \cos(\phi(l+1) + \alpha) + K_{l-1}(qr)(1-ls) \cos(\phi(l-1) + \alpha)] \\
 \mathcal{E}p_y(r, \phi, \alpha) &= -i \frac{C\beta}{\sqrt{2}q} [K_{l+1}(qr)(1+ls) \sin(\phi(l+1) + \alpha) - K_{l-1}(qr)(1-ls) \sin(\phi(l-1) + \alpha)] \\
 \mathcal{E}p_z(r, \phi, \alpha) &= \sqrt{2}C K_l(qr) \cos(l\phi + \alpha)
 \end{aligned}$$

$$\begin{aligned}
 \langle \mathbf{S}_z^p \rangle_{\text{out}} &= \left[K_{l+1}^2(qr)(1+ls)(1+ls_2) + K_{l-1}^2(qr)(1-ls)(1-ls_2) \right] \times \mathcal{N}^2 \frac{\beta}{\omega\mu_0} \frac{s}{s_2} \\
 &\quad - 2(l^2 s s_2 - 1) \cos(2l\phi + 2\alpha) K_{l+1}(qr) K_{l-1}(qr) \times \mathcal{N}^2 \frac{\beta}{\omega\mu_0} \frac{s}{s_2} \\
 \langle \mathbf{S}_z^p \rangle_{\text{in}} &= \left[J_{l+1}^2(hr)(1+ls)(1+ls_1) + J_{l-1}^2(hr)(1-ls)(1-ls_1) \right] \times \xi \mathcal{N}^2 \frac{\beta}{\omega\mu_0} \frac{s}{s_1} \\
 &\quad + 2(l^2 s s_1 - 1) \cos(2l\phi + 2\alpha) J_{l+1}(hr) J_{l-1}(hr) \times \xi \mathcal{N}^2 \frac{\beta}{\omega\mu_0} \frac{s}{s_1}
 \end{aligned}$$

Quasi-linear modes

Inside

$$\begin{aligned}
 |\mathcal{E}|^2 &= 2\mathcal{N}^2 \xi \left[J_{l+1}^2(hr)(1+ls)^2 + J_{l-1}^2(hr)(1-ls)^2 \right] \\
 &\quad + 2\mathcal{N}^2 \xi \left[-2J_{l+1}(hr) J_{l-1}(hr)(1+ls)(1-ls) \cos(2l\phi + 2\alpha) \right] \\
 &\quad + 2\mathcal{C}^2 \left(\frac{K_l(qa)}{J_l(ha)} \right)^2 J_l^2(hr) \cos(l\phi + \alpha)^2
 \end{aligned}$$

Outside

$$\begin{aligned}
 |\mathcal{E}|^2 &= 2\mathcal{N}^2 \left[K_{l+1}^2(qr)(1+ls)^2 + K_{l-1}^2(qr)(1-ls)^2 \right] \\
 &\quad + 2\mathcal{N}^2 \left[2K_{l+1}(qr) K_{l-1}(qr)(1+ls)(1-ls) \cos(2l\phi + 2\alpha) \right] \\
 &\quad + 2\mathcal{C}^2 K_l^2(qr) \cos(l\phi + \alpha)^2
 \end{aligned}$$



OPTICAL LIGHT INDUCED ZEEMAN SHIFTS

I see a tremendous amount of intricacy in the world and we have probably only begun to scratch at the surface of its intricacy.

— Roy J. Glauber

In this appendix chapter, we review, address and share our personal point of views on a few important fundamental challenges to consider for a nanofiber light-atom interface.

INTRODUCTION

The strong interaction of nonresonant light with atoms, such as in an optical trap for neutral atoms, can lead to both significant energy shifts and broadening of the internal states of the irradiated atoms [Cohen-Tannoudji and Dupont-Roc \(1972\)](#). The perturbation on the atomic states induced by light can be described in terms of fictitious magnetic fields and fictitious electric fields (in general static) as long as the dipole approximation is valid for the perturbed atomic charge distribution.

In relatively weak external magnetic fields, such perturbations can lift the Zeeman degeneracy of atomic states but also can couple different Zeeman levels together at a significant rate. These effects are detrimental for high resolution spectroscopy of atomic frequencies as well as for the manipulation and preservation of quantum coherence between Zeeman levels.

Using arguments based on the symmetry of the polarization of light beams¹, we explain the state-of-the-art strategies to eliminate or at least reduce the effect of light on the multiplicity of the hyperfine ground state of Cesium atoms. We will also mention the design of so-called state-intensitive optical dipole trap for neutral atoms based on magic wavelengths. In the dipole-electric interaction approximation, the nature of the fictitious magnetic and electric field is dictated by the polarization of the electric field at the atom location. Such field however has non trivial orientation and spatial distribution in the fundamental mode of an optical nanofiber compared to freely propagating light beams.

¹ which is connected to the symmetry of the *spin* of the photons in a given light mode.

We will mention situations where one would like to exploit such perturbing effects instead of avoiding them to prepare coherent superposition of Zeeman sublevels or to design subtle fictitious magnetic trap (Schneeweiss et al. (2014)) for instance. Finally we should find in these fictitious electric and magnetic interaction description nothing but the real composition of two angular momenta: the atom total angular momentum and the intrinsic angular momentum of light. When an atom gets dressed by a light field, one cannot consider these physical systems as separated anymore and their spin will compose to a new equilibria. Along the line of the physical mechanisms behind the fine and hyperfine structures of an atom one can view this additional spin coupling as an *ultrafine* structure.

C.1 INTERACTION HAMILTONIAN AND THE SYMMETRY OF LIGHT

C.1.1 *Light polarization*

When we consider the interaction between atoms and light within the dipole-electric approximation, aside from the strength, the coupling is entirely dictated on the light side by the orientation of the electric field vector at the location of the atom. This means that any transformation performed on the given interacting light mode, such as rotations, that leaves the electric field orientation at the position of the atom unchanged should leave the interaction energy invariant. Using symmetry arguments about the light mode, we will simplify greatly the physical understanding of the effects of light shifts on Zeeman atomic levels.

C.1.2 *Atom good quantum number*

We will assume that the generator of rotations is still given by the total angular momentum of the atoms. That is we consider F to be a “good” quantum number even in the presence of light if we assume that the light shifts and Zeeman degeneracy lifts are still a small deviation compared to the atomic hyperfine splitting. Such approximation is in general relevant for the ground states of alkali atoms where this splitting amounts to a few gigahertz or a thousand free radiative linewidths². We then describe the atomic states in the eigenstate basis of the atom total angular momentum to exploit rotational symmetries.

² To compare with light scalar shift of a few megahertz for standard millikelvin shallow conservative optical traps

C.2 SCALAR, VECTOR AND TENSOR LIGHT SHIFTS

C.2.1 *Effective hamiltonian*

The effective hamiltonian that describes optically induced Zeeman shifts is in principle not hermitian to account for both energy shift and broadening (Cohen-Tannoudji and Dupont-Roc (1972)). It was given in the formalism of the density matrix in Claude Cohen-Tannoudji’s thesis and his derivation can be found also in Barrat and Cohen-Tannoudji (1961) where the secular³ approximation and adiabatic elimination⁴ techniques were used. Here we only discuss light shifts and we shall postpone for the moment the broadening effects or in modern terms we will only look at the real part of the atomic response. Starting from $H = -\hat{\mathbf{d}} \cdot \hat{\mathbf{E}}$ and decomposing both operators into their analytic parts, one arrives at the following effective hamiltonian (Geremia et al. (2006))

$$\hat{H} = \sum_{f,f'} \hat{\mathbf{E}}^{(-)} \cdot \frac{\hat{P}_f \hat{\mathbf{d}} \hat{P}_{f'} \hat{\mathbf{d}}^\dagger \hat{P}_f}{\hbar \Delta_{f,f'}} \cdot \hat{\mathbf{E}}^{(+)} \quad (\text{C.1})$$

with the help of the rotating wave approximation and perturbation theory for instance. The positive (resp. negative) frequency part of the field $\hat{\mathbf{E}}^{(+)}$ (resp. $\hat{\mathbf{E}}^{(-)}$) represents the annihilation (resp. creation) of a photon for the given interacting light mode. While $\hat{\mathbf{d}}^\dagger$ (resp. $\hat{\mathbf{d}}$) is the atomic dipole operator raising (resp. lowering) excitation. The other unity scalar operators are projectors. $\hat{P}_f = \sum_m |f, m\rangle \langle f, m|$ is the projection onto the ground state f whereas $\hat{P}_{f'}$ is the projector for the excited states f' .

C.2.2 *Atomic polarizability tensor*

The atomic contribution in the effective hamiltonian appears as a dyadic or tensor product of two dipole vector operators. It is known nowadays as the atomic polarizability tensor $\hat{\alpha}$ which between two particular ground and excited states is

$$\hat{\alpha}_{f,f'} = \hat{P}_f \hat{\mathbf{d}} \hat{P}_{f'} \hat{\mathbf{d}}^\dagger \hat{P}_f. \quad (\text{C.2})$$

We shall comment it after explaining the effect of the hamiltonian onto the atomic Zeeman levels.

C.2.3 *Simplest case: interaction with $F = 1/2$*

We consider first the simplest non-trivial case of a total atomic spin $F = 1/2$. That is we only look at the effects of a light beam onto a

³ known nowadays as the rotating wave approximation.

⁴ Alternative techniques to perturbation theory lead to the same hamiltonian, for instance the resolvent method in .

given ground state F . Readily, its Zeeman multiplicity $(2F + 1)$ spans only a two-dimensional Hilbert space. This implies that the effective hamiltonian will read as a two-dimensional square matrix. Such matrix can be decomposed onto the Pauli matrices that form a basis of the Lie algebra of the $SU(2)$ group.

$$\mathcal{H}_{\text{eff}}(f = 1/2) = c_0 I_2 + \sum_i c_i \sigma_i. \quad (\text{C.3})$$

Here I_2 denotes the 2×2 identity matrix. A spin $1/2$, which can be expressed here as $\hat{F} = \frac{\hbar}{2} \hat{\sigma}$, possesses a magnetic moment $\vec{\mu} = \gamma \vec{F}$ where γ is the gyromagnetic ratio. Thus the scalar product in the above hamiltonian can be interpreted as a *fictitious* magnetic interaction $-\vec{\mu} \cdot \vec{B}$ by fixing the coefficients to $c_i = -\hbar \frac{\gamma}{2} B_i$. We then conclude that in general, the interaction between light and a spin $1/2$ ground state would result in two contributions behaving differently with respect to rotations. We have a scalar part which is independent of the angular orientation of the atomic spin equivalent to a constant center of mass light shift onto all the Zeeman level $|f, m\rangle$ and a pseudo-vectorial⁵ light shift Zeeman state dependent.

CONSEQUENCES OF THE LIGHT POLARIZATION Consider a light beam circularly polarized propagating along the z axis in free space. Any proper rotation of the beam around its propagating direction leaves its polarization invariant. Consequently, in the dipole-electric approximation, the effective hamiltonian should remain as well unchanged. Therefore any decomposition onto $\hat{\sigma}_x$ and $\hat{\sigma}_y$ should vanish such that the only remaining component of the fictitious magnetic field is along the propagation direction z . $\mathcal{H}_{\text{eff}} = c_0 I_2 + c_z \sigma_z$. Now consider that the helicity of the circular polarization is reversed which is like a xy plane mirror reflection, then the projection of the fictitious magnetic field will have also its sign reversed, $\mathcal{H}_{\text{eff}} = c_0 I_2 - c_z \sigma_z$. One will conclude that if one sends a superposition of σ^+ and σ^- circular polarization with equal intensity, the vector shift will cancel out such that an atomic spin $1/2$ only experiences scalar shifts from linearly polarized light. Aside this particular case, any unbalanced combination of circular polarizations, that is elliptical polarization, will induce a fictitious magnetic field. We shall see later that is then convenient to define a degree of ellipticity for the polarization that characterizes the strength of the vector light shift.

⁵ A magnetic field is a pseudo-vector or fully anti-symmetry rank 2 tensor with respect to rotations in 3D. i. e. depends on the sign of the rotation angle or the orientation of the basis axes.

c.2.4 *Fictitious magnetic field or spin composition*

Consider the following identity

$$(\vec{a} \cdot \vec{\sigma})(\vec{\sigma} \cdot \vec{b}) = (\vec{a} \cdot \vec{b})I_2 + i\vec{\sigma} \cdot (\vec{a} \times \vec{b}) \tag{C.4}$$

that holds when the vectors commute with the Pauli matrices. We remark that it can be applied to the effective hamiltonian (C.1) on the multiplicity of a ground state $F = 1/2$, where the electric field operator that acts on the field commutes with the atomic dipole operator. This would give for the vectorial shift $\vec{\sigma} \cdot [i\hat{\mathbf{E}}^{(-)} \times \hat{\mathbf{E}}^{(+)}]$. Interestingly, we have shown in an earlier chapter that the right vector in this scalar product is nothing but the intrinsic angular momentum of the light field. One can then interpret light shifts as the composition of the light intrinsic angular momentum with an atomic angular momentum. That is here the composition of two spin⁶ 1/2 leading to the direct sum of a spin 0 contribution and a spin 1. However, even though the true spin of light appears above, the atomic spin here is fictif as it maps the atomic dipole vector operator as SU(2) does for SO(3) (Feynman et al. (1957)). The previous results concerning the orientation of the fictitious magnetic field then readily resumes to the orientation of the spin angular momentum of light which can only be ported along the propagation direction in free space.

c.2.5 *General case $F > 1/2$: tensor shift*

A true vector, such as an atomic dipole, is by definition in physics an irreducible tensor of rank 1 with respect to rotations in the three-dimensional euclidian space. This is a requirement from the classical principle of relativity. However the composition of two such vectors through a dyadic product or tensor product forms a new representation, a rank 2 tensor that is not irreducible anymore. This is the case for instance in the effective hamiltonian (C.1) where one recognizes the dyadic product of two vector operators. To exploit the rotational symmetries of the atomic configuration, the most we can do is to decompose it into a direct sum of irreducible representations that transform independently among themselves with rotations. This decomposition is known as the Clebsch-Gordan decomposition. In the general case, the effective hamiltonian is a $(2F + 1) \times (2F + 1)$ matrix. We decompose it into irreducible tensor operators of rank k $T_q^{(k)}$ with spherical components $-k \leq q \leq k$ ($k = 0, 1, \dots, 2F$). Only up to the second rank, as this is the maximum rank that can be obtained by composition of two rank 1 tensors.

⁶ Light carries spin 1 in free space (photons are bosons) but only two components along the propagation can be detected.

$$H(f) = c_0^{(0)} + \sum_{q=-1}^1 c_q^{(1)} T_q^{(1)} + \sum_{q=-2}^2 c_q^{(2)} T_q^{(2)} \quad (\text{C.5})$$

The summation over the components of the rank 1 tensor can be rewritten as a linear combination of the cartesian components of the total angular momentum operator ($T_0^{(1)} \propto F_z$ and $T_{\pm 1}^{(1)} \propto (\mp F_x \pm iF_y)$). That is interpreted as before as a fictitious magnetic interaction with the dipole moment of the state f . In addition here the hamiltonian has a rank-2 tensor part leading to tensor shifts contrary to the case $F = 1/2$. The components of spherical rank 2 tensor can be expressed⁷ from the ones of the rank 1 tensor

$$\begin{aligned} T_{\pm 2}^{(2)} &\propto (F_x \pm iF_y)^2 \\ T_{\pm 1}^{(2)} &\propto \mp [F_z(F_x \pm iF_y) + (F_x \pm iF_y)F_z] \\ T_0^{(2)} &\propto 3F_z^2 - F(F+1) \end{aligned}$$

This may appear ugly to anyone who just sees component multiplications. However, the above expression is beautiful with respect to rotations. A magnetic dipole moment is a rank 1 tensor with respect to proper rotation⁸ and a traceless symmetric rank 2 tensor with respect to SO(3) is nothing but a pure quadrupole moment. Because a spin 1/2 has only two "polarities" that is only two opposite orientations, it cannot possess a quadrupole moment.

To sum up, the effects of light onto the Zeeman multiplicity of an atomic ground state f can be viewed as a monopole interaction (center of mass light shift), a dipole interaction (here a fictitious magnetic interaction) and a quadrupole interaction with the gradient of the electric field in the general case.

CONSEQUENCES OF THE LIGHT POLARIZATION Again, the rotational invariance of a circularly polarized beam of light propagating along the z axis would require that the contribution of all tensor components involving F_x and F_y should vanish. Therefore, $H(f) = a + bF_z + c [F_z^2 - F(F+1)]$ where only b changes sign for opposite circular polarization. For linear polarization, one only has a tensor shift in addition to the scalar shift.

⁷ Following the famous decomposition of a rank 2 cartesian tensor (i.e dyad product of two rank 1 tensor) into traceless fully antisymmetric tensor and symmetric tensors.

⁸ It is actually a rank 2 with SO(3) reduced to rank 1 as fully antisymmetric. It is a pseudo tensor but transform like rank 1 tensor upon proper rotation that is without inversion. The group of rotation is not continuous but composed of two disjoint sets (proper and improper rotations).

C.3 STATE-INSENSITIVE OPTICAL TRAP

We want to discuss in this section methods to minimize the effect of trap light onto the internal atomic states without calculation. The idea is to emphasize on the underlying physical mechanisms.

c.3.1 *Back-Goudsmit effect*

There is a very noteworthy comment at the end of the short article reporting the first significant light Zeeman shift (Dupont-Roc et al. (1967)). Light shifts can play the role of the atomic hyperfine structure. In view of designing an optical light trap for neutral atoms, the modification of the internal atomic states by the trapping mechanism is the last wanted effect for high resolution spectroscopy based on the measure of atomic frequencies but also for coherent and precise manipulation of the atomic states that would not be stationary anymore. However, in other situations, it is interesting that light can replace the role of the nuclear spin coupling. When the interaction with light is strong enough, one can actually uncouple the total electronic angular momentum J to the nuclear spin I leading to the Back-Goudsmit effect (Goudsmit and Bacher (1929); Gawlik (1991); Gawlik and Zachorowski (2002)). This effect is analog to the Paschen-Back effect where the total orbital momentum of the electron L gets decouple to its own spin S from a strong interaction with an external magnetic field.

c.3.2 *Magic and tune-out wavelengths*

Common optical light traps are based on the scalar or ac Stark shift when the electric field is inhomogeneous thereby creating a restoring gradient force. However the overall sign of the atomic polarizability depends on the relative position (detuning) of the light wavelength to the electronic states of the atoms which would either attract or repel the neutral atom from electric field intensity spatial maxima. This entails a limiting effect best summarized in the simple case where the light is assumed to act predominantly⁹ on only two such atomic levels. When the energy of the ground state gets red shifted the excited state gets blue shifted. Atoms in the excited state will then be anti-trapped. If one desires to also trap excited states¹⁰ (which have a short radiative lifetime contrary to ground states) it is possible to find so-called “magic” wavelengths (Ye et al. (2008)) that exploit the multi-level structure of the atom to produce a nearly identical scalar polarizability for a couple of levels that ensures a state-independent trap potential and a zero differential scalar shift.

⁹ when light is quasi-resonant with a transition

¹⁰ to exploit optical coherences between atomic states for instance

There also exists so-called “tune-out” wavelengths for which the dynamic scalar polarizability of ground state alkali atoms vanishes (LeBlanc and Thywissen (2007)). For instance, for Cesium atoms, the ground state will experience a zero Stark shift from an optical wavelength of 880.25 nm situated between the D1 and D2 lines (Arora et al. (2011)). There are more tune-out wavelengths for Cesium (460.22, 457.31, 389.029 in nanometres) which may be more difficult to produce. Obviously they cannot be used to optically trap directly a ground atomic state based on the scalar ac Stark shift. However, they permit novel trap schemes based on pure vectorial light shift for instance (that is light-induced magnetic trap) (Schneeweiss et al. (2014), here in a nanofiber). They initially have applications for sympathetic cooling where the tune-out wavelength could optically trap another atomic specie while a pre-cool buffer of tune-out alkali atoms would be little affected by the trap.

C.3.3 Differential Stark shift

To sound repetitive, for atomic clocks or quantum atomic coherences for metrology and computing, one should seek to design an optical light trap that little affects the frequency of the working atomic transition. And we have seen that the energy difference between two levels exhibits in general a non-zero differential Stark shift from the dressing of the trap light. On the one hand this affects the accuracy of the measurement of the transition frequency but also, on the other hand, leads to inhomogeneity from the motion of the atoms in the spatial profile of the trap light mode.

CANCELLATION FOR OPTICAL TRANSITIONS When the detuning of light is large compared to the hyperfine structure of the atomic excited states, its dressing will become independent of them, that is independent of f' . The indirect angular coupling with the nuclear spin through the electron angular momentum becomes negligible. In mathematical terms, this means that the total electronic angular momentum becomes a good quantum number for the rotational invariance of the dipole interaction. The atomic dipole operator acts only directly on the electronic variables. The tensor shift will therefore depend on J which for the ground states of alkali atoms $J = 1/2$ ($L = 0$, $S = 1/2$) will vanish (as the highest possible tensor rank is $2J + 1 = 1$). In absence of light polarization ellipticity, the vector shift vanishes as well. The remaining contribution to the differential Stark shift from the scalar shifts can be tackle using magic wavelengths. Cancellation of differential scalar shifts has been achieved very well for optical transition levels (see for example Bruschi et al. (2006); Boyd et al. (2006); Takamoto et al. (2005)).

NO MAGIC WAVELENGTH For the manipulation of hyperfine quantum coherences instead of optical ones, as more relevant to our work, the situation is more difficult. For instance, it was shown that there is no magic wavelength to cancel the differential Stark shift¹¹ on the clock states of Cesium [Rosenbusch et al. \(2009\)](#).

Indeed for atomic hyperfine transitions this is more difficult as the atomic polarizability of different f states of the same electronic state have quite the same dependence with the optical trap light frequency because this is actually what does¹² the far-detuned approximation which neglect the hyperfine structure from nuclear interaction. Indeed, we should strongly emphasize that the above results are for far-detuned light. It is possible to null the differential scalar shift on the ground hyperfine states by finding magic wavelengths provided now that they are near-detuned, that is falling between the hyperfine levels, whereby the frequency dependence of the hyperfine atomic polarizabilities can cross over. A smaller detuning has the cost of an increased scattering rate which is incompatible with the design of an optical light trap with deep depth and both long storage and coherence time.

VECTOR SHIFT AND MAGIC MAGNETIC FIELD As the most recent development in optical traps has shown, light vector shifts are important to discuss as they may be the source of increased trap losses. These trap losses will depend onto the spin polarization of the trapped atomic states ([Corwin et al. \(1999\)](#)). But again, the bilan is never black and white in physics.

It is interesting to consider that vector shifts could in turn be used to fight against differential scalar shifts when there exist no magic wavelengths to make them vanish. With elliptical light trap, it is then possible to program vector shifts to compensate scalar shifts [Chicireanu et al. \(2011\)](#). This idea has improved the coherence time of the hyperfine levels of trapped atoms [Dudin et al. \(2010\)](#).

The proposal of [Flambaum et al. \(2008\)](#) is worthnoting. Starting with a counter-intuitive circularly polarized optical light trap, one can find “magic” external magnetic field to subject the atoms to in order to compensate the scalar shifts with the vector shifts. When the magnetic field is large enough, it dictates the quantization axis. Henceforth, the relative angle θ between the magnetic field and the light propagation direction will modulate the vector shift contribution with $\cos\theta$. By varying the angle, which is found optimal close to $\pi/2$, any trap light frequency can be made magical. In fact, this shift is also proportional to the ellipticity of the light and then could alleviate the effect of the magnetic field orientation in traps with controlled polarization.

11 the result implicitly mean in conditions where light was linearly polarized for which the vector shifts cancel out. The tensor shift being absent in the ground state.

12 the polarizability of an hyperfine is in this approximation mainly given by the one of the fine structure up to the different detunings.

QUADRATIC ZEEMAN EFFECT STRATEGY Such previous compensation scheme can appear challenging. It requires first magnetic sensitive levels ($m_f \neq 0$) for which the vector shifts¹³ are in general much greater than both the scalar and the tensor parts. This would demand a very fine control of the ellipticity of light and/or of the overall orientation of the atom (through the fine control of the total magnetic field, effective + bias quantization field).

In order to tackle this shift on the clock states of the primary and secondary frequency standard (i. e. Cesium and Rubidium Zeeman hyperfine ground states with $m_f = 0$) the experimental demonstration of [Lundblad et al. \(2010\)](#) outstands. The idea may appear simple. It consists of making the originally first order magnetic Zeeman shift insensitive clock states $m_f = 0$, magnetically sensitive using the quadratic Zeeman shift in presence of a larger external magnetic field to create a vector shift of order comparable to the scalar shift. The obvious drawback of pursuing trap light intensity insensitivity with this method is making the atomic states sensitive to magnetic field fluctuations. For Cesium, this sensitivity, independent of the trap light detuning, is found to be 23 kHz/mT ¹⁴ ([Lundblad et al. \(2010\)](#)).

c.3.4 *Transition shift versus trap loading*

There is a very important issue of the light shifts with respect to the efficient loading of atoms into an optical dipole trap. By design purpose, the detuning of a Far-off resonant trap ([FORT](#)), for already several nanometers is such that the photon scattering rate is very low. This makes the optical [FORT](#) truly conservative. Atoms are in general pre-cooled before they can be transferred into such shallow trap. Because it is a conservative potential, the efficient loading of atoms into the optical trap requires a dissipative force such as a friction force that can be provided by the Doppler cooling effect at play in a [MOT](#) cooling reservoir for instance. Clearly, the existence of a large change in the atomic frequencies due to the Stark shift from the presence of the optical trap light is in general not compatible with Doppler cooling. Indeed, it can create a large red-shift or simply blue detune the [MOT](#) beams. This can be a great concern when trying to load into microscopic traps or into tightly-focused laser beam. By alternating optical trapping and dissipative (Doppler cooling) phases by chopping the dipole trap laser beam one would bypass this difficulty [Miller et al. \(1993\)](#).

To make optical trapping and optical cooling compatible for neutral atoms is actually the goal of sympathetic cooling but here in this thesis we are only working with a single atomic specie.

¹³ The atomic polarizability exhibits a vectorial nature already without the hyperfine interaction. It is a lower order contribution in perturbation theory compared to the scalar and tensor which are proportional to the hyperfine interaction.

¹⁴ 1 milli-tesla = 10 Gauss.

For a conservative trap, the maximum number of atoms that can be loaded into the trap can simply be estimated by the product nV of the trap volume V and the density of cold atoms from the MOT cloud n . Small trap volumes thus impose low number of atoms as it is difficult to increase n . Moreover, the volume can be small enough that the average number of atoms from a MOT cloud in the trap volume can be smaller than one.

Magic wavelengths, first for single color red-detuned FORT were then a great experimental advance in the loading of atoms. Not only did it solve the efficient loading of atoms in the small volume of an optical cavity for instance, the cancellation of the differential Stark shift also permitted the continuous observation of atoms in the trap. Such state-insensitive cooling and trapping was reported in McKeever et al. (2003) where a red-detuned magic-wavelength of 935 nm was used to cancel the differential shift on the cooling cyclic transition of Cesium atoms. This novel idea of such FORT compatible with Doppler cooling thanks to state-insensitive trapping via a magic wavelength was proposed and demonstrated by Katori et al. (1999) and Ido et al. (2000)

However, the transfert of atoms from a magneto-optical trap to an optical dipole trap is a dynamical and more subtle process. In the important experimental study of Kuppens et al. (2000), three key ingredients are highlighted for an efficient loading: increased detuning of the MOT light, reduction of the hyperfine repumping light and displacement of the center of the dipole trap with respect to the MOT. There is a noteworthy experimental curiosity in their report. The loading was also improved on the attempt to introduce a geometrical shadow in the repumping light beam whereby a disk protect the FORT region from being illuminated by repump light while it is still irradiating the surrounding MOT atoms. Could this shadow be realized with a nanofiber sustaining a dipole trap ?

Being able to operate a MOT with a dipole trap allows to reach high phase-space density that makes it possible to obtain Bose-Einstein condensation using fast optical methods Barrett et al. (2001); Salomon et al. (2014). After the efficient loading of a great number of atoms in the dipole trap, evaporative cooling could then be performed to reach the remaining needed phase-space density. Instead of the chopping method of Miller et al. (1993), a FORT can be efficiently loaded continuously from MOT cloud overlapping it by understanding the physical mechanisms that lead to losses during the transfert. An improvement of three orders of magnitude in the number of loaded atoms was achieved in Adams et al. (1995). This work highlights the central importance of the MOT repumping light during the loading stage. The repumping light scattering rate, which controls the number of atoms in the lowest ground state as well as the number of excited atoms, can damp density limiting processes such as radiative repulsion forces, light-assisted collisions and spin exchange/ground-state hyperfine changing

collisions. The last inelastic process leads to an energy exchange of about $h9.2\text{ GHz} \simeq k_B0.45\text{ mK}$ for Cesium. This would eject an atom from the shallow dipole trap of a nanofiber but could be re-captured in the MOT volume. Instead of ramping down the intensity of the repumping light of a standard MOT, one might consider applying the idea of the gray molasses or blue Sisyphus cooling to load into a nanofiber dipole trap to alleviate the effect of spin exchange collisions. The idea of [Borion et al. \(1998, 1996\)](#) should not represent an experimental challenge for our nanofiber experiment.

We note that the idea of the geometrically shadow in the repumping beam, overlaps with the principle of the dark MOT or dark Spontaneous-Force Optical Trap (SPOT) [Ketterle et al. \(1993\)](#).

C.3.5 *Magic wavelengths for optical nanofiber traps*

To allow for the simultaneous operation of a magneto-optical trap with a dipole trap engineered in the evanescent field of the fundamental mode carried by an optical nanofiber, [Le Kien et al. \(2005b\)](#) has found magic wavelengths compatible with the single-mode cut-off condition. Aside such fiber geometric criteria (evanescent decay length), the magic wavelengths are solely dictated by the atomic polarizability. The red-detuned magic wavelength of 934.5 nm for Cesium ground states is retained as in [McKeever et al. \(2003\)](#). For the two-color evanescent nanofiber trap, blue detuned magic wavelengths are in addition found to be 613 nm and 685.5 nm . The former being disregarded as too close to the fundamental cut-off wavelength of the fiber. For this choice, the maximally inhomogenous light shifts on the D2 line transition are shown to be only tens of megahertz. They will allow not only simultaneous operation of the trap with slightly detuned MOT light but also with simultaneous probing (continuous observation during trap motion). Finally, they offer the opportunity to trap both ground and excited states. However, vector-shifts due to the ellipticity of the polarization of the proposed trapping scheme therein were not investigated. Only the effects of the scalar and tensor shifts were studied.

In view of manipulating optical quantum coherence of atoms trap around an optical nanofiber, the group of Jeff Kimble, investigated the light shifts more precisely by taking into account the local ellipticity of the nanofiber mode field, that is, they studied the vector shifts for the nanofiber platform ([Lacroûte et al. \(2012\)](#)). They proposed and experimentally demonstrated a state-intensitive two-color dipole trap around a nanofiber based on the initial scheme presented and demonstrated in [Balykin et al. \(2004\)](#); [Vetsch et al. \(2010\)](#); [Dawkins et al. \(2011\)](#). It therefore comes with no surprise that the magic wavelengths given to cancel the scalar shifts are similar to those of [Le Kien et al. \(2005b\)](#). However, it could have been that from the many possible blue tuned wavelengths [Arora et al. \(2007\)](#) another one would have been better

suitable for a deep trap with few scattering events. The slight difference in wavelengths arises from the will to cancel exactly the differential scalar shift between the ground and $F' = 4'$ excited state with zero magnetic moment projection $m_f = 0$ of its respective hyperfine manifold. Indeed, also as in [Goban et al. \(2012\)](#), they report for the red wavelength **937 nm** and for the blue one **687 nm**.

As we have seen in previous sections, vector shifts arising from the ellipticity of the trapping light can be suppressed by using instead linear polarization (e. g. sending a counter-propagating trap beam with opposite ellipticity) or by orienting the total magnetic moment of the atom in a direction orthogonal to the local spin angular momentum orientation of light using an appropriate external bias magnetic field. The last point may be hardly applicable experimentally in the situation where the ellipticity of the light field is first inhomogeneous and second if its spatial variation happens on a scale smaller than the wavelength. This is the general situation for the evanescent fundamental mode of a nanofiber.

The main observations are as follows. Due to the presence of a longitudinal component of the electric field in the fundamental mode in quadrature to the transverse components, there can exist a significant elliptical polarization in the longitudinal plane even though the polarization in the transverse plane is quasi-linearly polarized. The polarization of a nanofiber mode is richer than a free space electromagnetic mode and exhibits the full complexity of a three-dimensional nature. The longitudinal component at the source of the ellipticity is maximum in a longitudinal plane containing the transversal linear polarization and vanishes in a longitudinal plane orthogonal to this first plane. From this we draw two temporary conclusions. In the two-color evanescent nanofiber trap scheme with orthogonal linear polarization (to ensure azimuthal confinement), atoms, which are trapped along the polarization direction of the red-detuned field, should experience then a non-negligible elliptical polarization. However, the red-detuned field is a standing wave one, such that the superposition of the counter-propagating red-detuned field with identical transverse linear polarization will balance out the longitudinal ellipticity. Because the blue-detuned field is singly propagating, it has the potential to introduce ellipticity at the trap location. However, it is polarized orthogonally to the red field polarization (along which the trap minimum is located) such that according to our previous remarks, the vector shifts should be cancelled at the trap minimum.

The main argument of the work reported in [Lacroûte et al. \(2012\)](#) is focused on the fluctuations of the atom position in the trap such as its natural harmonic motion around the minimum. This will lead to non-zero vector shifts. The azimuthal exploration of an atom in the trap motional ground state corresponds to tens of nanometers. This leads, through spatially inhomogeneous vector shift, to hundreds of kilohertz

splitting between the Zeeman sublevels of the ground state $|F = 4\rangle$. This estimates a spin coherence time of a few microseconds.

By adding a counter-propagating blue-detuned beam, one will reduce this vector shift along the same result as for the pair of red beams. However, the counter-propagating beam has to be detuned from its companion in order to avoid creating a blue-detuned standing wave, which would not be matched to the red one. The detuning is chosen such that the beat frequency is great compared to the atomic motion (trap frequency). The atom then sees an adiabatic total potential, being the sum of two independtly blue-detuned intensity with no interferences. The hyperfine coherence lifetime could then be limited only by residual scalar shifts for instance.

C.4 A COMMENT ON THE COLLISIONAL BLOCKADE REGIME

In this section, we argue whether the collision blockade regime is realistic in our nanofiber experiment.

The initial litterature, [Sagué et al. \(2008\)](#); [Vetsch et al. \(2010\)](#), on the trapping of atoms around a nanofiber expects the loading to operate in the particular collisional blockade regime. This belief may have turned into a claim even though no direct experimental evidences has been provided¹⁵ apart from expectation.

C.4.1 *Microscopic trap loading regimes*

Nanofiber traps have a small volume $< \lambda^3$ and one should expect its loading mechanism from a low density MOT to be the one of a microscopic optical dipole trap [Schlosser et al. \(2002\)](#). The equation for the evolution of the number of atoms N in a dipole trap is given as

$$\frac{dN}{dt} = R - \gamma N - \beta' N(N - 1). \quad (\text{C.6})$$

Here R , is the loading rate into the trap, γ the one-body loss rate and β' the two-body collisional loss rate. γ is attributed to mainly collisions of the trapped atoms with the room-temperature background gas atoms. β' sums up all kind of two-body inelastic collisions that eject the atoms from the trap. From (C.6), three loading regimes can be inferred in steady state.

WEAK LOADING When the third collisional term is negligible, we have in the steady state, $dN/dt = 0$, $\langle N \rangle = R/\gamma$. This happens for instance for very low loading rate R for which we imagine that the probability to have two-body collisions in the trap, before a collision with a background gas atom occurs, is low.

¹⁵ up to the knowledge of the author

STRONG LOADING When the loading rate R is high we imagine the opposite effect. The trap loss from background gas collisions becomes negligible due to the high flux of incoming atoms that participate in two-body collisions in the trap. One has $\langle N \rangle = \sqrt{R/\beta'}$.

COLLISION BLOCKADE LOADING When $\beta' \gg \gamma$, as soon as there is an atom in the trap brought by a loading rate comprise between γ and β , the much higher-occurrence of two-body collision will lock the statistics of the number of atoms in the trap to either 0 or 1 but never more than 1 such that on average $\langle N \rangle = 0.5$.

Therefore to ascertain the collisional blockade regime one needs the knowledge of the loading rate into a single nanofiber trap, the background gas loss and the two-body collisional rate. The first would be difficult to measure without single trap site resolution. We could then consider the process identical for all sites and then divide the total loading rate into the whole lattice by the number of trap sites. Even though this assumption would be valid, the loading rate, from the sub-Doppler cooling phase that changes the MOT light parameter largely and quickly for the efficient transfert will be a doubtful estimate.

C.4.2 Estimation of the rates

LOSS RATE DUE TO BACKGROUND The trap loss rate due to collision with the background gas is estimated from the background gas pressure in the chamber. More precisely from the different partial pressures of all different species (e. g. CO₂, N₂, H₂O) that possess different scattering cross-section with Cesium atom. For a van der Waals inter-nuclear distance interaction potential to the sixth power the collision rate of Bjorkholm (1988) becomes as in Arpornthip et al. (2012) as follows

$$\gamma_i = 1/\tau_i \simeq 6.8 \frac{P_i}{(k_B T)^{2/3}} \left(\frac{C_i}{m_i} \right)^{1/3} (Dm_0)^{-1/6}. \quad (\text{C.7})$$

Here, $P_i = n_i k_B T$ is the partial pressure of a given specie i , D the trap depth, m_0 the mass of the alkali atom and m_i of the background specie, C_i is the van der Waal potential approximation parameter $-C_i/r^6$. It can be estimated from the Slater-Kirkwood formula that takes into account the static polarizability and the number of valence electrons of the species. As a result it depends on the state of the atom and excited state will have a bit higher values. But we will estimate the order of magnitude of C_i from the collision rate between ground-state Cesium atom and hydrogen molecules, for a typical 1 K MOT deep trap and a room-temperature 300 K background gas. From Bali et al. (1999), $C_{\text{Cs-H}_2} = 170$ and $C_{\text{Cs-Cs}} = 6330$ in atomic units. This gives a reported value of $\gamma_{\text{H}_2}/P = 4.9 \times 10^{-7} \text{ Torr}^{-1} \text{ s}^{-1}$. Knowing the pressure in the chamber will allow to estimate the lifetime due to background collisions

with residual gas. γ_i depends weakly on the trap depth. Extrapolating to a milli-kelvin shallow trap will only multiply it by about 3. It actually depends in general weakly on all the specie parameter as well.

CHAMBER PRESSURE The volume of the vacuum chamber was measured to 810 ml^{16} by filling it up with acetone. The pressure in the chamber can be measured with the current of the ion pump (Varian Starcell 20 L/s pumping speed). Such measurement is less robust than from an ionization gauge as it is prone to leakage currents and other limiting offsets. After subtracting the offset from the ion pump indicator of 3.9 mV from the measured value of 4.8 mV from a good multimeter, we find a current of about $0.9\text{ }\mu\text{A}$ (the conversion factor being $1\text{ V} = 1\text{ mA}$). From Figure C.1, ($1\text{ mbar} \sim 0.75\text{ Torr}$ or mmHg) this brings us to a few 10^{-9} Torr . This value which has not changed over three years is compatible with a gauge measurement of about $2 \times 10^{-9}\text{ Torr}$ during the preparation of the vacuum with a turbo pump.

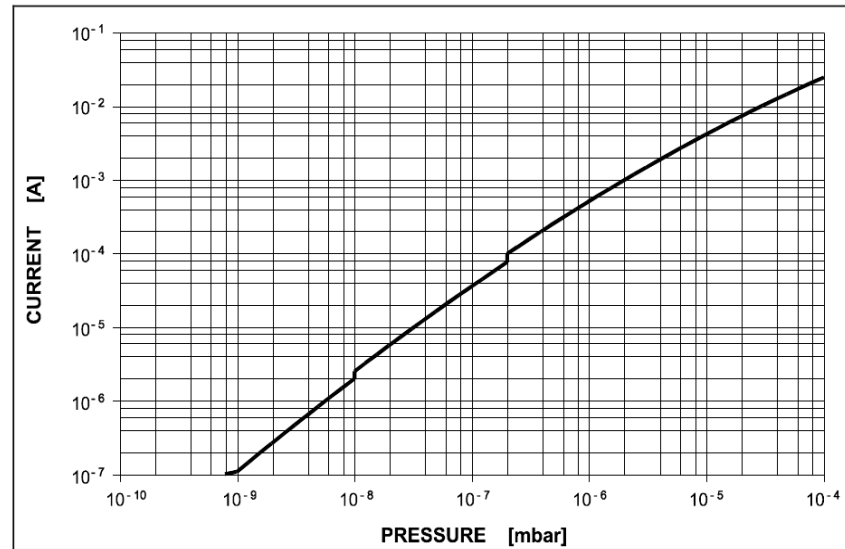


Fig. 5 - Pressure vs current diagram

Figure C.1: Ion pump technical pressure current calibration

The ion pump pressure measurement is a technique with comparable resolution has a pressure measurement inferred from the loading time τ of a magneto-optical trap. The low pressure floor being ultimately limited by collisions between atoms within the trap to less than $1 \times 10^{-9}\text{ Torr}$. From the recent interesting work of Arpornthip et al. (2012), a reliable conversion¹⁷ to vacuum pressure is given by $(2 \times 10^{-8}\text{ Torr s})/\tau$. Our pressure measurement is then compatible to our common $1/e$ loading time upper estimation of about 0.5 s .

¹⁶ comparable to the volume of a wine bottle.

¹⁷ The conversion factor is compatible with (Prentiss et al., 1988).

Based on all the above, a good range for the trap loss rate or trap lifetime due to background collision will be $0.1/\text{s} \leq \gamma \leq 1.0/\text{s}$ for a pressure ranging¹⁸ from 1 to 10×10^{-9} Torr, compatible with the estimation of [Sagué et al. \(2008\)](#). Any trap loading rate above $\gamma/2$ that is lower than the two-body collision loss rate ($\beta'/4$) (see [Schlosser et al. \(2002\)](#)) will fall into the collisional blockade regime. Interestingly, in the latter reference, a value of $\gamma = 0.2 \text{ Hz}$ for a vacuum chamber of a few 10^{-9} Torr is quoted showing that an estimation compatible to ours. Note that $\gamma = 1/\tau_{br} + 1/\tau_{Cs}$ if we were to take into account precisely additional collision due to untrapped Cesium atoms.

COLLISIONAL RATE From [Kuppens et al. \(2000\)](#) $\beta' = 0.016 \text{ Hz}$ for a gaussian trap volume with waist $w_0 = 40 \text{ }\mu\text{m}$ and wavelength $\sim 785 \text{ nm}$. The trap volume approximated to a cylinder depends on the fourth power of the waist ($V \propto w_0^2 z_R$ where $z_R \propto w_0^2$ is the Rayleigh range such that β' is rapidly varying function of the waist. This is why a value of $\beta' = 1000 \text{ Hz}$ as taken in [Schlosser et al. \(2002\)](#) will be a more than conservative value for a trap volume with typical sub-wavelength dimensions.

The collision blockage regime would then be accessible for at least three orders of magnitude of atom loading rate. We note that these regimes are expected to exhibit loading sub-Poissonian distribution of atom number in the trap.

LOADING RATE ESTIMATION [Sagué et al. \(2008\)](#) took the loading rate of the trap of [Schlosser et al. \(2002\)](#) to obtain the one for a single nanofiber trap. We know that the presence of the nanofiber affects the equilibrium number of atoms in a **MOT**. Collisions with the fiber itself or the presence of atoms sticking its surface might affect the dynamics of the loading as well as complex light assisted collisions from the **MOT** light crossing on the fiber. From the common number of atoms measured in the nanofiber trap and an estimate of the number of occupied sites from the volume overlap between the **MOT** and the dipole trap, after a sub-Doppler cooling transfert that last a time $\tau_{\text{sub-Doppler}}$ between 10 to maximum 100 ms , we would give a compatible estimate of $R \sim 1/\tau \sim 100 \text{ Hz}$ with the litterature. This shall not be taken as granted until experimental work provides quantitative measurement of the loading rate into a single nanofiber trap. In the recent work of [Vetsch et al. \(2012\)](#) a better experimental characterization of the nanofiber trap was conducted carefully to check *a priori* expectations about the trap, although evidences (sub-Doppler trap temperature) show that the laser cooling and loading mechanisms seem to work better than what might be expected in the vicinity of a nanofiber. However, the estimation of the loading rate, without direct measurements, is a guess similar as we just did. What is likely is that the loading rate

¹⁸ $\gamma/P = 1 \times 10^{-8} \text{ Torr}^{-1} \text{ s}^{-1}$

is bigger and not too far from γ and that $\beta/\gamma \gg 1$ due too the small trap volume.

D

DUAL-HETERODYNE NOTES

D.1 NOTATIONS

ASSUMPTION 1 Linear Response Detector Signal

$$\begin{aligned} \mathcal{S}(t) &= \int_{-\infty}^{+\infty} \mathcal{R}'(\tau) |E_{\text{tot}}(t - \tau)|^2 d\tau, \\ \mathcal{S}(t) &\stackrel{\text{causality}}{=} \int_{-\infty}^{+\infty} \underbrace{\theta(\tau) \mathcal{R}(\tau)}_{\mathcal{R}'(\tau), \tau \geq 0} |E_{\text{tot}}(t - \tau)|^2 d\tau. \end{aligned}$$

ASSUMPTION 2 Amplitudes and phases of all fields are slowly varying in time, i.e. nearly constant over an optical period oscillation.

$$E_{\text{tot}}(t) = \mathcal{E}_{\text{tot}}(t)/2 + c.c.,$$

with

$$\begin{aligned} \mathcal{E}_{\text{tot}}(t) &= \mathcal{E}_1 e^{i(\Phi_1 - \omega_1 t)} + \mathcal{E}_2 e^{i(\Phi_2 - \omega_2 t)} + \mathcal{E}_{\text{LO}} e^{i(\Phi_{\text{LO}} - \omega_{\text{LO}} t)}, \\ \omega_1 &= \omega_{\text{LO}} + \Omega \text{ and } \omega_2 = \omega_{\text{LO}} - \Omega. \end{aligned}$$

$$|E_{\text{tot}}|^2 = \frac{1}{4} \left[\underbrace{\mathcal{E}_{\text{tot}}^2 + \mathcal{E}_{\text{tot}}^{*2}}_{\text{optical freq.}} + 2|\mathcal{E}_{\text{tot}}|^2 \right].$$

Therefore

$$\mathcal{S}(t) \cong \frac{1}{2} \int_{-\infty}^{+\infty} \mathcal{R}'(\tau) |\mathcal{E}_{\text{tot}}(t - \tau)|^2 d\tau. \quad (\text{D.1})$$

QUICK PROOF

$$\begin{aligned} \mathcal{E}_{\text{tot}}^2 &= \mathcal{E}_1^2 e^{2i(\Phi_1 - \omega_1 t)} + \mathcal{E}_2^2 e^{2i(\Phi_2 - \omega_2 t)} + \mathcal{E}_{\text{LO}}^2 e^{2i(\Phi_{\text{LO}} - \omega_{\text{LO}} t)} \\ &+ 2\mathcal{E}_1 \mathcal{E}_2 e^{i(\Phi_1 + \Phi_2 - 2\omega_{\text{LO}} t)} + 2\mathcal{E}_1 \mathcal{E}_{\text{LO}} e^{i(\Phi_1 + \Phi_{\text{LO}} - 2\omega_{\text{LO}} t - \Omega t)} + 2\mathcal{E}_2 \mathcal{E}_{\text{LO}} e^{i(\Phi_2 + \Phi_{\text{LO}} - 2\omega_{\text{LO}} t + \Omega t)} \end{aligned}$$

$$\begin{aligned} \mathcal{S}'(t) &= \frac{1}{4} \int_{-\infty}^{+\infty} \mathcal{R}'(\tau) \left[\mathcal{E}_{\text{tot}}^2(t - \tau) + \mathcal{E}_{\text{tot}}^{*2}(t - \tau) \right] d\tau \\ &\stackrel{\text{first term}}{=} \int_{-\infty}^{+\infty} \mathcal{R}'(\tau) \mathcal{E}_1^2(t - \tau) \left[\cos(\Phi_1 - \omega_1(t - \tau))^2 - 1/2 \right] d\tau \sim 0 \end{aligned}$$

Within the previous assumption and if the detector response is very slow compare to $1/\omega_i$, all terms average to 0.

D.2 FILTERING

For real field amplitudes,

$$\begin{aligned}
 |\mathcal{E}_{\text{tot}}(t)|^2 &= \mathcal{E}_{\text{tot}}(t)^* \mathcal{E}_{\text{tot}}(t) \\
 &= \underbrace{\mathcal{E}_1^2 + \mathcal{E}_2^2 + \mathcal{E}_{\text{LO}}^2}_{\text{to high-pass filter}} + \underbrace{2\mathcal{E}_1\mathcal{E}_2 \cos(2\Omega t + \Delta\Phi)}_{\text{to low-pass filter (NOT LO quantum enhanced)}} \\
 &\quad + 2\mathcal{E}_1\mathcal{E}_{\text{LO}} \cos(\Omega t + \Phi_{\text{LO}} - \Phi_1) + 2\mathcal{E}_{\text{LO}}\mathcal{E}_2 \cos(\Omega t + \Phi_2 - \Phi_{\text{LO}})
 \end{aligned}$$

with $\Delta\Phi = \Phi_2 - \Phi_1$.

Of course the best approach is to reason in the frequency space, once the bandwidth of the detector is fully analytically known

$$\mathcal{S}(t) = \mathcal{R}' * |E_{\text{tot}}|^2 = \mathcal{F}^{-1} \left(\mathcal{F}\mathcal{R}'(t) \cdot \mathcal{F}|E_{\text{tot}}(t)|^2 \right) \quad (\text{D.2})$$

And if we simply consider the bandwidth of the detector centered on Ω and the electric field spectrum relatively sharp, we have, after the previously mentioned filtering stages,

$$\begin{aligned}
 \mathcal{S}(t) &\cong \frac{\text{Gain}(\Omega)}{2} \cos(\Omega t) \{ \mathcal{E}_1\mathcal{E}_{\text{LO}} \cos(\Phi_{\text{LO}} - \Phi_1) + \mathcal{E}_{\text{LO}}\mathcal{E}_2 \cos(\Phi_2 - \Phi_{\text{LO}}) \} \\
 &\quad - \sin(\Omega t) \{ \mathcal{E}_1\mathcal{E}_{\text{LO}} \sin(\Phi_{\text{LO}} - \Phi_1) + \mathcal{E}_{\text{LO}}\mathcal{E}_2 \sin(\Phi_2 - \Phi_{\text{LO}}) \}
 \end{aligned}$$

D.3 MIXING

After mixing, the in-phase component of the signal will be proportional to

$$\mathcal{S}(t)^{\text{in}} \propto \mathcal{E}_{\text{LO}} \{ \mathcal{E}_1 \cos(\Phi_{\text{LO}} - \Phi_1) + \mathcal{E}_2 \cos(\Phi_2 - \Phi_{\text{LO}}) \} \quad (\text{D.3})$$

$$\mathcal{S}(t)^{\text{in}} \propto \mathcal{E}_{\text{LO}} \{ \bar{\mathcal{E}} \cos(\Phi_{\text{ref}}) \cos(\Delta\bar{\Phi}) + \Delta\bar{\mathcal{E}} \sin(\Phi_{\text{ref}}) \sin(\Delta\bar{\Phi}) \} \quad (\text{D.4})$$

and the quadrature one

$$\mathcal{S}(t)^q \propto \mathcal{E}_{\text{LO}} \{ \mathcal{E}_1 \sin(\Phi_{\text{LO}} - \Phi_1) + \mathcal{E}_2 \sin(\Phi_2 - \Phi_{\text{LO}}) \} \quad (\text{D.5})$$

$$\mathcal{S}(t)^q \propto \mathcal{E}_{\text{LO}} \{ \bar{\mathcal{E}} \cos(\Phi_{\text{ref}}) \sin(\Delta\bar{\Phi}) - \Delta\bar{\mathcal{E}} \sin(\Phi_{\text{ref}}) \cos(\Delta\bar{\Phi}) \} \quad (\text{D.6})$$

if we introduce

$$\begin{aligned}
 \bar{\Phi} &= \frac{\Phi_1 + \Phi_2}{2}, \quad \Delta\bar{\Phi} = \frac{\Phi_2 - \Phi_1}{2}, \\
 \bar{\mathcal{E}} &= \frac{\mathcal{E}_1 + \mathcal{E}_2}{2}, \quad \Delta\bar{\mathcal{E}} = \frac{\mathcal{E}_2 - \mathcal{E}_1}{2}, \\
 \Phi_{\text{ref}} &= \Phi_{\text{LO}} - \bar{\Phi}.
 \end{aligned}$$

Common-mode phase noise rejection $\rightarrow \Delta\bar{\Phi} = \Delta\bar{\Phi}_{\text{atomic}}$. However $\bar{\Phi} = \Phi_{\text{physical length}} + \bar{\Phi}_{\text{atomic}}$ but the sidebands are symmetric around the

resonance and the dispersion profile is odd, we should nearly have $\Phi_{\text{atomic}} \sim 0$ such that

$$\Phi_{\text{ref}} \cong \Phi_{\text{LO}} - \Phi_{\text{physical length}}.$$

To have the best sensitivity over the atomic phase shifts we want to extract the term proportional to $\sin(\Delta\bar{\Phi})$. As we want the same coupling with the atoms for the two sidebands, we need $\Delta\bar{\mathcal{E}} \sim 0$. Thus, measuring $\mathcal{S}(t)^q$ when $\Phi_{\text{ref}} = 0 [2\pi]$ would be adequate.

BIBLIOGRAPHY

- Charles S. Adams, Heun Jin Lee, Nir Davidson, Mark Kasevich, and Steven Chu. Evaporative cooling in a crossed dipole trap. *Phys. Rev. Lett.*, 74:3577–3580, May 1995. doi: 10.1103/PhysRevLett.74.3577. URL <http://link.aps.org/doi/10.1103/PhysRevLett.74.3577>.
- C. G. Aminoff, A. M. Steane, P. Bouyer, P. Desbiolles, J. Dalibard, and C. Cohen-Tannoudji. Cesium atoms bouncing in a stable gravitational cavity. *Phys. Rev. Lett.*, 71:3083–3086, Nov 1993. doi: 10.1103/PhysRevLett.71.3083. URL <http://link.aps.org/doi/10.1103/PhysRevLett.71.3083>.
- M. R. Andrews, M.O. Mewes, N. J. van Druten, D. S. Durfee, D. M. Kurn, and W. Ketterle. Direct, nondestructive observation of a bose condensate. *Science*, 273(5271):84–87, 1996. doi: 10.1126/science.273.5271.84. URL <http://www.sciencemag.org/content/273/5271/84.abstract>.
- Jürgen Appel, Dallas Hoffman, Eden Figueroa, and A. I. Lvovsky. Electronic noise in optical homodyne tomography. *Phys. Rev. A*, 75:035802, Mar 2007. doi: 10.1103/PhysRevA.75.035802. URL <http://link.aps.org/doi/10.1103/PhysRevA.75.035802>.
- Jürgen Appel, Andrew MacRae, and A I Lvovsky. A versatile digital ghz phase lock for external cavity diode lasers. *Measurement Science and Technology*, 20(5):055302, 2009a. URL <http://stacks.iop.org/0957-0233/20/i=5/a=055302>.
- Jürgen Appel, Patrick Joachim Windpassinger, Daniel Oblak, U Busk Hoff, Niels Kjærgaard, and Eugene Simon Polzik. Mesoscopic atomic entanglement for precision measurements beyond the standard quantum limit. *Proceedings of the National Academy of Sciences*, 106(27):10960–10965, 2009b.
- Bindiya Arora, M. S. Safronova, and Charles W. Clark. Magic wavelengths for the np - ns transitions in alkali-metal atoms. *Phys. Rev. A*, 76:052509, Nov 2007. doi: 10.1103/PhysRevA.76.052509. URL <http://link.aps.org/doi/10.1103/PhysRevA.76.052509>.
- Bindiya Arora, M. S. Safronova, and Charles W. Clark. Tune-out wavelengths of alkali-metal atoms and their applications. *Phys. Rev. A*, 84:043401, Oct 2011. doi: 10.1103/PhysRevA.84.043401. URL <http://link.aps.org/doi/10.1103/PhysRevA.84.043401>.
- T. Arpornthip, C. A. Sackett, and K. J. Hughes. Vacuum-pressure measurement using a magneto-optical trap. *Phys. Rev. A*, 85:033420,

- Mar 2012. doi: 10.1103/PhysRevA.85.033420. URL <http://link.aps.org/doi/10.1103/PhysRevA.85.033420>.
- A. Ashkin. Trapping of atoms by resonance radiation pressure. *Phys. Rev. Lett.*, 40:729–732, Mar 1978. doi: 10.1103/PhysRevLett.40.729. URL <http://link.aps.org/doi/10.1103/PhysRevLett.40.729>.
- S. Bali, K. M. O’Hara, M. E. Gehm, S. R. Granade, and J. E. Thomas. Quantum-diffractive background gas collisions in atom-trap heating and loss. *Phys. Rev. A*, 60:R29–R32, Jul 1999. doi: 10.1103/PhysRevA.60.R29. URL <http://link.aps.org/doi/10.1103/PhysRevA.60.R29>.
- V. I. Balykin, V. S. Letokhov, Yu. B. Ovchinnikov, and A. I. Sidorov. Quantum-state-selective mirror reflection of atoms by laser light. *Phys. Rev. Lett.*, 60:2137–2140, May 1988. doi: 10.1103/PhysRevLett.60.2137. URL <http://link.aps.org/doi/10.1103/PhysRevLett.60.2137>.
- V. I. Balykin, K. Hakuta, Fam Le Kien, J. Q. Liang, and M. Morinaga. Atom trapping and guiding with a subwavelength-diameter optical fiber. *Phys. Rev. A*, 70:011401, Jul 2004. doi: 10.1103/PhysRevA.70.011401. URL <http://link.aps.org/doi/10.1103/PhysRevA.70.011401>.
- V.I. Balykin and V.S. Letokhov. Atomic cavity with light-induced mirrors. *Applied Physics B*, 48(6):517–523, 1989. ISSN 0946-2171. doi: 10.1007/BF00694689. URL <http://dx.doi.org/10.1007/BF00694689>.
- VI Balykin, VS Letokhov, Yu B Ovchinnikov, and AI Sidorov. Reflection of an atomic beam from a gradient of an optical field. *JETP Lett*, 45(6):353–356, 1987.
- A. H. Barnett, S. P. Smith, M. Olshanii, K. S. Johnson, A. W. Adams, and M. Prentiss. Substrate-based atom waveguide using guided two-color evanescent light fields. *Phys. Rev. A*, 61:023608, Jan 2000. doi: 10.1103/PhysRevA.61.023608. URL <http://link.aps.org/doi/10.1103/PhysRevA.61.023608>.
- Stephen M. Barnett. Resolution of the abraham-minkowski dilemma. *Phys. Rev. Lett.*, 104:070401, Feb 2010. doi: 10.1103/PhysRevLett.104.070401. URL <http://link.aps.org/doi/10.1103/PhysRevLett.104.070401>.
- Stephen M. Barnett and Rodney Loudon. The enigma of optical momentum in a medium. *Philosophical Transactions of the Royal Society of London A: Mathematical, Physical and Engineering Sciences*, 368(1914):927–939, 2010. ISSN 1364-503X. doi: 10.1098/rsta.2009.0207.

- J.P. Barrat and C. Cohen-Tannoudji. Étude du pompage optique dans le formalisme de la matrice densité. 1961. URL <http://hal.archives-ouvertes.fr/jpa-00236458>.
- M. D. Barrett, J. A. Sauer, and M. S. Chapman. All-optical formation of an atomic bose-einstein condensate. *Phys. Rev. Lett.*, 87:010404, Jun 2001. doi: 10.1103/PhysRevLett.87.010404. URL <http://link.aps.org/doi/10.1103/PhysRevLett.87.010404>.
- J.-B. Béguin, E. M. Bookjans, S. L. Christensen, H. L. Sørensen, J. H. Müller, E. S. Polzik, and J. Appel. Generation and detection of a sub-poissonian atom number distribution in a one-dimensional optical lattice. *Phys. Rev. Lett.*, 113:263603, Dec 2014. doi: 10.1103/PhysRevLett.113.263603. URL <http://link.aps.org/doi/10.1103/PhysRevLett.113.263603>.
- T. Bergeman, Gidon Erez, and Harold J. Metcalf. Magnetostatic trapping fields for neutral atoms. *Phys. Rev. A*, 35:1535–1546, Feb 1987. doi: 10.1103/PhysRevA.35.1535. URL <http://link.aps.org/doi/10.1103/PhysRevA.35.1535>.
- J. E. Bjorkholm. Collision-limited lifetimes of atom traps. *Phys. Rev. A*, 38:1599–1600, Aug 1988. doi: 10.1103/PhysRevA.38.1599. URL <http://link.aps.org/doi/10.1103/PhysRevA.38.1599>.
- R. Blümel and K. Dietrich. Quantum states of neutrons bound in the magnetic field of a rectilinear current. *Phys. Rev. A*, 43:22–28, Jan 1991. doi: 10.1103/PhysRevA.43.22. URL <http://link.aps.org/doi/10.1103/PhysRevA.43.22>.
- D. Boiron, A. Michaud, P. Lemonde, Y. Castin, C. Salomon, S. Weyers, K. Szymaniec, L. Cognet, and A. Clairon. Laser cooling of cesium atoms in gray optical molasses down to 1.1 μk . *Phys. Rev. A*, 53:R3734–R3737, Jun 1996. doi: 10.1103/PhysRevA.53.R3734. URL <http://link.aps.org/doi/10.1103/PhysRevA.53.R3734>.
- D. Boiron, A. Michaud, J. M. Fournier, L. Simard, M. Sprenger, G. Grynberg, and C. Salomon. Cold and dense cesium clouds in far-detuned dipole traps. *Phys. Rev. A*, 57:R4106–R4109, Jun 1998. doi: 10.1103/PhysRevA.57.R4106. URL <http://link.aps.org/doi/10.1103/PhysRevA.57.R4106>.
- M. Boustimi, J. Baudon, P. Candori, and J. Robert. van der waals interaction between an atom and a metallic nanowire. *Phys. Rev. B*, 65:155402, Mar 2002. doi: 10.1103/PhysRevB.65.155402. URL <http://link.aps.org/doi/10.1103/PhysRevB.65.155402>.
- M. Boustimi, J. Baudon, and J. Robert. Molecules interacting with a metallic nanowire. *Phys. Rev. B*, 67:045407, Jan 2003. doi: 10.1103/PhysRevB.67.045407. URL <http://link.aps.org/doi/10.1103/PhysRevB.67.045407>.

- L. Bouten, R. Van Handel, and M. James. An introduction to quantum filtering. *SIAM Journal on Control and Optimization*, 46(6):2199–2241, 2007. doi: 10.1137/060651239. URL <http://dx.doi.org/10.1137/060651239>.
- Martin M. Boyd, Tanya Zelevinsky, Andrew D. Ludlow, Seth M. Foreman, Sebastian Blatt, Tetsuya Ido, and Jun Ye. Optical atomic coherence at the 1-second time scale. *Science*, 314(5804):1430–1433, 2006. doi: 10.1126/science.1133732. URL <http://www.sciencemag.org/content/314/5804/1430.abstract>.
- Anders Brusch, Rodolphe Le Targat, Xavier Baillard, Mathilde Fouché, and Pierre Lemonde. Hyperpolarizability effects in a sr optical lattice clock. *Phys. Rev. Lett.*, 96:103003, Mar 2006. doi: 10.1103/PhysRevLett.96.103003. URL <http://link.aps.org/doi/10.1103/PhysRevLett.96.103003>.
- R.S. Bucy. Linear and nonlinear filtering. *Proceedings of the IEEE*, 58(6):854–864, June 1970. ISSN 0018-9219. doi: 10.1109/PROC.1970.7792.
- James P. Burke, Sai-Tak Chu, Garnett W. Bryant, C. J. Williams, and P. S. Julienne. Designing neutral-atom nanotraps with integrated optical waveguides. *Phys. Rev. A*, 65:043411, Apr 2002. doi: 10.1103/PhysRevA.65.043411. URL <http://link.aps.org/doi/10.1103/PhysRevA.65.043411>.
- D. E. Chang, L Jiang, A. V. Gorshkov, and H. J. Kimble. Cavity qed with atomic mirrors. *New Journal of Physics*, 14(6):063003, 2012. URL <http://stacks.iop.org/1367-2630/14/i=6/a=063003>.
- Ying-Cheng Chen, Yean-An Liao, Long Hsu, and Ite A. Yu. Simple technique for directly and accurately measuring the number of atoms in a magneto-optical trap. *Phys. Rev. A*, 64:031401, Aug 2001. doi: 10.1103/PhysRevA.64.031401. URL <http://link.aps.org/doi/10.1103/PhysRevA.64.031401>.
- R. Chicireanu, K. D. Nelson, S. Olmschenk, N. Lundblad, A. Derevianko, and J. V. Porto. Differential light-shift cancellation in a magnetic-field-insensitive transition of ^{87}Rb . *Phys. Rev. Lett.*, 106:063002, Feb 2011. doi: 10.1103/PhysRevLett.106.063002. URL <http://link.aps.org/doi/10.1103/PhysRevLett.106.063002>.
- S. L. Christensen, J.-B. Béguin, H. L. Sørensen, E. Bookjans, D. Oblak, J. H. Müller, J. Appel, and E. S. Polzik. Toward quantum state tomography of a single polariton state of an atomic ensemble. *New Journal of Physics*, 15(1):015002, 2013. URL <http://stacks.iop.org/1367-2630/15/i=1/a=015002>.

- S. L. Christensen, J.-B. Béguin, E. Bookjans, H. L. Sørensen, J. H. Müller, J. Appel, and E. S. Polzik. Quantum interference of a single spin excitation with a macroscopic atomic ensemble. *Phys. Rev. A*, 89:033801, Mar 2014. doi: 10.1103/PhysRevA.89.033801. URL <http://link.aps.org/doi/10.1103/PhysRevA.89.033801>.
- Steven Chu, J. E. Bjorkholm, A. Ashkin, and A. Cable. Experimental observation of optically trapped atoms. *Phys. Rev. Lett.*, 57:314–317, Jul 1986. doi: 10.1103/PhysRevLett.57.314. URL <http://link.aps.org/doi/10.1103/PhysRevLett.57.314>.
- M. A. Cirone, K. Rzażewski, W. P. Schleich, F. Straub, and J. A. Wheeler. Quantum anticentrifugal force. *Phys. Rev. A*, 65:022101, Dec 2001. doi: 10.1103/PhysRevA.65.022101. URL <http://link.aps.org/doi/10.1103/PhysRevA.65.022101>.
- Claude Cohen-Tannoudji and Jacques Dupont-Roc. Experimental study of zeeman light shifts in weak magnetic fields. *Phys. Rev. A*, 5:968–984, Feb 1972. doi: 10.1103/PhysRevA.5.968. URL <http://link.aps.org/doi/10.1103/PhysRevA.5.968>.
- Claude Cohen-Tannoudji and David Guéry-Odelin. *Advances in atomic physics*. World Scientific, 2011.
- Giorgio Colangelo, Robert J Sewell, Naeimeh Behbood, Ferran Martin Ciurana, Gil Triginer, and Morgan W Mitchell. Quantum atom-light interfaces in the gaussian description for spin-1 systems. *New Journal of Physics*, 15(10):103007, 2013. URL <http://stacks.iop.org/1367-2630/15/i=10/a=103007>.
- Richard J. Cook and Richard K. Hill. An electromagnetic mirror for neutral atoms. *Optics Communications*, 43:258–260, 1982. ISSN 0030-4018. doi: [http://dx.doi.org/10.1016/0030-4018\(82\)90392-3](http://dx.doi.org/10.1016/0030-4018(82)90392-3). URL <http://www.sciencedirect.com/science/article/pii/0030401882903923>.
- K. L. Corwin, S. J. M. Kuppens, D. Cho, and C. E. Wieman. Spin-polarized atoms in a circularly polarized optical dipole trap. *Phys. Rev. Lett.*, 83:1311–1314, Aug 1999. doi: 10.1103/PhysRevLett.83.1311. URL <http://link.aps.org/doi/10.1103/PhysRevLett.83.1311>.
- A Crubellier, S Liberman, D Pavolini, and P Pillet. Superradiance and subradiance. i. interatomic interference and symmetry properties in three-level systems. *Journal of Physics B: Atomic and Molecular Physics*, 18(18):3811, 1985. URL <http://stacks.iop.org/0022-3700/18/i=18/a=022>.
- Jean Dalibard and Jean-Louis Basdevant. *The quantum mechanics solver: how to apply quantum theory to modern physics*. Springer, 2005.

- K. B. Davis, M. O. Mewes, M. R. Andrews, N. J. van Druten, D. S. Durfee, D. M. Kurn, and W. Ketterle. Bose-einstein condensation in a gas of sodium atoms. *Phys. Rev. Lett.*, 75:3969–3973, Nov 1995. doi: 10.1103/PhysRevLett.75.3969. URL <http://link.aps.org/doi/10.1103/PhysRevLett.75.3969>.
- S. T. Dawkins, R. Mitsch, D. Reitz, E. Vetsch, and A. Rauschenbeutel. Dispersive optical interface based on nanofiber-trapped atoms. *Phys. Rev. Lett.*, 107:243601, Dec 2011. doi: 10.1103/PhysRevLett.107.243601. URL <http://link.aps.org/doi/10.1103/PhysRevLett.107.243601>.
- I. H. Deutsch, R. J. C. Spreeuw, S. L. Rolston, and W. D. Phillips. Photonic band gaps in optical lattices. *Phys. Rev. A*, 52:1394–1410, Aug 1995. doi: 10.1103/PhysRevA.52.1394. URL <http://link.aps.org/doi/10.1103/PhysRevA.52.1394>.
- R. H. Dicke. Coherence in spontaneous radiation processes. *Phys. Rev.*, 93:99–110, Jan 1954. doi: 10.1103/PhysRev.93.99. URL <http://link.aps.org/doi/10.1103/PhysRev.93.99>.
- L. M. Duan, M. D. Lukin, J. I. Cirac, and P. Zoller. Long-distance quantum communication with atomic ensembles and linear optics. *Nature*, 414(6862):413–418, 11 2001.
- Y. O. Dudin, R. Zhao, T. A. B. Kennedy, and A. Kuzmich. Light storage in a magnetically dressed optical lattice. *Phys. Rev. A*, 81:041805, Apr 2010. doi: 10.1103/PhysRevA.81.041805. URL <http://link.aps.org/doi/10.1103/PhysRevA.81.041805>.
- J. Dupont-Roc, N. Polonsky, C. Cohen-Tannoudji, and A. Kastler. Lifting of a zeeman degeneracy by interaction with a light beam. *Physics Letters A*, 25(2):87 – 88, 1967. ISSN 0375-9601. doi: [http://dx.doi.org/10.1016/0375-9601\(67\)90357-X](http://dx.doi.org/10.1016/0375-9601(67)90357-X). URL <http://www.sciencedirect.com/science/article/pii/037596016790357X>.
- K. Eckert, O. Romero-Isart, M. Rodriguez, M. Lewenstein, E. S. Polzik, and A. Sanpera. Quantum non-demolition detection of strongly correlated systems. *Nature Physics*, 4:50 – 54, Jan 2008. doi: 10.1038/nphys776.
- U. Fano. Description of states in quantum mechanics by density matrix and operator techniques. *Rev. Mod. Phys.*, 29:74–93, Jan 1957. doi: 10.1103/RevModPhys.29.74. URL <http://link.aps.org/doi/10.1103/RevModPhys.29.74>.
- R. Feynman. *The Feynman Lectures On Physics, The Definitive Edition Volume 3, 2/E*. The Feynman Lectures on Physics. Pearson Education, 1963. ISBN 9788131721667.

- Richard P. Feynman, Frank L. Vernon, and Robert W. Hellwarth. Geometrical representation of the schrödinger equation for solving maser problems. *Journal of Applied Physics*, 28(1):49–52, 1957. doi: <http://dx.doi.org/10.1063/1.1722572>. URL <http://scitation.aip.org/content/aip/journal/jap/28/1/10.1063/1.1722572>.
- V. V. Flambaum, V. A. Dzuba, and A. Derevianko. Magic frequencies for cesium primary-frequency standard. *Phys. Rev. Lett.*, 101:220801, Nov 2008. doi: 10.1103/PhysRevLett.101.220801. URL <http://link.aps.org/doi/10.1103/PhysRevLett.101.220801>.
- Wojciech Gawlik. Hyperfine interaction versus strong laser field-optical back-goudsmit (paschen-back) effect. *American Journal of Physics*, 59(8):706–710, 1991. doi: <http://dx.doi.org/10.1119/1.16748>. URL <http://scitation.aip.org/content/aapt/journal/ajp/59/8/10.1119/1.16748>.
- Wojciech Gawlik and Jerzy Zachorowski. Optical back-goudsmit effect: Laser decoupling of hyperfine interactions in atoms. *Acta Physica Polonica B*, 33:2243, 2002.
- J. M. Geremia, John K. Stockton, and Hideo Mabuchi. Tensor polarizability and dispersive quantum measurement of multilevel atoms. *Phys. Rev. A*, 73:042112, Apr 2006. doi: 10.1103/PhysRevA.73.042112. URL <http://link.aps.org/doi/10.1103/PhysRevA.73.042112>.
- JM Geremia, John K. Stockton, Andrew C. Doherty, and Hideo Mabuchi. Quantum kalman filtering and the heisenberg limit in atomic magnetometry. *Phys. Rev. Lett.*, 91:250801, Dec 2003. doi: 10.1103/PhysRevLett.91.250801. URL <http://link.aps.org/doi/10.1103/PhysRevLett.91.250801>.
- JM Geremia, John K. Stockton, and Hideo Mabuchi. Suppression of spin projection noise in broadband atomic magnetometry. *Phys. Rev. Lett.*, 94:203002, May 2005. doi: 10.1103/PhysRevLett.94.203002. URL <http://link.aps.org/doi/10.1103/PhysRevLett.94.203002>.
- R. J. Glauber. *Quantum Optics and Electronics (Les Houches)*. eds. C. de Witt, A. Blandin and C. Cohen-Tannoudji (New York: Gordon and Breach Science Publishers, Inc., 1965), 1964.
- Roy J. Glauber. Coherent and incoherent states of the radiation field. *Phys. Rev.*, 131:2766–2788, Sep 1963a. doi: 10.1103/PhysRev.131.2766. URL <http://link.aps.org/doi/10.1103/PhysRev.131.2766>.
- Roy J. Glauber. The quantum theory of optical coherence. *Phys. Rev.*, 130:2529–2539, Jun 1963b. doi: 10.1103/PhysRev.130.2529. URL <http://link.aps.org/doi/10.1103/PhysRev.130.2529>.

- A. Goban, K. S. Choi, D. J. Alton, D. Ding, C. Lacroûte, M. Pototschnig, T. Thiele, N. P. Stern, and H. J. Kimble. Demonstration of a state-insensitive, compensated nanofiber trap. *Phys. Rev. Lett.*, 109:033603, Jul 2012. doi: 10.1103/PhysRevLett.109.033603. URL <http://link.aps.org/doi/10.1103/PhysRevLett.109.033603>.
- S. Goudsmit and R. F. Bacher. The paschen-back effect of hyperfine structure. *Phys. Rev.*, 34:1499–1500, Dec 1929. doi: 10.1103/PhysRev.34.1499. URL <http://link.aps.org/doi/10.1103/PhysRev.34.1499>.
- A. Gozzini, F. Mango, J.H. Xu, G. Alzetta, F. Maccarrone, and R.A. Bernheim. Light-induced ejection of alkali atoms in polysiloxane coated cells. *Il Nuovo Cimento D*, 15(5):709–722, 1993. ISSN 0392-6737. doi: 10.1007/BF02482437. URL <http://dx.doi.org/10.1007/BF02482437>.
- Rudolf Grimm, Matthias Weideüller, and Yurii B. Ovchinnikov. Optical dipole traps for neutral atoms. 42:95–170, 2000. ISSN 1049-250X. doi: [http://dx.doi.org/10.1016/S1049-250X\(08\)60186-X](http://dx.doi.org/10.1016/S1049-250X(08)60186-X). URL <http://www.sciencedirect.com/science/article/pii/S1049250X0860186X>.
- Gilbert Grynberg, Alain Aspect, and Claude Fabre. *Introduction to quantum optics: from the semi-classical approach to quantized light*. Cambridge university press, 2010.
- Florian Haas, Jürgen Volz, Roger Gehr, Jakob Reichel, and Jérôme Estève. Entangled states of more than 40 atoms in an optical fiber cavity. *Science*, 344(6180):180–183, 2014. doi: 10.1126/science.1248905. URL <http://www.sciencemag.org/content/344/6180/180.abstract>.
- Klemens Hammerer, Anders S. Sørensen, and Eugene S. Polzik. Quantum interface between light and atomic ensembles. *Rev. Mod. Phys.*, 82:1041–1093, Apr 2010. doi: 10.1103/RevModPhys.82.1041. URL <http://link.aps.org/doi/10.1103/RevModPhys.82.1041>.
- T.W. Hänsch and A.L. Schawlow. Cooling of gases by laser radiation. *Optics Communications*, 13(1):68–69, 1975. ISSN 0030-4018. doi: [http://dx.doi.org/10.1016/0030-4018\(75\)90159-5](http://dx.doi.org/10.1016/0030-4018(75)90159-5). URL <http://www.sciencedirect.com/science/article/pii/0030401875901595>.
- Serge Haroche. Nobel lecture: Controlling photons in a box and exploring the quantum to classical boundary. *Rev. Mod. Phys.*, 85:1083–1102, Jul 2013. doi: 10.1103/RevModPhys.85.1083. URL <http://link.aps.org/doi/10.1103/RevModPhys.85.1083>.
- Serge Haroche and Jean-Michel Raimond. *Exploring the Quantum: Atoms, Cavities, and Photons (Oxford Graduate Texts)*. Oxford University Press, USA, 1st ed edition, 2006. ISBN 0198509146.

- Serge Haroche, Michel Brune, and Jean-Michel Raimond. Atomic clocks for controlling light fields. *Physics today*, 66(1):27–32, 2013. doi: 10.1063/PT.3.1856. URL <http://dx.doi.org/10.1063/PT.3.1856>.
- D. B. Hume, I. Stroescu, M. Joos, W. Muessel, H. Strobel, and M. K. Oberthaler. Accurate atom counting in mesoscopic ensembles. *Phys. Rev. Lett.*, 111:253001, Dec 2013. doi: 10.1103/PhysRevLett.111.253001. URL <http://link.aps.org/doi/10.1103/PhysRevLett.111.253001>.
- Tetsuya Ido, Yoshitomo Isoya, and Hidetoshi Katori. Optical-dipole trapping of sr atoms at a high phase-space density. *Phys. Rev. A*, 61:061403, May 2000. doi: 10.1103/PhysRevA.61.061403. URL <http://link.aps.org/doi/10.1103/PhysRevA.61.061403>.
- H. Ito, T. Nakata, K. Sakaki, M. Ohtsu, K. I. Lee, and W. Jhe. Laser spectroscopy of atoms guided by evanescent waves in micron-sized hollow optical fibers. *Phys. Rev. Lett.*, 76:4500–4503, Jun 1996. doi: 10.1103/PhysRevLett.76.4500. URL <http://link.aps.org/doi/10.1103/PhysRevLett.76.4500>.
- Rudolph E Kalman and Richard S Bucy. New results in linear filtering and prediction theory. *Journal of Fluids Engineering*, 83(1):95–108, 1961.
- KC Kao and George A Hockham. Dielectric-fibre surface waveguides for optical frequencies. In *Proceedings of the Institution of Electrical Engineers*, volume 113, pages 1151–1158. IET, 1966.
- Hidetoshi Katori, Tetsuya Ido, and Makoto Kuwata-Gonokami. Optimal design of dipole potentials for efficient loading of sr atoms. *Journal of the Physical Society of Japan*, 68(8):2479–2482, 1999. doi: 10.1143/JPSJ.68.2479. URL <http://dx.doi.org/10.1143/JPSJ.68.2479>.
- Wolfgang Ketterle, Kendall B. Davis, Michael A. Joffe, Alex Martin, and David E. Pritchard. High densities of cold atoms in a dark spontaneous-force optical trap. *Phys. Rev. Lett.*, 70:2253–2256, Apr 1993. doi: 10.1103/PhysRevLett.70.2253. URL <http://link.aps.org/doi/10.1103/PhysRevLett.70.2253>.
- Fam Le Kien, V. I. Balykin, and K. Hakuta. Angular momentum of light in an optical nanofiber. *Phys. Rev. A*, 73:053823, May 2006. doi: 10.1103/PhysRevA.73.053823. URL <http://link.aps.org/doi/10.1103/PhysRevA.73.053823>.
- T. Kiesel, W. Vogel, S. L. Christensen, J.-B. Béguin, J. Appel, and E. S. Polzik. Atomic nonclassicality quasiprobabilities. *Phys. Rev. A*, 86:042108, Oct 2012. doi: 10.1103/PhysRevA.86.042108. URL <http://link.aps.org/doi/10.1103/PhysRevA.86.042108>.

- Masahiro Kitagawa and Masahito Ueda. Squeezed spin states. *Phys. Rev. A*, 47:5138–5143, Jun 1993. doi: 10.1103/PhysRevA.47.5138. URL <http://link.aps.org/doi/10.1103/PhysRevA.47.5138>.
- S. J. M. Kuppens, K. L. Corwin, K. W. Miller, T. E. Chupp, and C. E. Wieman. Loading an optical dipole trap. *Phys. Rev. A*, 62:013406, Jun 2000. doi: 10.1103/PhysRevA.62.013406. URL <http://link.aps.org/doi/10.1103/PhysRevA.62.013406>.
- C. Lacroûte, K. S. Choi, A. Goban, D. J. Alton, D. Ding, N. P. Stern, and H. J. Kimble. A state-insensitive, compensated nanofiber trap. *New Journal of Physics*, 14(2):023056, 2012. URL <http://stacks.iop.org/1367-2630/14/i=2/a=023056>.
- Jr. Lamb, W.E. Anti-photon. *Applied Physics B*, 60(2-3):77–84, 1995. ISSN 0946-2171. doi: 10.1007/BF01135846. URL <http://dx.doi.org/10.1007/BF01135846>.
- J. Laurat, K. S. Choi, H. Deng, C. W. Chou, and H. J. Kimble. Heralded entanglement between atomic ensembles: Preparation, decoherence, and scaling. *Phys. Rev. Lett.*, 99:180504, Nov 2007. doi: 10.1103/PhysRevLett.99.180504. URL <http://link.aps.org/doi/10.1103/PhysRevLett.99.180504>.
- Fam Le Kien, V. I. Balykin, and K. Hakuta. Atom trap and waveguide using a two-color evanescent light field around a subwavelength-diameter optical fiber. *Phys. Rev. A*, 70:063403, Dec 2004. doi: 10.1103/PhysRevA.70.063403. URL <http://link.aps.org/doi/10.1103/PhysRevA.70.063403>.
- Fam Le Kien, S. Dutta Gupta, V. I. Balykin, and K. Hakuta. Spontaneous emission of a cesium atom near a nanofiber: Efficient coupling of light to guided modes. *Phys. Rev. A*, 72:032509, Sep 2005a. doi: 10.1103/PhysRevA.72.032509. URL <http://link.aps.org/doi/10.1103/PhysRevA.72.032509>.
- Fam Le Kien, Victor I. Balykin, and Kohzo Hakuta. State-insensitive trapping and guiding of cesium atoms using a two-color evanescent field around a subwavelength-diameter fiber. *Journal of the Physical Society of Japan*, 74(3):910–917, 2005b. doi: 10.1143/JPSJ.74.910. URL <http://dx.doi.org/10.1143/JPSJ.74.910>.
- L. J. LeBlanc and J. H. Thywissen. Species-specific optical lattices. *Phys. Rev. A*, 75:053612, May 2007. doi: 10.1103/PhysRevA.75.053612. URL <http://link.aps.org/doi/10.1103/PhysRevA.75.053612>.
- Mary Locke and Chad Fertig. Simultaneous unbalanced shared local oscillator heterodyne interferometry for high signal-to-noise-ratio, minimally destructive dispersive detection of time-dependent atomic

- spins. *J. Opt. Soc. Am. B*, 30(9):2409–2419, Sep 2013. doi: 10.1364/JOSAB.30.002409. URL <http://josab.osa.org/abstract.cfm?URI=josab-30-9-2409>.
- Anne Louchet-Chauvet, Jürgen Appel, Jelmer J Renema, Daniel Oblak, Niels Kjaergaard, and Eugene S Polzik. Entanglement-assisted atomic clock beyond the projection noise limit. *New Journal of Physics*, 12(6):065032, 2010. URL <http://stacks.iop.org/1367-2630/12/i=6/a=065032>.
- N. Lundblad, M. Schlosser, and J. V. Porto. Experimental observation of magic-wavelength behavior of ^{87}Rb atoms in an optical lattice. *Phys. Rev. A*, 81:031611, Mar 2010. doi: 10.1103/PhysRevA.81.031611. URL <http://link.aps.org/doi/10.1103/PhysRevA.81.031611>.
- J. E. Lye, J. J. Hope, and J. D. Close. Nondestructive dynamic detectors for bose-einstein condensates. *Phys. Rev. A*, 67:043609, Apr 2003. doi: 10.1103/PhysRevA.67.043609. URL <http://link.aps.org/doi/10.1103/PhysRevA.67.043609>.
- H. Mabuchi and H. J. Kimble. Atom galleries for whispering atoms: binding atoms in stable orbits around an optical resonator. *Opt. Lett.*, 19(10):749–751, May 1994. doi: 10.1364/OL.19.000749. URL <http://ol.osa.org/abstract.cfm?URI=ol-19-10-749>.
- Lorenzo Maccone and Arun K. Pati. Stronger uncertainty relations for all incompatible observables. *Phys. Rev. Lett.*, 113:260401, Dec 2014. doi: 10.1103/PhysRevLett.113.260401. URL <http://link.aps.org/doi/10.1103/PhysRevLett.113.260401>.
- Lars Bojer Madsen and Klaus Mølmer. Spin squeezing and precision probing with light and samples of atoms in the gaussian description. *Phys. Rev. A*, 70:052324, Nov 2004. doi: 10.1103/PhysRevA.70.052324. URL <http://link.aps.org/doi/10.1103/PhysRevA.70.052324>.
- J. McKeever, J. R. Buck, A. D. Boozer, A. Kuzmich, H.-C. Nägerl, D. M. Stamper-Kurn, and H. J. Kimble. State-insensitive cooling and trapping of single atoms in an optical cavity. *Phys. Rev. Lett.*, 90:133602, Apr 2003. doi: 10.1103/PhysRevLett.90.133602. URL <http://link.aps.org/doi/10.1103/PhysRevLett.90.133602>.
- A.D. McLachlan. Van der waals forces between an atom and a surface. *Molecular Physics*, 7(4):381–388, 1964. doi: 10.1080/00268976300101141. URL <http://dx.doi.org/10.1080/00268976300101141>.
- Alan L Migdall. Absolute quantum efficiency measurements using correlated photons: toward a measurement protocol. *IEEE Transac-*

- tions on Instrumentation and measurement*, 50(2):478–481, 2001. doi: 10.1109/19.918170.
- Alan L. Migdall, John V. Prodan, William D. Phillips, Thomas H. Bergeman, and Harold J. Metcalf. First observation of magnetically trapped neutral atoms. *Phys. Rev. Lett.*, 54:2596–2599, Jun 1985. doi: 10.1103/PhysRevLett.54.2596. URL <http://link.aps.org/doi/10.1103/PhysRevLett.54.2596>.
- J. D. Miller, R. A. Cline, and D. J. Heinzen. Far-off-resonance optical trapping of atoms. *Phys. Rev. A*, 47:R4567–R4570, Jun 1993. doi: 10.1103/PhysRevA.47.R4567. URL <http://link.aps.org/doi/10.1103/PhysRevA.47.R4567>.
- C. Monroe, W. Swann, H. Robinson, and C. Wieman. Very cold trapped atoms in a vapor cell. *Phys. Rev. Lett.*, 65:1571–1574, Sep 1990. doi: 10.1103/PhysRevLett.65.1571. URL <http://link.aps.org/doi/10.1103/PhysRevLett.65.1571>.
- K. P. Nayak, P. N. Melentiev, M. Morinaga, Fam Le Kien, V. I. Balykin, and K. Hakuta. Optical nanofiber as an efficient tool for manipulating and probing atomicfluorescence. *Opt. Express*, 15(9):5431–5438, Apr 2007. doi: 10.1364/OE.15.005431. URL <http://www.opticsexpress.org/abstract.cfm?URI=oe-15-9-5431>.
- Daniel Oblak, Plamen G. Petrov, Carlos L. Garrido Alzar, Wolfgang Tittel, Anton K. Vershovski, Jens K. Mikkelsen, Jens L. Sørensen, and Eugene S. Polzik. Quantum-noise-limited interferometric measurement of atomic noise: Towards spin squeezing on the cs clock transition. *Phys. Rev. A*, 71:043807, Apr 2005. doi: 10.1103/PhysRevA.71.043807. URL <http://link.aps.org/doi/10.1103/PhysRevA.71.043807>.
- Harold Ollivier and Wojciech H. Zurek. Quantum discord: A measure of the quantumness of correlations. *Phys. Rev. Lett.*, 88:017901, Dec 2001. doi: 10.1103/PhysRevLett.88.017901. URL <http://link.aps.org/doi/10.1103/PhysRevLett.88.017901>.
- M.A. Ol’Shanii, Yu.B. Ovchinnikov, and V.S. Letokhov. Laser guiding of atoms in a hollow optical fiber. *Optics Communications*, 98(1-3):77–79, 1993. ISSN 0030-4018. doi: [http://dx.doi.org/10.1016/0030-4018\(93\)90761-S](http://dx.doi.org/10.1016/0030-4018(93)90761-S). URL <http://www.sciencedirect.com/science/article/pii/003040189390761S>.
- U Österberg and Walter Margulis. Dye laser pumped by nd:yag laser pulses frequency doubled in a glass optical fiber. *Optics letters*, 11(8):516–518, 1986.
- Y B Ovchinnikov, S V Shul’ga, and V I Balykin. An atomic trap based on evanescent light waves. *Journal of Physics B: Atomic, Molecular*

- and Optical Physics*, 24(14):3173, 1991. URL <http://stacks.iop.org/0953-4075/24/i=14/a=009>.
- J. M. Pino, R. J. Wild, P. Makotyn, D. S. Jin, and E. A. Cornell. Photon counting for bragg spectroscopy of quantum gases. *Phys. Rev. A*, 83:033615, Mar 2011. doi: 10.1103/PhysRevA.83.033615. URL <http://link.aps.org/doi/10.1103/PhysRevA.83.033615>.
- M. Prentiss, E. L. Raab, D. E. Pritchard, A. Cable, J. E. Bjorkholm, and Steven Chu. Atomic-density-dependent losses in an optical trap. *Opt. Lett.*, 13(6):452–454, Jun 1988. doi: 10.1364/OL.13.000452. URL <http://ol.osa.org/abstract.cfm?URI=ol-13-6-452>.
- E. L. Raab, M. Prentiss, Alex Cable, Steven Chu, and D. E. Pritchard. Trapping of neutral sodium atoms with radiation pressure. *Phys. Rev. Lett.*, 59:2631–2634, Dec 1987. doi: 10.1103/PhysRevLett.59.2631. URL <http://link.aps.org/doi/10.1103/PhysRevLett.59.2631>.
- Simon Ramo, John R. Whinnery, and Theodore V. Van Duzer. *Fields and Waves in Communication Electronics*. Wiley, January 1994. ISBN 0471585513.
- Norman F Ramsey. The method of successive oscillatory fields. *Phys. Today*, 33(7):25–30, 1980. doi: 10.1063/PT.3.1857. URL <http://dx.doi.org/10.1063/PT.3.1857>.
- Norman F. Ramsey. Experiments with separated oscillatory fields and hydrogen masers. *Rev. Mod. Phys.*, 62:541–552, Jul 1990. doi: 10.1103/RevModPhys.62.541. URL <http://link.aps.org/doi/10.1103/RevModPhys.62.541>.
- Andreas Reiserer, Stephan Ritter, and Gerhard Rempe. Nondestructive detection of an optical photon. *Science*, 342(6164):1349–1351, 2013. doi: 10.1126/science.1246164. URL <http://www.sciencemag.org/content/342/6164/1349.abstract>.
- D. Reitz, C. Sayrin, B. Albrecht, I. Mazets, R. Mitsch, P. Schneeweiss, and A. Rauschenbeutel. Backscattering properties of a waveguide-coupled array of atoms in the strongly nonparaxial regime. *Phys. Rev. A*, 89:031804, Mar 2014. doi: 10.1103/PhysRevA.89.031804. URL <http://link.aps.org/doi/10.1103/PhysRevA.89.031804>.
- M. J. Renn, D. Montgomery, O. Vdovin, D. Z. Anderson, C. E. Wieman, and E. A. Cornell. Laser-guided atoms in hollow-core optical fibers. *Phys. Rev. Lett.*, 75:3253–3256, Oct 1995. doi: 10.1103/PhysRevLett.75.3253. URL <http://link.aps.org/doi/10.1103/PhysRevLett.75.3253>.
- P. Rosenbusch, S. Ghezali, V. A. Dzuba, V. V. Flambaum, K. Beloy, and A. Derevianko. ac stark shift of the cs microwave atomic

- clock transitions. *Phys. Rev. A*, 79:013404, Jan 2009. doi: 10.1103/PhysRevA.79.013404. URL <http://link.aps.org/doi/10.1103/PhysRevA.79.013404>.
- M. Saffman, D. Oblak, J. Appel, and E. S. Polzik. Spin squeezing of atomic ensembles by multicolor quantum nondemolition measurements. *Phys. Rev. A*, 79:023831, Feb 2009. doi: 10.1103/PhysRevA.79.023831. URL <http://link.aps.org/doi/10.1103/PhysRevA.79.023831>.
- G. Sagué, A. Baade, and A. Rauschenbeutel. Blue-detuned evanescent field surface traps for neutral atoms based on mode interference in ultrathin optical fibres. *New Journal of Physics*, 10(11):113008, 2008. URL <http://stacks.iop.org/1367-2630/10/i=11/a=113008>.
- G. Salomon, L. Fouché, S. Lepoutre, A. Aspect, and T. Bourdel. All-optical cooling of ^{39}K to bose-einstein condensation. *Phys. Rev. A*, 90:033405, Sep 2014. doi: 10.1103/PhysRevA.90.033405. URL <http://link.aps.org/doi/10.1103/PhysRevA.90.033405>.
- Monika H. Schleier-Smith, Ian D. Leroux, and Vladan Vuletić. States of an ensemble of two-level atoms with reduced quantum uncertainty. *Phys. Rev. Lett.*, 104:073604, Feb 2010. doi: 10.1103/PhysRevLett.104.073604. URL <http://link.aps.org/doi/10.1103/PhysRevLett.104.073604>.
- N. Schlosser, G. Reymond, and P. Grangier. Collisional blockade in microscopic optical dipole traps. *Phys. Rev. Lett.*, 89:023005, Jun 2002. doi: 10.1103/PhysRevLett.89.023005. URL <http://link.aps.org/doi/10.1103/PhysRevLett.89.023005>.
- Jörg Schmiedmayer. Guiding and trapping a neutral atom on a wire. *Phys. Rev. A*, 52:R13–R16, Jul 1995. doi: 10.1103/PhysRevA.52.R13. URL <http://link.aps.org/doi/10.1103/PhysRevA.52.R13>.
- Philipp Schneeweiss, Fam Le Kien, and Arno Rauschenbeutel. Nanofiber-based atom trap created by combining fictitious and real magnetic fields. *New Journal of Physics*, 16(1):013014, 2014. URL <http://stacks.iop.org/1367-2630/16/i=1/a=013014>.
- Dieter Schuch. Nonlinear riccati equations as a unifying link between linear quantum mechanics and other fields of physics. *Journal of Physics: Conference Series*, 504(1):012005, 2014. URL <http://stacks.iop.org/1742-6596/504/i=1/a=012005>.
- Elias Snitzer. Cylindrical dielectric waveguide modes. *JOSA*, 51(5):491–498, 1961.
- A. Soerensen, L. M. Duan, J. I. Cirac, and P. Zoller. Many-particle entanglement with bose-einstein condensates. *Nature*, 409(6816):63–66, 01 2001.

- Daniel. A. Steck. Cesium d line data revision 2.1.4. 2010. URL <http://steck.us/alkalidata>.
- John K. Stockton, J. M. Geremia, Andrew C. Doherty, and Hideo Mabuchi. Characterizing the entanglement of symmetric many-particle spin- $\frac{1}{2}$ systems. *Phys. Rev. A*, 67:022112, Feb 2003. doi: 10.1103/PhysRevA.67.022112. URL <http://link.aps.org/doi/10.1103/PhysRevA.67.022112>.
- John K. Stockton, Ramon van Handel, and Hideo Mabuchi. Deterministic dicke-state preparation with continuous measurement and control. *Phys. Rev. A*, 70:022106, Aug 2004. doi: 10.1103/PhysRevA.70.022106. URL <http://link.aps.org/doi/10.1103/PhysRevA.70.022106>.
- Masao Takamoto, Feng-Lei Hong, Ryoichi Higashi, and Hidetoshi Katori. An optical lattice clock. *Nature*, 435(7040):321–324, 05 2005. URL <http://dx.doi.org/10.1038/nature03541>.
- Limin Tong, Rafael R. Gattass, Jonathan B. Ashcom, Sailing He, Jingyi Lou, Mengyan Shen, Iva Maxwell, and Eric Mazur. Subwavelength-diameter silica wires for low-loss optical wave guiding. *Nature*, 426(6968):816–819, 12 2003. URL <http://dx.doi.org/10.1038/nature02193>.
- Lene Vestergaard Hau, J. A. Golovchenko, and Michael M. Burns. Supersymmetry and the binding of a magnetic atom to a filamentary current. *Phys. Rev. Lett.*, 74:3138–3140, Apr 1995. doi: 10.1103/PhysRevLett.74.3138. URL <http://link.aps.org/doi/10.1103/PhysRevLett.74.3138>.
- E. Vetsch, D. Reitz, G. Sagué, R. Schmidt, S. T. Dawkins, and A. Rauschenbeutel. Optical interface created by laser-cooled atoms trapped in the evanescent field surrounding an optical nanofiber. *Phys. Rev. Lett.*, 104:203603, May 2010. doi: 10.1103/PhysRevLett.104.203603. URL <http://link.aps.org/doi/10.1103/PhysRevLett.104.203603>.
- E. Vetsch, S.T. Dawkins, R. Mitsch, D. Reitz, P. Schneeweiss, and A. Rauschenbeutel. Nanofiber-based optical trapping of cold neutral atoms. *Selected Topics in Quantum Electronics, IEEE Journal of*, 18(6):1763–1770, Nov 2012. ISSN 1077-260X. doi: 10.1109/JSTQE.2012.2196025. URL <http://dx.doi.org/10.1109/JSTQE.2012.2196025>.
- C. Wieman and T. W. Hänsch. Doppler-free laser polarization spectroscopy. *Phys. Rev. Lett.*, 36:1170–1173, May 1976. doi: 10.1103/PhysRevLett.36.1170. URL <http://link.aps.org/doi/10.1103/PhysRevLett.36.1170>.

- D. J. Wineland, J. J. Bollinger, W. M. Itano, and D. J. Heinzen. Squeezed atomic states and projection noise in spectroscopy. *Phys. Rev. A*, 50:67–88, Jul 1994. doi: 10.1103/PhysRevA.50.67. URL <http://link.aps.org/doi/10.1103/PhysRevA.50.67>.
- Steffen Wolf, Steven J. Oliver, and David S. Weiss. Suppression of recoil heating by an optical lattice. *Phys. Rev. Lett.*, 85:4249–4252, Nov 2000. doi: 10.1103/PhysRevLett.85.4249. URL <http://link.aps.org/doi/10.1103/PhysRevLett.85.4249>.
- Jun Ye, H. J. Kimble, and Hidetoshi Katori. Quantum state engineering and precision metrology using state-insensitive light traps. *Science*, 320(5884):1734–1738, 2008. doi: 10.1126/science.1148259. URL <http://www.sciencemag.org/content/320/5884/1734.abstract>.
- Hao Zhang, Robert McConnell, Senka Čuk, Qian Lin, Monika H. Schleier-Smith, Ian D. Leroux, and Vladan Vuletić. Collective state measurement of mesoscopic ensembles with single-atom resolution. *Phys. Rev. Lett.*, 109:133603, Sep 2012. doi: 10.1103/PhysRevLett.109.133603. URL <http://link.aps.org/doi/10.1103/PhysRevLett.109.133603>.
- W. H. Zurek. Decoherence and the transition from quantum to classical. *Phys. Today*, 44:36, 1991. doi: 10.1063/1.881293. URL <http://dx.doi.org/10.1063/1.881293>.
- W. H. Zurek. Decoherence and the transition from quantum to classical – revisited. *eprint arXiv:quant-ph/0306072*, June 2003.
- Wojciech Hubert Zurek. Decoherence, einselection, and the quantum origins of the classical. *Rev. Mod. Phys.*, 75:715–775, May 2003. doi: 10.1103/RevModPhys.75.715. URL <http://link.aps.org/doi/10.1103/RevModPhys.75.715>.

COLOPHON

This document was typeset using the typographical look-and-feel `classicthesis` developed by André Miede. The style was inspired by Robert Bringhurst's seminal book on typography "*The Elements of Typographic Style*".

Final Version as of April 21, 2015 (JB `thesis` version 1.2).